A CRITICAL ASSESSMENT OF SAMPLING BIASES IN GEOMETRIC MORPHOMETRIC ANALYSIS: THE CASE OF *HOMO ERECTUS*

by

Chi Zhang

Bachelor of Science, Nanjing University of Posts and Telecommunications and New York Institute of Technology, 2012

Submitted to the Graduate Faculty of

The Dietrich School of Arts and Sciences in partial fulfillment

of the requirements for the degree of

Doctor of Philosophy

University of Pittsburgh

2020

UNIVERSITY OF PITTSBURGH

DIETRICH SCHOOL OF ARTS AND SCIENCES

This dissertation was presented

by

Chi Zhang

It was defended on

February 27, 2020

and approved by

Bryan K. Hanks, PhD, Associate Professor and Department Chair, Department of Anthropology, University of Pittsburgh

William Harcourt-Smith, PhD, Assistant Professor, Department of Anthropology, City University of New York Lehman College

Margaret Judd, PhD, Associate Professor, Department Anthropology, University of Pittsburgh

Dissertation Advisor and Chair: Jeffrey H. Schwartz, PhD, Professor Emeritus, Department of Anthropology and History & Philosophy of Science, University of Pittsburgh

HOMINID SYSTEMATICS:
A CRITICAL ASSESSMENT OF SAMPLING BIASES IN GEOMETRIC MORPHOMETRIC ANALYSIS

Chi Zhang, PhD

University of Pittsburgh, 2020

This study primarily explores the potential of GMA in capturing and recognizing specific morphological features of specimens commonly allocated to *H. erectus*. For these purposes, four surface semilandmark datasets were collected for analyzing the gross morphology of the entire crania, posterior crania, temporal bones, and frontal bones.

Results show that though dense surface semilandmarks can potentially capture many morphological features that cannot be included by using discrete landmarks, some shape differences visualized by PCA, include those in lateral cranial profiles, the trajectories of the squamosal sutures and the inclinations of the nuchal planes, do not match observed morphology. Procrustes superimposition is identified as an important, yet usually ignored, factor that may contribute to some incompatibilities between visualized shape differences and observed morphology. This is because Procrustes superimposition rotates configurations to different orientations to minimize their overall differences, while observed morphology is based on aligning specimens in the Frankfurt plane.

This study also assesses three sampling issues associated with statistical analyses commonly used for testing whether *H. erectus* is too variable to be a single species based on landmark data. The first two are whether densities of semilandmarks and focusing on different cranial regions can yield inconsistent results of the same statistical analyses. The third is whether including a large sample of *H. sapiens* may affect results of PCAs.

Results suggest that semilandmarks used in this study are oversampled, because using a much smaller number of semilandmarks can yield nearly identical results. The reason is that GMA places more weight on gross shape differences than details. Furthermore, the analyses of the temporal and frontal bones show results incompatible with those of the entire and posterior crania, likely because the former analyses focus on shapes of individual bones, while the latter analyses focus on gross cranial shapes. In addition, including a large sample of *H. sapiens* with fossils cause higher-ranked PCs to emphasize variations within *H. sapiens*. In this case, it is also important to examine lower PCs to understand shape differences between fossils.

TABLE OF CONTENTS

LIST OF TABLES

LIST OF FIGURES

DEDICATION

To my mom Xueling Qiu, my dad Haifeng Zhang, and my wife Shengyu Wang, without whom none of this work would have been possible.

ACKNOWLEDGEMENT

Without the support and encouragement of many people, I could not have made it through my doctoral studies and dissertation. I am very delighted to express my gratitude to them.

First and foremost, I thank my academic advisor, Dr. Jeffrey Schwartz, for guiding and mentoring me through my Ph.D., his great effort in editing my dissertation, and his encouragement and inspiration for battling against received wisdom. I have gained invaluable knowledge from him. I feel grateful to be his student. All of these years under his mentoring has created one of the most important and unforgettable periods in my life. I also want to thank him for the great contribution to the study of human evolution and biological anthropology.

I owe much to the tremendous support and intellectual inspiration of Dr. William Harcourt-Smith, one of my dissertation committee members. Dr. Harcourt-Smith took care of me as if I were his own student. He mentored me on using morphometrics to pursue biological questions and guided me during data collection and analysis. He generously made available to me hardware and software tools for collecting data. He patiently reviewed my statistical analysis and provided me invaluable suggestions. I feel very lucky to have worked with him. Without him, I could not have finished this project. I would also like to say that Dr. William Harcourt-Smith has become a great friend.

I would like to thank Dr. Margaret Judd and Dr. Bryan Hanks, also members of my dissertation committee, for generously supporting my study, patiently reading my dissertation and offering invaluable suggestions. I am grateful to have had them on my committee. Their advice has inspired my future studies and made me a more professional scholar.

For data collection, I thank Dr. Ian Tattersall, The American Museum of Natural History (AMNH), for letting me scan his collection of fossil casts, and Dr. Eric Delson, also of the AMNH, for generously offering his 3D scans of *Homo sapiens* and fossil hominids. I thank the Swanson Center for Product Innovation, University of Pittsburgh, for granting permission to use their software to process raw 3D scans.

I want to express my gratitude to the Department of Anthropology, University of Pittsburgh, especially our wonderful staff members, Phyllis Deasy and Lynn Lantz, for their support of all graduate students, including me. Many thanks to colleagues and friends for their encouragement and inspiration. I

thank the faculty of the Department of Anthropology for educating me as an anthropologist. I also thank Dr. Seth Weinberg, Center for Craniofacial and Dental enetics, for giving me crucial experience in geometric morphometric analysis and academic publication.

I thank Mr. Tom Aspell of the Writing Center, University of Pittsburgh, for offering invaluable help in writing professional English. I enjoyed working with him. I also thank the staff of Hillman Library, University of Pittsburgh. I spent most time writing my dissertation in Hillman Library in which they provided an energetic study environment.

Finally, none of my work would have been possible without the love, encouragement and support of my parents, Xueling Qiu and Haifeng Zhang, and my wife Shengyu Wang. They always believed in, and stood with me. Words cannot express my gratitude to them.

PREFACE

The *Homo erectus* problem – is it a single species or a group of species – has been one of the major controversies in paleoanthropology. Recently, a relatively new quantitative method, geometric morphometric analysis (GMA), which quantifies biological shapes using landmark data, has been applied to the study of *Homo erectus* (Baab, 2008a, 2016; Lordkipanidze et al., 2013; Terhune, 2007). These analyses almost unanimously support the single species hypothesis by suggesting that this group of specimens is not more variable in morphology than extant species, e.g. *Homo sapiens* and chimpanzees. On the other hand, some cladistics analyses, which define groups by unique morphological features, conclude that *Homo erectus* comprises multiple species (Andrews, 1984; Schwartz, 2004, 2016; Zeitoun, 2009).

In discussing these contradictory studies, some authors believe that GMA is more appropriate because it can quantify overall morphology (i.e., phenetic) and continuous variation between specimens (Adams et al., 2004, 2013; Baab, 2016; Baab et al., 2012; Terhune et al., 2007). Cladistic analysis is believed to be subjective because it relies on visual comparison and verbal description, which focuses on discontinuous features (Adams et al., 2004, 2013; Baab, 2016; Baab et al., 2012; Terhune et al., 2007).

Nevertheless, when comparing results of these methodologically different studies, it is also imperative to examine what morphological information is actually incorporated. This is because morphology is the most direct evidence of hominid biological evolution. In fact, most GMAs of *Homo erectus* can only focus on gross shapes because they sample discrete landmarks scattered across the entire cranium (Baab, 2016; Schwartz et al., 2014; Spoor, 2013; Villmoare, 2005). In these analyses, because of missing many observed details, the large-scale cranial contours may not be fully captured.

Yet, quantifying detailed morphology has not been the major focus of GMA or previous multivariate analysesof craniometrical data (cf. Chapter 1). Most efforts have been on developing sophisticated statistical techniques to extract patterns of overall similarity within a given dataset, rather than assessing the information content of this dataset. While these statistical techniques are subjective, the landmark choice, which determinesthe morphological features included in an analysis, can also be subjective (Zelditch et al., 2012). Because of the limited morphological information of landmark datasets, previous GMAs of *Homo erectus* should not simply be viewed as a test of the results of cladistics

analyses by capturing continuous variation and overall morphology of hominid specimens. Many features incorporated in cladistics analyses are not included in GMAs (Baab, 2016; Schwartz et al., 2014; Spoor, 2013; Villmoare, 2005).

An associated problem is the reliance on using principal components (PCs) to understand "the most variable aspects" of morphological differences between specimens (Baab, 2016, p. 8; Harvati et al., 2010; Terhune et al., 2007). PCs are mathematical constructions and statistically meaningful because each explains a proportion of shape differences (Zelditch et al., 2012). However, visualized differences of a PC or a combination of two PCs may not fully reveal actual morphological differences between individual specimens, although they may account for a substantial amount of total shape difference. In some cases, even large-scale differences of the entire cranium cannot be linked directly to observed conditions (cf. Chapter 9). Paleoanthropologists usually do not pay sufficient attention to individual specimens but verify the morphological capability of their GMAs by citing generalized morphological comparisons of designated groups (e.g., Asian versus African *Homo erectus*). Yet, to have a basic understanding of *Homo erectus*, the morphology of individual specimens should be examined since each may have the potential to represent a new species if it exhibits some unique features (Schwartz 2004, 2016; Schwartz & Tattersall, 2002, 2003; Zeitoun, 2009).

In order to make GMA a better morphological tool for testing hypotheses of hominid species, I have developed two main, interconnected objectives for this study. The first is to explore the potential of GMA for capturing more subtle morphological features by sampling dense semilandmarks across the surface of the entire cranium. The second goal is to assess whether visualized differences between PCs can be treated as representing real morphological differences. In particular, this study examines whether observed morphological details of individual specimens can be extracted from PCs.

There are also three relevant sampling issues that may affect results of statistical analyses regarding the matter of *Homo erectus* being too variable to be a single species. These statistical analyses typically focus on three hypotheses (e.g., Baab, 2008a, 2016; Terhune, 2007; Lordkipanidze et al., 2013):

1. *H. erectus sensu lato* (which will simply be referred to as *H. erectus*) is significantly more variable than *H. sapiens*.
2. The overall variability in Asian *H. erectus* and in African *H. ergaster* exceeds that of *H. sapiens*.
3. Differences between Asian *H. erectus sensu stricto* (which will be referred to as Asian *H. erectus*) and African *Homo ergaster* exceeds those between geographical subsets of *H. sapiens*.

The first issue concerns the density of semilandmarks. Sampling too few semilandmarks can lead to loss of morphological information. Sampling too many landmarks can be time consuming and may

create redundancy in statistical analyses. Relevant here is the method of Landmark Sampling Evaluation Curve (LASEC), which is designed to evaluate how many landmarks or semilandmarks are able to capture sufficient "shape information" (Watanabe, 2018, p. 12). Because the study here samples dense semilandmarks in order to capture more morphological differences, it would be interesting to use LASEC to assess if the datasets used here are too dense to capture a certain amount of "morphological information".

The second sampling issue concerns collecting landmarks and semilandmarks from different cranial regions. Most studies of *Homo erectus* sample landmarks from the entire cranium (Baab, 2008a, 2016; Lordkipanidze et al., 2013). They almost unanimously conclude that *Homo erectus* is less variable in overall cranial shape than *Homo sapiens* or various non-human primates . Therefore, it is important to test whether quantifying shapes of the temporal and frontal bones can alter the results of statistical tests of *Homo erectus* variability.

This study also assesses the influence on PCA of including a very large sample of *Homo sapiens*. In previous studies, researchers usually used samples of extant species, such as *Homo sapiens* and chimpanzees. However, in these studies, higher-ordered PCs may focus on differences that separate specimens of extant taxa from each other and from fossil hominids, as well as differences between specimens of extant taxa when sample sizes are large. Therefore, this study also explores whether patterns of shape difference revealed by PCs of fossil hominids can be demonstrated by the PCA that includes both *Homo sapiens* and fossil hominids.

Lastly, given the increasing weight of "technology" in studies not only in biological anthropology, but anthropology in general, as well as in non-anthropological disciplines, it is my hope that the results of, and questions arising from this study will cause a rethinking of how data is captured, compared, and analyzed.

1.0 HISTORY OF MORPHOMETRIC ANALYSES IN PALEOANTHROPOLOGY

1.1 INTRODUCTION

Morphometrics refers to a group of statistical shape analytical methods using quantitative data (Reyment, 2010). In this chapter, this term is used interchangeably with statistical or quantitative methods. Recently, a particular category of morphometric methods—geometric morphometric analysis (GMA)—has gained popularity in paleoanthropology for its use in quantifying the overall shape of hominid fossils (here, the term "hominid" refers to humans and their fossil relatives).

This chapter presents a historical review to understand how and why people use GMA to human fossils and even to infer their phylogenetic relationships. GMA has been hailed as a "morphometric revolution" because it uses landmark data to quantify and visualize actual shape variation (Rohlf & Marcus, 1993). GMA is also called "modern morphometrics" as it is distinct from traditional or multivariate morphometrics, which can only indirectly reflect shape differences because the raw data are simply a list of unilinear measurements or angles and has been criticized for not differentiating size from shape (Adams et al., 2004; Bookstein, 1997, 1998; Rohlf & Marcus, 1993).

Though methodologically distinct, GMA and multivariate morphometrics are used consistently by paleoanthropologists to group specimens. Both measure degree of overall similarity, which constitutes the basis for classifying fossil specimens and inferring phylogenetic relatedness. For paleoanthropologists, GMA allows them to use a category of more appropriate shape data for the same kind of analysis (Adams et al., 2004, 2013; Baab et al., 2012). Consequently, to understand from a historical perspective how and why paleoanthropologists perform GMA, it is necessary to start with the application of multivariate methods.

This chapter focuses on two factors underlying the use of GMA in paleoanthropology. The first is the theory of continuous evolution, whereby differences among hominids taken as continuous variation. The second is the desire to quantify overall similarity, or "total morphological pattern". While researchers have developed and applied a variety of statistically rigorous methods to extract patterns and degrees of overall similarity from a list of measurements or landmarks, less attention has been paid to whether their data can capture sufficient significant and potentially systematically relevant morphological detail. In fact,

the majority of multivariate analyses and GMAs deal only with gross shape differences (Kaifu et al., 2008; Schwartz et al., 2014; Spoor, 2013; Spoor et al., 2008; Villmoare, 2005). Furthermore, even though GMA provides powerful visualization tools, interpreting localized morphological difference has been claimed to be difficult or even misleading (Baab et al., 2012; Klingenberg, 2013; Richtsmeier et al., 2002).

Some researchers also view quantitative analysis based on morphometrics, particularly GMA, as more appropriate than cladistic analysis because of its ability to reflect the continuous nature of morphological difference, especially among hominids. The is because cladistic analysis has usually been viewed as the opposite of morphometrics because it generates a list of discontinuous character states as the basis for inferring clades as distinct entities (Baab, 2016; Harvati et al., 2010; Wood, 1991a, 1991b). Nevertheless, the foundation of cladistic analysis is to recognize and compare specific morphological features, which could be highly localized and detailed (Schwartz, 2004; Schwartz and Tattersall, 2002, 2003; Tattersall, 2000; Zeitoun, 2009). Based on these comparisons, unique morphological conditions are then summarized as the basis for reconstructing taxa and their phylogenetic relationships (Schwartz and Tattersall, 2002, 2003; Tattersall, 2000; Zeitoun, 2009). GMA has yet to become a powerful morphological tool in identifying and comparing specific morphological features because paleoanthropologists have primarily using it to compute gross shape differences (Klingenberg, 2013; Richtsmeier et al., 2002; Schwartz et al., 2014; Spoor, 2013; Zelditch et al., 2012). Therefore, this chapter suggests the significance of exploring the potential of GMA in capturing specific morphological features, especially observed detail.

1.2 SIMPSON, THE THEORY OF CONTINUOUS EVOLUTION, AND MORPHOMETRICS

G. G. Simpson's (1943) assertion that classification is essentially a statistical problem had a profound influence on paleoanthropology. Simpson realized that members of species vary, as "no two organisms are exactly alike" (Simpson, 1943, p. 151). Because no one could study every individual of every species, the process of defining a "morphological species" (a population) must come from inferring the "characters and limits" from a sample of individuals, i.e., determining how similar members of a group are in degree so they can be allocated to the same taxon or different taxa at different ranks. Simpson's ultimate goal was to use "morphological species" to infer "genetic species", which was, for him, the real natural species, which he defined as a genetic and reproductive entity. Because all taxa are populations, classification is, in a broad sense, a statistical process.

However, Simpson (1943) was challenged by colleagues who argued that a taxon can be defined qualitatively, using the "presence" or "absence" of morphological characters. Thus, differences between species or higher taxa are qualitative, while differences within a species (intraspecific variation) are quantitative and continuous. Obviously, if a species can be defined qualitatively, there is no need to measure the degree of similarity between individuals or groups for statistical inference because morphological differences are already definitive.

Methodologically, Simpson (1943) argued that the majority of qualitative morphological differences enumerated by fellow taxonomists, such as the prominence of a tooth's crests, would be seen as varying continuously along a scale if properly quantified. Nevertheless, this procedure is insufficient for rejecting the distinctiveness of qualitative versus quantitative characters. It simply narrows the commonality of qualitative characters that distinguish groups.

In rejecting the reality of qualitative differences, Simpson (1943) went on to cite the theory of Darwinian continuous evolution, which depicts evolutionary change as an ongoing process of accumulation of small, intraspecific variations that ultimately lead to the divergence of characters. Simpson (1943, p.158) went on to use the phrase "quantitative increase of differences by increments" to summarize the continuous evolutionary process. Therefore, differences in corresponding characters between individuals, subspecies, species, genera, or higher taxa are merely differences in degree that can be measured on "a continuous scale" (Simpson, 1943, p. 158). According to this view of evolution, the qualitative differences that taxonomists recognize are merely large-scale quantitative differences, which are ultimately produced by the extinction of transitional forms.

By transforming all morphological differences to matters of degree, Simpson (1943) argued that classification is indeed a type of statistical inference based on quantifying the degree of similarity. For proper inference, Simpson suggested using "allied forms" to model the degree of variability at different taxonomic levels, though he questioned the existence of a universal degree of variability that defines a particular level. Although Simpson did not offer a practical example, his suggestion predates by almost 40 years the widely accepted approach to classification that has used the degree of variability of extant, "closely related" taxa to test the validity of hominid species.

1.3 EARLY APPLICATIONS OF MULTIVARIATE MORPHOMETRICS IN PALEOANTHROPOLOGY

1.3.1 Statistics as the uniform scale

Solly Zuckerman (1950, 1951) was one of the first paleoanthropologists to promote the use of statistical methods in classifying fossil primates and hominids. By adopting Simpson's (1943) view that classification is essentially a statistical problem, Zuckerman (1950, 1951) argued that paleoanthropological classifications should begin by summarizing the degree of variability within known species, against which the degree of variability of fossil specimens could then be compared.

Zuckerman's (1933, 1940) insistence on using statistical methods was also prompted by a particular paleoanthropological issue at that time: the redundancy of taxonomic names. Before the 1950s, discoverers of hominid fossils created taxonomic names usually without providing rigorous morphological reasoning. These included *Homo modjokertensis*, *Homo rhodesiensis*, *Pithecanthropus robustus*, and *Javanthropus soloensis*. For Zuckerman (1933, 1940, 1950, 1951), this chaotic situation was due to lack of a uniform scale for quantifying degree of similarity, which statistics did provide.

1.3.2 The development of multivariate morphometrics for classification

As a user of statistics, Zuckerman (1950, 1951) also noted the value of the emerging field multivariate statistics, which provided a single variable—"distance"—to summarize degree of overall similarity within a list of measurements, rather than evaluating each measurement individually. Thus, a multivariate approach could provide a more holistic view of how similar specimens are. Later, multivariate statistics was referred to as multivariate morphometrics (Blackith & Reyment, 1971).

Regarding the predecessor of multivariate morphometrics, Karl Pearson (1926) had already pointed out, "We need a single numerical measure of the whole system of differences, something which will express by a single coefficient the measure of resemblance (or divergence) of the two races or groups" (p. 105). However, Pearson's "coefficient of racial likeness" has been criticized as measuring only the probability of misclassification rather than the actual degree of overall similarity (Blackith & Reyment, 1971; Fisher, 1936; Mahalanobis, 1936, 1949).

A historical development in multivariate statistics is the "generalized distance of statistics" or the "Mahalanobis distance, D^2", developed by Mahalanobis (1936, 1949), which is a continuous variable that quantifies overall similarity. D^2 is still used to facilitate discrimination between known groups by

eliminating correlations between metrical variables in order to reduce redundancy, and by transforming the variance of each variable to the unit quantity in order to assign each variable equal weight in distance calculation (Blackith & Reyment, 1971; Mahalanobis, 1936, 1949; Rao, 1952).

Another fundamental development in multivariate statistics was R. A. Fisher's (1936, 1938) "linear discriminant analysis", which looks for a linear combination (discriminant function) of the selected set of variables to maximally separate individuals into two groups. A linear combination is in the form:

$$y = \beta_1 x_1 + \beta_2 x_2 + \beta_3 x_3 + ... + \beta_n x_n$$

where "x" denotes each variable and "y" is the newly generated variable, i.e., the discriminant score. "β" is the correlation coefficient of each variable that indicates each variable's contribution to the discriminant score. These correlation coefficients are computed such that the discriminant scores of individuals from the two groups are maximally separated.

D^2 and Fisher's linear discriminant analysis are intercorrelated, such that after transforming the covariance matrix for constructing a discriminate function, the difference between the means of two groups is equal to the calculated D^2 (Blackith & Reyment, 1971; N. A. Campbell & Atchley, 1981; Fisher, 1938; Mahalanobis, 1949). Combining the principles of these two analyses, Rao (1948, 1952) extended Fisher's linear discriminant analyses, which considers only two groups, to multiple discriminant analysis, which can discriminate between multiple groups (Blackith & Reyment, 1971; N. A. Campbell & Atchley, 1981). This is also called canonical variate analysis (CVA).

As a typical multivariate analysis, CVA looks for the orthogonal axes in transformed multivariate space (Blackith & Reyment, 1971; N. A. Campbell & Atchley, 1981). Each axis is a new variable called a canonical variate, which is essentially a linear combination of the original variables and a discriminant function. These canonical variates are ordered by their power of group discrimination. Thus, by the first canonical variate, the variability of group means is maximized, and the variability within each group is minimized (Blackith & Reyment, 1971; N. A. Campbell & Atchley, 1981). Researchers usually employ the first two canonical variates to visualize the separation of groups. Moreover, transformation of the covariance matrix that eliminates the effect of correlations and unequal variance, as in Fisher's linear discrimination, ensures that differences between group means are simply equal to the D^2 between them (N. A. Campbell & Atchley, 1981; Rao, 1948, 1952). To determine the group identity of a specimen, one usually chooses the first two canonical variates to construct a two-dimensional space for visualizing the distribution of groups and how close that particular specimen is to different group means.

Noticing these developments of multivariate methods that allow analyzing an entire structure, or even individual, as an entity, Bronowski and Long (1952) applied a linear discriminant analysis to classify the Taung and Kromdraai juvenile mandibles using four measurements of the deciduous teeth.

They found that the discriminant scores of the fossils were closer to the scores of extant humans than to chimpanzees, suggesting a closer relationship between the former and humans. Inspired by Bronowski and Long (1952), Ashton et al. (1957) performed a CVA to assess the "affinity" between the teeth of fossil hominids and fossil hominoids as well as extant hominoids and humans. By reading the "distance" chart constructed by the first two canonical variates, they found that the teeth of the Zhoukoudian hominid remains were closer to Australian Aborigines, while those of *Proconsul* were closer to chimpanzees.

1.4 THE SIMPSONIAN CLASSIFICATION AND MULTIVARIATE MORPHOMETRICS IN PALEOANTHROPOLOGY

Paleoanthropologists did not seriously discuss the role of multivariate morphometrics in paleoanthropological classification until the 1960s. In 1962, an international symposium was held at Burg Wartenstein (the European conference center of the Wenner-Gren Foundation) for the express purpose of discussing and regulating the classification of human fossils (Washburn, 1963). There, Simpson (1963) introduced the principle of "modern taxonomy", which, as explained in his earlier paper in 1943, states that classification is a statistical problem.

Similar to Zuckerman (1950, 1951), Simpson (1963, p. 4) suggested that the "chaos of anthropological nomenclature" was a result of not recognizing taxa as varying populations and of inconsistently evaluating the degree of similarity. He claimed that if one used proper statistical analysis, the degree of differences that separate some hominid genera (such as *Pithecanthropus* and *Atlanthropus*) would not even merit species-level (Simpson, 1963). However, he still cautioned that "there is no absolute criterion for the degree of difference to be called generic, and it is particularly here that experience and common sense are required" (Simpson, 1963, p. 8). Simpson (1963) also reminded paleoanthropologists that their observed discontinuities might be artificial, created by the elimination or a lack of discovery of intermediate populations within a single lineage. In the same symposium, Mayr (1963) concurred with Simpson (1963) that continuity should be the theme of human evolution, though he did also think there might be some divergence between gracile and robust australopiths.

Bernard Campbell (1963) embraced Simpson (1963) and Mayr's (1963) notion that boundaries between hominid taxa were unreal and only degree of similarity is real. He then went on to argue that if properly controlling for factors such as differential rates of evolution, multivariate statistical methods, which measure the degree of overall similarity in a whole set of measurements, can reflect the actual amount of overall morphological change without the need to subjectively choose measurements. Like his

predecessors, such as Ashton, Zuckerman, and Bronowski, Campbell (1963) realized that D^2 was an appropriate way to represent degree of overall similarity between population means. He further embraced Ashton et al.'s (1957) approach of using CVA to visualize distances between populations without losing a significant amount of overall variation.

Howells (1969, 1972, 1973) believed that multivariate analysis a properly expressed "population thinking" because only multivariate analysis allowed quantifying each individual as an integrated entity. On the other hand, the univariate method was not an expression of such theory because a single measurement is not an individual. However, Howells (1969, 1972, 1973) worked on only living human populations, and also performed another kind of multivariate analysis, principal component analysis (PCA), which aims to analyze overall variation among individuals rather than discriminating between groups.

Since the 1960s, because of rapidly developing computer techniques, discriminant analyses and D^2 quickly have become the most popular multivariate methods used by paleoanthropologists, even though they were designed only to discriminate between known groups and to classify individuals accordingly. This is probably because they had been well developed and widely used by statisticians. This popularity also reflects a lack of examination of the commonly accepted classificatory system in paleoanthropology. For example, to quantify degree of similarity in "total morphological patterns", Bilsborough (1971; 1973, p. 387) viewed D^2 as a proper measure of the degree of overall morphological change within the human lineage, which could serve as a basis for classifying fossil humans. To further serve this purpose, he then performed CVA to investigate patterns of overall variability in presumed hominid groups. In another study, van Vark (1984) used D^2 values between known hominid groups to estimate the closeness of their affinities. Rightmire (1970a, 1970b) also used D^2 along with CVA to assess the similarity of several extant African *Homo sapiens* populations as a basis for classifying recent African human skeletal remains.

1.5 THE PROBLEM OF INTERPRETATION: THE "PATTERNS" OF VARIABILITY

1.5.1 Criticism of discriminant analysis and D^2

In the 1970s, some statisticians began to realize that D^2 may not be an objective representation of the degree of overall variability, though it is calculated from a covariance matrix constructed from a set of linear measurements (Corruccini, 1975; Kowalski, 1972) These criticisms were mainly from

methodological perspectives, such as the assumption of normality and equal covariance matrices for all assumed groups (Corruccini, 1975; Kowalski, 1972). After recognizing these methodological deficiencies, Corruccini (1975) rejected Howells' (1969, 1972, 1973) notion that multivariate analysis expresses population thinking. Among these critiques, Kowalski (1972) in particular pointed out that the results of multivariate analysis are subject to the choice of measurements and that it is difficult to differentiate shape differences from size differences. Furthermore, noticing the difficulty in interpreting the results of discriminant analyses and D^2, Kowalski (1972) also suggested that univariate analysis may still be useful for analyzing shape variation due to its clarity.

On the other hand, paleoanthropologists during that period did not pay too much attention to these limitations of D^2. Some of them seem to have used D^2 and discriminant analyses simply because it provided a continuous variable with which to quantify overall similarity, thus meeting the theoretical requirement of continuous evolution (e.g., Bilsborough, 1971, 1973; Rightmire, 1970a, 1970b; van Vark, 1984). These applications usually do not include a careful assessment of which morphological differences the raw measurements can capture or how to interpret the results in order to understand which features contribute to the resultant D^2.

1.5.2 Discriminant topology in paleoanthropology

Although evaluating the results of multivariate analyses from a morphological perspective was usually missing from anthropological applications, some statisticians became aware of the problem of interpretation. Blackith and Reyment (1971; Blackith, 1957) noticed that in a CVA, a canonical variate or discriminant function, as an axis in a multivariate space, not only explains a fraction of the overall variation in group means measured by D^2 but also specifies a direction of shape differences. For instance, in their hypothetical case, the first canonical variate specified a direction of shape difference from "thinness" to "fatness" between two ends; the second canonical variate specified a direction from "shortness" to "tallness". Interpretation of what a canonical variate describes comes from reading the "loading" of each variable, which is the correlation coefficient between a variable and a canonical variate. In other words, a "loading" specifies the contribution that a variable makes to a canonical variate. This process of interpretation is called "discriminant topology" (Blackith, 1957; Blackith and Reyment, 1971, p.272). Accordingly, Blackith and Reyment (1971) assigned an explanatory property to multivariate analyses and established the field of multivariate morphometrics.

Some paleoanthropologists also began to realize the explanatory power of multivariate analyses. Oxnard (1968a, 1968b, 1972, 1983) found he could interpret each canonical variate to sort out aspects of differences associated with functional adaptations of primate taxa. For example, he discovered that in one

of his earlier CVAs based on measurements of shoulder girdles, the first canonical variate that separated apes from the Old World monkeys suggested differences associated with the endurance of tensile force during locomotion (Oxnard, 1968a, 1968b, 1972). Another CVA of postcranial skeletons plotted arboreal mammals close to primates, reflecting similar functional adaptations in locomotion (Oxnard, 1968a).

Echoing Oxnard (1972, 1983), Howells (1972, 1973, 1984) also highlighted the importance of interpretation. Instead of CVA, he performed PCA, which analyzes overall variation among individuals without an *a priori* group identity or transformation of the covariance matrix. PCA looks for orthogonal axes, which are statistically independent principal components (PCs), in a multivariate dataset, in the original multivariate Euclidean space (N. Campbell & Atchley, 1981; Howells, 1973; Zelditch et al., 2012). These PCs are ordered according to the proportion of total variance among individuals they explain. Each PC is essentially a linear combination of metric variables, such that it can be interpreted by looking at the "loading" of each variable (N. Campbell & Atchley, 1981; Howells, 1973; Zelditch et al., 2012). To visualize clustering of individuals, researchers usually chose the two PCs from the first few PCs that explain a large proportion of the total variance (N. Campbell & Atchley, 1981; Howells, 1973; Zelditch et al., 2012). This has been seen as advantageous for reducing the complexity of the original dataset (N. Campbell & Atchley, 1981; Zelditch et al., 2012). Because PCA does not transform the covariance matrix, the overall similarity between individuals is simply the Euclidean distance, which is the root of the sum of squared differences between every pair of variables (N. Campbell & Atchley, 1981; Howells, 1973; Zelditch et al., 2012).

Because of these properties, Howells (1972, 1973) used PCA to generate "factors" of morphological differences that explained major aspects of variation in 70 craniofacial measurements taken from samples of 17 living human populations. In the initial analysis, he chose the first 18 PCs as morphological factors and interpreted them by reading the loadings. These factors covered aspects of variation associated with the degree of forward extension of the facial skeleton, vault breadth, general upper facial breadth, and general midfacial breadth. He also performed CVA and generated a list of discriminant functions to find aspects of variation that facilitated population identification. Howells (1972, 1973) suggested the next step would be explaining these factors from a biological perspective. Most likely because PCA relies on fewer assumptions, such as group identity, it later became the most popular analysis for data visualization and interpretation in paleoanthropology, even in GMA.

1.6 CONTROVERSIES OF CLADISTIC ANALYSIS

While multivariate analysis was gradually becoming popular in paleoanthropology in the 1980s, cladistics (i.e., cladistic analysis) was applied to hominid systematics (Andrews, 1984; Delson et al., 1977; Stringer, 1984; Wood, 1984). Cladistic analysis stands in sharp contrast to multivariate analyses, since its principle explicitly states that overall similarity could be misleading because, for instance, some similarity between two specimens could be inherited from a distant ancestor and therefore was not indicative of a close relationship between them. Instead, to define a group, cladistic analysis looks for the group's unique, or apomorphous features (shared derived features). In this way, a species is also defined in a clear-cut manner, while the degree of similarity plays no role. As the "inventor", Willi Hennig (1966, p. 92) stressed, "When we distinguish different conditions of a character as plesiomorphous and relatively apomorphous, we do not take the magnitude between these conditions into account in any way". Following these principles, some paleoanthropologists tested the morphological definition of *Homo erectus* (*H. erectus*) and concluded that its hypodigm should be split into two species: an Asian group, which is the real *H. erectus* (*sensu stricto*) that can be defined by a short list of unique features, and an African group, *Homo ergaster* (Andrews, 1984; Stringer, 1984; Wood, 1984, 1991a).

Cladistic analysis clashes with the conventional view of human evolution as a continuous process, in which boundaries between the majority of hominid taxa, which are variable populations, are considered arbitrary (Harrison, 1993; Pope, 1992; Rightmire, 1993; Trinkaus, 1990; Turner & Chamberlain, 1989). Some paleoanthropologists who held a similar view continued to embrace the notion that, although a limited amount of speciation may have occurred, there were insufficient geographical barriers and time to prevent gene flow and create stable gaps between hominid groups (Harrison, 1993; Trinkaus, 1990).

Similar to Simpson (1943, 1963), many scholars believed that by appropriately evaluating variation, especially through quantification, one should expect that a majority of visually observed discontinuities would be seen as arbitrary. For example, a series of analyses showed how variable features supposedly unique to *H. erectus sensu stricto* could be, such that the truly unique features of this hypodigm were rare (Bräuer, 1990; Bräuer & Mbua, 1992; Kennedy, 1991; Pimentcl & Riggins, 1987). There are also extreme views in which no hominid taxa are real because they are too variable and in any case, there were no boundaries between them at any time or in any geographical region (Thorne & Wolpoff, 1981; Wolpoff et al., 1994). All of these efforts were meant to point out the inappropriateness of using cladistics to recognize hominid species as distinct entities (Bräuer, 1990; Bräuer & Mbua, 1992; Kennedy, 1991; Turner & Chamberlain, 1989).

To cope with the "seamless continuity" in hominid evolution, "remarkable variability" in hominid taxa, and to understand total morphological patterns rather than a few features, paleoanthropologists came

up with strategies to recognize and classify hominid species. For example, Wood (1984, 1991b) and Rightmire (1993) recommended using a combination of features, ancestral and derived, to assess total morphological pattern. In this way, a hominid species could be identified as possessing a group of features, even though some were also present in other taxa.

Reacting to cladistics, some paleoanthropologists continued to conduct multivariate analyses, such as PCA and CVA, to visualize the clustering of individuals, as this category of methods was designed to analyze the degree of overall similarity in a set of measurements (e.g., Antón, 2002, 2003; Bilsborough & Wood, 1988; Bräuer, 1994). In particular, PCA gradually became more popular, probably because it could analyze overall similarity between individuals without group assumption. For example, Bräuer (1994) and Antón (2002) were in agreement that Asian and African *H. erectus* should belong to the same species because of the overlap between two clusters demonstrated by their PCAs. Antón (2002) also interpreted patterns of overall variability by reading loadings of metric variables. Most likely because of realizing that her PCAs captured only general shape rather than morphological detail, Antón (2002) supplemented the PCAs with a more detailed visual comparative analysis.

1.7 VARIABILITY OF SPECIES

1.7.1 Using the degree of variability of extant taxa to model extinct taxa

Although PCA is a powerful tool for visualizing patterns and degrees of overall similarity between individual specimens, it cannot directly assess whether the hypothesis "species" is valid. Therefore, some scholars embraced Simpson's (1943, 1963) approach which uses variability of extant taxa as the yard stick against which to evaluate if the variability of the fossil group is acceptable (Bilsborough, 1984; Bilsborough & Wood, 1988; Godfrey & Marks, 1991; Harrison, 1993). For example, like Simpson (1943, 1963), Godfrey and Marks (1991) stated that a real species or "biospecies", which is a genetic and reproductive entity, can be identified only via molecular analysis. Thus, the determination of fossil biospecies, which can be inferred only from morphology, is always less reliable than the determination of extant biospecies, the genetic structure of which could be studied. For these authors, this unfortunate fact highlighted the importance of using variability of extant biospecies as a proper criterion for validating the identification of fossil species.

The theoretical background for using extant species to model extinct species appears to be sound, but selecting proper extant species is complicated. The most commonly used extant taxa are *H. sapiens*,

Gorilla and the two species of *Pan*, because molecular analysis are believed to show that *H. sapiens* and African great apes are the closest living relatives, and because it is expected that closely related taxa have similar patterns of variability. However, people have noticed that these closely related taxa may differ considerably in their expression of variability. For example, *Gorilla* is usually more while chimpanzees and humans less variable and sexually dimorphic (Kramer et al., 1995; Lockwood et al., 1996; Wood, 1991b). Thus, *Gorilla* samples are usually used to provide a conservative hypothesis of hominid species diversity. Some people also suggest that extant species do not capture the temporal dimension of variation, leading to underestimating the number of hominid species (Kimbel & White, 1988; Lieberman et al., 1988; Wood, 1991b). Because of this, Wood (1991b, 1993) even suggested using other extinct hominid species as modeling taxa, though the validity of these hominid taxa is also problematic.

1.7.2 Univariate and multivariate methods quantifying variability

Earlier approaches to testing the variability of fossil taxa were univariate (e.g., Kramer, 1993; Kramer et al., 1995; Lockwood et al., 1996; Wood, 1991b, 1993; Wood et al., 1991). The most popular method was the "coefficient of variance" (CV), which was used to quantify the variability of each measurement. The calculation of CVs takes the sample mean, sample size, and standard deviation into consideration. Researchers also use patterns of CVs to visualize patterns of variability. This kind of analysis was first used in the early 1980s to test the validity of Miocene hominoid species by comparing their CVs with the CVs of extant great ape species (Kay, 1982; Martin, 1983).

For scholars who questioned the usefulness of cladistic analysis, however, univariate analysis remained insufficient for testing the validity of species because they believed that species recognition was based on evaluating the total morphological pattern (Godfrey and Marks, 1991; Harrison, 1993; Wood, 1993). The solution was to use distances achieved with multivariate analyses (Godfrey & Marks, 1991; Harrison, 1993; Wood, 1993). For example, Kramer (1993) and Grine et al. (1996) used mean pairwise Euclidean distances as a measure of overall variability in an early *Homo* sample in comparison with an extant *H. sapiens* sample. Villmoare (2005) calculated the mean pairwise distances between all possible pairs of specimens from the Asian and African subsets of *H. erectus* to investigate whether differences between these two subsets were larger than between African and Asian *H. sapiens* samples.

On the other hand, researchers have paid less attention to patterns of variability, though some suggested that a species may have a distinct pattern of variability (Ackermann, 2002; Kramer et al., 1995; Wood, 1993; Wood et al., 1991). The definition of " pattern of variability" is obscure, as many statistical analyses are not directly associated with a detailed interpretation of which features vary and how they vary. For univariate analysis, the most common way to diagrammatically demonstrate patterns of

variability is to draw a CV profile by connecting dots that represent all CV values (e.g., Kramer, 1993; Kramer et al., 1995; Wood, 1993; Wood et al., 1991). For example, Kramer et al. (1995) found that the CV profile of *Homo habilis* was different from extant hominoids based on a visual comparison and calculated rank-order correlation. The results led them to reject the hypothesis that *H. habilis* was a single species, though its degree of overall variability was not exceptionally large.

For multivariate analyses, Ackermann (2002) assessed similarity between the covariance matrixes of different hominoid species and *H. sapiens*, which are frequently used to model extinct hominid species. Her study suggests that these species do have different patterns of variability, and that their similarity is consistent with molecular phylogenetic analyses. However, she focused only on sophisticated mathematical characteristics, such as correlations between matrices, which are difficult to interpret morphologically. The most straightforward way to understand patterns of overall variability still seems to be reading major PCs in a PCA (e.g., Antón, 2002).

1.8 GEOMETRIC MORPHOMETRICS IN PALEOANTHROPOLOGY

1.8.1 Methodological overview

Since the late 1990s, GMA has been increasingly used to classify hominid fossils. GMA is believed to be a revolutionary shape analytical tool compared to traditional morphometrics because it directly quantifies overall shapes by using landmark data (Baab et al., 2012; Zelditch et al., 2012). In particular, shape information is isolated by using Procrustes superimposition to remove irrelevant information regarding size, location and orientation (Baab et al., 2012; Zelditch et al., 2012). Subsequently, specimens are collapsed as points into a curved hyperdimensional shape space. For example, the simplest shape space is a spherical space of triangles. In this space, each random point represents a possible triangle. Overall shape differences are calculated as Procrustes distances between any pair of points in this shape space.

An advantage of GMA over multivariate analysis is that it can visualize shape differences, which helps researchers better interpret the results of statistical analyses (Baab et al., 2012; Harvati et al., 2010; Terhune et al., 2007; Zelditch et al., 2012). A common method of visualization is to simply add vectors to each landmark to show the direction and magnitude of mapping landmarks of one shape relative to another shape. Another interesting way to visualize shape differences by mapping correspondent

landmarks is to use the thin-plate spline method, which interpolates a function to smoothly deform a reference shape into a targeted shape (Bookstein, 1997; Zelditch et al., 2012).

Landmark data of GMA can also be submitted to conventional multivariate techniques (such as the most popular, PCA) to analyze overall shape differences (Zelditch et al., 2012) because one can project points in a shape space into a Euclidean space, which is analogous to converting a globe into a flat map (Klingenberg, 2013). The spatial relationship between points is still preserved, and the Euclidean distances in the projected space are essentially equal to the original Procrustes distances. After this procedure, shape data can be submitted to multivariate analyses. Furthermore, shape differences described by a PC can be visualized, while in conventional multivariate analyses based on linear measurements, one can interpret a PC only indirectly by reading the loadings of variables.

1.8.2 GMA in paleoanthropology

Some paleoanthropologists quickly realized that landmark data were more appropriate than linear measurements for directly quantifying an overall shape as both an integrated entity and a continuous variable, while the results of GMA could be visualized as shape differences (Baab, 2016; Baab et al., 2012; Harvati et al., 2010; Lockwood et al., 2002; Terhune et al., 2007). The advantages of GMA also provoked discussion in the late 1980s about quantitative methods being more suitable morphological tools than visual analysis, because quantitative methods are supposed to be more objective, repeatable, and accurate in reflecting the supposed continuous nature of morphological difference (Baab, 2016; Cranston & Humphries, 1988; Gómez-Robles et al., 2011; González-José et al., 2008; Humphries, 2002; MacLeod & Forey, 2002).

Most likely because landmark data work well with conventional multivariate analyses, the ways in which paleoanthropologists use GMA to classify human fossils and infer their relationships are the same as when earlier multivariate analyses were used. Researchers usually perform PCA to demonstrate clustering of specimens according to degree of overall similarity that is based on a few higher-ranked PCs that can explain a substantial amount of the total variance (e.g. Baab, 2008b, 2016; Harvati et al., 2010; Lordkipanidze et al., 2013; Terhune et al., 2007). They then make inferences of classification based on distributions of points in these PCs. For example, Delson et al.'s (2001) GMA showed that in the PC diagram, the Sambungmacan (SM) 3 skull was intermediate between other Asian *H. erectus* and Middle Pleistocene "archaic *H. sapiens*". This result allowed them to propose that SM 3 represented a phylogenetically intermediate population.

GMA greatly facilitates interpretation of each PC by allowing researchers to visualize shape differences as a shape changes from one end to another end of this PC (Klingenberg, 2013; Zelditch et al.,

2012). For example, Terhune et al. (2007) used PCA to analyze the overall variation in the temporal bones of *H. erectus*. They then interpreted each PC by reading the dislocation of landmarks along a PC to understand major components of shape differences within *H. erectus*. These researchers also tentatively compared shape differences revealed by major PCs to observed morphological differences (e.g., Baab, 2016; Terhune et al., 2007)

Some paleoanthropologists quantify degree of variability using landmark data to test the validity of hominid species. The test statistic that quantifies overall variability is the Procrustes distance. For example, Baab (2008b) used the sum of pairwise Procrustes distances to measure degree of overall variability in each sample of *H. erectus* and extant taxa to test whether the fossil sample was too variable to be considered a single species.

1.8.3 The use of semilandmarks in paleoanthropological classification

Most GMAs use a small number of discrete anatomical landmarks. Thus, features in landmark-free regions are frequently overlooked (Freidline, Gunz, Harvati, et al., 2012; Freidline, Gunz, Janković, et al., 2012; Harvati et al., 2010; Villmoare, 2005). One solution is to use semilandmarks, which are randomly generated points between discrete landmarks (Freidline, Gunz, Harvati, et al., 2012; Freidline, Gunz, Janković, et al., 2012; Gunz & Mitteroecker, 2013). There are two kinds of semilandmarks: 1) curved semilandmarks, which are points evenly spaced along the curvature between two landmarks, and 2) surface semilandmarks, which are points placed evenly on the surface defined by some landmarks. During the process of Procrustes superimposition, semilandmarks need to slide along the tangential line or surface to minimize variation generated by the arbitrary positioning of these points (Gunz & Mitteroecker, 2013). After this procedure, they are treated the same as discrete landmarks.

A few GMAs use curvature semilandmarks to quantify variation along the sagittal profile (e.g., Delson et al., 2001; Harvati et al., 2010). Analyses of surface semilandmarks focus primarily on the frontofacial region of Middle Pleistocene hominids. For example, Freidline, Gunz, Janković, et al. (2012) conducted a GMA of the affinity of a Zuttiyeh fossil with other hominids. They placed semilandmarks across the frontal and midfacial bones. Using PCA, they concluded that overall, the Zuttiyeh fossil was morphologically consistent with other Middle Pleistocene archaic *H. sapiens*. This skull may also represent an early form of Neanderthal due to its similarity with Shanidar 5, a Near Eastern Neanderthal cranium. In another study, Freidline, Gunz, Harvati, et al. (2012) analyzed Middle Pleistocene archaic *H. sapiens*, placing semilandmarks on the supraorbital region and the face. Their PCA demonstrated a temporal trend of morphological change from the Middle Pleistocene archaic forms to the younger anatomically modern *H. sapiens.*

1.9 DISCUSSION

This chapter shows that researchers favored traditional multivariate morphometrics because they can quantify overall similarity by using continuous variables as well as represent each specimen as a single entity. Therefore, the problem of paleoanthropological classification transformed into determining how similar groups or subsets of specimens are so they can be taxonomically grouped. This method contrasts with cladistic analysis, which generates a series of independent and discrete features that could delineate species. When comparing these methods, some researchers view multivariate morphometrics as a more appropriate morphological tool because it can capture the continuous nature of morphological difference, which is believed to be the common phenomenon. As a phenetic method, morphometrics can also evaluate total morphological patterns rather than arbitrarily selecting a few measurements.

However, to determine if a methodology is suited for analyzing morphology, it is necessary to ask what morphological features are captured and how they can be identified (Zelditch et al., 2004). Though claimed to be phenetic, the most multivariate analyses used in paleoanthropological research include only a very limited number of morphological differences, because they use only a few craniofacial measurements (Kaifu et al., 2008; Villmoare, 2005). Furthermore, it is difficult to use linear measurements to capture many morphological features (Baab, 2016; Baab et al., 2012; Harvati et al., 2010; Zelditch et al., 2012). It is also difficult to identify features, if captured, from the results of multivariate analyses, such as PCAs (Baab, 2016; Baab et al., 2012; Harvati et al., 2010; Zelditch et al., 2012). From this perspective, it is inappropriate to say that linear measurement-based multivariate morphometrics is more suitable than visual analysis in systematic studies. The gap between them is a problem not only of "continuous vs. discontinuous variation", but also of the fact that traditional morphometric analysis is not able to capture detailed morphology.

GMA has been viewed as revolutionary compared to traditional morphometrics because landmark data can directly capture the geometry of biological shapes. Results of GMA can also be easily visualized as shape differences. The ability to work with conventional multivariate analyses also encourages paleoanthropologists to use landmark data instead of linear measurements. However, most GMAs focus on gross shape rather than morphological detail (Baab, 2016; Harvati et al., 2010; Schwartz et al., 2014; Spoor, 2013; Spoor et al., 2008; Villmoare, 2005). An important reason for this limitation is that many GMAs sample only a small number of discrete landmarks (Harvati et al., 2010; Schwartz et al., 2014; Villmoare, 2005).

Moreover, although GMA offers a powerful visualization toolkit, identifying morphological features, especially from results of the most popular method, PCA, could be challenging. First, as GMA treats each shape as an integrated entity, higher-ranked PCs that explains a large proportion of the total

variance may focus on large-scale, gross shape differences, such as overall cranial contours and proportions of major cranial bones. This is because gross shape differences usually subsume many landmarks, which contribute substantially to overall shape differences. However, detailed shape differences, if included in landmark data, can still be difficult to be read from higher-ranked PCs. This is because details are usually about differences located in some specific structures or small cranial regions, such as the shape of the mandibular fossa and mastoid process. Thus, detailed differences usually involve only a relatively small number of landmarks or semilandmarks, which contribute little to overall shape difference. In addition, PCs are essentially arbitrary axes in the original shape space that is dependent on the sampled landmarks and specimens included (Adams et al., 2011; Baab, 2016; Zelditch et al., 2012). Therefore, shape differences revealed by a single PC does not necessarily match actual morphological features (Adams et al., 2011; Baab, 2016; Zelditch et al., 2012).

An important, yet usually ignored, factor that may cause problems in identifying morphological features from shape differences visualized by a GMA is Procrustes superimposition (Richtsmeier et al., 2002). This is because shape differences captured and revealed by a GMA depend on how specimens are superimposed with each other (Richtsmeier et al., 2002). In particular, during Procrustes superimposition, superimposed landmark configurations are rotated away from a consistent orientation until the overall Procrustes sum of squares are minimized (Klingenberg, 2013; Richtsmeier et al., 2002; Zelditch et al., 2012). However, observed morphology, such as degree of frontal rise and inclination of the nuchal plane, are based on orienting specimens in the Frankfurt plane. This inconsistency of orientating specimen may create incompatibility between shape differences revealed by a GMA and observed morphology. Specifically, the effect of Procrustes superimposition is difficult to predict and control because this process depends on the specimens included in the analysis as well as on the sampled landmarks (Richtsmeier et al., 2002).

Overall, the incompatibility between GMA and systematics based on cladistic analysis should not be viewed simply as the former focusing on continuous variation and overall similarity, and the latter arbitrarily creating a list of discrete features. It also happens because the potential for capturing and properly identifying morphological features, especially morphological detail, via landmark data has not been thoroughly explored.

1.10 RESEARCH GOALS

As discussed, in paleoanthropology, little attention has been paid to exploring the potential of GMA in capturing and recognizing morphological features. Therefore, a primary goal of this dissertation is to use curvature and surface semilandmarks to capture more observed cranial features of hominids, which cannot be recorded by discrete landmarks, into GMA. An equally important goal is to explore whether specific features can be identified from shape differences visualized by PCA, which is the most commonly used method in GMA to demonstrate degrees and patterns of overall shape difference. Particularly, I assess how Procrustes superimposition, which changes the orientations of specimens, can create inconsistency between shape differences revealed by PCA and observed morphology.

I also assess whether three other sampling issues related to testing whether *Homo erectus* is too variable to constitute a single species. There are three specific hypotheses that are usually tested:

1. *H. erectus sensu lato* (referred to here as *H. erectus*) is significantly more variable than *H. sapiens*.
2. The overall variability in Asian *H. erectus* and African *H. ergaster* exceeds that of *H. sapiens*.
3. Differences between Asian *H. erectus sensu stricto* (referred to here as Asian *H. erectus*) and African *Homo ergaster* exceeds those between geographical subsets of *H. sapiens*.

The first issue concerns semilandmark density. Some researchers believe that oversampling landmarks, i.e., sampling too many landmarks relative to a small sample size of specimens, can cause low efficiency in data collection and affect statistical analyses (Watanabe, 2018). However, sampling too few landmarks can lead to serious loss of information (Gunz & Mitteroecker, 2013; Watanabe, 2018). Gunz and Mitteroecker (2013) propose that oversampling of landmarks is actually beneficial to biological research because it facilitates interpretation. Thus, I compare the same statistical analyses based on semilandmark and landmark datasets with different densities to assess whether the denser semilandmark datasets can include more shape information and affect the results of statistical analyses.

The second matter is whether analyses of different cranial regions yield different results by focusing on different aspects of morphological differences. Most of previous GMAs sample points across the entire cranium. However, if one focuses only on a single cranial bone, the analyses may yield alternative results by emphasizing more shape differences in individual cranial bones.

The third issue concerns reference taxa. Usually, researchers include a large sample of reference taxa, such as *H. sapiens* and extant hominoids, both to increase sample size and to demonstrate differences between hominids and these taxa (Baab, 2008b; Freidline, Gunz, Janković, et al., 2012; Harvati et al., 2010; Lordkipanidze et al., 2013; Terhune et al., 2007). However, when adding too many

specimens relative to the small sample size of fossils, major PCs might be affected by differences between or within taxa. Important aspects of shape differences within the fossil sample might be concealed.

In assessing these sampling issues, I focus on specimens commonly allocated to *H. erectus* because the validity of *H. erectus*—i.e., whether a single species or an invalid hypodigm that subsumes multiple species—has been a central issue of paleoanthropology, and a major focus of GMAs (e.g., Baab, 2008a, 2016; Terhune et al., 2007) (Table A.1 in Appendix A). However, these studies only used discrete landmarks. Thus, it is interesting to explore whether surface semilandmarks can capture observed features of specimens usually assigned to *H. erectus*. It is also interesting to explore whether commonly used statistical analyses that aimed to test the validity of *H. erectus* can yield alternative results when semilandmarks are used.

The second chapter reviews the history of the problem of *H. erectus* to provide background information on the hypotheses to be tested. It also focuses on morphometric analyses that test hypotheses about this taxon. The third is a detailed descriptive overview of specimens commonly assigned to *H. erectus* for the purpose of comparing them with shape differences revealed by the GMAs in this study. The fourth presents the hypotheses to be tested by GMA and the methods that will be used to test them. The fifth to eighth chapters present the results of GMA of the entire cranium, posterior cranium, the temporal region, and the frontal region. The last chapter synthesizes these results, discusses the significance of this research, and suggests potential future research directions.

2.0 HISTORY OF *HOMO ERECTUS*

2.1 INTRODUCTION

This chapter offers a historical review of how commonly accepted ideas of *Homo erectus* (*H. erectus*) developed. It also provides background for hypotheses to be tested in the following chapters via geometric morphometric analysis (GMA). It attempts to demonstrate how a set of descriptive features, such as a bar-like supraorbital region and occipital torus, and a long, low cranium with an angular torus, have been "recycled" in the studies of *H. erectus.* These features are rooted in Weidenreich's (1943) description of a group of fossils from Zhoukoudian, China. Even the cladistic analyses of the 1980s that suggested splitting the *H. erectus* hypodigm into two species were based on evaluating the distribution of these features in hominids (Andrews, 1984; Stringer, 1984; Wood, 1984). Nevertheless, some of these features are overgeneralized or even poorly defined (Schwartz, 2004, 2016; Schwartz & Tattersall, 2002, 2003).

This review also focuses on morphometric analyses that test taxonomic hypotheses about *H. erectus*. As reviewed in the previous chapter, the use of morphometrics in paleoanthropology is closely associated with studies of *H. erectus*. The initial promotion of multivariate morphometrics in paleoanthropology was triggered by the numerous taxonomic names applied to hominid specimens, many of which were later sunk into *H. erectus*. Later, in the 1980s, criticisms of cladistic analyses that aimed to define *H. erectus* triggered a new wave of multivariate analyses to re-examine the validity of this taxon from a phenetic perspective. In the last decade, some paleoanthropologists have performed the same statistical tests with landmark data. Most of these morphometric analyses consistently support that *H. erectus*, though highly variable, is not too variable to be a single species.

Nevertheless, this chapter shows that these GMAs still focus on gross shapes rather than on specific details. One probable underlying factor that may constrain researchers from evaluating whether their landmark sets can capture sufficient details is their reliance on commonly cited features. They then use these features as references to check the morphological capacity of their GMAs. Consequently, this chapter highlights the importance of reexamining and synthesizing descriptive features of *H. erectus*

specimens as the first step in examining whether GMA has the potential to capture observed, especially detailed, morphological features.

2.2 BEFORE THE 1950S: A CHAOS OF TAXONOMIC NAMES

In 1891, Eugene Dubois discovered the Trinil 2 skullcap, which later became the type specimen of *H. erectus*. Based on this skullcap and a femur recovered one year later at the same site, Dubois (1892) created the new species, *Anthropopithecus erectus*, which he later changed to *Pithecanthropus erectus* (*P. erectus*) (Dubois, 1896). He believed that the "ape-like" cranium and the "human-like" femur indicated that the species was the missing link between humans and apes (Dubois, 1892, 1896, 1898).

From 1936 to 1941, Ralph von Koenigswald and his team discovered in Sangiran, Java a number of hominid cranial and mandibular remains, cataloged from Sangiran 1 (S 1) to Sangiran 6 (S 6). In the original analysis, von Koenigswald and Weidenreich (1939) allocated S 1 to S 4 to *P. erectus* primarily because the cranial remains S 2 and S 3 were comparable to the Trinil 2 skullcap, though they believed that the extremely large S 4 , which includes a maxilla, might have belonged to a more primitive form. Later, S 4 was assigned a new name: *Pithecanthropus robustus* (Weidenreich, 1945). The last Sangiran cranial specimen discovered before the 1950s was the Sangiran 6 partial mandible (1941). Due to its great robustness, it was referred to the new taxon *Meganthropus paleojavanicus* (Weidenreich, 1944).

Eleven partial crania were found at the site of Ngandong, Java during excavations between 1931 and 1933. Oppenoorth (1932) created *Homo soloensis* for these specimens, which were characterized for example, by marked postorbital constriction, stout brows, and a sloping nuchal plane with marked muscle marking. However, in the same announcement, he also offered *Javanthropus soloensis* as the genus and species for the Ngandong remains and Kabwe 1 (later allocated to *Homo heidelbergensis*).

In China, the Zhoukoudian site yielded another important group of specimens that were eventually included in *H. erectus*. In 1927, Davidson Black used a lower left, and possibly the first, molar recovered from this site as the type specimen of a new genus and species, *Sinanthropus pekinensis*. Excavations over the next 10 years yielded numerous fossils that were allocated to this taxon, including Skull I to Skull XIV (Weidenreich, 1943). Among these skulls, the most complete were three adult calvariae, i.e., Skull X, XI, and XII from Locus L (Weidenreich, 1943). Primarily using these three calvariae, Weidenreich (1943) assessed the morphology of *Sinanthropus* cranial remains. His descriptions served as the protocol for the "classic description" of *H. erectus* that paleoanthropologists commonly use (Antón, 2002, p. 313; 2003). These descriptions include straight, shelf-like brows continuous over the

glabellar region, cranium widest across the supramastoid regions, angular torus on the parietals, and bar-like occipital torus.

In comparing the Zhoukoudian with other Asian specimens, Weidenreich (1943, 1945) observed some differences. For example, *Sinanthropus* had a supraorbital torus separated from the forehead by a sulcus, a swollen forehead, and a flat region of obelion. *Pithecanthropus*, on the other hand, had a supraorbital region that was confluent with the forehead, a flat forehead, and a vaulted region of obelion. *H. soloensis* was similar to *Pithecanthropus* in these features, suggesting their affinity. However, Weidenreich (1943, p.228) still considered these hominids to belong to the same species because "the difference between these two hominids forms … are of the same kind and magnitude as modern racial differences". In response to criticisms from Le Gros Clark (1940) and Zuckerman (1933, 1940) about his confusing use of taxonomic names, Weidenreich (1943) explained that he kept the name "*Sinanthropus pekinensis*" only to commemorate Davidson Black. He also suggested that hominid taxonomic names could be used merely as informal labels without referring taxonomic meaning.

Further complicating anthropological nomenclature, von Koenigswald (1948) created more names for these Asian specimens without providing sufficient morphological assessments. He assigned S1, S 4, and the Mojokerto infant skull to *Pithecanthropus mojokertensis* for unspecified "morphological and stratigraphic reasons" (von Koenigswald, 1948, p. 59). S 5 was assigned the name *Pithecanthropus dubius* because Weidenreich was uncertain about its taxonomic status.

2.3 "*HOMO ERECTUS*" AS BOTH A GRADE AND A POLYTYPIC SPECIES

2.3.1 *Homo erectus* as a grade

Since the 1940s, paleoanthropologists have been increasingly aware of the chaotic state of paleoanthropological nomenclature. Le Gros Clark (1940) and Zuckerman (1933, 1940) both argued that Weidenreich's (1943) use of the genus names *Pithecanthropus* and *Sinanthropus* was confusing, and even Weidenreich (1936, 1943) confessed that their differences might only be racial. Zuckerman (1950) further called for a thorough reclassification of hominids involving statistical methods to measure the degree of similarity consistently.

Finally, Mayr (1950) proposed that all known hominids should be lumped into only three time-consecutive species within a single genus: *H. transvaalensis*, *H. erectus*, and *H. sapiens* (Howells, 1976; Tattersall & Schwartz, 2009). *H. transvaalensis* included all australopiths. *H. erectus* included the

chronologically intermediate Javanese and Chinese fossil hominids, including those assigned to *Pithecanthropus*, *Meganthropus*, *Sinanthropus*, and *H. soloensis*. All hominids younger than *H. erectus* were placed into *H. sapiens*. Nevertheless, Mayr (1950) did not provide any morphological evidence for his classification, though he suggested that his fellow paleoanthropologists often exaggerated intraspecific differences to differences at the specific or even generic level (Tattersall & Schwartz, 2009). Mayr's ecological perspective ultimately led him to believe there was only one species at any time during human evolution. For him, members of the genus *Homo* were, from the beginning, able to occupy virtually all regions of the world because their possession of culture freed them from needing to physically adapt to different environments (Mayr, 1950). As a result, hominids never speciated.

Not all paleoanthropologists adopted Mayr's classification of hominids as a formal system, but Mayr's idea of arranging species into chronologically consecutive grades was generally accepted. Consequently, some preferred to use informal names such as "Pithecanthropine" to combine specimens originally allocated to *Pithecanthropus*, *Sinanthropus*, and *H. soloensis* into a grade intermediate between older and younger hominids (Clark, 1957, 1964; Howells, 1976; Straus Jr, 1956). However, separation between grades was unclear, as a result of continuous evolution (Robinson, 1953).

Some scholars did not strictly follow Mayr's linear-grade approach. Robinson (1953) proposed parallel Asian and African lineages. He divided hominid evolution into two grades: Australopithecine and Euhominine. In Africa, Euhominine evolved from African australopiths. In Asia, the australopithecine grade represented by *Meganthropus* (S 6 partial lower jaw) gave rise to Asian euhominines, which included *Sinanthropus* and *Pithecanthropus.* Tobias and von Koenigswald (1964) embraced Robinson's (1953) view of coexisting Asian and African lineages. They assigned *Meganthropus* (including the Sangiran 8 mandible discovered in 1952) to the same primitive grade as the newly discovered *Homo habilis* from Olduvai Gorge. The next grade was "*Pithecanthropus mojokertensis*", which included specimens of *Sinanthropus* and *Pithecanthropus*. Though this name was proposed by von Koenigswald (1948), these authors shied away from assigning formal taxonomic names because sorting out lineages was more important. Following Campbell (1963), they also suggested *Sinanthropus* and *Pithecanthropus* could be replaced by *H. erectus pekinensis* and *H. erectus erectus*, respectively.

2.3.2 *Homo erectus* as a species

In the first edition of his influential book, *The Fossil Evidence for Human Evolution*, Le Gros Clark (1957) kept the name *P. erectus* for the Zhoukoudian and Javanese specimens, as he still believed that the degree of difference between specimens of *Pithecanthropus* and *Homo* was comparable to that between *Pan* and *Gorilla*. *Pithecanthropus* could also be viewed as a grade. Of the studies that focused on

sorting out grades before the 1970s, only Le Gros Clark (1957) attempted to provide a morphological "definition" of *H. erectus* (Howells, 1976). However, his "definition" was only a generalized description that consisted of a list of very generalized features, such as a low and flat cranium, marked postorbital constriction, well-developed supraorbital torus, and a brain size of approximately 1,000 cc.

At the Wenner-Gren Foundation's conference at Burg Wartenstein held in 1963 to discuss paleoanthropological classification, Campbell (1963) provided a formal taxonomic system for fossil hominids. In that system, *H. erectus* became a formal taxonomic name for the specimens from Trinil, Sangiran, Ngandong, and Zhoukoudian. He further placed all Javanese specimens of *Pithecanthropus*, *Meganthropus*, and *H. soloensis* in the subspecies *H. erectus erectus* and those of *S. pekinensis* in *H. erectus pekinensis*.

The following year, in the second edition of *The Fossil Evidence for Human Evolution*, Le Gros Clark (1964, p. 88) modified the name "*Pithecanthropus erectus*" to "*Homo erectus*" because there was "a general consensus of opinions that they are more properly to be included in the genus *Homo*, but specifically distinct from *H. sapiens* and *H. neanderthalensis*". He argued, "the morphological arguments for this change of nomenclature seem to be well-founded", though he did not specifically discuss any morphological evidence (Le Gros Clark, 1964, p. 88). Additionally, he suggested that in order to help his colleagues become familiar with the name "*Homo erectus*", they could use informal names such as "Pithecanthropine" to "ease the transitional period of nomenclature change" (Le Gros Clark, 1964, p. 89).

2.3.3 The expanding *Homo erectus* hypodigm

As the morphological assessment of *H. erectus* remained vague, subsequently discovered, contemporaneous specimens were assigned this taxonomic name without much morphological reasoning. These fossils included the skullcap OH 9 and a more fragmentary skull, OH 12, which were found by L. S. B. Leakey at Olduvai Gorge in 1960 (L. S. B. Leakey, 1961). Two other major discoveries of "*H. erectus*" were the skulls KNM-ER 3733 and KNM-ER 3883, found in 1973 at Koobi Fora (M. G. Leakey & Leakey, 1978; R. E. Leakey & Walker, 1976; Wood, 1991a). Without any morphological basis, Meave Leakey and Richard Leakey (1978) allocated them to *H. erectus*, and suggested they might have evolved from *H. habilis*.

By the end of the 1970s, many cranial, mandibular, and dental fragments were recovered from the Sangiran region (Jacob, 1972). Most were allocated to *Pithecanthropus* without proper descriptions (Jacob, 1972). Among them, the best preserved is Sangiran 17 (S 17), found in 1969. In the original description, Sartono (1971) allocated it to *Pithecanthropus* and suggested it was very similar to the Sangiran 2 skullcap. Jacob (1973) classified it as *Pithecanthropus soloensis* along with Ngandong

specimens and the Sambungmacan SM 1 calvaria based on “overall similarity”. However, Jacob (1973) also stated that all *Pithecanthropus* subgroups were consistent in overall morphology, including having a prominent supraorbital torus, a low vault, and marked postorbital constriction.

Later, Sartono (1982) replaced *Pithecanthropus* with *H. erectus.* He also believed there was a distinct robust lineage in Indonesia, represented by mandibular remains, such as S 8, S 12, S 27, and S 31, which he allocated to *Meganthropus palaeojavanicus*. He then changed this name to *Homo palaeojavanicus* without providing specific reasoning.

After the 1950s, a series of specimens later allocated to *H. erectus* were found in China. The most remarkable are a mandible and cranium from two sites in the Lantian Region, Northwest China. The mandible was excavated at the Chenjiawo site in 1963 (Aigner & Laughlin, 1973; von Koenigswald, 1968; R. Wu, 1964, 1966; X. Wu & Poirier, 1995). In the original description, R. Wu (1964) found that this mandible differed from *Sinanthropus pekinensis* in a few features, which led him to establish a new species, *Sinanthropus lantianensis*, for it. The partial cranium was found at Gongwangling in 1966. It preserved large portions of the frontal, right temporal, and parietal bones, as well as two maxillae. R. Wu (1966) found that the skull was similar overall to the skulls of Javanese *Pithecanthropus erectus* in having a smooth transition between the supraorbital torus and the forehead. However, similar to the *Sinanthropus pekinensis* skulls, the Lantian skull bore a cross-like elevation at bregma. Overall, this skull was seen as more primitive than the Zhoukoudian remains because it had more pronounced postorbital constriction, lower cranial height, an extraordinarily thick cranial wall, and smaller brain (775 cc to 783 cc) (von Koenigswald, 1968; R. Wu, 1966).

When discussing Lantian remains, which did not attract much international attention because of a lack of communication, Aigner and Laughlin (1973) simply called them *H. erectus*. They concurred with R. Wu’s (1964) description and idea that the Gongwangling skull was more primitive than the Zhoukoudian skulls because of an older date based on faunal remains (Aigner & Laughlin, 1973). They then summarized trends of evolution within *H. erectus* based on the primitiveness of the skull, including the expansion of the brain, reduction in the masticatory complex, thinning of the cranial wall, and flexing of the cranial base.

2.4 CONTROVERSIES OF CLADISTIC ANALYSIS

2.4.1 Reappraisal of *Homo erectus* and the introduction of cladistic analysis

Since the 1970s, awareness of the inadequate morphological assessment of the greatly expanded *H. erectus* hypodigm has increased. Rightmire (1979) focused on OH 9 and OH 12 because little attention had been paid to them since their discovery in the early 1960s. He found they shared many features with KNM-ER 3733 and the Zhoukoudian specimens. He then called for a comprehensive morphological assessment of all Asian and African specimens found after the 1950s.

Howells (1976, p. 82) pointed out that *H. erectus*, and even the genus *Homo*, had never been properly defined, but existed as a concept based on the notion that hominids "were not speciating at a time when elephants, equids, and suids were doing so freely". In particular, Howells (1976) knew of the value of a newly emerged methodology, cladistic analysis, in recognizing and defining species on the basis of their derived (unique) features. For him, cladistic analysis was also supported by the theory of *punctuated equilibrium*, which postulated rapid periods of speciation followed by stasis. Thus, potential hominid species could be recognized as distinct entities. Consequently, Howells (1976) encouraged using cladistic analysis to redefine *H. erectus*, which could then serve as a pivoted point in re-evaluating scenarios of human evolution. However, a few years later, Howells (1980) confessed that it was extremely difficult to produce a strict morphological definition for such a polytypic, intermediate species. Like other paleoanthropologists, Howells (1980) only produced a list of common descriptive features of *H. erectus*, including a low frontal bone, a straight supraorbital torus, sagittal keeling, and a sharply angled occipital profile.

Although, in the end, Howells (1980) shunned cladistic analysis, other paleoanthropologists emphasized its value in generating testable hypotheses of phylogenetic relationships. However, rather than testing hypotheses about species, they simply used commonly accepted hominid taxa as working units in creating cladograms. For example, Delson et al. (1977) used *H. erectus* as a clade and suggested that the generalized features briefly summarized by Macintosh and Larnach (1972), such as undivided brows, marked postorbital constriction, a small mastoid process, and a mound-shaped occipital torus, were its derived features.

Santa Luca (1980) was the only one at that time who critically examined previous descriptions as a basis for performing a cladistic analysis to sort out relationships among Ngandong and other Asian specimens. He recognized discontinuous variation in several characters, including the configurations of frontal bone, sagittal and coronal keeling, the relationship between the supramastoid and mastoid crests, detailed aspects of the angular torus, and the development and morphology of the occipital torus. As a

result, the Ngandong specimens formed a distinct morph based on the derived condition of having a metopic ridge isolated from the bregmatic eminence and longer coronal ridge. This morph grouped with S 4, because of their uniquely having separated mastoid and supramastoid crests as well as a sharply defined junction between the well-developed occipital torus and occipital squama. These specimens were more closely related to the clade that contained S 2, S 17, and Trinil 2 than they were to the clade of Zhoukoudian specimens. The descriptions and the cladistic analysis provided by Santa Luca (1980) were usually ignored, though many researchers cited his work to show that Asian *H. erectus* specimens presented generalized features, such as an angular torus and a cruciate bregmatic eminence (e.g., Andrews, 1984; Baab, 2016; Stringer, 1984).

Santa Luca's (1980) view of cladistic analysis was complicated. He argued that previous phylogenetic analyses of *H. erectus* fell into the "gradualist fallacy", whereby specimens were arbitrarily ordered into segments along a presumed transformation series, via features such as "the reduction of the supraorbital torus, the expansion of the lateral cranial wall and reduction of supramastoid crest, or the expansion of the cranial vault" (Santa Luca, 1980, p. 124). In contrast, cladistic analysis allowed one to detect subtle discontinuous variation as a basis for delineating distinct groups and their relationships (Santa Luca, 1980). However, Santa Luca (1980) refrained from using cladistic analysis to test the validity of *H. erectus*. He first determined that the commonly accepted *H. erectus* hypodigm represented a valid species because its members shared the same "Bauplan" in overall cranial shape that was captured by craniometric measurements and general cranial profiles.

2.4.2 Cladistic analysis and the emergence of *Homo ergaster*

The most influential cladistic analyses of *H. erectus* were those of Andrews (1984), Stringer (1984), and Wood (1984) in the mid-1980s. However, rather than searching for unique features with which to delineate species, these cladistic analyses focused primarily on reexamining the distribution of commonly cited descriptive features, such as a long and low cranium, continuous brows, marked postorbital constriction, greatest cranial width across the supramastoid crests, thick vault bone, angular torus, upper occipital plane shorter than the lower (nuchal plane), prognathic face, and sulcus behind the supraorbital torus. They reported that many of these features could be found in other hominids and even non-human primates, while others were unique to Asian specimens. Consequently, they proposed that the expanding *H. erectus (sensu lato)* (*H. erectus s. l.*) hypodigm should be split into two species: 1) the real *H. erectus*, which was later called *H. erectus sensu stricto* (*H. erectus s. s.*), consisting primarily of the Asian specimens; 2) the African specimens from the Turkana region, represented by KNM-ER 3733 and KNM-ER 3883, which were later classified as *Homo ergaster* (*H. ergaster*) (Wood, 1991a, 1991b).

Andrews (1984) was the most radical of all as he realized that previous analyses focused only on features, such as the cranial capacity, that facilitated defining *H. erectus* as an intermediate grade, while a species should be recognized as an entity even though broad trends in human evolution may still exist. He argued that only Asian specimens were the real *H. erectus* as they were unique in having frontal keeling, thick cranial vault bone, an angular torus on the parietal bone, and bilateral mastoid fissures. Stringer (1984) was more conservative. He identified 12 possibly unique features of the Asian specimens, including a strong occipital torus, an occipital plane that was shorter than the nuchal plane, an angular torus on the parietal bone, a robust tympanic plate, and thick cranial bone. However, he confessed that "it would take a brave worker to say that therefore the latter (African) fossils do not represent *H. erectus*" (Stringer, 1984, p. 137).

Wood (1984) also identified a short list of potentially unique *H. erectus* features, including an occipital torus continuous with the angular torus and supramastoid crest, posttoral sulcus, sharply angled occipital profile, and longer occipital than nuchal planes. Based on this list, Wood (1984) removed KNM-ER 3733 and KNM-3883 from *H. erectus* while keeping OH 9 and OH 12 in it. However, Wood (1984) was not a devotee of cladistic analysis. He believed that the advantage of cladistic analysis was defining species only by unique features. Nevertheless, he found that a combination of features, regardless of their being primitive or derived, could also be useful in diagnosing species. For example, although *H. habilis* specimens had a long and low cranium and *H. heidelbergensis* had robust brows and a thick vault, only *H. erectus* presented a combination of these features. Based on this approach, the *H. erectus* hypodigm did not need to be split up (Wood, 1991a).

Later, Wood (1991a, 1991b) allocated KNM-ER 3733 and KNM-ER 3883, which were excluded from *H. erectus* as a result of cladistic analysis, to *H. ergaster*, whose type specimen was the KNM-ER 992 mandible (Groves & Mazak, 1975). Notably, neither KNM-ER 3733 and KNM-ER 3883 was associated with a lower jaw. The reason Wood (1991a) excluded these specimens from *H. erectus* was that they exhibited a combination of primitive retentions shared with Asian *H. erectus* and several features shared with *H. sapiens*, such as increased parietal breadth, relatively longer occipital bone, broader nasal aperture, and shorter cranial base. Thus, he suggested *H. ergaster* was more likely than Asian *H. erectus* to be an "ancestor", because the latter was too derived.

2.4.3 The problem of variation and covariation

As discussed in the previous chapter, the cladistic analyses that suggested splitting *H. erectus* soon met a wave of criticism, as many paleoanthropologists argued that cladistic analyses arbitrarily treat potentially continuous variants as discrete that were scored as either "present" or "absent" (Bräuer, 1990;

Bräuer & Mbua, 1992; Hublin, 1986; Kennedy, 1991; Trinkaus, 1990). For example, Bräuer and Mbua (1992) showed that Andrews' (1984) seven "derived features" of Asian *H. erectus* were variably expressed in both the Asian and African subsets. Consequently, it was difficult to draw a clear boundary around *H. erectus*. For many researchers, this confirmed the view that continuity was the theme in human evolution. Moreover, some researchers argued that cladistic analysis ignored correlation or covariation between morphological features because discrete features were treated independently (Bräuer & Mbua, 1992; Kennedy, 1991; Pope, 1992). For example, Bräuer and Mbua (1992) observed that keeling, angular torus, and vault bone thickness covaried because they usually appeared together. Overall, variation and covariation rendered cladistic analysis unsuitable for recognizing hominid species (Bräuer & Mbua, 1992; Harrison, 1993; Kennedy, 1991; Pope, 1992).

These criticisms influenced the classification of new discoveries. When assessing the "Nariokotome boy" (KNM-WT 15000), found in the West Turkana region in 1985, Walker and Leakey (1993) concurred with Bräuer (1990) and Kennedy (1991), who viewed cladistic analysis as unsuitable for defining hominid species. Therefore, they chose not to split the *H. erectus* hypodigm, and thus allocated KNM-WT 15000 to *H. erectus* (*sensu lato*) because of overall cranial similarity. They suggested that, if one split the *H. erectus* hypodigm, KNM-WT 15000 must be classified as *H. ergaster*.

2.4.4 The total morphological pattern

2.4.4.1 The combination of features

Convinced that cladistic analysis was not suitable for recognizing hominid species, paleoanthropologists shifted to assessing overall similarity in order to test the validity of *H. erectus*. One approach was to use a combination of features (Harrison, 1993; Pope, 1992; Rightmire, 1993; Wood, 1984, 1991a, 1991b).

Rightmire (1993) was fully aware of the limitations of cladistic analyses in recognizing *H. erectus* as a discrete taxon. Although he listed nine features, including thick and continuous brows, frontal midline keeling, angular torus, transverse occipital torus, and strong petrosal crest as possible derived features of *H. erectus*, he admitted these features were variably expressed. Instead, he realized that all specimens of *H. erectus* (*s. l.*) were similar in many descriptive features. Due to their "striking" degree of overall similarity, differences between Asian and African subsets were unremarkable and comparable to differences between geographical groups within a species.

To further support the idea that *H. erectus* was a good paleospecies rather than a segment of a continuous evolutionary sequence, as viewed by "the most committed gradualist" (p. 185), Rightmire (1993) proposed two other lines of evidence. First, *H. erectus* was different overall from other hominid

taxa. The only group that somewhat overlapped with *H. erectus* was Middle Pleistocene "archaic" *H. sapiens*, later referred to *H. heidelbergensis* (Rightmire, 1998). However, these specimens presented only a few *H. erectus* features, rather than the common *H. erectus* plan. The presence of a few *H. erectus* features in the Middle Pleistocene group also suggested to Rightmire that the latter might have descended from the former. For Rightmire (1993), this proved the advantage of his approach, since it allowed one to hypothesize an ancestor-descendant relationship, which was not a feature of cladistic analysis. Further, he found no significant chronological trend within *H. erectus* when comparing craniometric measurements. This suggested that *H. erectus* was stable over a long period of time rather than an evolving lineage.

2.4.4.2 Multivariate analysis

A quantitative expression of the phenetic approach, which focuses on overall similarity, is multivariate analysis (Bilsborough & Wood, 1988; Howells, 1972, 1973; Rightmire, 1998). Multivariate analysis assesses overall similarity in a set of linear measurements by constructing new continuous variables such as principal components (PCs) and distances. This process of taking continuous variation and total morphological patterns into consideration at the same time encouraged some paleoanthropologists to apply these methods to re-evaluating the validity of *H. erectus* (Bilsborough & Wood, 1988; Bräuer, 1994; Kramer, 1993; Wood, 1993; Wood et al., 1991). For example, Bräuer's (1994) principle component analysis (PCA) demonstrated great overlap between Asian and African subsets of *H. erectus*. Anton's (2002) extensive PCAs yielded similar results.

Some paleoanthropologists used multivariate techniques to quantify the degree of overall variability in *H. erectus (s. l.)* in order to test if *H. erectus* was too variable to be a single species by comparing this variability with extant hominoids and *H. sapiens*. For instance, Kramer (1993) found that the degree of overall variability in *H. erectus* (*s. l.*) was comparable to his *H. sapiens* sample. The failure to find excessive variability suggested that the single species hypothesis could not be rejected. Villmoare (2005) also carried out multivariate analyses, which again showed that differences between Asian and African subsets of *H. erectus* were comparable to those between geographical subsets of *H. sapiens*. However, it should be noted that these multivariate analyses relied on only a short list of measurements, so they can only capture general shapes rather than details (Kaifu et al., 2008; Villmoare, 2005).

2.5 THE FURTHER EXPANDING *HOMO ERECTUS* HYPODIGM

Since the 1990s, cladistic analyses of the validity of *H. erectus* have largely been absent. Some paleoanthropologists even suggested that using only discrete unique features could be misleading (Antón, 2002, 2003; Asfaw, 2008; Bräuer, 1990; Pope, 1992). The majority of cladistic analyses focused only on sorting out the phylogenetic relationships among australopiths, while using *H. erectus* or *H. ergaster* as operational units (e.g., Lieberman et al., 1996; Strait & Grine, 1999; Strait et al., 1997). As a result, *H. erectus* remained a polytypic species. More specimens were added to *H. erectus* as long as they presented some of commonly used descriptive features and the resultant expanded group was not too variable.

2.5.1 The role of the Dmanisi specimens

A remarkable group of specimens added to *H. erectus* was found at Dmanisi, Georgia. In the description of the first two skulls, D2280 and D2282, which were found in 1999, Gabunia et al. (2000) concluded they were more similar to the skulls of early African *H. erectus* (so-called *H. ergaster*) than to those of Asian *H. erectus* (*s. s.*). Because these fossils also displayed a few distinct features, Gabunia et al. (2000, p. 1021) temporarily named them "*Homo ex gr. ergaster*". A third cranium, D2700, which was a subadult, and its associated mandible, D2735, were described as being consistent in overall morphology with the first two crania (Vekua et al., 2002). Vekua et al. (2002) allocated them to *H. erectus* because they displayed a typical combination of features, such as the morphology of the supraorbital torus, faint midline keeling, a low rear profile, and a long and low temporal squama.

Following Rightmire's (1993) descriptive protocol, Lordkipanidze et al. (2006) also allocated the Dmanisi remains, including the fourth skull, D3444, to *H. erectus*, because they displayed a combination of classic *H. erectus* features, such as a bar-like occipital torus, sharp occipital angulation, and sagittal keeling. On the other hand, they observed that the Dmanisi fossils presented a combination of Asian and African regional *H. erectus* features. Thus, they suggested, the Dmanisi "paleodeme" might be closely related to the common ancestor of the African and Asian subsets.

In a more comprehensive morphological analysis, Rightmire et al. (2006) discussed the importance of using a combination of features to allocate the Dmanisi remains to *H. erectus* rather than relying on a much shorter list of diagnostic features, such as bregmatic eminence, well-developed supramastoid crest, and sagittal keeling. These authors also noted that similarities between KNM-ER 1813 and D2700 blurred the boundary between *H. habilis* and *H. erectus*. Therefore, Rightmire et al. (2006) regarded the Dmanisi population as a primitive subspecies of *H. erectus*, *H. erectus georgicus*,

which was again suggested to be close to the origin of *H. erectus*. However, *H. habilis* and *H. erectus* were still considered separate paleospecies, as they did not share the same combination of features.

Based on their previous assessment, Lordkipanidze et al. (2013) allocated the fifth Dmanisi skull, D4500, to *H. erectus*. They believed that in adding this skull, the Dmanisi group validated the single species concept of *H. erectus*, since they showed how variable a group of species could be when assuming that specimens from the same site could be the same species (Schwartz et al., 2014). They further supported this notion by using GMA to show that the degree of variability in *H. erectus* after adding the Dmanisi group was still tolerable when comparing the degree of variability within *H. erectus* to samples of *H. sapiens* and chimpanzees.

2.5.2 New African *Homo erectus*

Some African specimens discovered after the 1980s were allocated to *H. erectus*. One well-preserved calvaria was the Daka skull (BOU-VP-2/66), which was discovered in 1992. Asfaw (2008) observed that this specimen displayed a mosaic of "typical" *H. erectus* features. As a result of his computerized cladistic analysis, which was based on coding previously described features as discrete states, Gilbert (2008) found that this skull grouped with other *H. erectus* specimens. However, similar to many other paleoanthropologists, Gilbert (2008) was pessimistic about the cladistic approach because it ignored variation as well as supposed genetic, developmental and functional correlations.

Another important African specimen is the small-brained KNM-ER 42700 calvaria recovered from Koobi Fora in 2000. Spoor et al. (2008) allocated it to *H. erectus* since it expressed a list of conventional *H. erectus* features, including frontal and parietal keeling, a shorter occipital plane, a narrow glenoid fossa, and angulation between the tympanic and petrous portions. They also performed a PCA using a few craniofacial measurements to show that this skull was very similar overall to other *H. erectus*. However, Baab's (2008a, 2016) GMA, which focused on gross cranial shapes, revealed that this remain was somewhat distant from most *H. erectus*.

2.5.3 New Asian *Homo erectus*

When China was reopened to the world in the late 1970s, Chinese paleoanthropologists quickly adopted the name *H. erectus* to replace the old name *Sinanthropus* (R. Wu & Dong, 1985; X. Wu & Poirier, 1995). They also lumped many fossils discovered after the 1980s, such as those from Hexian, Yunxian and Tangshan, into *H. erectus* because they displayed a combination of *H. erectus* features

commonly used in other studies (Etler, 1996; Li & Etler, 1992; Liu et al., 2005; R. Wu & Dong, 1985; X. Wu & Poirier, 1995).

Instead of testing the validity of *H. erectus*, Chinese researchers were more interested in fitting their discoveries to scenarios of hominid evolution. For example, Liu et al. (2005) performed a PCA based on seven cranial measurements and found that Nanjing No. 1 plotted closer to specimens from Zhoukoudian, Dmanisi, and Africa than those from Sangiran and Sambungmacan. This result was consistent with the expectation that *H. erectus* was more isolated in Southeast Asia than in Eurasia and Africa, between which there was supposedly more gene flow.

A group of paleoanthropologists who focused on Asian human evolution also endeavored to demonstrate regional continuity between Asian *H. erectus* and Middle Pleistocene "archaic *H. sapiens*", such as from Maba, Xujiayao, and Dali (Bae, 2010; Pope, 1992; Rosenberg & Wu, 2013; Wolpoff et al., 1994; X. Wu & Poirier, 1995; X. Wu & Wu, 1985). These authors showed that the boundary between Asian *H. erectus* and "archaic" *H. sapiens* was blurred because some *H. erectus* specimens displayed several "archaic" *H. sapiens* features and vice versa (Rosenberg & Wu, 2013; X. Wu, 1996). For example, X. Wu (1996) observed an angular torus and a sharply angled occipital bone in the Dali skull, marked postorbital constriction in the Maba cranium, and sagittal keeling in all three Asian Mid-Pleistocene hominids, i.e., from Dali, Maba, and Jinniushan. This "observation" was explained as the result of "mosaic evolution", meaning that different features of *H. erectus* evolved at different rates (X. Wu, 1996). In addition, the evolutionary rate of the same structures also differed in specimens across geographical regions (Rosenberg & X. Wu, 2013; X. Wu, 1996).

There were also a series of new discoveries in Southeast Asia. One is Sangiran IX, recovered in 1993. In the original description, Arif et al. (2002) observed that this skull displayed "a unique combination of characters," including an elongated supraorbital region, narrow vault, and bumped forehead. They concluded that this fossil is best viewed as representing individual variation within the Sangiran-Trinil group.

Another well-preserved cranium is Sambungmacan 3 (SM 3), which was "rediscovered" in a natural history store in New York City (Márquez et al., 2001). Márquez et al. (2001) found that most of SM 3's cranial measurements fell within the range of Javanese *H. erectus*. However, SM 3 also differed from other Javanese *H. erectus* in having no angular torus at the posteroinferior side of the parietal, discontinuous supraorbital tori at glabella, a more obtuse occipital angle, a rounder vault, and a less sloped frontal bone. These differences led the authors to propose that this specimen either represented a new species or an extension of the range of variation of *H. erectus*.

In a subsequent analysis, Delson et al. (2001) ruled out the possibility that SM 3 represented a new species. They showed that SM 3 was most similar to SM 1 and the Ngandong and Ngawi specimens

in having a gracile supraorbital torus, a similar degree of postorbital constriction, a characteristic tympanic-mastoid fissure, and a supramastoid crest separated from the mastoid crest by a sulcus. On the other hand, SM 3 also showed some similarity with "archaic *H. sapiens*". A PCA based on landmark data plotted SM 3 in an intermediate position between *H. erectus* and Asian "archaic" *H. sapiens* groups. Based on these observations, Delson et al. (2001) listed another three possibilities for SM 3: (1) SM 3 represented a population of *H. erectus* evolving toward *H. sapiens*; (2) SM 3 represented a distinct population of *H. erectus* that eventually went extinct; (3) SM 3 was just an "odd" *H. erectus*.

In 2001, the third Sambungmacan skull, SM 4, was discovered (Baba et al., 2003). Based on morphological analysis and PCA, Baba et al. (2003) suggested that this and other Sambungmacan specimens bridged the gap between an older Trinil/Sangiran group and a younger Ngandong-Sambungmacan group, though they were more similar to the latter. Kaifu et al. (2008) supported the view of chronological continuity within the Indonesian *H. erectus* group based on extensive univariate analysis. They also suggested that these late Indonesian specimens did not contribute to Southeast Asian human ancestry because they were too derived in having features such as a laterally thickened supraorbital torus, no postglabellar depression, an extensive angular torus, a special mandibular fossa morphology, and a very projecting occipital torus (Kaifu et al., 2008).

2.5.4 A reappraisal of regional variation in Asian *Homo erectus*

Because the Asian *H. erectus* subset was greatly expanded in the late 1990s, Antón (2002) felt it necessary to reassess the degree and patterns of variability within this group. She concluded that northern Chinese specimens were consistent with the "standard description" provided by Weidenreich (1943), such as having a continuous and straight supraorbital torus, a small mastoid process, and a horizontal occipital torus (Antón 2002, p. 313). Indonesian specimens, though highly variable, consistently deviated from the "standard description" because they displayed prominent shelf-like supraorbital tori projecting mostly in the glabellar region and a supramastoid sulcus, but lacked a supraorbital sulcus or "gutter". Nevertheless, Antón's (2002) PCAs, based on several craniofacial measurements, confirmed that the Indonesian and northern Chinese fossils shared the same "Bauplan" as *H. erectus* because they overlapped greatly and were well separated from *H. sapiens*. In addition, Antón (2002) found that chronological variation within the general Asian group was strongly correlated with an increase in cranial capacity.

When considering this variation within the context of all specimens included in *H. erectus*, Antón (2003) still believed their overall similarity was overwhelming compared to their regional differences. Therefore, she tended to support the single species hypothesis. It should be noted that Antón (2003) seems to have viewed the effort to define *H. erectus* as trivial. Instead, she recommended focusing on

patterns of variation to decipher "more interesting questions of energetics, local adaptation, life history, dispersal, development, and group interaction at boundaries", rather than endless controversies between "lumpers" and "splitters" (Anton, 2003, p. 155).

2.5.5 The application of geometric morphometric analysis (GMA)

In the last two decades, some paleoanthropologists brought in the revolutionary technique of GMA to re-examine the degrees and patterns of overall variability in *H. erectus* and to test its validity as a species (Baab, 2008b, 2016; Delson et al., 2001; Lordkipanidze et al., 2013; Terhune et al., 2007). Proponents believed that GMA has an advantage over linear measurement-based multivariate analyses because landmark data could reflect actual shape variation and was easily visualized for facilitating interpretation (Baab, 2012, 2016; Terhune et al., 2007).

One of the first applications was Delson et al.'s (2001), which suggested that SM 3 was consistent in overall shape with other Indonesian *H. erectus* specimens. Later, Terhune et al. (2007) used discrete landmarks to quantify the overall morphology of the temporal bone. They chose this bone because Lockwood et al.'s (2002) GMA of extant hominoid temporal bones showed groupings consistent with molecular analyses. Interestingly, Terhune et al.'s (2007) statistical analyses revealed that the variability of *H. erectus* was most comparable to differences that separated extant ape taxa. Furthermore, the distance between Asian and African *H. erectus* was greater than between geographical subsets within *H. sapiens* or ape species. This is the only statistical analysis that supports splitting *H. erectus* into two species.

Baab (2008a, 2008b, 2016) also performed a series of GMAs that used discrete landmarks to quantify the overall cranial shapes of *H. erectus*. Her analyses showed that, in general, *H. erectus* was less variable than many extant taxa, including chimpanzees, gorillas, *H. sapiens* and some other anthropoids. In another recent analysis, Lordkipanidze et al. (2013) showed that after adding Dmanisi specimens, *H. erectus* was still less variable than *H. sapiens* and chimpanzees. They went on to support the idea of there being only one species at any time during human evolution.

Importantly, these GMAs apply only discrete landmarks and thus can capture gross shapes but not details (Baab, 2016; Schwartz et al., 2014; Spoor et al., 2008; Villmoare, 2005). Some researchers also relied on commonly used *H. erectus* descriptive features to show the morphological relevance of their data (Baab, 2008a, 2008b, 2016; Terhune et al., 2007). For example, Baab (2016) found that she was able to capture features that separated *H. erectus* from *H. sapiens*, such as a sloped frontal, prominent brows, and greater postorbital constriction, as well as those that differentiated *H. erectus* from early *Homo*, including a longer and lower cranium, greater posterior placement of inion, and a wider

neurocranium. Nevertheless, she stated that her analysis did not capture other specific features, such as parietal bossing and an angular torus.

2.6 ALTERNATIVE HYPOTHESES ABOUT *HOMO ERECTUS*

2.6.1 Indonesian mandibular remains

There are still alternative views regarding the definition of *H. erectus*. Some paleoanthropologists have proposed possible taxic diversity within the Javanese mandibular remains. For example, Tyler (1994, 1996) showed that the Javanese mandibles were statistically more variable than in gorillas. Krantz (1975, 1994) argued that the S 4 and S 5 mandibles represented a distinct species, *Pongo brevirostris*, because they exhibited some orangutan-like features and tooth wear patterns. However, his view was rejected by Durband (2008), who also used the Dmanisi group as an example to show how variable *H. erectus* could be.

Kaifu et al. (2005, p. 518) also argued that "the multiple-species hypothesis cannot be dismissed easily" after showing that Indonesian mandibular remains found between 1956 and 1986 could be divided into a "gracile" group and a "robust" group, each of which had distinct features. In particular, they observed that within the robust group, most specimens displayed a ridge that demarcated the anterior border of the masseteric fossa. Interestingly, the observing of a similar ridge in both S 5 and S 9 led von Koenigswald (1948, 1968) to allocate them to *Pithecanthropus dubius*.

2.6.2 Cladistic analyses

Although cladistic analysis has suffered much criticism, some applications continue to suggest taxic diversity within *H. erectus*. For example, Widianto and Zeitoun's (2003) computerized cladistic analysis based on 127 coded characters showed that the Ngawi 1, Sambungmacan, and Ngandong specimens belonged to one clade (Sambungmacan-Ngandong series), while the Trinil and Sangiran specimens constituted another (Sangiran-Trinil series). Consequently, Widianto and Zeitoun (2003, p. 347) pointed out that only "the Trinil-Sangiran series, including the type specimen Trinil 2, can be considered as the only *Homo erectus* in the strict sense". However, they identified the Sambungmacan-Ngandong series as "advanced *Homo erectus*" and the Sangiran-Trinil series as "classical *Homo erectus*" (p. 348).

Zeitoun (2009) himself realized the necessity of using his own morphological observation in a cladistic analysis and treating each specimen as an operational unit. His cladogram showed Trinil 2, the Sangiran specimens S 2, S 12, and S 17, and KNM-WT 15000 forming a clade because of shared-derived features, such as similar degree of postorbital constriction, large temporal band on the frontal bone, somewhat "squat" upper parietal with the superior longer than the inferior length, and occipital torus continuous with the superior temporal line. Among other specimens, because ZKD III was a distinct clade, he allocated it to the new species, *Homo pekinensis*. ZKD XI grouped with the Bodo skull, Petralona 1, and the Arago skull, which were together referred to archaic *H. sapiens*. The Ngandong specimens, Ngawi 1, and Sangiran 4 formed a distinct morph, *H. soloensis*. On the other hand, the "*H. ergaster*" crania, KNM-ER 3733, KNM-ER 3883, and KNM-WT 15000, were assigned to different groups. Although Zeitoun (2009) admitted it was too early to transform this cladogram into a formal Linnaean classification, he suggested that the marked taxic diversity subsumed in genus *Homo* should not be ignored.

Schwartz (2004, 2016; Schwartz & Tattersall, 2000) called for a radical reappraisal of the definition of *H. erectus* based strictly on the unique features of the type specimen, Trinil 2. Schwartz (2004, 2016) observed that only Sangiran cranial specimens (except for S 17 and S IX) displayed the same set of unique features seen in Trinil 2, e.g., a pair of depressions delineating the "sagittal keeling" and a supraorbital torus that flows continuously into the gently sloping forehead. In this way, only Trinil/Sangiran specimens could reliably be called *H. erectus*. In addition, in S 2 and 4, in which the petrotemporal region was well preserved, the sigmoid sinus arborized before draining into the jugular foramen. Accordingly, other specimens are not *H. erectus*.

2.7 CONCLUDING REMARKS

This review has showed that a series of "standard" *H. erectus* features (Antón, 2002, p. 313) have been "recycled" or reused from one paleoanthropological study to another in studies addressing the taxonomic validity of *H. erectus*. These features include a shelf-like and continuous supraorbital torus, long and low cranium, small and inwardly oriented mastoid process, sagittal keeling, angular torus, straight occipital torus, sharply angled occipital bone, mastoid fissure, and supramastoid sulcus (e.g., Antón, 2002, 2003; Cartmill and Smith, 2009; Rightmire, 1993; Wood, 1984). For example, as reviewed in this chapter, specimens such as the Dmanisi skulls, Sangiran IX, and KNM-ER 42700 are grouped into *Homo erectus* because they more-or-less exhibit a combination these features (e.g., Arif et al., 2002; Rightmire et al., 2006; Spoor et al., 2008; Vekua et al., 2002). By assessing features such as "long, low

cranium", "angular torus" and "sharp occipital flexure", some scholars even proposed that the boundary between *Homo erectus* and Mid-Pleistocene "archaic" *Homo erectus* is blurred (e.g., Rosenberg & X. Wu, 2013; X. Wu, 1996).

The fact that these descriptions of *Homo erectus* features have been reused in many studies reveals that detailed morphological analysis of the actual specimens has been insufficient. As discussed in this chapter, the investigation of a morphological definition of *Homo erectus* was stimulated by several cladistics analyses conducted in the 1980s (e.g., Andrews, 1984; Wood, 1984), which suggested that splitting *H. erectus s. l.* into distinct Asian and an African species was also based on assessing the presence of features cited in previous literates (e.g., "long, low cranium", "angular torus", and "sharp occipital flexure") in *H. erectus* specimens. Subsequent studies that argued that *H. erectus* should not be split into multiple species only focused on how variable such features could be (e.g., Bräuer and Mbua, 1992; Rightmire, 1993). However, descriptions of these commonly cited *H. erectus* features are usually very generalized and not well defined (Wood, 1993; Schwartz and Tattersall, 2001; Zeitoun, 2009). Some morphological studies that scrutinize original specimens without relying on previous descriptions continue to show that species diversity within the conventional *H. erectus* group should not be ignored (e.g., Schwartz, 2004; Zeitoun, 2009). Yet, these studies are usually ignored.

Recent GMAs almost unanimously support the single species hypothesis of *H. erectus* (e.g., Baab, 2008a, 2016; Lordkipanidze et al., 2013). These analyses have been criticized for focusing on gross shape rather than on morphological detail (Schwartz et al., 2013; Spoor et al., 2008; Villmoare, 2005). One reason is that researchers only cited *H. erectus* features summarized in previous analyses to check the extent of morphological features can be captured by their landmark datasets. Consequently, little attention has been paid to alternative ideas of species diversity within *H. erectus* that are based on the morphological details of actual specimens.

This study aims to explore the potential of GMA in capturing and detecting morphological details and assess how results of statistical analyses can be influenced if more morphological details are included. To serve these goals, it is necessary to thoroughly study morphology of *Homo erectus* specimens. Consequently, the following chapter provides a detailed description of morphology of the *H. erectus* specimens used in this study.

3.0 MORPHOLOGY OF SPECIMENS COMMONLY ALLOCATED TO *HOMO ERECTUS*

3.1 INTRODUCTION

As discussed in the Preface and first chapter, a major goal of this dissertation is to use landmark data to capture and identify detailed morphology. Therefore, it is important to first have a thorough understanding of morphology. Consequently, in this chapter, I critically examine and synthesize previous descriptions based on well-made casts in the Physical Anthropology Laboratory of the University of Pittsburgh. The specimens listed in this chapter are used in the following statistical analyses (see Table A.1 in Appendix A). The morphologies I focus on are those that can be potentially captured using semilandmarks and landmarks.

3.2 OVERALL PROFILE

The overall cranial profile of *H. erectus* is usually described as "long and low", reflecting such features as a flat and receding frontal, short and flat parietal, and sloped occipital plane with sharp angulation (Antón, 2003; Baab, 2016; Cartmill & Smith, 2009; Rightmire, 1993; Stringer, 1984; Weidenreich, 1943; Wood, 1984). In superior view, postorbital constriction is usually marked. In posterior view, the low and wide cranium is widest at the level of the supramastoid crest (Antón, 2003; Cartmill & Smith, 2009; Rightmire, 1993; Stringer, 1984; Weidenreich, 1943; Wood, 1984).

Other details are noteworthy (Schwartz & Tattersall, 2003). Trinil 2 and S 2 (and other Sangiran specimens except S 17) share a unique overall profile (Schwartz, 2004, 2016; Schwartz & Tattersall, 2003). In lateral view, the frontal squama is long and flat, peaking at a posteriorly situated bregma. The parietal is flat along its anterior half. It then curves gently down and back toward the occipital flexure, which is uniquely "V-shaped" because the occipital and nuchal planes are both relatively flat and form the same angle with the transverse plane (Schwartz, 2004, p. 53; Schwartz & Tattersall, 2003, p. 484). Overall, the rear profile is uniquely "wider mediolaterally than superoinferiorly tall" (Schwartz, 2016, p.

95; Schwartz & Tattersall, 2003). The almost flat roof curves down nearly at a right-angle midway across the parietal width into the slightly outwardly inclined side wall (Schwartz, 2016; Schwartz & Tattersall, 2003). The rear profile then tilts inward at the level of the parietal notch (Schwartz & Tattersall, 2003). In superior view, the postorbital constriction is not marked as the lateral brows and orbits do not significantly flare out (Schwartz & Tattersall, 2003). The superior profile is widest above the mastoid region and curves medially into the anteroposteriorly short occipital region

S 17 has a very long, low, and flat frontal that peaks at bregma, which is relatively posteriorly placed, level with the articular eminence (Schwartz & Tattersall, 2003). The lateral profile then gently curves downward toward the occipital flexure, which lies below asterion (Schwartz & Tattersall, 2003). Lambda is fairly low (Kaifu et al., 2008). The nuchal plane is nearly horizontal, and the occipital plane is nearly vertical, such that the occipital flexure is not V-shaped (Schwartz & Tattersall, 2003). In rear view, the slightly sloped, flat roof curves via a distinct and somewhat obtuse angle at the midwidth of the parietal into the slightly outwardly tilted side wall (Schwartz & Tattersall, 2003). The rear profile then curves inward at the level of the supramastoid crest. In superior view, the contour of the brow curves gently backward from the glabellar region. A small lateral part of the orbit flares out from the frontal squama, and postorbital constriction is moderate. The superior profile is equally wide at both the supraorbital and supramastoid regions.

The Ngandong specimens have a taller profile overall (Schwartz and Tattersall, 2003). In lateral view, the slightly curved frontal profile rises relatively steeply. The lateral profile peaks at the weak bregmatic eminence, from which the contour flattens along the anterior half of the parietal and then curves gently downward. From the fairly low-placed, bulging lambda, the profile becomes even more vertical before the occipital angle, which is roughly at the same level as asterion. The nuchal plane is relatively less downwardly inclined (Schwartz & Tattersall, 2003). The coronal profile is tall, narrow, and rounded (Schwartz & Tattersall, 2003). In rear view, the downwardly sloping roof curves smoothly into the slightly outwardly tilted side wall roughly at the temporal line. From the superior mastoid portion behind the meatus, the rear profile proceeds down and slightly inward. In superior view, the supraorbital contour is flat across the glabellar region, curving slightly backward in the lateral halves. The postorbital constriction is relatively weak (Schwartz & Tattersall, 2003). The posterior contour at the supramastoid crest is slightly wider than the supraorbital region. SM 3 has a similar contour, though it is smaller and rounder.

ZKD 11 has an overall long and low neurocranium, but it differs from the Indonesian specimens in many details (Schwartz & Tattersall, 2003). In lateral view, the frontal bone is highly arched because it first rises nearly vertically behind the posttoral sulcus and then curves slightly downwardly to peak at bregma (Schwartz & Tattersall, 2003). The profile then becomes flat and horizontal along the anterior

half of the parietal and then curves gently downward to course straight to lambda. From there, the profile becomes nearly vertical before reaching the occipital angle, which lies slightly higher than the parietomastoid notch but level with asterion (Schwartz & Tattersall, 2003). The long nuchal plane is downwardly inclined, but the occipital angle is not as perfectly V-shaped as in Trinil 2 and Sangiran 2 (Schwartz & Tattersall, 2003). From the midline, the somewhat downwardly sloping roof curves smoothly into the flat and somewhat outwardly tilted side wall via a very obtuse angle level with and medial to the temporal line (Schwartz & Tattersall, 2003). At the height of the supramastoid crest, the rear profile tilts inward. Overall, the coronal profile is wide and low, but not as extreme as in Trinil 2 and Sangiran 2 (Schwartz & Tattersall, 2003). In superior view, the contour of the brow is nearly straight across the glabellar region. Postorbital constriction is moderate as only the lateral margin of the orbit flares out. The cranium is widest across the supramastoid regions. The occipital region is relatively long anteroposteriorly (Schwartz & Tattersall, 2003).

ZKD 12's profile is rounder than ZKD 11. The frontal rise is less steep. The contour curves smoothly up and back, peaks at bregma, and then curves smoothly down and back. It becomes more vertical at the occipital squama until reaching the occipital angle, which lies slightly higher than asterion. The rear profile is even somewhat roundedly triangular because the side wall is relatively more outwardly tilted. The lateral end of each brow curves slightly back, but overall, the superior profile still resembles ZKD 11 (Schwartz & Tattersall, 2003).

In D2700, the frontal squama is flat, receding, and relatively long. From bregma, the lateral contour curves down and back across the parietal. From lambda, this contour curves sharply down, becoming nearly vertical before reaching the occipital flexure, which lies lower than the parietomastoid suture. The nuchal plane is nearly horizontal. The rear profile resembles ZKD 11, though the roof is slightly more horizontal. Overall, the superior profile is short anteroposteriorly. The brows angle straight back from glabella. Postorbital constriction is marked. The vault is widest across the supramastoid regions, which is relatively anteriorly placed.

Although the cranial roof is quite broken, OH 9's lateral profile is fairly tall and rounded (Schwartz & Tattersall, 2003). The frontal squama rises fairly steeply; it curves back just anterior to bregma (Schwartz & Tattersall, 2003). The rest of the inferior occipital squama is nearly vertical. The nuchal plane also slopes strongly downward (Schwartz and Tattersall, 2003). The posterior profile is "roundedly triangular" (Schwartz, 2004, p.54). The very outwardly tilted side wall curves only in the mastoid region posterior to the midpoint of the auditory meatus. In superior view, the brow angles gently back from the depressed glabellar region, curving more strongly back at the lateral end. The brow flares remarkedly outward such that the width of the supraorbital region is greater than the relatively posteriorly positioned supramastoid region.

KNM-ER 3733 also has a fairly tall and rounded vault. In lateral view, the frontal profile rises in a relatively straight up course and then curves back to peak slightly anterior to bregma (Schwartz and Tattersall, 2003). From there, the profile curves smoothly back and down and becomes more vertical after passing beyond the fairly inferiorly positioned lambda. Thus, the posterior vault is superoinferiorly shorter than the frontal region (Schwartz and Tattersall, 2003). The nuchal plane is only slightly downwardly inclined. The occipital angle is higher than the parietomastoid suture. In posterior view, the roof is curved. It flows smoothly via an obtuse angle into the slightly outwardly tilted side wall, which only curves to become nearly vertical posterior to the middle of the auditory meatus. In superior view, the brow courses roughly straight across glabella and then curves back laterally to the highest point of the superior margin. Postorbital constriction is marked. The maximum width occurs in both the supraorbital and the supramastoid regions.

KNM-ER 3883 has a long and low neurocranium. The frontal is fairly long, low and only slightly domed. The lateral profile curves smoothly to become more horizontal across bregma and peaks near the middle of the parietal (Schwartz and Tattersall, 2003). From there, the contour curves down to the bulge at lambda and then becomes nearly vertical along the short occipital plane. Thus, overall the cranium is superoinferiorly shorter at the anterior half and expands superoinferiorly at the posterior half (Schwartz and Tattersall, 2003). The lateral profile angles into the moderately downwardly sloping nuchal plane via an obtuse angle roughly level with the parietomastoid suture. In posterior view, the roof curves gently across the midline and then into the slightly outwardly tilted side wall. The profile tilts inward inferior to the supramastoid region. The rear profile is wide and fairly low but again not as extreme as Trinil 2 and Sangiran 2. In superior view, the brow region is flat across glabella and curves backward lateral to mid-orbit (Schwarz and Tattersall, 2003). Postorbital constriction is marked. The supraorbital region is slightly narrower than the posteriorly positioned supramastoid region.

KNM-WT 15000 has a rounded, low, and fairly long neurocranium (Schwartz and Tattersall, 2003). The frontal profile rises gently and then curves smoothly into bregma. The profile then becomes flat and horizontal across the anterior half of the parietal. From there, it curves steeply across lambda into the short and somewhat inclined occipital plane. The fairly large occipital angle lies inferior to the parietomastoid suture (Schwartz and Tattersall, 2003). In posterior view, the profile is similarly tall superoinferiorly and wide mediolaterally. The roof curves slightly across the midline and then angles smoothly into the slightly outwardly tilted side wall, which then tilts inward below the supramastoid region. In superior view, postorbital constriction is moderate. The profile is widest across the supramastoid region, which is fairly posteriorly positioned.

3.3 THE SUPRAORBITAL REGION

H. erectus is usually described as having a robust, straight, and bar-like supraorbital torus that is continuous over a similarly configured glabellar region (Andrews, 1984; Antón, 2003; Baab, 2016; Cartmill & Smith, 2009; Lordkipanidze et al., 2006; Rightmire, 1993; Stringer, 1984; Wood, 1984). The tori are usually described as "shelf-like", suggesting they protrude over the orbits and create a supraorbital plane (Antón, 2002, 2003; Baab, 2016; Cartmill and Smith, 2009; Rightmire, 1993). This plane is frequently hollowed such that there appears to be a posttoral sulcus running bilaterally (Andrews, 1984; Antón, 2003; Baab, 2016; Cartmill and Smith, 2009; Rightmire, 1990; Stringer, 1994; Wood, 1984). These descriptions are derived from Weidenreich (1943), who reported that the Zhoukoudian specimens consistently possessed a frontal torus that is confluent across an equally configured glabellar region, and is well separated from the frontal squama by a furrow. Some paleoanthropologists also commented on how variable this region is in thickness and configuration of the sulcus (Antón, 2002, 2003; Baab, 2016; Rightmire, 1990; Stringer, 1984; Wood, 1984).

Schwartz and Tattersall (2003), however, criticized paleoanthropologists for making the term "supraorbital torus" a "blanket term" that conceals morphological differences. The term should apply to a supraorbital rim with a defined superior margin (Schwartz and Tattersall, 2003). Specimens of the Trinil 2-Sangiran (except Sangiran 17) morph do not have an isolated torus as the supraorbital region flows smoothly into the frontal squama through a very short posttoral plane (Schwartz, 2016). Viewed from above, the ledge-like brows of Trinil 2 are straight across (Antón, 2002; Schwartz and Tattersall, 2003).

Differing from other Sangiran specimens, S 17 has flat and moderately long posttoral and postglabellar planes (Schwartz, 2016). The somewhat arched supraorbital tori are uniformly thick and confluent across the slightly concave glabellar region, which protrudes more anteriorly than in other Sangiran specimens (Schwartz and Tattersall, 2003). The descending and ascending parts of each brow of S 17 are quite straight (Schwartz and Tattersall, 2003). The surfaces of the tori and glabellar regions are superoinferiorly tall, flat, and anteriorly facing.

The Ngandong specimens have morphologically consistent supraorbital regions, i.e., their supraorbital tori are truly bar-like and straight, and thicken laterally (Santa Luca, 1980; Schwartz and Tattersall, 2003). From the midline, the medial ascending part of each torus is short, such that the highest point of each brow is very medially placed. The glabellar region is variably depressed. A postglabellar plane is absent because the glabellar region is confluent with the frontal squama. The posttoral plane is a slightly hollowed triangular plateau (Santa Luca, 1980). The supraorbital regions of Ngawi 1 and SM 3 are similar.

The Zhoukoudian specimens are usually described as having a shelf-like supraorbital torus that is continuous across glabella and a posttoral sulcus that is confluent with the postglabellar plane (Antón, 2002; Santa Luca, 1980). In ZKD 11, the tori are straight across, thin superoinferiorly, and somewhat thickened laterally (Schwartz and Tattersall, 2003). The highest point of the superior margin is rather medially placed. The posttoral plane is moderately long and slightly concave before rising sharply into the frontal (Schwartz and Tattersall, 2003). This plane gradually elongates anteroposteriorly toward the lateral end; it is more concave at the slightly downwardly sloping postglabellar plane (Antón, 2002; Schwartz and Tattersall, 2003). In ZKD 12, the tori and glabellar region are relatively thick superoinferiorly; their anterior surfaces are relatively flat and anteriorly facing (rather than ridge-like as in ZKD 11). The torus is slightly arched and in general uniformly thick, with the highest point positioned slightly medial to the midpoint of the orbit (Schwartz and Tattersall, 2003). The posttoral sulcus is more pronounced than ZKD 11 because the sharper superior margin of the torus protrudes more superiorly.

Rather than actual supraorbital tori, juvenile D2700 has slightly superoinferiorly thickened supraorbital rims without defined superior margins. The laterally thinning brows are somewhat arched, following the contours of the orbits. The surface above the wide and shallow supraorbital notch is concave. Lateral to the somewhat medially placed highest point of the superior margin, the supraorbital rim is less developed. Its surface flows backward and is confluent with the horizontal posttoral plane, which also flows smoothly into the frontal squama. The more anteriorly protruded glabellar region is relatively robust; its lateral profile is nearly vertical such that nasion is not inwardly hidden. The postglabellar plane is slightly sloping and is continuous with the frontal squama.

OH 9 has very robust tori, which are, in general, straight across, uniformly thick superoinferiorly, and very anteriorly protruding (Schwartz and Tattersall, 2003). The ascending medial part is very short mediolaterally and thickened laterally; its peak is lies roughly above the superomedial corner of each orbit. Lateral to its peak, the brow is uniformly thick superoinferiorly. The glabellar region is broad and strongly concave (Schwartz and Tattersall, 2003). In superior view, it is depressed relative to the adjacent brows. The posttoral plane is anteroposteriorly long and horizontal, confluent with the similarly anteroposteriorly long, but deeper and slightly downwardly sloped postglabellar plane (Anton, 2002). There is no posttoral sulcus, and the posttoral plane is not sharply contrasted with the moderately steep frontal rise. The supraorbital surface is rounded and essentially anteriorly facing.

The three *H. ergaster* specimens have very different supraorbital morphologies. KNM-ER 3733 has double-arched brows that are uniformly thin superoinferiorly, and that protrude both anteriorly and superiorly (Schwartz and Tattersall, 2004; Wood, 1991). The uniformly anteroposteriorly long posttoral sulcus is well formed and deepest in the also anteroposteriorly long postglabellar region. Behind the sulcus, the frontal rise is quite steep. The brow's anterior surface is rounded and anterosuperiorly facing.

It also bears a blunt tubercle just lateral to the shallow supraorbital notch, from which a distinct concavity courses upward (Schwartz and Tattersall, 2003). In superior view, the supraorbital tori are confluent across the depressed glabellar region, such that only the lateral ends of the tori curve backward (Wood, 1991). The lateral glabellar profile goes inward to reach the nasion (Schwartz and Tattersall, 2003).

KNM-ER 3883's brows are slightly arched; they thin markedly laterally (Schwartz and Tattersall, 2003; Wood, 1991a). The brows are confluent across the slightly concave glabellar region (Schwartz and Tattersall, 2003). The highest point of the superior margin lies medial to the midpoint of the orbit. On each side, the moderately anteroposteriorly long posttoral plane is flat and horizontal, connected by a flat, slightly concave, downwardly sloped postglabellar plane that is confluent with the low frontal squama (Wood, 1991a).

Most of KNM-WT 15000's supraorbital region is broken. The preserved left lateral end shows that the torus is somewhat tall superoinferiorly and appears to be uniformly thick (Schwartz and Tattersall, 2003). Contrary to Walker and Leakey's (1993) description, KNM-WT 15000 does not have a clearly developed posttoral sulcus; rather, the brows only protrude anteriorly, creating a posttoral plane rather than a sulcus.

3.4 FRONTAL SQUAMA AND KEEL-LIKE STRUCTURES

Specimens of *H. erectus* are frequently described as possessing various keel-like structures, i.e., frontal, coronal, and sagittal keels, as well as a bregmatic eminence (Baab, 2016; Rightmire, 1993; Stringer, 1984; Weidenreich, 1943; Wood, 1984). Other authors also mentioned that several *H. erectus* specimens show a cruciate bregmatic eminence, suggesting confluence between frontal, coronal, and sagittal keels at bregma. The sagittal keel is usually with a "parasagittal depression", which makes the vault look flat. Andrews (1984) in particular emphasized that frontal keeling might be unique to *H. erectus* in Asia.

The presence and morphology of these keel-like structures are certainly very different between relevant specimens. Trinil 2 and the Sangiran specimens' frontal "keel" is unique in being defined by a pair of anteroposteriorly long and mediolaterally wide depressions in the frontal squama (Schwartz, 2004, 2016). These specimens also exhibit a faint bregmatic eminence that does not extend bilaterally into coronal keels or posteriorly into a sagittal keel, though a pair of small depressions are located posterior to bregma. These depressions make the parietal bones appear flat in lateral view. S 17 has no apparent frontal keel but displays a low and wide bregmatic eminence with a pair of faint lateral "arms", as well as

a short and indistinct sagittal extension (Santa Luca, 1980). Some parasagittal hollowing is observed posterior to bregma.

According to Santa Luca (1980), the Ngandong specimens are unique in having a frontal keel that is separated from the bregmatic eminence, while the coronal keel and sagittal keel form a T-shaped structure. These structures are actually variably expressed (Schwartz and Tattersall, 2003; Santa Luca, 1980). Another interesting feature of the Ngandong specimens is a depression in the posterior parietal region that terminates at lambda. SM 3 is a gracile skull with a faint sagittal keel bounded by a pair of parasagittal hollowed areas. There is no coronal keel. A depression is also present but less prominent in the posterior parietal region.

ZKD 11 and ZKD 12 present a low frontal keel at the midline that begins at the middle of the frontal squama and extends to the bregmatic eminence, which is very low, without apparent lateral extensions (Santa Luca, 1980). The parasagittal depression behind the bregmatic eminence is faint. A low and short sagittal keel extends from the bregmatic eminence and terminates before reaching the middle of the sagittal suture (Santa Luca, 1980; Schwartz and Tattersall, 2003).

D2700 has a low and flat frontal squama with no midline keeling. The frontal bone is more elevated than the parietal bone along the coronal suture. However, there is no bregmatic eminence. The low sagittal keel that emanates from bregma is bounded on each side by a small flattened area. The keel is initially faint but becomes more marked along the posterior third of the sagittal suture, where the parietal regions on the two sides flatten.

KNM-ER 3733 does not have a typical frontal keel, but it does have a distinct swelling, or "keel-like pre-bregmatic bulge", anterior to bregma (Schwartz and Tattersall, 2003, p. 143). Otherwise, the generally rounded vault lacks a bregmatic eminence and coronal and sagittal keels, as is also the case in KNM-ER 3883 and KNM-WT 15000 (Schwartz and Tattersall, 2003).

3.5 THE OCCIPITAL TORUS

A frequently mentioned feature of *H. erectus* is a variably expressed bar-like "transverse occipital torus", which was used by Weidenreich (1943) in describing the Zhoukoudian specimens (Antón, 2003; Baab, 2016; Rightmire, 1993; Stringer, 1984; Wood, 1984). Cartmill and Smith (2009, p. 244) preferred the term "nuchal torus", which they defined as a "thickening of the vault where the neck muscle attaches". Rightmire (1993) also noted that the lower border was defined by the nuchal lines. Furthermore, there is no external occipital protuberance (Baab, 2016; Cartmill and Smith, 2009; Rightmire, 1993) but sometimes a linear tubercle produced by the convergence of right and left superior

nuchal lines (Rightmire, 1993). The upper border is supposed to be defined by a supratoral sulcus (Cartmill and Smith, 2009; Wood, 1984). Asfaw (2008) emphasized the variability of the occipital torus, which could be uniformly thick and "bar-like", more pronounced in the midline, or double arched (Asfaw, 2008).

On the other hand, Schwartz and Tattersall (2003) pointed out that the term "occipital torus" has been mistakenly used for a condition in which the occipital plane is undercut by the nuchal lines. Instead, the term "occipital torus" should be used to refer to a "raised bar" of bone (Schwartz and Tattersall, 2003). Following this definition, the Trinil-Sangiran morph represented by Trinil 2 and S 2 does not have a true occipital torus. These specimens present only a concave suprainiac region on the midline above the faint nuchal lines (Schwartz and Tattersall 2003). The occipital angle is very obtuse and extends to the supramastoid region (Schwartz and Tattersall, 2003).

In S 17, there is a weak and blunt occipital torus. Its superior border is delineated by a faint supratoral sulcus across the width of the occipital squama, similar to the Zhoukoudian specimens. The torus is delineated inferiorly by a sulcus that courses across the width of the nuchal plane (Schwartz and Tattersall, 2003). A linear tubercle is absent. The nuchal undercut is moderate, and the nuchal plane is flat.

In all Ngandong specimens, the occipital torus is well developed, though its prominence varies (Schwartz and Tattersall 2003). The torus is most protrusive and thickest at the midline. The suprainiac fossa is short superoinferiorly; it becomes shallower laterally until reaching a depression that is bounded laterally by a raised bony plateau around asterion. The occipital torus extends laterally to join this plateau slightly medial to asterion. The torus also varies from horizontally protruding to inferiorly protruding; and it is delineated inferiorly by deep undercut of nuchal muscles (Schwartz and Tattersall, 2003). The two curved nuchal lines join at the midline to produce a prominent external occipital protuberance. Therefore, on each side, the inferior border of the torus appears bow shaped. This explains why Asfaw (2008) described the occipital torus of the Ngandong specimens as double-arched. In SM 3, the morphology of the occipital torus is similar to the Ngandong specimens, but less prominent. Ngawi 1 also presents an occipital torus similar to that in the Ngandong specimens (Schwartz and Tattersall, 2003).

In ZKD 11, the occipital torus swells out and is delineated superiorly by a narrow and shallow sulcus that runs across the most of the occipital squama; it diminishes gradually laterally (Schwartz and Tattersall, 2003). It is poorly delineated inferiorly by a nuchal undercut (Schwartz and Tattersall, 2003). The torus is uniformly thick overall; it is only slightly superoinferiorly thicker and more protruding at the midline (Asfaw, 2008). In ZKD 12, the more pronounced occipital torus is also weakly delineated inferiorly by a nuchal line that courses straight across the width of the nuchal plane. Overall, the torus is not as raised as in the Ngandong specimens.

In juvenile D2700, there is no torus. The surfaces of the occipital squama and nuchal plane are quite smooth. OH 9 also does not possess a true occipital torus, though the inferior border of the occipital plane is undercut by strong nuchal muscles markers. An occipital torus is not found in KNM-ER 3733, KNM-ER 3883 or KNM-WT 15000. However, in KNM-ER 3733, there is a slight bulge in the middle of the occipital flexure.

3.6 ANGULAR TORUS

H. erectus is usually described as variably possessing an angular torus on each parietal (Antón, 2003; Baab, 2016; Cartmill and Smith, 2009; Rightmire, 1993; Stringer, 1984; Wood, 1994). The angular torus is defined as a posterior expansion of the temporal line at the parietal mastoid angle or near the lambdoid suture (Asfaw, 2008; Cartmill and Smith, 2009; Rightmire, 1993). Andrews (1984) argued that an angular torus may be unique to Asian *H. erectus* rather than any African counterpart, though others have claimed that this feature is variably expressed in both the Asian and African subsets (e.g., Bräuer & Mbua, 1992).

Santa Luca (1980) believed that the Ngandong specimens had a unique version of an angular torus, which he described as a "flat, plateau-like swelling of the posterior part of the superior temporal line" (Santa Luca, 1980, p. 102). This triangular plateau is so extensive that it not only covers the region between the superior temporal line near the parietomastoid angle and the parietal notch, it also extends across the lambdoid suture to meet the lateral arm of the occipital torus (Santa Luca, 1980). On each side, this plateau bounds a depression medial to asterion. SM 3 also presents a similar morphology in this region. Most likely because it is more gracile, the depression medial to the plateau is not marked.

In both ZKD 11 and ZKD 12, the temporal line terminates in a small bulge at the parietal notch (Santa Luca, 1980). It is most prominent just above asterion. The Euro-African specimens do not possess an angular torus or significant thickening in the posterior portion of the temporal line. Specifically, in OH 9, the temporal line bifurcates at its posterior extremity (Schwartz and Tattersall, 2003). The superior line curves downward to reach the upper border of the mastoid portion of the temporal. The inferior line curves anteroinferiorly toward the parietal notch. However, no raised plateau or bulge is produced in between.

3.7 SUPRAMASTOID, SUPRAMEATAL, AND MASTOID CRESTS AND THE "GENERAL REINFORCEMENT SYSTEM"

H. erectus is usually described as presenting "well-developed or marked" mastoid and supramastoid crests, which are either separated from each other by a supramastoid sulcus or in some cases fused (Antón, 2003; Asfaw, 2008; Baab, 2016; Rightmire, 1993; Stringer, 1984; Wood, 1984). These two crests, the suprameatal crest that overhangs the acoustic meatus, the angular torus, and the occipital torus, which are overall connected with each other, represent the "generalized hypertrophy" of the *H. erectus* cranium (Antón, 2002; Cartmill and Smith, 2009; Rightmire, 1993; Wood, 1984). Weidenreich (1943) originally used the term "basal series of the general reinforcement system" to refer to the confluence of these hypertrophic structures, as well as the supraorbital torus, as a characteristic of *Sinanthropus*, *Pithecanthropus,* and *Homo soloensis*.

Nevertheless, the development and configuration of the supramastoid and mastoid crests as well as whether or how they are connected with the angular and occipital torus are not the same in all specimens of *H. erectus* (Santa Luca, 1980; Schwartz and Tattersall, 2003). In most of specimens, the supramastoid crest courses obliquely upward from the suprameatal crest, terminating at the squamosal suture just anterior to the deepest point of the parietal notch. In S 2, S 17, ZKD 11, and ZKD 12, the supramastoid crest and mastoid "bulge" form a Y-shaped elevated area. In Ngandong specimens, the two blunt, raised crests, though separated by a sulcus, form an elevated area that is confluent with an "angular torus".

In the majority of specimens, the supramastoid crest flows somewhat obliquely upward from the suprameatal crest. In OH 9, however, the low and obliquely oriented suprameatal crest curves somewhat inferiorly into a more-or-less horizontal and less developed supramastoid crest. The mastoid crest is a blunt bony ridge that is more elevated than the supramastoid crest. They merge into a single crest that courses to meet the parietal notch, and are confluent with the anterior arm of the bifurcated posterior temporal line (Schwartz and Tattersall, 2003). In many specimens, the suprameatal crest is shelf-like. In KNM-ER 3733, this structure is quite thin superoinferiorly and the supramastoid crest is also nearly horizontal. KNM-WT 15000 has a very superoinferiorly thick, low and horizontally oriented suprameatal crest that curves upward into the extremely large and obliquely oriented supramastoid crest.

3.8 THE GENERAL CONTOUR OF THE TEMPORAL BONE

The temporal bone of *H. erectus* is usually described as long and low with a straight squamosal suture (Antón, 2003; Asfaw, 2008; Baab, 2016; Cartmill and Smith, 2009; Rightmire, 1993; Stringer, 1984; Weidenreich, 1943; Wood, 1984). Schwartz and Tattersall (2003) also focused on several aspects of the squamous temporal, such as the position of the tallest point, the shape of the upper border, the depth and shape of the parietal notches, and the contour of the parietomastoid suture.

S 2 has a long and low squamosal. The slightly posteriorly sloping sphenotemporal suture curves smoothly into the overall horizontal and straight squamosal suture (Schwartz and Tattersall, 2003). The parietal notch is very shallow. The parietomastoid suture is very short and essentially horizontal; it is only slightly arced at its midpoint. The mastoid portion and asterion are lower than the lateral end of the occipital flexure. Relative to the squamosal portion, the mastoid portion is short anteroposteriorly but tall superoinferiorly.

S 17's sphenotemporal suture curves smoothly into the squamosal suture (Schwartz and Tattersall, 2003). The squamosal suture peaks anteriorly, close to pterion, and then gently courses down to the wide and shallow parietal notch. A very short vertical component of the squamosal suture bounds the notch anteriorly. The mastoid portion is shorter anteroposteriorly and less tall superoinferiorly, with a straight parietomastoid suture.

In Ngandong specimens, the nearly vertical sphenotemporal suture curves sharply into the squamosal suture, which is essentially straight and horizontal. Near its posterior end, the suture curves sharply downward toward the parietal notch, producing a relatively long and vertical (or even anteriorly sloped) component of the squamosal suture that in some specimens bounds the parietal notch anteriorly (Santa Luca, 1980). From the moderately deep notch, the parietomastoid suture courses up and then becomes essentially horizontal until reaching asterion (Schwartz and Tattersall, 2003). Overall, the parietomastoid suture lies higher than the occipital torus and nearly level with the squamosal suture. Therefore, in general, the mastoid portion is both long anteroposteriorly and tall superoinferiorly. SM 3 is similar to the Ngandong specimens in these respects.

In ZKD 11 and ZKD 12, the vertical sphenotemporal suture also angles sharply into the squamosal suture, which is only slightly curved and peaked anteriorly. Just before passing the supramastoid crest, the squamosal suture curves sharply downward to a short vertical component (shorter than in the Ngandong specimens), terminating at the parietal notch. In ZKD 11, the very long, low and straight parietomastoid suture courses upward slightly to reach asterion. Thus, the parietal notch is relatively narrow and deep (Schwartz and Tattersall, 2003). In ZKD 12, the parietomastoid suture is also straight but shorter anteroposteriorly; It courses downward slightly to reach asterion. Thus, the parietal

notch of ZKD 12 is quite open, and the mastoid portion is relatively shorter anteroposteriorly and much shorter superoinferiorly than that in ZKD 11. In both specimens, the parietomastoid sutures are situated somewhat below the occipital angle.

In D2700, the very slightly backwardly sloping sphenotemporal suture transitions via a slightly obtuse angle into the somewhat curved squamosal suture, which peaks roughly in the middle above the anterior root of the zygomatic process; it then courses gently downward. Near the posterior end, it curves sharply anteroinferiorly toward the mediolaterally narrow but not superoinferiorly deep parietal notch. The parietomastoid suture then courses horizontally for a very short distance to reach asterion. Thus, the mastoid region is very small in all dimensions, although the upper border lies higher than the occipital angle.

In OH 9, the vertical sphenotemporal suture curves smoothly via an obtuse angle into the slightly arced squamosal suture, which peaks in the middle, above the anterior root of the zygomatic process. It then courses slightly downward to reach the wide and shallow parietal notch. The parietomastoid suture is very short, horizontally oriented, and essentially level with the occipital angle. The mastoid region is very short superoinferiorly and small.

In KNM-ER 3733, the squamosal portion is relatively tall superoinferiorly and long anteroposteriorly (Schwartz and Tattersall, 2003). The nearly vertical sphenotemporal suture curves sharply via a right angle into the relatively more arced squamosal suture, which peaks above the posterior root of the zygomatic process. It then gently curves downward. At its posterior end, the squamosal suture curves downward into a very short vertical component before reaching the wide and shallow parietal notch. The slightly arced and moderately anteroposteriorly short parietomastoid suture curves slightly downward to reach asterion. This suture lies slightly below the occipital angle. The mastoid region is also relatively shorter anteroposteriorly and less tall superoinferiorly.

In KNM-ER 3883, the squamosal portion is relatively tall superoinferiorly and long anteroposteriorly (Schwartz and Tattersall, 2003). The slightly anteriorly sloping sphenotemporal suture curves sharply to the squamosal suture, which is arced and peaks anteriorly, above the anterior root of the zygomatic process. This suture then courses gently downwardly to the very shallow and open parietal notch. The horizontal and anteroposteriorly short parietal suture lies roughly at the same level as the occipital angle. The mastoid region is anteroposteriorly short and superoinferiorly low relative to the squamosal portion.

KNM-WT 15000 has an anteroposteriorly long and superoinferiorly low squamosal portion. The vertical sphenotemporal suture sharply curves via a right angle into the overall straight squamosal suture, which peaks at its anterior end. It then courses slightly downward and then curves sharply into a superoinferiorly short vertical component that extends to the relatively narrow and deep parietal notch.

The parietomastoid suture is relatively long and arched. Asterion lies at the same level as the parietal notch. Overall, the mastoid portion is relatively long anteroposteriorly and nearly as superoinferiorly tall as the mastoid portion.

3.9 MANDIBULAR FOSSA AND THE TYMPANIC PLATE

In *H. erectus* specimens, the morphology of the glenoid region is usually complicated, and descriptions often inconsistent. Based on previous literature, Baab (2016) noted that *H. erectus* usually has a "wide" glenoid/mandibular/digastric fossa and no postglenoid process. Rightmire (1993, p. 177) commented that the glenoid fossa "may be hollowed", while the anterior border of the fossa is usually confluent with the preglenoid planum. This description follows Weidenreich (1943), who stated that in *Sinanthropus* and *Pithecanthropus*, the "articular tubercle" is replaced by a "planum preglenoidale" (Weidenreich, 1943, p. 201). On the other hand, from literature that included Weidenreich and Rightmire's work, Cartmill and Smith (2009) stated that in *H. erectus* the glenoid fossa is deep and the anterior articular eminence pronounced.

The mandibular fossa is bounded posteriorly by the tympanic plate, which is usually described as thick and transversely oriented (Asfaw, 2008; Baab, 2016; Rightmire, 1993; Weidenreich, 1943; Wood, 1984). The mastoid process is usually separated from the tympanic plate by a distinct "mastoid fissure" (Baab, 2016; Cartmill and Smith, 2009; Stringer, 1984). Baab (2016) also noted that the lateral part of the posterior margin of the mandibular fossa often does not bear a postglenoid process. However, Cartmill and Smith (2009) summarized the literature as indicating that the posterior margin is marked with a large postglenoid process. In addition, the petrous bone curves anteriorly and forms an acute angle with the tympanic plate (Asfaw, 2008; Baab, 2016; Weidenreich, 1943; Wood, 1984).

In S 2, the deep mandibular fossa is anteroposteriorly shorter laterally than medially. Its long axis is oriented transversely (Schwartz and Tattersall, 2003). The articular eminence is very low, partly due to remodeling. It curves posteriorly into an anteroposteriorly oriented medial wall, which does not terminate as an entoglenoid tubercle (Schwartz and Tattersall, 2003). The transversely oriented tympanic plate is low, rounded and thick, and surrounds the small and rounded auditory meatus (Schwartz and Tattersall, 2003). It bounds almost the entire posterior margin of the mandibular fossa; a postglenoid process is absent. The low vaginal process peaks quite medially (Schwartz and Tattersall, 2003). The mandibular fossa is quite open laterally. Its anterior and posterior margins are both short and straight. Only a small portion of the mandibular fossa flares out from the cranium. There is a narrow recess between the entoglenoid region and the tympanic plate.

S 17's large and deep mandibular fossa is equally anteroposteriorly long and mediolaterally wide (Schwartz and Tattersall, 2003). The deepest point is approximately in the center. The mediolateral axis is slightly oriented obliquely. Both the anterior and posterior margins are curved, such that the mandibular fossa is shorter anteroposteriorly at the two ends and longest anteroposteriorly in the middle. The fossa is open medially because there is a broad but shallow gap between the entoglenoid region and the tympanic plate (Schwartz and Tattersall, 2003). The low articular eminence terminates in a small swelling that might be an entoglenoid tubercle. The lateral part of the posterior margin is bound by a small postglenoid process, which is a thin and low bony ridge (Schwartz and Tattersall, 2003). The medial part of the posterior margin of the fossa—the tympanic plate—is mediolaterally short and essentially transversely oriented. Its medial end curves anteriorly, and its anterior surface slopes back. The posterior surface of the tympanic plate tightly abuts the mastoid region. The tympanic plate surrounds a small and subrounded auditory meatus (Schwartz and Tattersall, 2003). The articular eminence and tympanic plate are equally tall.

In the Ngandong specimens, the mandibular fossa is relatively anteroposteriorly short, mediolaterally wide and quite deep. The lateral half flares significantly away from the cranial base. The mediolateral axis is oriented obliquely (Schwartz and Tattersall, 2003). The blunt, tall and vertical articular eminence is concave in the middle (Schwartz and Tattersall, 2003). The mandibular fossa becomes shorter anteroposteriorly along its medial side and longer anteroposteriorly along its lateral side. Its medial end and tympanic plate are either fused or separated by a narrow recess. There is no entoglenoid tubercle. A short lateral part of the posterior margin of the mandibular fossa is open, due to absence of a postglenoid process. The prominent, mediolaterally short, and transversely oriented tympanic plate is taller than the articular eminence; its anterior surface is convex. The low, thick vaginal process does not extend to the oval and vertically oriented auditory meatus; it is well separated from the mastoid process (Schwartz and Tattersall, 2003). In lateral view, the profile of the mandibular fossa is narrowly V-shaped, with a vertically oriented posterior wall and slightly forwardly sloping anterior wall. The deepest point is along the roof of the posterior wall. The configuration of the mandibular fossa and tympanic plate of SM 3 is similar to that of the Ngandong specimens, though the long axis of the former's fossa is slightly more transversely oriented.

ZKD 11's and ZKD 12's mandibular fossae are in general short anteroposteriorly, wide mediolaterally, deep, and moderate in size (Schwartz and Tattersall, 2003). Most of the fossa sits under the braincase. The mediolateral axis is obliquely oriented. The steep anterior wall curves smoothly into the preglenoid plane without producing a distinct articular eminence (Schwartz and Tattersall, 2003). Though the lateral end is broken, the fossa should become shorter anteroposteriorly at both the medial and lateral ends. The anterior margin is curved and concave in the middle, while the posterior margin is

relatively straight and slightly convex (Schwartz and Tattersall, 2003). Thus, the mandibular fossa is oval and longest anteroposteriorly in the middle. The roof is deepest near its midpoints. An entoglenoid tubercle is absent, and there is only a shallow and narrow recess at the medial end of the anterior wall. The thick, short, and tall tympanic plate is transversely oriented; it bounds the medial part of the fossa posteriorly (Schwartz and Tattersall, 2003). The ovoid, narrow and small auditory meatus is posteriorly sloping. In the better-preserved ZKD 12, the lateral half of the posterior margin lacks a distinct postglenoid process; only a low and rounded bony ridge is present.

There are also some differences between these two specimens. In ZKD 11, the tympanic plate protrudes vertically downward. The thick, extremely large, and medially placed vaginal process extends nearly to the auditory meatus and is separated from the mastoid process by a narrow groove. In ZKD 12, the tympanic plate follows the orientation of the auditory meatus. Thus, its posterior wall is very backwardly sloping; the lateral extension of the vaginal process tightly abuts the mastoid region.

D2700's relatively shallow mandibular fossa is also relatively wide mediolaterally and short anteroposteriorly. The deepest point is roughly at the center. The mediolateral axis is oriented obliquely. The anterior wall is forwardly sloping; it curves smoothly into the preglenoid surface and arcs in the middle, while the posterior wall is relatively straight. Thus, the mandibular fossa also becomes shorter anteroposteriorly at both medial and lateral side but longer anteroposteriorly slightly more at its lateral end. The entoglenoid end which lacks a tubercle, contacts the tympanic plate. The moderately thick and slightly obliquely oriented tympanic plate angles smoothly anteriorly into the petrosal region. It bounds the medial half of the posterior margin of the fossa. The lateral half of the posterior portion of the mandibular fossa is bound by a blunt but well-elevated postglenoid process. The vaginal process is tall and pointed, extending almost to the oval and vertically oriented auditory meatus, of which the inferior tip is unfused.

In OH 9, the better-preserved mandibular fossa on the right side is deep, mediolaterally wide and anteroposteriorly short (Schwartz and Tattersall, 2003). The fossa does not flare much from the cranial base. Its long axis is oriented obliquely. The fossa is deeper near the anteromedial corner. Similar to the Ngandong specimens, the fossa becomes anteroposteriorly shorter medially and anteroposteriorly longer laterally. The medial end of the anterior wall terminates in an entoglenoid tubercle (Schwartz and Tattersall, 2003). The curved and tall anterior wall of the mandibular fossa rises steeply. The lateral half of the posterior margin is bound by a distinct and blunt postglenoid process (Schwartz and Tattersall, 2003). The medial half of the posterior wall of the mandibular fossa is represented by the tall, thick, and transversely oriented tympanic plate. Its posterior surface seems to tightly abut the broken mastoid process. The vaginal process is blunt and prominent but does not extend as far as the narrow and vertically oriented auditory meatus (Schwartz and Tattersall, 2003). The anterior wall and the tympanic

plate incline anteriorly and posteriorly to a similar degree. The superior moiety is shorter anteroposteriorly. Thus, the lateral profile is widely V-shaped.

KNM-ER 3733's mandibular fossa is wide mediolaterally, moderately long anteroposteriorly, and quite shallow. Its mediolateral axis is also oriented obliquely (Schwartz and Tattersall, 2003). The fossa is shorter anteroposteriorly medially than laterally. The mediolaterally short, curved anterior wall inclines significantly forward and terminates medially at each end in a tubercle (Schwartz and Tattersall, 2003). The thick, rounded and mediolaterally short tympanic plate bounds the medial half of the posterior margin of the fossa and is separated from the entoglenoid tubercle by a deep, narrow fissure. The vaginal process is low, pointed, and restricted to the region just posterior to the entoglenoid tubercle. The posterior surface of the tympanic plate is separated from the mastoid process by a wide and shallow groove. The ovoid auditory meatus is superoinferiorly short and slightly posteriorly tilted (Schwartz and Tattersall, 2003).

KNM-ER 3883's mandibular fossa is relatively large, deep, anteroposteriorly short, and mediolaterally wide. The long axis is oriented obliquely. The fossa is shorter anteroposteriorly laterally than medially. It flares prominently from the cranial base. The rounded and thick articular eminence is essentially straight, only curving slightly back at its medial end into a rounded and thick entoglenoid region, which is separated from the tympanic plate by a widely V-shaped recess (Schwartz and Tattersall, 2003). The mediolaterally long and blunt postglenoid plate bounds the majority of the posterior margin, almost covering the region anterior to the lateral half of the tympanic plate; it is also oriented obliquely, similar to the anterior wall and the mediolateral axis of the fossa (Schwartz and Tattersall, 2003). The thick, slightly posteriorly inclined, transversely oriented tympanic plate bounds the medial half of the fossa and wraps the large, superoinferiorly short oval auditory meatus (Schwartz and Tattersall, 2003). The low and double-peaked vaginal process is restricted to the area just anterior to the styloid pit (Schwartz and Tattersall, 2003). The lateral end of the tympanic plate tightly abuts the mastoid process.

In KNM-WT 15000, the mandibular fossa is large, deep, anteroposteriorly long, and mediolaterally wide. It flares somewhat from the cranial base. The long axis is oriented obliquely. The fossa is uniformly deep, shorter anteroposteriorly at the medial end, and open on the lateral side (Schwartz and Tattersall, 2003). The quite anteriorly inclined anterior wall flows smoothly into the preglenoid plane; an articular eminence is absent (Schwartz and Tattersall, 2003); only its medial end curves backward into a ridge in the entoglenoid region, which is separated from the tympanic plate by a V-shaped recess. Most of the posterior margin is bound by an mediolaterally short, thick, and transversely oriented tympanic plate (Schwartz and Tattersall, 2003). A small lateral part of the posterior margin is open (a postglenoid plate is absent). The tympanic plate is also vertically protrusive, reflecting the vertical orientation of the short, ovoid auditory meatus. The tympanic plate is also much taller superoinferiorly

than the anterior wall; the top is anteroposteriorly narrow, creating a V-shaped lateral profile of the mandibular fossa. The superoinferiorly tall and thick vaginal process extends much more inferiorly than the anterior wall and extends laterally nearly to the auditory meatus (Schwartz and Tattersall, 2003). The lateral extension is separated from the mastoid process by a shallow and narrow groove.

3.10 THE MASTOID PROCESS

The mastoid "process" of *H. erectus* is usually described as small and tilted medially, though its size is variable (Antón, 2003; Asfaw, 2008; Baab, 2016; Rightmire, 1993; Wood, 1984). The detailed configurations of the mastoid process are actually very different between specimens of *H. erectus*. In S 2, the surface of the mastoid process is damaged. It appears that there is no projecting process but a small swelling, of which the lateral contour inclines medially (Schwartz and Tattersall, 2003).

S 17 has a small mastoid process that extends inferiorly from the base and slightly over the tympanic plate. The lateral contour is straight, not swollen, and inwardly tilted (Schwartz and Tattersall, 2003). In inferior view, it is narrow mediolaterally, resembling an anteroposteriorly oriented ridge (Schwartz and Tattersall, 2003).

In general, the Ngandong specimens have prominent, bulky, and pyramid-shaped mastoid processes (Schwartz and Tattersall, 2003). The triangular base is similarly mediolaterally wide and anteroposteriorly long. The rounded tip is placed nearly in the center. The anterior margin is transversely oriented. The process projects below the tympanic plate. The lateral profile is slightly swollen and only slightly tilted inward (Schwartz and Tattersall, 2003). In SM 3, the tip of the mastoid process is broken, but the general shape resembles the Ngandong specimens.

ZKD 11 has a small, gracile, blunt, and ridge-like mastoid process. In inferior view, it is narrow mediolaterally and oriented obliquely posteromedially—anteromedially. It extends a lot below the tympanic plate. The lateral profile is straight and tilted inward (Schwartz and Tattersall, 2003). Though the tip is broken, ZKD 12's mastoid process is similar.

D2700 does not have a distinct mastoid process; the swollen mastoid region extends below the tympanic plate. The lateral profile is tilted inward and bulky laterally.

In OH 9, the tip of the mastoid process is broken. It should be extremely large, based on the size of the base. The base is triangular and wide mediolaterally but differs from the Ngandong specimens, because its anterior base is oriented obliquely, posterolaterally—anteromedially. The lateral profile tilts medially.

In KNM-ER 3733, the inferior tip of the mastoid process is eroded, but the process is mostly preserved. It is very small and extends to the level of the tympanic plate (Schwartz and Tattersall, 2003). The lateral profile is bulky superiorly and slightly tilted inward. The base of the process is also triangular and equally mediolaterally wide and anteroposteriorly long. The medial margin is straight and undercut by a distinct mastoid notch (Schwartz and Tattersall, 2003).

KNM-ER 3883 has an extremely large, sharply pointed, and pyramidally-shaped mastoid process. It is also similarly wide mediolaterally and long anteroposteriorly. The tip lies essentially centrally. The posterior profile is slightly tilted inward and bulbous in its superior half.

KNM-WT 15000 has a very small and pointed mastoid process that does not extend beyond the tympanic plate (Schwartz and Tattersall, 2003). The base is triangular and equally wide mediolaterally and long anteroposteriorly. The lateral profile is bulbous in its superior half and tilted inward.

4.0 MATERIAL AND METHODS

4.1 INTRODUCTION

This chapter presents materials and statistical methods for this dissertation study. As stated in the Preface and Chapter 1, a major goal of this study is to use surface semilandmarks to capture and identify morphological details. In addition, this dissertation also examines whether changing densities of semilandmarks and analyzing different individual cranial bones (e.g. frontal and temporal) can affect the results of statistical analyses commonly used in the study of *Homo erectus*.

The hypotheses these statistical analyses aim to test concern whether *Homo erectus* and its geographical subsets are more variable than extant species, such as *Homo sapiens* and chimpanzees (e.g., Baab, 2008b; Lordkipanidze et al., 2013; Terhune et al., 2007). This study particularly focuses on three hypotheses of *Homo erectus* common to previous studies:

1. *H. erectus sensu lato* (which will simply be called *H. erectus* in the following chapters) is significantly more variable than *H. sapiens*.
2. The overall variability in Asian *H. erectus* and *H. ergaster* exceeds that of *H. sapiens*.
3. The difference between Asian *H. erectus sensu stricto* (which will be called Asian *H. erectus*) and *Homo ergaster* exceeds that between geographical subsets of *H. sapiens*.

4.2 MATERIAL

4.2.1 Specimens

Landmarks and semilandmarks are acquired from 3D models of well-preserved fossil hominid and *Homo sapiens* crania (Table A.1, Table A.2 and Table A.3 in Appendix A). The study primarily focuses on the vault rather than the face because only a few hominid specimens preserve facial skeletons (Table A.1 in Appendix A). Some of the 3D models of fossil hominid specimens are scanned by the

author (Table A.1 in Appendix A). These fine hominid cranial casts, including the original casts of ZKD 11 and ZKD 12 made by Franz Weidenreich (1943), were generously provided by Dr. Ian Tattersall at the American Museum of Natural History (AMNH). The other groups of 3D models that include crania of both fossil hominids and *H. sapiens* were generously provided by Dr. Eric Delson and Dr. William Harcourt-Smith from the AMNH. The *H. sapiens* samples comprise skulls from Mongolia, Australia, Egypt, and Ethiopia (Table A.3). The degree of overall variability of the *H. sapiens* sample is used as a yardstick in order to test whether the *H. erectus* hypodigm is too variable to be a single species.

The catalog of Ngandong specimens (Ng 6, Ng 7, Ng 10, and Ng 12) follows the common catalog system provided by Oakley et al. (1976) (Table A.1). The majority of the specimens are adults, except for KNM-WT 15000 and D2700. These two specimens were frequently included in previous analyses of *H. erectus*; thus, including them in this study, which aims to assess sampling issues in commonly used statistical analyses, should be acceptable (Terhune et al., 2007). In addition, D2700's third molar is erupted, such that the differences between it and the adult specimen it would have grown into should be insignificant (Baab, 2016; Rightmire et al., 2006; Vekua et al., 2002). The geographical subsets that each fossil belongs to are also summarized in Appendix A (Table A.4).

4.2.2 Scanning tool

The Artec Space Spider 3D industrial scanner (Artec 3D, Inc., Luxembourg), courtesy of Dr. William Harcourt-Smith at the AMNH, is capable of accurately capturing complex geometry and fine details at the surface of calvaria at a speed of 15 frames per second. The resultant high-quality models in ".ply" format can have a resolution up to 0.05 mm. During scanning, each specimen is put on a turntable and scanned from multiple angles. These scans of a single specimen are then aligned and fused to produce a complete single model by using the Artec Studio 13 software (Artec 3D Inc., 2018), courtesy of Dr. William Harcourt-Smith at the AMNH. Some scans are also repaired by using the Geomagic Studio 2015 software (Geomagic Inc., 2015), courtesy of the Swanson Center for Product Innovation, University of Pittsburgh.

4.2.3 3D model reconstruction

The majority of 3D models of incomplete fossil casts are reconstructed by using Artec Studio 13 (Artec 3D Inc., 2018). Ng 6, Ng 7, Ng 12, and Kabwe are reconstructed by using both Geomagic Studio 2015 (Geomagic Inc., 2015) and Artec Studio 13. The 3D models are rescaled using Meshlab (Cignoni et

al., 2008). The reconstructed hominid models are summarized in Appendix A (Section A.2, Figure A.1 to Figure A.17).

To reconstruct a structure missing on one side, I used a mirror image of its counterpart on the other side of the cranium. In both Geomagic and Artec Studio software, the original models and mirrored patches are first aligned by selecting several common points and then further registered by using either the "Global Registration" function in Geomatic Studio 2015 or the "Align" function in Artec Studio 13. This procedure is repeated a couple of times as needed until the original model and patches are well aligned. They are then fused to produce a single reconstructed model (Appendix A.2, Figure A.1 to Figure A.17).

The major cracks in the cranial surface, such as those at the vault of Sangiran 17, are "filled" using the "Defeature" function in Artec Studio 13 (Figure A.9). This function first removes the surface within the selected area to create a hole, which is then filled by creating a surface that is confluent with the adjacent area. This function is useful for the vault because its surface is relatively smooth.

4.3 LANDMARKS AND SEMILANDMARKS

4.3.1 Reasons for landmark choice and the use of semilandmarks

4.3.1.1 Correspondence of landmarks

Landmarks are the raw data of geometric morphometric analysis (GMA). One of the important criterion for picking landmarks is correspondence (Bookstein, 1997; Lele & Richtsmeier, 2001; Zelditch et al., 2012). When landmarks of a group of specimens are corresponding, these points are sampled from the same anatomical loci, such as joints between the sagittal and lambdoid sutures (Bookstein, 1997; Zelditch et al., 2012).

Researchers commonly use the term "homology" in replacement of "correspondence" (Bookstein, 1997; Lele & Richtsmeier, 2001; Zelditch et al., 2012). However, the "homology" of landmarks does not suggest structures derived from a common ancestor as in evolutionary biology, but only correspondence of anatomical loci (Lele & Richtsmeier, 2001; Zelditch et al., 2012). Therefore, to avoid confusion, "correspondence", rather than "homology" is used in this dissertation (Lele & Richtsmeier, 2001; Zelditch et al., 2012).

Bookstein (1997) classified discrete landmarks into three categories, reflecting three levels of reliability in being corresponding. Type I landmarks are most reliable in being corresponding because

they are located at the junctions of structures, such as bregma, which is located at the joint of the frontal and two parietal bones. Type II landmarks are less reliable because they are usually located at curvature maxima, such as the point at the tip of the incisor. Type III landmarks are the least reliable to be corresponding because they are artificially constructed, such as those placed at the endpoints of a diameter. These points are usually designed to take measurements, such as the maximum width of the skull.

4.3.1.2 Repeatability

Another important aspect of landmark design is repeatability, which means that landmarks should be reliably found in many specimens (Zelditch et al., 2012). Repeatability is associated with Bookstein's (1997) classification of landmarks because Type II and Type III landmarks are usually less repeatable in a group of specimens. This criterion of repeatability is especially relevant for studies that include potentially different species with different structures. If some specimens of a distinct species do not present a correspondent structure, there is no way to place a certain landmark in a repeatable manner. For example, in adult chimpanzees, lambdoid sutures are usually obliterated, so it is difficult to accurately locate lambda.

4.3.1.3 Coverage of information

Bookstein's (1997) purpose for classifying landmarks into three types was to use dislocations of corresponding landmarks to reflect covariations of structures for further exploring underlying developmental and functional factors. Thus, Type I landmarks, which are placed at the junction of structures, are most useful. Type II landmarks have less power to reflect covariations as they are placed on only one structure. Type III landmarks are viewed as almost useless since they are almost artificial.

Nevertheless, the extent of morphological variations included in an analysis is similarly important in landmark design because landmarks determine which morphological differences are analyzed (Harvati et al., 2010; Zelditch et al., 2012). Zelditch et al. (2012) suggested that sometimes one has to use more Type II and even Type III landmarks to include desired features, though according to Bookstein's (1997) definition, Type II and Type III landmarks are not as reliable in guaranteeing correspondence as Type I landmarks (Zelditch et al., 2012). Although using only landmarks to design cranial measurements, Howells (1973) also argued that one should pay more attention to the anatomical meaning of landmarks, i.e., what features landmarks can capture, rather than only pursuing precision. For example, instead of defining "bregma" as the point strictly at the junction between the frontal bone and two parietal bones, this point should highlight the overall posterior boundary of the frontal bone (Howells, 1973). Therefore, when the frontal bone is slightly invaginated posteriorly into the parietal bones, bregma should not be

used to mark this small variation (Howells, 1973). Howells (1973) also encouraged developing new landmarks to measure morphological features, even if doing so may not guarantee accuracy of placing landmarks.

Nonetheless, a natural limitation of discrete landmarks is that many morphological features are located in landmark-free regions (Freidline, Gunz, Janković, et al., 2012; Gunz & Mitteroecker, 2013; Villmoare, 2005; Zelditch et al., 2012). In particular, features that define hominid species are usually detailed and localized (Schwartz, 2004, 2016; Schwartz and Tattersall, 2003; Schwartz et al., 2013; Spoor et al., 2008). For this reason, GMAs based on discrete landmarks may not be sufficient for exploring detailed morphological differences in *H. erectus*.

Consequently, this analysis follows Howells' (1973) and Zelditch et al.'s (2012) suggestions that a balance between adequate coverage of information and the correspondence of landmarks is important to landmark design. It is better to attempt to capture detailed features than to not try at all, even though some degree of repeatability and correspondence might be sacrificed.

4.3.1.4 The use of semilandmarks

This study uses surface semilandmarks because they are designed to capture morphological differences in landmark-free regions (Gunz and Mitteroecker, 2013). Semilandmarks are points placed equidistantly on a curve or surface defined by a set of discrete landmarks (Gunz and Mitteroecker, 2013). To reduce the excessive variations created by initial arbitrary placement of these points, they should be slid to minimize either the bending energy or the total Procrustes sum of squares before actual statistical analysis (Gunz and Mitteroecker, 2013). After sliding, semilandmarks are treated as if they are corresponding discrete landmarks when computing shape differences (Gunz and Mitteroecker, 2013). It is important to note that a single semilandmark cannot be interpreted independently but should be understood in the context of differences in the whole semilandmark configurations (Gunz & Mitteroecker, 2013; Klingenberg, 2013).

There are several limitations of using semilandmarks. First, semilandmarks are not suitable for a surface that is too complex (Gunz and Mitteroecker, 2013). Second, the use of semilandmarks has a higher requirement of specimen preservation because they are placed across a region of the cranial surface rather than at a few anatomical loci. Third, sampling too many semilandmarks and landmarks relative to a small sample size of specimens, which is sometimes unavoidable in paleoanthropological research due to the small number of available fossils, may arguably affect statistical efficiency (Collyer et al., 2015; Watanabe, 2018). Sampling too many semilandmarks can also be time consuming.

In terms of the first limitation, this study focuses primarily on the surface of the calvaria, which should be essentially smooth overall. The second limitation of incomplete fossil records is inherent to all

paleoanthropological research. 3D model reconstruction may somewhat buffer this problem. Regarding the problem of oversampling, the opinions of scholars are inconsistent. Gunz and Mitteroecker (2013) still encourage sampling dense semilandmarks because it is crucial for interpretation and exploring underlying biological explanation. As the coverage of information is also fundamental for GMA, it is still worth applying a dense semilandmark set in a small sample of fossil calvaria to capture more morphological differences that were missed in previous analyses. The possibility of oversampling can be evaluated at the same time.

4.3.2 Landmark and semilandmark collection

4.3.2.1 Landmark collection tool

The software Landmark Editor (Wiley et al., 2005) developed by the Institute for Data Analysis and Visualization (IDAV) and the University of California, Davis, is used to collect landmarks and semilandmarks from the 3D surface models. The software allows users to place semilandmarks as patches of points, each of which is defined by nine (3×3) discrete anchor points. One can drag these anchor points to place the patch across the desired area. The density of semilandmarks in each patch can be altered.

A complete specimen, such as a *H. sapiens* cranium, is first chosen as the template for placing a sequence of semilandmark patches. A series of anchor points, which are discrete landmarks, are then placed on the rest of specimens in a user-defined order to map semilandmark patches from the template specimen onto these specimens.

4.3.2.2 The design of semilandmark patches

The anchor points and patches of semilandmarks are summarized in the Appendix. The anchor points are essentially discrete landmarks that are composed of Type I, Type II, and Type III landmarks. The use of Type III landmarks is unavoidable because each patch requires nine anchor points. For example, a few anchor points must be placed in the middle of the sagittal suture between the bregma and lambda. Nevertheless, many of these Type III anchor points are slid similar to other semilandmarks to minimize their arbitrariness (Appendix A.3, Table A.4 to Table A.20). Furthermore, the error of placing anchor points in this study is weighed down by the use of a large number of semilandmarks because dislocations of all these points are treated as a whole in GMA to calculate overall shape differences. As the focus of this study is the use of semilandmarks to capture more shape differences, sacrificing a small degree of accuracy and correspondence should be tolerable as long as these points can be repeatedly sampled.

4.3.2.3 Anchor points at obscure suture joints

In several specimens, such as S 2, S 17, KNM-ER 3883 and KNM-ER 1813, some cranial sutures are untraceable (Appendix A.4). Therefore, a few important landmarks, such as the bregma and lambda, cannot be located accurately in these specimens. In these cases, the positions of these landmarks must be estimated from other published sources.

One source is published metrical data because many cranial measurements are defined by discrete landmarks (Table A.24). To estimate the positions of these points with the help of cranial measurements, the "Dimension" function in Landmark Editor (Wiley et al., 2005) is employed. For example, to determine the position of bregma in KNM ER 1813 (Table A.22 and Figure A.24), the first step is to use the "Dimension" function to put measurements between preserved anatomical landmarks, such as the glabellar-nasion and glabellar-basion distances. The actual values of these measurements, which are derived from the work of Wood (1991a), are input to scale the 3D model to the actual size. The next step is to place a landmark in an area that may contain the bregma. A few measurements defined by the "bregma" and other preserved landmarks, such as glabella, basion and asterion, are taken. After this, the potential bregma is moved around until all the chord distances are similar overall to published values. Differences of a few millimeters are allowed. The disadvantage of this method is that it relies on the estimation of other sources, which are not guaranteed to be perfectly accurate (Kaifu et al., 2008).

A specific case is S 17, which does not preserve a bregma and lambda on its cranial surface. The estimation of the positions of the lambda is based on pictures provided by Kaifu et al. (2008). These authors used CT scanning to trace the lambdoid sutures underneath the cranial surface to determine the position of lambda. Bregma is placed in the middle of the bregmatic eminence (Kaifu et al., 2008).

4.4 STATISTICAL ANALYSES

4.4.1 Programming software

General Procrustes analysis (GPA), which is the first and fundamental step of GMA, is performed by using the "geomorph" package in the statistical language R (Adams et al., 2018; R Core Team, 2018; Sherratt, 2014; Zelditch et al., 2019). Statistical analyses are performed by using functions in both the geomorph package and other built-in packages in R. Visualization is performed by using relevant functions in the geomorph package (Adams et al., 2018; Sherratt, 2014; Zelditch et al., 2019). The Morphologika software (O'Higgins & Jones, 2006) is also used to aid visualization because it is able to

demonstrate shape differences as shape change between any two points (specimens) in a space of two PCs. Specifically, the analysis of the landmark sampling evaluation curve (LASEC), which will be introduced in the following text, is performed by using the LaSEC function from the R package "LaMBDA" (R Core Team, 2018; Watanabe, 2017). The Procrustes ANOVA of size-shape relationship of each PC, which will be introduced in the following text, is performed by using the R package "permuco" (Frossard & Renaud, 2019; R Core Team, 2018)

4.4.2 The general Procrustes analysis, shape space and Procrustes distances

This study employs GMA to quantify overall shape differences. The backbone of GMA is GPA, which employs Procrustes superimposition to remove the effect of size, location, and orientation, which are believed to be irrelevant to shape differences (Adams et al., 2018; Baab et al., 2012; Zelditch et al., 2012). The effects of location and orientation, which are produced during the acquisition of 3D models, are removed by transforming the centroids of all landmark configurations into the same point. The size of each configuration is calculated as the centroid size, which is the sum of squared differences between each point in this configuration and its centroid. To remove the size effect, the centroid sizes are scaled to the unit quantity. The last step is to remove the effect of orientation. To do this, landmark configurations are rotated until they are best aligned (Baab et al., 2012; Zelditch et al., 2012). The criterion for the best alignment for a group of landmark configurations it to minimize Procrustes sum of squares, which is the sum of positional differences (i.e., squared distances) between all corresponding landmarks of a group of configurations (Baab et al., 2012; Zelditch et al., 2012). Therefore, overall shape differences in a group of configurations, calculated as Procrustes sum of squares, are minimized (Baab et al., 2012; Zelditch et al., 2012).

After GPA, landmark configurations become shapes. These shapes are then collapsed to a group of points in a curved hyperdimensional shape space, of which the dimensions are determined by the number of landmarks (Adams et al., 2004; Baab et al., 2012; Zelditch et al., 2012). Each point in this shape space represents a specific shape. The distance between two points in the space is called the Procrustes distance, which represents the degree of overall differences between two shapes (Baab et al., 2012; Zelditch et al., 2012). This distance is just the Procrustes sum of squares between these two specimens, which is calculated as the sum of squared distances between all corresponding landmarks of these two configurations (Baab et al., 2012; Zelditch et al., 2012).

When a group of points in a shape space are close enough to each other, which is the case for most biological studies, these points can be projected into a Euclidean space that is tangent to the centroid of the cluster (Adams et al., 2004; Baab et al., 2012; Zelditch et al., 2012). The spatial relationship among

these points is preserved in the Euclidean space, which is analogous to projecting cities from a globe onto a flat map (Adams et al., 2013; Klingenberg, 2013, 2016; Zelditch et al., 2012). Therefore, the Euclidean distances in the tangent space, which are calculated as the sum of squared differences between every pair of corresponding landmarks, can be used to represent the Procrustes distances (Klingenberg, 2013, 2016; Zelditch et al., 2012). In this dissertation, the term "Procrustes distance" is used to avoid confusion. The ability to project points from the shape space into a tangent Euclidean space allows submitting landmark data to conventional multivariate analyses, such as principal component analysis (PCA), because these analyses operate in the Euclidean space (Adams et al., 2004; Baab et al., 2012; Klingenberg, 2013, 2016; Zelditch et al., 2012).

4.4.3 Methods for sliding surface and curve semilandmarks

As discussed previously, in the last step of GPA, each semilandmark must be slid in a direction tangent to the curve or surface where it is located to reduce excessive variations created by arbitrary equidistant positioning (Gunz & Mitteroecker, 2013). There are two approaches for sliding semilandmarks. The first approach is to minimize the bending energy among shapes with thin-plate spline (TPS) transformation (Gunz and Mitteroecker, 2013). TPS interpolates a function to smoothly deform one shape into another shape through a minimum amount of overall change, which is calculated as bending energy (Bookstein, 1997; Gunz & Mitteroecker, 2013; Zelditch et al., 2012). The second approach aims to literally minimize the overall Procrustes distances among shapes (Gunz and Mitteroecker, 2013).

If the amount of overall difference is quite limited, the two approaches yield similar results (Gunz and Mitterocker, 2013). However, if the amount of variation is large, the bending energy approach yields better results because it generates fewer arbitrary landmark dislocations (Gunz and Mitteroecker, 2013). After some experimenting, I found the bending energy approach to be able because the Procrustes distance approach causes some semilandmarks to slide into abnormal positions. For example, some surface semilandmarks located in the supraorbital region are slid out of its superior or inferior margins.

Curve semilandmarks are specified by using the "curvslide" function in the "geomorph" package in R (Adams et al., 2018) to prevent surface semilandmarks in one region from sliding into another region, as suggested by Gunz and Mitteroecker (2013). This is also helpful for specifying curves that may convey interesting morphological information, such as the morphology of the midsagittal contour and the superior margin of the supraorbital torus. Curvatures and points that are not allowed to slide are marked in Appendix A.

4.4.4 Visualization

This study employs a variety of techniques to visualize shape differences. The "geomorph" package provides three methods of visualization (Adams et al., 2018; Sherratt, 2014; Zelditch et al., 2012). The first method is to show the overlap between any two landmark configurations after GPA and the sliding of semilandmarks. The second method is to add vectors to each landmark to mark its magnitude and direction of dislocation. The third method, which is the popular TPS deformation, is not employed. TPS is derived from D'Arcy Thompson's conception of overall morphological differences as deforming a whole reference shape into a target shape based on transformation grids (Bookstein, 1997; Gunz & Mitteroecker, 2013; Klingenberg, 2013; Zelditch et al., 2012). However, it is more suitable for visualizing two-dimensional data (Baab et al., 2012). Furthermore, the "geomorph" package offers only two-dimensional diagrams of transformation grids in lateral and superior views (Adams et al., 2018).

In particular, the software Morphologika offers a very powerful and convenient tool with which to visualize shape change along a PC obtained from PCA (O'Higgins & Jones, 2006). On the other hand, the version of the "geomorph" package used in this study offers only allows comparing shapes at two ends of a PC, making interpretation less straightforward (Adams et al., 2018).

4.4.5 Principal component analysis (PCA)

PCA is probably the most popular statistical method used by paleoanthropologists to visualize patterns and degree of overall shape differences in GMA. This approach is rooted in the nature of GMA, which treats each biological shape as an integrated entity and collapses it into a point that occupies a unique position in a hyper-dimensional shape space (Zelditch et al., 2012). It is impossible to directly visualize overall shape differences and distribution of points in shape space, because the shape space has too many dimensions (Slice et al., 2007; Zelditch et al., 2012). Therefore, researchers use PCA to simply the process of interpretation by constructing new variables, Principal components (PCs), which are mutually orthogonal axes that goes through the center of a group of points in shape space (Zelditch et al., 2012).

PCs are ordered by proportions of the total variance each of them explains (Zelditch et al., 2012). Therefore, PC 1 explains highest amount of the total variance. This means that when projecting to PC 1, a group of points that represent shapes distributed wider than to any other directions. In other words, PC 1 specifies a direction that specimens differ most from each other overall. Following this process, PC 2 lies in the direction that shows wider separation of points than any other directions orthogonal to PC 1

(Zelditch et al., 2012). Mathematically, PCs are eigenvectors calculated from the variance-covariance matrix that contains variances and covariances of all landmark coordinates (Zeldithc et al., 2012).

When all possible PCs are used, a replica of the original shape space is generated. In actual analyses, researchers usually pick up two higher-ranked PCs to plot specimens, because these PCs can explain a substantial proportion of the total variance. In this way, a few higher-ranked PCs are used to recapitulate distribution of point in the original shape space. This is why PCA is called a "dimension-reduction technique" (Slice et al., 2007; Zelditch et al., 2004).

A PC, as an axis in a shape space, also specifies a "direction" of shape differences. This direction of differences can be visualized by moving a point, representing a start shape, at the negative end of a PC toward a point, representing a target shape, at the positive end of a PC along the direction of this PC (Klingenberg, 2013). The whole process is equal to mapping all landmarks in a start shape toward a target shape at two sides of a PC (Klingenberg, 2013). During this process, each landmark in the start shape dislocates in a particular direction toward its corresponding landmark in the target shape. Thus, the process of visualizating shape differences a PC specifies can also be treated as if gradually changing the start shape into a target shape through infinitesimal steps along this PC (Klingenberg, 2013). When projecting to a PC, a group shapes, which represent specimens, occupy different positions in this PC. Thus, these shapes are ordered along this PC from the negative end to positive end. Specimens can then be assigned PC scores to mark their positions in this PC (Zelditch et al., 2012). Therefore, differences between PC scores of two specimens represent degree of differences between these specimens along the direction a PC specifies. For example, Lordkipanidze et al.'s (2013) found that PC 1 specifies a direction of shape differences so that specimens can be ordered from small-faced to large-faced individuals. Therefore, specimens that have higher PC scores, i.e., closer to this PC's positive end, have larger face than those have lower scores.

As discussed previously, shape differences along a PC can be efficiently viewed by using Morphologika software (O'higgins & Jones, 2006). The "geomorph" package also generates shapes at two ends of each PC as well as the amount of variance each PC explains (Adams et al., 2018; Sherratt, 2014; Zelditch et al., 2019). Notably, PCs are arbitrary axes generated according to distribution of shapes in a shape space; therefore, shape differences revealed by a single PC do not necessarily represent specific morphological features (Adams et al., 2011; Baab, 2016; Zelditch et al., 2012). Therefore, shape differences demonstrated by a PC should be carefully interpreted as actual morphological differences (Adams et al., 2011; Zelditch et al., 2012).

4.4.6 The bootstrap method

As discussed in the first two chapters, the essence of testing the validity of *H. erectus* has been transformed to assessing if its hypodigm is more variable than some extant taxa. One way to quantify overall similarity is to use the sum of all pairwise Procrustes distances (SSD) (Baab, 2008b). Similarly, the mean pairwise distance of a sample can also be calculated to approximate overall variability. However, fossil samples usually have a very small sample size, and their frequency distribution is unknown because they may come from distinct populations (Baab, 2008b; Hesterberg et al., 2003; Zelditch et al., 2012). Therefore, they cannot be directly compared with *H. sapiens* samples, whose sample size is much larger, using conventional tests such as the t-test. To allow directly comparing fossil and *H. sapiens* samples, researchers usually employ randomization procedures to resample the *H. sapiens* sample many times (Baab, 2008b; Hesterberg et al., 2003; Lockwood et al., 1996; Terhune et al., 2007; Zelditch et al., 2012).

One commonly used resampling method is the bootstrap method (Baab, 2008b; Villmoare, 2005; Zelditch et al., 2012). This method resamples the *H. sapiens* sample a great number of times with replacement, which means that after each round of resampling, the randomly selected specimens will be put back to the original sample before the next round. In this study, the *H. sapiens* sample is resampled 10,000 times. Each randomly generated sample of *H. sapiens* has the same size as the fossil sample. The SSD and mean pairwise distance of each random sample is then calculated. Consequently, frequency distributions of 10,000 *H. sapiens* SSDs and mean pairwise distances are generated. The SSD and mean pairwise distance of the fossil sample can then be directly compared with the bootstrapped SSDs and mean pairwise distances of *H. sapiens* to calculate the proportion of *H. sapiens* SSD values that it exceeds. Following Baab (2008b), if the SSD of the fossil sample exceeds 90% of the *H. sapiens* SSDs, the fossil sample is considered significantly more variable than the *H. sapiens* sample. What the bootstrapped method actually does is to estimate the possibility that one can randomly achieve an SSD or mean pairwise distance of *H. sapiens* that exceeds the SSD or mean pairwise of fossils respectively (Baab, 2008b; Villmoare, 2005; Zelditch et al., 2012). For example, when the fossil SSD exceeds more 90% bootstrapped *H. sapiens* values, it means that there is only less than 10% of possibility that one can get an SSD of *H. sapiens* by chance that exceeds the SSD of fossils.

The bootstrap method is also used to test the significance of differences between means of fossil geographical subsets (Villmoare, 2005). To do this, the Asian and African *H. sapiens* subsets are resampled 10,000 separate times. The random sample of each geographical *H. sapiens* subset has the same size as the corresponding fossil geographical subset (Villmoare, 2005). For each round of resampling, a Procrustes distance between the mean shapes of the two geographical *H. sapiens* samples is

calculated, resulting in a frequency distribution of 10,000 Procrustes distances between means. The empirical distance between the means of fossil geographical subsets is then used to assess the proportion of *H. sapiens* cases it exceeds. Again, if the fossil value exceeds more than 90% of *H. sapiens* cases, the distance between means of fossil geographical subsets is significantly greater than that between geographical subsets of *H. sapiens*.

4.4.7 Procrustes analysis of variance with permutation tests

To further test the significance of the difference between means of two geographical subsets, Procrustes analysis of variance (ANOVA) is carried out (Goodall, 1991; Klingenberg, 2015; Zelditch et al., 2012, 2019). This analysis tests if a significant amount of the total variance is correlated with the separation of group means based on *a priori* group assignment. The test statistic is the empirical F-value, which is calculated as the ratio between the variances explained by the separation of group means and the total variances of a sample. Thus, the F-value specifies the proportion of the total variance that can be explained by the separation of geographical subsets. This analysis then uses a permutation test, which is another kind of randomization process, to test the significance of the empirical F-value (Baab, 2008b; Harcourt-Smith, 2003; Terhune et al., 2007; Zelditch et al., 2012). Each permutation randomly assigns specimens to the "Asian" and "African" subsets, both of which have the same sample size as the actual geographical subsets in a pooled sample (Baab, 2008; Harcourt-Smith, 2003; Terhune et al., 2007; Zelditch et al., 2012). An F-value is then calculated for each permutation. This calculation generates a distribution of permutated F-values.

The empirical F-value is then compared to the permutated F-values to determine how many cases the former exceeds (Zelditch et al., 2012, 2019). The logic is that if the amount of the total variance explained by the separation of group means is insignificant, the empirical F-value should not be too different from the randomly achieved F-values (Baab, 2008, Zelditch et al., 2012, 2019). Therefore, if the empirical F-value exceeds more than 95% of all cases (the p-value < 0.05), then the null hypothesis, which is that the amount of the total variance explained by group separation is insignificant, is rejected, because the probability of achieving larger F-values by chance is less than 5%. In other words, the amount of the total variance correlated with the separation of subsets is significantly large (Zelditch et al., 2012). For the *H. sapiens* sample, 10,000 permutations are performed. For the *H. erectus* sample, all permutations are used because the sample size is too small (Baab, 2008). Procrustes ANOVA is carried out by using the "ProcD.lm()" function in the "geomorph" package (Adams et al., 2018; Sherratt, 2014; Zelditch et al., 2012, 2019).

ANOVA with permutation method is also used to test the significance of the size-shape relationship of each PC based on 1,000 permutations (Harcourt-Smith, 2003; Sherratt, 2014; Zelditch et al., 2012, 2019). The test statistic is the empirical F-value, which is the ratio between variances explained by size and the total variance. Thus, this value specifies the proportion of the total variance that is associated with size difference. If the p-value falls below 0.05, the null hypothesis that there is no significant size-shape relationship is rejected. The result of the size-shape relationship of each major PC in each analysis is listed in Appendix B.

4.4.8 The unweighted pair group method with arithmetic mean

The unweighted pair group method with arithmetic mean (UPGMA) generates a hierarchical dendrogram that shows the clustering of specimens based on their degrees of overall similarity, which are calculated as pairwise Procrustes distances between specimens (Harcourt-Smith, 2003; Saitou & Nei, 1987; Terhune et al., 2007; Zelditch et al., 2012, 2019). The resulting dendrogram is the simplest one that minimizes the sum of distances along all branches (Harcourt-Smith, 2003; Saitou & Nei, 1987; Terhune et al., 2007; Zelditch et al., 2012, 2019). This analysis uses each specimen as an operational taxonomic unit (OTU) without *a priori* group assignment (Harcourt-Smith, 2003; Saitou & Nei, 1987; Terhune et al., 2007; Zelditch et al., 2012, 2019). Notably, the dendrogram does not reflect actual phylogenetic relationships. The purpose of this analysis is to visualize the overall similarity among individual specimens by grouping specimens that are relatively close to each other in distances into clusters.

4.4.9 Landmark sampling evaluation curve

This study employs the landmark sampling evaluation curve (LASEC) method designed by Watanabe (2018) to assess the effect of landmark density. The core of this method is that it randomly pick up landmarks in each configuration of the original dataset at a lower landmark density to construct a subsampled dataset (Watanabe, 2018). It then evaluates how well this subsampled dataset is aligned with the original dataset in shape space (Watanabe, 2018).

First, the original and subsampled datasets must be placed in the same shape space. Configurations in a subsampled dataset cannot be directly put into the same shape space of the original dataset. This is because the dimension of a shape space is determined by numbers of landmarks in each configuration in a dataset. Therefore, a sufficient number of zeros is added to each configuration of the subsampled dataset to ensure that all of these configurations have the same number of landmarks as

configurations of the original dataset. In this way, the subsampled dataset can be put into the same shape space of the original dataset. These "dummy" landmarks of zeros do not affect the calculation of shape differences between configurations of the subsampled and original datasets (Watanabe 2018, p.4).

After projecting the subsampled and original datasets into the same shape space, Procrustes sum of squares (PSS) is calculated (Watanabe, 2018). In the analysis of LASEC, PSS does not represent overall shape differences between configurations, but represents the degree of differences between distributions of points of two datasets in a shape space (Watanabe, 2018). Watanabe (2018) then created a fit value that is equal to 1-PSS to measure how well two datasets are aligned in a shape space. Consequently, when the number of randomly selected landmarks in a subsampled dataset is equal to the original dataset (that is, these datasets are identical), the PSS between the shapes in the two datasets is zero. This is because distributions of points of two datasets in shape space are perfectly aligned. Thus, the fit between two datasets is one. When the number of randomly selected landmarks of the subsampled dataset is much smaller than the original dataset, the PSS approaches one and the fit value of two datasets approaches zero.

The analysis beginning by randomly selecting three landmarks in each landmark configuration of the original dataset to construct a subsample and then calculating a fit value between the subsampled and original datasets (Watanabe, 2018). The next step is randomly selecting four landmarks in each configuration of the original dataset to construct a new subsample. A new fit is then calculated. This process is iterated until the number of landmarks in a subsampled dataset is identical to original dataset (Watanabe, 2018). During this process, the fit value gradually increases and approaches "1", suggesting that the final subsampled and original datasets are perfectly aligned in shape space. As a result, a curve of fit values called LASEC can be generated by plotting fit values against the number of randomly selected landmarks in each subsample (Watanabe, 2018). A LASEC demonstrates that when number of landmarks in a subsample increases, the fit value increases until reaches "1" (Watanabe, 2018). The entire process can also be repeated for multiple times to construct a mean LASEC. One can then estimate the number of landmarks needed to capture a similar amount of information as that in the original dataset by visually examine where the fit of the LASEC closely approaches "1" so that a plateau appears in the mean LASEC.

4.5 THE STRUCTURE OF ANALYSES

The results are divided into four chapters, reflecting the four cranial regions: entire cranium, the posterior cranium (without the frontal region), temporal bone, and frontal bone. For the analysis of the entire and posterior crania as well as of the temporal bones, the maximum-semilandmark dataset is designed to maximize cranial regions covered by semilandmarks, while the maximum-specimen set is designed to including more specimens following Baab's (2016) practice. In the analysis based on the maximum-specimen dataset of the entire and posterior crania, the semilandmark patches at the mandibular fossae and the mastoid processes are taken out (Appendix A 3.1 and A 3.2). For the analysis based on the maximum-specimen dataset of the temporal bones, only semilandmark patches at the mastoid processes are removed (Appendix A.3.3).

For each semilandmark dataset, three PCAs are performed. The first one includes only fossil hominids. The second also includes thirty-five *H. sapiens* crania along with the fossil specimens (see Appendix A). The third includes only eight *H. sapiens* crania along with the fossil specimens. The purpose of performing these three PCAs is to assess how large and small samples of *H. sapiens* can affect the ability of PCA to capture major aspects of shape differences within fossil hominids. These PCAs are also used to examine the shape differences included by semilandmark data of each cranial region. In the discussion chapter (Chapter 9), I assessed whether these shape differences revealed by PCAs can match actual morphology.

The statistical analyses listed previously are also performed for each landmark set based on the GMA of both fossils and a large *H. sapiens* sample. The bootstrapped analyses of the SSD and mean pairwise distance are used to assess the overall variability in *H. erectus* and its subsets in comparison to *H. sapiens*. The bootstrapped analyses of the pairwise distances between means and Procrustes ANOVA are used to evaluate differences between geographical subsets of the *H. erectus* sample. To understand detailed patterns of overall differences, measured by Procrustes distances, between individual specimens that may be concealed by SSDs and mean pairwise distances, individual pairwise distances between fossil specimens are examined with the aid of boxplot and UPGMA dendrogram.

To assess the effect of densities of points, PCA and the same statistical analyses are repeated for the datasets that only include anchor points, as well as the datasets only include discrete landmarks (Appendix A 3.5). The consistencies between results of the analyses for these datasets are evaluated. To further assess if the datasets with lower landmark densities are able to convey a similar amount of information, the LASECs for these datasets are also calculated. For the analysis of LASEC, the large sample of *H. sapiens* is included along with the fossil sample to increase the sample size and the efficiency of calculation. The results of these analyses are synthesized in the last chapter.

5.0 THE ENTIRE CRANIUM

5.1 THE PCA BASED ON THE MAXIMUM-SEMILANDMARK SET

5.1.1 The first PCA: The fossil sample

Table 5.1 The first PCA of the entire cranium: The percentage variance explained by the first seven PCs

	Percentage of Variance	Cumulative Percentage
PC 1	33.876%	33.876%
PC 2	17.137%	51.013%
PC 3	11.95%	62.96%
PC 4	8.404%	71.365%
PC 5	6.237%	77.601%
PC 6	5.907%	83.508%
PC 7	4.475%	87.983%

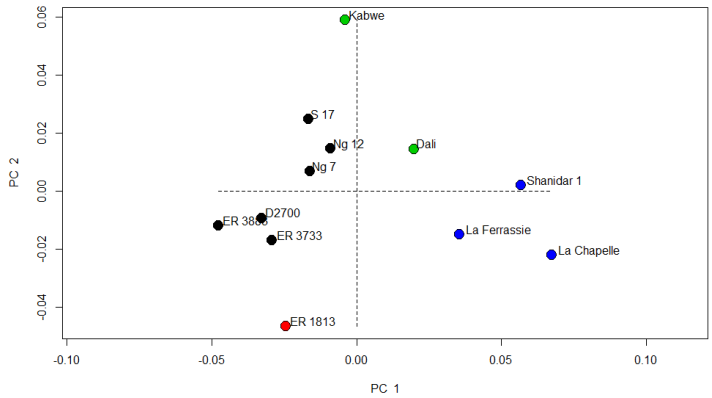

Figure 5.1 The first PCA of the entire cranium: The plot of PC 1 and PC 2
The black dots: *H. erectus*. The red dot: *H. habilis*. The green dots: Mid-Pleistocene *Homo*. The blue dots: Neanderthals.

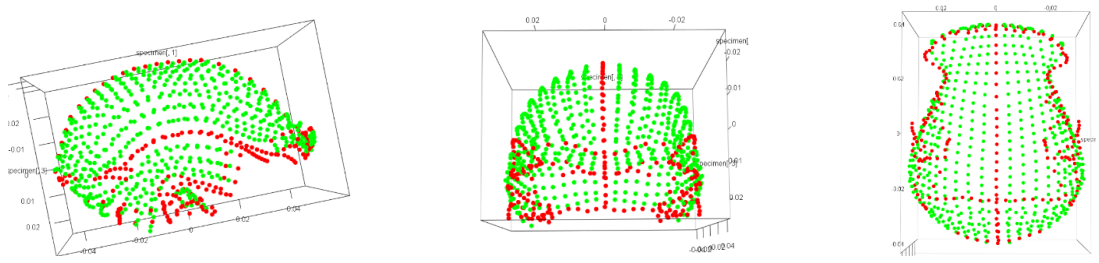

(A)

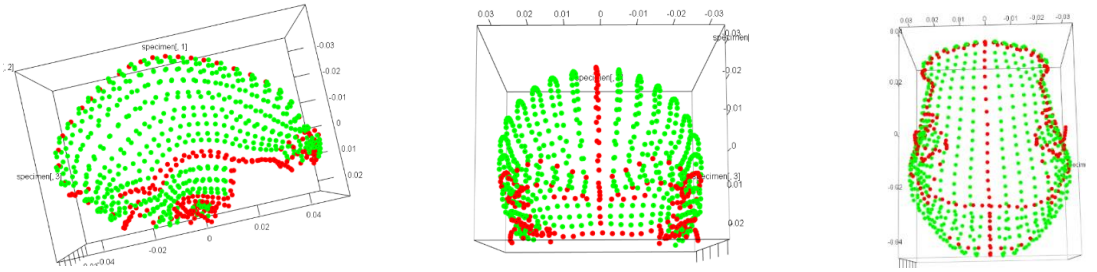

(B)

Figure 5.2 The first PCA of the overall cranium: The shapes at the two ends of PC 1
(A) The shape at the negative end. (B) The shape at the positive end. From left to right: lateral view, anterior view, and inferior view. The red dots are curve semilandmarks and discrete semilandmarks. The yellow dots are surface semilandmarks.

The first seven principal components (PCs) explain 87.983% of the total variance (Table 5.1). Procrustes ANOVA with 1,000 random permutations shows a significant size-shape relationship for PC 1, 38% of the total variance in which is associated with size (Table B.1 in Appendix B). This is likely because the specimens with higher PC 1 scores are the relatively large Dali and Neanderthal skulls.

PC 1 accounts for 33.876% of the total variance (Figure 5.1 and Figure 5.2). The *Homo erectus* specimens, KNM-ER 1813, and Kabwe 1 have negative scores for PC 1. D2700, KNM-ER 3733, and KNM-ER 1813 are intermediate between the specimen with the most negative score (ER 3883) and the specimens with the least negative scores (S17, Ng 7, Ng 12, and Kabwe 1). The Dali skull is intermediate between the Neanderthals, which have the most positive scores, and other hominids.

As the PC score increases, the temporal region decreases in size, while the vault expands (Figure 5.2). In particular, the midfrontal, midparietal, and midoccipital regions expand superiorly to a higher degree than other areas. Thus, in lateral view, the frontal rise becomes more vertical, the peak gradually shifts to the midparietal region, and the posterior most point shifts to the midoccipital region when approaching the positive end. Two flattened areas across the bregma and lambda are also observed as these areas expand to a lesser degree.

In anterior and posterior views, the points on the temporal region also roughly converge to the center of the cranial base, while the vault superior to the temporal region expands laterally. Consequently, the orientation of the side wall gradually becomes inwardly tilted, and the widest level shifts upward from the supramastoid region to around the temporal line.

The frontal bone also expands laterally, while its base along the alisphenoid remains relatively stable, causing the postorbital constriction to weaken. The highest point of the brow's superior margin and the mid-point of the upper orbit shift laterally, such that the ascending part of the brow elongates. As the lateral end moves slightly posteroinferiorly, the brow becomes somewhat more arched. In superior view, the lateral end also shifts slightly backward and inward.

In inferior view, the mandibular fossa decreases in size overall. Its long axis becomes more transversely oriented. The tympanic plate becomes more obliquely oriented. In lateral view, the fossa becomes more narrowly V-shaped since the posterior wall becomes more vertical. The degree of lateral flaring from the cranial base does not change significantly as the side wall also becomes more inwardly tilted. The mastoid process shifts anteromedially and becomes slightly narrower mediolaterally. The greatest width of the superior profile remains in the mastoid region. The nuchal plane also becomes narrower mediolaterally. Overall, the occipital region in superior view becomes anteroposteriorly elongated and mediolaterally narrower.

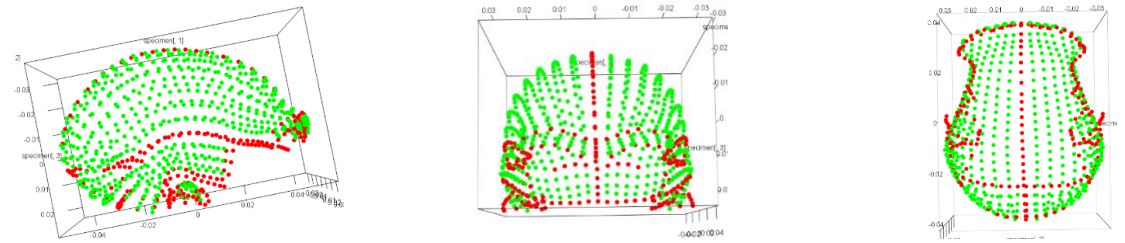

(A)

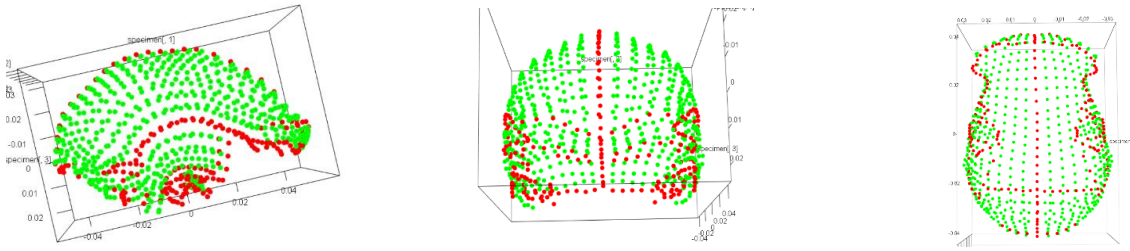

(B)

Figure 5.3 The first PCA of the entire cranium: The shapes at the two ends of PC 2
(A) The shape at the negative end. (B) The shape at the positive end. From left to right: lateral view, anterior view, and inferior view. The red dots are curve semilandmarks and discrete semilandmarks. The yellow dots are surface semilandmarks.

PC 2, which accounts for 17.137% of the total variance, contrasts Kabwe 1 (positive end) and KNM-ER 1813 (negative end) (Figure 5.1 and Figure 5.3). The *H. erectus* sample is separated into two somewhat separated clusters. D2700, KNM-ER 3733, and KNM-ER 3883 have negative PC scores, while S 17, Ng 7, and Ng 12 have positive scores. These specimens overlap with the Dali skull and the Neanderthals but have slightly more positive values.

Moving toward the positive end, the supraorbital and glabellar regions move forward and slightly downward, driving the entire frontal region to elongate anteroinferiorly, while the bregmatic region remains stable (Figure 5.3). The parietal region elongates posteriorly as the lambda moves posteroinferiorly. The parietal region before curving downward and the region anterior to lambda both become hollowed. Inion also slightly moves upward, such that the occipital bone shortens superoinferiorly.

The supraorbital region thickens superoinferiorly. The surface of the supraorbital and glabellar regions changes from slightly anterosuperiorly facing to anteroinferiorly facing as their superior margin shifts anteroinferiorly, while the inferior margin only moves downward. The surface of the descending

part of the brow is less anteroinferiorly facing. In superior view, the medial ascending part becomes more bulged. The superior contour of the supraorbital region curves more backward from the midline.

The superior squamosal portion expands. The squamosal suture becomes more arced as the anterior half raises upward. The inferior squamosal portion shortens anteroposteriorly as the mandibular fossa and points above it shift anteriorly. The suprameatal crest becomes thinner and more horizontal as auriculare shifts downward. The mastoid portion shifts anteroinferiorly. The parietal notch is more anteroinferiorly invaginated, creating a vertical component of the squamosal suture at the posterior end. As the asterion remains relatively still, the supramastoid portion also elongates anteroposteriorly. Overall, the entire mastoid portion becomes relatively lower than the squamosal portion.

The mastoid portion and the inferior squamosal portion also shift medially. Points superior to the squamosal suture shift somewhat superolaterally. Thus, the side wall changes from outwardly tilted and widest across the supramastoid region to slightly inwardly tilted and widest across the region above the squamosal suture. Points on both sides of the midline slightly shift downward, making the roof flatter.

The mastoid process is more inferiorly protruded. Its base becomes longer anteroinferiorly and shorter mediolaterally. The mandibular fossa becomes more narrower mediolaterally and less flared out from the cranial base. The medial end shortens anteroposteriorly more than the lateral end. The posterior wall becomes both more vertical and taller than the anterior wall. The fossa becomes slightly deeper. The tympanic plate becomes more obliquely oriented.

In inferior view, both the mandibular fossa and the mastoid process move anteromedially. The nuchal plane anterior to inion becomes less bulging and eventually becomes more concave in the positive half of this PC. It also elongates anteriorly. The superior profile is similarly wide in both the supraorbital region and the supramastoid region as the width at the former level expands mediolaterally, while that at the latter level becomes narrower mediolaterally.

5.1.2 The second PCA: The large sample of *Homo sapiens* sample and the fossil sample

Table 5.2 The second PCA of the overall cranium: The percentage variance explained by the first seven PCs

	Percentage of Variance	Cumulative Percentage
PC 1	42.27%	46.7%
PC 2	11.483%	53.756%
PC 3	9.234%	62.99%
PC 4	6.128%	69.117%
PC 5	4.492%	73.609%
PC 6	3.476%	77.085%
PC 7	2.607%	79.692%

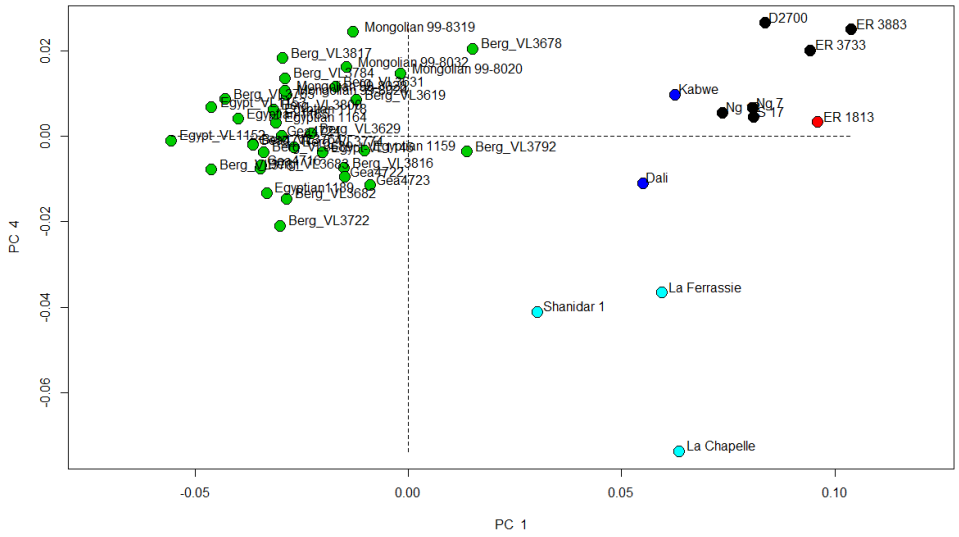

Figure 5.4 The second PCA of the overall cranium: The plot of PC 1 and PC 4
The black dots: The *H. erectus s. l.* specimens. The red dot: The *H. habilis* specimen. The dark blue dots: The Mid-Pleistocene *Homo* specimens. The light blue dots: the Neanderthal specimens. The green dots: The *H. sapiens* specimens.

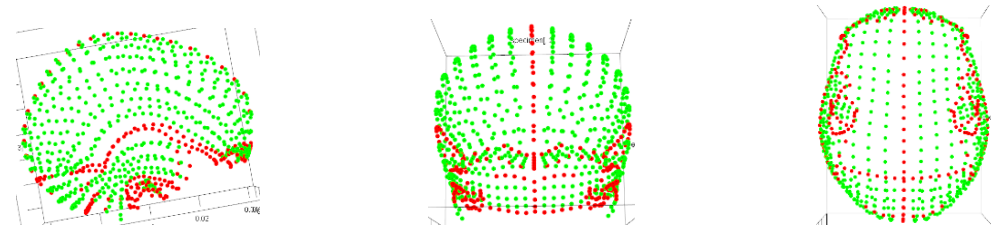

(A)

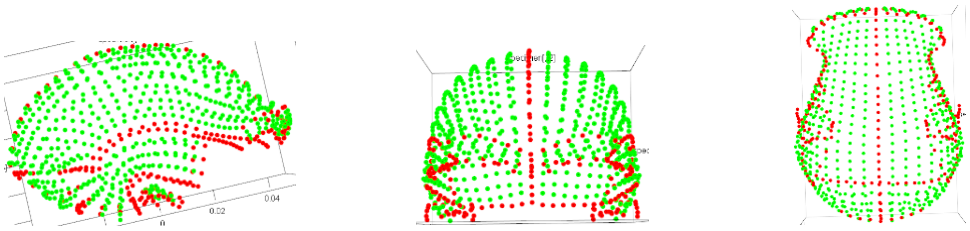

(B)

Figure 5.5 The second PCA of the entire cranium: The shapes at the two ends of PC 1
(A) The shape at the negative end. (B) The shape at the positive end. From left to right: lateral view, anterior view, and inferior view. The red dots are curve semilandmarks and discrete semilandmarks. The yellow dots are surface semilandmarks.

This set includes thirty-five *Homo sapiens* specimens along with fossil hominids. The first seven PCs explain 79.342% of the total variance (Figure 5.4, Table 5.2, and Table B.2). PC 1, which explains 42.27% of the total variance, particularly separates modern *H. sapiens* from all fossil hominids (Figure 5.4 and Figure 5.5). In general, fossil hominids have more positive scores than *H. sapiens*. KNM-ER 3883 is the fossil specimen with the most positive score. KNM-ER 3883 and KNM-ER 1813 are plotted to less positive positions. The Asian *H. erectus* specimens and D2700 have more negative scores. Kabwe 1, the Dali skull, and Neanderthals are intermediate between *H. sapiens* and *H. erectus*.

Closer to KNM-ER 3883 at the positive end, the vault becomes flatter and anteroposteriorly elongated (Figure 5.5). With bregma remaining relatively stable, the supraorbital region shifts anterosuperiorly. Thus, the frontal bone elongates anterosuperiorly and becomes lower and flatter. A horizontal posttoral plane is gradually produced near the positive end. The points at the midparietal region move downward faster than the points at the anterior and posterior parietal. Thus, the parietal region becomes flat, and the peak of the vault shifts to bregma when PC scores are higher than those of the Neanderthals. The region of inion shifts posterosuperiorly. As lambda remains relatively stable, the occipital squama becomes flatter, shorter superoinferiorly, and more inclined. The nuchal plane becomes

less inclined. Therefore, the occipital angle becomes sharper, and the posterior-most point of the vault shifts from the midoccipital region to inion when PC scores are higher than that of the Dali skull.

In anterior view, the roof becomes flatter. The side wall changes from inwardly tilted to outwardly tilted when scores are higher than those of the Neanderthals. Thus, the greatest width shifts downwardly from above the squamosal suture to the supramastoid region. The supraorbital and glabellar regions gradually expand mediolaterally and superoinferiorly. The ascending part of each brow and the glabellar region consistently face anteroinferiorly, while the descending part consistently faces anteroinferiorly. In superior view, the brow flares more laterally, while the frontal bone becomes narrower mediolaterally.

The temporal region elongates slightly anteroposteriorly. The squamosal suture becomes straighter, though the overall height of the temporal region does not change significantly. Auriculare moves posterosuperiorly, indicating that the suprameatal and supramastoid crests become more robust and oblique. The mandibular fossa shifts slightly laterally, expands mediolaterally, and flares more from the cranial base. Its posterior wall, the tympanic plate, becomes more transversely oriented and backwardly sloping.

The part of the superior contour posterior to the auditory meatus shortens anteroposteriorly and widens mediolaterally as the mastoid region shifts laterally. The base of the mastoid process, which protrudes less inferiorly, widens mediolaterally. The greatest width of the superior profile shifts from the auditory meatus to the mastoid region.

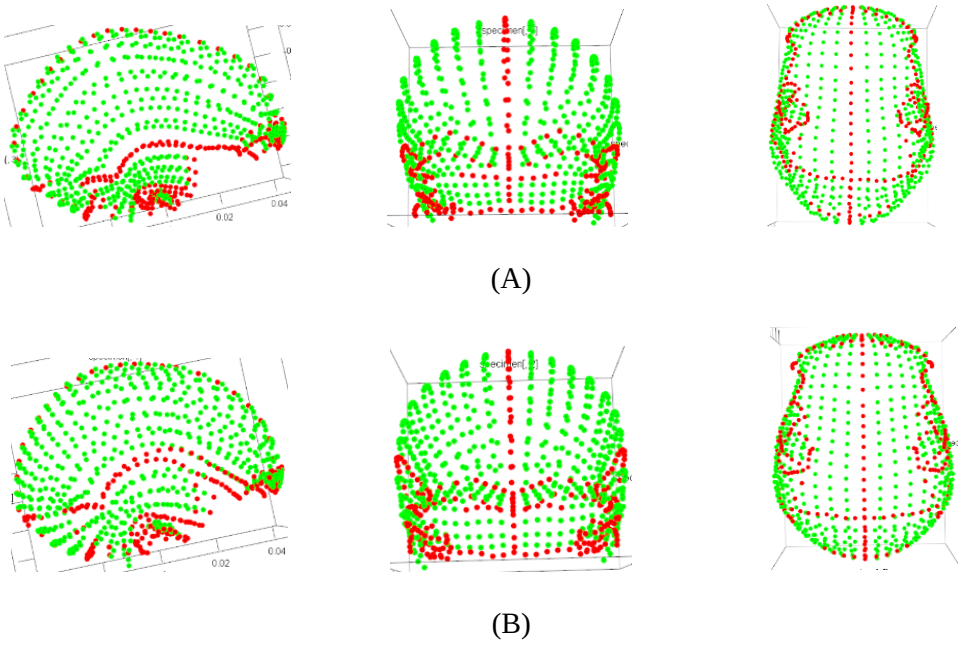

Figure 5.6 The second PCA of the overall cranium: The shapes at the two ends of PC 4
(A) The shape at the negative end. (B) The shape at the positive end. From left to right: lateral view, anterior view, and inferior view. The red dots are curve semilandmarks and discrete semilandmarks. The yellow dots are surface semilandmarks.

PC 2 and PC 3 primarily explain variation within the *H. sapiens* sample because of its large sample size. The fossil hominids are distributed in a relatively tight cluster. PC 4, which explains 6.128% of the total variance, shows a similar distribution of specimens as PC 1 from the analysis that includes only fossil hominids (Table 5.2, Figure 5.4 and Figure 5.6). Again, the three Neanderthals are separated from other specimens, including *H. sapiens*, by having more negative scores. The other fossils overlap the *H. sapiens* sample. The distribution of fossil specimens is also similar overall to that produced by PC 1 from the first analysis, with some minor differences. In this case, D2700, not KNM-ER 3883, is placed at the end opposite to the Neanderthals. KNM-ER 1813 overlaps the Indonesian specimens. PC 4 shows a significant size-shape relationship. This is likely because the three Neanderthal specimens are somewhat larger than the *H. sapiens* and other fossil specimens.

This PC also describes shape differences similar to those described by PC 1 in the first PCA (Figure 5.6). When approaching the Neanderthal end, the temporal region decreases in size and converges to the middle of the bottom, while the vault expands. Similarly, the midfrontal and midoccipital regions become more bulging, creating two flattened areas, one across bregma and another across lambda. The side wall also becomes inwardly tilted. Slightly different, this PC does not show much change in the

supraorbital region. The weakening of the postorbital constriction is solely driven by the widening of the frontal bone since the width of the supraorbital region remains unchanged.

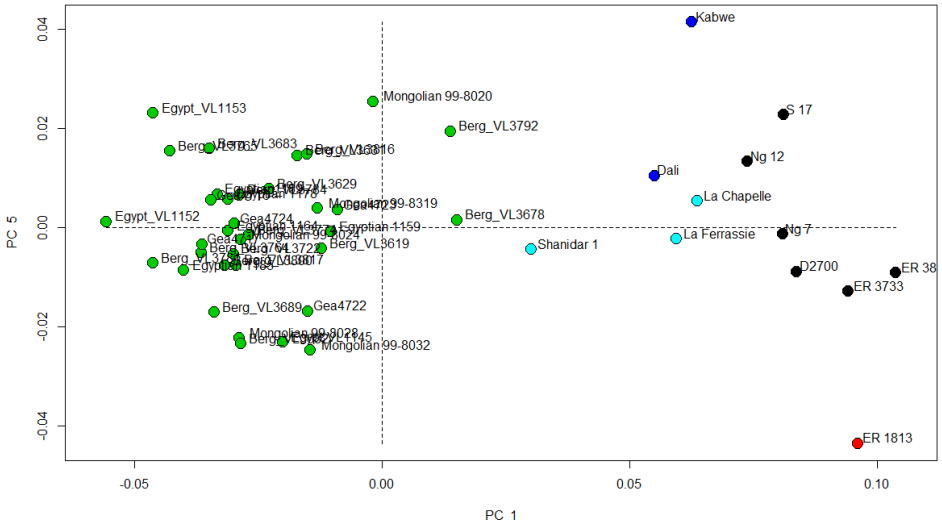

Figure 5.7 The second PCA of the entire cranium: The plot of PC 1 and PC 5
The black dots: The *H. erectus s. l.* specimens. The red dot: The *H. habilis* specimen. The dark blue dots: The Mid-Pleistocene *Homo* specimens. The light blue dots: the Neanderthal specimens. The green dots: The *H. sapiens* specimens.

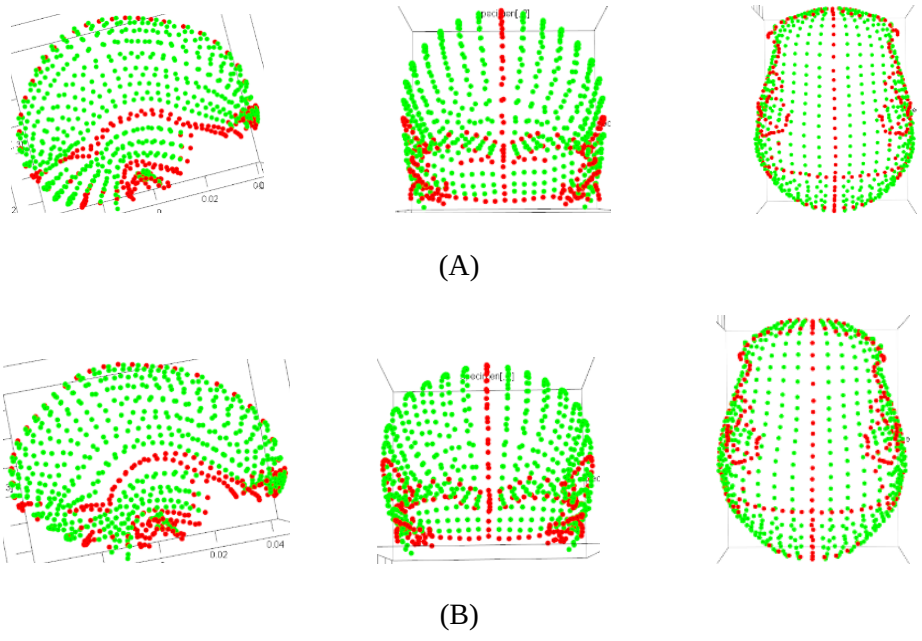

Figure 5.8 The second PCA of the entire cranium: The shapes at the two ends of PC 5
(A) The shape at the negative end. (B) The shape at the positive end. From left to right: lateral view, anterior view, and inferior view. The red dots are curve semilandmarks and discrete semilandmarks. The yellow dots are surface semilandmarks.

PC 5, which explains 4.492% of the total variance, shows a distribution of fossil specimens similar to PC 2 in the first analysis. This PC also contrasts Kabwe 1 and ER KNM-ER 1813 at its two ends (Table 5.2 and Figure 5.7). The other fossils overlap *H. sapiens*. PC 5 shows a significant correlation between size and shape (Table B.2). This is probably because KNM-ER 1813 is smaller than *H. sapiens* specimens, which are relatively large. PC 5 also describes patterns of shape differences very similar to those described by PC 2 in the first analysis, such as the anteroinferior elongation of the frontal, posterior elongation of the parietal, shortening of the occipital squama, and concavity at the nuchal plane (Figure 5.8). Slightly different, this PC shows nearly no change in the height of the squamosal portion. The squamosal portion becomes more arced because points at the posterior squamosal shift anteroinferiorly. The mastoid portion also decreases in size. In addition, the orientation of the posterior wall of the mandibular fossa remains constant rather than becoming more vertical.

5.1.3 The third PCA: The small sample of *Homo sapiens* and the fossil sample

Table 5.3 The third PCA of the entire cranium: The percentage variance explained by the first seven PCs

	Percentage of Variance	Cumulative Percentage
PC 1	45.897%	45.897%
PC 2	11.947%	57.844%
PC 3	7.996%	65.840%
PC 4	5.901%	71.741%
PC 5	5.015%	76.756%
PC 6	4.108%	80.865%
PC 7	3.638%	84.502%

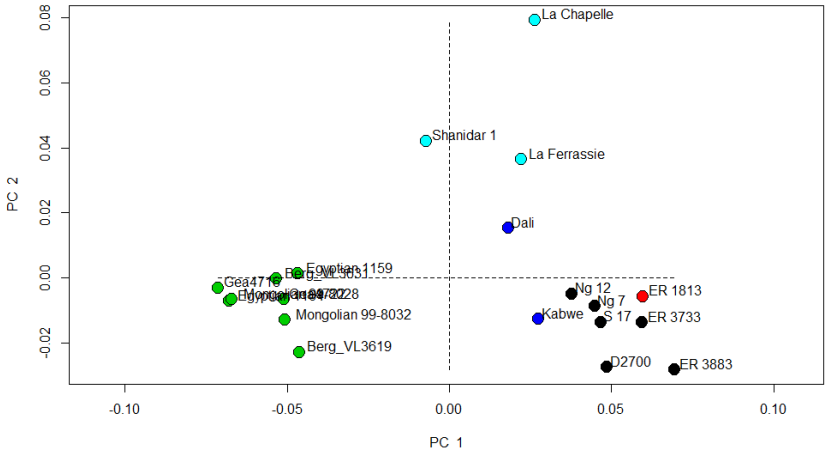

Figure 5.9 The third PCA of the entire cranium: The plot of PC 1 and PC 2
The black dots: The *H. erectus s. l.* specimens. The red dot: The *H. habilis* specimen. The dark blue dots: The Mid-Pleistocene *Homo* specimens. The light blue dots: the Neanderthal specimens. The green dots: The *H. sapiens* specimens.

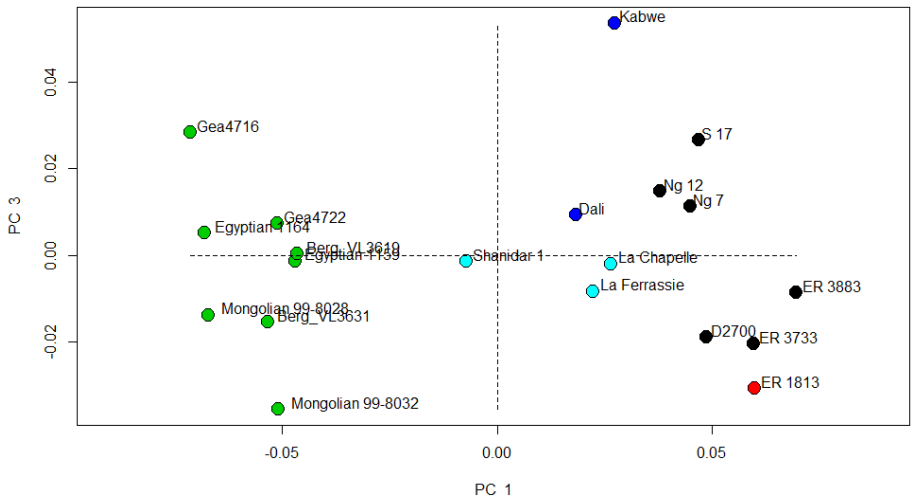

Figure 5.10 The third PCA of the entire cranium: The plot of PC 1 and PC 3
The black dots: The *H. erectus s. l.* specimens. The red dot: The *H. habilis* specimen. The dark blue dots: The Mid-Pleistocene *Homo* specimens. The light blue dots: the Neanderthal specimens. The green dots: The *H. sapiens* specimens.

After reducing the sample size of *H. sapiens* to eight, the higher-ranked PCs cease to explain variation within it. Instead, the first three PCs are consistent overall with PC 1, PC 4, and PC 5 of the second analysis that includes a large sample of *H. sapiens* (see Table 5.3, Figure 5.9 and Figure 5.10; Figure B.1 to Figure B.3 in Appendix B). These three PCs also show a significant size-shape relationship (Table B.3).

Only PC 3 shows slight inconsistencies with PC 5 of the second analysis (Figure 5.10 and Figure B.3). In this PC, KNM-ER 1813, though still lying at the end opposite to Kabwe 1, overlaps *H. sapiens*. Thus, this PC better emphasizes the distinction of Kabwe 1 from other fossils. PC 3 in this analysis also describes slightly different detailed shape differences. For example, moving toward the end of Kabwe 1, the anterior wall of the mandibular fossa becomes more horizontal, and the posterior wall becomes more vertical. The orientation of the side wall in anterior or posterior view almost does not change.

5.2 THE PCA BASED ON THE MAXIMUM-SPECIMEN LANDMARK SET

5.2.1 The fourth PCA: Only hominid specimens

Table 5.4 The fourth PCA of the entire cranium: The percentage variance explained by the first seven PCs

	Percentage of Variance	Cumulative Percentage
PC 1	30.185%	30.185%
PC 2	13.285%	43.470%
PC 3	11.652%	55.123%
PC 4	9.650%	64.773%
PC 5	6.854%	71.627%
PC 6	4.698%	76.325%
PC 7	4.621%	80.946%

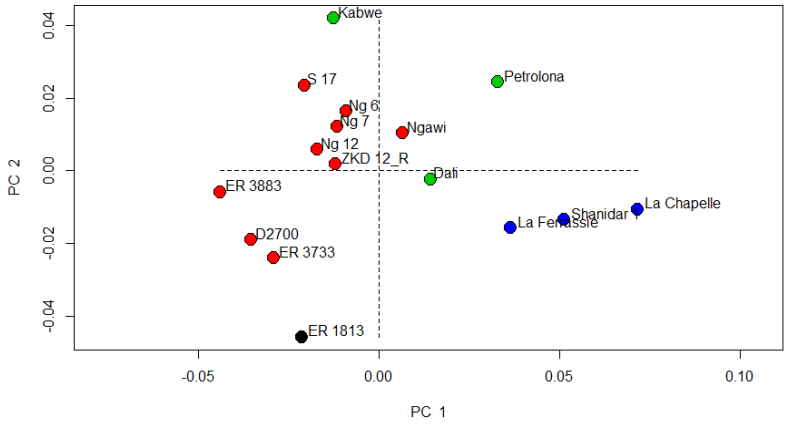

Figure 5.11 The fourth PCA of the entire cranium: The plot of PC 1 and PC 2
The red dots: The *H. erectus s. l.* specimens. The black dot: The *H. habilis* specimen. The green dots: The Mid-Pleistocene *Homo* specimens. The blue dots: the Neanderthal specimens. The graphs are generated by the Geomorph R package (Adams et al., 2018).

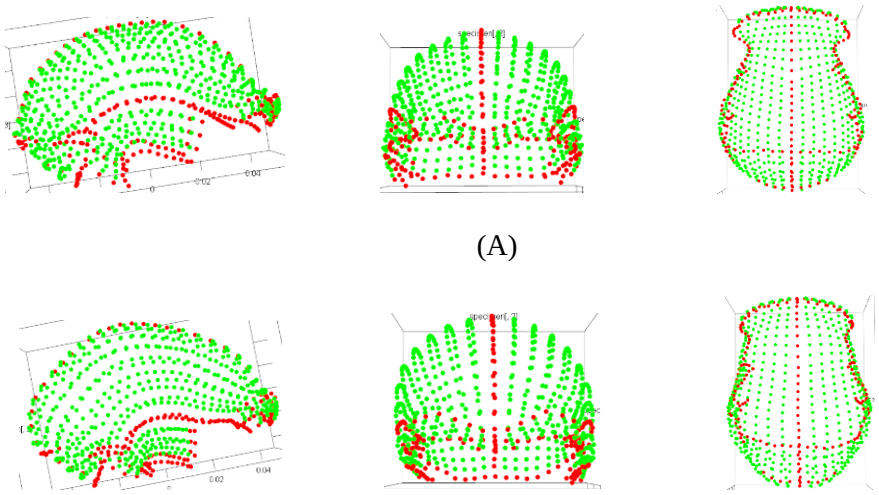

Figure 5.12 The fourth PCA of the entire cranium: The shapes at the two ends of PC 1
(A) The shape at the negative end. (B) The shape at the positive end. From left to right: lateral view, anterior view, and inferior view. The graphs are generated by the Geomorph R package (Adams et al., 2018).

This semilandmark dataset does not include semilandmarks and landmarks on the mandibular fossae and mastoid processes because these regions are often broken in hominid remains. This dataet allows further inclusion of Ng 6, ZKD 12, Ngawi 1, and the Petralona skull (Appendix A.3.1.2).

After adding a few more hominid specimens, the first two PCs are overall consistent with the first two PCs from the first analysis of the maximum-semilandmark set. PC 1, which explains 30.185% of the total variance, also contrasts the three Neanderthal specimens with KNM-ER 3883 and captures similar shape differences such as decreasing in size of the temporal region and the expansion of the vault (Table 5.4, Figure 5.11 and Figure 5.12). This PC shows a strong size-shape relationship, again because the three Neanderthals are relatively larger (Table B.4). Among the newly added specimens, Ng 6 and ZKD 12 have nearly identical scores to the other Indonesian specimens. Ngawi 1 is placed intermediate to the Dali skull and the Asian cluster. Petrolona turns out to be very close to the negative boundary of Neanderthals.

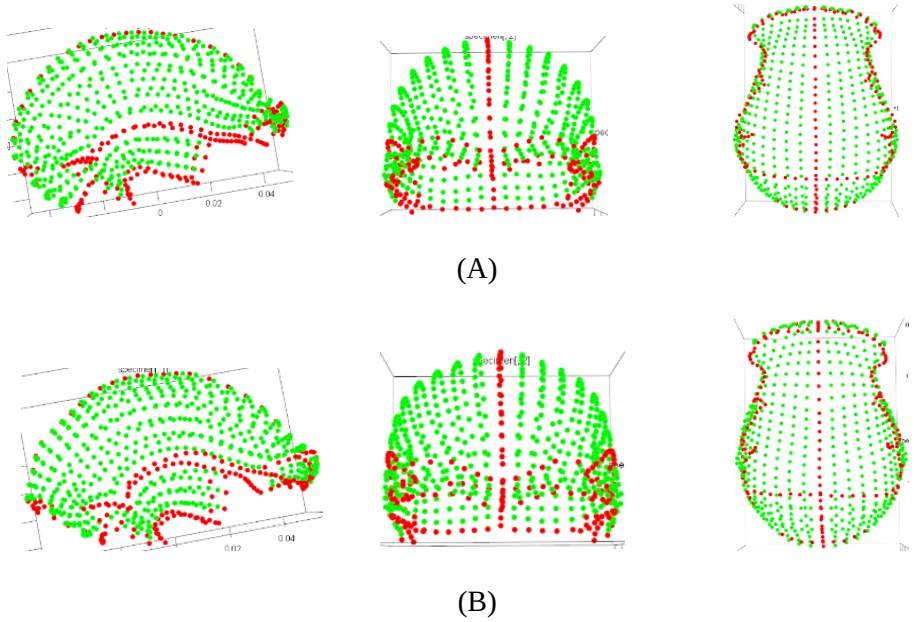

Figure 5.13 The fourth PCA of the entire cranium: The shapes at the two ends of PC 2
(A) The shape at the negative end. (B) The shape at the positive end. From left to right: lateral view, anterior view, and inferior view. The red dots are curve semilandmarks and discrete semilandmarks. The yellow dots are surface semilandmarks. The graphs are generated by the Geomorph R package (Adams et al., 2018).

PC 2, which explains 13.285% of the total variance, also places KNM-ER 1813 with Kabwe 1 at its two ends (Table 5.4 and Figure 5.11). Again, Ng 6, ZKD 12, and Ngawi 1 are grouped tightly with the other Indonesian remains. Petrolona is particularly close to S 17 and is relatively close to Kabwe 1. Slightly different from PC 2 of the first analysis of the maximum-semilandmark set, KNM-ER 3883 is more distant from D 2700 and KNM-ER 3733. This PC also demonstrates a strong size-shape relationship, probably because of the size difference between the small KNM-ER 1813 and the large Kabwe 1 (Table B.4). This PC also captures shape differences similar to those captured by PC 2 in the first analysis of the maximum-semilandmark set, such as the anteroinferior shift of the supraorbital region, the posterior elongation of the parietal bone and the superoinferior shortening of the occipital squama toward the Kabwe end. Slightly different from PC in the first analysis, the squamosal portion generally expands superiorly and shortens anteroposteriorly (Figure 5.12).

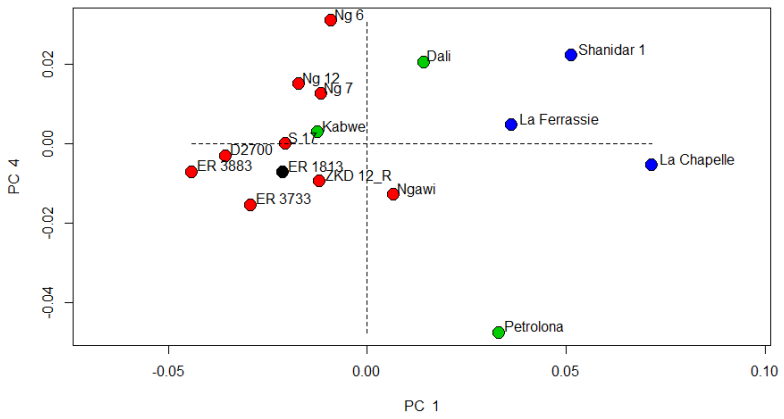

Figure 5.14 The fourth PCA of the entire cranium: The plot of PC 1 and PC 4
The red dots: The *H. erectus s. l.* specimens. The black dot: The *H. habilis* specimen. The green dots: The Mid-Pleistocene *Homo* specimens. The blue dots: the Neanderthal specimens. The red dots are curve semilandmarks and discrete semilandmarks. The yellow dots are surface semilandmarks. The graphs are generated by the Geomorph R package (Adams et al., 2018).

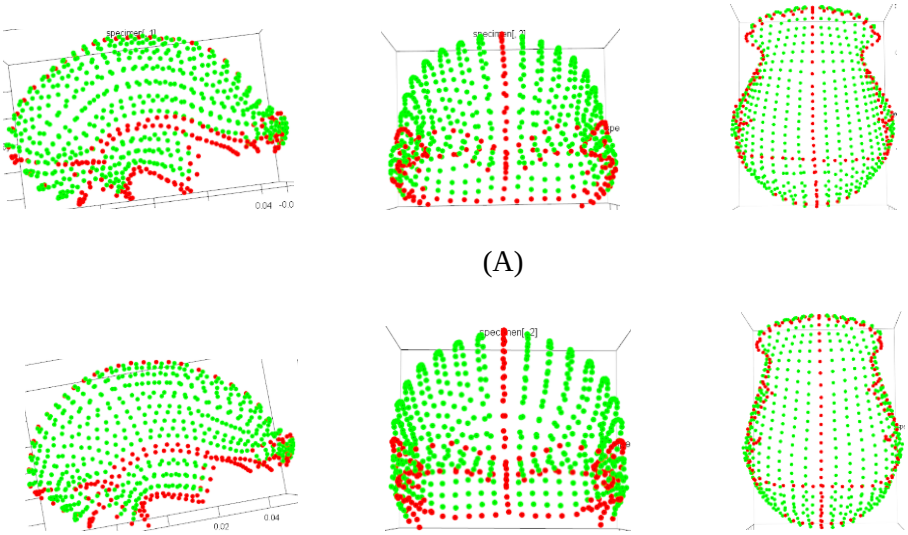

(A)

(B)

Figure 5.15 The fourth PCA of the entire cranium: The shapes at the two ends of PC 4
(A) The shape at the negative end. (B) The shape at the positive end. From left to right: lateral view, anterior view, and inferior view. The red dots are curve semilandmarks and discrete semilandmarks. The yellow dots are surface semilandmarks. The graphs are generated by the Geomorph R package (Adams et al., 2018).

PCs lower than the PC 4 are overall inconsistent with the corresponding PCs in the PCA of the maximum-semilandmark dataset that only includes fossils, partly because the newly added specimens are different in gross shapes. Specifically, PC 4 distinguishes Petralona 1 from the other hominids (see Table 5.4, Figure 5.14 and Figure 5.15). Closer to Petralona 1 (negative end), the parietal region shortens anteroposteriorly because the occipital squama elongates anterosuperiorly, creating a flattened area across lambda (Figure 5.15). Inion shifts slightly posterosuperiorly. The lateral ends of the brows flare more laterally. The mastoid portion becomes shortens anteroposteriorly. In inferior view, the width across the mastoid regions increases bilaterally. The inferior end of the anterior margin of the squamosal portion protrudes inferiorly.

5.2.2 The fifth PCA: The large sample of *Homo sapiens* and the fossil sample

Table 5.5 The fifth PCA of the entire cranium: The percentage variance explained by the first seven PCs

	Percentage of Variance	Cumulative Percentage
PC 1	46.609%	46.609%
PC 2	10.577%	57.187%
PC 3	8.452%	65.579%
PC 4	5.964%	71.603%
PC 5	4.025%	75.627%
PC 6	2.864%	78.491%
PC 7	2.581%	81.072%

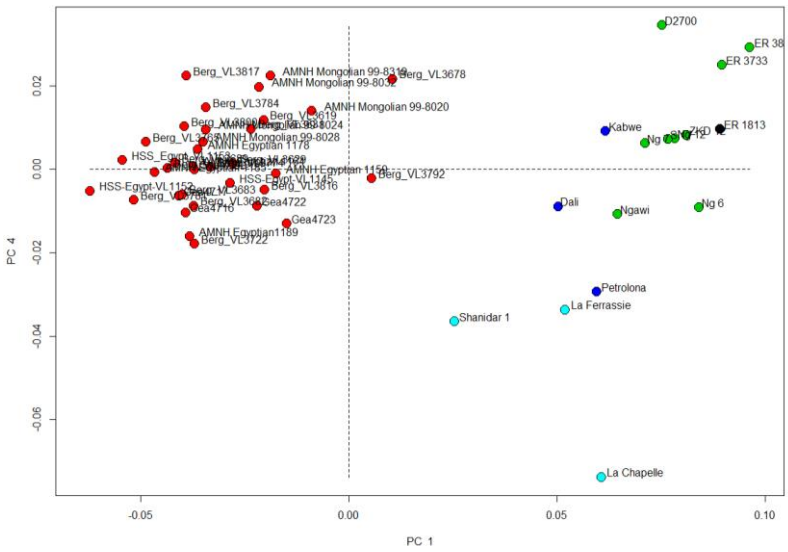

Figure 5.16 The fourth PCA of the entire cranium: The plot of PC 1 and PC 4
The green dots: The *H. erectus s. l.* specimens. The black dot: The *H. habilis* specimen. The dark blue dots: The Mid-Pleistocene *Homo* specimens. The light blue dots: the Neanderthal specimens. The red dots: The *H. sapiens* specimens. The graphs are generated by the Geomorph R package (Adams et al., 2018).

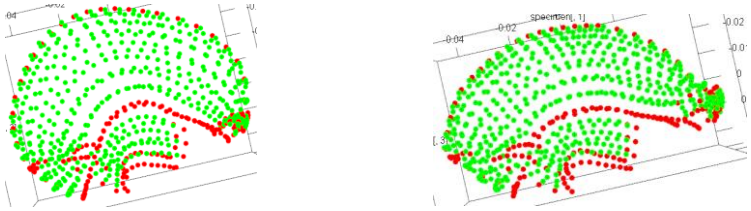

(A)

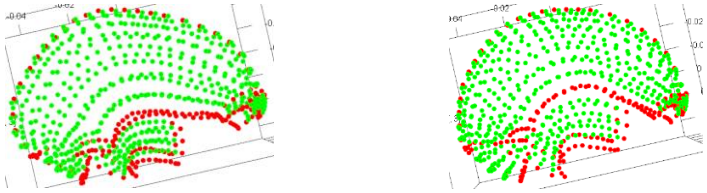

(B)

Figure 5.17 The fifth PCA of the entire cranium: The shapes at the two ends of PC 1 and PC 4
(A) Left: The shape at the negative end of PC 1; Right: The shape at the positive end of PC 1 (B) Left: The shape at the negative end of PC 4; Right: The shape at the positive end of PC 4. The red dots are curve semilandmarks and discrete semilandmarks. The yellow dots are surface semilandmarks. The graphs are generated by the Geomorph R package (Adams et al., 2018).

In this analysis, the first six PCs are overall consistent with the corresponding PCs in the PCA of the maximum-semilandmark dataset that includes the large *H. sapiens* and fossil samples, again suggesting that the effect of removing the mastoid process and mandibular fossa on PCA is little. PC 1 continues to separate the *H. sapiens* sample from the fossil sample by having more negative scores (Table 5.5, Figure 5.16 and Figure 5.17; also see Figure B.4 in Appendix B). ZKD 12 and Ng 6 overlap with the other Asian specimens. Ngawi 1 is placed at the negative end of the Asian *H. erectus* cluster. Petrolona, which is very close to Kabwe, is positioned at the positive boundary of Neanderthals.

PC 4 also separates Neanderthals from all other specimens (see Table 5.5 and Figure 5.16). The Asian *H. erectus* specimens, Kabwe 1, and the Dali skull are fairly close to each other. Petralona 1 is very close to the positive boundary of the Neanderthal cluster. Similar to PC 4 from the second analysis of the maximum-semilandmark set, this PC continues to show that the temporal region decreases in size relative to the vault in a specimen closer to Neanderthals (see Figure 5.17 and Figure B.5).

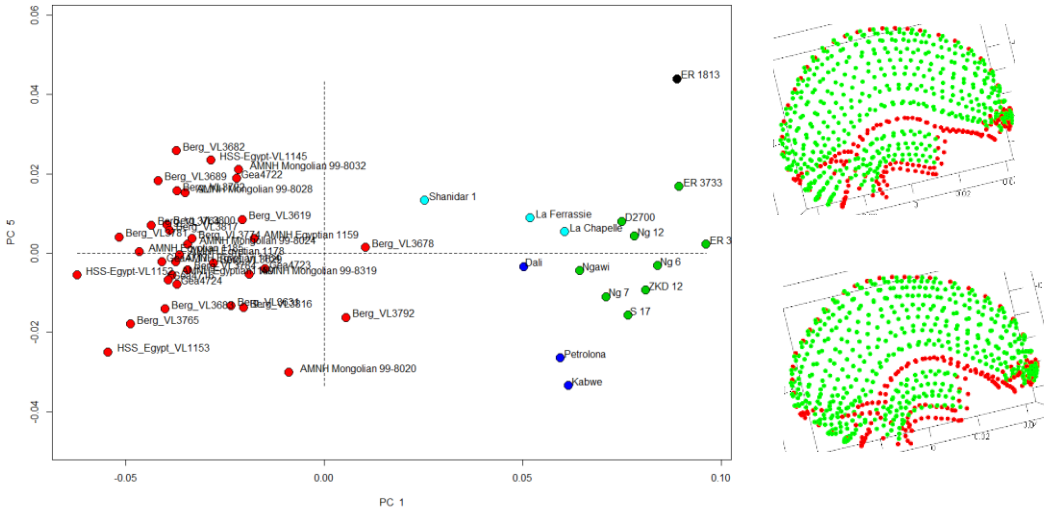

Figure 5.18 The fourth PCA of the entire cranium: The plot of PC 1 and PC 5
The below landmark configuration at the right side shows the negative-most shape of PC 5. The above landmark configuration side shows the positive-most shape of PC 5. The green dots: The *H. erectus s. l.* specimens. The black dot: The *H. habilis* specimen. The dark blue dots: The Mid-Pleistocene *Homo* specimens. The light blue dots: the Neanderthal specimens. The red dots: The *H. sapiens* specimens. The graphs are generated by the Geomorph R package (Adams et al., 2018).

PC 5, which explains only 4.025% of the total variance, also contrasts Kabwe 1 and KNM-ER 1813 at its two ends (Table 5.5 and Figure 5.18). The newly added Petralona 1 lies very close to Kabwe 1.

The other fossil specimens are fairly close to each other across the origin. This PC also reveals similar shape differences as the corresponding PC of the second analysis of the maximum semilandmark set, such as the anteroinferior elongation of the frontal and the posterior elongation of the parietal as well as the superoposterior shift of inion (Figure 5.18 and Figure B.6). Slightly different, this PC also reveals an asymmetrical component of shape differences: closer to Kabwe 1, the right mastoid region shifts medially more than the left side.

5.2.3 The sixth PCA: The small sample of *Homo sapiens* and the fossil sample

Table 5.6 The sixth PCA of the overall cranium: The percentage variance explained by the first seven PCs

	Percentage of Variance	Cumulative Percentage
PC 1	45.857%	45.857%
PC 2	11.454%	57.310%
PC 3	7.261%	64.571%
PC 4	5.191%	69.762%
PC 5	4.809%	74.571%
PC 6	4.399%	78.970%
PC 7	3.499%	82.469%

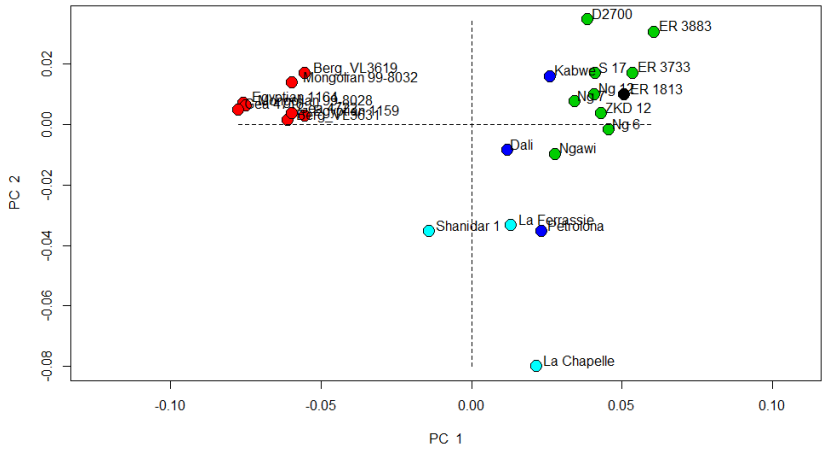

Figure 5.19 The fourth PCA of the entire cranium: The plot of PC 1 and PC 2
The red dots: The *H. erectus s. l.* specimens. The black dot: The *H. habilis* specimen. The green dots: The Mid-Pleistocene *Homo* specimens. The blue dots: the Neanderthal specimens.

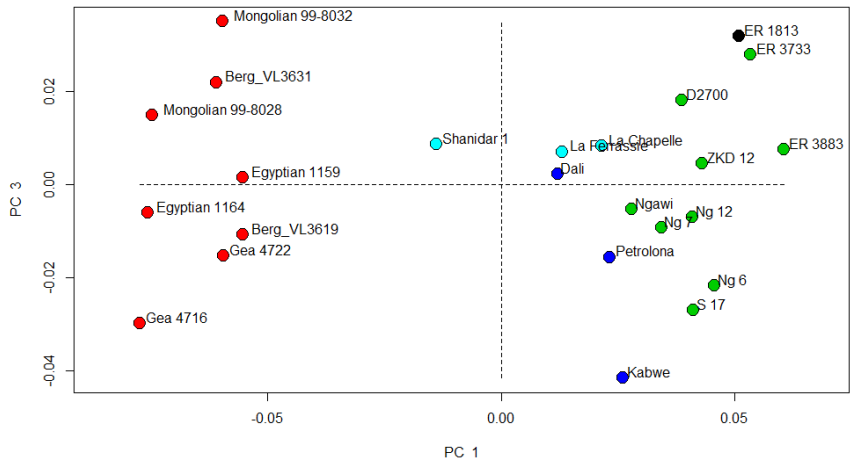

Figure 5.20 The fourth PCA of the entire cranium: The plot of PC 1 and PC 3
The red dots: The *H. erectus s. l.* specimens. The black dot: The *H. habilis* specimen. The green dots: The Mid-Pleistocene *Homo* specimens. The blue dots: the Neanderthal specimens. The graphs are generated by the Geomorph R package (Adams et al., 2018).

After decreasing the sample size of *H. sapiens* to eight, the first three PCs are consistent with PC 1, PC 4, and PC 5 of the analysis of the large sample of *H. sapiens* (Table 5.6, Figure 5.19 and Figure 5.20; also see Figure B.7, Figure B.8 and Figure B.9). Thus, the major PCs again cease to focus on variations within the *H. sapiens* sample. PC 3 shows some degree of inconsistency with PC 5 of the second analysis as well as PC 2 of the first analysis of the maximum-specimen set (Figure 5.20). Though this PC continues to contrast KNM-ER 1813 and Kabwe 1, these specimens are less separated from the other fossil hominid and *H. sapiens* specimens. However, overall, this PC still describes similar shape differences to PC 5 (Figure B.9). Other lower-ranked PCs are inconsistent with lower-ranked PCs from the other analyses. This is perhaps affected by both adding new specimens and removing the mastoid processes and mandibular fossae.

5.3 BOOTSTRAP ANALYSIS OF OVERALL VARIABILITY

5.3.1 Sum of squared Procrustes distances (SSDs)

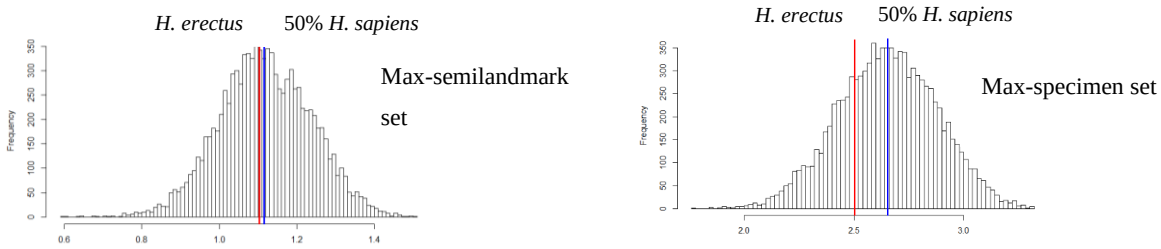

(A) *H. erectus* s. l. vs. *H. sapiens*

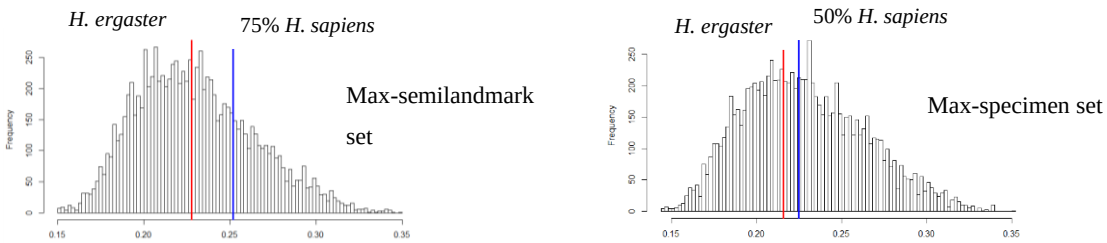

(B) *H. ergaster* (with D2700) vs. *H. sapiens*

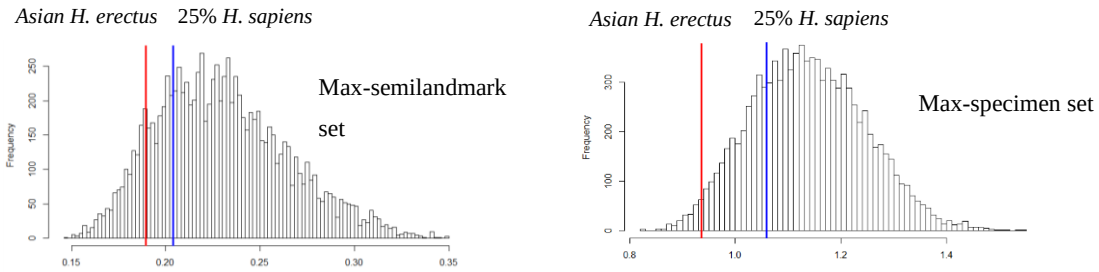

(C) Asian *H. erectus* vs. *H. sapiens*

Figure 5.21 The bootstrapped analyses of SSDs of the entire cranium
The histograms show the distributions of 10,000 bootstrapped SSDs for the *H. sapiens* samples based on the maximum-semilandmark set (left) and the maximum-specimen set (right). In (A), (B), and (C), the red lines indicate the SSDs of the *H. erectus s. l.*, *H. ergaster* (with D2700), and Asian *H. erectus* samples. In (A), the blue line indicates the 50th percentile of the *H. sapiens* SSDs. In (B), the blue line indicates the 75th percentile of the *H. sapiens* SSDs in the left graph and the 50th percentile in the right graph. In (C), the blue line indicates the 25th percentile of the *H. sapiens* SSDs.

Based on the maximum-semilandmark dataset, the sum of squared Procrustes distances (SSDs) of *H. erectus s. l.* and its subsets are not significantly greater than the bootstrapped SSDs of the *H. sapiens* sample (Figure 5.21 and Table B.7). The SSD of *H. erectus s. l.* falls below the 50th percentile of the *H. sapiens* SSDs: it exceeds 4,610 (46.10%) of the 10,000 *H. sapiens* SSDs. The SSD of *H. ergaster* that includes D2700 only slightly exceeds the 50th percentile of *H. sapiens* SSDs because it is greater than 5,168 *H. sapiens* SSDs. The SSD of Asian *H. erectus* is even less because it falls well below the 25th percentile of *H. sapiens* SSDs (greater than only 1,145 *H. sapiens* SSDs).

The results based on the maximum-specimen dataset show that the variability in *H. erectus* and its subsets are even less than in *H. sapiens* (Figure 5.21 and Table B.7). The SSD of *H. erectus s. l.* slightly exceeds the 25th percentile of *H. sapiens* as it is greater than 2,596 *H. sapiens* SSDs. The SSD of the *H. ergaster* sample that includes D2700 falls below the 50th percentile by exceeding 4,053 of the 10,000 *H. sapiens* SSDs. The SSD of Asian *H. erectus* becomes very small as it exceeds only 199 bootstrapped *H. sapiens* SSDs.

5.3.2 Mean pairwise Procrustes distances

(A) *H. erectus* s. l. vs. *H. sapiens*

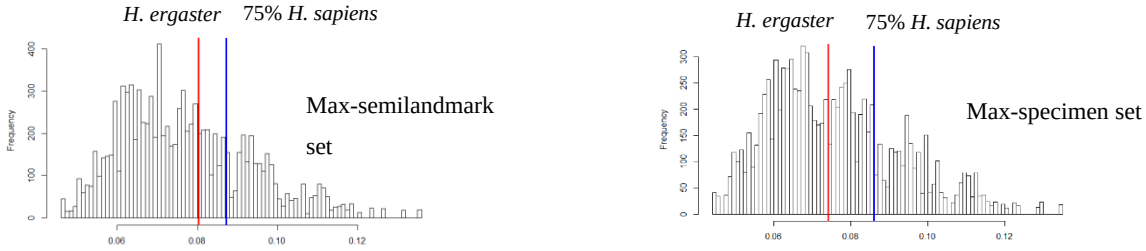

(B) African *H. ergaster* (ER 3733 and ER 3883) vs. *H. sapiens*

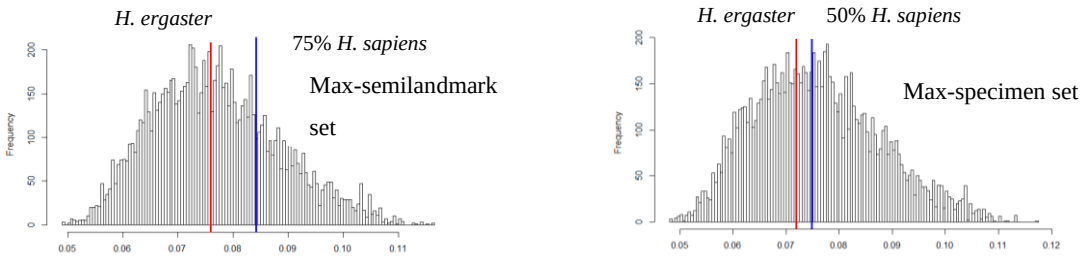

(B) *H. ergaster* (with D2700) vs. *H. sapiens*

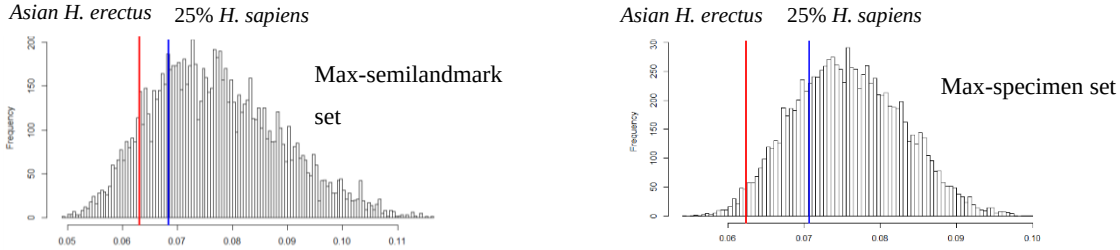

(C) Asian *H. erectus* vs. *H. sapiens*

Figure 5.22 The bootstrap analyses of mean pairwise distances of the entire cranium
The histograms show the distributions of 10,000 bootstrapped mean pairwise distances for the *H. sapiens* samples based on the maximum-semilandmark set (left) and the maximum-specimen set (right). In (A), (B), (C) and (D), the red lines indicate the mean pairwise distances of the *H. erectus s. l.*, *H. ergaster* (with and without D2700), and Asian *H. erectus* samples. In (A), the blue lines indicate the 50th percentile of the *H. sapiens* SSDs in both graphs. In (B), the blue lines indicate the 75th percentile of the *H. sapiens* SSDs in both graphs. In (C), the blue lines indicate the 75th percentile and 50th percentile of the *H. sapiens* SSDs in the left and right graphs respectively. In (D), the blue lines indicate the 25th percentile of the *H. sapiens* SSDs in both graphs.

Based on bootstrap analyses, the mean pairwise distances in *H. erectus s. l.* and its subsets are generally consistent with the SSDs in being not significantly greater than in *H. sapiens* (Figure 5.22 and Table B.7). Based on the maximum-semilandmark dataset, the mean distance of *H. erectus s. l.* is less than the 50th percentile of the *H. sapiens* mean distance as it exceeds 3,544 (35.44%) *H. sapiens* distances. The distance between KNM-ER 3733 and KNM-ER 3883, which is the only pairwise distance within the small African *H. ergaster* sample, is greater than 6,316 (63.16%) *H. sapiens* mean distances. When adding D2700, the mean distance of the *H. ergaster* sample exceeds 5,035 (50.35%) of the *H. sapiens* distances. The mean pairwise distance of Asian *H. erectus* is again very small as it exceeds only 1,068 (10.68%) of the 10,000 bootstrap distances of the *H. sapiens* sample.

Again, based on the maximum-specimen dataset, the mean distances of the *H. erectus s. l.* sample and its subsets are relatively small (Figure 5.21 and Table B.7). The mean distance of *H. erectus s. l.* is greater than only 1,187 (11.87%) of the 10,000 bootstrapped mean distances of the *H. sapiens* sample.

The distance between KNM-ER 3733 and KNM-ER 3883 is greater than 5,207 (52.07) of the *H. sapiens* distances. The mean distance of the *H. ergaster* sample including D2700 exceeds 4,074 (40.74%) of the *H. sapiens* distances. The mean pairwise distance with the Asian *H. erectus* sample exceeds only 209 (2.09%) of the *H. sapiens* distances.

5.4 INDIVIDUAL PAIRWISE DISTANCES

5.4.1 Maximum-semilandmark dataset

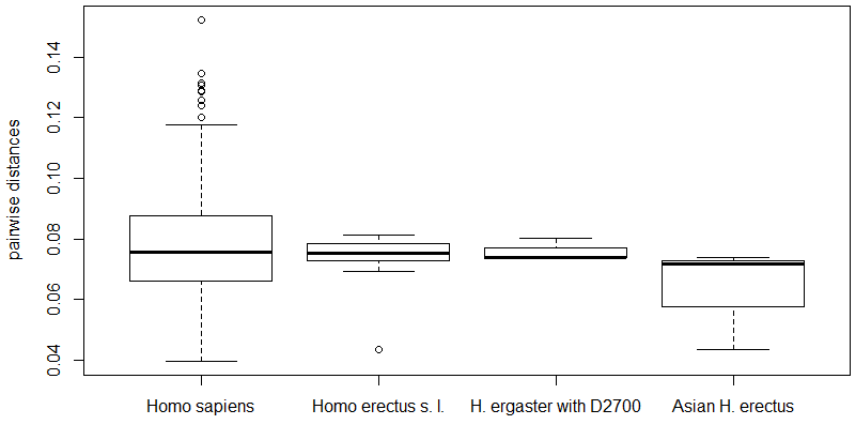

Figure 5.23 The boxplot of pairwise distances (maximum-semilandmark set of the entire cranium)

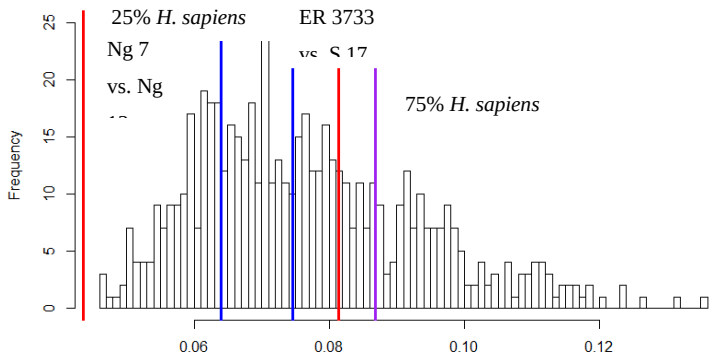

Figure 5.24 Individual *H. erectus* pairwise distances (the maximum-semilandmark set of the entire cranium) The histogram shows the distribution of all pairwise distances within the *H. sapiens* sample. From left to right, the blue lines indicate the 25th, 50th, and 75th percentiles of the *H. sapiens* pairwise distances. The left red line indicates the distance between Ng 7 and Ng 12, which is the smallest *H. erectus* distance. The right red line indicates the distance between ER 3733 and S 17, which is the largest *H. erectus* distance.

Table 5.7 Distribution of pairwise distances in the *H. sapiens* and *H. erectus* samples based on the maximum-semilandmark set of the entire cranium

	Mean	Min	25th	50th	75th	90th	Max
H. sapiens	0.0765	0.0461	0.0640	0.0745	0.0868	0.0986	0.135
H. erectus s. l.	0.0736	0.0436	0.0727	0.0753	0.0784	0.808	0.0815

Table 5.8 Individual pairwise distances of the *H. erectus* sample based on the maximum-semilandmark set of the entire cranium

(A) The pairwise distance that is less than the 25th percentile of the H. sapiens distances; (B) The pairwise distances that fall between the 45th and 65th percentiles of the H. sapiens distances.

(A)

	Ng 7 vs. Ng 12 (minimum)
Pairwise distance	0.0436

(B)

	ER 3733 vs. S 17 (maximum)	D2700 vs. ER 3733	D2700 vs. ER 3883	D2700 vs. Ng 7	D2700 vs. Ng 12	ER 3733 vs. ER 3883
Pairwise distance	0.0815	0.0735	0.0740	0.0811	0.0778	0.0803

	ER 3733 vs. Ng 12	ER 3883 vs. Ng 7	ER 3883 vs. Ng 12	ER 3883 vs. S 17	Ng 7 vs. S 17	Ng 12 vs. S 17
Pairwise distance	0.0761	0.0753	0.0767	0.0789	0.0738	0.0719

When assessing individual pairwise distances using the boxplot and histogram, none of the pairwise distances within *H. erectus s. l.* is significantly greater than *H. sapiens* pairwise distances, as the majority of former fall near the median of *H. sapiens* distances (Figure 5.23 and Figure 5.24). Furthermore, *H. ergaster* (including D2700) seems to be slightly more variable than Asian *H. erectus*.

Based on the individual pairwise distances between *H. erectus* specimens, the smallest pairwise distance is between Ng 7 and Ng 12 (Figure 5.24 and Table 5.8). This value is less than all the pairwise distances within the *H. sapiens* sample. The existence of this extreme value also explains why the SSD and mean pairwise distance of Asian *H. erectus* are much less than *H. erectus s. l.* and *H. ergaster*. However, all other pairwise distances, including between S 17 and the two Ngandong specimens, fall between the 45th and 65th percentiles of *H. sapiens* distances (Table 5.8). Thus, the distances among the other *H. erectus* specimens are not significantly greater than *H. sapiens* but are quite great if using the small distance between the two Ngandong specimens as a yardstick.

5.4.2 Maximum-specimen set

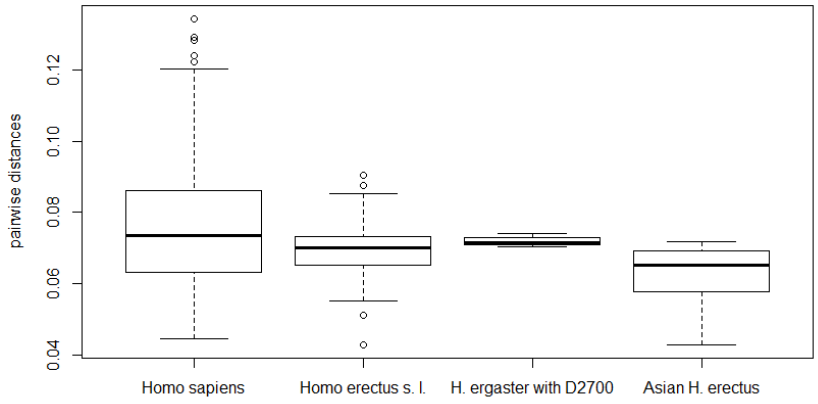

Figure 5.25 The boxplot of pairwise distances based on the maximum-specimen set of the entire cranium

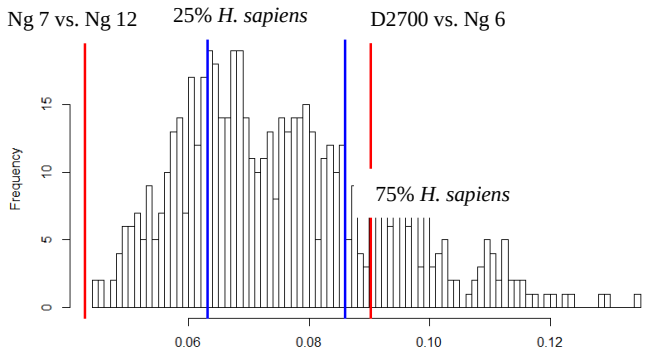

Figure 5.26 The histogram of individual pairwise distances of the *H. erectus* and *H. sapiens* samples based on the maximum-semilandmark set of the entire cranium

The histogram shows the distribution of all pairwise distances within the *H. sapiens* sample. From left to right, the blue lines indicate the 25th and 75th percentiles of the *H. sapiens* pairwise distances. The left red line indicates the distance between Ng 7 and Ng 12, which is the smallest *H. erectus* distance. The right red line indicates the distance between D2709 and Ng 6, which is the largest *H. erectus* distance.

Table 5.9 Distribution of pairwise distances in the *H. sapiens* and *H. erectus* samples based on the maximum-specimen set of the entire cranium

	Mean	Min	25th	50th	75th	90th	Max
H. sapiens	0.0760	0.0445	0.0632	0.0733	0.0860	0.0990	0.134
H. erectus s. l.	0.0695	0,0428	0.0654	0.0701	0.0729	0.0816	0.0858

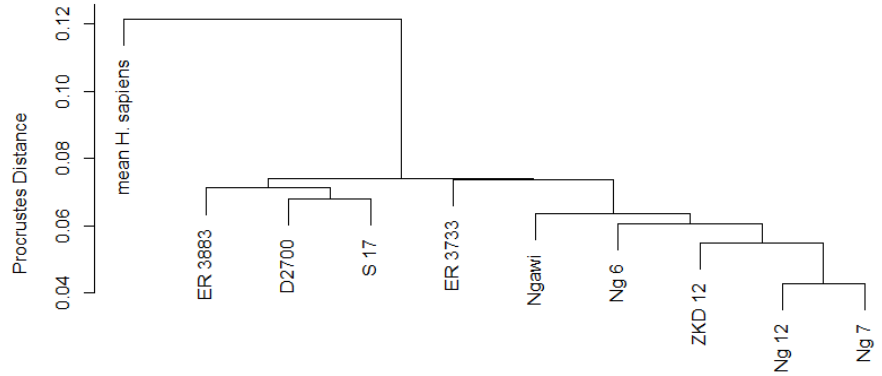

Figure 5.27 The UPGMA dendrogram of the *H. erectus* specimens and the mean shape of *H. sapiens* based on the maximum-specimen dataset of the entire crania

Table 5.10 Individual pairwise distances of the *H. erectus* sample based on the maximum-specimen set of the entire cranium

(A) The pairwise distances that is less than the 25th percentile of the *H. sapiens* distances; (B) The pairwise distances that fall between the 45th and 75th percentiles of the *H. sapiens* distances; (C) The pairwise distances that exceed the 75th percentile of the *H. sapiens* distances.

(A)

	Ng 7 vs. Ng 12 (minimum)	Ng 6 vs. Ng 12	Ng 12 vs. ZKD 12	Ng 6 vs. Ng 7	Ng 7 vs. Ngawi 1	Ng 7 vs. ZKD 12	Ngawi 1 vs. ZKD 12
Pairwise distance	0.0428	0.0550	0.0587	0.0568	0.0605	0.0511	0.0615

(B)

	D2700 vs. ER 3733	D2700 vs. Ng 12	D2700 vs. Ngawi	D2700 vs. Ng 7	ER 3733 vs. ER 3883	ER 3733 vs. Ngawi
Pairwise distance	0.0715	0.0775	0.0821	0.0725	0.0741	0.0812

	ER 3733 vs. S 17	ER 3883 vs. Ng 12	ER 3883 vs. Ng 6	ER 3883 vs. Ng 7	ER 3883 vs. Ngawi 1	ER 3883 vs. S 17	Ng 6 vs. S 17
Pairwise distance	0.0808	0.0710	0.0852	0.0706	0.0792	0.0723	0.0716

(C)

	D2700 vs. Ng 6 (max)	ER 3733 vs. Ng 6
Pairwise distance	0.0903	0.0874

The results based on the maximum-specimen dataset are similar overall with those based on the maximum-semilandmark dataset, as most of the pairwise distances within *H. erectus* are not significantly greater than the *H. sapiens* distances (Table 5.9, Table 5.10, Figure 5.25 and Figure 5.25). The three Ngandong and Ngawi 1 specimens are still very close to each other in distances. They are also very close to ZKD 12. In fact, all seven pairwise distances that below the 25th percentile of *H. sapiens* distances fall between these Asian specimens. The smallest distance, which is between Ng 7 and Ng 12, is also less than all *H. sapiens* distances. The only three pairwise distances that exceed the 25th percentile of *H. sapiens* distances within the Ngandong-Ngawi-ZKD group are those between Ng 6 and ZKD 12, Ng 12 and Ngawi 1, and Ng 6 and Ngawi 1, respectively. The distance between Ng 6 and Ngawi 1 is slightly less than the 45th percentile of *H. sapiens* distances, while the other two are both less than the 35th percentile of *H. sapiens* distances.

Nevertheless, overall the specimens of the Ngandong-Ngawi-ZKD group are more separated from S 17 than from each other (Table 5.10). Their distances fall between the 30th and 50th percentiles of the *H. sapiens* distances. The least distance is between Ng 7 and S 17, which falls between the 30th and 35th percentiles of the *H. sapiens* distances. The greatest distance is that between Ng 6 and S 17, which falls between the 45th and 50th percentiles of the *H. sapiens* distances.

The three pairwise distances among three *H. ergaster* fall between the 45th and 55th percentiles of the *H. sapiens* distances (Table 5.10 and Figure 5.25). Among these distances, the longest is that between ER 3733 and ER 3883, which is slightly shorter than the 55th percentile of the *H. sapiens* distances. The shortest distance is between KNM-ER 3883 and D2700, which is very slightly shorter than the 45th percentile of the *H. sapiens* distances.

The *H. ergaster* specimens are similarly separated from the Indonesian specimens. Among all fifteen pairwise distances, twelve exceed the 45th percentile of the *H. sapiens* distances (Table 5.10). The distance between KNM-ER 3733 and Ng 6 and the distance between D2700 and Ng 6 even exceed the 75th percentile of the *H. sapiens* distances (Table 5.10 and Figure 5.26). Eight other pairs fall between the 50th and 75th percentiles of the *H. sapiens* distances. The three pairs that fall below the 45th percentile of the *H. sapiens* distances are D2700-S 17, KNM-ER 3733-Ng 7, and KNM-ER 3733-Ng 12. In particular, KNM-ER 3733 and Ng 12 are relatively close, as the distance between them falls approximately at the 30th percentile of the *H. sapiens* distances.

In addition, the *H. ergaster* specimens generally differ less from ZKD 12 than from the Indonesian specimens. The distances between specimens from these two groups mostly fall between the 25th and 50th percentiles of the *H. sapiens* distances. Thus, ZKD 12 seems to be intermediate between other specimens in terms of pairwise distances.

In general, the Ngandong-Ngawi-ZKD specimens are very close to each other. Despite this cluster, the other specimens are different from each other to a similar degree. The distances among the three *H. ergaster* specimens as well as those between these *H. ergaster* and Indonesian specimens are relatively large. The somewhat smaller distances between ZKD 12 and the *H. ergaster* specimens are comparable to those between S 17 and specimens of the Ngandong-Ngawi-ZKD cluster. The unweighted pair group method with arithmetic mean (UPGMA) dendrogram roughly reflects these patterns of pairwise distances but should be interpreted carefully (Figure 5.27). It successfully groups the Ngandong-Ngawi-ZKD specimens into a cluster. KNM-ER 3733 is placed near the root of this cluster because it is fairly close to Ng 7 and Ng 12. S 17 is grouped with D2700 because the distance between them is slightly less than those between S 17 and other specimens.

5.5 DIFFERENCES BETWEEN GROUP MEANS

5.5.1 Bootstrap analysis

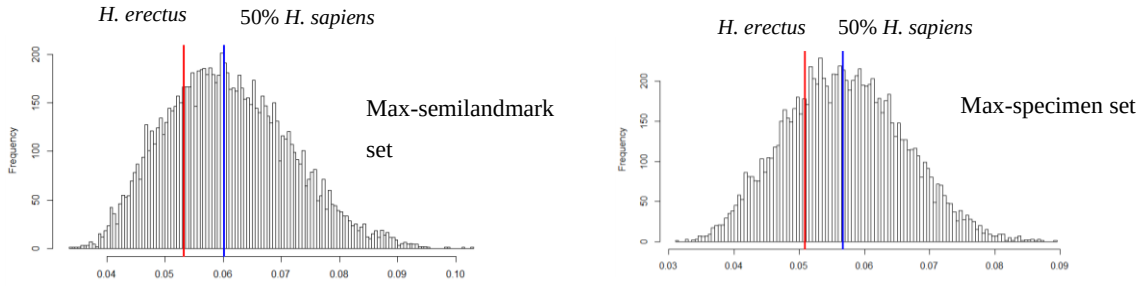

(A) *H. ergaster* (no D2700) vs. Asian *H. erectus*

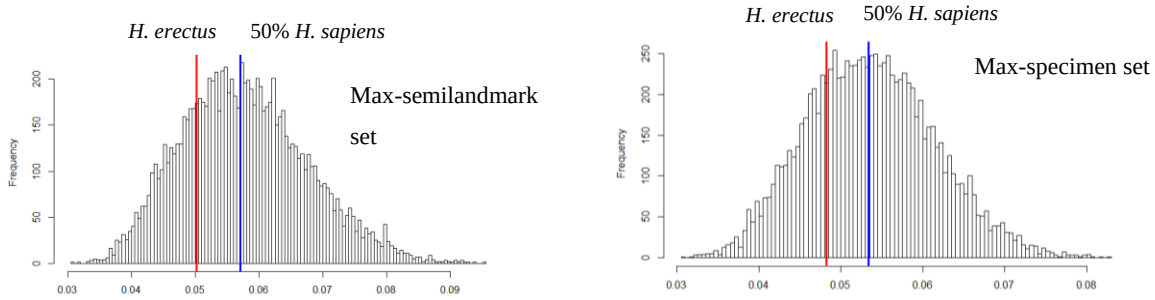

(B) *H. ergaster* (with D2700) vs. Asian *H. erectus*

Figure 5.28 The bootstrap analyses of distances between the means of *H. erectus* geographical subsets
In both (A) and (B), the left graph is based on the maximum-semilandmark set, while the right graph is based on the maximum-specimen landmark set. The blue line represents the 50th percentile of the 10,000 bootstrapped *H. sapiens* distances. (A) The red line represents the distance between the means of *H. ergaster* (no D2700) and Asian *H. erectus*. (B) The red line represents the distance between the means of *H. ergaster* (with D2700) and Asian *H. erectus*.

Differences between the mean shapes of subsets of *H. erectus* are insignificant compared to distances between bootstrapped mean shapes of *H. sapiens* subsets (Figure 5.28). For the maximum-semilandmark set, the distance between African *H. ergaster* and Asian *H. erectus* means exceeds only 2,581 (25.81%) of the 10,000 bootstrapped *H. sapiens* distances. The distance between *H. ergaster* (including D2700) and Asian *H. erectus* means exceeds only 2,387 (23.87%) of the 10,000 bootstrapped distances. For the maximum-specimen dataset, the results are consistent. The former pairwise distance exceeds 2,667 of the bootstrapped *H. sapiens* distances, while the latter distance exceeds 2,587 *H. sapiens* distances. These results are expected because pairwise distances within the *H. erectus* sample are not exceptionally great relative to the *H. sapiens* subsets. Furthermore, ZKD 12 is not very different from the *H. ergaster* specimens, while S 17 and D2700 are very close to each other.

5.5.2 Procrustes ANOVA

Table 5.11 The Procrustes ANOVA of the *H. sapiens* geographical subsets
(A) The Procrustes ANOVA based on the maximum-semilandmark set. (B) The Procrustes ANOVA based on the maximum specimen set. For each analysis, 10,000 permutations were carried out.

(A)

	Degrees of Freedom	Sum of Squares	Mean Square	R Squared (Coefficient of Determination)	F-value	P-value
Asian vs. African *H. sapiens*	1	0.016369	0.0163691	0.1566	6.1274	0.001
Residuals	33	0.088158	0.0026715	0.8434		
Total	34	0.104528				

(B)

	Degrees of Freedom	Sum of Squares	Mean Square	R Squared (Coefficient of Determination)	F-value	P-value
Asian vs. African *H. sapiens*	1	0.016398	0.0163982	0.15996	6.2837	0.0004
Residuals	33	0.086118	0.0026096	0.84004		
Total	34	0.102516				

Table 5.12 The Procrustes ANOVA of the *H. erectus* geographical subsets (84 permutations)
(A) *H. ergaster* (no D2700) vs. Asian *H. erectus* based on the maximum-semilandmark set. Ten permutations were carried out. (B) *H. ergaster* (no D2700) vs. Asian *H. erectus* based on the maximum-specimen set. 28 permutations were carried out. (C) *H. ergaster* (with D2700) vs. Asian *H. erectus* based on the maximum-semilandmark set. 20 permutations were carried out. (D) *H. ergaster* (with D2700) vs. Asian *H. erectus* based on the maximum-specimen set. 84 permutations were carried out.

(A)

	Degrees of Freedom	Sum of Squares	Mean Square	R Squared (Coefficient of Determination)	F-value	P-value
H. ergaster (no D2700) vs. Asian *H. erectus*	1	0.0034004	0.0034004	0.31503	1.3797	0.3
Residuals	3	0.0073937	0.0024646	0.68497		
Total	4	0.107942				

(B)

	Degrees of Freedom	Sum of Squares	Mean Square	R Squared (Coefficient of Determination)	F-value	P-value
H. ergaster (no D2700) vs. Asian *H. erectus*	1	0.0038765	0.0038765	0.23492	1.8423	0.03571
Residuals	6	0.0126249	0.0021042	0.76508		
Total	7	0.165014				

(C)

	Degrees of Freedom	Sum of Squares	Mean Square	R Squared (Coefficient of Determination)	F-value	P-value
H. ergaster (with D2700) vs. Asian *H. erectus*	1	0.0037773	0.0037773	0.27528	1.5194	0.2
Residuals	4	0.0099440	0.0024860	0.72472		
Total	5	0.0137213				

(D)

	Degrees of Freedom	Sum of Squares	Mean Square	R Squared (Coefficient of Determination)	F-value	P-value
H. ergaster (with D2700) vs. Asian *H. erectus*	1	0.0046554	0.0046554	0.23614	2.164	0.02381
Residuals	7	0.0150591	0.0021513	0.76386		
Total	8	0.0197146				

The Procrustes ANOVA of both the maximum-semilandmark and maximum-specimen datasets shows that a significant amount of the total variance is correlated with the separation of the two geographical subsets, as the p-values are much less than 0.05 (Table 5.12).

The Procrustes ANOVAs of the *H. erectus* subsets are limited by the small sample sizes. The Procrustes ANOVA of the difference between the means of African *H. ergaster* and Asian *H. erectus* based on the maximum-semilandmark dataset yields a p-value of 0.3 (Table 5.12 A). However, the number of total random permutations is only 10. This means that the empirical F-value calculated from the difference between the African and Asian group means exceeds six of the nine permutated F-values. After adding D2700 to the *H. ergaster* sample, the p-value becomes 0.2 (Table 5.12 B). As the number of total permutations is 20, the empirical F-value now exceeds 16 of the 19 permutated F-values.

When using the maximum-specimen dataset, the p-value based on 28 total permutations of the differences between the mean of African *H. ergaster* and that of Asian *H. erectus* drops to 0.03571 (Table 5.13 C). Therefore, the empirical F-value exceeds 26 of the 27 permutated F-values. After adding D2700 to the *H. ergaster* sample, the p-value based on the 84 total permutations drops to 0.02381, meaning that the empirical F-value exceeds 81 of the 83 permutated F-values.

Notably, the p-values of the *H. sapiens* geographical subsets based on both landmark sets fall well below the 0.05 critical value, indicating that even the p-value suggests that a significant amount of variance can be explained by the separation of group means, which may not indicate different species (Table 5.12 C and D). Furthermore, the differences between means of the *H. erectus* geographical subsets are likely driven by the distinct Ngandong-Ngawi cluster. The specimens within the *H. ergaster* cluster remain different from each other when using the Ngandong-Ngawi cluster as a yardstick.

5.6 OVERALL SIMILARITY WITH OTHER FOSSIL SPECIMENS

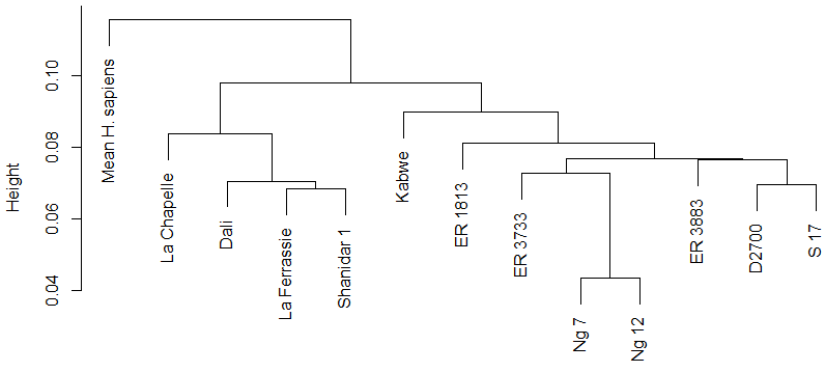

(A)

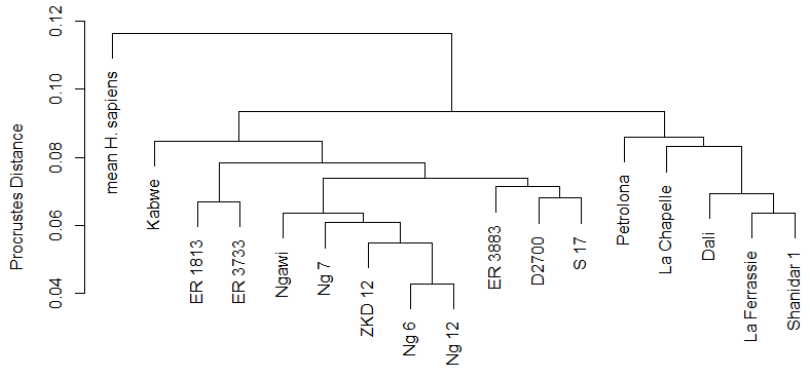

(B)

Figure 5.29 The UPGMA dendrogram of the fossil specimens and the mean shape of *H. sapiens*
(A) The maximum-semilandmark set. (B) The maximum-specimen set.

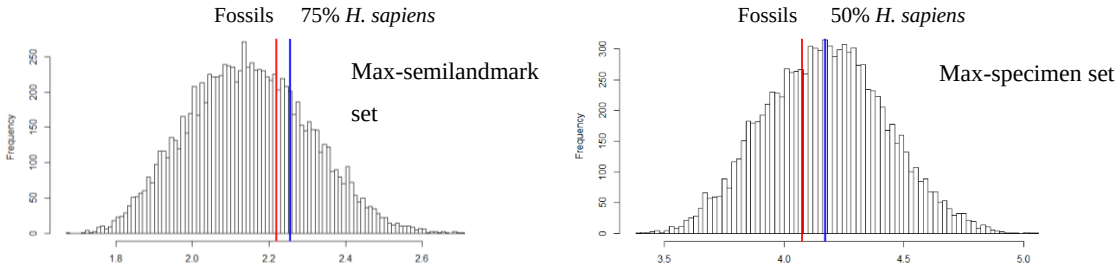

Figure 5.30 The bootstrapped analyses of fossil SSDs of the entire cranium
The fossil set includes ER 1813 and Kabwe. The left graph is based on the maximum-semilandmark set. The red line represents the SSD of the fossil set. The blue line represents the 75th percentile of the *H. sapiens* SSDs. The right graph is based on the maximum-specimen set. The blue line represents the 50th percentile of the *H. sapiens* SSDs.

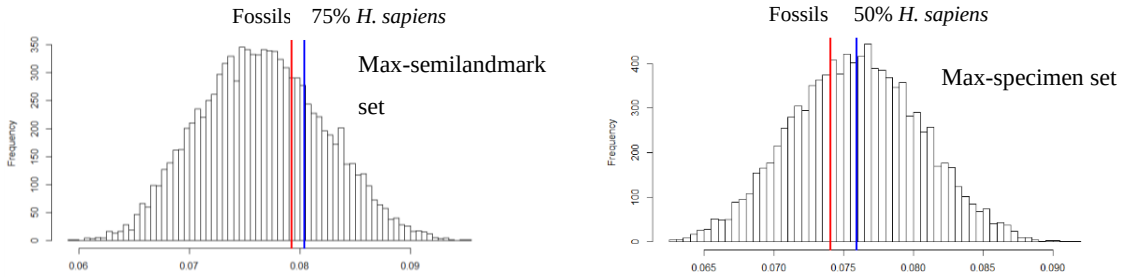

Figure 5.31 The bootstrapped analyses of mean pairwise distances of the entire cranium
The fossil set includes ER 1813 and Kabwe. The left graph is based on the maximum-semilandmark set. The blue line represents the 75th percentile of the *H. sapiens* SSDs. The right graph is based on the maximum-specimen set. The blue line represents the 50th percentile of the *H. sapiens* SSDs.

After adding other hominid specimens, the UPGMA dendrograms based on both the maximum-semilandmark and maximum-specimen datasets show consistent results overall (Figure 5.29). Neanderthals, the Dali skull, and Petralona 1 are allocated to a cluster that is separated from *H. erectus*. KNM-ER 1813 and Kabwe 1 are allocated to the *H. erectus* cluster. In the analyses based on both data sets, Kabwe 1 is placed near the root of this cluster, indicating that it differs more from the other *H. erectus* specimens than KNM-ER 1813. In the analysis based on the maximum-specimen dataset, KNM-ER 1813 is even grouped with ER 3733.

After adding Kabwe and ER 1813 to the *H. erectus* cluster, the SSD based on the maximum-semilandmark set still falls below the 75th percentile of the bootstrapped *H. sapiens* SSDs, as it exceeds only 6,746 (67.46%) *H. sapiens* SSDs (Figure 5.30). The mean pairwise distance based on the same

landmark set also exceeds only 6,809 (68.09%) bootstrapped *H. sapiens* distances (Figure 5.31). Using the maximum-specimen set, the SSD of the cluster that includes the *H. erectus* specimens, ER 1813 and Kabwe exceeds only 3,559 (35.59%) bootstrapped *H. sapiens* SSDs (Figure 5.30). The mean pairwise distance of this cluster exceeds only 3,506 (35.06%) bootstrapped *H. sapiens* distances (Figure 5.31).

5.7 LOWER LANDMARK DENSITIES

5.7.1 One hundred fifty-nine anchor points

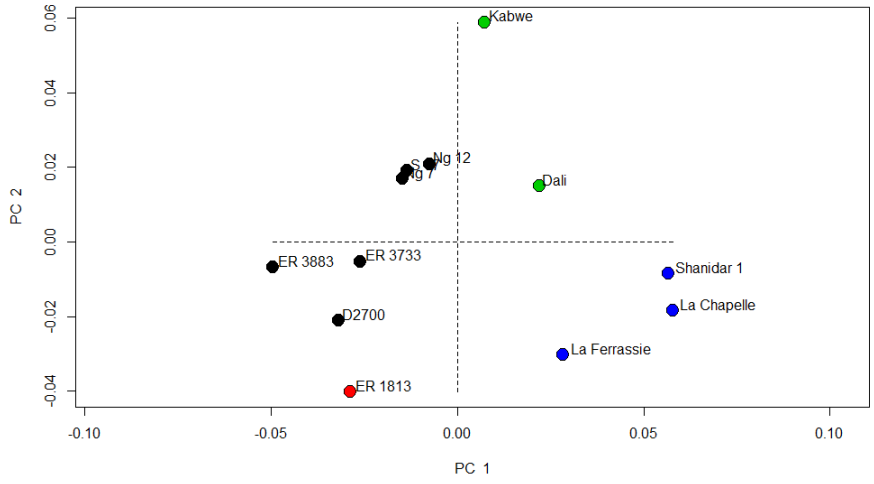

Figure 5.32 The plot of PC 1 and PC 2 of the fossil sample based on the anchor points of the overall cranium

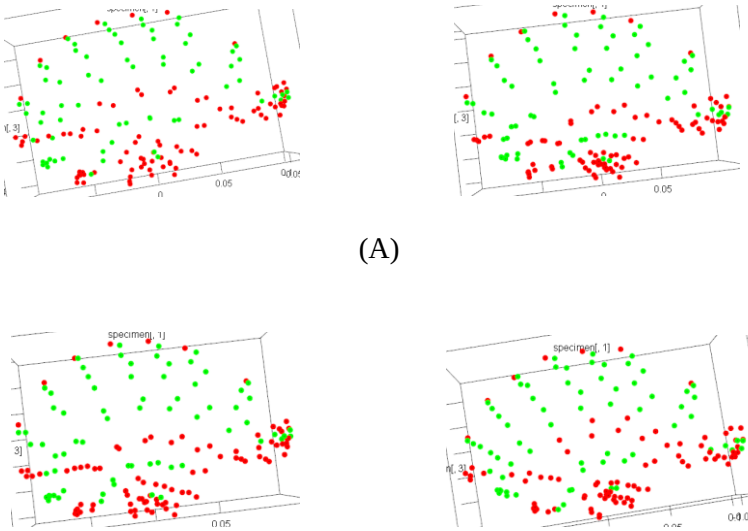

(A)

(B)

Figure 5.33 The shapes at the two ends of PC 1 and PC 2 based on the anchor points of the entire cranium
(A) Left: The shape at the negative end of PC 1; Right: The shape at the positive end of PC 1 (B) Left: The shape at the negative end of PC 2; Right: The shape at the positive end of PC 2. The graphs are generated by the Geomorph R package (Adams et al., 2018).

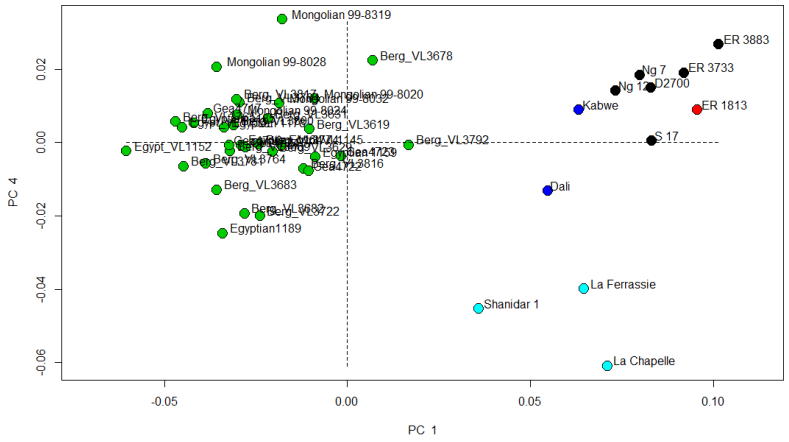

Figure 5.34 The PC 1 and PC 4 plot of *H. sapiens* and fossils (the anchor points of the entire cranium)

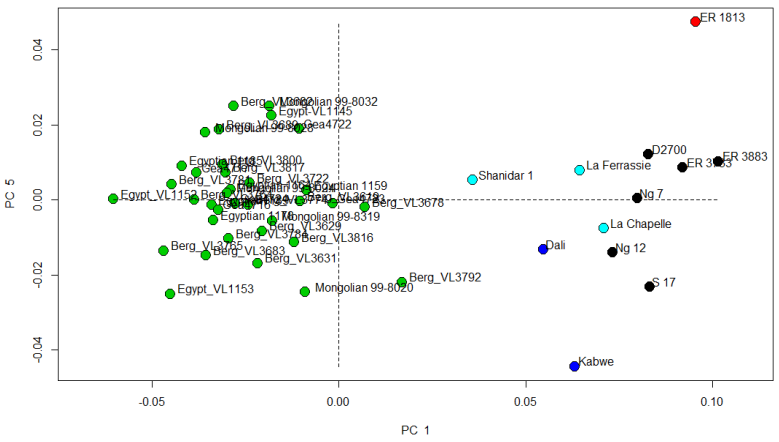

Figure 5.35 The PC 1 and PC 5 plot of the *H. sapiens* and fossils (the anchor points of the overall cranium)

When 159 anchor points are used to analyze specimens in the maximum-semilandmark dataset, the results of the statistical analyses are only slightly affected. This is probably because these 159 points reflect similar aspects of large-scale shape differences. For the analysis that includes only fossil hominids, PC 1 continues to separate Neanderthals from other specimens as a reflection of an the overall expansion of the vault relative to the decrease in size of the temporal region, though some localized differences, such as hollowing across lambda and bregma, are not fully captured due to the lower density of points in these regions (Figure 5.32 and Figure 5.33; also see Figure B.10 in Appendix B). PC 2 also contrasts KNM-ER 1813 and Kabwe 1 at its two ends (Figure 5.32 and Figure 5.33; also see Figure B.11). Closer to Kabwe 1, this PC again reflects an anteroinferior elongation of the frontal bone, thickening of the brow, flattening of the parietal region, superoinferior shortening of the occipital squama due to the superoposterior shifting of inion, and flattening of the nuchal plane. It does not capture some localized, such as the concavity at the nuchal plane just anterior to the superior nuchal line. For the analysis that includes the large sample of *H. sapiens*, PC 1 still separates them from fossil specimens, while PC 4 and PC 5 are consistent overall with PC 1 and PC 2 in the analysis that of only fossil specimens (Figure 5.34 and Figure 5.35; also see Figure B.12 to B.14 in Appendix B).

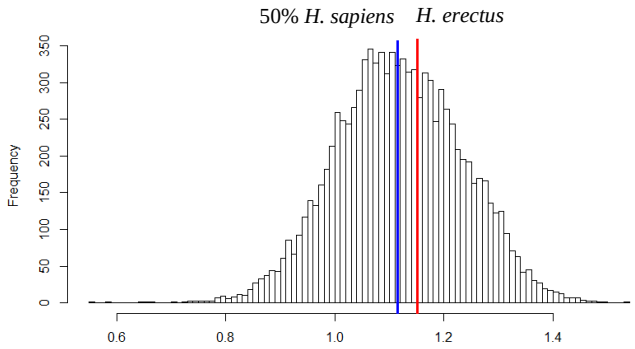

Figure 5.36 The bootstrap analysis of SSDs based on the anchor points of the overall cranium

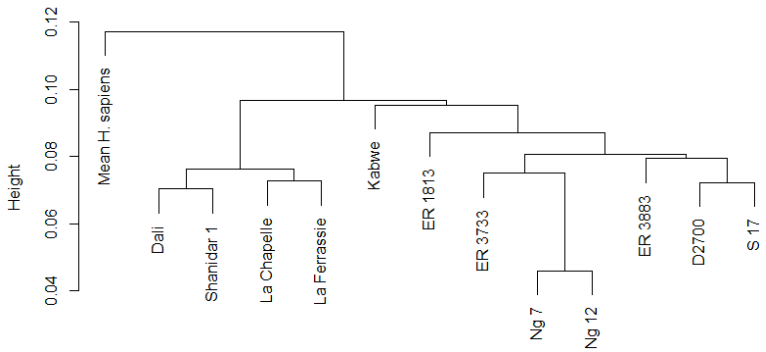

Figure 5.37 The UPGMA dendrogram of the fossil specimens and the mean shape of *H. sapiens* based on the anchor points of the overall cranium

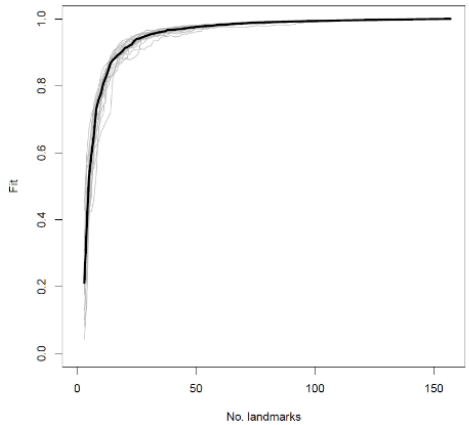

Figure 5.38 The mean LASEC based on the anchor points of the overall cranium

The statistical analyses are also consistent. The bootstrap analysis of SSDs shows that the SSD of six *H. erectus s. l.* specimens becomes somewhat greater but exceeds only 6,148 (61.48%) bootstrapped *H. sapiens* SSDs (Figure 5.36). The UPGMA tree for the anchor-point dataset also shows a distribution of specimens nearly identical to that in the analysis of the maximum-semilandmark dataset (Figure 5.37). Similarly, the distance between two Ngandong specimens are still the smallest. KNM-ER 3733 is slightly closer to the Ngandong specimens than to KNM-ER 3883. D2700 and S 17 are still grouped together. They are also grouped with KNM-ER 3883. These three *H. erectus* specimens are also clustered with KNM-ER 1813 and Kabwe 1. The three Neanderthals and the Dali skull form a distinct cluster.

The mean landmark sampling evaluation curve (LASEC) obtained by resampling the anchor point sets 20 times shows a plateau of the fit value when the number of landmarks is slightly less than 50 (Figure 5.38). The slope of this plateau is near zero, which means that the fit closely approaches 1 when the number of landmarks approaches 100. It can be expected that when the number of landmarks increases, the fit value will not specifically be able to increase signifantly. In terms of the statistical analyses used here, these results show that the original semilandmark dataset is oversampled.

5.7.2 Thirty-nine landmarks

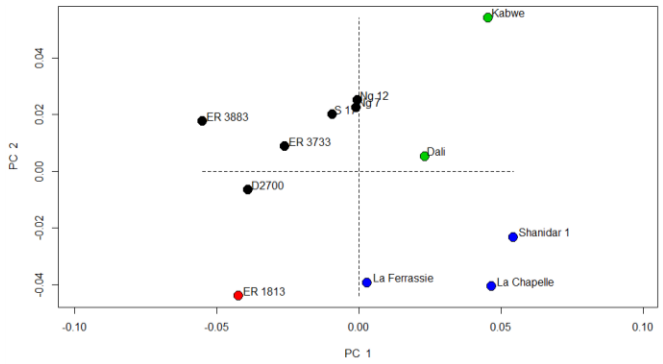

Figure 5.39 The PC 1 and PC 2 plot of the fossil sample (the discrete landmarks of the entire cranium)

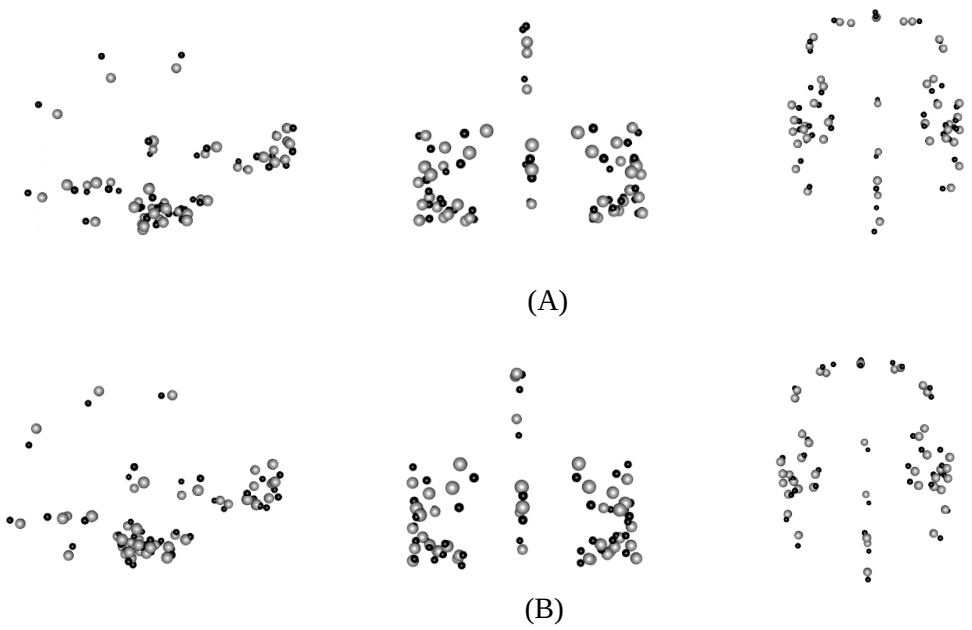

Figure 5.40 Shape change in PC 1 and PC 2 based on the discrete landmarks of the entire cranium
(A) The shapes at the two ends of PC 1. (B) The shapes at the two ends of PC 2. The grey points represent the shape at the negative end. The black points represent the shape at the positive end. From left to right: lateral view, anterior view, and inferior view. The graphs are generated by the Geomorph R package (Adams et al., 2018).

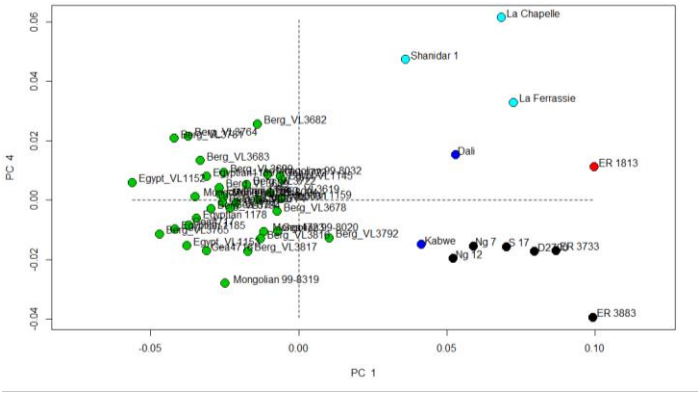

Figure 5.41 The PC 1 and PC 4 plot of *H. sapiens* and fossils (the discrete landmarks of the entire cranium)

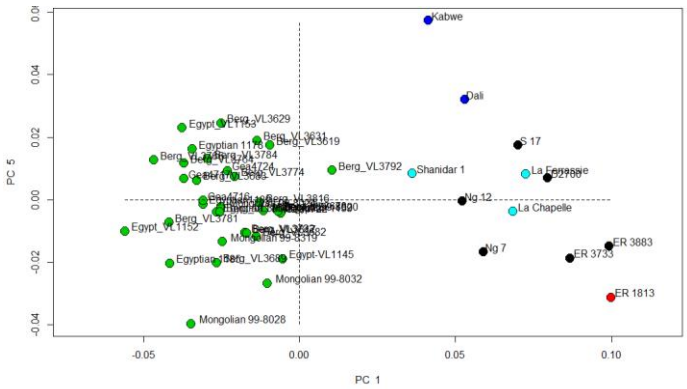

Figure 5.42 The PC 1 and PC 5 plot of *H. sapiens* and fossils based on the anchor points of the entire cranium

When using 39 discrete landmarks, the major PC axes still show a distribution of specimens roughly similar to analyses based on anchor points and semilandmarks. Nevertheless, the results show more inconsistencies with the analyses that use semilandmarks than with the analyses that use 159 anchor points. This is probably because the small number of discrete landmarks fails to capture morphological differences in landmark free-regions, such as the surface of the supraorbital region, frontal squama, cranial side walls, and occipital squama. PC 1, which includes only fossil hominids, still separates the three Neanderthals from all other specimens, since these points are sufficient to show global shape differences, such as the diminution of the temporal region relative to the vault. However, Neanderthals become less separated from fossils as they overlap with both Kabwe 1 and the Dali skull (Figure 5.39 and Figure 5.40). PC 2 still contrasts Kabwe 1 and KNM-ER 1813, as this PC is able to reflect similar shape differences such as those in the position of the supraorbital region, the relative length of the frontal occipital squamae, and the position of inion (Figure 5.39 and Figure 5.40).

For the analysis that also includes a large sample of *H. sapiens*, PC 1 is still able to separate *H. sapiens* from fossil specimens based on features such as the size of the brow, the height and length of the vault, and the angulation in the occipital region, among others (Figure 5.41 and Figure B.15). However, the three Neanderthals begin to overlap with Kabwe 1, the Dali skull, and Asian *H. erectus*. PC 4 produces a distribution of specimens that is roughly similar to PC 1 of fossils but shows a tighter clustering of the *H. erectus* specimens except KNM-ER 3883, which is plotted to this PC's negative end (Figure 5.41 and Figure B.16). PC 5 is also roughly consistent with PC 2 of fossils (Figure 5.42 and Figure B.17).

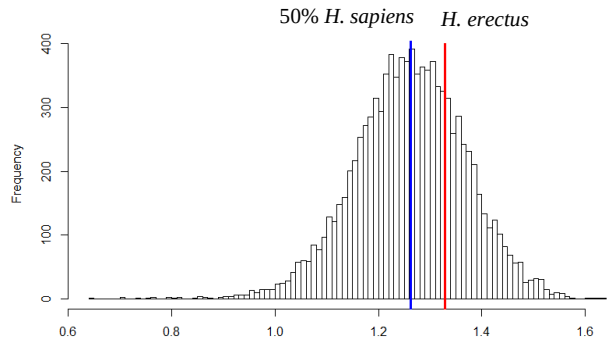

Figure 5.43 The bootstrapped analysis of SSDs based on the discrete landmarks of the overall cranium
The red line represents the SSD of the *H. erectus* sample. The blue line indicates the 50th percentile of the bootstrapped *H. sapiens* SSDs.

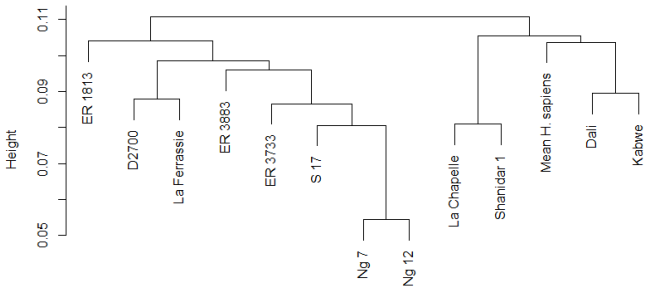

Figure 5.44 The UPGMA dendrogram of the fossil specimens and the mean shape of *H. sapiens* based on the discrete landmarks of the overall cranium

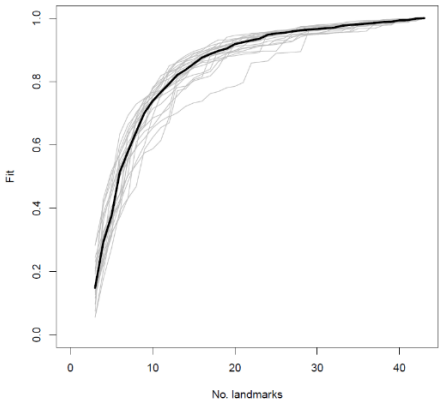

Figure 5.45 The mean LASEC based on the discrete landmarks of the overall cranium

The bootstrap analysis shows that the SSD of the *H. erectus s. l.* sample increases as it approaches the 75th percentile of the *H. sapiens* SSDs (greater than 7,346 of the 10,000 *H. sapiens* SSDs) (Figure 5.43). The UPGMA dendrogram also shows more inconsistencies. S 17 is grouped with the two Ngandong specimens (Figure 5.44). La Ferrassie is grouped with D 2700. Kabwe and Dali are also grouped together, along with the other two Neanderthals and the mean of *H. sapiens*, which is less different from the other fossils and is not placed at the root of this dendrogram.

The mean LASEC obtained from twenty rounds of resampling 39 discrete points shows a continuous increase in fit value without an apparent plateau (Figure 5.45). These analyses show that reducing the number of landmarks to a certain degree may cause a loss of morphological information and affect statistical results.

6.0 THE POSTERIOR CRANIUM

6.1 THE PCA OF THE MAXIMUM-SEMILANDMARK SET

6.1.1 The first PCA: The fossil sample

Table 6.1 The first PCA of the posterior cranium: The percentage variance explained by the first seven PCs

	Percentage of Variance	Cumulative Percentage
PC 1	34.64%	34.64%
PC 2	14.466%	49.109%
PC 3	13.650%	62.759%
PC 4	8.813%	71.365%
PC 5	5.886%	77.458%
PC 6	5.380%	82.838%
PC 7	4.123%	86.961%

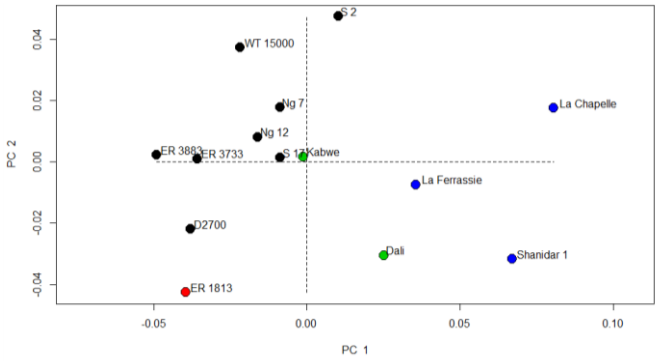

Figure 6.1 The first PCA of the posterior cranium: The plot of PC 1 and PC 2
The black dots: The *H. erectus s. l.* specimens. The red dot: The *H. habilis* specimen. The green dots: The Mid-Pleistocene *Homo* specimens. The blue dots: the Neanderthal specimens. The graphs are generated by the Geomorph R package (Adams et al., 2018).

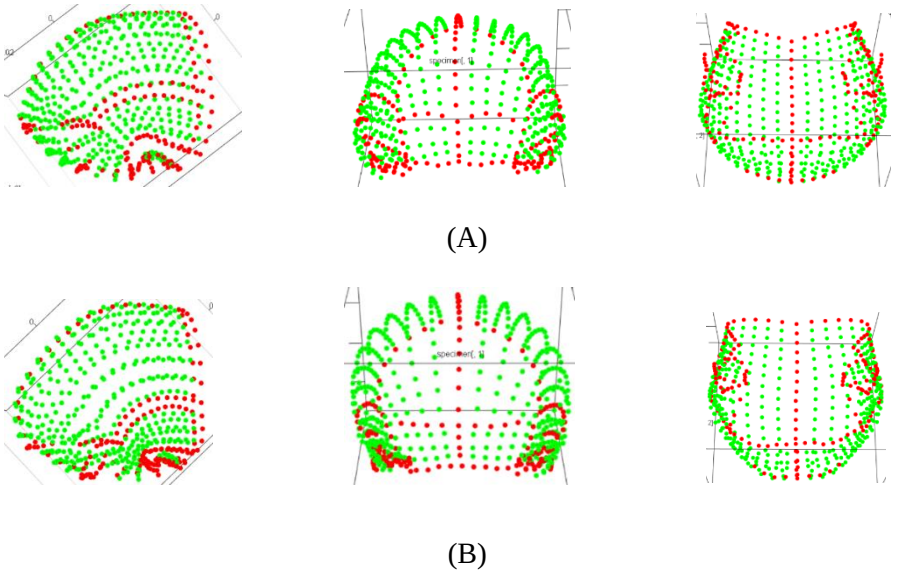

Figure 6.2 The first PCA of the posterior cranium: The shapes at the two ends of PC 1
(A) The shape at the negative end. (B) The shape at the positive end. From left to right: lateral view, posterior view, and inferior view. The graphs are generated by the Geomorph R package (Adams et al., 2018).

The semilandmark datasets of posterior crania exclude the frontal region in order to include S 2 and KNM-WT 15000. PC 1, which explains 34.64% of the total variance, shows a distribution of specimens similar to PC 1 in the PCAs of the entire cranium of fossils (Figure 6.1 and Table 6.1). This PC separates Neanderthals from other hominids, which are ordered roughly similarly. This is the only PC that is strongly correlated with size (the p-value is 0.0031), probably because the large sized Neanderthals scored highest (Table B.9). KNM-ER 3883 is again at the end opposite to Neanderthals. KNM-ER 1813 overlaps with KNM-ER 3733 and D2700, while Kabwe 1 overlaps with the Indonesian specimens, which are plotted closer to Neanderthals overall. The newly added KNM-WT 15000 is intermediate between the *Homo ergaster* and Indonesian groups. Interestingly, S 2 scored higher than Kabwe 1 and all other Indonesian specimens.

PC 1 also describes patterns of shape differences that are very similar to those described by PC 1 in the analyses of the entire crania of fossils (Figure 6.2). In a specimen closer to Neanderthals, the temporal region decreases in size and tilts to the midline, while the vault increases in size. In particular, the midoccipital and midparietal regions bulge more, creating flattened areas across bregma and lambda. Thus, the peak of the vault shifts backward from the bregmatic to the midparietal regions, the posterior-most point of the vault shifts upward to the midoccipital region, and the greatest width of the rear profile shifts upward from the supramastoid regions to above the squamosal sutures. The mandibular fossa

decreases in overall size, flares less from the base and shifts anteriorly. The fossa becomes more narrowly V-shaped in lateral view as its posterior wall becomes more vertically oriented.

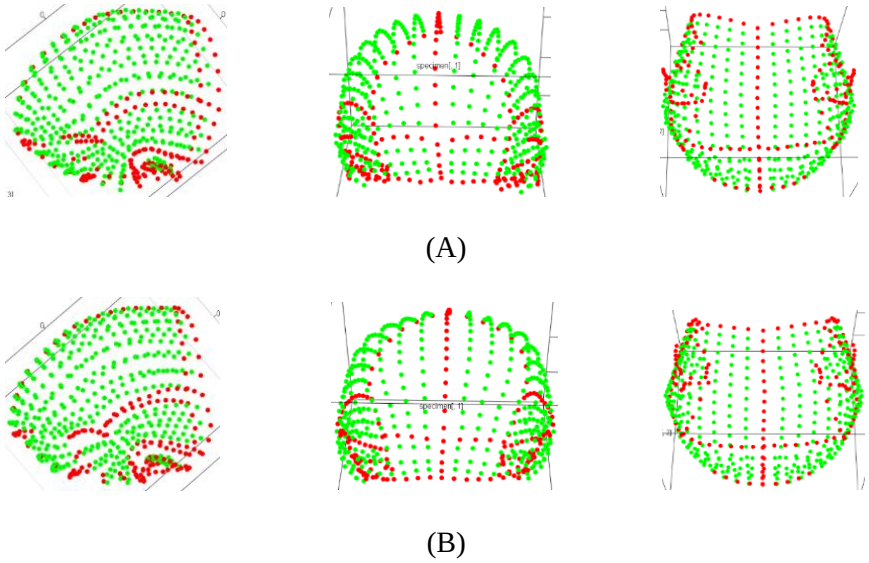

Figure 6.3 The first PCA of the posterior cranium: The shapes at the two ends of PC 2
(A) The shape at the negative end. (B) The shape at the positive end. From left to right: lateral view, posterior view, and inferior view. The graphs are generated by the Geomorph R package (Adams et al., 2018).

PC 2, which accounts for 14.47% of the total variance, plots S 2 and KNM-ER 1813 at opposite ends (Figure 6.1). KNM-WT 15000 lies closest to S 17, while D2700 is the *Homo erectus* specimen with the greatest negative score. KNM-ER 3733, KNM-ER 3883, S 17, and Kabwe 1 are placed almost at the origin, while Ng 7 and Ng 12 have slightly more positive scores. The three Neanderthals are widely separated along this PC. The Dali skull lies very close to KNM-ER 1813.

In a specimen closer to S 17, the rear profile becomes shorter superoinferiorly, and the roof becomes flatter (Figure 6.3). The parietal region shortens slightly anteroposteriorly. Inion lies more upwardly. The occipital squama and the region across lambda flatten and incline more forward. The angle at the occipital flexure becomes sharper. The squamosal portion shortens anteroposteriorly. The squamosal suture straightens. Its peak shifts anteriorly, and its anterior end lies more backwardly. The parietomastoid suture becomes more arched and shortens as asterion moves anteriorly. The mastoid process becomes less protruding relative to the tympanic plate. The mandibular fossa becomes narrower mediolaterally and flares less from the cranial base. It elongates anteroinferiorly as the anterior wall elongates and becomes more horizontal. This PC also captures some asymmetrical variations as the

inferior tip of the auditory meatus and mandibular fossa shift somewhat superomedially on the left while shifting more inferiorly on the right in posterior view.

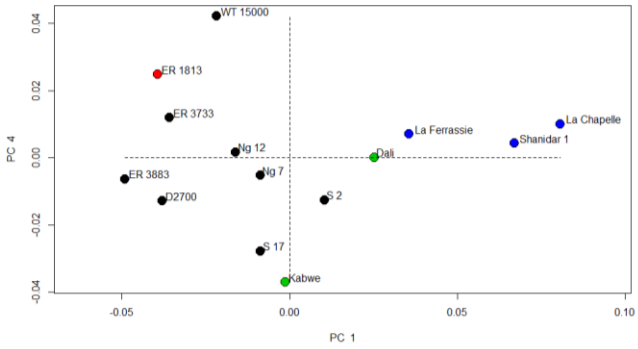

Figure 6.4 The first PCA of the posterior cranium: The plot of PC 1 and PC 4
The black dots: The *H. erectus s. l.* specimens. The red dot: The *H. habilis* specimen. The green dots: The Mid-Pleistocene *Homo* specimens. The blue dots: the Neanderthal specimens. The graphs are generated by the Geomorph R package (Adams et al., 2018).

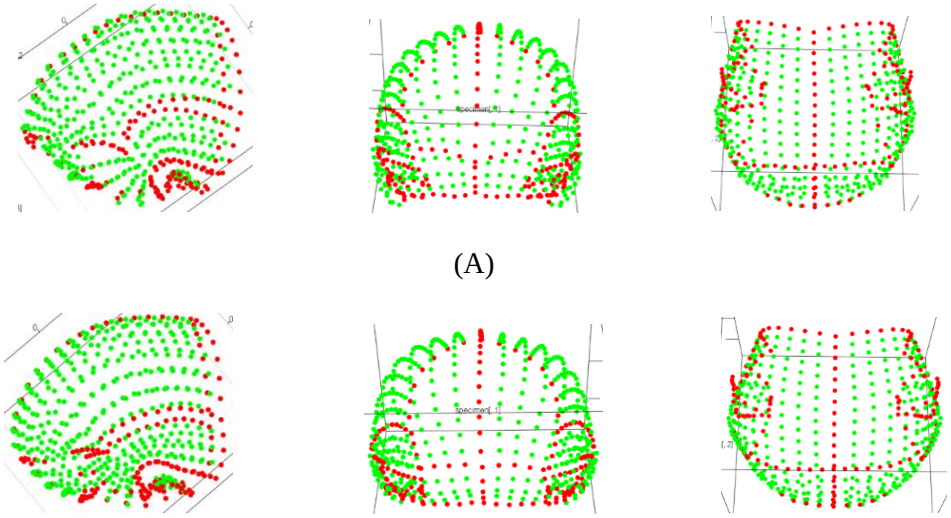

(A)

(B)

Figure 6.5 The first PCA of the posterior cranium: The shapes at the two ends of PC 4
(A) The shape at the negative end. (B) The shape at the positive end. From left to right: lateral view, posterior view, and inferior view. The graphs are generated by the Geomorph R package (Adams et al., 2018).

PC 4, which explains 8.813% of the total variance, places Kabwe 1 and KNM-WT 15000 at opposite ends (Table 1.1 and Figure 6.4). S 17 lies very close to Kabwe 1, while KNM-ER 1813 lies close to KNM-WT 15000. The other specimens are generally distributed across the origin of the plot. The three Neanderthals lie especially close to each other.

This PC demonstrates shape differences similar to those revealed by PC 2 in the analyses based on the entire crania of fossils (Figure 6.5). In a specimen lies closer to KNM-WT 15000, the lateral contour of the parietals becomes rounded. Semilandmarks in the posterior parietal region lie slightly more posterosuperiorly so the area across lambda gradually bulges. Semilandmarks at the superior occipital squama lie slightly more anterosuperiorly, while those near inion shift slightly inferiorly, causing the occipital squama to elongate superoinferiorly and become less forwardly inclined. The nuchal plane becomes bulging. The concavity anterior to inion disappears. Thus, the occipital flexure becomes rounded and more obtuse. The rear profile becomes slightly taller superoinferiorly and narrower mediolaterally.

The squamosal suture becomes more curved; its peak shifts anteriorly as the anterior squamosal portion expands superoinferiorly. The mastoid portion shortens anteroposteriorly, since semilandmarks there lie closer to its anterior boundary. The parietal mastoid suture straightens and becomes more horizontal. The tympanic plate becomes more transversely oriented as the vaginal process shifts slightly posterolaterally. The mandibular fossa becomes smaller overall and less laterally flaring. The fossa deepens and becomes more narrowly V-shaped in lateral view as its anterior wall orients more vertically. while the posterior wall orients more vertically and extending more inferiorly. The mastoid process protrudes less downwardly.

6.1.2 The second PCA: The large sample of *H. sapiens* and the fossil sample

Table 6.2 The second PCA of the posterior cranium: The percentage variance explained by the first seven PCs

	Percentage of Variance	Cumulative Percentage
PC 1	37.565%	37.565%
PC 2	15.148%	52.713%
PC 3	8.786%	61.498%
PC 4	5.152%	66.650%
PC 5	4.598%	71.248%
PC 6	3.654%	74.902%
PC 7	3.050%	77.951%

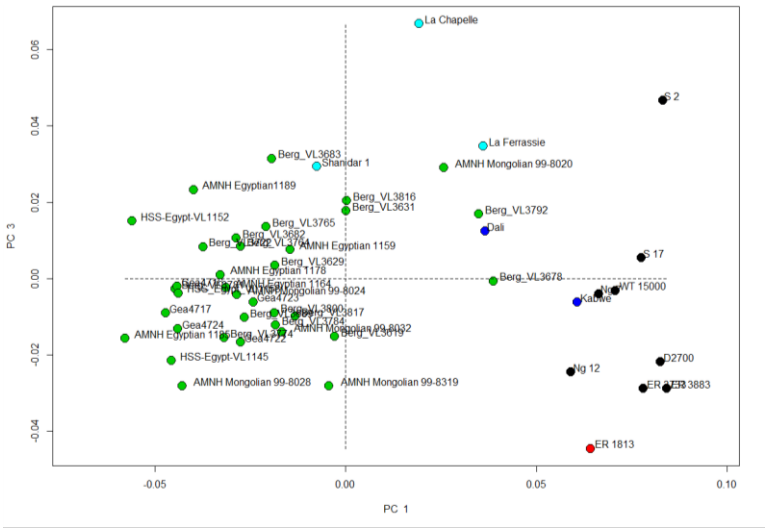

Figure 6.6 The second PCA of the posterior cranium: The plot of PC 1 and PC 4
The green dots: The *H. erectus s. l.* specimens. The black dot: The *H. habilis* specimen. The dark blue dots: The Mid-Pleistocene *Homo* specimens. The light blue dots: the Neanderthal specimens. The red dots: The *H. sapiens* specimens. The graphs are generated by the Geomorph R package (Adams et al., 2018).

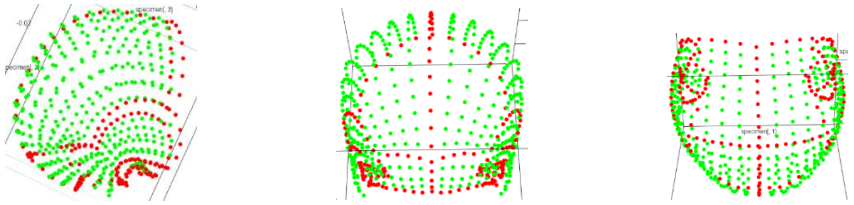

(A)

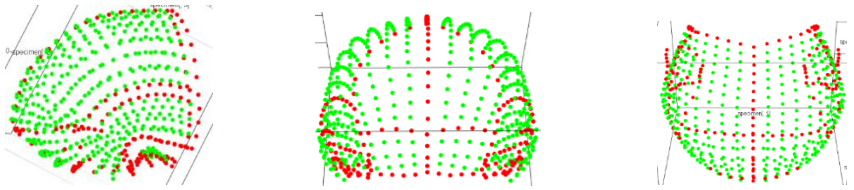

(B)

Figure 6.7 The second PCA of the posterior cranium: The shapes at the two ends of PC 1
(A) The shape at the negative end. (B) The shape at the positive end. From left to right: lateral view, posterior view, and inferior view. The graphs are generated by the Geomorph R package (Adams et al., 2018).

After adding 35 *H. sapiens* specimens, PC 1 primarily separates *Homo sapiens* from fossils (Table 6.2 and Figure 6.6). Along this PC, the *H. erectus* specimens, KNM-ER 1813 and Kabwe 1 cluster fairly tightly and are well separated from *H. sapiens*. Within this cluster, KNM-ER 3883 is located at the positive end and very close to S 2, S 17, KNM-ER 3733, and D2700. Ng 7, Ng 12, KNM-WT 15000, Kabwe 1, and KNM-ER 1813 have somewhat less positive scores. The three Neanderthals and Dali specimens overlap with a few *H. sapiens* specimens. The Shanidar specimen falls well within the positive portion of the *H. sapiens* cluster. PC 1 is strongly correlated with size, likely because the *H. sapiens* specimens are generally larger than most fossils except Neanderthals (Table B.10).

This PC shows shape differences similar to those demonstrated by PC 1 in the analyses of the entire crania (Figure 6.7). In a specimen plotted closer to KNM-ER 3883, the vault flattened, shorter superoinferiorly and elongated anteroposteriorly. Semilandmarks at the midparietal region lie downwardly to a higher degree, such that the peak shifts anteriorly toward bregma. Inion shifts superoposteriorly. The occipital squama shortens superoinferiorly and inclines more forward. The angle at the occipital flexure sharpens. The squamosal suture become elongated anteroposteriorly and straightened. The cranial roof flattened and narrowing mediolaterally, while the side walls tilt laterally. Thus, the greatest width of the rear profile shifts downwardly toward the supramastoid region. The inferior tip of the mastoid process tilts more medially.

The distance between the suprameatal crest and the mandibular fossa increases. The mastoid process becomes less downwardly protruded. In inferior view, the mastoid region becomes wider mediolaterally and lies more laterally. Thus, the mediolateral width of the vault increases. The mandibular fossa becomes larger and more laterally flared. The lateral profile becomes shallower and anteroposteriorly elongated primarily because the anterior wall elongates and inclines more anteriorly. The bottom of the mandibular fossa also becomes anteriorly elongated.

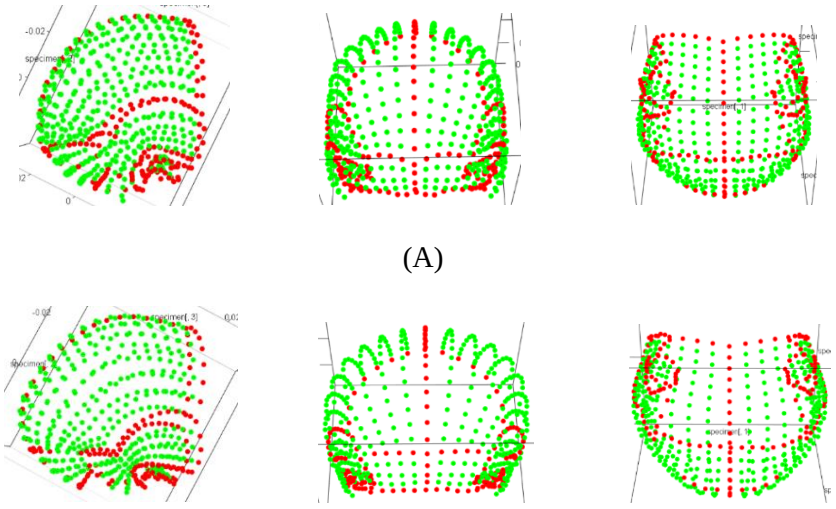

(A)

(B)

Figure 6.8 The second PCA of the posterior cranium: The shapes at the two ends of PC 3
(A) The shape at the negative end. (B) The shape at the positive end. From left to right: lateral view, posterior view, and inferior view. The graphs are generated by the Geomorph R package (Adams et al., 2018).

PC 3, which explains 8.786% of the total variance, shows a distribution roughly consistent with PC 1 from the analysis of the posterior crania of fossils, by placing Neanderthals at the positive end (Table and Figure). The three *H. ergaster* specimens and Ng 12 are relatively close to KNM-ER 1813 at the negative end. KNM-WT 15000, Kabwe 1 and the other Indonesian specimens have more positive scores. The Dali skull is again intermediate between most other fossils and Neanderthals. Interestingly, S 2 overlaps with Neanderthals. In addition, Shanidar 1 overlaps with the positive boundary of the *H. sapiens* cluster.

Similar to PC 1 from the first analysis, this PC also captures a reduction in the overall size of the temporal region relative to the vault in a specimen lies closer to Neanderthals (Figure). The vault itself does not appear to significantly increases in height. The midoccipital region still bulges out, while the

bulging of the midparietal region is created by a slightly downward shift of points in both the anterior and posterior parietal regions. The side walls also tilt more inward as the vault expands laterally. The mandibular fossa decreases in overall size and becomes shallower. The base of the mastoid process narrowing mediolaterally and shifts medially. Thus, the greatest width of the superior profile shifts slightly anteriorly toward the auditory meatus.

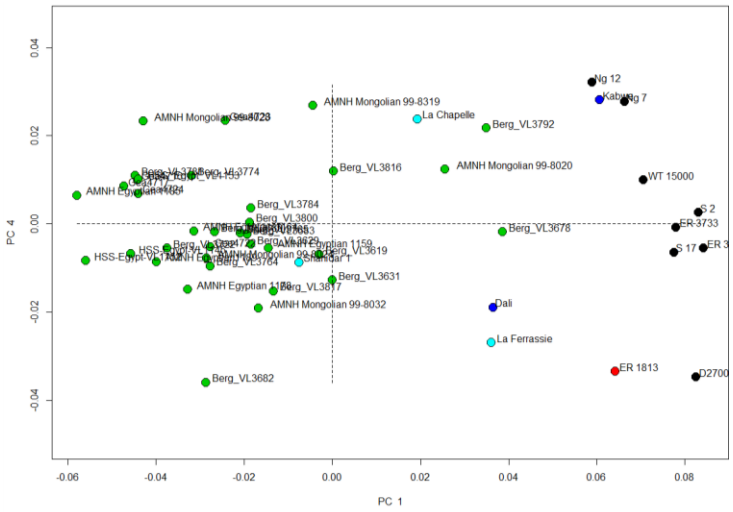

Figure 6.9 The second PCA of the posterior cranium: The plot of PC 1 and PC 4
The green dots: The *H. erectus s. l.* specimens. The black dot: The *H. habilis* specimen. The dark blue dots: The Mid-Pleistocene *Homo* specimens. The light blue dots: the Neanderthal specimens. The red dots: The *H. sapiens* specimens. The graphs are generated by the Geomorph R package (Adams et al., 2018).

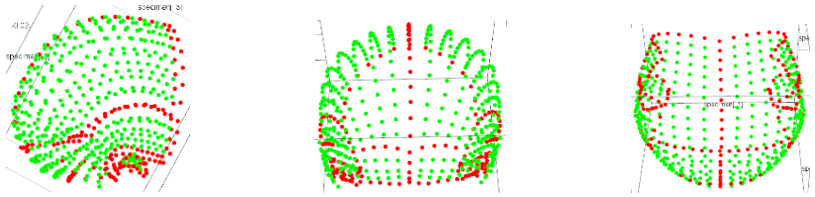

(A)

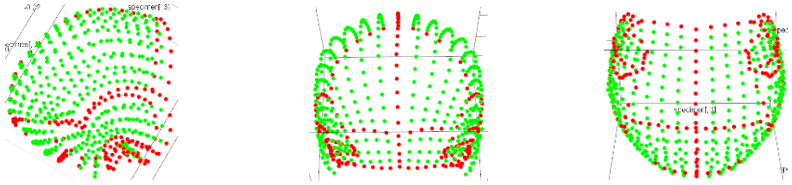

(B)

Figure 6.10 The second PCA of the posterior cranium: The shapes at the two ends of PC 4
(A) The shape at the negative end. (B) The shape at the positive end. From left to right: lateral view, posterior view, and inferior view. The graphs are generated by the Geomorph R package (Adams et al., 2018).

PC 4, which explains 5.152% of the total variance, divides the non-Neanderthal fossil specimens into roughly three clusters (Table 6.2 and Figure 6.9). Ng 7, Ng 12, and Kabwe 1 are plotted at the positive end. KNM-ER 1813 and D2700 are at the negative end. The other specimens are in the middle. Dali is somewhat intermediate between the last two clusters. On the other hand, the *H. sapiens* and Neanderthal clusters are widely separated along this PC.

In a specimen lies closer the positive end, the occipital squama shortens superoinferiorly and inclines more anteriorly (Figure 6.10). Inion shifts posterosuperiorly. The nuchal plane elongates anteroposteriorly and flattens. The angle at the occipital flexure becomes sharper. The region just anterior to lambda flattened. The mastoid portion expands anteroposteriorly. The parietomastoid suture elongates as well as becomes more upwardly obliquely oriented as asterion shifts posterosuperiorly, while the parietal notch shifts anteroinferiorly. The squamosal suture becomes more arced and shorter anteroposteriorly as the anterior end of the squamosal suture shifts backward. The anterior margin of the squamosal suture also becomes more vertically oriented. The mastoid process protrudes more inferiorly. The mandibular fossa shifts anteriorly and elongates somewhat anteroposteriorly. The width across the mastoid regions also somewhat decreases.

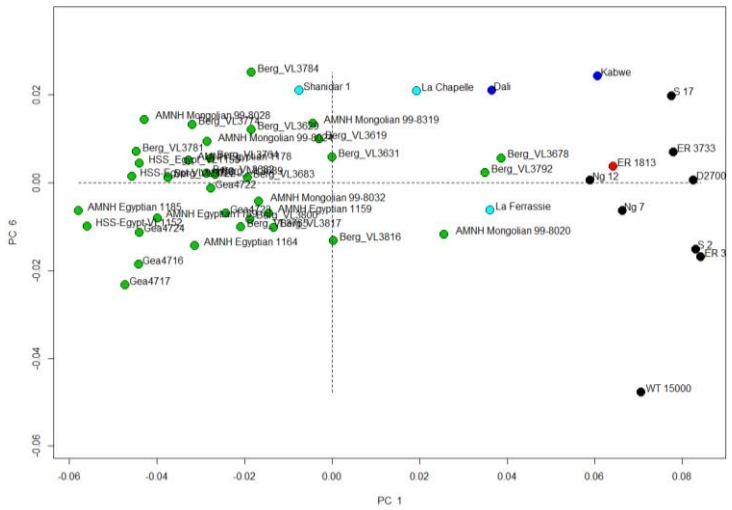

Figure 6.11 The second PCA of the posterior cranium: The plot of PC 1 and PC 6
The green dots: The *H. erectus s. l.* specimens. The black dot: The *H. habilis* specimen. The dark blue dots: The Mid-Pleistocene *Homo* specimens. The light blue dots: the Neanderthal specimens. The red dots: The *H. sapiens* specimens. The graphs are generated by the Geomorph R package (Adams et al., 2018).

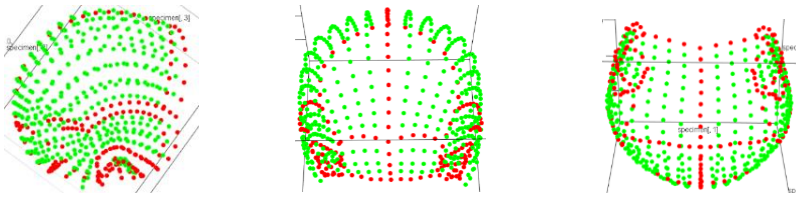

(A)

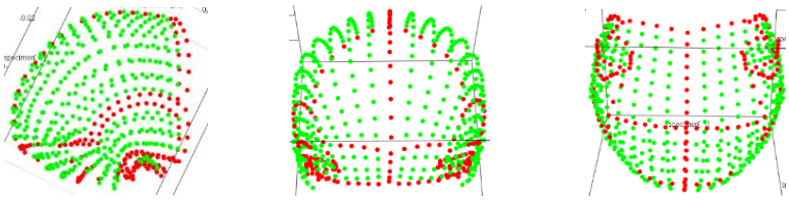

(B)

Figure 6.12 The second PCA of the posterior cranium: The shapes at the two ends of PC 4
(A) The shape at the negative end. (B) The shape at the positive end. From left to right: lateral view, posterior view, and inferior view. The graphs are generated by the Geomorph R package (Adams et al., 2018).

Another interesting lower-ranked PC is PC 6, which explains only 3.654% of the total variance (Table 6.2). This PC primarily separates KNM-WT 15000 from other specimens (Figure 6.11). The fossil specimens lie closest to KNM-WT 15000 are KNM-ER 3733 and S2. Kabwe 1, the Dali skull, and S 17 are placed at the end opposite KNM-WT 15000. Neanderthals and *H. sapiens* are widely distributed. When PC scores gradually approach KNM-WT 15000 at the negative end, the posterior cranium generally becomes rounder and shorter anteroposteriorly (Figure 6.12). The occipital flexure shifts anteriorly and becomes more obtuse. The nuchal plane bulges out. The squamosal suture becomes less arched. The squamosal portion shortens anteroposteriorly as the parietal notch shifts somewhat anteriorly. The mastoid portion becomes nearly as tall as the squamosal portion. It also becomes more vertically oriented as the mastoid process and the auditory meatus both shift backward. The long axis of the mandibular fossa becomes more obliquely oriented as the vaginal process shifts posterolaterally. The fossa becomes more widely V-shaped in lateral view as the posterior wall elongates and tilts more posteriorly.

6.1.3 The third PCA: A smaller *H. sapiens* sample with fossil specimens

Table 6.3 The third PCA of the posterior cranium: The percentage variance explained by the first seven PCs

	Percentage of Variance	Cumulative Percentage
PC 1	39.256%	39.256%
PC 2	14.590%	53.846%
PC 3	8.479%	62.325%
PC 4	6.392%	68.718%
PC 5	5.249%	73.967%
PC 6	4.793%	78.760%
PC 7	3.649%	82.409%

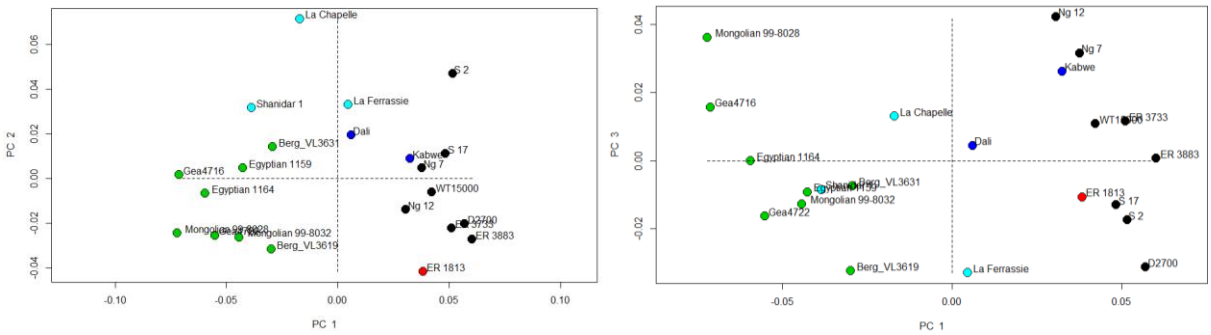

(A) (B)

Figure 6.13 The plot of the third PCA of the posterior cranium
(A) PC 1 and PC 2 plot. (B) PC 1 and PC 3 plot. The green dots: The *H. erectus s. l.* specimens. The black dot: The *H. habilis* specimen. The dark blue dots: The Mid-Pleistocene *Homo* specimens. The light blue dots: the Neanderthal specimens. The red dots: The *H. sapiens* specimens. The graphs are generated by the Geomorph R package (Adams et al., 2018).

When reducing the sample size of *H. sapiens* to eight, PCs such as PC 2 in the previous analysis that emphasize the variability within *H. sapiens* disappear. PC 1, PC 2, and PC 3 are similar to PC 1, PC 3 and PC 4 in the second PCA of the posterior crania, respectively (Table 6.3 and Figure 6.13; also see Figure B.18 to Figure B.20 in Appendix B). PC 1 continues to differentiate *H. erectus* from *H. sapiens*. PC 2 also separates Neanderthals and S 2 from other specimens and plots KNM-ER 1813 at the opposite end. PC 1 and PC 2 also correlate significantly with size, as these PCs distinguish large Neanderthal and *H. sapiens* specimens from small fossil hominids (Table B.11).

PC 3 shows a distribution of specimens roughly similar to that shown by PC 4 in the second PCA of the posterior crania (Figure 6.13). In this case, however, specimens are not divided into clear clusters but form a continuum. PC 3 still describes similar gross shape differences, such as superoinferior shortening of the occipital plane, flattening of the nuchal plane, increase in size of the mastoid portion and greater inferior distension of the mastoid process (Figure B.20). Slightly different, this PC shows that the parietomastoid suture elongates and arcs to a higher degree in a specimen lies closer to this PC's positive end.

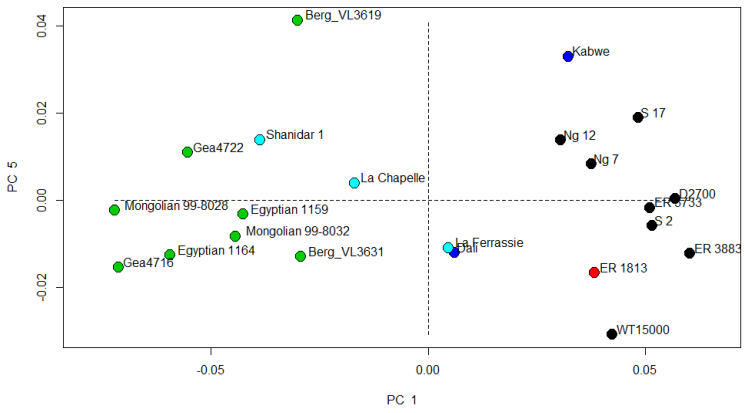

Figure 6.14 The PC 1 and PC 4 plot of the third PCA of the posterior cranium
The green dots: The *H. erectus s. l.* specimens. The black dot: The *H. habilis* specimen. The dark blue dots: The Mid-Pleistocene *Homo* specimens. The light blue dots: the Neanderthal specimens. The red dots: The *H. sapiens* specimens. The graphs are generated by the Geomorph R package (Adams et al., 2018).

PC 5 is roughly consistent with PC 4 in the first analysis of posterior crania. This PC plots KNM-WT 15000 and Kabwe 1 at the opposite side of the fossil cluster (Figure 6.14). Differently, this PC plots Ng 7 and Ng 12 close to the other *H. erectus* specimens rather than Kabwe 1. This PC also describes similar shape differences, such as shortening of the occipital squama, concavity at the nuchal plane, and flattening of the posterior parietal, when moving toward the Kabwe end (Figure B.21). In this case, however, the contours of the squamosal suture barely show differences. The anterior margin of the squamosal portion becomes more vertical.

6.2 MAXIMUM-SPECIMEN DATASET

6.2.1 The fourth PCA: The fossil specimens only

Table 6.4 The fourth PCA of the posterior cranium: The percentage variance explained by the first seven PCs

	Percentage of Variance	Cumulative Percentage
PC 1	28.316%	28.316%
PC 2	16.328%	44.644%
PC 3	9.984%	54.628%
PC 4	8.811%	63.439%
PC 5	6.825%	70.264%
PC 6	5.212%	75.477%
PC 7	4.132%	79.609%

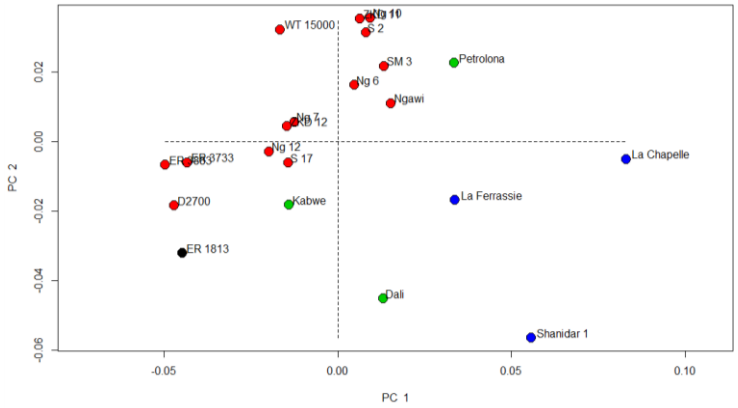

Figure 6.15 The fourth PCA of the posterior cranium: The plot of PC 1 and PC 2
The black dots: The *H. erectus s. l.* specimens. The red dot: The *H. habilis* specimen. The green dots: The Mid-Pleistocene *Homo* specimens. The blue dots: the Neanderthal specimens. The graphs are generated by the Geomorph R package (Adams et al., 2018).

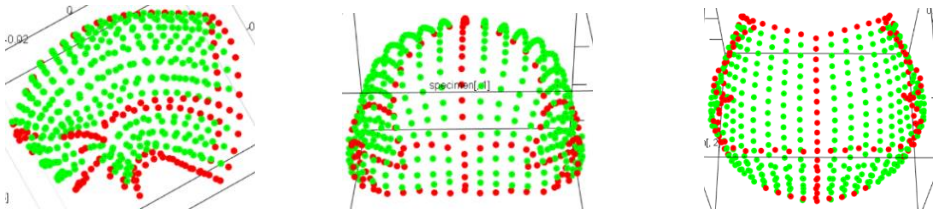

(A)

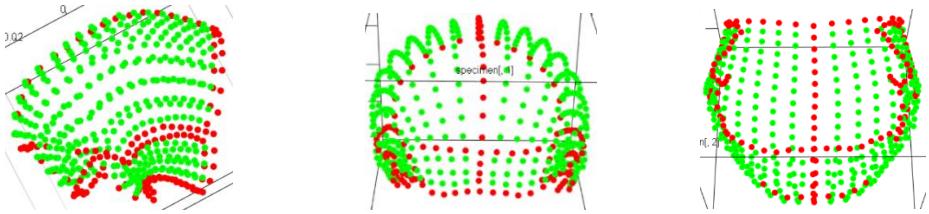

(B)

Figure 6.16 The fourth PCA of the posterior cranium: The shapes at the two ends of PC 1
(A) The shape at the negative end. (B) The shape at the positive end. From left to right: lateral view, posterior view, and inferior view. The graphs are generated by the Geomorph R package (Adams et al., 2018).

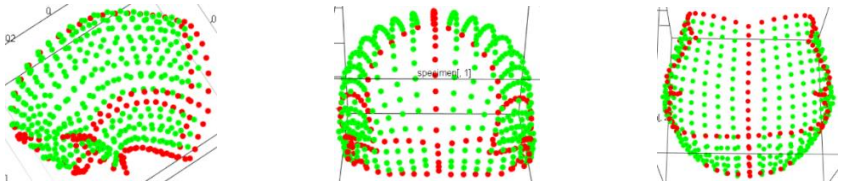

(A)

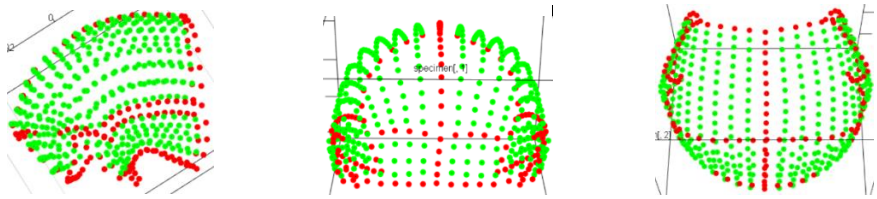

(B)

Figure 6.17 The fourth PCA of the posterior cranium: The shapes at the two ends of PC 2
(A) The shape at the negative end. (B) The shape at the positive end. From left to right: lateral view, posterior view, and inferior view. The graphs are generated by the Geomorph R package (Adams et al., 2018).

By excluding the mandibular fossae and mastoid processes, the maximum-specimen dataset includes more fossil specimens. Though distribution of specimens become more complicated than the maximum-specimen dataset, PC 1 and PC 2 still roughly show the same distributions and shape differences as the first two PCs in the first PCA based on the maximum-specimen dataset. PC 1, which explains 28.316% of the total variance, still plots Neanderthals at the positive end and the Koobi Fora specimens as well as D2700 at the negative end (Table 6.4, Figure 6.15 and Figure 6.16). Among the newly added specimens, ZKD 12 groups tightly with Ng 7, Ng 12, S 17, KNM-WT 15000 and Kabwe 1 at the center of the *H. erectus* cluster. Ng 6, Ng 10, Ngawi 1, SM 3, and ZKD 11 are located on the positive side of the *H. erectus* cluster, along with S 2 and Dali. Petralona 1 is placed at the negative end of Neanderthals. PC 1 is the only PC among the first seven PCs that is significantly correlated with size (Table B.12).

PC 2, which explains 16.328% of the total variance, is roughly comparable to PC 2 of the first analysis of the maximum-semilandmark set (Table 6.4, Figure 6.15 and Figure 6.17). In this case, KNM-WT 15000 is plotted very close to S 2 at the positive end. The newly added Ng 10 and ZKD 11 are also placed near S 2. SM 3, Ng 6, Ngawi 1 and Petralona 1 are plotted slightly away from S 2. ZKD 12 is placed near other *H. erectus* across the origin. Neanderthals are widely separated in this PC. Shanidar 1 and the Dali skull are even more negative than ER 1813. Similarly, this PC also shows that in a specimen plotted closer to S 2 (positive end), the vault becomes somewhat lower superoinferiorly and wider mediolaterally as the side walls tilt more outward. The vault elongates slightly posteriorly as inion moves lies more posterosuperiorly. The occipital plane flattens and inclines more anteriorly. The mastoid portion increases in height. The squamosal suture becomes straighter.

6.2.2 The fifth PCA: A larger *H. sapiens* sample with fossil specimens

Table 6.5 The fifth PCA of the posterior cranium: The percentage variance explained by the first seven PCs

	Percentage of Variance	Cumulative Percentage
PC 1	41.894%	41.894%
PC 2	14.211%	56.105%
PC 3	8.523%	64.628%
PC 4	4.392%	69.020%
PC 5	4.109%	73.128%
PC 6	3.563%	76.692%
PC 7	2.507%	79.198%

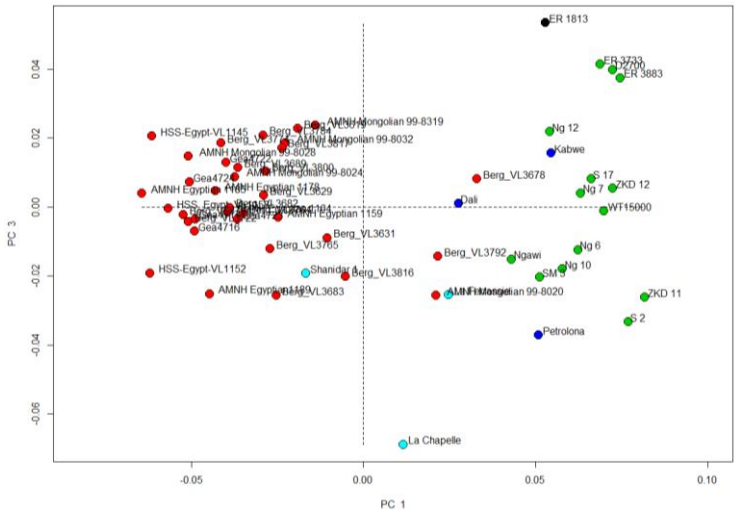

Figure 6.18 The PC 1 and PC 3 plot of the fifth PCA of the posterior cranium
The green dots: The *H. erectus s. l.* specimens. The black dot: The *H. habilis* specimen. The dark blue dots: The Mid-Pleistocene *Homo* specimens. The light blue dots: the Neanderthal specimens. The red dots: The *H. sapiens* specimens. The graphs are generated by the Geomorph R package (Adams et al., 2018).

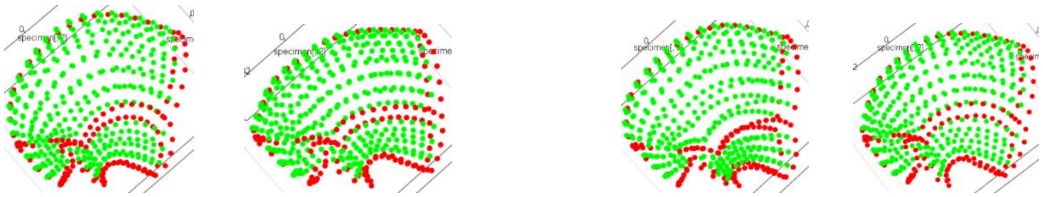

(A) (B)

Figure 6.19 The fourth PCA of the posterior cranium: The shapes at the two ends of PC 1 and PC 3
(A) The shape at the two ends of PC 1. (B) The shape at the two ends of PC 3. The left graph represents the negatove end. The right graph represents the positive end. The graphs are generated by the Geomorph R package (Adams et al., 2018).

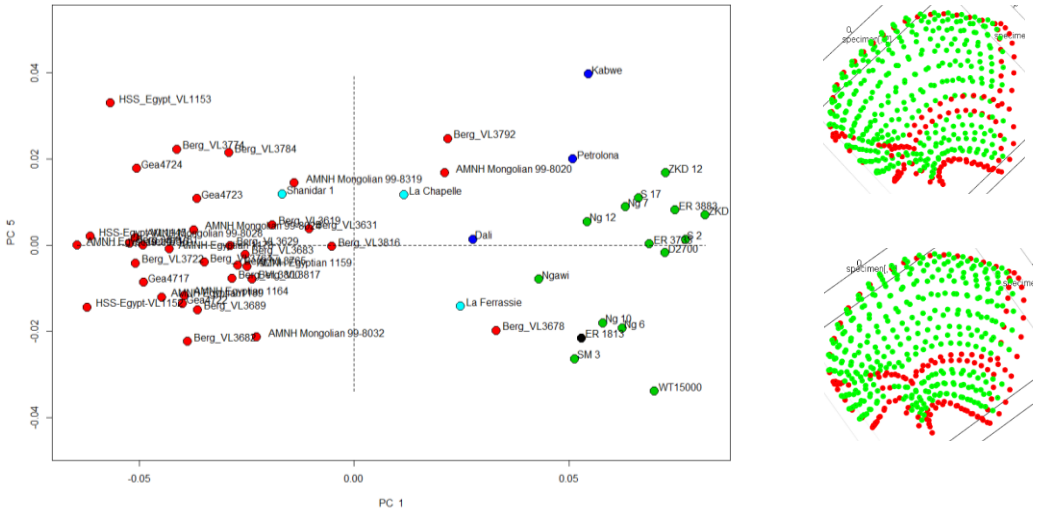

Figure 6.20 The fifth PCA of the overall cranium: The plot of PC 1 and PC 5
The below landmark configuration at the right side shows the negative-most shape of PC 5. The above landmark configuration side shows the positive-most shape of PC 5. The green dots: The *H. erectus s. l.* specimens. The black dot: The *H. habilis* specimen. The dark blue dots: The Mid-Pleistocene *Homo* specimens. The light blue dots: the Neanderthal specimens. The red dots: The *H. sapiens* specimens. The graphs are generated by the Geomorph R package (Adams et al., 2018).

After adding 35 *H. sapiens* specimens to the analysis, PC 1, which explains 41.894% of the total variance, again separates *H. sapiens* specimens from most fossils because the former have taller, shorter and rounder vaults (Table 6.5, Figure 6.18 and Figure 6.19; also see Appendix B). PC 3, which explains 8.523% of the total variance, also places Neanderthals at one end because of their relatively smaller temporal region, more bulging midparietal and midoccipital regions, and inwardly tilted side walls. S 2, ZKD 11 and Petralona 1 also overlap with Neanderthals (Figure 6.5, Figure 6.18 and Figure 6.19; also see

Figure B.22 and B.23). Similar to the PC 3 in the second PCA based on the maximum-semilandmark dataset, the vault does not significantly increase in height.

PC 5 is roughly consistent with PC 6 from the second analysis of posterior crania set by plotting KNM-WT 15000 and Kabwe 1 at its two ends (Table 6.5, Figure 6.20; also see Figure B.24). Nevertheless, the other specimens do not show obvious clustering. Moving toward Kabwe 1, this PC also demonstrates that the occipital squama shortens superoinferiorly, the region across the lambda flattens, the mastoid portion decreases in size, and the squamosal portion increases in size.

6.2.3 The sixth PCA: Smaller *H. sapiens* sample with fossils

Table 6.6 The sixth PCA of the posterior cranium: The percentage variance explained by the first seven PCs

	Percentage of Variance	Cumulative Percentage
PC 1	38.451%	38.451%
PC 2	13.901%	52.351%
PC 3	7.557%	59.909%
PC 4	6.332%	66.240%
PC 5	5.566%	71.806%
PC 6	4.467%	76.273%
PC 7	3.309%	79.582%

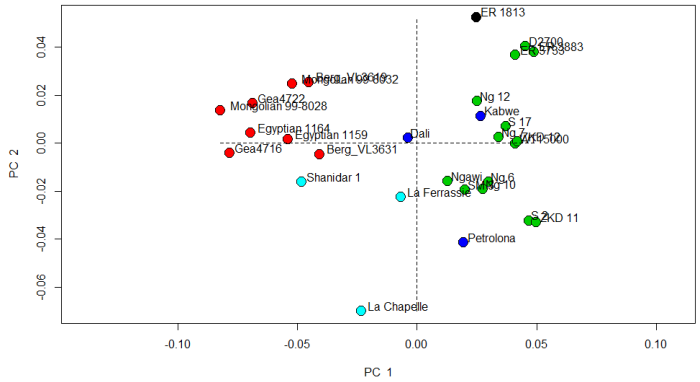

Figure 6.21 The PC 1 and PC 2 plot of the sixth PCA of the posterior cranium
The green dots: *H. erectus*. The black dot: *H. habilis*. The dark blue dots: Mid-Pleistocene *Homo*. The light blue dots: Neanderthals. The red dots: *H. sapiens*.

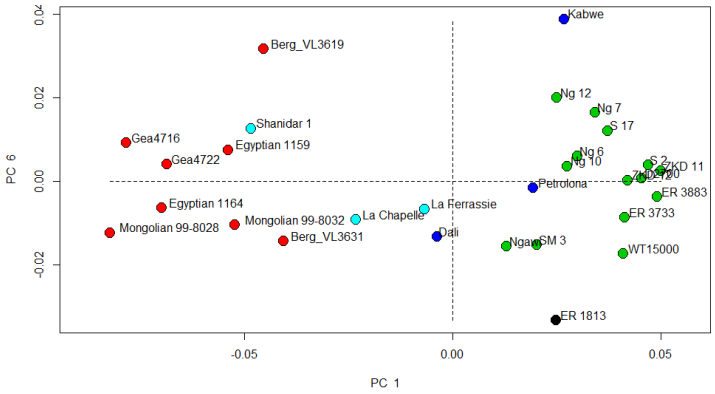

Figure 6.22 The PC 1 and PC 6 plot of the fifth PCA of the posterior cranium
The green dots: The *H. erectus s. l.* specimens. The black dot: The *H. habilis* specimen. The dark blue dots: The Mid-Pleistocene *Homo* specimens. The light blue dots: the Neanderthal specimens. The red dots: The *H. sapiens* specimens. The graphs are generated by the Geomorph R package (Adams et al., 2018).

When reducing the *H. sapiens* sample size to eight, PC 1 and PC 2 are still consistent with PC 1 and PC 3 in the fifth PCA that includes the large *H. sapiens* sample (Table 6.6, and Figure 6.21; also see Figure B.25 and Figure B.26). PC 6, which explains only 4.467% of the total variance, appears to be roughly consistent with PC 5 in the fifth PCA (Table 6.6 and Figure 6.22; also see Figure B.27). This PC plots KNM-ER 1813 and Kabwe 1 at its two ends. In a specimen plotted closer Kabwe 1, this PC also shows that the occipital squama becomes shorter superoinferiorly and more vertical, the region across lambda flattens, the nuchal plane becomes concave, especially in the area anterior to inion, the squamosal portion increases in size, and the mastoid portion becomes smaller.

6.3 BOOTSTRAP ANALYSIS OF OVERALL VARIABILITY

6.3.1 Sum of squared pairwise Procrustes distances (SSD)

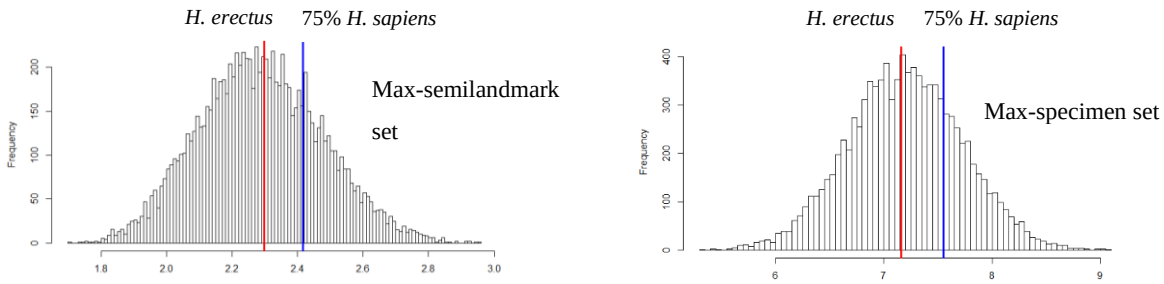

(A) *H. erectus s. l.* vs. *H. sapiens*

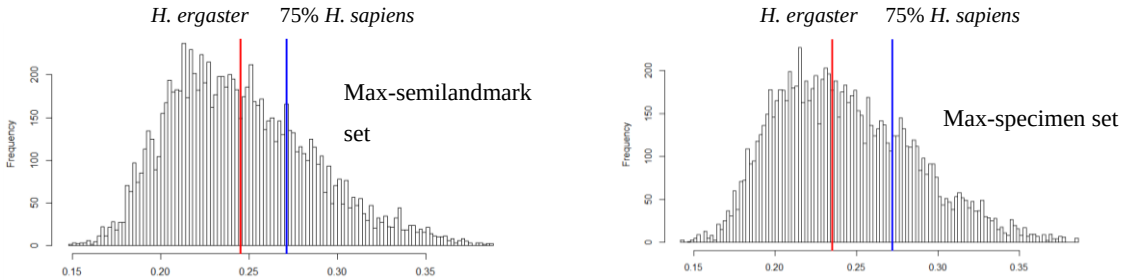

(B) African *H. ergaster* (no D2700) vs. *H. sapiens*

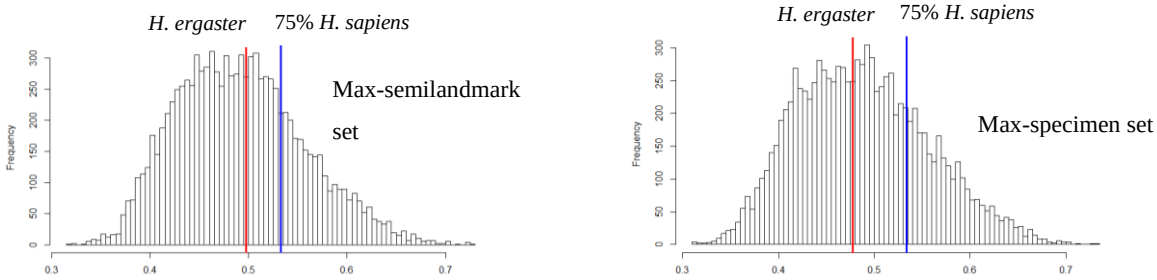

(C) *H. ergaster* (with D2700) vs. *H. sapiens*

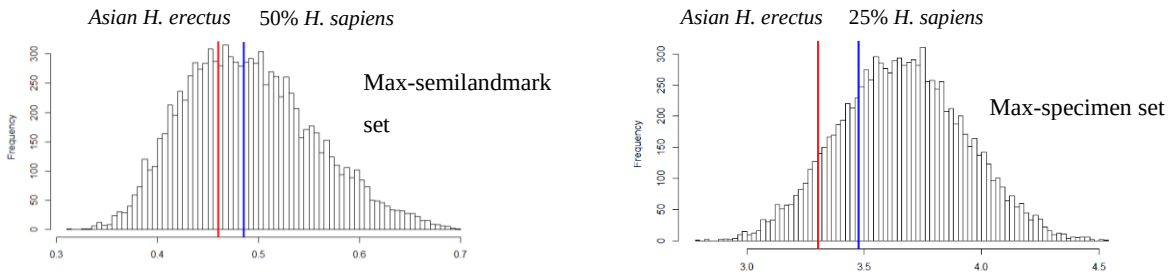

(D) Asian *H. erectus* vs. *H. sapiens*

Figure 6.23 The bootstrapped analyses of SSDs of the posterior cranium
The histograms show the distributions of 10,000 bootstrapped SSDs for the *H. sapiens* samples based on the maximum-semilandmark set (left) and the maximum-specimen set (right). In (A), (B), (C) and (D), the red lines indicate the SSDs of the *H. erectus s. l.*, *H. ergaster* (without D2700), *H. ergaster* (with D2700), and Asian *H. erectus* samples respectively. In (A), (B) and (C), the blue line indicates the 50th percentile of the *H. sapiens* SSDs. In (D), the blue line indicates the 50th percentile of the *H. sapiens* SSDs in the left graph and the 25th percentile in the right graph.

The bootstrap analyses of the posterior crania show that the SSDs of the *H. erectus* sample and its subsets remain insignificant relative to the bootstrapped SSDs of the *H. sapiens* sample (Figure 6.23 and Table B.15). Using the maximum semilandmark dataset, the *H. erectus s. l.* SSD exceeds 5345 (53.45%) bootstrapped *H. sapiens* SSDs. The SSD of the *H. ergaster* samples with and without D2700 exceed 5437 (54.37%) and 5,669 (56.69%) of *H. sapiens* SSDs, respectively. The SSD of the Asian *H. erectus* sample is relatively smaller as it exceeds only 3,534 (35.34%) of all *H. sapiens* SSDs.

The maximum specimen dataset shows that the SSDs of the *H. erectus* sample and its subsets are smaller than those in the *H. sapiens* sample (Figure 6.23 and Table B.15). The SSD of the expanded *H. erectus s. l.* sample is greater than 4,725 (47.25%) out of 10,000 *H. sapiens* bootstrapped SSDs. The SSD of the *H. ergaster* sample without D2700 is greater than 4,741 (47.41%) *H. sapiens* cases, while the SSD of *H. ergaster* sample after adding D2700 exceeds 4,677 (46.77%) of the *H. sapiens* cases. The SSD of the expanded Asian *H. erectus* sample is greater than only 928 (9.28%) of bootstrapped *H. sapiens* SSDs.

6.3.2 Mean pairwise Procrustes distances

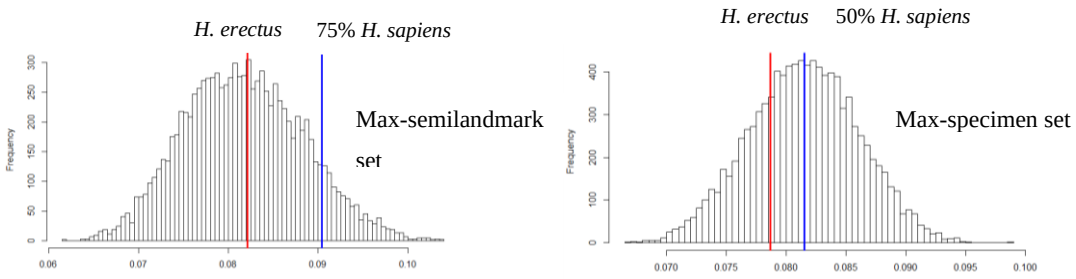

(A) *H. erectus s. l.* vs. *H. sapiens*

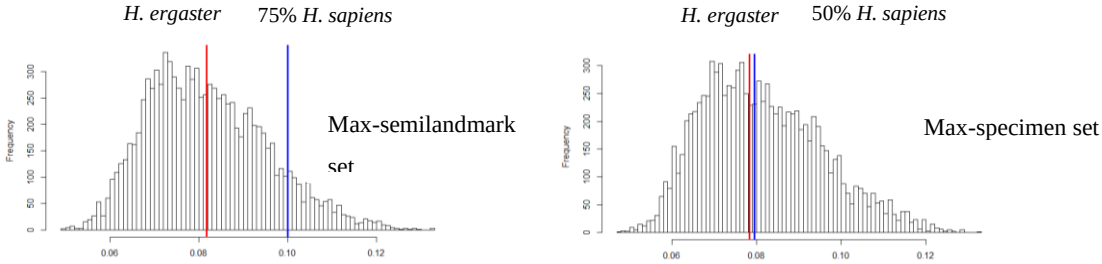

(B) *H. ergaster* (no D2700) vs. *H. sapiens*

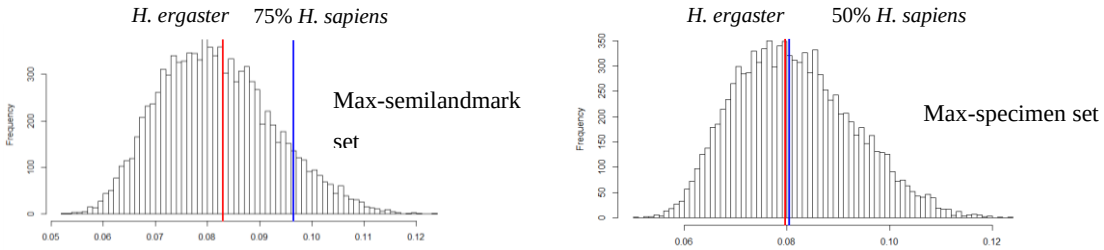

(C) *H. ergaster* (with D2700) vs. *H. sapiens*

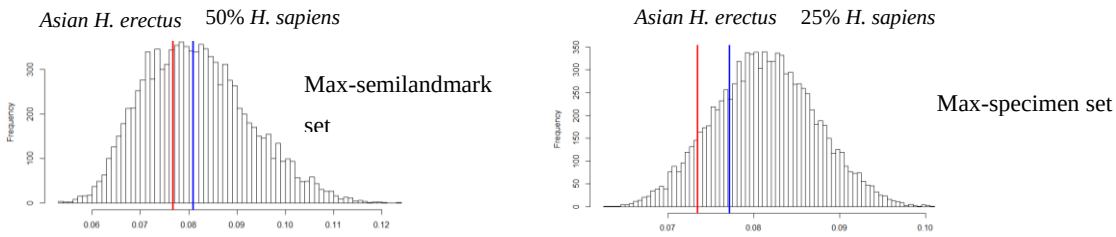

(D) Asian *H. erectus* vs. *H. sapiens*

Figure 6.24 The bootstrapped analyses of mean pairwise distances of the overall cranium
The histograms show the distributions of 10,000 bootstrapped mean pairwise distances for the *H. sapiens* samples based on the maximum-semilandmark set (left) and the maximum-specimen set (right). In (A), (B), (C) and (D), the red lines indicate the mean pairwise distances of the *H. erectus s. l.*, *H. ergaster* (without D2700), *H. ergaster* (with D2700), and Asian *H. erectus* samples respectively. In (A), (B) and (C), the blue lines indicate the 75th percentile (left) and 50th percentile (right) of the *H. sapiens* SSDs. In (D), the blue lines indicate the 50th (left) and 25th percentile (right) of the *H. sapiens* SSDs.

The mean pairwise distances of *H. erectus* and its subsets are quite small comparing to the bootstrapped *H. sapiens* pairwise distances. Using the maximum-semilandmark set, the mean pairwise distance of the *H. erectus s. l.* exceeds 5,294 (52.94%) bootstrapped *H. sapiens* distances (Figure 6.24 and Table B.16). The mean pairwise distances of the *H. ergaster* samples (without and with D2700) exceed 5,419 (54.19%) and 5,660 (56.60%) bootstrapped *H. sapiens* cases, respectively. The mean pairwise distance of the Asian *H. erectus* sample is greater than only 3,442 (34.42%) *H. sapiens* cases (Figure 6.24 and Table B.16).

For the maximum-specimen dataset, the mean pairwise distances become overall smaller (Figure 6.24 and Table B.16). The distance of the expanded *H. erectus s. l.* sample exceeds only 2,750 (27.50%) *H. sapiens* distances. The mean distances of the *H. ergaster* samples (without and with D2700) exceed 4,643 (46.43%) and 4,647 (46.47%) bootstrapped *H. sapiens* cases, respectively. The expanded Asian *H. erectus* sample shows a much-reduced mean pairwise distance, which is only greater than only 926 (9.26%) bootstrapped *H. sapiens* distances.

6.4 INDIVIDUAL PAIRWISE DISTANCES

6.4.1 The maximum-semilandmark set

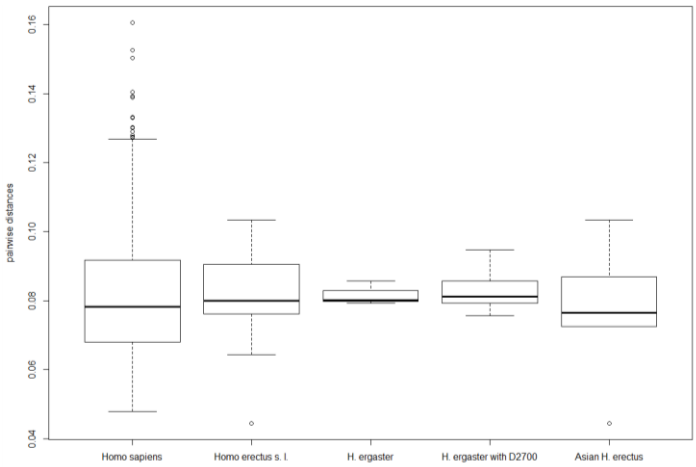

Figure 6.25 The boxplot of pairwise distances (the maximum-semilandmark set of the posterior cranium)

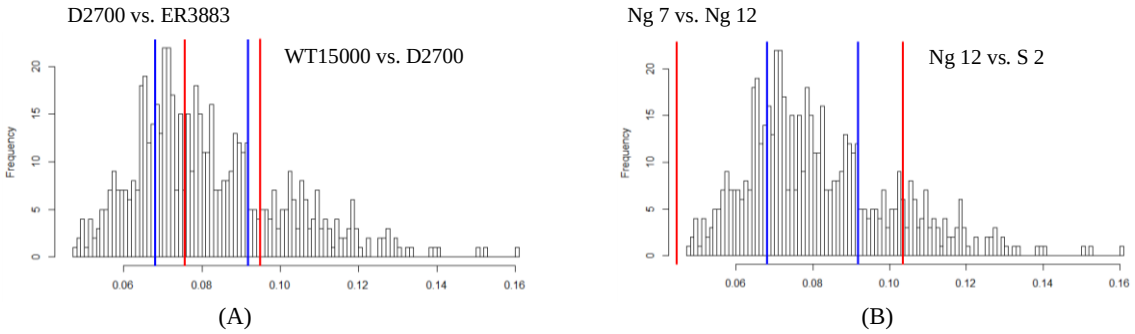

Figure 6.26 Pairwise distances of *H. erectus* (the maximum-semilandmark set of the posterior cranium)
The histogram shows the distribution of all pairwise distances within the *H. sapiens* sample. From left to right, the blue lines indicate the 25th and 75th percentiles of the *H. sapiens* pairwise distances in (A) and (B). In (A), the left red line represents the distance between D2700 and ER 3883, which is the smallest *H. ergaster* distance. The right red line represents the distance between WT 15000 and D2700, which is the largest *H. ergaster* distance. In (B), the left red line distance between Ng 7 and Ng 12, which is the smallest *H. erectus* distance, which is the smallest *H. erectus* distance. The right red line represents the distance between S 2 and Ng 12, which is the largest *H. erectus* distance.

Table 6.7 Distribution of pairwise distances in the *H. sapiens* and *H. erectus* samples based on the maximum-semilandmark set of the overall cranium

	Mean distance	Min	25th percentile	50th percentile	75th percentile	90th percentile	Max
H. sapiens	0.0817	0.0479	0.0681	0.0782	0.0917	0.109	0.161
H. erectus s. l.	0.0821	0.0445	0.0765	0.0799	0.0894	0.0950	0.103

Table 6.8 Individual pairwise distances of the *H. erectus* sample based on the maximum-semilandmark set of the overall cranium

(A) The pairwise distance that is smaller than the 25th percentile of the *H. sapiens* distances; (B) The pairwise distances that exceed the 75th percentile of the *H. sapiens* distances.

(A)

	Ng 7 vs. Ng 12 (min)	D2700 vs. S 17
Pairwise distance	0.0445	0.0643

(B)

	S 2 vs. Ng 12 (max)	D2700 vs. Ng 12	D2700 vs. S2	D2700 vs. WT 15000	ER 3733 vs. S 2	ER 3883 vs. S 2	S 2 vs. WT 15000
Pairwise distance	0.103	0.0927	0.0940	0.0948	0.0955	0.102	0.0929

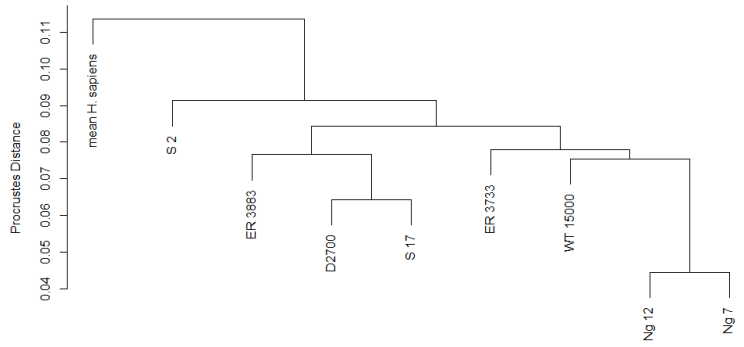

Figure 6.27 The UPGMA dendrogram of the *H. erectus* specimens and the mean shape of *H. sapiens* based on the maximum-specimen set of the posterior cranium

The boxplot shows that the three pairwise distances between three African *H. ergaster*, KNM-ER 3733, KNM-ER 3883, and KNM-WT 15000, are consistently somewhat greater than the 50th percentile of the *H. sapiens* distances (Figure 6.25). After adding D2700, the upper whisker of the *H. ergaster* box extends over the 75th percentile of the *H. sapiens* distances (Figure 6.25). The upper whisker represents the distance between KNM-WT 15000 and D2700, which exceeds the 75th percentiles of *H. sapiens* distances (Table 6.8, Figure 6.25 and Figure 6.26 A). The lower whisker, which represents the distance between KNM-ER 3883 and D2700, falls slightly below the 50th percentile of the *H. sapiens* distribution (Table 6.8; Figure 6.25 and 6.26A).

The distances of the Asian *H. erectus* cluster appear to be more variable, as the boxplot shows (Figure 6.25). The smallest distance is between Ng 7 and Ng 12, which is smaller than all the *H. sapiens* pairwise distances (Figure 6.26 A). The other distances generally fall between the 25th and 75th percentiles of the *H. sapiens* distances. In particular, the distances between S 2 and the two Ngandong specimens exceed the 50th percentile of the *H. sapiens* distances. The one between S 2 and Ng 12 even exceeds the 75th percentile of the *H. sapiens* distances (Figure 6.26 B and Table 6.8). The distance between S 2 and S 17 is slightly smaller than the 40th percentile of the *H. sapiens* distances.

Pooling all *H. erectus* specimens together, the greatest distance is still between Ng 12 and S 2 (Figure 6.26 B). Interestingly, the distances between S 2 and the *H. ergaster* specimens all exceed the 75th percentile of the *H. sapiens* distances. In addition, the distances between D2700 and WT 15000 and between D2700 and Ng 12 both exceed the 75th percentile of the *H. sapiens* distances. S 17 is very close to D2700, but the distances between it and the other *H. ergaster* specimens all exceed the 50th percentile of the *H. sapiens* sample.

In general, the two Ngandong specimens remain extremely close. The other pairwise distances are comparable and are great if using the Ngandong specimens as a measure. The distance between S 2 and S 17, as well as the distance between KNM-WT 15000 and Ng 7, is slightly smaller. The distances between S 2 and all the *H. ergaster* specimens, between D2700 and KNM-WT 15000, and between D2700 and Ng 7 are somewhat greater.

These patterns of pairwise distances are captured by the unweighted pair group method with arithmetic mean (UPGMA) dendrogram, which groups Ng 7 and Ng 12 in the tightest cluster (Figure 6.27). D2700 and S 17 are also grouped together. S 2 is placed near the root of the *H. erectus* cluster because it differs more from the other specimens than they do from each other.

6.4.2 The maximum-specimen set

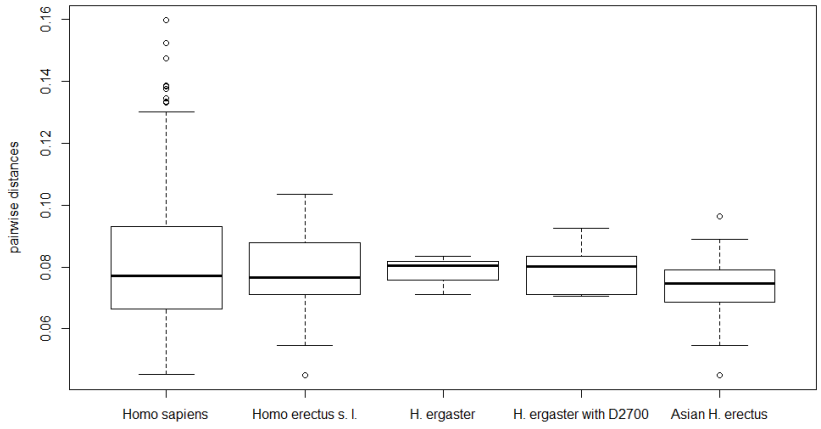

Figure 6.28 The boxplot of pairwise distances based on the maximum-specimen set of the posterior cranium

Table 6.9 Distribution of pairwise distances in the *H. sapiens* and *H. erectus* samples based on the maximum-specimen set of the posterior cranium

	Mean distance	Min	25th percentile	50th percentile	75th percentile	90th percentile	Max
H. sapiens	0.0814	0.0452	0.0665	0.0772	0.0931	0.111	0.160
H. erectus s. l.	0.0787	0.0451	0.0711	0.0767	0.0878	0.0947	0.103

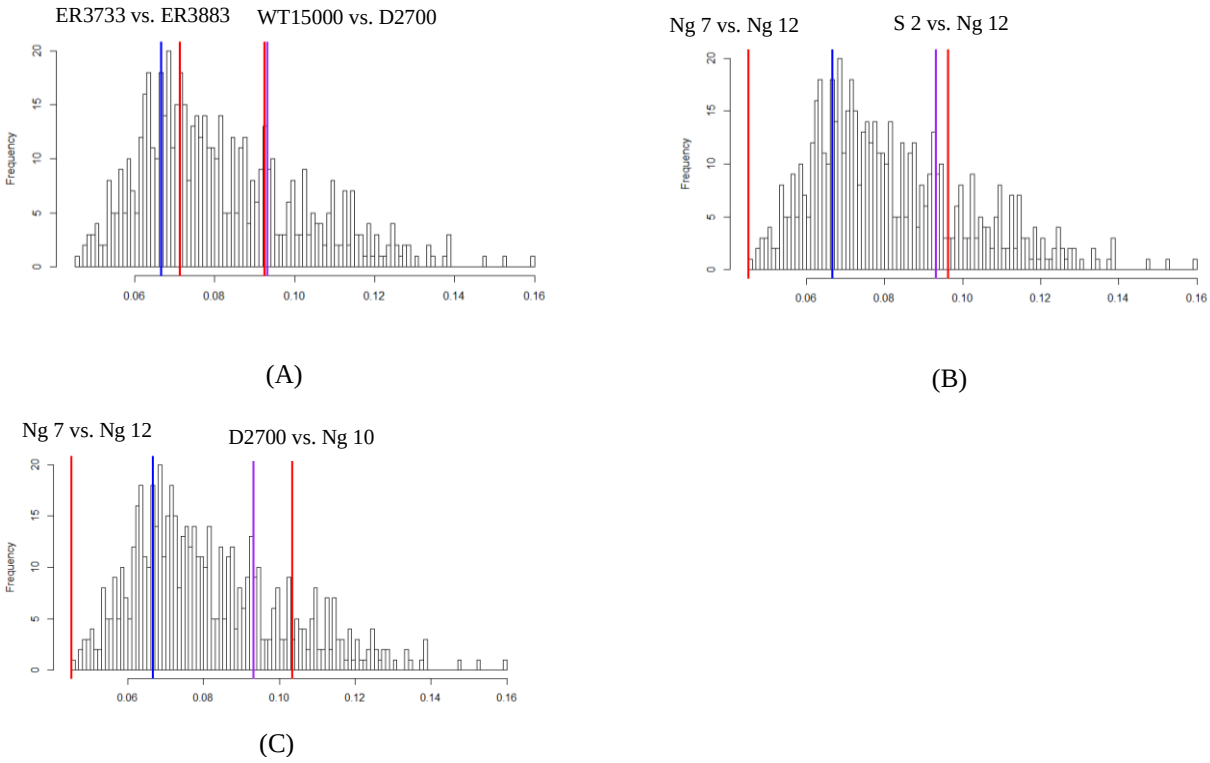

Figure 6.29 Individual pairwise distances of the *H. erectus* and *H. sapiens* samples based on the maximum-semilandmark set of the posterior cranium

The histogram shows the distribution of all pairwise distances within the *H. sapiens* sample. From left to right, the blue lines indicate the 25th and 75th percentiles of the *H. sapiens* pairwise distances in each graph. In (A), the left red line represents the distance between ER3733 and ER 3883, which is the smallest *H. ergaster* distance. The right red line represents the distance between WT 15000 and D2700, which is the largest *H. ergaster* distance. In (B), the left red line distance between Ng 7 and Ng 12, which is the smallest *H. erectus* distance, which is the smallest *H. erectus* distance. The right red line represents the distance between S 2 and Ng 12, which is the largest Asian *H. erectus* distance. In (C), the left red line distance between Ng 7 and Ng 12. The right red line represents the distance between D2700 and Ng 10, which is the largest *H. erectus* distance.

Table 6.10 Individual pairwise distances of the *H. erectus* sample based on the maximum-specimen set of the posterior cranium

(A) The pairwise distances that is smaller than the 25th percentile of the *H. sapiens* distances; (B) The pairwise distances that exceed the 75th percentile of the *H. sapiens* distances.

(A)

	Ng 12 vs. Ng 7 (Minimum)	Ng 12 vs. Ng 6	Ng 10 vs. Ngawi 1	Ng 10 vs. SM 3	Ng 6 vs. Ng 7	Ngawi vs. SM 3
Pairwise distance	0.0451	0.0658	0.0637	0.0640	0.0582	0.0546

	Ng 7 vs. S 17	Ng 7 vs. ZKD 12	ZKD 11 vs. ZKD 12	D2700 vs. S 17
Pairwise distance	0.0659	0.0554	0.0667	0.0601

(B)

	D2700 vs. Ng 10 (Maximum)	D2700 vs. Ng 6	D2700 vs. Ngawi 1	D2700 vs. ZKD 11	ER3733 vs. Ng 6	ER3733 vs. S 2
Pairwise distance	0.103	0.100	0.0910	0.103	0.0948	0.0984

	ER 3733 vs. SM 3	ER 3883 vs. Ng 10	ER 3883 vs. Ng 6	ER 3883 vs. ZKD 11	Ng 12 vs. S 2
Pairwise distance	0.0966	0.101	0.103	0.102	0.0963

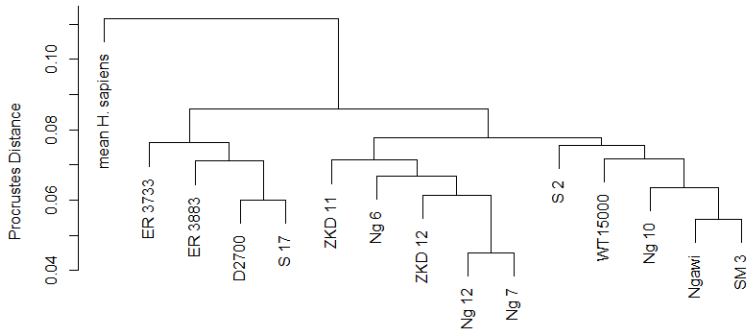

Figure 6.30 The UPGMA dendrogram of the *H. erectus* specimens and the mean shape of *H. sapiens* based on the maximum-specimen set of the posterior cranium

The boxplot demonstrates that the distributions of *H. erectus* and its subsets based on the maximum-specimen set are consistent with those based on the maximum-semilandmark set when compared to the pairwise distances of *H. sapiens* (Figure 6.28). Overall, most pairwise distances in the *H. erectus* sample fall below the 75th percentile of the *H. sapiens* distances (Figure 6.28 and Table 6.9). Nevertheless, the actual patterns of pairwise distances are complicated.

Distances between the *H. ergaster* specimens generally fall between the 35th and 75th percentiles of the *H. sapiens* distances (Figure 6.28 and 6.29A). The distances between KNM-WT 15000 and the other three *H. ergaster* specimens are relatively large, as they exceed the 55th percentile of the *H. sapiens* distances, as does the distance between D2700 and ER 3733. The distance between ER 3733 and ER 3883, as well as the distance between D2700 and ER 3883, fall below the 40th percentile of the *H. sapiens* distances.

The distances within Asian *H. erectus* are again more variable (Figure 6.28 and 6.29B). Upon adding more specimens, the late Indonesian specimens from Ngandong, Sambungmaçan, and Ngawi are still relatively close. Six of fifteen distances fall below the 25th percentile of the *H. sapiens* distances (Table 6.10). However, three pairs of distances that even exceed the 50th percentile of the *H. sapiens* distances (Ng 12-Ng10, Ng 6-Ngawi, and Ng 12-Ngawi). The distances between ZKD 11 and ZKD 12 and between ZKD 12 and Ng 7 also fall below the 25th percentile of the *H. sapiens* distances. The only distance that exceeds the 75th percentile in the *H. sapiens* sample is the one between S 2 and Ng 12.

When pooling Asian and African specimens together, the upper whisker of the boxplot increases slightly compared to the Asian *H. erectus* sample. In fact, among 10 of 11 pairwise distances exceeding the 75th percentile of *H. sapiens* distances, four are between D2700 and Asian specimens, and six between African *H. ergaster* and Asian specimens (Table 6.10 and Figure 6.29C). The distance between

D2700 and Ng 10 is the greatest (Table 6.10 and Figure 6.29C). Nevertheless, D 2700 is very close to S 17, as in the analysis based on the maximum-specimen set.

Consequently, the distribution of individual pairwise distances is somewhat different from that obtained with the analysis based on the maximum-semilandmark dataset. Overall, the separation between S 2 and other fossils is reduced. The late Indonesian specimens also do not form a very tight cluster, though they are still relatively close to each other. KNM-WT 15000 differs more from the other *H. ergaster* specimens than they do from each other. These patterns are reflected in the UPGMA dendrogram. In this diagram, the late Indonesian cluster is divided into two subclusters, in which ZKD 11, ZKD 12, KNM-WT 15000, and S 2 intermingle. KNM-ER 3733 is placed in another cluster with ER 3883, D2700 and S 17 (Figure 6.30).

6.5 DIFFERENCES BETWEEN GROUP MEANS

6.5.1 Bootstrap analysis

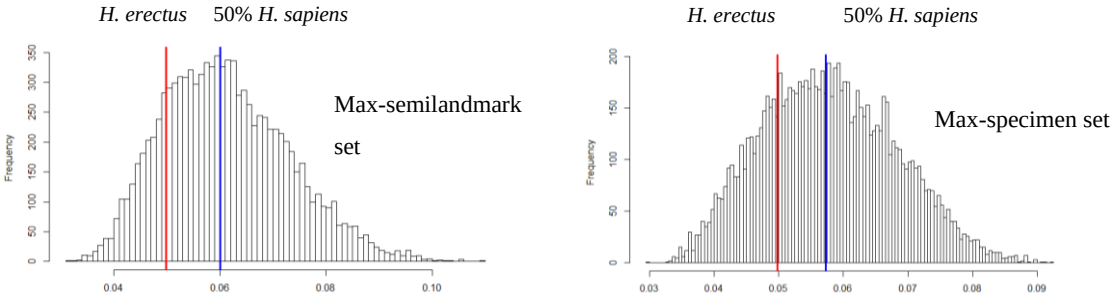

(A) *H. ergaster* (no D2700) vs. Asian *H. erectus*

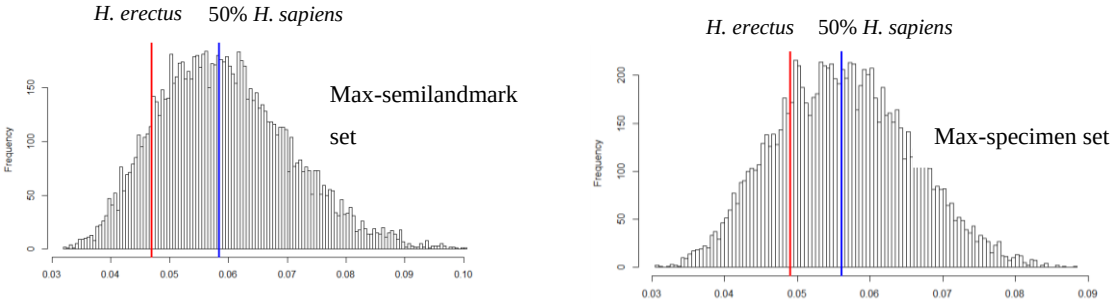

(B) *H. ergaster* (with D2700) vs. Asian *H. erectus*

Figure 6.31 The bootstrapped analyses of pairwise distances between the means of *H. erectus* geographical subsets (the posterior cranium)

In both (A) and (B), the left graph is based on the maximum-semilandmark set, while the right graph is based on the maximum-specimen landmark set. The blue line represents the 50th percentile of the 10,000 bootstrapped *H. sapiens* distances. (A) The red line represents the distance between the means of *H. ergaster* (no D2700) and Asian *H. erectus*. (B) The red line represents the distance between the means of *H. ergaster* (with D2700) and Asian *H. erectus*.

The bootstrap analysis of the group means based on the maximum-semilandmark set shows that the empirical distance between the means of *H. ergaster* (no D2700) and Asian *H. erectus* only exceeds 1,812 (18.12%) of the 10,0000 *H. sapiens* SSDs (Figure 6.31 and Table B.17). After adding D2700 to the *H. ergaster* sample, the empirical distance becomes relatively smaller, since it is greater than only 1,287 (12.87%) of the *H. sapiens* distances (Figure 6.31 and Table B.17). This is probably because D2700 is very close to S 17.

The maximum-specimen set shows that the distances between the means of the *H. erectus* geographical subsets somewhat increase, but still insignificant compared to the *H. sapiens* cases (Figure 6.31 and Table B.17). The distance between the mean African *H. ergaster* and the mean Asian *H. erectus* is larger than only 2,438 (24.38%) *H. sapiens* distances. The distance between the mean *H. ergaster* distance after adding D2700 and the mean Asian *H. erectus* distance is greater than only 2,273 (22.73%) *H. sapiens* cases.

6.5.2 Permutation tests of group means

Table 6.11 The Procrustes ANOVA of the *H. sapiens* geographical subsets (the posterior cranium)
(A) The Procrustes ANOVA based on the maximum-semilandmark set. (B) The Procrustes ANOVA based on the maximum specimen set. For each analysis, 10,000 permutations were carried out.

(A)

	Degree of Freedom	Sum of Square	Mean square	R square (coefficient of determination)	F-value	P-value
Asian vs. African *Homo sapiens*	1	0.020890	0.020890	0.17444	6.9729	0.0004
Residuals	33	0.098863	0.0029958	0.82556		
Total	34	0.119752				

(B)

	Degree of Freedom	Sum of Square	Mean square	R square (coefficient of determination)	F-value	P-value
Asian vs. African *Homo sapiens*	1	0.021535	0.021535	0.18035	7.2613	0.001
Residuals	33	0.097867	0.0029657	0.81985		
Total	34	0.119401				

Table 6.12 The Procrustes ANOVA of the *H*. erectus geographical subsets (the posterior cranium)
(A) *H. ergaster* (no D2700) vs. Asian *H. erectus* based on the maximum-semilandmark set. 35 permutations were carried out. (B) *H. ergaster* (no D2700) vs. Asian *H. erectus* based on the maximum-specimen set. 715 permutations were carried out. (C) *H. ergaster* (with D2700) vs. Asian *H. erectus* based on the maximum-semilandmark set. 70 permutations were carried out. (D) *H. ergaster* (with D2700) vs. Asian *H. erectus* based on the maximum-specimen set. 1001 permutations were carried out.

(A)

	Degree of Freedom	Sum of Square	Mean square	R square (coefficient of determination)	F-value	P-value
H. ergaster (no D2700) vs. Asian *H. erectus*	1	0.0042663	0.0042663	0.2107	1.3348	0.2857
Residuals	5	0.0159814	0.0031963	0.7893		
Total	6	0.0202476				

(B)

	Degree of Freedom	Sum of Square	Mean square	R square (coefficient of determination)	F-value	P-value
H. ergaster (no D2700) vs. Asian *H. erectus*	1	0.005715	0.005717	0.15648	2.0406	0.01259
Residuals	11	0.030819	0.0028017	0.84352		
Total	12	0.036536				

(C)

	Degree of Freedom	Sum of Square	Mean square	R square (coefficient of determination)	F-value	P-value
H. ergaster (with D2700) vs. Asian *H. erectus*	1	0.0044004	0.0044004	0.18282	1.3423	0.1786
Residuals	6	0.0196691	0.0032782	0.81718		
Total	7	0.0240695				

(D)

	Degree of Freedom	Sum of Square	Mean square	R square (coefficient of determination)	F-value	P-value
H. ergaster (with D2700) vs. Asian *H. erectus*	1	0.006870	0.0068696	0.1671	2.4075	0.006494
Residuals	12	0.034242	0.0028535	0.8329		
Total	13	0.041111				

Results of the Procrustes ANOVA are consistent overall with those based on the datasets of the entire cranium. The analysis comparing the African *H. ergaster* sample and the Asian *H. erectus* sample based on the maximum-semilandmark set yields a p-value of 0.2857, meaning that the empirical F-value is smaller than 10 of the 34 randomly permutated F-values (Table 6.12A). When including D2700 to the *H. ergaster* cluster, the p-value becomes 0.1786, meaning that the empirical F-value is less than 12 of the 69 other permutated F-values (Table 6.12C).

When using the maximum-specimen set, the ANOVA that compares the African *H. ergaster* sample and Asian *H. erectus* samples produces a p-value of 0.01259, meaning that the empirical F-value is less than only 9 of the 714 permutated F-values (Table 6.12B). After adding D2700 to the *H. ergaster* cluster, the p-value drops to 0.006494, meaning that the p-value is smaller than only approximately 6 permutated F-values (Table 6.12D). Therefore, there is only an insignificant amount of the total variance can be explained by the separation of group means.

Nevertheless, the p-values of the analyses comparing the geographical subsets of the *H. sapiens* sample fall well below the 0.05 critical value (Table 6.11). This suggests that a significant separation of the group means, as indicated by the F-test, does not necessarily imply an intra-sample species diversity. Again, the pattern of group separation detected by the ANOVA within the fossil samples may be driven by a separation of the late Indonesian specimens (i.e., the Ngandong, Ngawi and Sambungmaçan specimens) from other fossils. Notably, the absolute proportions of the total variance explained by the separation of group means (i.e., R squares) are not exceptionally large as they are all less than 20%.

6.6 OVERALL SIMILARITY WITH OTHER FOSSIL SPECIMENS

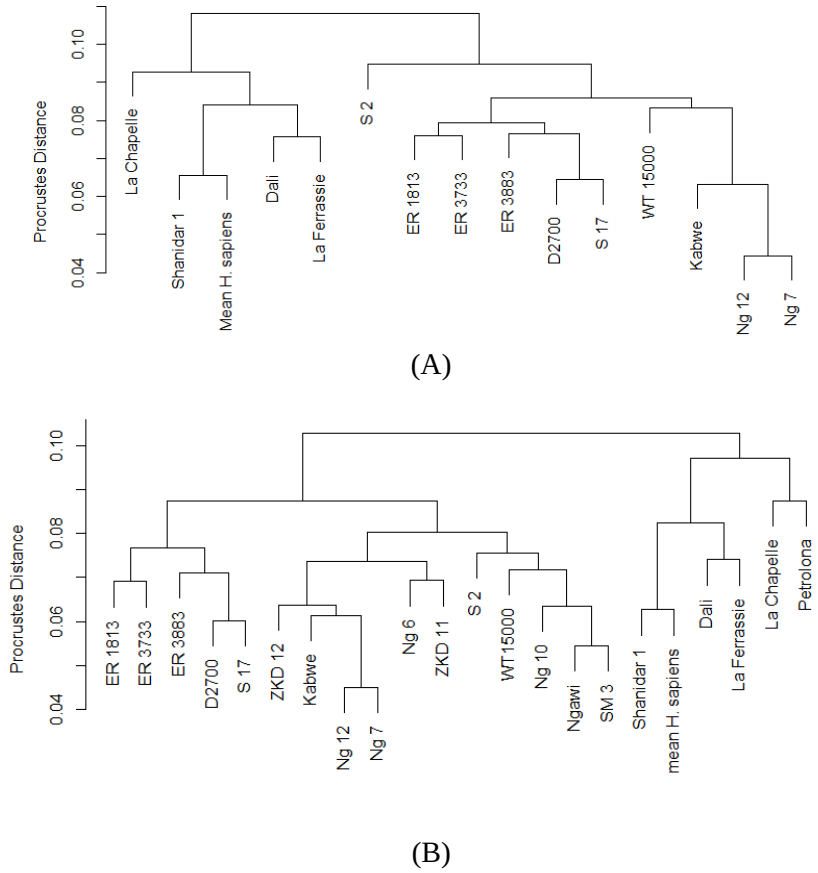

Figure 6.32 The UPGMA dendrogram of the fossil specimens (the posterior cranium)
(A) The maximum-semilandmark set. (B) The maximum-specimen set.

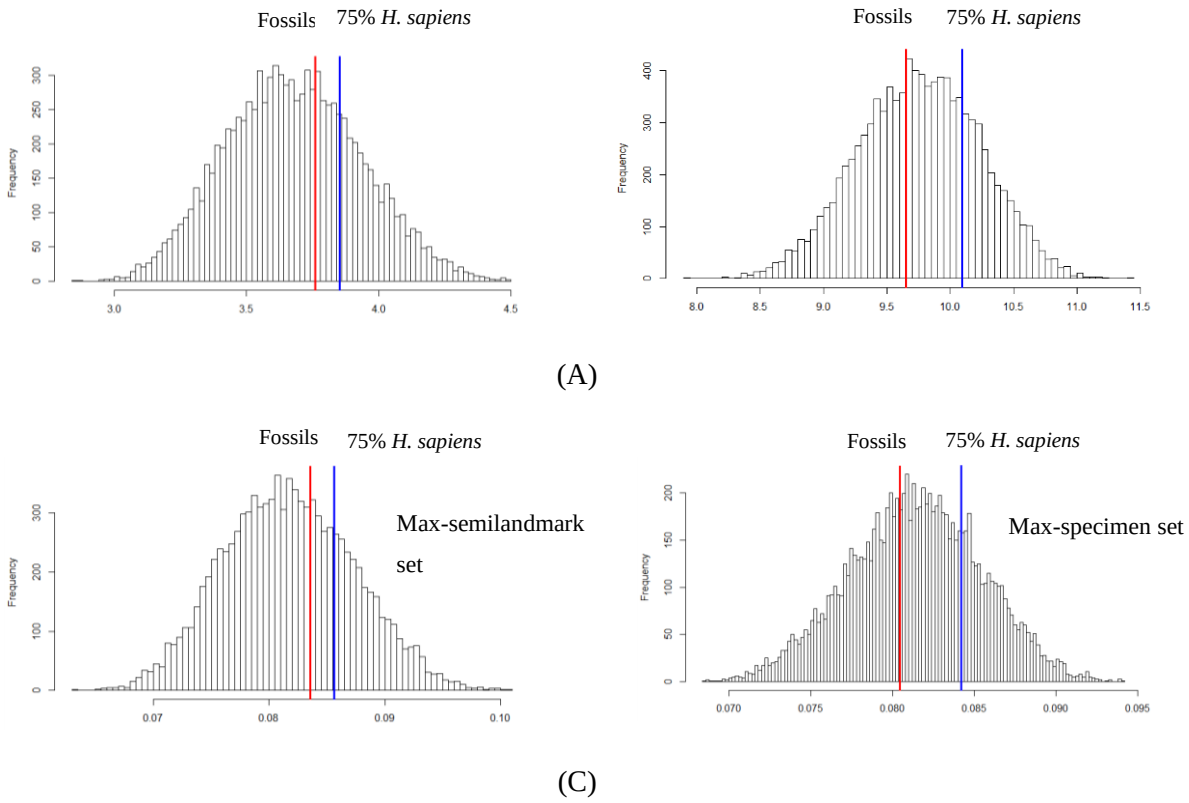

Figure 6.33 The bootstrapped analyses of mean pairwise distances of the posterior cranium
The fossil set includes KNM-ER 1813 and Kabwe 1. The left graph is based on the maximum-semilandmark set. The blue line represents the 75th percentile of the *H. sapiens* SSDs. The right graph is based on the maximum-specimen set. The blue line represents the 50th percentile of the *H. sapiens* SSDs.

After adding the other hominid specimens, the UPGMA dendrogram based on the maximum-semilandmark dataset again allocates Kabwe 1 and KNM-ER 1813 into the *H. erectus* cluster, while Dali, the Neanderthals, and the mean shape of the *H. sapiens* into a separate cluster (Figure 6.32A). In particular, KNM-ER 1813 is closest to KNM-ER 3733, while Kabwe 1 is closest to Ng 7 and Ng 12. Using the maximum-specimen dataset, the positions of Kabwe 1 and KNM-ER 1813 remain the same (Figure 6.32B). Further, Petrolona 1 is allocated to the Neanderthal cluster.

Upon adding the Kabwe 1 and KNM-ER 1813 to the *H. erectus* cluster, the SSDs of both the maximum-semilandmark and maximum-specimen sets, though relatively greater, do not exceed the 75th percentile of the bootstrapped *H. sapiens* SSDs (Figure 6.33). The former exceeds 6,225 (62.25%) *H. sapiens* SSDs, while the latter only 4,114 (41.14%) SSDs. The mean pairwise distance of the maximum-semilandmark set exceeds 6,210 (62.10%) *H. sapiens* cases, whereas the distance of the maximum specimen set is greater than only 4,038 (40.38%) *H. sapiens* cases.

6.7 LOWER LANDMARK DENSITIES

6.7.1 One hundred twenty-one anchor points

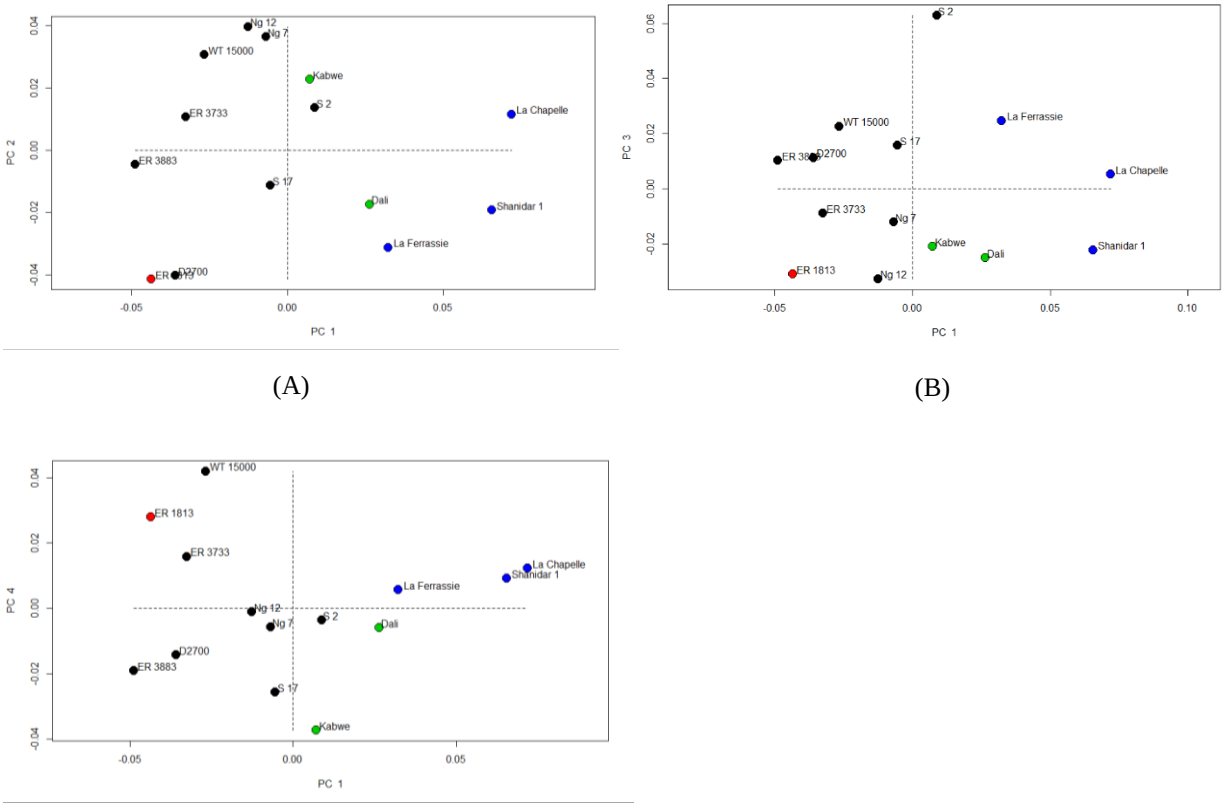

Figure 6.34 PCA plots of the fossil sample based on the anchor points of the overall cranium
(A) PC 1 and PC 2. (B) PC 1 and PC 3. (C) PC 1 and PC 4. The graphs are generated by the Geomorph R package (Adams et al., 2018).

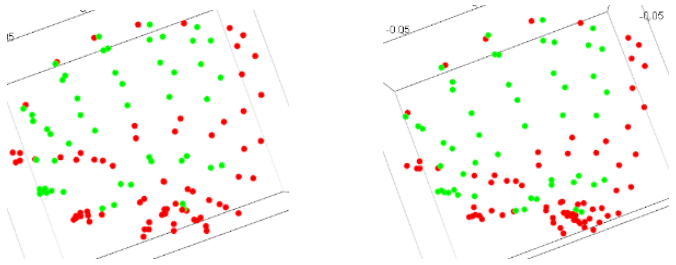

(A)

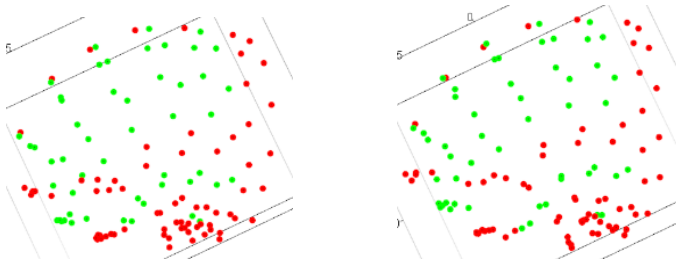

(B)

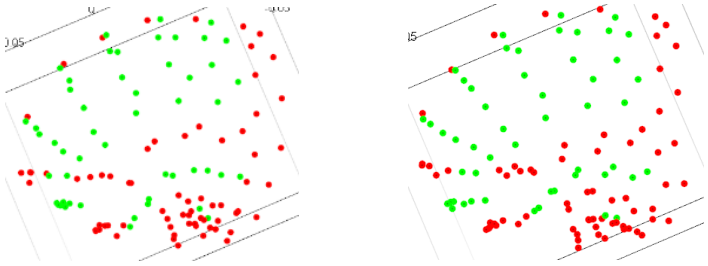

(C)

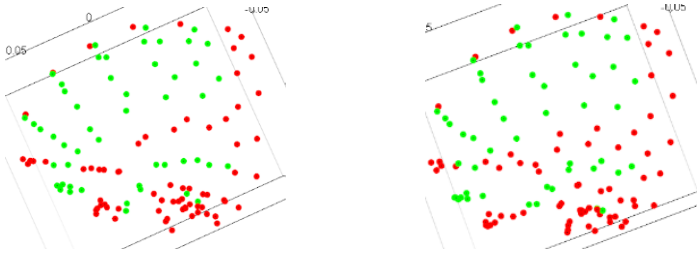

(D)

Figure 6.35 The shapes at the two ends of PCs based on the anchor points of the posterior cranium
In (A), (B), (C) and (D), the left graph represents the shape at the negative end, while the right graph represents the shape at the positive end of a PC. (A) PC1; (B) PC 2; (C) PC 3; (D) PC4. The graphs are generated by the Geomorph R package (Adams et al., 2018).

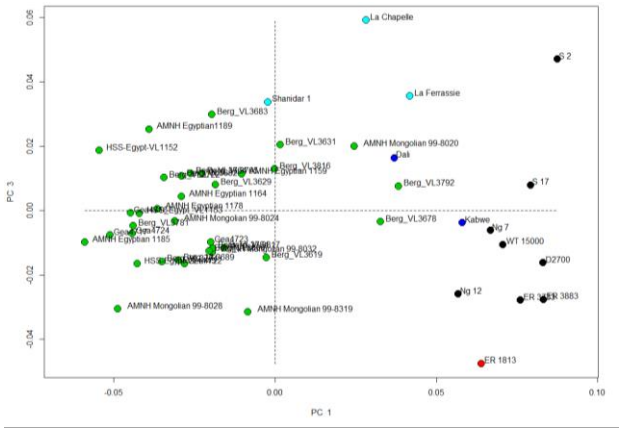

(A)

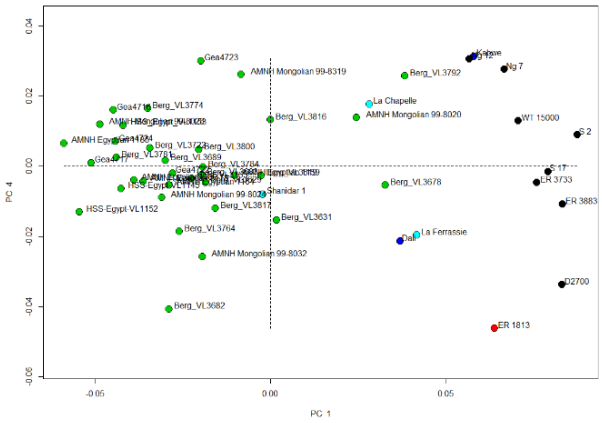

(B)

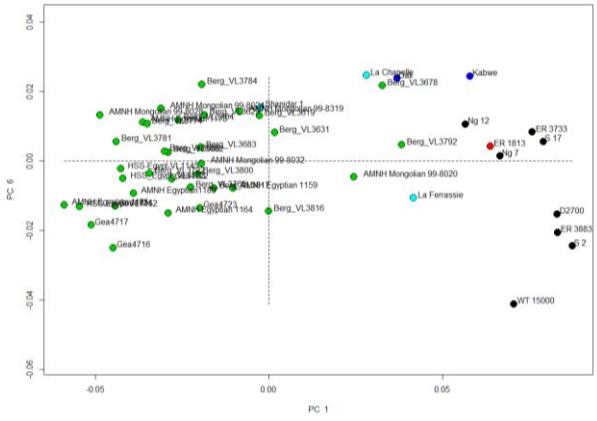

(C)

Figure 6.36 The PCA plots of *H. sapiens* and fossils based on the anchor points of the overall cranium
(A) PC 1 and PC 3. (B) PC 1 and PC 4. (C) PC 1 and PC 6.

When using 121 anchor points, the higher-ranked PCs are generally consistent with those of the original analyses based on the maximum-semilandmark set. For the analysis that includes only fossil specimens, PC 1, PC 2, and PC 4 are consistent with the corresponding PCs from the original analysis. PC 1 continues to show similar patterns of shape differences, e.g., decrease in size of the temporal region and the nuchal plane in specimens plotted closer to Neanderthals (Figure 6.34A, Figure 6.35A, and Figure B.28).

Both PC 2 and PC 3 of the fossil set are inconsistent with the corresponding PCs from the analysis based on the maximum-semilandmark dataset (Figure 6.34, Figure 6.35, Figure B.29 and Figure B.30). PC 2 plots the two Ngandong specimens at the positive end, but places KNM-ER 1813 and D2700 at the negative end. Moving toward the Ngandong side, the mastoid portion increases in size, the parietal notch shifts anteroinferiorly, inion shifts posteriorly, and the nuchal plane flattens.

PC 3 of the fossil sample is roughly similar to PC 2 from the analysis based on the maximum-semilandmark dataset (Figure 6.34B, Figure 6.35C, Figure B.30). It also separates S 2 from the rest of the fossil specimens, all of which are fairly close to each other. KNM-ER 1813 remains at the opposite end, while Ng 12 has a similar negative score. This PC also describes similar aspects of shape differences. Moving toward S 2, the rear profile becomes slightly shorter superoinferiorly and wider mediolaterally. The parietomastoid suture shortens, arcs, and shifts anteriorly. The squamosal suture straightens. The occipital angle sharpens. Inion shifts upward, and the occipital squama becomes shorter superoinferiorly.

PC 4 of the fossil sample is also fairly consistent with PC 4 from the first analysis based on the maximum-semilandmark set by placing KNM-WT 15000 and KNM-ER 1813 at the positive end while placing Kabwe 1 at the negative end (Figure 6.34C, Figure 6.35D, and Figure B.31). In a specimen plotted closer to KNM-WT 15000, the cranium becomes overall rounder, anteroposteriorly shorter and superoinferiorly taller, as inion moves anteriorly, the squamosal suture becomes flatter, the mandibular fossa increases slightly in size and becomes more laterally flared. However, this PC also shows that the parietomastoid suture becomes elongated anteroposteriorly and arced, which is the opposite of shape differences that PC 4 from the first analysis describes.

Upon including the large *H. sapiens* sample in the analysis with the fossil specimens, the major PCs are consistent overall with the corresponding PCs from the second analysis of the maximum-semilandmark dataset (Figure 6.36; also see Figure B.32 to Figure B.35). PC 1 separates *H. sapiens* from the fossil hominids. PC 3 separates S 2 and Neanderthals from the other specimens. PC 4 continues to place D2700 and KNM-ER 1813 at the end opposite to the Ngandong specimens and Kabwe 1. PC 6 also separates KNM-WT 15000 from the other hominids.

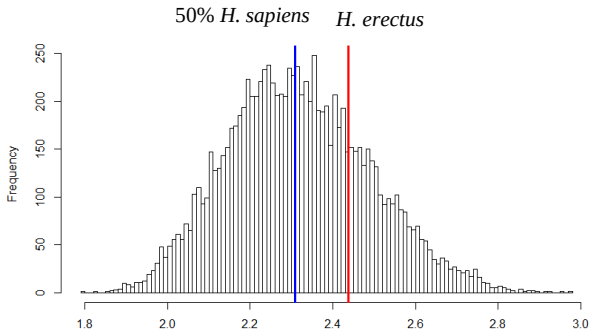

Figure 6.37 The bootstrap analysis of SSDs based on the anchor points of the posterior cranium

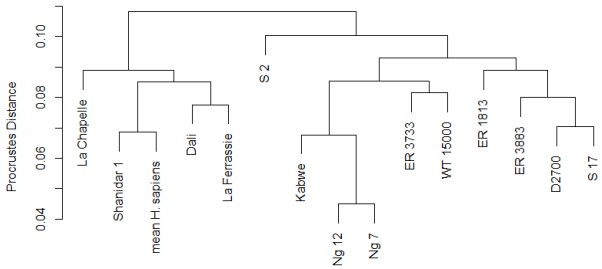

Figure 6.38 The UPGMA dendrogram (the anchor points of the posterior cranium)

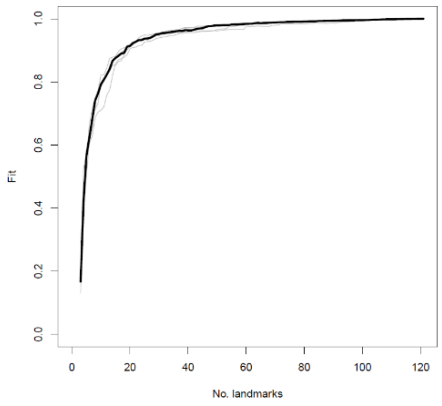

Figure 6.39 The mean LASEC based on the anchor points of the overall cranium

The bootstrap analysis shows that the sum of squared Procrustes distance (SSD) of *H. erectus s. l.* based on the anchor point dataset exceeds slightly the 75th percentile of the bootstrapped *H. sapiens* SSDs (greater than 7,567 (75.67%) *H. sapiens* distances) (Figure 6.37). Therefore, *H. erectus* appears to be more variable, as measured by SSD. The UPGMA tree shows a distribution of specimens nearly identical to that obtained from the maximum-semilandmark dataset (Figure 6.38). Differing the previous analysis, rather than grouping with KNM-ER 1813, KNM-ER 3733 and KNM-WT 15000 are part of the cluster close to the cluster containing Ng 7, Ng 12, and Kabwe 1. However, as these specimens are still close to the root of the *H. erectus* cluster, the distances between them remain similar in degree.

The mean landmark sampling evaluation curve (LASEC) obtained with five rounds of random sampling shows that when the number of randomly selected landmarks exceeds 20, the slope drops significantly, and a plateau appears (Figure 6.39). After the number of points exceeds 60, the slope approaches zero as the fit value approaches 1. This means that 60 or more points randomly selected from 159 anchor points will yield similar statistical results.

6.7.2 Thirty-three landmarks

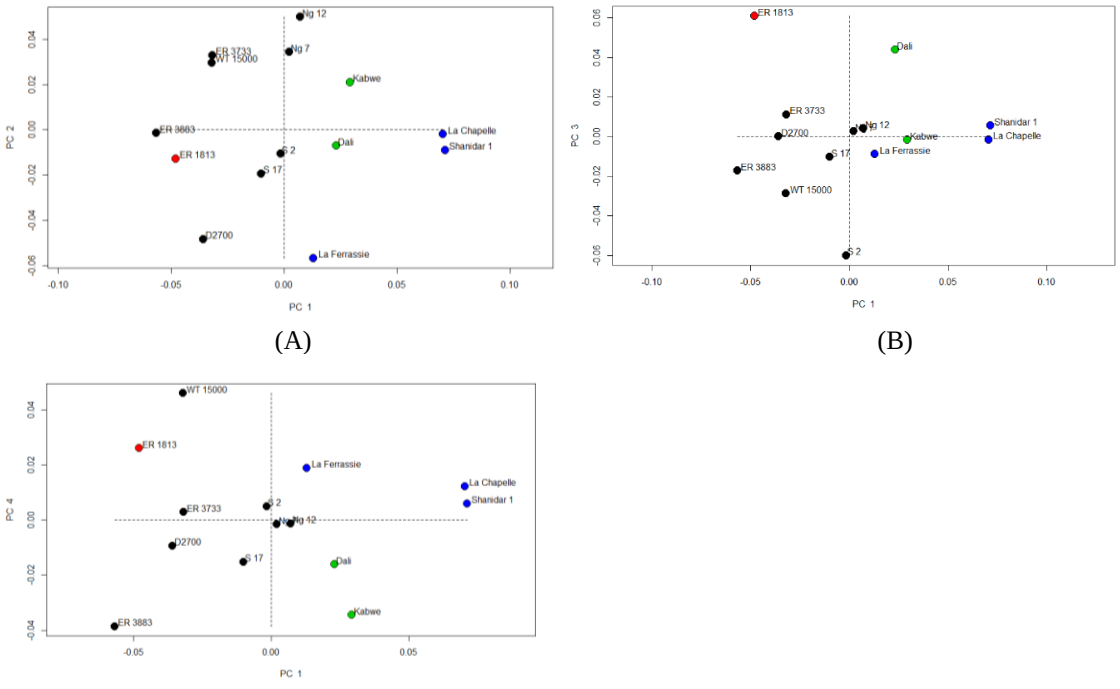

Figure 6.40 PCA plots of the fossil sample based on the discrete landmarks of the overall cranium
(A) PC 1 and PC 2. (B) PC 1 and PC 3. (C) PC 1 and PC 4.

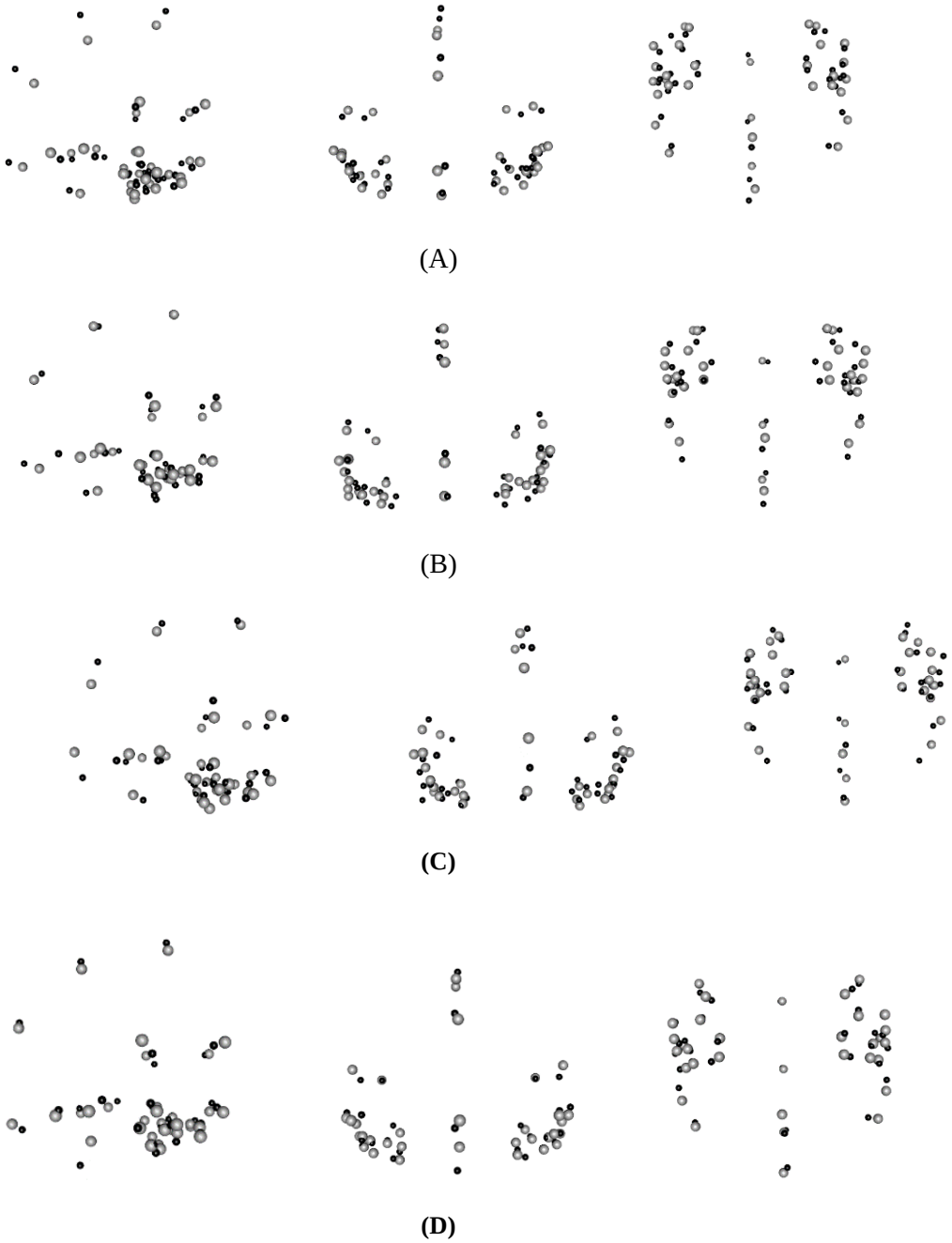

Figure 6.41 The shapes at the two ends of PCs based on the discrete landmarks of the posterior cranium
(A) PC 1. (B) PC 2. (C) PC 3. (D) PC 4. The grey points represent the shape at the negative end. The black points represent the shape at the positive end. From left to right: lateral view, anterior view, and inferior view. The graphs are generated by the Geomorph R package (Adams et al., 2018).

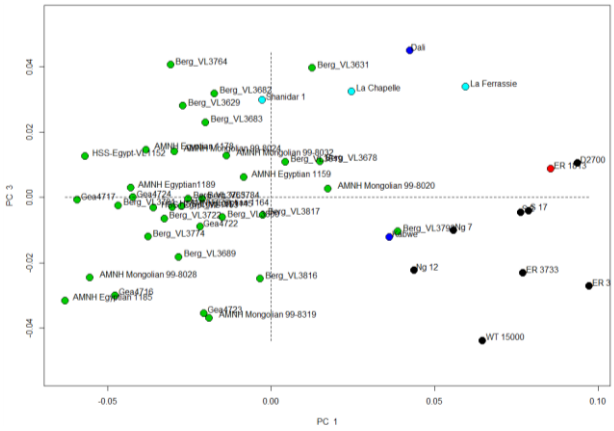

(A)

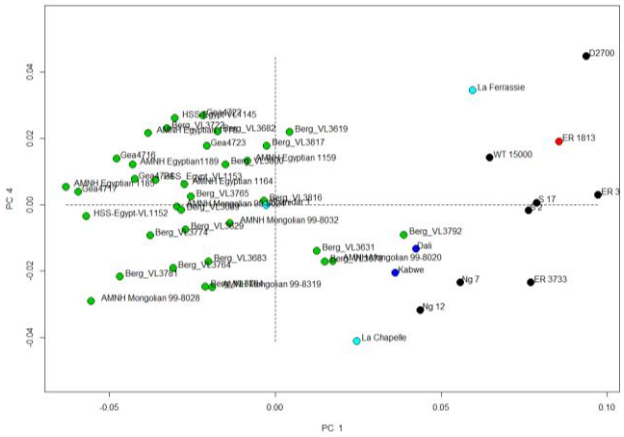

(B)

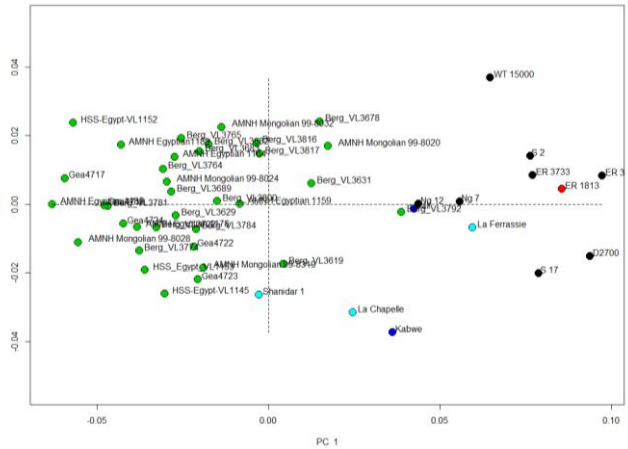

(C)

Figure 6.42 PCA plots of the fossil sample based on the discrete landmarks of the overall cranium
(A) PC 1 and PC 3. (B) PC 1 and PC 4. (C) PC 1 and PC 6

When using 33 discrete landmarks, the major PCs are roughly consistent with the corresponding PCs from the PCAs based on the 121-anchor point set. These discrete landmarks still capture gross shape differences in posterior crania. For example, PC 1 of the fossil sample continues to show an increase in size of the vault relative to a decrease in size of the temporal region (Figure 6.40A and 6.41A). PC 2 of the fossil sample can still reflect the posterior shift of inion, relative an increase in size of the mastoid region, and an anterior shift of the parietal notch (Figure 6.40A and 6.41B). PC 3 of the fossil sample also reflects the overall superoinferior shortening and mediolateral widening of the rear profile, superoinferior shortening of the squamosal portion, anteroinferior shortening of the parietomastoid suture and upward shifting of the inion (Figure 6.40B and Figure 6.41C). Most likely because many localized shape differences at landmark-free regions are not included, distribution of some specimens in this PC is different from the corresponding PC in the analyses based on the semilandmark or anchor-point datasets. For instance, for the analyses of the fossil sample, PC 1 shows more overlap between Neanderthals and rest of the fossils. PC 2 assigns KNM-ER 1813 a rather less negative score than plotting it at the negative end. PC 3 plots KNM-ER 1813 and Dali away from the other hominids. PC 4 places KNM-ER 3883 at the negative end rather than near D2700 (Figure 6.40C and Figure 6.41D). When including the large *H. sapiens* sample, the major PCs remain more or less similar to the corresponding PCs from the PCA based on the anchor points or the maximum-semilandmark dataset (Figure 6.42 and Appendix B 2.6).

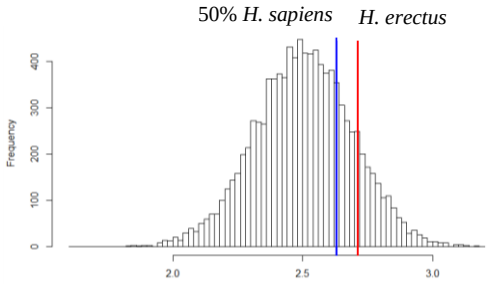

Figure 6.43 The bootstrapped analysis of SSDs based on the discrete landmarks of the posterior cranium
The red line represents the SSD of the *H. erectus* sample. The blue line indicates the 50th percentile of the bootstrapped *H. sapiens* SSDs.

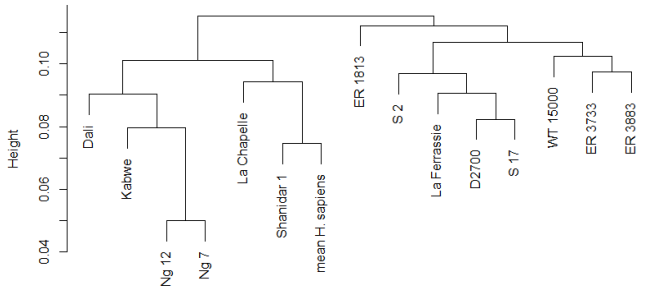

Figure 6.44 The UPGMA dendrogram (the discrete landmarks of the posterior cranium)

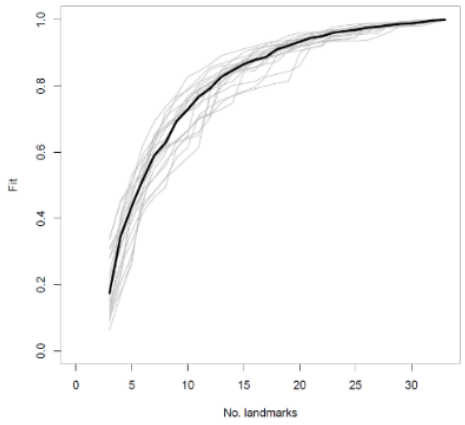

Figure 6.45 The mean LASEC based on the discrete landmarks of the posterior cranium

Interestingly, the bootstrap analysis shows that the SSD of the *H. erectus* sample becomes even greater relative to the *H. sapiens* distances, as it exceeds 8,667 (86.67%) of *H. sapiens* distances (Figure 6.43). The UPGMA dendrogram is more inconsistent with the original dendrogram based on the maximum-semilandmark dataset than the dendrogram based on the anchor-point set does (Figure 6.44). Though Ng 12 and Ng 7 remain closest to each other, they are further grouped with Dali and two Neanderthals rather than with KNM-WT 15000. KNM-ER 3733 is now closest to KNM-ER 3883 rather than to KNM-ER 1813. S 2 is grouped with the D2700-S 17 cluster rather than KNM-ER 1813, along with La Ferrassie 1. These patterns based on pairwise Procrustes distances are consistent with the distribution of specimens for major PCs, which shows that the Neanderthal specimens are less separated from the other hominid remains.

The mean LASEC obtained with 20 rounds of resampling of 33 discrete landmarks shows that when the number of landmarks increases, the fit value continuously increases, though the slope gradually

decreases (Figure 6.45). Thus, for the current landmark set, removing a few landmarks has more remarkable effects on the statistical results than the anchor-point dataset. This result is consistent with the LASEC obtained from the analysis of the 121-anchor point set.

7.0 THE TEMPORAL REGION

7.1 THE PCA BASED ON THE MAXIMUM-SEMILANDMARK SET

7.1.1 The first PCA: The fossil sample

Table 7.1 The first PCA of the temporal region: The percentage variance explained by the first seven PCs

	Percentage of Variance	Cumulative Percentage
PC 1	20.477%	20.477%
PC 2	16.821%	37.298%
PC 3	13.987%	51.258%
PC 4	10.532%	61.817%
PC 5	7.487%	69.303%
PC 6	6.358%	75.662%
PC 7	5.398%	81.059%

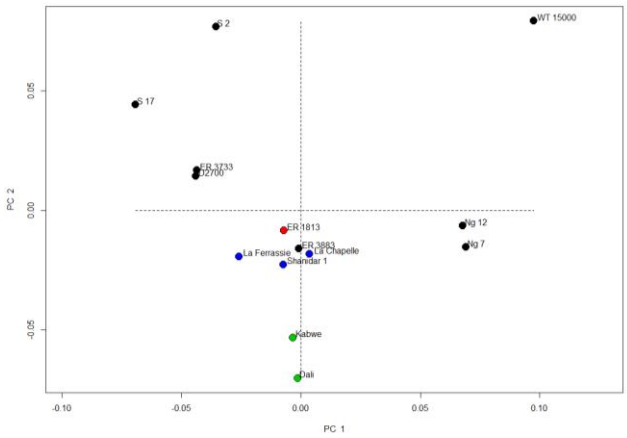

Figure 7.1 The first PCA of the temporal region: The plot of PC 1 and PC 2
The black dots: The *H. erectus s. l.* specimens. The red dot: The *H. habilis* specimen. The green dots: The Mid-Pleistocene *Homo* specimens. The blue dots: the Neanderthal specimens.

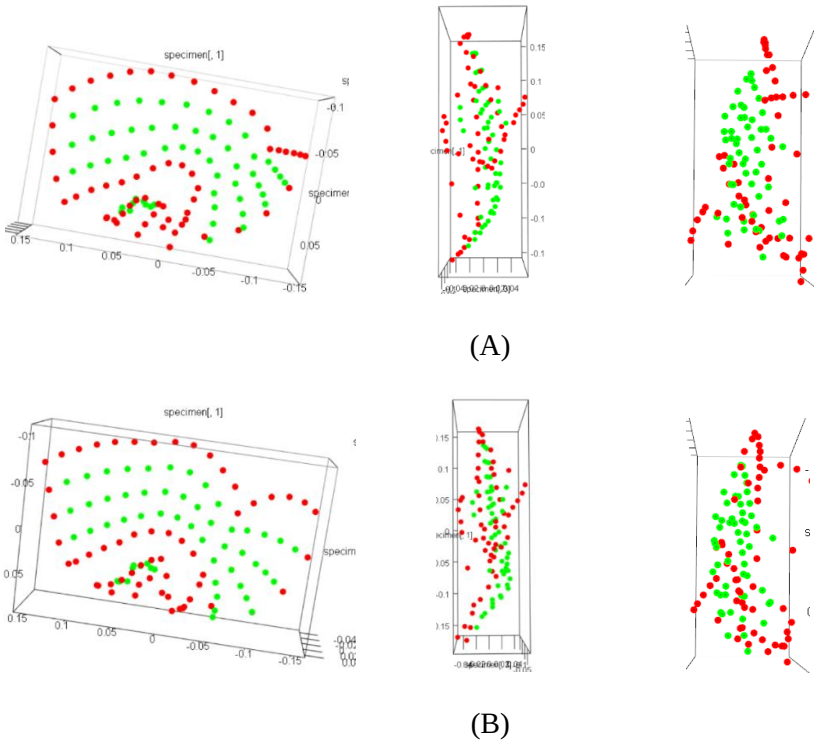

Figure 7.2 The first PCA of the temporal region: The shapes at the two ends of PC 1
(A) The shape at the negative end. (B) The shape at the positive end. From left to right: lateral view, anterior view, and inferior view. The graphs are generated by the Geomorph R package (Adams et al., 2018).

The principal component analysis (PCA) of the temporal region shows a complicated distribution. None of the first seven PCs is significantly correlated with size (Table B.18). PC 1, which explains 20.477% of the total variance, places S 17 and WT 15000 at opposite ends (Table 7.1 and Figure 7.1). S 2, KNM-ER 3733, and KNM-ER 3883 lie close to S 17, while Ng 7 and Ng 12, which score nearly the same, lie close to KNM-WT 15000. KNM-ER 1813, KNM-ER 3883, Neanderthals, Kabwe 1, and the Dali skull are distributed near the origin.

In a specimen plotted closer to KNM-WT 15000, the mastoid portion elongates anteroposteriorly. The squamosal suture becomes shorter anteroposteriorly, and the parietomastoid suture becomes longer anteroposteriorly as the parietomastoid suture lies more anteriorly and the position of asterion remains relatively stable (Figure 7.2). The auditory meatus lies more posteroinferiorly such that its posterior margin lies nearly underneath the parietal notch and the mastoid region becomes more vertically oriented. The peak of the squamosal suture shifts posteriorly from the midpoint as the posterior squamosal portion becomes taller superoinferiorly. The mastoid portion increases superoinferiorly in height because the parietomastoid suture arcs at its midpoint.

The tympanic plate becomes less inferiorly distended relative to the mastoid process (Figure 7.2). In inferior view, the mastoid portion becomes slightly elongated posteriorly. The mandibular fossa deepens as it protrudes into the cranial base, and its posterior wall becomes superoinferiorly taller and more vertically oriented. Its inferior moiety becomes shorter anteroposteriorly, such that the lateral profile changes from U- to V-shaped. The deepest point shifts from the medial to lateral end. The anterior margin of the fossa becomes wider mediolaterally and more arced than the posterior margin. The fossa also becomes wider laterally as the postglenoid region and the anterior wall of the auditory meatus lies more posteroinferiorly.

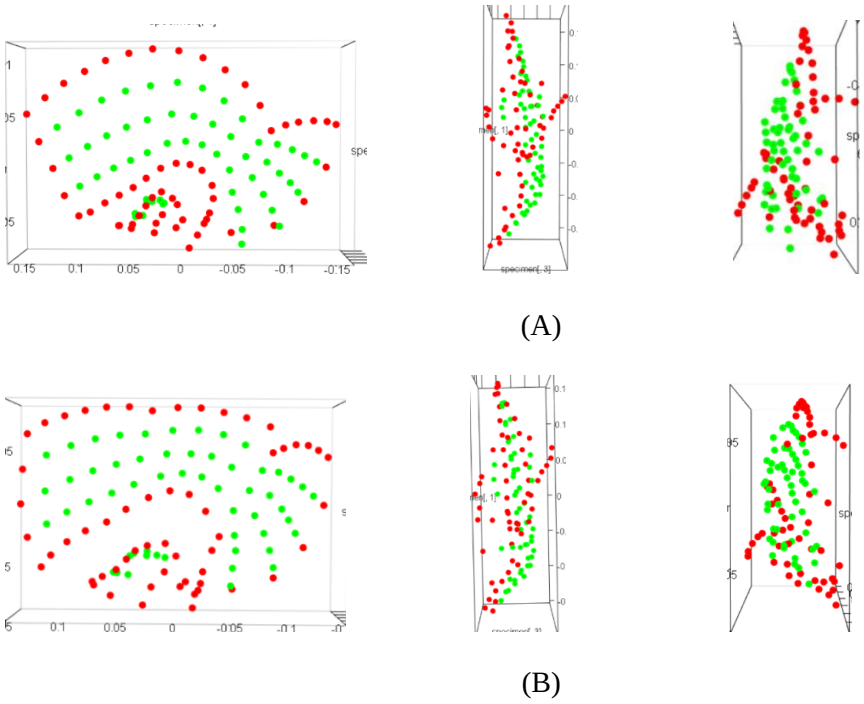

Figure 7.3 The first PCA of the temporal region: The shapes at the two ends of PC 2
(A) The shape at the negative end. (B) The shape at the positive end. From left to right: lateral view, anterior view, and inferior view. The graphs are generated by the Geomorph R package (Adams et al., 2018).

PC 2, which explains 16.821% of the total variance, plots S 2 and KNM-WT 15000 at the positive end and the Dali skull and Kabwe 1 at the negative end. KNM-ER 3883, KNM-ER 1813, Neanderthals, and the two Ngandong specimens cluster tightly just negative of the origin (Table 7.1 and Figure 7.1). KNM-ER 3733 and D2700 have nearly the same positive scores. S 17 is intermediate between these two specimens and the positive end.

In a specimen plotted closer to the positive end, the squamosal portion, especially the posterior part above the mandibular fossa, becomes shorter superoinferiorly, such that the squamosal suture becomes lower and straighter (Figure 7.3). The point just anterior to the parietal notch lies more posterosuperiorly, creating a short vertical component that bounds the notch anteriorly. The anterior corner of the squamosal suture lies more posteriorly, making the anterior margin of the squamosal portion more posteriorly sloping. The mastoid portion becomes taller superoinferiorly. The parietomastoid suture shortens anteroinferiorly. The parietal notch moves to the same height with as asterion. The mastoid process gradually becomes less distended. Its lateral profile becomes less inwardly tilting. Asterion slightly shifts laterally in the posterior view. Points at the suprameatal crest shift posterosuperiorly, indicating that this crest becomes more robust and obliquely oriented.

Overall, the mandibular fossa becomes longer anteroposteriorly (Figure 7.3). The mediolateral axis is more obliquely oriented as the lateral border lies more anteriorly, while the medial end lies slightly more posteriorly. The tympanic plate becomes more horizontally oriented. Lateral profile becomes shallower and broadly V-shaped as the anterior wall becomes more anteriorly sloped.

7.1.2 The second PCA: The large sample of *Homo sapiens* and the fossil sample

Table 7.2 The second PCA of the overall cranium: The percentage variance explained by the first seven PCs

	Percentage of Variance	Cumulative Percentage
PC 1	27.230%	27.230%
PC 2	13.577%	40.806%
PC 3	9.455%	50.261%
PC 4	5.905%	56.166%
PC 5	4.858%	61.025%
PC 6	4.234%	65.259%
PC 7	3.907%	69.166%

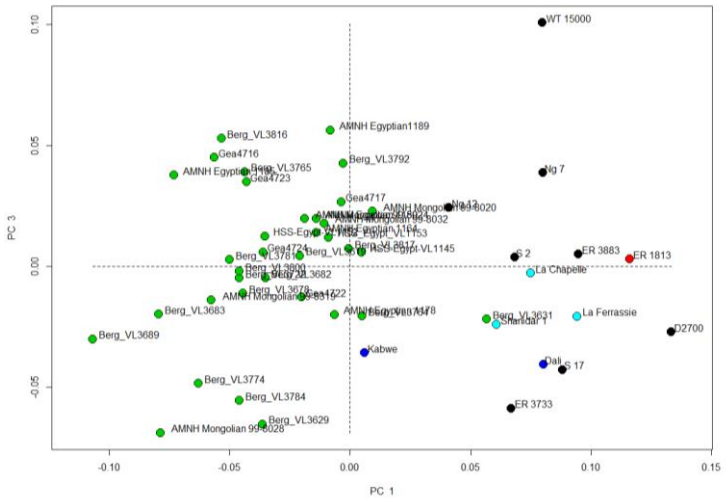

Figure 7.4 The second PCA of the temporal region: The plot of PC 1 and PC 3
The black dots: The *H. erectus s. l.* specimens. The red dot: The *H. habilis* specimen. The dark blue dots: The Mid-Pleistocene *Homo* specimens. The light blue dots: the Neanderthal specimens. The green dots: The *H. sapiens* specimens.

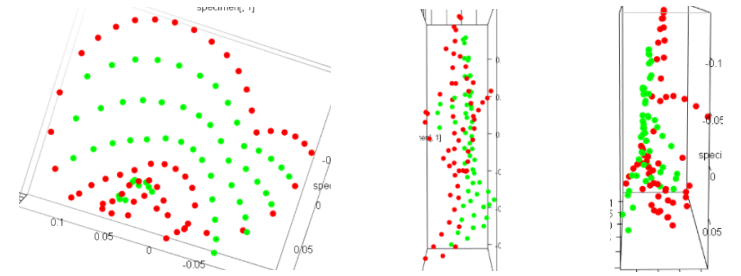

(A)

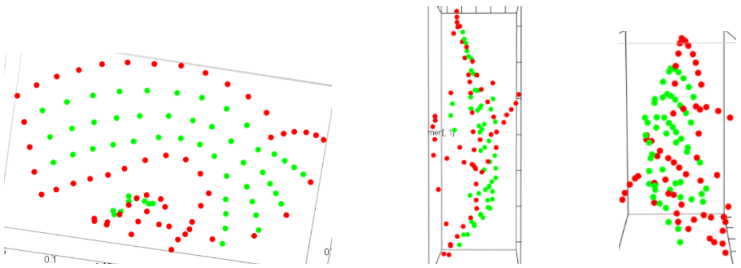

(B)

Figure 7.5 The second PCA of the temporal region: The shapes at the two ends of PC 1
(A) The shape at the negative end. (B) The shape at the positive end. From left to right: lateral view, anterior view, and inferior view. The graphs are generated by the Geomorph R package (Adams et al., 2018).

Upon adding 35 *H. sapiens* specimens to the analysis of the fossil specimens, no PC shows a significant size-shape relationship (Table B.19). PC 1, which explains 27.230% of the total variance, separates most fossils from *H. sapiens* (Table 7.2 and Figure 7.4). However, probably because Neanderthals overlap with other fossils, this PC is still insignificantly correlated with size. Kabwe 1 is located at the positive boundary of the *H. sapiens* sample. One of *H. sapiens* specimens also falls on the negative side of the fossil cluster. Among fossils, D2700 has the most positive score, while Ng 12 has the most negative score. The other fossil specimens do not form clear clusters along this PC.

In a specimen closer to D2700, the temporal bone becomes shorter superoinferiorly (Figure 7.5). The posterior extremity of the squamosal suture shifts posteriorly slightly more than the parietal notch, producing a short vertical component that is anterior to the notch. The squamosal portion becomes longer anteroposteriorly, while the squamosal suture flattens. The posterior extremity of the squamosal suture shifts posteriorly, producing a short superoinferiorly vertical component anterior to the notch. The anterosuperior corner lies more anteriorly, such that the anterior margin of the temporal region tilts more anteriorly. The mastoid portion becomes relatively shorter anteroposteriorly as the parietal notch lies more posteriorly. Semilandmarks at the suprameatal crest lie more posterosuperiorly, indicating that the suprameatal crest becomes more robust and oblique. The mastoid process becomes less distended. The posterior profile of the mastoid region tilts more medially. In inferior view, the base of the mastoid process becomes mediolaterally wider. The mandibular fossa becomes larger, and flares more laterally from the cranial base. It also becomes slightly shallower superoinferiorly.

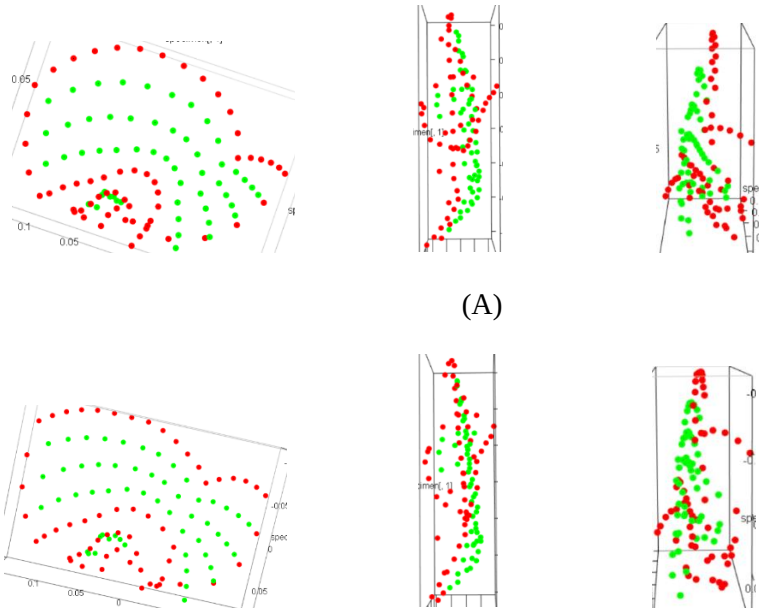

Figure 7.6 The second PCA of the temporal region: The shapes at the two ends of PC 3
(A) The shape at the negative end. (B) The shape at the positive end. From left to right: lateral view, anterior view, and inferior view. The graphs are generated by the Geomorph R package (Adams et al., 2018).

PC 3, which explains 9.455% of the total variance, separates KNM-WT 15000 from extant *H. sapiens* and other fossils (Table 7.2). Within the fossil group, while the Ngandong specimens are closer to KNM-WT 15000, they do not lie out of the range of *H. sapiens*. KNM-ER 3733 is the fossil specimen with the most negative score, and does not exceed the negative boundary of *H. sapiens*. The other specimens do not show clear clusters.

This PC shows shape differences similar to PC 1 and PC 2 in the first PCA that includes only fossils (Figure 7.6). In a specimen plotted closer to KNM-WT 15000, the posterior part of the squamosal portion becomes shorter superoinferiorly relative to the slightly superoinferiorly expanded anterior portion. The squamosal suture becomes less arced, and its peak shifts anteriorly. In lateral vie, the mastoid region expands becomes longer anteroposteriorly and taller superoinferiorly. The parietomastoid suture becomes longer anteroposteriorly as the parietal notch shifts anteroposteriorly. The mastoid process and the posterior margin of the auditory meatus shift posteriorly and slightly downwardly. The mastoid process becomes slightly more inferiorly protruding. The auditory meatus increases in size. In inferior view, the base of the mastoid process becomes shorter anteroposteriorly. The mandibular fossa becomes longer anteroposteriorly and narrower mediolaterally, especially on its posterior side. Its lateral profile becomes wider mediolaterally and deeper superoinferiorly.

7.1.3 The third PCA: The small sample of *H. sapiens* and the fossil sample

Table 7.3 The third PCA of the overall cranium: The percentage variance explained by the first seven PCs

	Percentage of Variance	Cumulative Percentage
PC 1	27.041%	27.041%
PC 2	14.410%	41.452%
PC 3	12.37%	53.82%
PC 4	8.256%	62.080%
PC 5	5.217%	67.297%
PC 6	5.002%	72.299%
PC 7	4.064%	76.363%

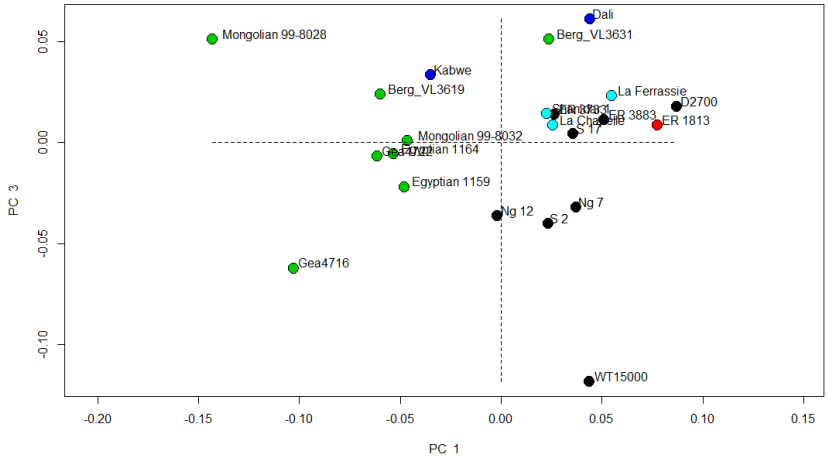

Figure 7.7 The third PCA of the temporal bones: The plot of PC 1 and PC 3
The black dots: The *H. erectus s. l.* specimens. The red dot: The *H. habilis* specimen. The dark blue dots: The Mid-Pleistocene *Homo* specimens. The light blue dots: the Neanderthal specimens. The green dots: The *H. sapiens* specimens. The graphs are generated by the Geomorph R package (Adams et al., 2018).

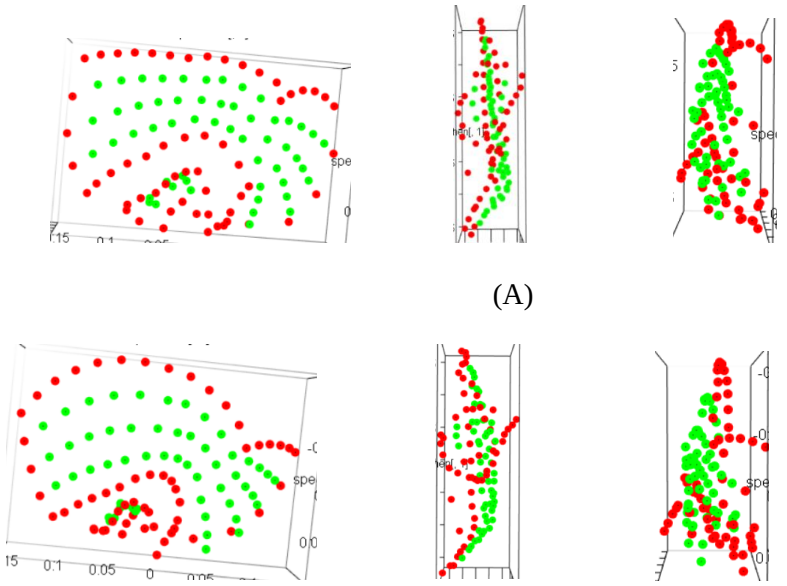

Figure 7.8 The second PCA of the temporal region: The shapes at the two ends of PC 3
(A) The shape at the negative end. (B) The shape at the positive end. From left to right: lateral view, anterior view, and inferior view. The graphs are generated by the Geomorph R package (Adams et al., 2018).

When reducing the sample size of *H. sapiens* to eight, none of the major PCs is significantly correlated with size (see Appendix B). The first three PCs are consistent with the corresponding PCs from the analysis that includes the large *H. sapiens* sample. PC 1, which explains 27.041% of the total variance, continues to separate the *H. sapiens* sample from most fossils as its temporal bone is shorter anteroposteriorly and increases in height superoinferiorly (Table 7.3, Figure 7.7 and Appendix).

PC 3, which explains 12.37% of the total variance, also separates KNM-WT 15000 from the other specimens (Table 7.3 and Figure 7.7). In this case, The Dali skull is placed at the opposite end, while KNM-ER 3733 overlaps with the less negatively scored Neanderthals, KNM-ER 3883, and D2700. In a specimen plotted closer to KNM-WT 15000 end, this PC describes similar shape differences. For example, the posterior squamosal portion decreases in height superoinferiorly, the parietomastoid suture becomes in longer anteroposteriorly and the mastoid process lies more posteroinferiorly (Figure 7.8).

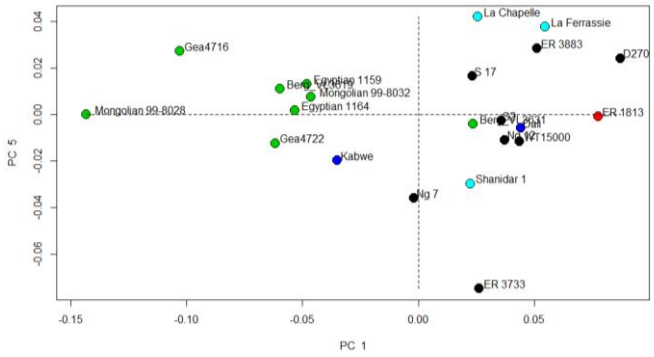

Figure 7.9 The third PCA of the temporal bones: The plot of PC 1 and PC 5
The black dots: The *H. erectus s. l.* specimens. The red dot: The *H. habilis* specimen. The dark blue dots: The Mid-Pleistocene *Homo* specimens. The light blue dots: the Neanderthal specimens. The green dots: The *H. sapiens* specimens.

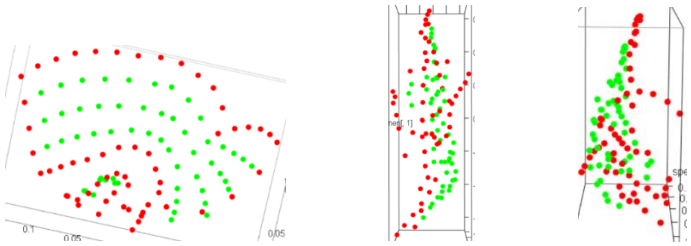

(A)

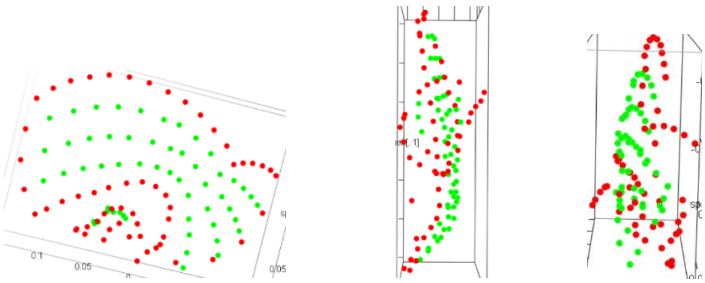

(B)

Figure 7.10 The second PCA of the temporal bones: The shapes at the two ends of PC 5
(A) The shape at the negative end. (B) The shape at the positive end. From left to right: lateral view, anterior view, and inferior view. The graphs are generated by the Geomorph R package (Adams et al., 2018).

Another interesting PC not shown in the first two analyses is PC 5, which explains 5.217% of the total variance (Table 7.3). This PC separates KNM-ER 3733 from others (Figure 7.9). Within the fossil sample, Ng 12, KNM-WT 15000, The Dali skull, and KNM-ER 1813 form a tight cluster on the negative

side of the origin. Ng 7 and Shanidar 1 are intermediate between this cluster and KNM-ER 3733. S 17, D2700, ER 3883, and the other two Neanderthal specimens have similar positive scores.

In a specimen closer to KNM-ER 3733, the squamosal portion (Figure 7.10). The squamosal suture becomes shorter superoinferiorly and straighter. The anterosuperior corner of the squamosal portion shifts forward, while the point at the infratemporal crest shifts backward. The parietal notch shifts anteriorly, creating a short vertical component of the posterior squamosal suture that bounds it anteriorly. The auditory meatus becomes narrower. The mastoid process is less inferiorly protroding. The supramastoid portion bulges more laterally in posterior view. Asterion shifts slightly medially. The tympanic plate becomes more transversely oriented. The lateral profile of the mandibular fossa becomes deeper superoinferiorly and more narrowly V-shaped as the posterior wall becomes more vertical. The entire fossa slightly lies more medially.

7.2 THE PCA BASED ON THE MAXIMUM-SPECIMEN SET

7.2.1 The fourth PCA: The fossil sample

Table 7.4 The fourth PCA of the overall cranium: The percentage variance explained by the first seven PCs

	Percentage of Variance	Cumulative Percentage
PC 1	22.986%	22.986%
PC 2	16.461%	39.447%
PC 3	12.171%	51.618%
PC 4	9.512%	61.131%
PC 5	7.949%	69.097%
PC 6	5.374%	74.453%
PC 7	5.110%	79.563%

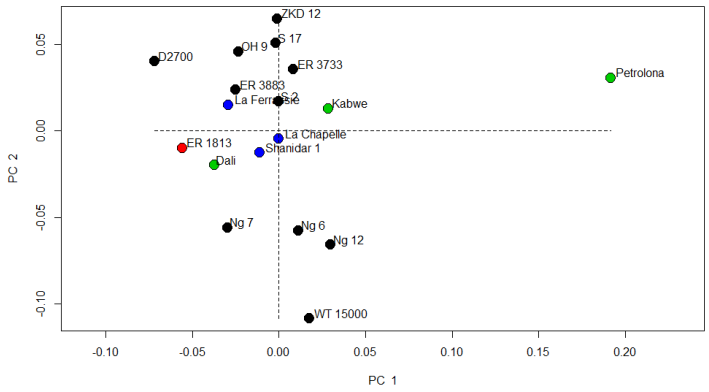

Figure 7.11 The fourth PCA of the temporal bones: The plot of PC 1 and PC 2
The black dots: The *H. erectus s. l.* specimens. The red dot: The *H. habilis* specimen. The green dots: The Mid-Pleistocene *Homo* specimens. The blue dots: the Neanderthal specimens. The graphs are generated by the Geomorph R package (Adams et al., 2018).

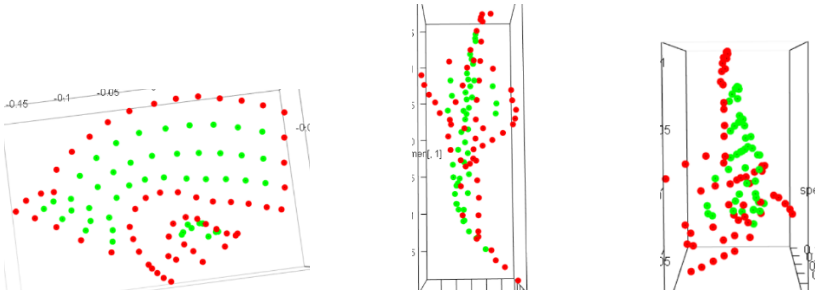

(A)

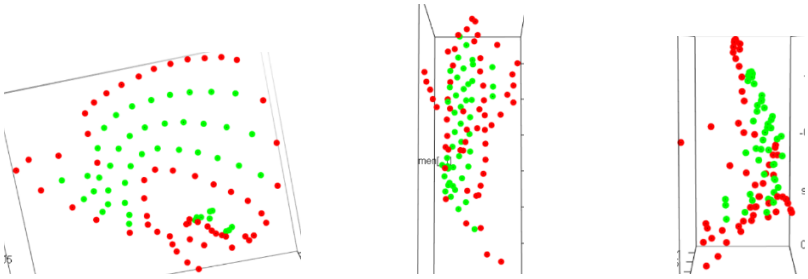

(B)

Figure 7.12 The fourth PCA of the temporal bones: The shapes at the two ends of PC 1
(A) The shape at the negative end. (B) The shape at the positive end. From left to right: lateral view, anterior view, and inferior view. The graphs are generated by the Geomorph R package (Adams et al., 2018).

For the maximum-specimen dataset that excludes the mastoid process, PC 1, which explains 22.986% of the total variance, primarily separates Petralona 1 from all others (Table 7.4 and Figure 7.11). In a specimen plotted closer to Petralona, semilandmarks at the anterosuperiorly corner of the squamosal portion lie more posterosuperiorly. Semilandmarks at the infratemporal region lie more posteroinferiorly (Figure 7.12). The parietal notch lies more anteroinferiorly. Therefore, the squamosal portion becomes taller superoinferiorly anteriorly at its anterior portion and shorter anteroposteriorly overall. There is a superoinferiorly long vertical component of the squamosal suture that bounds the parietal notch anteriorly. Moreover, the mastoid portion becomes anteroposteriorly longer.

The tympanic plate becomes less inferiorly projecting. Additionally, the vaginal process becomes more inferiorly projecting. The mediolateral axis of the mandibular fossa becomes less obliquely oriented as its medial end lies more anteriorly. The roof of the fossa becomes shorter anteroposteriorly. The mandibular fossa also lies slightly more anteriorly.

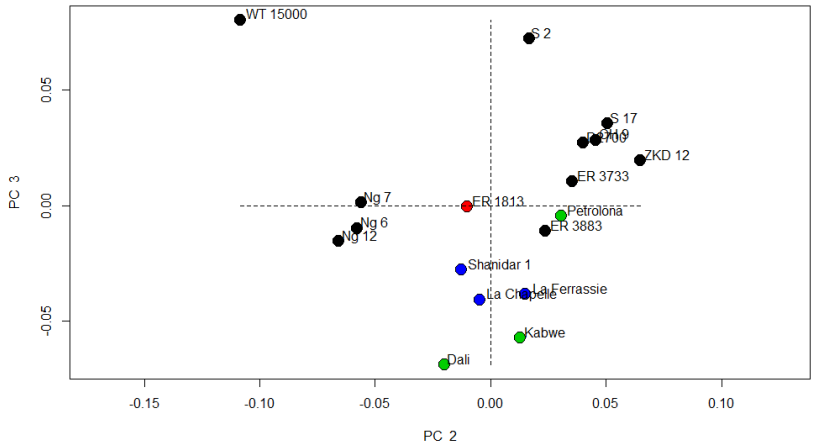

Figure 7.13 The fourth PCA of the temporal bones: The plot of PC 2 and PC 3
The black dots: The *H. erectus s. l.* specimens. The red dot: The *H. habilis* specimen. The green dots: The Mid-Pleistocene *Homo* specimens. The blue dots: the Neanderthal specimens.

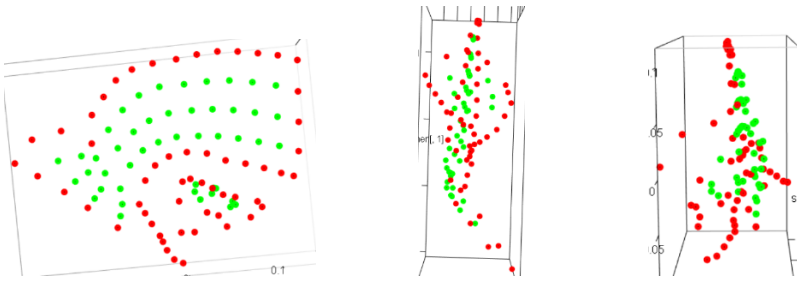

(A)

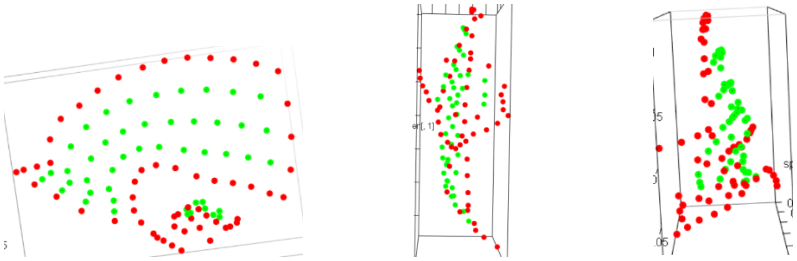

(B)

Figure 7.14 The fourth PCA of the temporal bones: The shapes at the two ends of PC 2
(A) The shape at the negative end. (B) The shape at the positive end. From left to right: lateral view, anterior view, and inferior view.

PC 2, which explains 16.461% of the total variance, is consistent overall with PC 1 from the first analysis of the maximum-semilandmark dataset (Table 7.4 and Figure 7.13). This PC also plots KNM-WT 15000 at one end (Figure 7.13). The newly added Ng 6 groups tightly with Ng 7 and Ng 12 near the KNM-WT 15000. OH 9 groups with other *H. erectus* in the positive side of PC 2. ZKD 12 lies at the end opposite to KNM-WT 15000 and near S 17. Neanderthals and mid-Pleistocene specimens are placed across the origin. This PC describes shape differences similar to those described by PC 1 in the first analysis of the maximum-semilandmark set (Figure 7.14). For example, in a specimen closer to KNM-WT 15000, the mastoid portion increases in size relative to the squamosal portion, which decreases in size. The mandibular fossa becomes deeper superoinferiorly, and its posterior wall more vertically oriented.

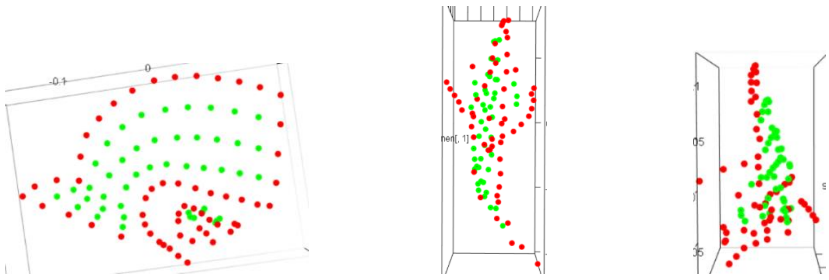

(A)

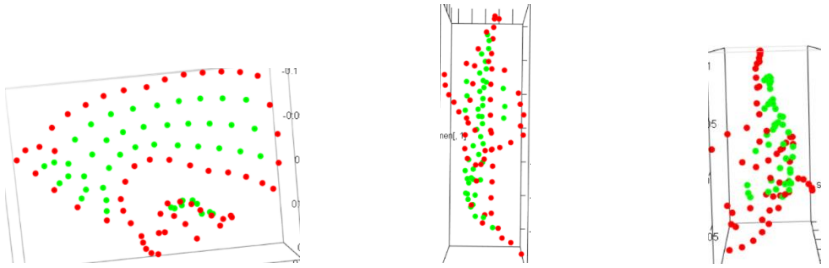

(B)

Figure 7.15 The fourth PCA of the temporal region: The shapes at the two ends of PC 3
(A) The shape at the negative end. (B) The shape at the positive end. From left to right: lateral view, anterior view, and inferior view. The graphs are generated by the Geomorph R package (Adams et al., 2018).

PC 3, which explains 12.171% of the total variance, is similar to PC 2 from the first analysis based on the maximum-semilandmark dataset (Table 7.4 and Figure 7.13). This PC places KNM-WT 15000 and S 2 at the end opposite to Kabwe 1 and the Dali skull. S 17, OH 9, D2700, ZKD 12, and KNM-ER 3733 are closer to KNM-WT 15000 (Figure 7.13). The three Ngandong specimens, KNM-ER 3883, KNM-ER 1813, and Petralona 1 are placed across the origin. They are not clearly separated from other mid-Pleistocene specimens and Neanderthals, which have slightly more negative scores. This PC shows patterns of shape differences similar to those shown by PC 2 in the first analysis (Figure 7.15). For example, moving toward the positive end (KNM-WT 15000 and S 2), the squamosal portion becomes longer anteroposteriorly and shorter superoinferiorly, while the mastoid portion becomes shorter anteroposteriorly and taller superoinferiorly. The mandibular fossa becomes anteroposteriorly longer and its lateral profile more widely V-shaped. Its mediolateral axis becomes more obliquely oriented.

7.2.2 The fifth PCA: A large sample *H. sapiens* and the fossil sample

Table 7.5 The fifth PCA of the overall cranium: The percentage variance explained by the first seven PCs

	Percentage of Variance	Cumulative Percentage
PC 1	26.660%	26.660%
PC 2	16.438%	43.098%
PC 3	8.948%	52.046%
PC 4	5.998%	58.044%
PC 5	5.295%	63.339%
PC 6	4.402%	67.741%
PC 7	3.579%	71.500%

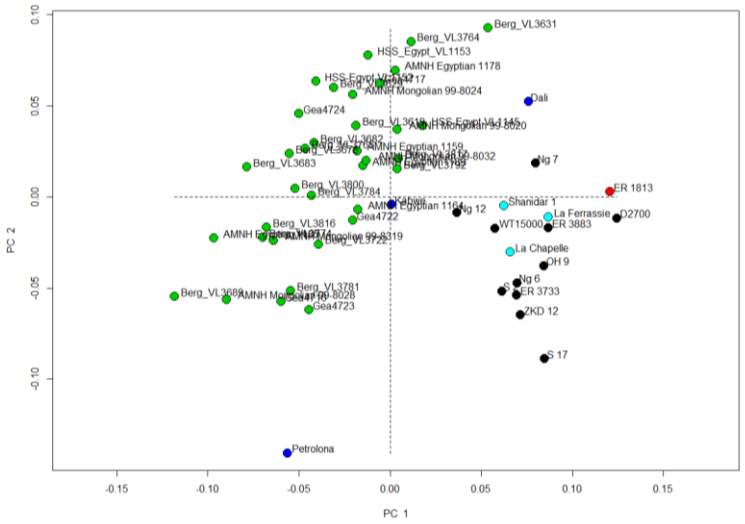

Figure 7.16 The fifth PCA of the temporal region: The plot of PC 1 and PC 2
The black dots: The *H. erectus s. l.* specimens. The red dot: The *H. habilis* specimen. The dark blue dots: The Mid-Pleistocene *Homo* specimens. The light blue dots: the Neanderthal specimens. The green dots: The *H. sapiens* specimens. The graphs are generated by the Geomorph R package (Adams et al., 2018).

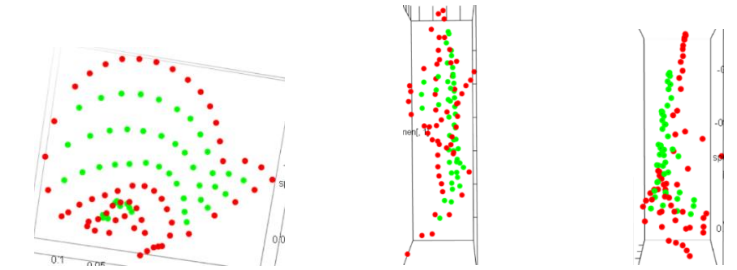

(A)

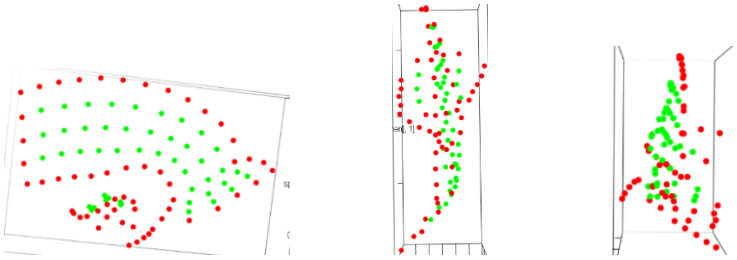

(B)

Figure 7.17 The fifth PCA of the temporal region: The shapes at the two ends of PC 1
(A) The shape at the negative end. (B) The shape at the positive end. From left to right: lateral view, anterior view, and inferior view. The graphs are generated by the Geomorph R package (Adams et al., 2018).

Upon adding the large *H. sapiens* sample, PC 1 is similar overall to PC 1 from the second analysis based on the maximum-semilandmark dataset. The newly added Petralona 1 specimen falls well within the *H. sapiens* cluster (Table 7.5 and Figure 7.16). Similarly, PC 1 shows that from the negative end to the positive end, the temporal region generally becomes shorter superoinferiorly and longer anteroposteriorly, the distance between the auricular region and the mandibular fossa increases, and the mandibular fossa becomes wider mediolaterally and flares more laterally from the cranial base (Figure 7.17).

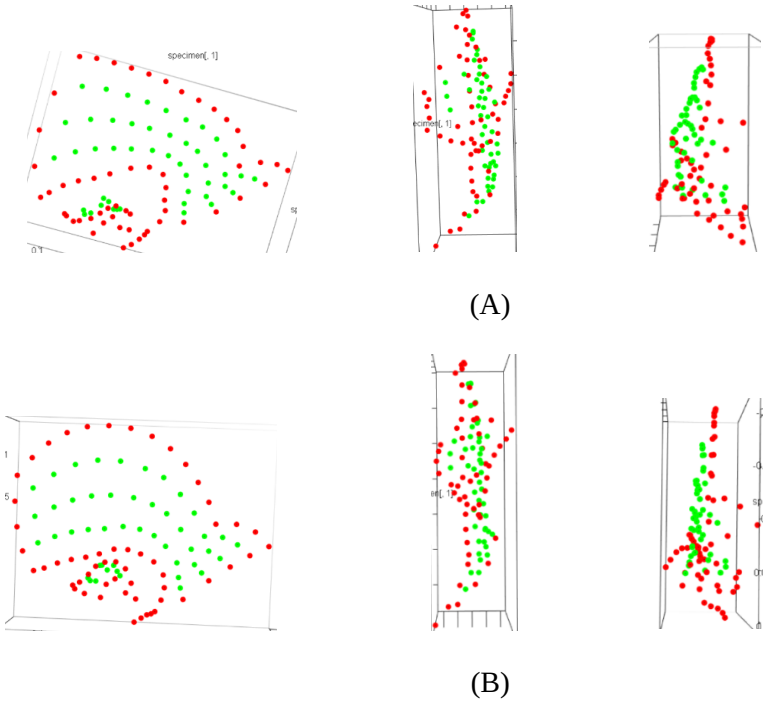

Figure 7.18 The fifth PCA of the temporal region: The shapes at the two ends of PC 2
(A) The shape at the negative end. (B) The shape at the positive end. From left to right: lateral view, anterior view, and inferior view. The graphs are generated by the Geomorph R package (Adams et al., 2018).

PC 2, which explains 16.438% of the total variance, separates Petralona 1 from all other specimens. S 17 lies relatively close to Petralona 1 (Table 7.5 and Figure 7.16). The other fossils overlap with the *H. sapiens* cluster. ZKD 12, KNM-ER 3733, S 2, Ng 7, and OH 9 have more negative scores, while the others scatter across the origin. This PC reflects shape differences similar to those reflected by PC 1 in the first PCA based on the maximum-semilandmark dataset of fossils (Figure 7.18). In a specimen plotted closer to Petralona 1, the squamosal portion also becomes taller superoinferiorly at its anterior portion and shorter superoinferiorly at its posterior portion. The mandibular fossa increases in size and becomes shallower superoinferiorly.

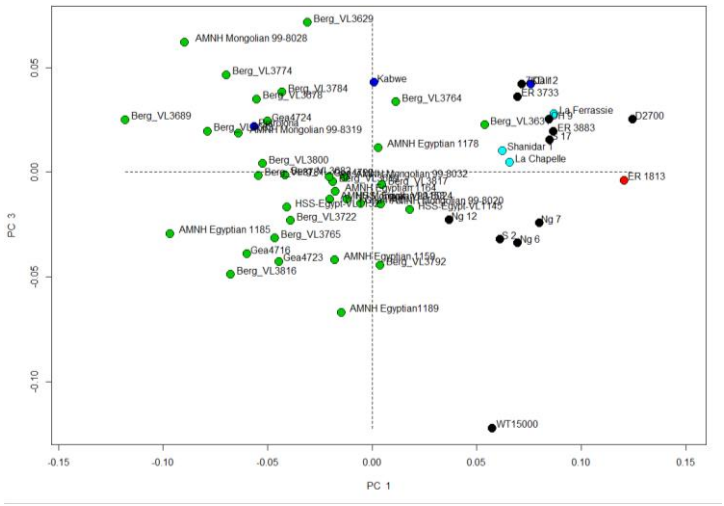

Figure 7.19 The fifth PCA of the temporal region: The plot of PC 1 and PC 3
The black dots: The *H. erectus s. l.* specimens. The red dot: The *H. habilis* specimen. The dark blue dots: The Mid-Pleistocene *Homo* specimens. The light blue dots: the Neanderthal specimens. The green dots: The *H. sapiens* specimens.

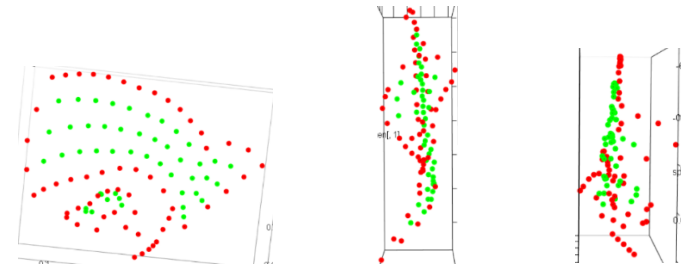

(A)

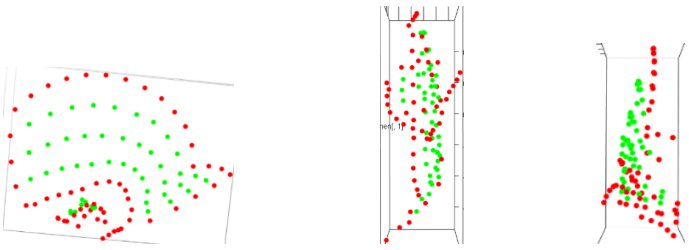

(B)

Figure 7.20 The fifth PCA of the temporal region: The shapes at the two ends of PC 3
(A) The shape at the negative end. (B) The shape at the positive end. From left to right: lateral view, anterior view, and inferior view. The graphs are generated by the Geomorph R package (Adams et al., 2018).

PC 3 resembles PC 2 from the fourth PCA by separating KNM-WT 15000 from others (Table 7.5 and Figure 7.19). Within the fossil sample, Ng 6, Ng 7, Ng 12, and S 17 are grouped together on the negative side. The other specimens are placed at the positive half of this PC. In a specimen closer to KNM-WT 15000, this PC also shows that the mastoid part increases in size, while the squamosal part becomes shorter superoinferiorly (Figure 7.20). The mandibular fossa becomes longer anteroposteriorly. In lateral view, the lateral profile of the fossa becomes more deeply widely V-shaped. PC 3 is also significantly correlated with size. This is probably because the small sized KNM-WT 15000 is well separated from *H. sapiens*.

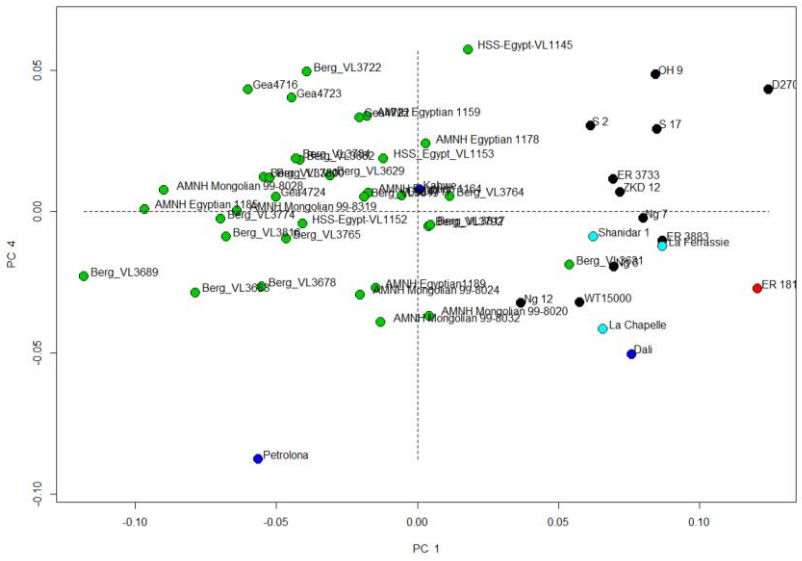

Figure 7.21 The fifth PCA of the temporal region: The plot of PC 1 and PC 4
The black dots: The *H. erectus s. l.* specimens. The red dot: The *H. habilis* specimen. The dark blue dots: The Mid-Pleistocene *Homo* specimens. The light blue dots: the Neanderthal specimens. The green dots: The *H. sapiens* specimens. The graphs are generated by the Geomorph R package (Adams et al., 2018).

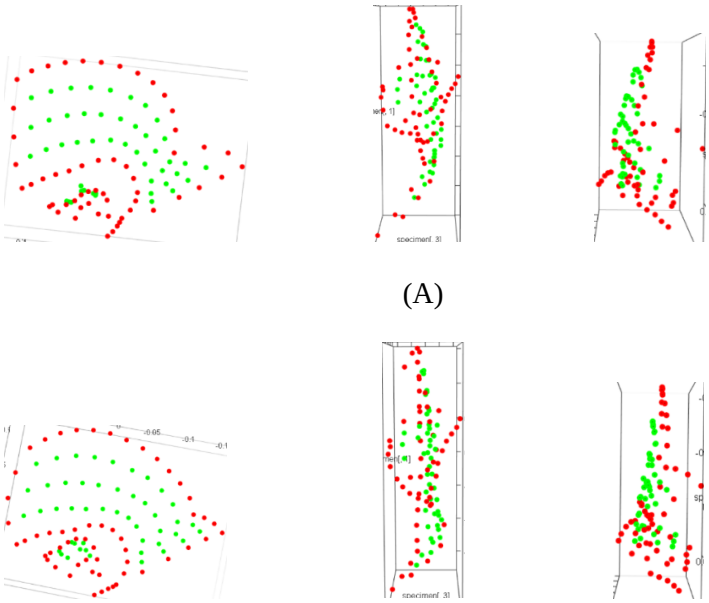

Figure 7.22 The fifth PCA of the temporal region: The shapes at the two ends of PC 4
(A) The shape at the negative end. (B) The shape at the positive end. From left to right: lateral view, anterior view, and inferior view. The graphs are generated by the Geomorph R package (Adams et al., 2018).

PC 4, which explains 5.998% of the total variance, also separates Petralona 1 from the others (Table 7.5 and Figure 7.21). Among the fossils, the Ngandong specimens and KNM-WT 15000 have negative scores, overlapping with KNM-ER 1813, the Dali skull, and Neanderthals. Kabwe 1 and the other *H. erectus* all have positive scores. The specimen at the end opposite to Petralona 1 is OH 9. In a specimen closer to Petralona 1, the parietal notch lies more anteroinferiorly, such that the parietomastoid suture becomes longer anteroposteriorly (Figure 7.22). The auricular region lies more posterosuperiorly. The mandibular fossa becomes wider mediolaterally. Its mediolateral axis becomes more transversely oriented as its lateral margin lies more posteriorly and becomes shorter anteroposteriorly. The tympanic plate also becomes less obliquely oriented. The lateral profile of the fossa becomes more narrowly V-shaped. The anterior wall of the fossa becomes more concave. The auditory meatus decreases in size.

7.2.3 The sixth PCA: A small *H. sapiens* sample with fossil specimens

Table 7.6 The sixth PCA of the overall cranium: The percentage variance explained by the first seven PCs

	Percentage of Variance	Cumulative Percentage
PC 1	25.022%	25.022%
PC 2	15.399%	40.421%
PC 3	10.732%	51.153%
PC 4	8.333%	59.478%
PC 5	6.947%	66.433%
PC 6	4.928%	71.361%
PC 7	4.345%	75.706%

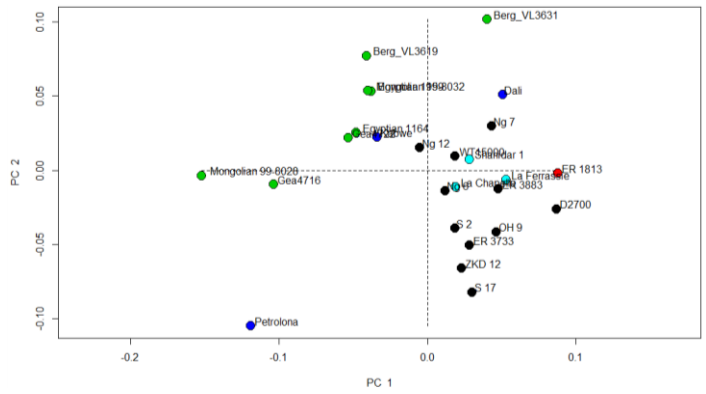

(A)

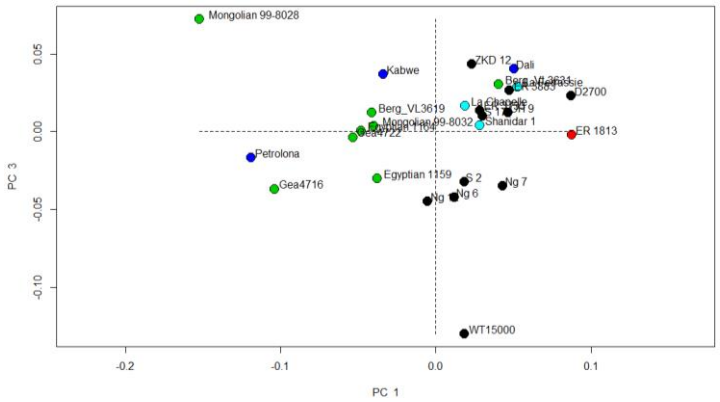

(B)

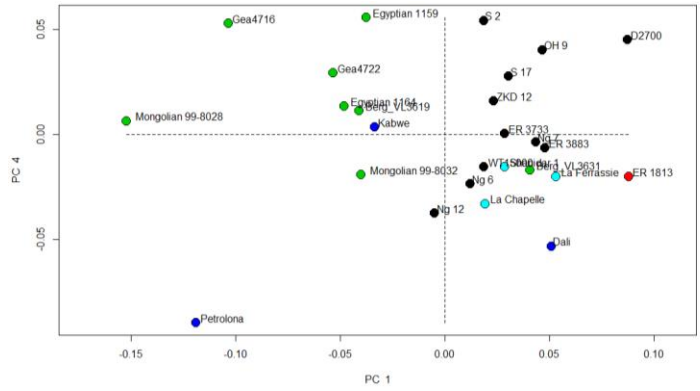

(C)

Figure 7.23 The plots of the fourth PCA of the overall cranium

The red dots: The *H. erectus s. l.* specimens. The black dot: The *H. habilis* specimen. The green dots: The Mid-Pleistocene *Homo* specimens. The blue dots: the Neanderthal specimens. (A) PC 1and PC 2. (B) PC 1 and PC 3. (C) PC 1 and PC 4.

After reducing the sample size of *H. sapiens* to eight, none of the first seven PCs are significantly correlated with size (Table B.23). The first four PCs are similar to corresponding PCs in the fifth PCA of the temporal bones (Table 7.6, Figure 7.23; also see Appendix B 3.1.6).

PC 1 continues to separate the majority of the fossils from the *H. sapiens* sample based on differences in the overall superoinferior height of the temporal bone. As the sample size of *H. sapiens* decreases, Petralona 1 even falls near the negative end of the *H. sapiens* cluster. PC 2 also separates Petralona 1 from other fossils and *H. sapiens*. However, the separation between them is less obvious than PC 2 in the fifth PCA of the temporal bones, as specimens such as S2, ZKD 12, ER 3733, OH 9, and S 17 are fairly close to Petralona 1. PC 3 shows clear separation between KNM-WT 15000 and all the other specimens. The three Ngandong specimens and S 17 again form a tight cluster intermediate between KNM-WT 15000 and other fossils. PC 4 also separates Petralona 1 from others because of similar shape differences. S 2 and D2700 lie in more positive positions than OH 9.

7.3 BOOTSTRAP ANALYSIS OF OVERALL VARIABILITY

7.3.1 Sum of squared pairwise distances

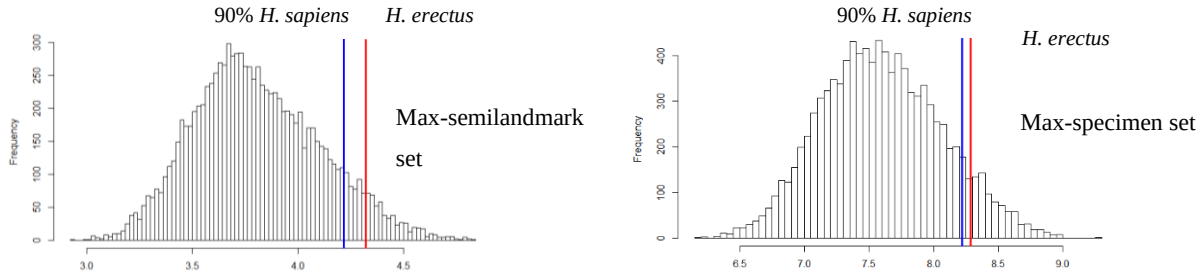

(A) *H. erectus s. l.* vs. *H. sapiens*

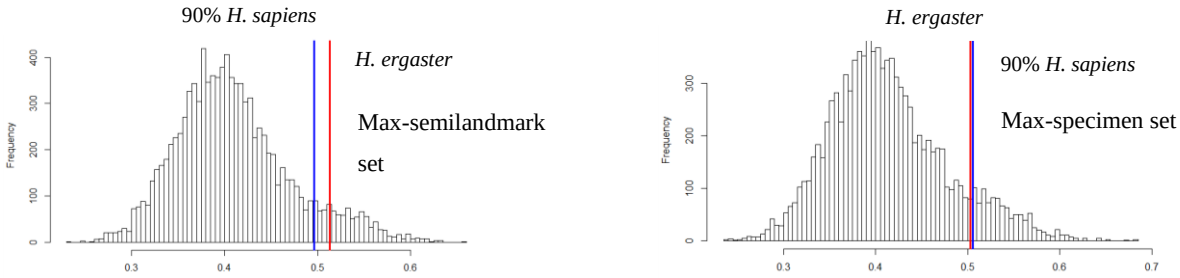

(B) *H. ergaster* (no D2700) vs. *H. sapiens*

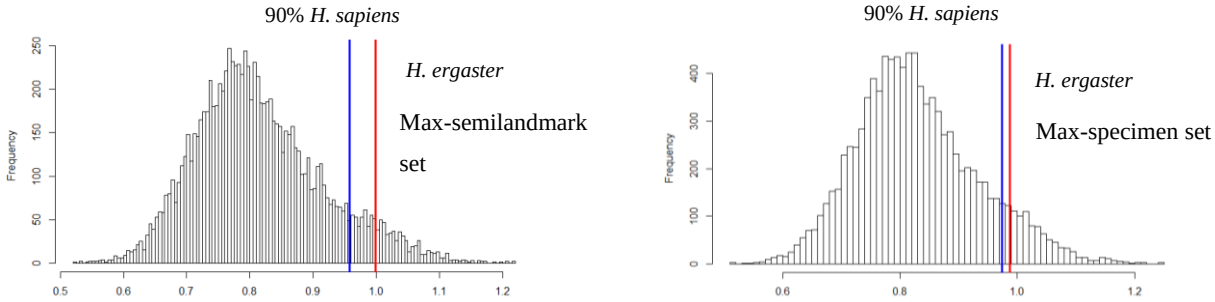

(C) *H. ergaster* (with D2700) vs. *H. sapiens*

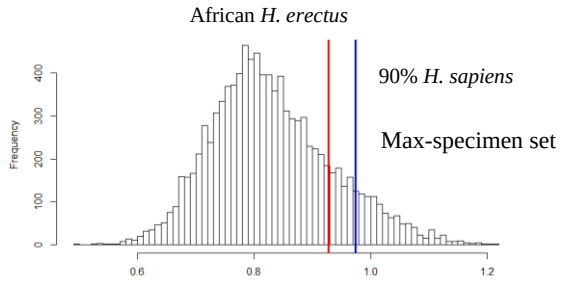

(D) African *H. erectus* (with OH 9) vs. *H. sapiens*

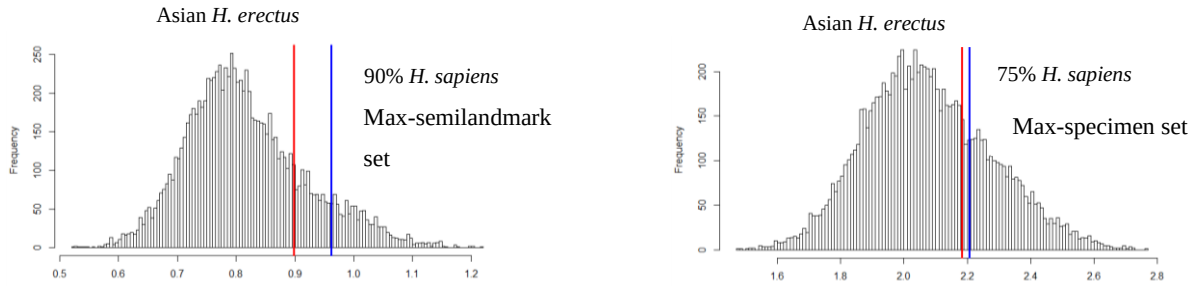

(E) Asian *H. erectus* vs. *H. sapiens*

Figure 7.24 The bootstrapped analyses of SSDs of the temporal

The histograms show the distributions of 10,000 bootstrapped SSDs for the *H. sapiens* samples based on the maximum-semilandmark set (left) and the maximum-specimen set (right). The red lines indicate the SSDs of the *H. erectus s. l.* (A), *H. ergaster* (without D2700) (B), *H. ergaster* (with D2700) (C), African *H. erectus* (D) and Asian *H. erectus* (E) samples. In (A) to (D), the the blue line indicates the 90th percentile of the *H. sapiens* SSDs. In (E), the blue line indicates the 90th percentiles of the *H. sapiens* SSDs in the left graph and the 75th percentile in the right graph.

For the temporal region, the SSDs of the *H. erectus s. l.* sample and its subsets increase dramatically compared to those achieved from datasets of the overall and posterior crania when using the bootstrapped SSDs of the *H. sapiens* samples as a yardstick (Figure 7.24 and Table B.24). For the maximum-semilandmark dataset, the SSD of the *H. erectus s. l.* sample is significantly greater than those of the *H. sapiens* sample as it exceeds 9,449 (94.49%) bootstrapped *H. sapiens* SSDs. The SSD of the African *H. ergaster* (KNM-ER 3733, KNM-ER 3883, and KNM-WT 15000) also exceed the 90th percentile of the *H. sapiens* SSDs as it is larger than 9,297 (92.97%) *H. sapiens* distances. After adding D2700 to *H. ergaster*, its SSD is still larger than 9,148 (91.48%) *H. sapiens* SSDs. The SSD of the four Asian *H. erectus* is relatively smaller, but still exceeds 7,996 (79.96%) of the bootstrapped *H. sapiens* SSDs.

The results based on the maximum-specimen dataset are generally similar (Figure 7.24 and Table B.24). The SSDs of the *H. erectus s. l.*, African *H. ergaster*, and *H. ergaster* plus D2700 samples exceed 9,203 (92.03%), 8,950 (89.50%), 9,148 (91.48%) of the *H. sapiens* SSDs, respectively. The SSD of the African *H. erectus* sample, which includes OH 9 and the African *H. ergaster* specimens, is greater than 8,214 (82.14%) of the *H. sapiens* SSDs. The SSD of the expanded Asian *H. erectus* sample falls below the 75th percentile of the *H. sapiens* distances as it only exceeds 7,177 (71.77%) of the *H. sapiens* SSDs.

7.3.2 Mean pairwise Procrustes distances

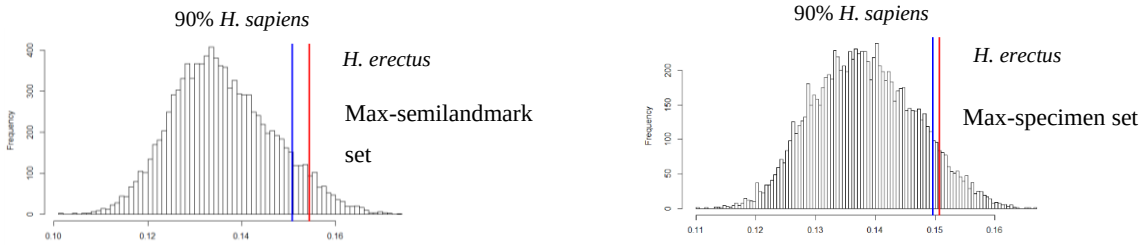

(A) *H. erectus s. l.* vs. *H. sapiens*

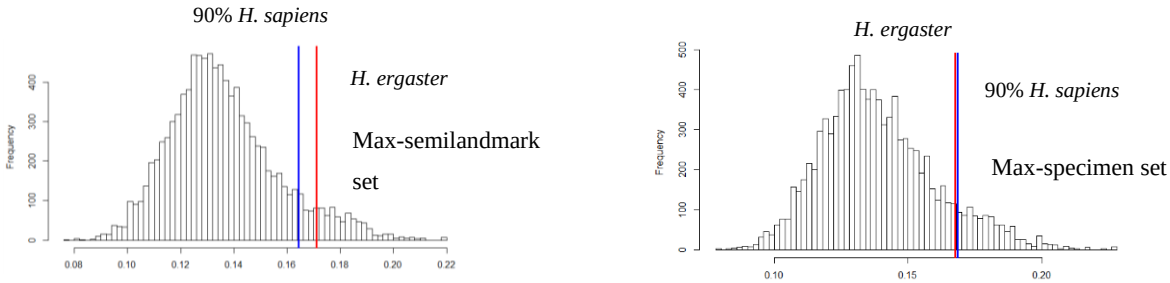

(B) *H ergaster* (no D2700) vs. *H. sapiens*

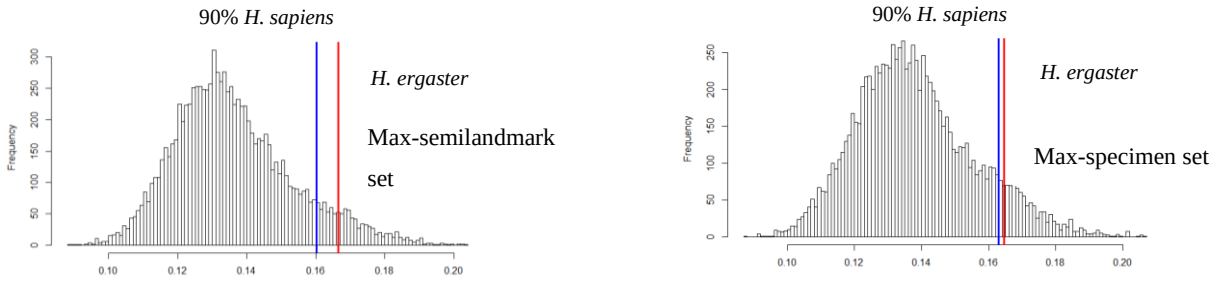

(C) *H. ergaster* (with D2700) vs. *H. sapiens*

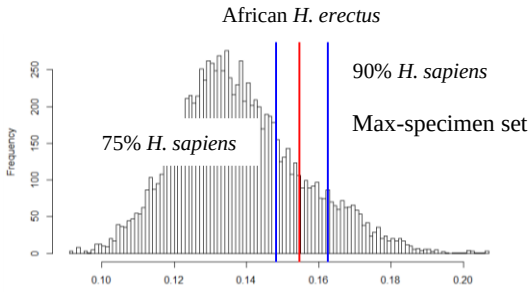

(D) African *H. erectus* vs. *H. sapiens*

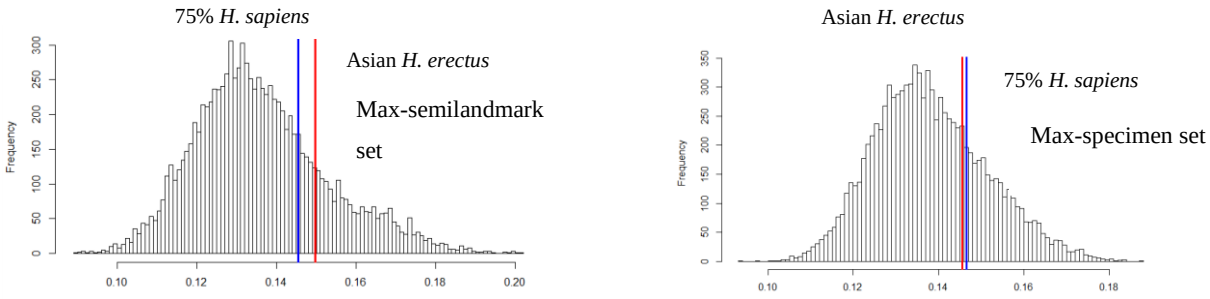

(E) Asian *H. erectus* vs. *H. sapiens*

Figure 7.25 The bootstrapped analyses of mean pairwise distances of the temporal region
The histograms show the distributions of 10,000 bootstrapped SSDs for the *H. sapiens* samples based on the maximum-semilandmark set (left) and the maximum-specimen set (right). The red lines indicate the SSDs of the *H. erectus s. l.* (A), *H. ergaster* (without D2700) (B), *H. ergaster* (with D2700) (C), African *H. erectus* (D) and Asian *H. erectus* (E) samples. In (A) to (C), the the blue line indicates the 90th percentile of the *H. sapiens* SSDs. In (D), the left blue line indicates the 75th percentiles of the *H. sapiens* SSDs; the right blue line indicates the 90th percentile of the *H. sapiens* SSDs. In (E), the blue line indicates the 75th percentiles of the *H. sapiens* SSDs.

Results of the mean pairwise distances of the *H. erectus s. l.* and its subsets are overall similar to the analyses of SSDs (Figure 7.25 and Table B.25). For the maximum-semilandmark set, the mean distances of the *H. erectus s. l.*, African *H. ergaster*, *H. ergaster* plus D2700 samples exceed 9,436 (94.36%), 9,295 (92.95%), and 9,366 (93.66%) of the *H. sapiens* cases, respectively (Figure 7.25 and Appendix). Again, the mean pairwise distance of the Asian *H. erectus* sample is relatively smaller as it exceeds 8,092 (80.92%) of the bootstrapped distances of the *H. sapiens* sample.

Based on the maximum specimen dataset, the results are also similar (Figure 7.25 and Table B.25). The mean pairwise distances of the *H. erectus s. l.*, African *H. ergaster*, *H. ergaster* (with D2700) samples exceed 9,206 (92.06%), 9,295 (89.56%), and 9,206 (92.06%) of the *H. sapiens* distances respectively. The mean pairwise distance of African *H. erectus* including OH 9, is greater than 8,308 (83.08%) of *H. sapiens* mean pairwise distances. The mean distance of the Asian *H. erectus* sample falls slightly below the 75th percentile of bootstrapped *H. sapiens* mean pairwise distances as it exceeds 7,282 (72.82%) of the *H. sapiens* cases.

7.4 INDIVIDUAL PAIRWISE DISTANCES

7.4.1 The maximum-semilandmark set

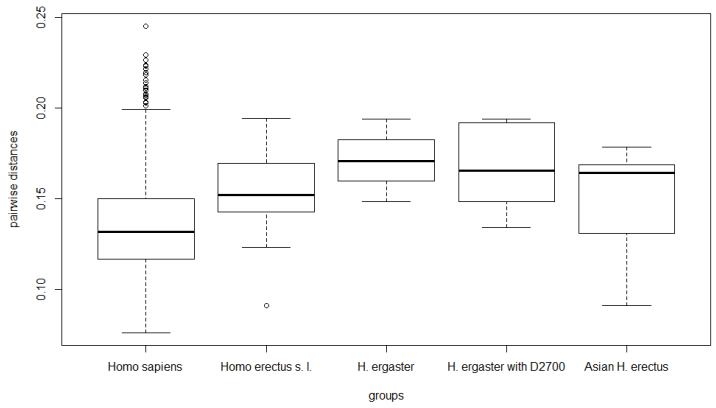

Figure 7.26 The boxplot of pairwise distances (the maximum-semilandmark set of the overall cranium)

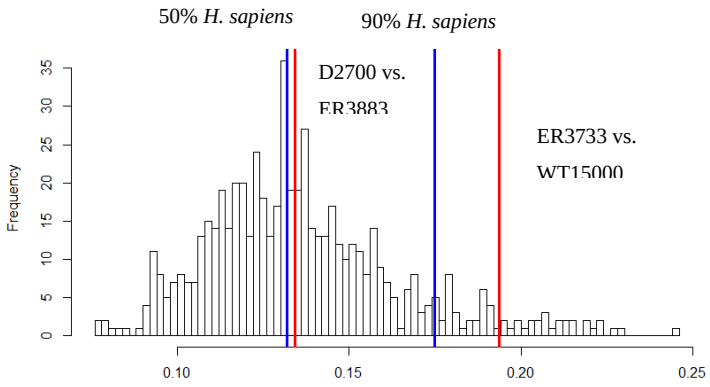

(A)

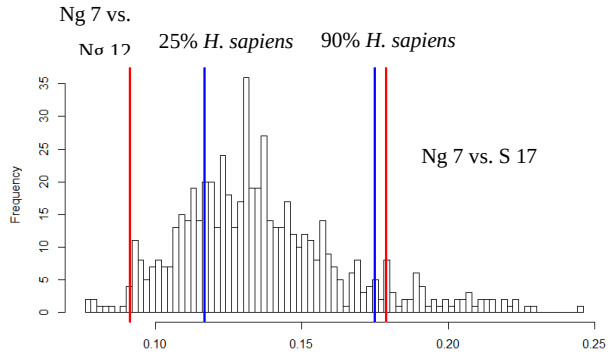

(B)

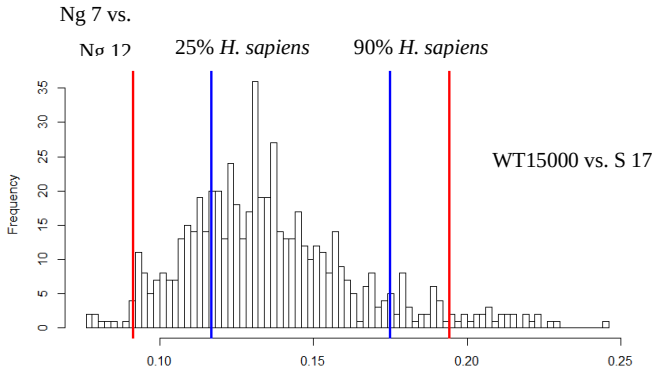

(C)

Figure 7.27 Individual pairwise distances (the maximum-semilandmark set of the temporal region)
The histogram shows the distribution of all pairwise distances within the *H. sapiens* sample. From left to right, the blue lines indicate the 50th and 90th percentiles of the *H. sapiens* pairwise distances in (A), 25th and 90th percentiles in (B) and (C). In (A), the left red line represents the distance between D2700 and ER 3883, which is the smallest *H. ergaster* distance. The right red line represents the distance between WT 15000 and ER3733, which is the largest *H. ergaster* distance. In (B), the left red line represents the distance between Ng 7 and Ng 12, which is the smallest *H. erectus* distance. The right red line represents the distance between Ng 7 and S 17, which is the largest Asian *H. erectus* distance. In (C), the left red line represents the distance between Ng 7 and Ng 12, while the right red line represents the distance between WT 15000 and S 17, which is the largest *H. erectus* distance.

Table 7.7 Distribution of pairwise distances in the *H. sapiens* and *H. erectus* samples based on the maximum-semilandmark set of the overall cranium

	Mean distance	Min	25th percentile	50th percentile	75th percentile	90th percentile	Max
H. sapiens	0.136	0.0762	0.117	0.132	0.150	0.175	0.245
H. erectus s. l.	0.154	0.0913	0.143	0.152	0.169	0.183	0.194

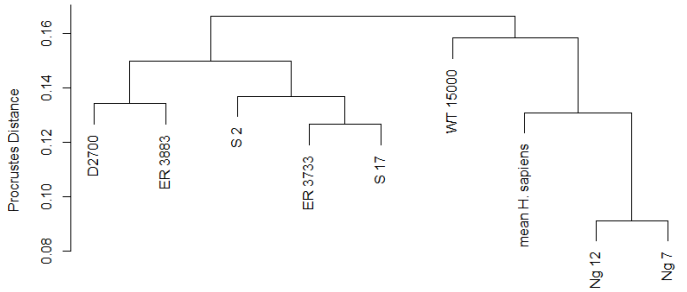

Figure 7.28 The UPGMA dendrogram of the *H. erectus* specimens and the mean shape of *H. sapiens* based on the maximum-specimen set

Most pairwise distances within *H. erectus s. l.* and its subsets exceed the 50th percentile of the *H. sapiens* distances, except for ones between ER 3883 and Ng 7 and between Ng 7 and Ng 12 (Table 7.7, Table 7.8, Figure 7.26). Moreover, the pairwise distances of the *H. erectus s. l.* sample and its subsets are also quite variable compared to those obtained with the landmark sets that cover the overall and posterior calvaria.

The three pairwise distances within the African *H. ergaster* sample fall at, or exceed the 75th percentile of the *H. sapiens* distances (Table 7.8 and Figure 7.26). The smallest distance, which is between KNM-ER 3733 and KNM-ER 3883, is only slightly lower than the 75th percentile of the *H. sapiens* distances. After adding D2700, the lower whisker falls below the 75th percentile of the *H. sapiens* box because the distance between D2700 and ER 3883 only slightly exceeds the median of the *H. sapiens* distances (Table 7.8, Figure 7.26 and Figure 7.27). The additional pairwise distances are all well above the 75th percentile of the *H. sapiens* distribution of distances. KNM-WT 15000 is separated from most fossils. The distances between KNM-WT 15000 and the other *H. ergaster* specimens exceed or fall slightly below the 90th percentile of the *H. sapiens* distances (Table 7.8 and Figure 7.27A).

Table 7.8 Individual pairwise distances of the *H. erectus* sample based on the maximum-semilandmark set of the temporal region

(A) The pairwise distance that is smaller than the 25th percentile of the *H. sapiens* distances; (B) The pairwise distances that exceed the 75th percentiles of the *H. sapiens* distances. (C) The pairwise distances that exceed the 90th percentiles of the *H. sapiens* distances.

(A)

	Ng 7 vs. Ng 12 (minimum)
Pairwise distance	0.09

(B)

	D2700 vs. ER 3733	D2700 vs. Ng 7	ER 3733 vs. Ng 7	ER 3883 vs. S 17	ER 3883 vs. S 2	ER 3883 vs. WT 15000
Pairwise distance	0.160	0.153	0.164	0.152	0. 154	0. 171

	Ng 12 vs. S 17	Ng 12 vs. S 2	Ng 7 vs. S 2	WT 15000 vs. S 2
Pairwise distance	0.164	0.164	0.169	0.170

(C)

	WT 15000 vs. S 17 (maximum)	D2700 vs. Ng 12	D2700 vs. WT 15000	Ng 7 vs. S 17	ER 3733 vs. WT 15000
Pairwise distance	0.194	0.175	0.192	0.179	0.194

The Asian sample shows a broader distribution of pairwise distances (Figure 7.26 and 7.27). The main reason is that the Ng 7 and Ng 12 are not only very close to each other, they also are well separated from either S 2 or S 17. In fact, the distance between Ng 7 and Ng 12 is the only one that falls below the 25th percentile of the *H. sapiens* distances. Furthermore, the pairwise distances between the Ngandong specimens and the two Sangiran specimens exceed the 85th percentile of the *H. sapiens* distances. However, the distance between S 2 and S 17 is relatively short, exceeding only the 50th percentile of the *H. sapiens* pairwise distances.

When pooling Asian and African *H. erectus*, the pairwise distances become more variable (Figure 7.26 and Figure 7.27). WT 15000 is especially different from the two Sangiran specimens. The distance between KNM-WT 15000 and S 17 is the longest pairwise distance in the *H. erectus s. l.* sample, and comparable to the distance between KNM-WT 15000 and KNM-ER 3733 (Table 7.8, Figure 7.26 and Figure 7.27). The two Ngandong specimens are also quite different from the other specimens, especially D2700 and ER 3733. The distances between the two Ngandong specimens and D2700 and between KNM-ER 3733 and Ng 7 exceed the 75th percentile of *H. sapiens*, while that between KNM-ER 3733 and Ng 12 is only slightly less than this value. KNM-ER 3883 is well separated from the Sangiran specimens as the distances between them exceed the 75th percentile of the *H. sapiens* distances.

Overall, the Ngandong specimens remain distant from the others and very close to each other. This explains why the SSDs and mean pairwise distances of the Asian *H. erectus* sample in the maximum-semilandmark and maximum-specimen datasets fall below the 75th percentile of the *H. sapiens* distances. KNM-WT 15000 is also very different from the majority of the other fossil specimens. For the other specimens, it is difficult to sort out patterns of clustering based on pairwise distances. With a few exceptions, these specimens are consistently distant from each other.

These patterns of distances are captured overall by the unweighted pair group method with arithmetic mean (UPGMA) dendrogram (Figure 7.28). KNM-WT 15000 is placed in the Ngandong. Interestingly, the mean shape of the *H. sapiens* sample is even to that of the mean Ngandong specimens than KNM-WT 15000 is. All the other specimens constitute another cluster. However, it should be noted that the distances among them are all quite great if using the Ngandong specimens as a yardstick.

7.4.2 The maximum-specimen set

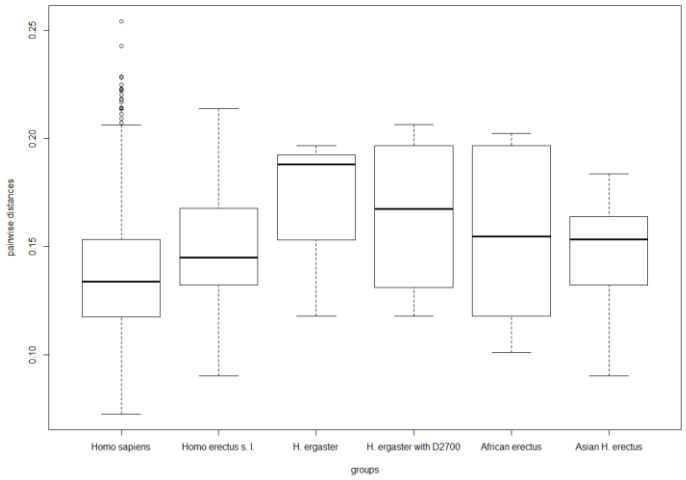

Figure 7.29 The boxplot of pairwise distances based on the maximum-specimen set of the temporal region

The boxplot based on the maximum-specimen dataset shows that the majority of pairwise distances in the *H. erectus s. l.* sample continue to exceed the median of the *H. sapiens* distances (Figure 7.29 and Table 7.9). However, the distances in the *H. erectus s. l.* sample and its subsets become widely separated (Figure 7.29). For the African *H. ergaster* sample, the smallest distance remains between KNM-ER 3733 and KNM-ER 3883, which is nearly the same as the 25th percentile of the *H. sapiens* pairwise distances (Figure 7.30A). The distances between KNM-WT 15000 and the two Koobi Fora, and that between D2700 and KNM-WT 15000 again exceed the 90th percentile of the *H. sapiens* distances (Table 7.10). However, D2700 is close to both KNM-ER 3733 and KNM-ER 3883, as the distances between them fall below the 75th percentile of the *H. sapiens* distances (Table 7.10).

The African *H. erectus* box shows even greater variability in pairwise distances (Figure 7.29 and Figure 7.30B). The distance between OH 9 and KNM-WT 15000 exceeds the 95th percentile of the *H. sapien*s pairwise distances (Figure 7.30B and Table 7.10). Nevertheless, the distances between OH 9 and the two Koobi Fora specimens fall around the 25th percentile of the *H. sapien*s distances, as does that between D2700 and OH 9 (Figure 7.30B and Table 7.10). These results confirm that KNM-WT 15000 is widely separated from the African and Dmanisi specimens in terms of Procrustes distances.

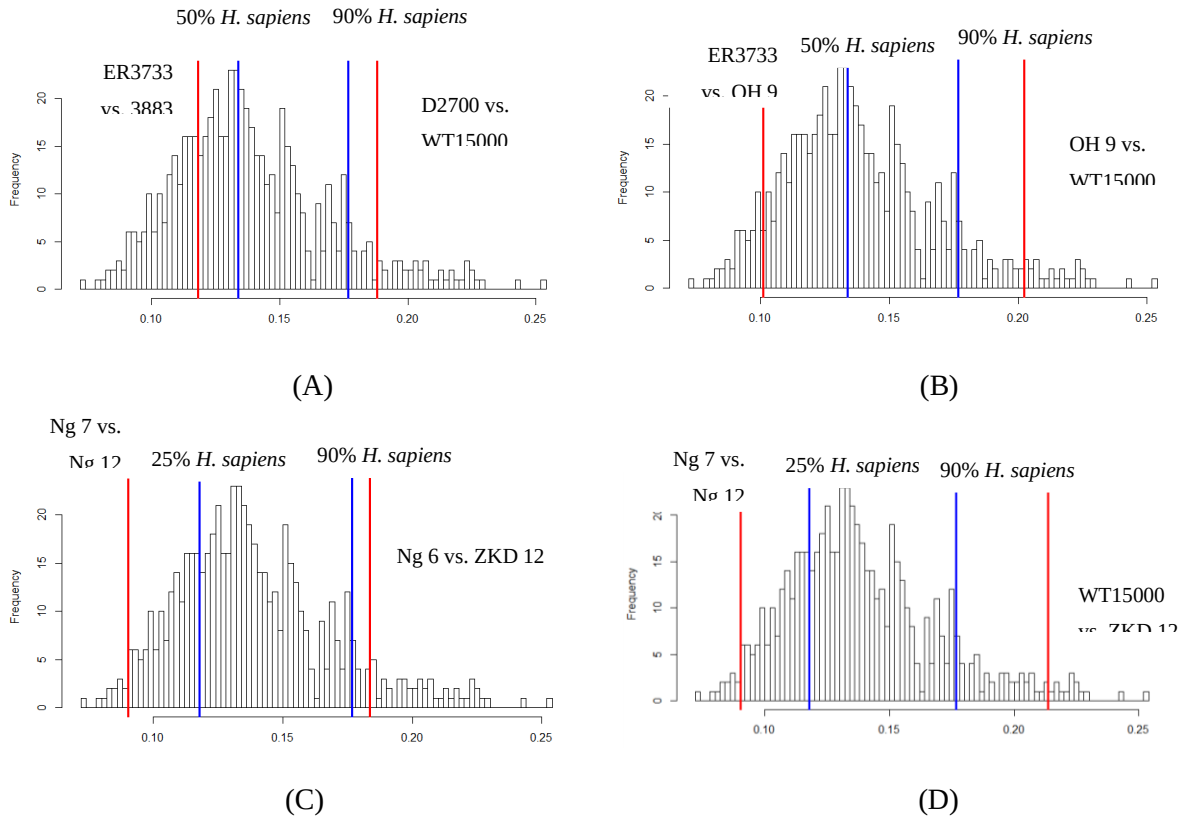

Figure 7.30 Individual pairwise distances (the maximum-specimen set of the temporal region)
The histogram shows the distribution of all pairwise distances within the *H. sapiens* sample. From left to right, the blue lines indicate the 50th and 90th percentiles of the *H. sapiens* pairwise distances in (A) and (B), 25th and 90th percentiles in (C) and (D). In (A), the left red line represents the distance between ER3733 and ER 3883, which is the smallest *H. ergaster* distance. The right red line represents the distance between WT 15000 and D2700, which is the largest *H. ergaster* distance. In (B), the left red line represents the distance between ER 3733 and OH 9, which is the smallest African *H. erectus* distance. The right red line represents the distance between WT 15000 and OH 9, which is the largest African *H. erectus* distance. In (C), the left red line represents the distance between Ng 7 and Ng 12, which is the smallest *H. erectus* distance. The right red line represents the distance between Ng 6 and ZKD 12, which is the largest Asian *H. erectus* distance. In (C), the left red line represents the distance between Ng 7 and Ng 12, while the right red line represents the distance between WT 15000 and ZKD 12, which is the largest *H. erectus* distance.

Table 7.9 Distribution of pairwise distances in the *H. sapiens* and *H. erectus* samples based on the maximum-specimen set of the temporal region

	Mean distance	Min	25th percentile	50th percentile	75th percentile	90th percentile	Max
H. sapiens	0.138	0.0728	0.118	0.134	0.154	0.176	0.254
H. erectus s. l.	0.151	0.0729	0.132	0.145	0.168	0.192	0.214

The Asian *H. erectus* sample shows a distribution of pairwise distances comparable to that of the *H. sapiens* sample (Figure 7.29, Figure 7.30 and Table 7.10). The distances between the Ng 6, Ng 7, and Ng 12 again constitute the lower extremity of the box of the Asian *H. erectus* sample because these distances all fall around the 25th percentile of the *H. sapiens* distances.

The distance between S 2 and S 17 is not exceptionally great as it falls near the median of the *H. sapiens* distances. S 2 and S 17 are also similarly distant from the Ngandong specimens. Excluding the distance between Ng 7 and S 2, which falls at approximately the 65th percentile of the *H. sapiens* distances, the pairwise distances between these groups either exceed or fall very slightly below the 75th percentile of the *H. sapiens* distances.

ZKD 12 is relatively close to the S 2 and S 17. The distance between ZKD 12 and S 2 falls slightly below the 50th percentile of the *H. sapiens* distances, while that between ZKD 12 and S 17 even falls below the 25th percentile of the *H. sapiens* distances. ZKD 12 is well separated from the three Ngandong specimens. The distances between them fall around the 90th percentile of the *H. sapiens* distances.

After pooling all *H. erectus s. l.* specimens, KNM-WT 15000 is consistently well separated from the Asian specimens (Figure 7.29, Figure 7.30 and Table 7.10). The distances between KNM-WT 15000 and the Sangiran specimens as well as ZKD 12 are either slightly smaller or larger than the 90th percentile of the *H. sapiens* distances. KNM-WT 15000 is somewhat closer to the Ngandong specimens, as the distances between them either exceed or fall slightly below the 75th percentile of the *H. sapiens* distances.

Table 7.10 Individual pairwise distances of the *H. erectus* sample based on the maximum-specimen set of the overall cranium

(A) The pairwise distances that is smaller than the 25th percentile of the *H. sapiens* distances; (B) The pairwise distances that fall between the 45th and 75th percentiles of the *H. sapiens* distances; (C) The pairwise distances that exceed the 75th percentile of the *H. sapiens* distances.

(A)

	Ng 7 vs. Ng 12 (minimum)	Ng 6 vs. Ng 12	D2700 vs. OH 9	ER 3733 vs. OH 9	S 17 vs. ZKD 12
Pairwise distance	0.0904	0.114	0.117	0.101	0.111

(B)

	D2700 vs. Ng 12	ER 3733 vs. Ng 6	ER 3883 vs. Ng 12	OH 9 vs. Ng 12	S2 vs. Ng 12	S 17 vs. Ng 12	WT 15000 vs. Ng 12
Pairwise distance	0.175	0.158	0.164	0.155	0.163	0.157	0.155

	ZKD 12 vs. Ng 12	OH 9 vs. Ng 6	S 17 vs. Ng 6	ZKD 12 vs. Ng 7	S 17 vs. WT 15000
Pairwise distance	0.172	0.176	0.173	0.165	0.170

(C)

	WT 15000 vs. ZKD 12 (maximum)	D2700 vs. Ng 6	D2700 vs. WT 15000	ER 3733 vs. WT 15000	ER 3883 vs. WT 15000	Ng 6 vs. WT 15000
Pairwise distance	0.214	0.193	0.206	0.197	0.188	0.191

	Ng 6 vs. ZKD 12	OH 9 vs. WT 15000	S 17 vs. WT 15000	ER 3733 vs. WT 15000
Pairwise distance	0.184	0.202	0.202	0.197

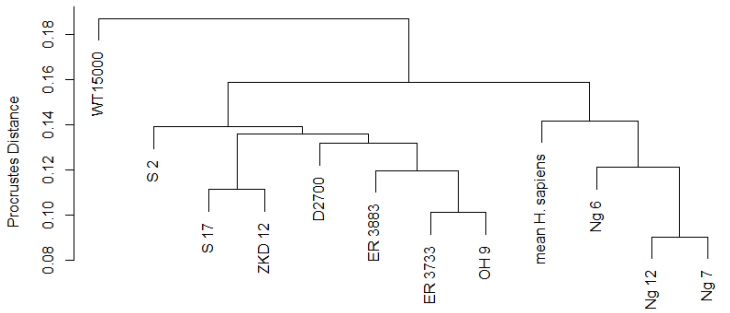

Figure 7.31 The UPGMA dendrogram of the *H. erectus* specimens and the mean shape of *H. sapiens* based on the maximum-specimen set

Patterns of pairwise distances between KNM-ER 3733, KNM-ER 3883, D2700 and OH 9 and Asian specimens are complicated. All of these distances well exceed the 50th percentile of the *H. sapiens* distances. In particular, the distances between Ng 7 and Euro-African specimens, between Ng 6 and D2700 and between Ng 6 and OH 9 exceed the 75th percentile of the *H. sapiens* distances. However, Ng 12 and the two Sangiran specimens are not particularly separated from these Euro-African specimens as their pairwise distances fall well below the 75th percentile of the *H. sapiens* distances.

Overall, similar to the pattern observed in the analysis based on the maximum-specimen dataset, KNM-WT 15000 is again well separated from the majority of the *H. erectus* specimens. The Ngandong specimens are also well separated from others. Overall, KNM-WT 15000 is somewhat closer to the Ngandong specimens than others. For the other specimens, it is difficult to sort out clear clustering. Their differences are generally insignificant if using the 75th percentile of the *H. sapiens* distances as a yardstick. In particular, ZKD 12 is very close to S 17, while OH 9 is very close to ER 3733, ER 3883, and D2700.

The UPGMA dendrogram reflects these patterns of pairwise distances (Figure 7.31). It shows that KNM-WT 15000 is well separated from others by placing it at its root. The Ngandong specimens also form a separate cluster that groups with the mean shape of the *H. sapiens* sample. All other specimens are placed in another cluster, within which OH 9, D2700, ER 3733, and ER 3883 constitute a subcluster. Another subcluster contains the three Asian specimens, within which ZKD 12 and S 17 are grouped together.

7.5 DIFFERENCES BETWEEN GROUP MEANS

7.5.1 Bootstrap analysis

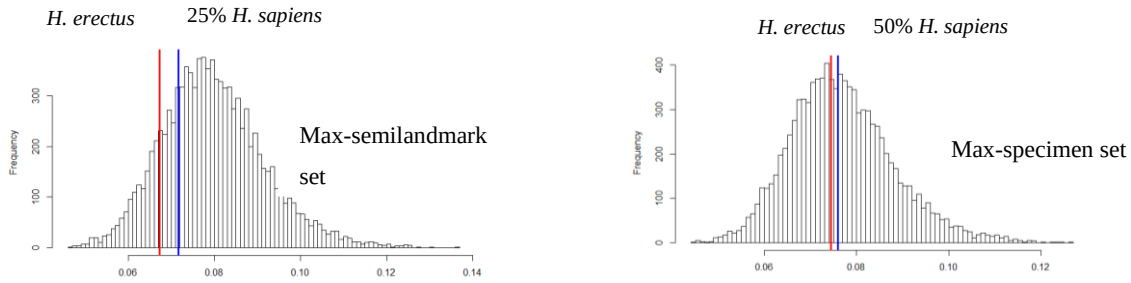

(A) *H. ergaster* (no D2700) vs. Asian *H. erectus*

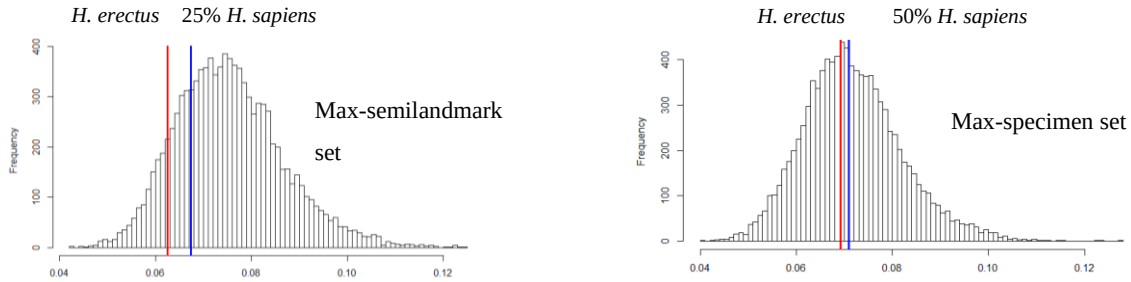

(B) *H. ergaster* (with D2700) vs. Asian *H. erectus*

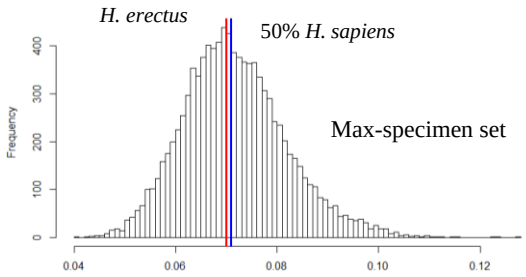

(C) African *H. erectus* (with OH 9) vs. Asian *H. erectus*

Figure 7.32 The bootstrap analyses of pairwise distances between the means of geographical subsets
In (A), (B) and (C), the left graph is based on the maximum-semilandmark set, while the right graph is based on the maximum-specimen landmark set. The blue line represents the 25th percentile of the 10,000 bootstrapped *H. sapiens* distances in each graph of the maximum-semilandmark set and 50th percentile in each graph of the maximum-specimen set. (A) The red line represents the distance between the means of *H. ergaster* (no D2700) and Asian *H. erectus*. (B) The red line represents the distance between the means of *H. ergaster* (with D2700) and Asian *H. erectus*. (C) The red line represents the distance between the means of African and Asian *H. erectus*.

Though the SSDs and mean pairwise distances within the *H. erectus* sample and its subsets are relatively large, differences between the mean shapes of the geographical subsets of *H. erectus* are all nonsignificant compared to the *H. sapiens* distances (Figure 7.32 and Table B.26). For the maximum-semilandmark set, the distance between the mean shapes of both African *H. ergaster* and Asian *H. erectus* samples and of the *H. ergaster* (with D2700) and Asian *H. erectus* samples fall well underneath the 25th percentile of the bootstrapped *H. sapiens* distances. The former exceeds only 1,379 (13.79%) bootstrapped distances of the *H. sapiens* sample, and the latter only 1,136 (11.36%) *H. sapiens* distances.

For the maximum specimen dataset, the distance between the mean shapes of the African *H. ergaster* and expanded Asian *H. erectus* samples falls just within the 50% confidence interval as it is larger than 4,576 (45.76%) *H. sapiens* distances. The distance between the means of the *H. ergaster* sample with D2700 and the Asian *H. erectus* sample exceeds 4,196 (41.96%) of *H. sapiens* cases. The distance between the African and Asian *H. erectus* mean shapes also exceeds 4,537 (45.37%) of the *H. sapiens* distances.

7.5.2 Procrustes ANOVA

Table 7.11 The Procrustes ANOVA of the *H. sapiens* geographical subsets (temporal region)
(A) The Procrustes ANOVA based on the maximum-semilandmark set. (B) The Procrustes ANOVA based on the maximum specimen set. For each analysis, 10,000 permutations were carried out.

(A)

	Degree of Freedom	Sum of Square	Mean square	R square (coefficient of determination)	F-value	P-value
Asian vs. African *Homo sapiens*	1	0.01899	0.01899	0.05786	2.0265	0.0205
Residuals	33	0.30916	0.009369	0.94214		
Total	34	0.32814				

(B)

	Degree of Freedom	Sum of Square	Mean square	R square (coefficient of determination)	F-value	P-value
Asian vs. African *Homo sapiens*	1	0.02000	0.0199976	0.05886	2.064	0.0275
Residuals	33	0.31937	0.0096888	0.94114		
Total	34	0.33973				

Table 7.12 The Procrustes ANOVA of the *H. erectus* geographical subsets (temporal region)
(A) *H. ergaster* (no D2700) vs. Asian *H. erectus* based on the maximum-semilandmark set. Ten permutations were carried out. (B) *H. ergaster* (no D2700) vs. Asian *H. erectus* based on the maximum-specimen set. 28 permutations were carried out. (C) *H. ergaster* (with D2700) vs. Asian *H. erectus* based on the maximum-semilandmark set. 20 permutations were carried out. (D) *H. ergaster* (with D2700) vs. Asian *H. erectus* based on the maximum-specimen set. 84 permutations were carried out. (E) African vs. Asian *H. erectus* based on the maximum-specimen set.

(A)

	Degree of Freedom	Sum of Square	Mean square	R square (coefficient of determination)	F-value	P-value
H. ergaster (no D2700) vs. Asian *H. erectus*	1	0.007748	0.007748	0.10714	0.6	0.8857
Residuals	5	0.064564	0.012913	0.98286		
Total	6	0.072312				

(B)

	Degree of Freedom	Sum of Square	Mean square	R square (coefficient of determination)	F-value	P-value
H. ergaster (no D2700) vs. Asian *H. erectus*	1	0.011078	0.011078	0.11671	0.9249	0.5238
Residuals	7	0.083840	0.088329	0.88329		
Total	8	0.094918				

(C)

	Degree of Freedom	Sum of Square	Mean square	R square (coefficient of determination)	F-value	P-value
H. ergaster (with D2700) vs. Asian *H. erectus*	1	0.007818	0.0078177	0.09187	0.607	0.8571
Residuals	6	0.077276	0.0128794	0.90813		
Total	7	0.085094				

(D)

	Degree of Freedom	Sum of Square	Mean square	R square (coefficient of determination)	F-value	P-value
H. ergaster (with D2700) vs. Asian *H. erectus*	1	0.011472	0.011472	0.10589	0..9474	0.4524
Residuals	8	0.096864	0.012108	0.89411		
Total	9	0.108336				

(E)

	Degree of Freedom	Sum of Square	Mean square	R square (coefficient of determination)	F-value	P-value
African (with OH9) vs. Asian *H. erectus*	1	0.011750	0.011750	0.11221	1.0111	0.3952
Residuals	8	0.092965	0.011621	0.88779		
Total	9	0.104715				

Results of the Procrustes ANOVAs are similar to those of the bootstrapped analyses. For all three pairs of geographical subsets based on both the maximum-semilandmark and maximum specimen datasets, all empirical F-values fall well within the 95% confidence interval (Table 7.12). Furthermore, in all comparisons, only around 10% of the total variance can be explained by the separation of group means. On the other hand, the ANOVA of the *H. sapiens* geographical subsets continue to show that a significant amount of the total variance can be explained by the separation of geographical group means (Table 7.11). This results further supports that there is no clear pattern of geographical group separation in the *H. erectus s. l.* sample.

7.6 OVERALL SIMILARITY WITH OTHER FOSSIL SPECIMENS

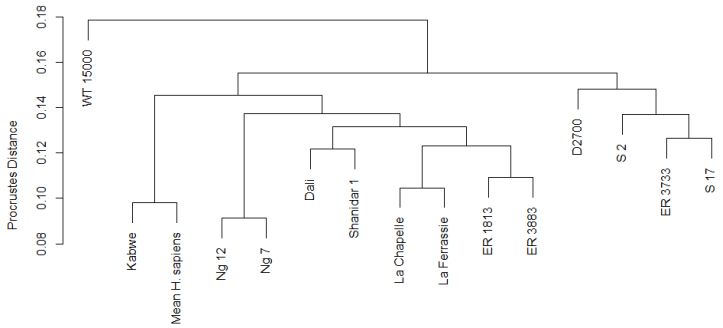

(A)

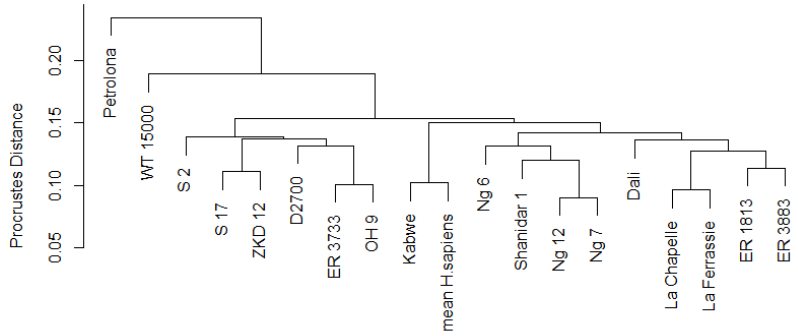

(B)

Figure 7.33 The UPGMA dendrogram of all fossil specimens (the temporal region)
(A) The maximum-semilandmark set. (B) The maximum-specimen set.

Upon adding the other fossil specimens, the UPGMA dendrograms based on both the maximum-semilandmark and maximum-specimen datasets reflect a complicated distribution of specimens (Figure 7.33). For the maximum-semilandmark dataset, KNM-WT 15000 shifts to the root as it is well separated from other fossils. KNM-ER 1813 and KNM-ER 3883 are grouped together and are then grouped with the three Neanderthals, the Dali skull, and the two Ngandong specimens. This larger cluster is linked with another cluster that contains Kabwe 1 and the mean shape of the *H. sapiens* sample. As the PCA shows, Kabwe 1 overlaps with the *H. sapiens* specimens. The other *H. erectus* specimens, S 17, KNM-ER 3733, D2700 and S 2 continue to constitute an independent cluster.

For the maximum-specimen dataset, the distribution of specimens is generally similar to the maximum semilandmark dataset. However, differing from the previous analysis, Shanidar 1 is grouped within the cluster of Ngandong specimens. KNM-ER 3733 is clustered with the newly added OH 9 as the pairwise distance between them is very short. S 17 is grouped with ZKD 12. WT 15000 is still distinct from all the other specimens. Another specimen widely separated from other fossils is Petralona 1, which is placed at the root of this dendrogram. Thus, the three mid-Pleistocene *Homo* specimens are widely separated from each other in terms of pairwise distances of the temporal region.

7.7 LOWER LANDMARK DENSITY

7.7.1 Twenty-nine anchor points

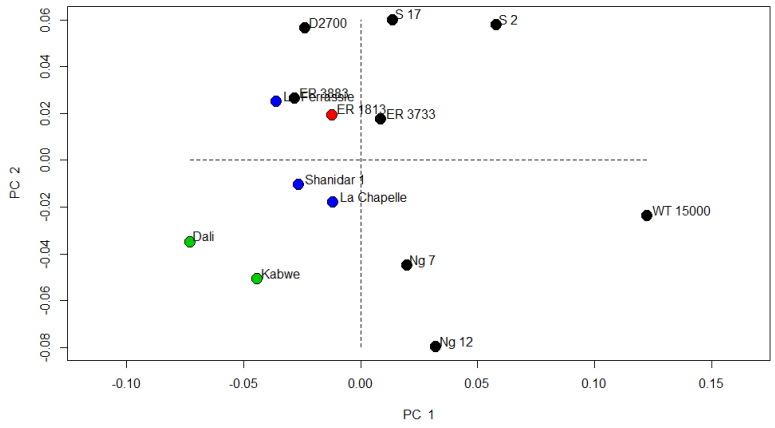

Figure 7.34 The plot of PC 1 and PC 2 of the fossil sample based on the anchor points of the temporal region

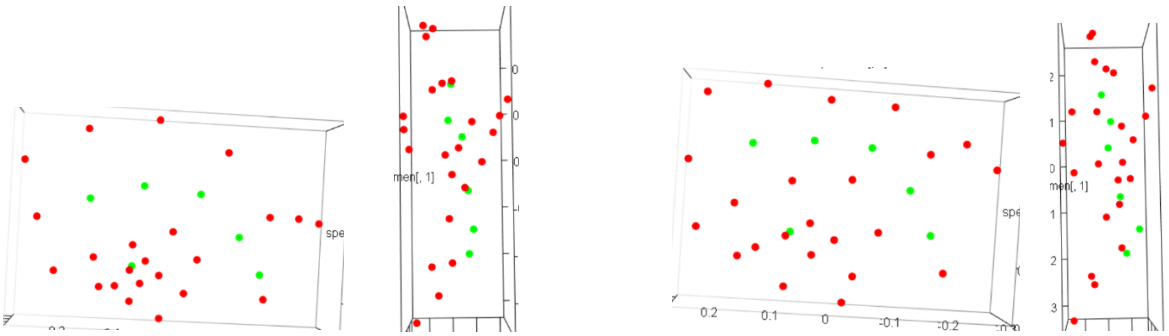

(A) (B)

Figure 7.35 The shapes at the two ends of PC 1 of the fossil sample (the anchor points of the temporal region) (A) The shape at the negative end of PC 1 (left: lateral view; right: inferior view); (B) The shape at the positive end of PC 1 (left: lateral view; right: inferior view).

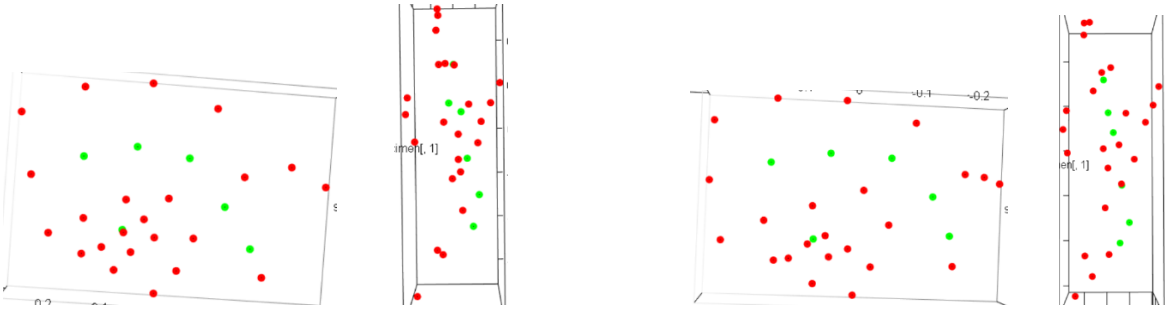

(A) (B)

Figure 7.36 The shapes at the two ends of PC 2 of the fossil sample (anchor points of the temporal region) (A) The shape at the negative end of PC 2 (left: lateral view; right: inferior view); (B) The shape at the positive end of PC 2 (left: lateral view; right: inferior view). The graphs are generated by the Geomorph R package (Adams et al., 2018).

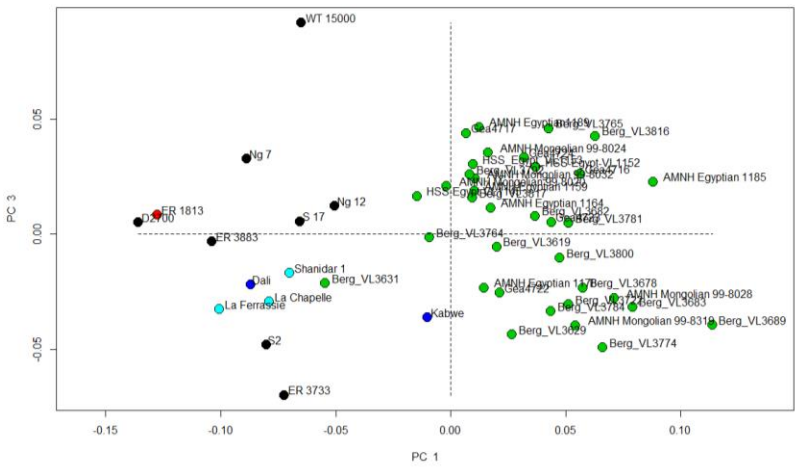

Figure 7.37 The PC 1 and PC 3 plot of *H. sapiens* and fossils (the anchor points of the temporal region)

Using the 29 anchor points, the PCAs show some different results compared to those obtained with the maximum-semilandmark set. When using only the fossil specimens, PC 1 continues to separate KNM-WT 15000 from the other fossil specimens, as did PC 2 from the first analysis of the maximum-semilandmark set (Figure 7.34). However, the distribution of the other specimens is altered. For example, in PC 1 of the anchor-points dataset, the Ngandong specimens are less close KNM-WT 15000 than S 2, while in PC 1 of the semilandmark dataset, the Ngandong specimens lie very close to KNM-WT 15000. The Dali skull and Kabwe 1, on the other hand, are plotted farther away from KNM-WT 15000. However, PC 1 continues to capture similar shape differences that separates KNM-WT 15000 from others (Figure 7.35). These aspects include the straightness of the squamosal suture because of inferior shifting of points above the auditory meatus, a more arced parietomastoid suture without significant anteroposterior elongation, a superior shift of the auricular region, and a posterior shift of the anterior end of the squamosal suture. The mandibular fossa also becomes anteroposteriorly longer. Differing from PC 1 of the semilandmark dataset, PC 1 of the anchor-point dataset also shows an increase in superoinferior height of the mastoid portion.

The other PCs are less comparable to the corresponding PCs from the first analysis of the maximum-semilandmark set. For example, PC 2 puts S 17, S 2, and D2700 at its positive end but Ng 12 at the negative end (Figure 7.34). The other specimens are intermediate overall. Moving toward the positive end, this PC captures the anteroposterior shortening, straightening of the parietomastoid suture as well as an anteroposterior shortening of the mandibular fossa (Figure 7.36). However, this PC does not demonstrate an increase in superoinferior height of the mastoid portion.

After including the large *H. sapiens* sample in the analysis, PC 1 still separates the majority of fossil specimens from the *H. sapiens* sample because they have a superoinferiorly shorter, anteroposteriorly longer temporal region as well as a mediolaterally wider mandibular fossa (Figure 7.37 and Figure 7.38). PC 3 is also similar overall to the corresponding PC in the second PCA based on the maximum-semilandmark set by separating KNM-WT 15000 from the other specimens because of its relatively larger mastoid portion and anteroposteriorly shorter squamosal portion (Figure 7.37 and Figure 7.39).

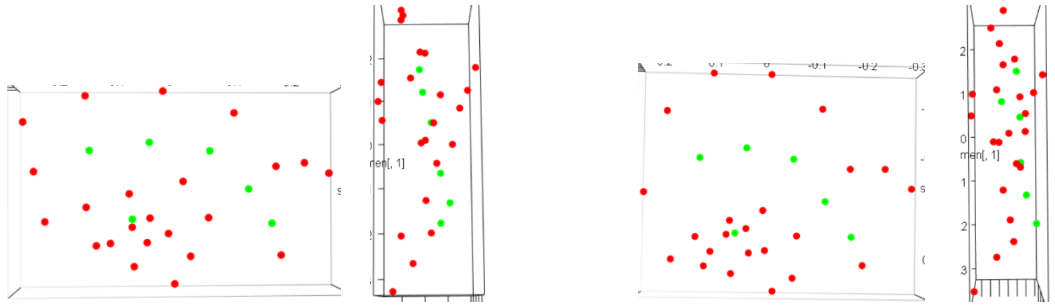

(A) (B)

Figure 7.38 Shape changes in PC 1 of *H. sapiens* and fossils (anchor points of the temporal region)
(A) The shape at the negative end of PC 1 (left: lateral view; right: inferior view); (B) The shape at the positive end of PC 1 (left: lateral view; right: inferior view).

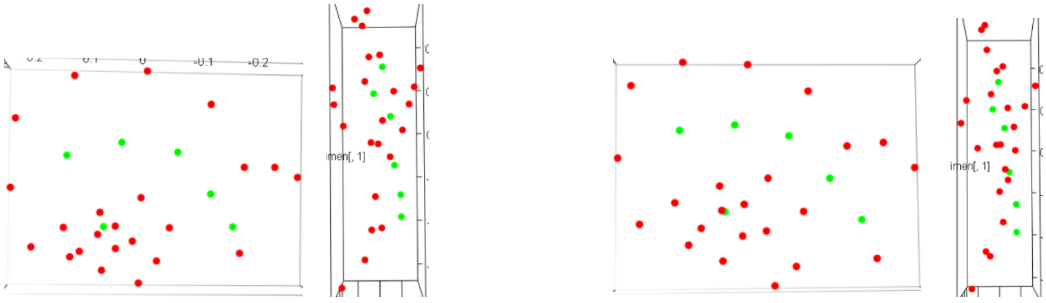

(A) (B)

Figure 7.39 Shape changes in PC 3 of *H. sapiens* and fossils (anchor points of the temporal region)
(A) The shape at the negative end of PC 3 (left: lateral view; right: inferior view); (B) The shape at the positive end of PC 3 (left: lateral view; right: inferior view). The graphs are generated by the Geomorph R package (Adams et al., 2018).

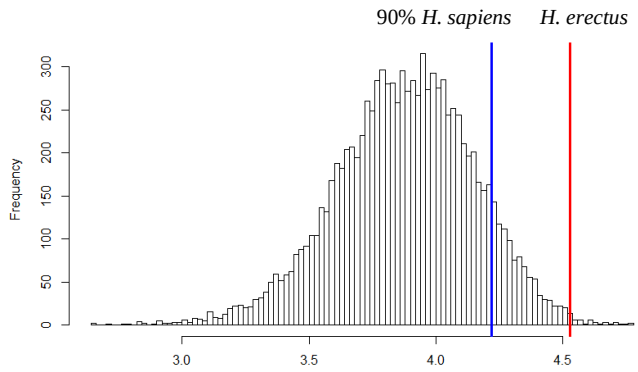

Figure 7.40 The bootstrapped analysis of SSDs based on the anchor points of the temporal region
The red line represents the SSD of the *H. erectus* sample. The blue line indicates the 90th percentile of the bootstrapped *H. sapiens* SSDs.

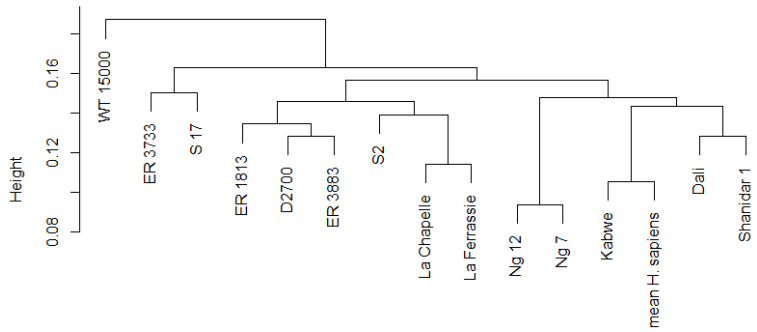

Figure 7.41 The UPGMA dendrogram of the fossil specimens (the anchor points of the temporal region)

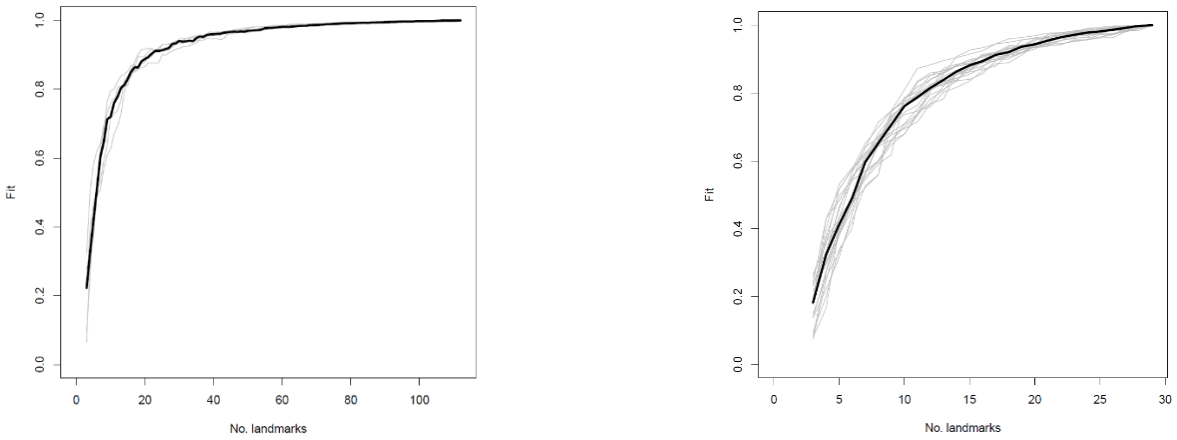

(A) (B)

Figure 7.42 The mean LASEC based on the semilandmark and anchor point sets of the temporal region
(A) The mean LASEC based on the maximum-semilandmark sets. (B) The mean LASEC based on the anchor points.

The bootstrap analysis still shows that the SSD of *H. erectus s. l.* significantly greatly exceeds the bootstrap SSDs of the *H. sapiens* sample, exceeding 9,960 (96.60%) of the *H. sapiens* distances (Figure 7.40). The UPGMA shows some inconsistent results, though KNM-WT 15000 continues to separate from all the other specimens (Figure 7.41). In this case, S 2 is grouped in the same cluster with Le Ferrassie and La Chapelle. They are further grouped with ER 3883, ER 1813, and D 2700, rather than with Shanidar 1, Dali, and Kabwe.

The mean landmark sampling evaluation curve (LASEC) obtained with 20 iterations of resampling shows that the fit continuously increases until the number of randomly selected landmarks reaches 29, without producing a plateau (Figure 7.42B). This suggests that the anchor point set is insufficient to capture a similar amount of shape information as that obtained with the original maximum-semilandmark set. The mean LASEC obtained with five rounds of resampling of the landmark set confirms this result as the fit becomes relatively stable after the number of randomly resampled landmarks roughly exceeds 40 (Figure 7.42A).

7.7.2 Fourteen discrete landmarks

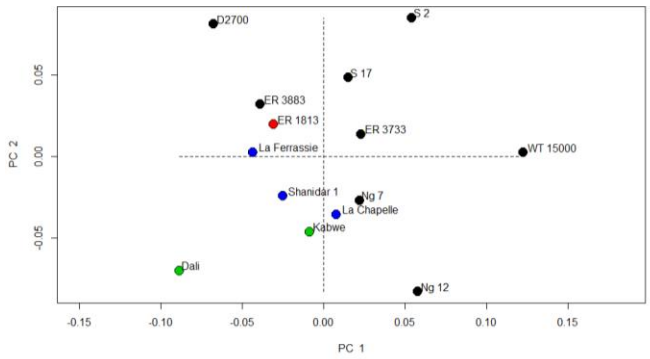

Figure 7.43 The PC 1 and PC 2 plot of the fossil sample based on the discrete landmarks of the temporal region

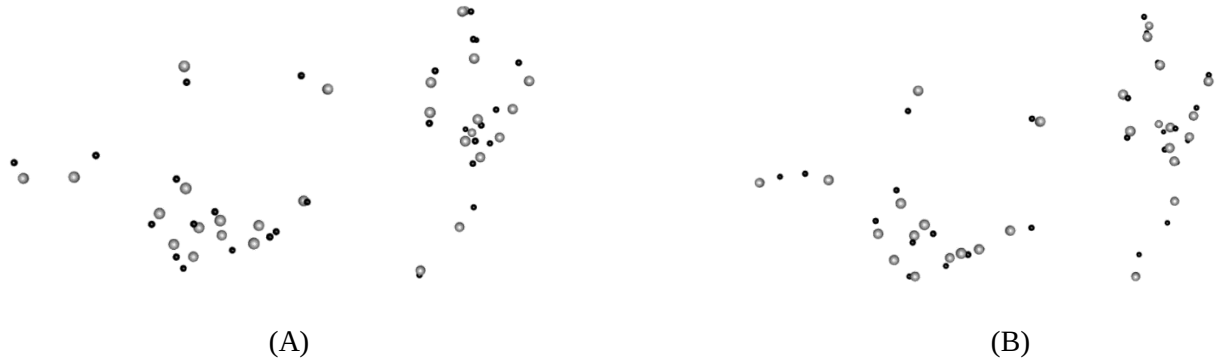

(A) (B)

Figure 7.44 Shape changes in PC 1 and 2 of *H. sapiens* and fossils (discrete landmarks of the temporal region)
(A) The shapes at the two ends of PC 1. (B) The shapes at the two ends of PC 2. The grey points represent the shape at the negative end. The black points represent the shape at the positive end. From left to right: lateral view and inferior view. The graphs are generated by the Geomorph R package (Adams et al., 2018).

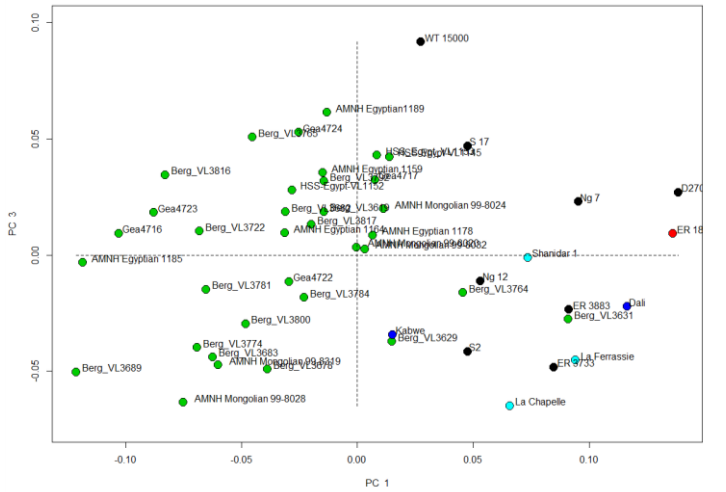

Figure 7.45 The PC 1 and PC 4 plot of *H. sapiens* and fossils based on the discrete landmarks of the temporal region

(A) (B)

Figure 7.46 Shape changes in PC 1 and 3 of *H. sapiens* and fossils (discrete landmarks of the temporal region) (A) The shapes at the two ends of PC 1. (B) The shapes at the two ends of PC 2. The grey points represent the shape at the negative end. The black points represent the shape at the positive end. From left to right: lateral view and inferior view. The graphs are generated by the Geomorph R package (Adams et al., 2018).

When using only 14 discrete points, the major PCs are roughly similar to the corresponding PCs based on the anchor-point dataset. PC 1 continues to separate KNM-WT 15000 from other fossils and places the Dali skull at the opposite end as these discrete landmarks can still reflect the straightness of the squamosal suture, the position of the parietomastoid suture, and anteroinferior length of the mandibular fossa (Figure 7.43 and Figure 7.43). PC 2 is also similar with PC 2 from the anchor-point dataset. Other PCs are different from corresponding PCs of the anchor-point dataset (Figure 7.43 and Figure 7.44).

After adding the large *H. sapiens* sample to the analysis, PC 1 still separates the majority of the fossils from *H. sapiens* because these discrete landmarks can show differences in the overall dimensions of the temporal region (Figure 7.45 and Figure 7.46). Similarly, PC 3 also separates KNM-WT 15000 from the other specimens because this landmark dataset can capture differences such as the straightness of the squamosal suture and anteroposterior length of the mandibular fossa (Figure 7.45 and 7.46). Probably because of the very low density of discrete landmarks, KNM-WT 15000 is less separated from others.

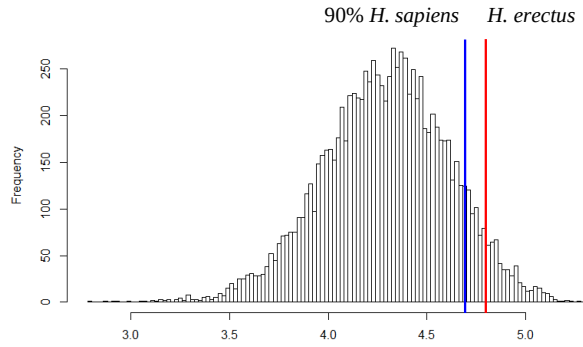

Figure 7.47 The bootstrapped analysis of SSDs based on the discrete landmarks of the temporal region
The red line represents the SSD of the *H. erectus* sample. The blue line indicates the 90th percentile of the bootstrapped *H. sapiens* SSDs.

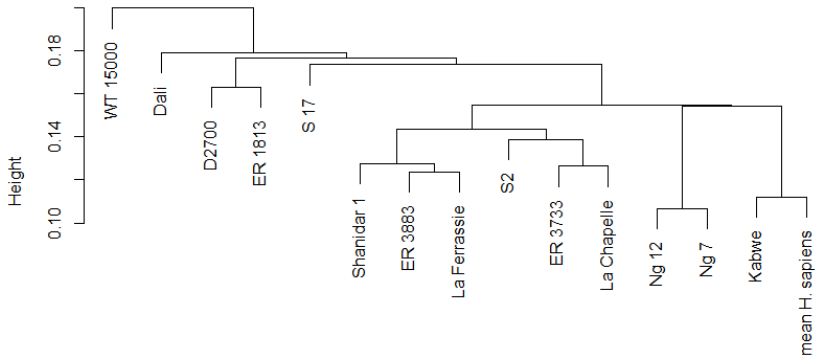

Figure 7.48 The UPGMA dendrogram of the fossil specimens (the discrete landmarks of the temporal region)

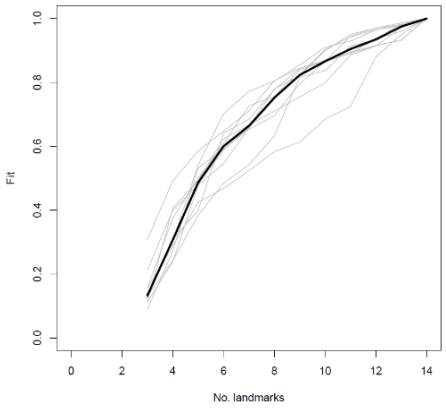

Figure 7.49 The mean LASEC based on the discrete landmarks of the overall cranium

The bootstrap analysis again shows that the SSD of the *H. erectus s. l.* sample is significantly greater than that of the *H. sapiens* sample, as it exceeds 9,489 (94.89%) of the 10,000 bootstrapped *H. sapiens* SSDs (Figure 7.47). The UPGMA dendrogram continues to plot KNM-WT 15000 at the root (Figure 7.48). However, this dendrogram is further different from the original dendrogram based on the maximum-semilandmark dataset. For example, KNM-ER 3733 is grouped with La Chapelle 1 rather than S 17. KNM-ER 3883 is grouped with two other Neanderthal specimens. The mean LASEC curve obtained with ten iterations of resampling shows that the fit increases sharply as the number of landmarks increases (Figure 7.49). This result is consistent with the previous LASEC curves that are based on greater landmark densities.

8.0 THE FRONTAL REGION

8.1 THE PCA OF THE MAXIMUM-SEMILANDMARK SET

8.1.1 The first PCA: The fossil sample

Table 8.1 The first PCA of the frontal region: The percentage variance explained by the first seven PCs

	Percentage of Variance	Cumulative Percentage
PC 1	35.013%	35.013%
PC 2	17.848%	52.861%
PC 3	11.830%	64.691%
PC 4	6.470%	71.161%
PC 5	6.011%	77.172%
PC 6	5.408%	82.580%
PC 7	3.884%	86.464%

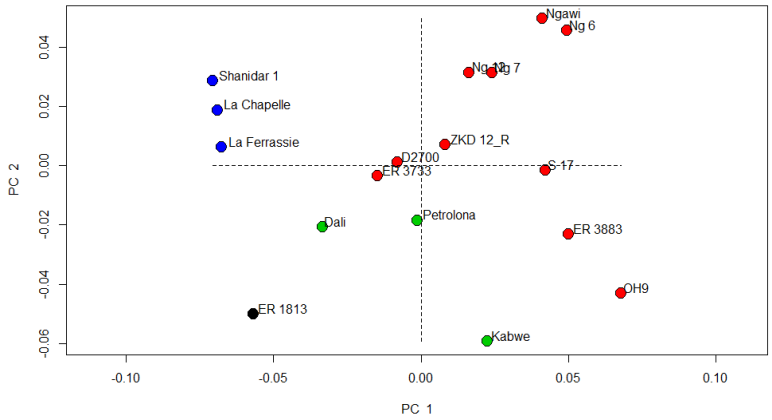

Figure 8.1 The first PCA of the frontal region: The plot of PC 1 and PC 2
The red dots: The *H. erectus s. l.* specimens. The black dot: The *H. habilis* specimen. The green dots: The Mid-Pleistocene *Homo* specimens. The blue dots: the Neanderthal specimens.

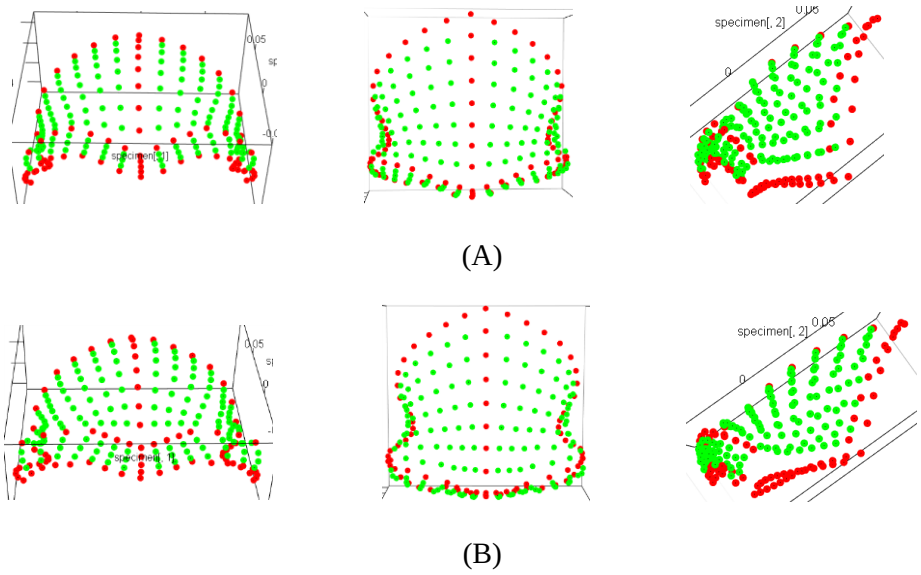

Figure 8.2 The first PCA of the frontal region: The shapes at the two ends of PC 1
(A) The shape at the negative end. (B) The shape at the positive end. From left to right: lateral view, superior view, and lateral view. The graphs are generated by the Geomorph package (Adams et al., 2018).

Principal component analysis (PCA) reveals a complicated distribution of the fossil specimens. PC 1, which explains 35.013% of the total variance, does not show clear clustering (Table 8.1 and Figure 8.1; also see Table B.27 for size-shape relationship). The three Neanderthals, which scored nearly identically, are placed at the negative end. KNM-ER 1813 has an only slightly less negative score. KNM-ER 3733, D2700, ZKD 12 and the mid-Pleistocene specimens are distributed across the origin. The Ngandong and Ngawi specimens have somewhat more positive scores. OH 9 is placed at the positive end.

In a specimen plotted closer to the positive end, the supraorbital and glabellar regions become thicker superoinferiorly and slightly less arced superiorly (Figure 8.2). The highest point of the superior margin of the brow shifts medially, such that the ascending part of each brow becomes shorter mediolaterally relative to the descending part, which becomes thicker to a slightly higher degree before reaching the zygomaticofrontal suture. In lateral view, the superior margin lies more anteriorly, more so than the inferior margin, creating an anteroposteriorly long posttoral plane that flows smoothly into the frontal squama. The supraorbital and glabellar surfaces also change from more anteroinferiorly faced to more anteroinferiorly faced. The frontal bone also becomes longer anteroposteriorly, and the frontal rise becomes gentler. In superior view, the supraorbital region flares more laterally. The glabellar region protrudes less, such that the superior contour becomes flatter across the glabella.

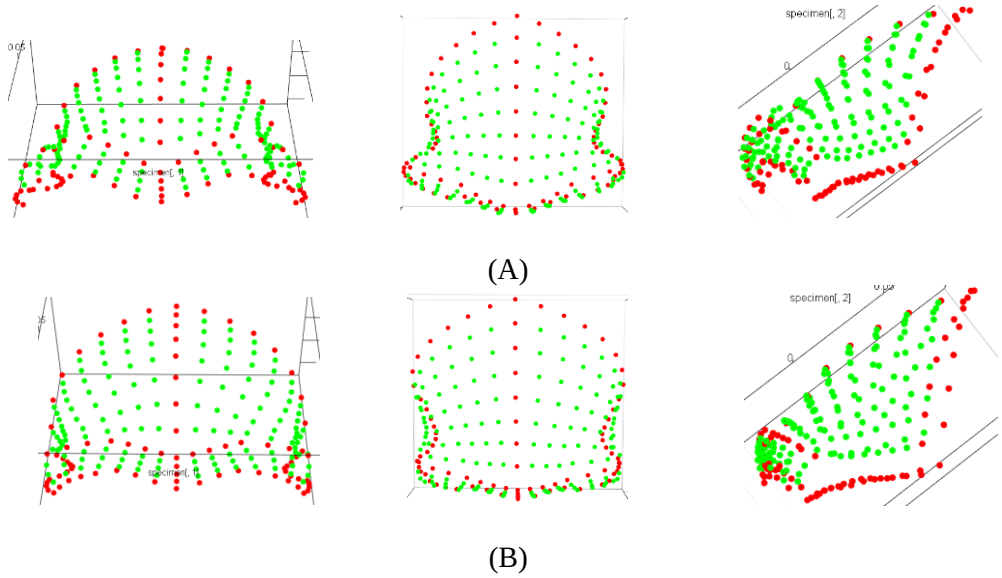

Figure 8.3 The first PCA of the frontal region: The shapes at the two ends of PC 2
(A) The shape at the negative end. (B) The shape at the positive end. From left to right: lateral view, superior view, and lateral view. The graphs are generated by the Geomorph package (Adams et al., 2018).

PC 2, which explains 17.848% of the total variance, plots the three Ngandong specimens (Ng 6, Ng 7, and Ng 12) and Ngawi 1, which have similar positive scores, at its positive half (Table 1 and Figure 1). The three Neanderthal specimens score somewhat less positively. ZKD 12, D2700, KNM-ER 3733 and S 17 are very close to each other, positioned around the origin. OH 9 and KNM-ER 1813 have more negative scores. Kabwe 1 is placed at the negative end.

From the negative to the positive end, PC 2 describes an overall decrease in size of the supraorbital relative to the glabellar region, such that that the brow becomes less flared laterally and the postorbital constriction decreases (Figure 8.3). Additionally, the glabellar region shifts slightly upward, such that that the ascending part of the brow becomes more horizontal. The glabellar region also recedes posteriorly, while the medial part of the supraorbital region on either side becomes more concave. Overall, the superior contour of the brow region is flatter. In lateral view, the glabellar region becomes more backwardly sloped relative to the supraorbital region. The frontal rise also becomes steeper.

Although none of the PCs reveal isolated clustering of the specimens, taking these two PCs together, the Neanderthals form a distinct cluster, while the Ngandong and Ngawi specimens form another somewhat isolated group (Figure 8.1).

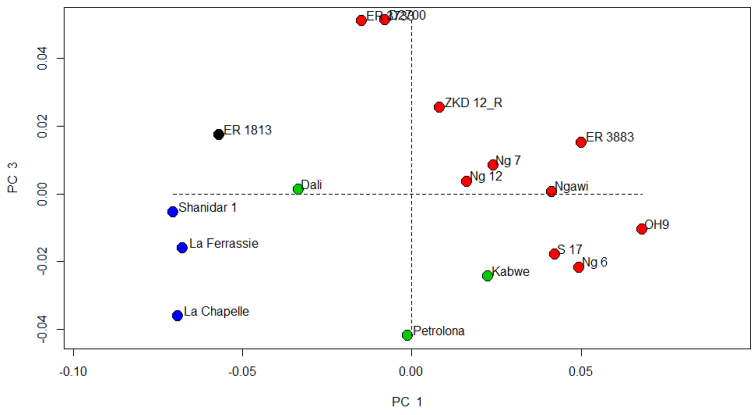

Figure 8.4 The first PCA of the frontal region: The plot of PC 1 and PC 3
The red dots: The *H. erectus s. l.* specimens. The black dot: The *H. habilis* specimen. The green dots: The Mid-Pleistocene *Homo* specimens. The blue dots: the Neanderthal specimens.

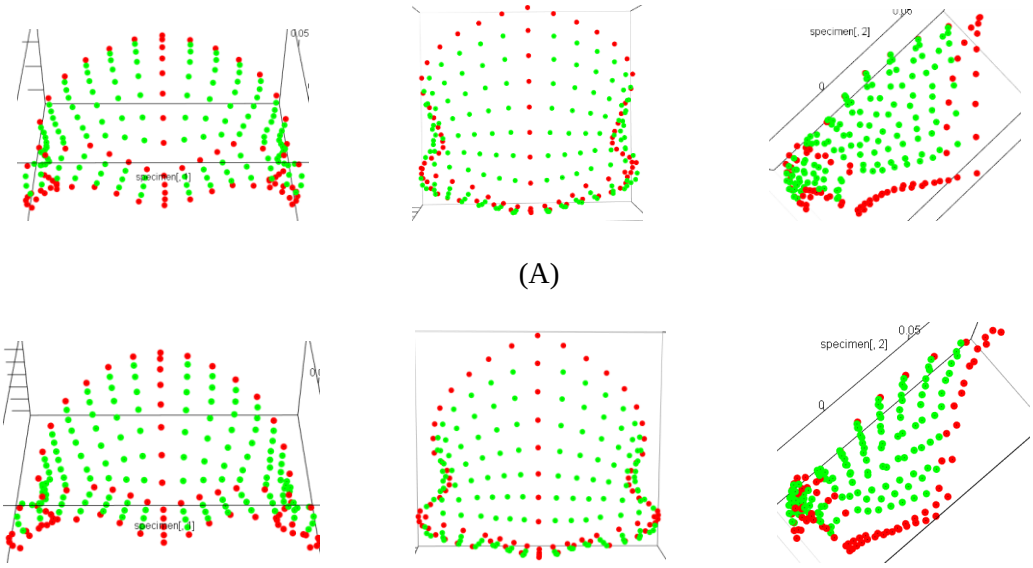

Figure 8.5 The first PCA of the frontal region: The shapes at the two ends of PC 3
(A) The shape at the negative end. (B) The shape at the positive end. From left to right: lateral view, superior view, and lateral view. The graphs are generated by the Geomorph package (Adams et al., 2018).

PC 3, which explains 11.83% of the total variance, separates ER 3733 and D2700, which have nearly identical positive scores, from other specimens (Table 1 and Figure 8.4). ZKD 12 is closest to these specimens but is still separated from them by a clear gap. The specimen with the most negative score is

Petralona 1. Other specimens scatter in between, with no clear pattern of grouping. PC 3 is also the only higher-ranked PC that is significantly correlated with size, probably because it plots Neanderthals and mid-Pleistocene specimens, which are large in size, in the negative half.

In a specimen plotted to PC 3's positive end, the supraorbital region becomes thinner superoinferiorly overall relative to the glabellar region (Figure 8.5). The brow becomes thinning laterally. The lateral end flares more laterally from the frontal squama, which becomes longer as bregma lies more posterosuperiorly. Points posterior to the superior margin of the brow lie more backward and downward, so that a horizontal posttoral plane appears in specimens plotted very close to this PC 3's positive end. The glabellar surface becomes more posteriorly sloping than the adjacent supraorbital plane. The surface just at the ascending part of the brow becomes more concave. Near the positive end, a low and blunt supraorbital tubercle becomes more apparent bilaterally, just lateral to the highest point of the orbital margin.

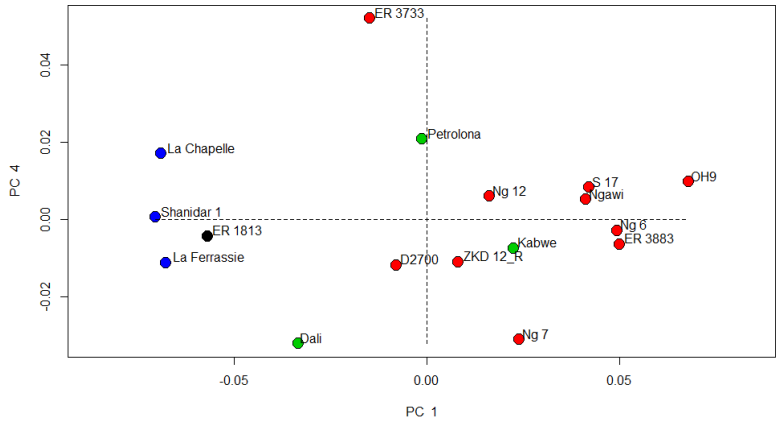

Figure 8.6 The first PCA of the frontal region: The plot of PC 1 and PC 4
The red dots: The *H. erectus s. l.* specimens. The black dot: The *H. habilis* specimen. The green dots: The Mid-Pleistocene *Homo* specimens. The blue dots: the Neanderthal specimens. The graphs are generated by the Geomorph package (Adams et al., 2018).

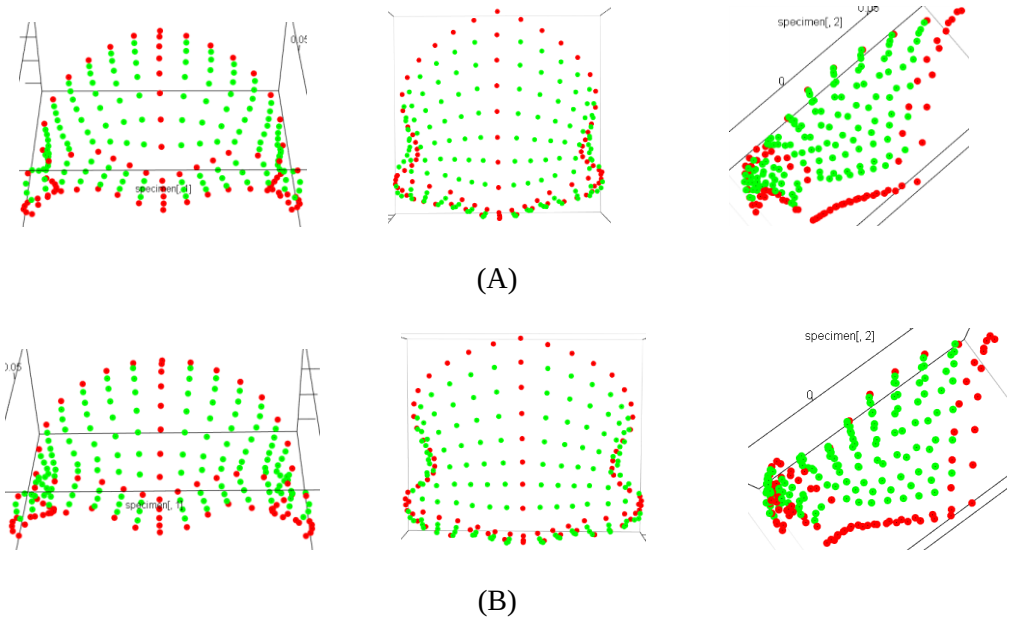

Figure 8.7 The first PCA of the frontal region: The shapes at the two ends of PC 4
(A) The shape at the negative end. (B) The shape at the positive end. From left to right: lateral view, superior view, and lateral view. The graphs are generated by the Geomorph package (Adams et al., 2018).

PC 4, which explains only 6.470% of the total variance, separates KNM-ER 3733 from the other fossil specimens (Table 8.1 and Figure 8.6). This PC demonstrates that in a specimen plotted very close to KNM-ER 3733, the highest point of the brow lies more laterally, such that the ascending part becomes longer mediolaterally (Figure 8.7). The brow becomes superoinferiorly thinner overall relative to the glabellar region. The brow also becomes thinning laterally. In superior view, the glabellar region lies more posteriorly. The surface of the ascending part of the brow becomes concave. The lateral part of the brow becomes more bulging. Overall, the superior contour is more transversely oriented. The lateral end of the brow flares out, while the anterior frontal squama becomes narrower, such that the postorbital constriction becomes stronger. In lateral view, the supraorbital surface changes from anteroinferiorly to anteriorly facing. Semilandmarks posterior to the superior margin of the brow lie more posteroinferiorly, creating a shallow sulcus at the KNM-ER 3733 end. Specifically, the postglabellar surface at the midline is more concave than the adjacent posttoral plane. The frontal rise becomes steeper. Furthermore, semilandmarks just anterior to the bregma shift anteriorly, reflecting a bulging area in KNM-ER 3733 anterior to bregma.

8.1.2 The second PCA: A large *Homo sapiens* sample with the fossil specimens

Table 8.2 The second PCA of the frontal region: The percentage variance explained by the first seven PCs

	Percentage of Variance	Cumulative Percentage
PC 1	54.816%	54.816%
PC 2	12.723%	67.539%
PC 3	6.863%	74.401%
PC 4	5.161%	79.563%
PC 5	3.370%	82.932%
PC 6	2.455%	85.377%
PC 7	1.897%	87.274%

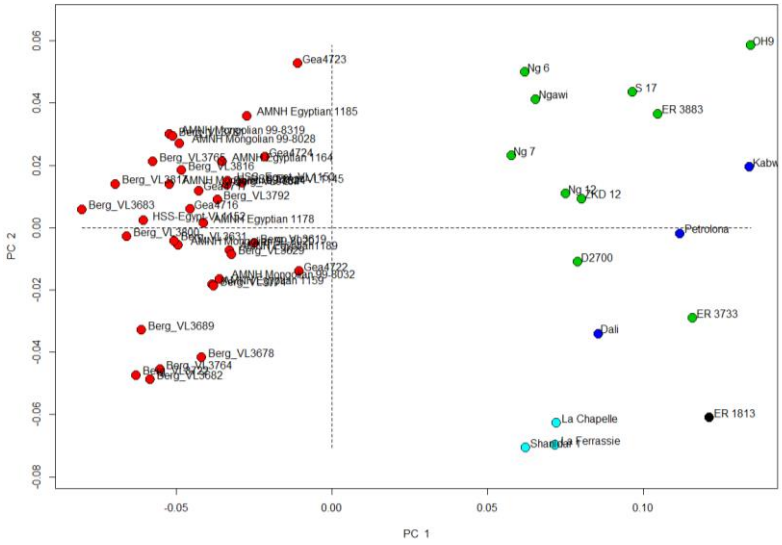

Figure 8.8 The second PCA of the frontal region: The plot of PC 1 and PC 2
The green dots: The *H. erectus s. l.* specimens. The black dot: The *H. habilis* specimen. The dark blue dots: The Mid-Pleistocene *Homo* specimens. The light blue dots: the Neanderthal specimens. The red dots: The *H. sapiens* specimens.

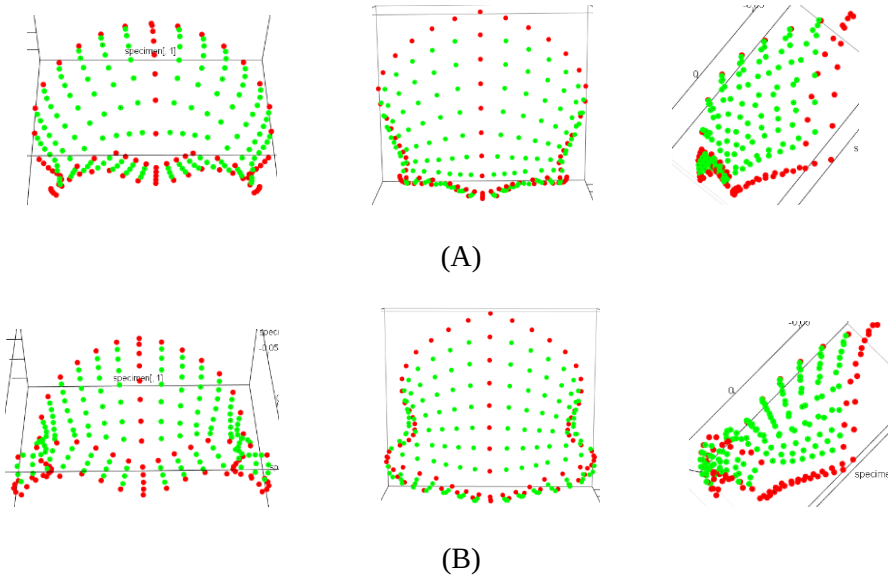

Figure 8.9 The second PCA of the frontal region: The shapes at the two ends of PC 1
(A) The shape at the negative end. (B) The shape at the positive end. From left to right: lateral view, superior view, and lateral view. The graphs are generated by the Geomorph package (Adams et al., 2018).

PC 1, which explains 54.816% of the total variance, clearly separates *H. sapiens* from fossil by placing them at its negative and positive halves, respectively, as two fairly tight clusters (Table 8.2 and Figure 8.8; also see Table B.28 for size-shape relationship). The Ngandong specimens, D2700, Ngawi 1, ZKD 12, the Dali skull and the Neanderthals have less positive scores. OH 9 and Kabwe 1 are the specimens with the most positive scores. S17, KNM-ER 3733, KNM-ER 3883, KNM-ER 1813 and Petralona 1 have intermediate scores.

In a specimen lies closer to the positive end (OH 9), PC 1 describes an overall increase in size of the supraorbital region relative to the frontal squama, which also becomes lower, flatter and mediolaterally narrower (Figure 8.9). Postorbital constriction becomes stronger, and the brow rounder. The lateral profile of the glabellar region become more anteriorly sloping as glabella lies more anteriorly than nasion. The supraorbital region becomes more anteriorly protruding, creating a horizontal posttoral plane.

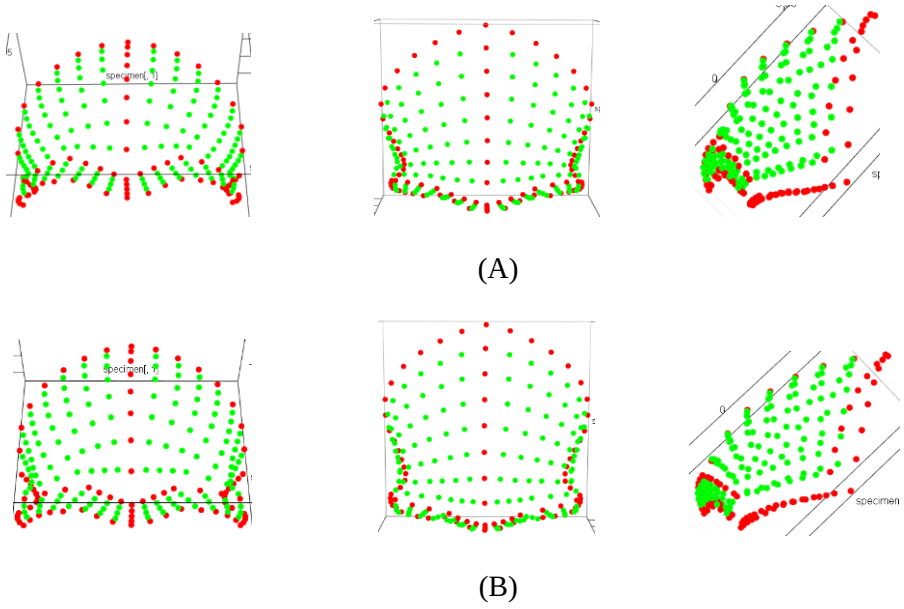

Figure 8.10 The second PCA of the frontal region: The shapes at the two ends of PC 2
(A) The shape at the negative end. (B) The shape at the positive end. From left to right: lateral view, superior view, and lateral view. The graphs are generated by the Geomorph package (Adams et al., 2018).

PC 2, which explains 12.723% of the total variance, shows a distribution of fossils very similar to that of PC 1 in the first PCA, though fossils greatly overlap *H. sapiens* (Table 8.2 and Figure 8.8). Similarly, Neanderthals and KNM-ER 1813 are placed at the negative end. D2700 and KNM-ER 3733 are the *H. erectus* specimens with the most negative scores. OH 9 is again placed at the positive end. From the negative to the positive end, this PC also shows that the ascending part of the brow becomes superoinferiorly shorter, while laterally descending part becomes superoinferiorly thicker (Figure 8.10). The frontal squama becomes anteroposteriorly longer, and the supraorbital surface becomes slightly more anteroinferiorly facing. The other PCs are not in accord with lower PCs in the previous analysis that includes only the fossil specimens.

8.1.3 The third PCA: A smaller *H. sapiens* sample with fossil samples

Table 8.3 The third PCA of the frontal region: The percentage variance explained by the first seven PCs

	Percentage of Variance	Cumulative Percentage
PC 1	49.983%	49.983%
PC 2	17.180%	67.163%
PC 3	6.862%	74.025%
PC 4	5.660%	79.680%
PC 5	3.380%	83.006%
PC 6	2.804%	85.869%
PC 7	2.306%	88.175%

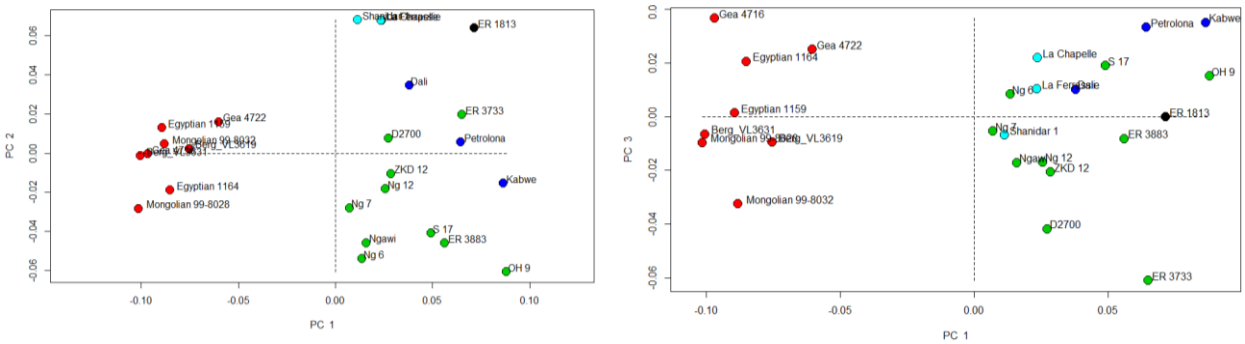

(A) (B)

Figure 8.11 The plots of the third PCA of the frontal region
(A) PC 1 and PC 2. (B) PC 1 and PC 3. The green dots: The *H. erectus s. l.* specimens. The black dot: The *H. habilis* specimen. The dark blue dots: The Mid-Pleistocene *Homo* specimens. The light blue dots: the Neanderthal specimens. The red dots: The *H. sapiens* specimens. The graphs are generated by the Geomorph package (Adams et al., 2018).

When reducing the sample size of *H. sapiens* to eight, PC 1 and PC 2 are similar to the corresponding PCs in the analysis that includes the large *H. sapiens* sample and fossils (see Table B.29 for size-shape relationship). PC 1 continues to separate *H. sapiens* from fossils based on the overall size of the supraorbital region relative to the frontal squama (Table 8.3 and Figure 8.11A; also see Figure B.45). PC 2 also places Neanderthals and KNM-ER 1813 at one end and OH 9 at the other (Table 8.3 and Figure 8.11A; also see Figure B.46).

PC 3 is similar to PC 3 from the first analysis that includes only fossils by separating KNM-ER 3733 from others (Figure 8.11B). Differing from PC 3 in the first analysis, D2700 lies intermediate between KNM-ER 3733 and other fossils rather than at nearly identical positions. In a specimens plotted closer to KNM-ER 3733, the supraorbital region also becomes superoinferiorly thinner than the glabellar region. In superior view, the ascending part of the brow becomes more concave, while the descending part becomes more rounded (Figure B.47). Semilandmarks at the anterior frontal squama lie more posteroinferiorly, creating a horizontal posttoral plane with a steeper frontal rise.

8.2 BOOTSTRAP ANALYSIS OF OVERALL VARIABILITY

8.2.1 Sum of squared pairwise distances

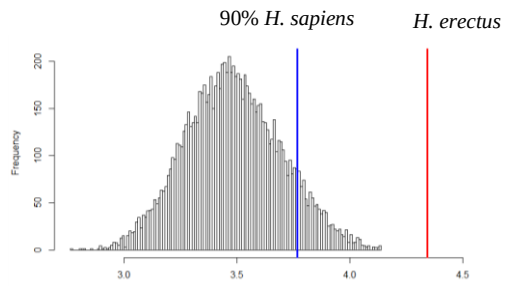

(A) *H. erectus s. l.* vs. *H. sapiens*

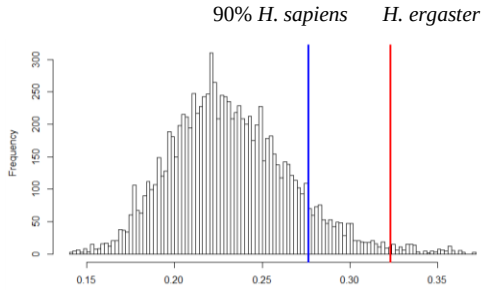

(B) *H. ergaster* (with D2700) vs. *H. sapiens*

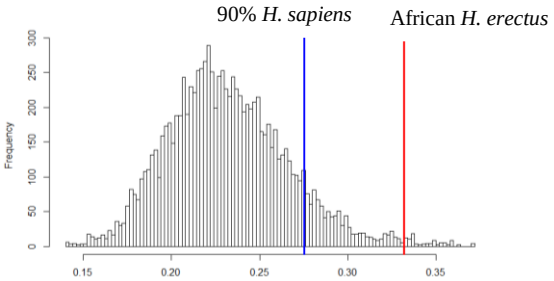

(C) African *H. erectus* (with OH 9) vs. *H. sapiens*

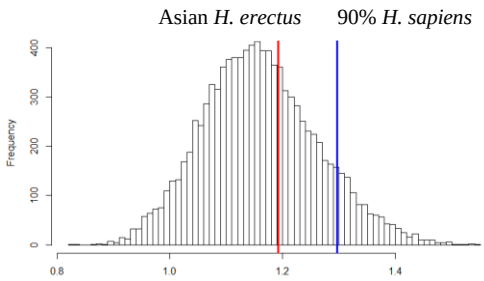

(D) Asian *H. erectus* vs. *H. sapiens*

Figure 8.12 The bootstrapped analyses of SSDs of the frontal region
The histograms show the distributions of 10,000 bootstrapped SSDs for the *H. sapiens* samples based on the maximum-semilandmark set (left) and the maximum-specimen set (right). In (A), (B), (C) and (D), the red line represents the SSD of the *H. erectus s. l.*, *H. ergaster* (with D2700), and Asian *H. erectus* samples respectively. The blue line in each graph represents the 90th percentile of the *H. sapiens* SSDs.

All the SSDs of the *H. erectus s. l.* sample and its subsets are significantly large relative to the bootstrapped SSDs of the *H. sapiens* sample (Figure 8.12 and Table B.30). The SSD of the *H. erectus s. l.* sample exceeds all the 10,000 bootstrapped SSDs of the *H. sapiens* sample. The SSD of *H. ergaster* specimens plus D2700 exceeds 9,855 (98.55%) of all *H. sapiens* SSDs. The SSD of African *H. erectus* (ER 3733, ER 3883, and OH 9) is greater than 9,908 (99.08%) SSDs of *H. sapiens*. Thus, the SSDs of these fossil samples are all significantly greater than those of *H. sapiens*. The only exception is the SSD of the Asian *H. erectus*, which only exceeds 6.454 (64.53%) of all bootstrapped *H. sapiens* SSDs.

The mean pairwise distances of the *H. erectus s. l.* sample and its subsets are significantly greater than bootstrapped mean pairwise distances in the *H. sapiens* sample (Figure 8.13 and Table B.31). The mean distance of the *H. erectus s. l.* sample again exceeds all of the 10,000 bootstrapped distances of the *H. sapiens* sample. The distance between KNM-ER 3733 and KNM-ER 3883 is greater than 9.826 (98.26%) of all *H. sapiens* distances. The mean pairwise distance of *H. ergaster* plus D2700 also exceeds 9,915 (98.50%) of *H. sapiens*. The mean pairwise distance of the African *H. erectus* sample (ER 3733, ER 3883, OH 9) also exceeds 9,915 (99.15%) of the *H. sapiens* distances. However, the mean pairwise distance of Asian *H. erectus* exceeds only 6,333 (63.33%) bootstrapped distances of *H. sapiens* sample.

8.2.2 Mean pairwise Procrustes distances

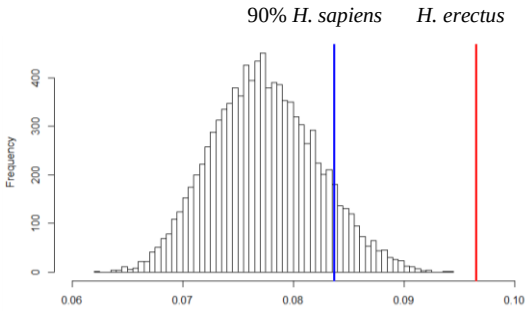

(A) *H. erectus s. l.* vs. H. sapiens

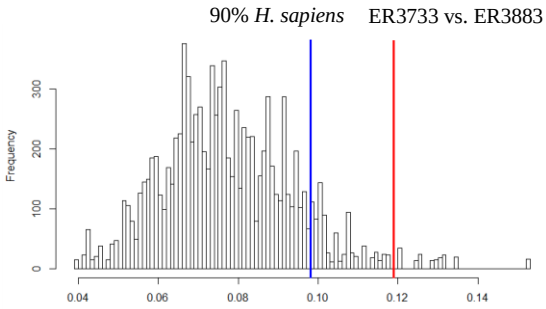

(B) *ER 3733-ER3883* vs. H. sapiens

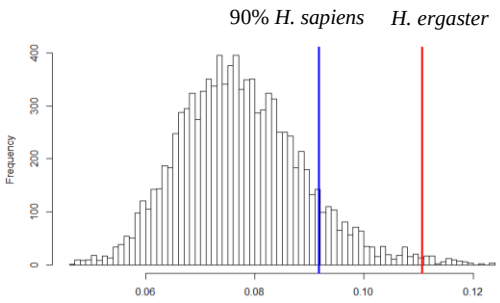

(C) *H. ergaster* (no D2700) vs. *H. sapiens*

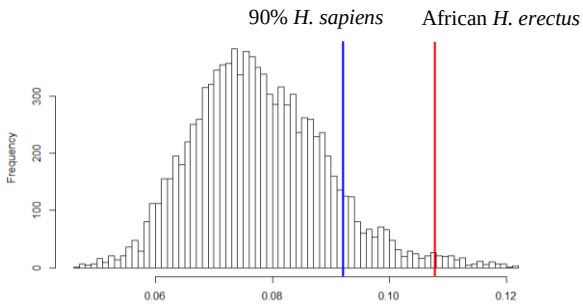

(D) African H. erectus vs. H. sapiens

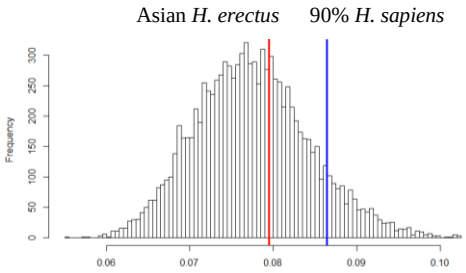

(E) Asian *H. erectus* vs. *H. sapiens*

Figure 8.13 The bootstrapped analyses of mean pairwise distances of the frontal region
The histograms show the distributions of 10,000 bootstrapped distances for the *H. sapiens* samples based on the maximum-semilandmark set (left) and the maximum-specimen set (right). In (A), (B), (C) and (D), the red line represents the mean pairwise distance of the *H. erectus s. l.*, *H. ergaster* (with D2700), and Asian *H. erectus* samples respectively. The blue line in each graph represents the 90th percentile of the *H. sapiens* distances.

8.3 INDIVIDUAL PAIRWISE DISTANCES

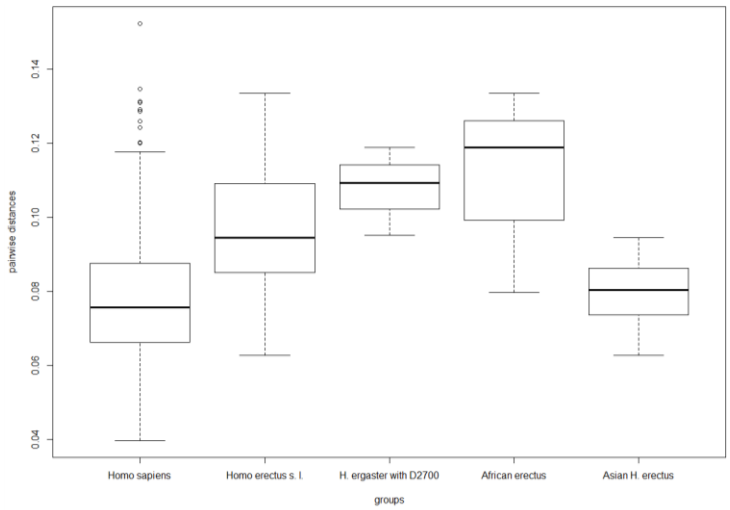

Figure 8.14 The boxplot of pairwise distances based on the maximum-semilandmark set of the frontal region

Table 8.4 Distribution of pairwise distances (the frontal region)

	Mean distance	Min	25th percentile	50th percentile	75th percentile	90th percentile	Max
H. sapiens	0.0772	0.0397	0.0663	0.0756	0.0876	0.0983	0.152
H. erectus s. l.	0.0965	0.0626	0.0850	0.0945	0.109	0.118	0.133

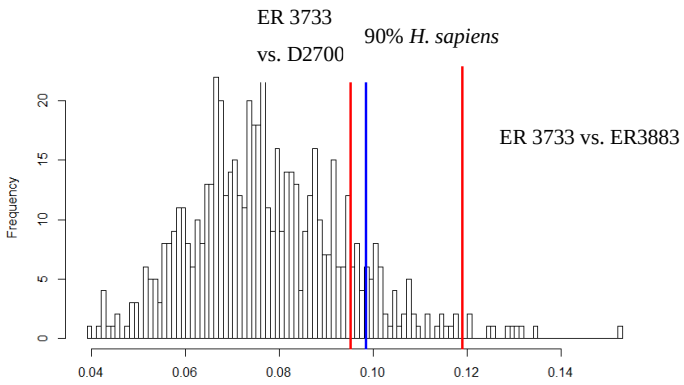
ER 3733
vs. D2700
90% H. sapiens
ER 3733 vs. ER3883
Frequency
0
5
10
15
20
0.04
0.06
0.08
0.10
0.12
0.14

(A)

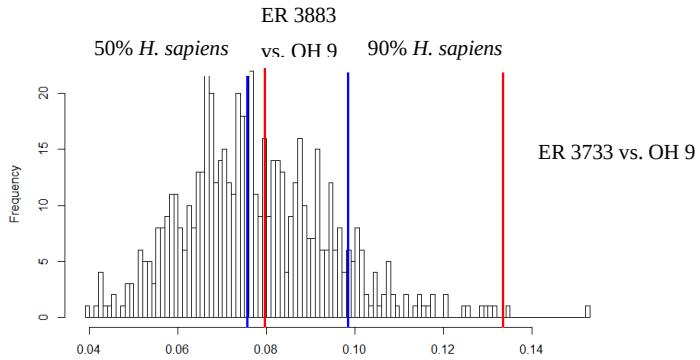
ER 3883
50% H. sapiens
vs. OH 9
90% H. sapiens
ER 3733 vs. OH 9
Frequency
0
5
10
15
20
0.04
0.06
0.08
0.10
0.12
0.14

(B)

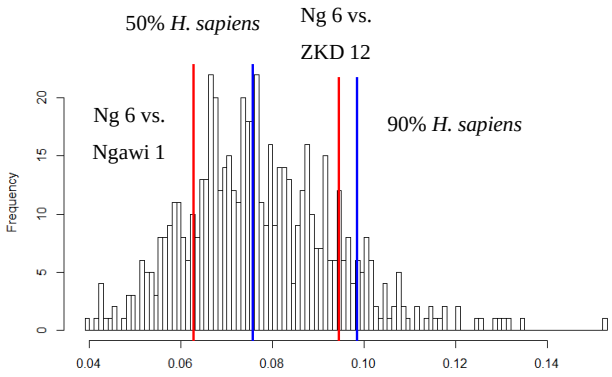
50% H. sapiens
Ng 6 vs.
ZKD 12
Ng 6 vs.
Ngawi 1
90% H. sapiens
Frequency
0
5
10
15
20
0.04
0.06
0.08
0.10
0.12
0.14

(C)

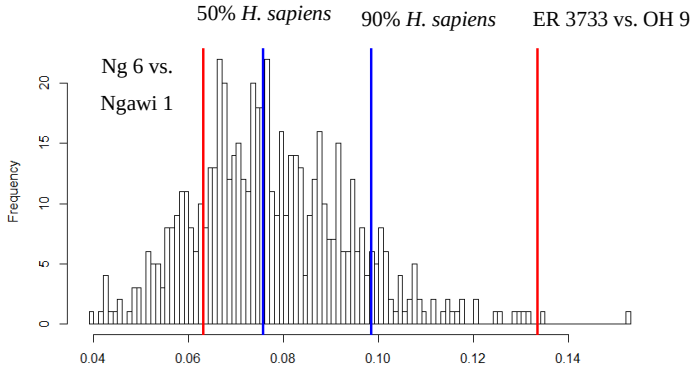

(D)

Figure 8.15 Pairwise distances of the *H. erectus* and *H. sapiens* samples based on the frontal region
The histogram shows the distribution of all pairwise distances within the *H. sapiens* sample. In (A), the blue line represents the 90th percentiles of the *H. sapiens* pairwise distance. In (B), (C) and (D), the blue left and right blue lines represent the 50th and 90th percentiles of the *H. sapiens* pairwise distances respectively. In (A), the left red line represents the distance between ER3733 and D2700, which is the smallest *H. ergaster* distance. The right red line represents the distance between ER3733 and ER3883, which is the largest *H. ergaster* distance. In (B), the left red line represents the distance between ER 3883 and OH 9, which is the smallest African *H. erectus* distance. The right red line represents the distance between ER 3733 and OH 9, which is the largest *H. erectus* distance. In (C), the left red line represents the distance between Ng 6 and Ngawi 1, which is the smallest *H. erectus* distance. The right red line represents the distance between Ng 6 and ZKD 12, which is the largest Asian *H. erectus* distance. In (C), the left red line represents the distance between Ng 6 and Ngawi 1, while the right red line represents the distance between ER 3733 and OH 9. These are also the smallest and largest distances of the whole H. erectus sample.

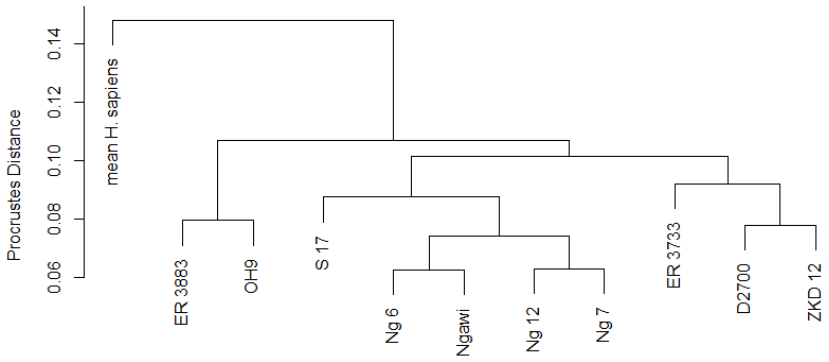

Figure 8.16 The UPGMA dendrogram (the frontal region)

Table 8.5 Individual pairwise distances of the *H. erectus* sample based on the maximum-semilandmark set of the frontal region

(A) The pairwise distance that is smaller than the 50th percentile of the *H. sapiens* distances; (B) The pairwise distances that fall between the 50th and 75th percentiles of the *H. sapiens* distances.

(A)

	Ng 6 vs. Ngawi (minimum)	Ng 6 vs. Ng 12	Ng 7 vs. Ng 12	Ng 12 vs. Ngawi	Ng 7 vs. Ngawi	Ng 12 vs. ZKD 12
Pairwise distance	0.0626	0.0757	0.0631	0.0652	0.0718	0.0756

(B)

	Ng 12 vs. S 17	Ng 6 vs. Ng 7	Ng 6 vs. S 17	Ng 7 vs. ZKD 12	Ngawi 1 vs. ZKD 12	S 17 vs. ZKD 12
Pairwise distance	0.0854	0.0840	0.0804	0.0774	0.0851	0.0869

	D2700 vs. ZKD 12	ER 3883 vs. OH 9
Pairwise distance	0.779	0.0796

The boxplot shows that most pairwise distances (31 of 45) within the *H. erectus s. l.* sample exceed the 75th percentile of the *H. sapiens* distances (Table 8.4 and Figure 8.14). Nineteen of the 45 pairwise distances even exceed the 90th percentile.

In *H. ergaster* (KNM-ER 3733, KNM-ER 3883, and D2700), the smallest distance, which falls between the 75th and 90th percentiles of the *H. sapiens* distances, is the one between D2700 and KNM-ER 3733 (Figure 8.15A). The other two distances far exceed the 90th percentile of the *H. sapiens* distances (Figure 8.14 and Figure 8.15A).

The lower extremity of the African *H. erectus* sample (KNM-ER 3733, KNM-ER 3883, and OH 9) falls below the 75th percentile of the *H. sapiens* distances because of the relatively small distance between KNM-ER 3883 and OH 9 (Table 8.5, Figure 8.14 and Figure 8.15B). The distance between KNM-ER 3733 and OH 9, however, becomes the greatest distance, even in the pooled *H. erectus s. l.* sample (Figure 8.14 and Figure 8.15B).

The majority of the pairwise distances (12 of 15) in the Asian *H. erectus* sample fall within the 25th and 75th percentiles of the *H. sapiens* distances (Figure 8.14 and Table 8.5). The Ngandong and

Ngawi specimens are again very close to each other. Among the six pairwise distances within the Ngandong-Ngawi subset, five fall below the 25th percentile of the *H. sapiens* distances (Table 8.5). Among the other distances, the only three that reach the interval between the 75th and 90th percentiles of the *H. sapiens* distances are between Ng 7 and S 17, between Ngawi 1 and S 17, and between Ng 6 and ZKD 12 (Figure 8.15C). The other seven pairwise distances within the Asian sample fall between the 50th and 75th percentiles of the *H. sapiens* bootstrapped distances (Table 8.5).

Upon pooling *H. erectus* specimens together, all pairwise distances between the Asian and Euro-African specimens well exceed the 75th percentile of the *H. sapiens* distances, except the distance between D2700 and ZKD 12, which falls between the 50th and 75th percentiles of the *H. sapiens* bootstrapped distances (Table 8.5). Sixteen of 24 pairwise distances between specimens from these two geographical regions exceed the 90th percentiles of the *H. sapiens* distances (Figure 8.14 and Figure 8.15D).

Overall, the Ngandong-Ngawi specimens remain close to each other. The Asian specimens are also relatively close to each other when using the 75th percentile of the *H. sapiens* distances as a yardstick. The distances within the Euro-African sample are greater than those in the Asian sample but are generally comparable to the distances between these specimens and those specimens of the Asian group, with the exception of the small distances between D2700 and ZKD 12 and between KNM-ER 3883 and OH 9.

The unweighted pair group method with arithmetic mean (UPGMA) dendrogram reflects these patterns of pairwise distances (Figure 8.16). The Ngandong specimens and Ngawi 1 are grouped into a tight cluster. S 17 is close to this cluster. ZKD 12 and D2700 group together because of the small distance between them. They are further clustered with KNM-ER 3733, whereas KNM-ER 3883 and OH 9 are placed in a separate cluster because the distance between them falls below the 75th percentile of the *H. sapiens* distances. The mean shape of *H. sapiens* is placed at the root because it is distinct from all *H. erectus* shapes in terms of overall similarity.

8.4 DIFFERENCES BETWEEN GEOGRAPHICAL SUBSETS

8.4.1 Bootstrap analysis of distances between group means

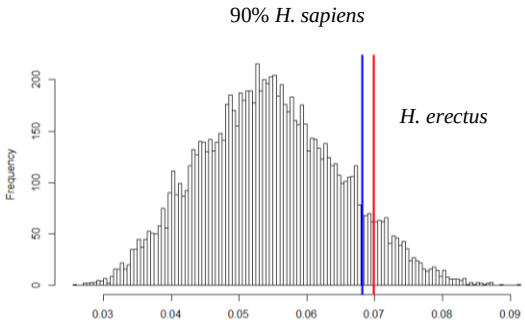

(A) *H. ergaster* (no D2700) vs. *H. sapiens*

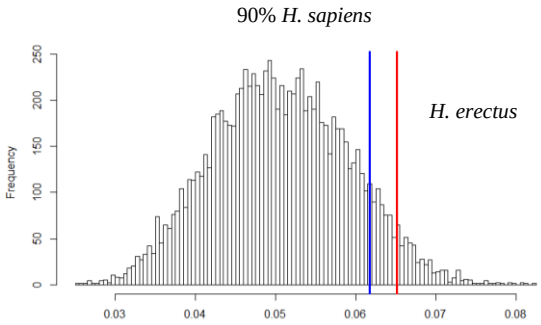

(B) *H. ergaster* (with D2700) vs. *H. sapiens*

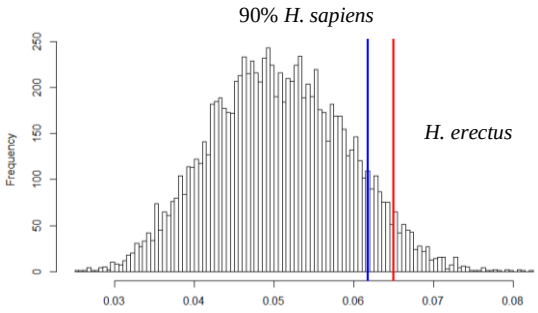

(C) African *H. erectus* and African *H. erectus*

Figure 8.17 The pairwise distances between the means of *H. erectus* geographical subsets compared to bootstrapped *H. sapiens* distances (the frontal region)
The blue line in each graph represents the 90th percentile of the 10,000 bootstrapped *H. sapiens* distances. (A) The red line represents the distance between the means of *H. ergaster* (no D2700) and Asian *H. erectus*. (B) The red line represents the distance between the means of *H. ergaster* (with D2700) and Asian *H. erectus*. (C) The red line represents the distance between the means of African and Asian *H. erectus*.

Bootstrap analyses show that the distance between the means of African *H. ergaster* (KNM-ER 3733 and KNM-ER 3883) and Asian *H. erectus* exceeds 9,266 (92.66%) of the *H. sapiens* distances (Figure 8.17A and Table B.32). The distance between the means of *H. ergaster* plus D2700 and Asian *H. erectus* is greater than 9547 (95.47%) of *H. sapiens* (Figure 8.17B). Furthermore, the distance between the means of African and Asian *H. erectus* exceeds 9,529 (95.29%) of all *H. sapiens* cases (Figure

8.17C). These results show that the distances between the means of the *H. erectus* geographical subsets are significantly greater than those between the *H. sapiens* geographical subsets. However, this result may be a byproduct of relatively great individual pairwise distances in the *H. erectus* sample as reported in the previous section.

8.4.2 Procrustes ANOVA

Table 8.6 The Procrustes ANOVA of the *H. sapiens* geographical subsets (the frontal region)

	Degree of Freedom	Sum of Square	Mean square	R square (coefficient of determination)	F-value	P-value
Asian vs. African *Homo sapiens*	1	0.023849	0.0128487	0.12071	4.5303	0.0004
Residuals	33	0.093595	0.0028362	0.87929		
Total	34	0.106444				

The Procrustes ANOVAs are limited by small sample sizes. The ANOVA of the African *H. ergaster* and Asian *H. erectus* samples yields a p-value of 0.1786, which means that the amount of the total variance explained by the geographical group separation is insignificant (Table 8.7A). However, the empirical F-values still exceeds 23 out of 27 permutated F-values. The ANOVA of the *H. ergaster* (with D2700) and the Asian *H. erectus* samples results in a p-value of 0.0592, which slightly exceeds the 0.05 critical value (Figure 8.7B). This shows that the empirical F-value exceeds 78 of 83 permutated F-values. The ANOVA of the African and Asian *H. erectus* samples yields the same p-value of 0.0592 (Figure 8.7C). This again means that the empirical F-value exceeds 78 of 83 permutated F-values in this analysis. Thus, these ANOVAs still indicate that patterns of group separation may still exist within the *H. erectus* sample. Notably, these patterns of group separation might be driven by the distinctiveness of the Ngandong-Ngawi group as previously shown.

However, the amount of the total variance explained by the separation of the geographical subsets in *H. sapiens* sample is also significantly great as the p-value falls well below the 0.05 critical value (Table 8.6). This seems to weaken the power of Procrustes ANOVA in showing the coexistence of two geographical species a sample. However, The R-square value shows that only 12% of the total variance in the *H. sapiens* sample can be explained by the group means, while more than 20% of the total variance within the fossil sets can be explained by the separation of group means.

Table 8.7 The Procrustes ANOVA of the *H. erectus* geographical subsets

(A) *H. ergaster* (no D2700) vs. Asian *H. erectus*. 28 permutations were carried out. (B) *H. ergaster* (with D2700) vs. Asian *H. erectus*. 84 permutations were carried out. (C) African *H. erectus* vs. Asian *H. erectus*. 84 permutations were carried out.

(A)

	Degree of Freedom	Sum of Square	Mean square	R square (coefficient of determination)	F-value	P-value
H. ergaster (no D2700) vs. Asian *H. erectus*	1	0.0073274	0.0073274	0.24077	1.9027	0.1786
Residuals	6	0.0231059	0.0038510	0.75923		
Total	7	0.0304334				

(B)

	Degree of Freedom	Sum of Square	Mean square	R square (coefficient of determination)	F-value	P-value
H. ergaster (with D2700) vs. Asian *H. erectus*	1	0.008487	0.0084865	0.23424	2.1413	0.05952
Residuals	7	0.027743	0.0039633	0.76576		
Total	8	0.036230				

(C)

	Degree of Freedom	Sum of Square	Mean square	R square (coefficient of determination)	F-value	P-value
African *H. erectus* vs. Asian *H. erectus*	1	0.008431	0.0084305	0.22648	2.0495	0.05952
Residuals	7	0.028794	0.0041135	0.77352		
Total	8	0.037225				

8.5 THE UPGMA DENDROGRAM OF ALL THE FOSSIL SPECIMENS

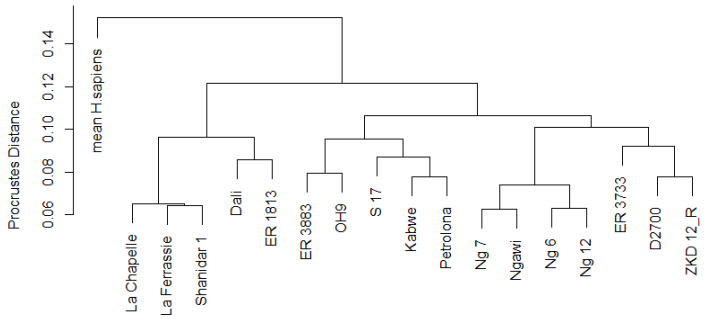

Figure 8.18 The UPGMA dendrogram of the fossil specimens (the frontal region)

Upon adding the other hominid specimens, the UPGMA dendrogram plots Kabwe 1 and Petralona with the *H. erectus* specimens (Figure 8.18). They are particularly grouped with S 17. The three Neanderthals are added to a distinct cluster. Interestingly, The Dali skull groups with KNM-ER 1813 rather than with the other mid-Pleistocene specimens. The Dali skull and KNM-ER 1813 are further group with Neanderthals into a cluster parallel to the *H. erectus* cluster. The mean shape of *H. sapiens* is placed at the root, suggesting that it is far separated from all fossils.

8.6 LOWER LANDMARK DENSITY

8.6.1 The 45-anchor point set

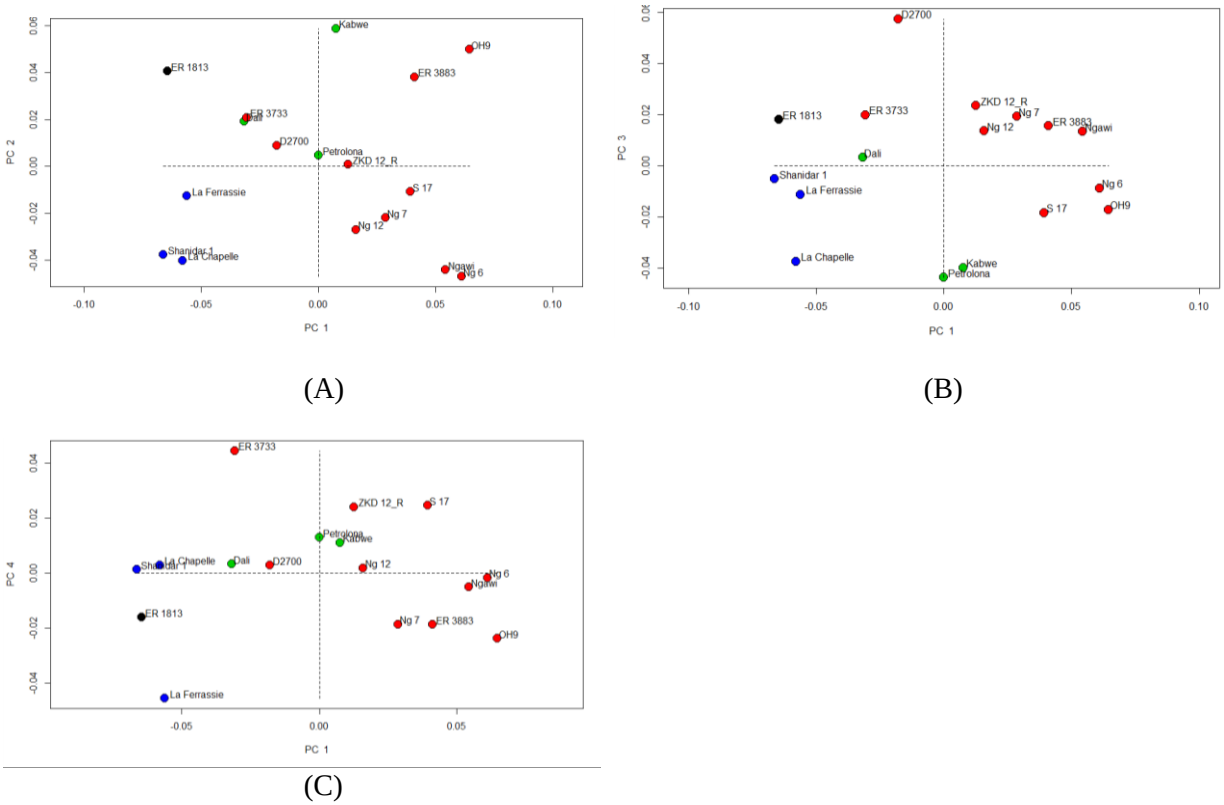

Figure 8.19 The PCA plots of the fossil sample based on the anchor points of the frontal region
(A) PC 1 and PC 2. (B) PC 1 and PC 3. (C) PC 1 and PC 4.

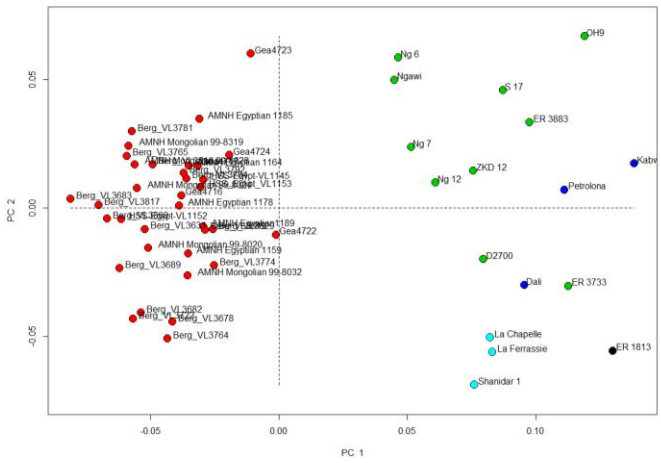

Figure 8.20 The PC 1 and PC 2 plot of *H. sapiens* and fossils based on the anchor points of the overall cranium

Based on 45 anchor points, PC 1 to PC 4 are similar overall to the corresponding PCs from the first PCA of the maximum-semilandmark dataset (Figure 8.19 and Appendix B.4.5). PC 1 continues to demonstrate shape differences that separate specimens with higher scores from specimens with lower scores, such as overall and lateral superoinferior thickening of the brow, an anterior protrusion of the brow region, a more anteroinferiorly facing supraorbital and glabellar surface, and anteroposterior elongation of the frontal bone (Figure 8.19A and Figure B.48). PC 2 still plots the Ngandong-Ngawi specimens at the end opposite to Kabwe 1 (Figure 8.19A and Figure B.49). PC 2 also shows that in a specimen plotted closer to the late Indonesian specimens, the brow decreases in size relative to both the glabellar region and the mediolaterally wider frontal squama. The ascending part of the brow becomes more horizontal as the glabellar region lies more posterosuperiorly.

PC 3 is somewhat different from PC3 of the maximum-semilandmark set (Figure 8.19B and Figure B.50). Instead of being positioned at the positive end with D2700, KNM-ER 3733 is aligned with the other fossil specimens with relatively higher scores, such as ZKD 12 and KNM-ER 1813. Similar to PC 3 of the maximum-semilandmark dataset, PC 3 continue to show shape differences that separate D2700 from other fossils, such as more lateral flaring and lateral thinning the supraorbital rim, a more posteriorly sloping glabellar profile, and a more posteroinferior position of bregma. However, it does not reveal the presence of a posttoral plane because no achor point is placed at the post-toral region. This probably explains why KNM-ER 3733 lies closer to other fossils than to D2700 in PC 3 of the anchor-point set.

PC 4 is able to separates KNM-ER 3733 from other fossils, though it again fails to reveal differences that separate KNM-ER 3733 from other fossils, such as the presences posttoral sulcus and a

bulging area anterior to bregma (Figure 8.19C and Figure B.51). This PC still demonstrates that KNM-ER 3733 differs from other fossils in having a more anterosuperiorly facing supraorbital and glabellar surfaces, a straighter anterior contour of the supraorbital region as the lateral end of the brow lies more anteriorly and extends laterally, and a posterosuperior shift of bregma.

Upon including the large *H. sapiens* sample, higher-ranked PCs are also similar overall to the corresponding PCs from the second analysis of the maximum-semilandmark set (Figure 8.20 and Appendix B.4.5). PC 1 continues to separate the fossils from *H. sapiens* based on the size of the brow and overall configuration of the frontal squama. PC 2 also shows a nearly identical distribution of fossils by placing Neanderthals and KNM-ER 1813 at its negative and OH 9 at its positive end. In a specimen plotted closer to OH end, the highest point of the superior margin of the brow lies more medially, the supraorbital surface become more anteroinferiorly facing, and the frontal squama becomes longer anteroposteriorly.

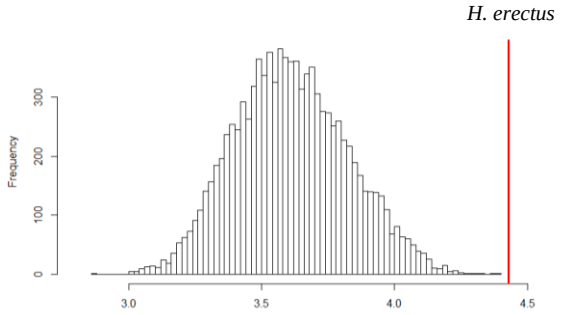

Figure 8.21 The bootstrapped analysis of SSDs based on the anchor points of the overall cranium
The histogram demonstrates the distribution of 10,000 *H. sapiens* SSDs. The red line represents the SSD of the *H. erectus* sample.

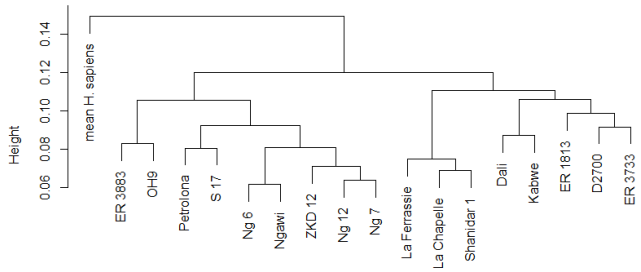

Figure 8.22 The UPGMA dendrogram of the fossil specimens (the anchor points of the overall cranium)

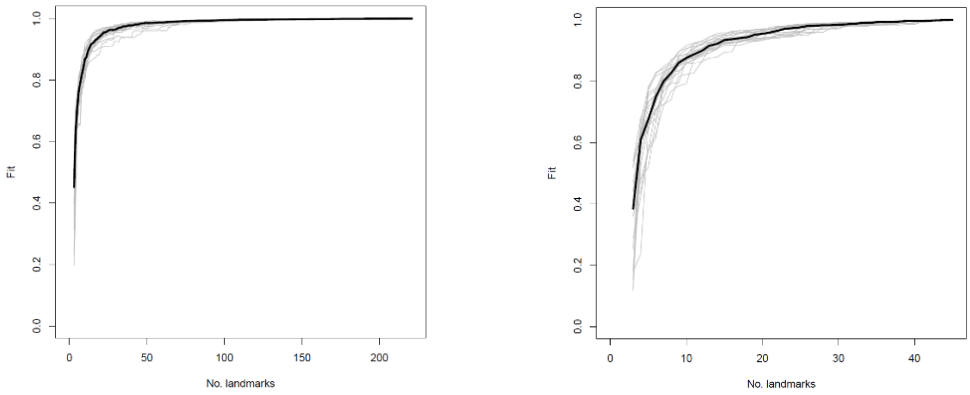

(A) (B)

Figure 8.23 The mean LASEC based on the semilandmark and anchor point sets of the frontal region
(A) The mean LASEC based on the maximum-semilandmark sets. (B) The mean LASEC based on the anchor points.

The bootstrap analysis again shows that the sum of squared Procrustes distance (SSD) of the *H. erectus s. l.* sample exceeds all 10,000 bootstrapped *H. sapiens* SSDs (Figure 8.21). The UPGMA dendrogram shows a very similar distribution of specimens (Figure 8.22). In this case, ZKD 12 is clustered with the Ngandong-Ngawi specimens rather than with D2700 and KNM-ER 3733. Kabwe 1 groups with the Dali skull rather than Petralona 1 and S 17.

For the anchor point dataset, the mean landmark sampling evaluation curve (LASEC) obtained with 20 rounds of resampling shows that the slope significantly decreases after the number of landmarks roughly exceeds ten (Figure 8.23B). The fit approaches 1 when the number of landmarks roughly exceeds a value close to 40. Based on the maximum-semilandmark set, the mean LASEC obtained with 20 rounds of resampling yields similar results (Figure 8.23A). This demonstrates that when the number of landmarks exceeds 50, the fit value closely approaches 1.

8.6.2 The fifteen-discrete landmark set

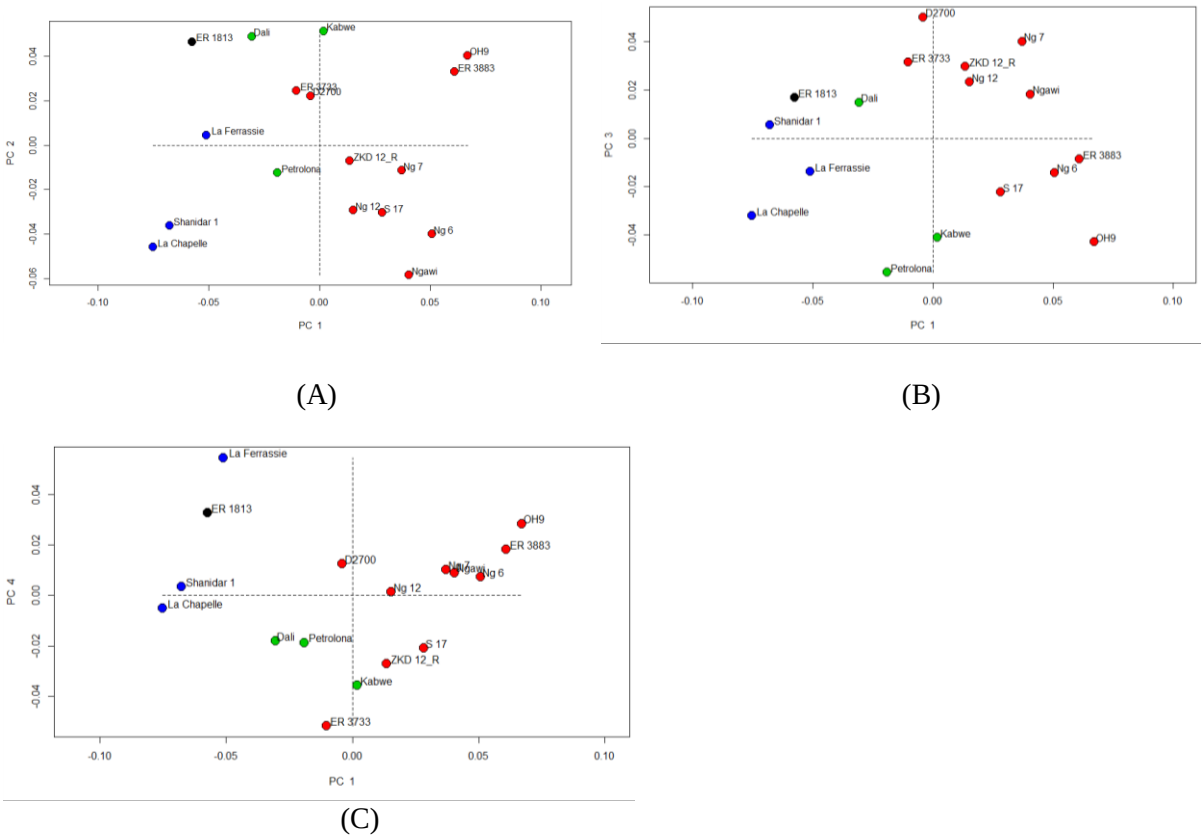

Figure 8.24 The PCA plots of the fossil sample (discrete landmarks of the frontal region)
(A) PC 1 and PC 2. (B) PC 1 and PC 3. (C) PC 1 and PC 4.

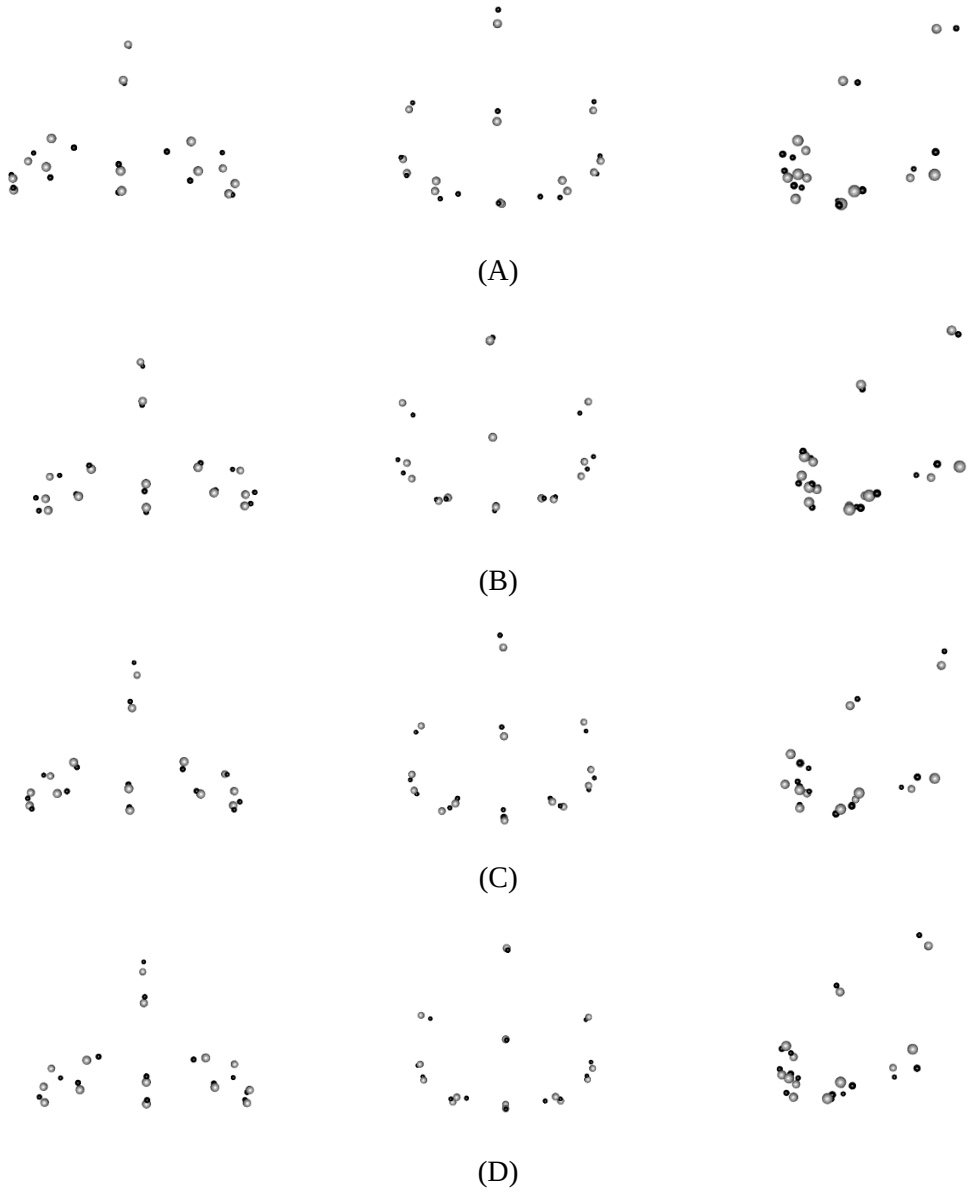

Figure 8.25 Shape changes in PC 1 to 4 of *H. sapiens* and fossils (discrete landmarks of the frontal region) (A) The shapes at the two ends of PC 1. (B) The shapes at the two ends of PC 2. (C) The shapes at the two ends of PC 3. (D) The shapes at the two ends of PC 4. The grey points represent the shape at the negative end. The black points represent the shape at the positive end. From left to right: lateral view, superior view and lateral view. The graphs are generated by the Geomorph R package (Adams et al., 2018).

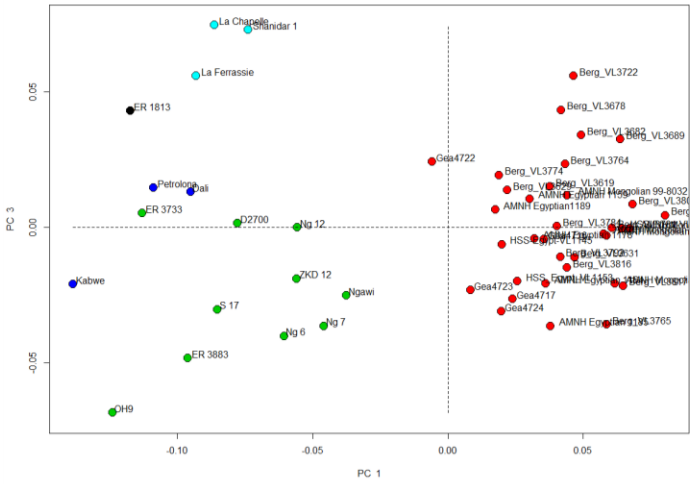

Figure 8.26 The PC 1 and PC 3 plot of *H. sapiens* and fossils (discrete landmarks of the frontal region)

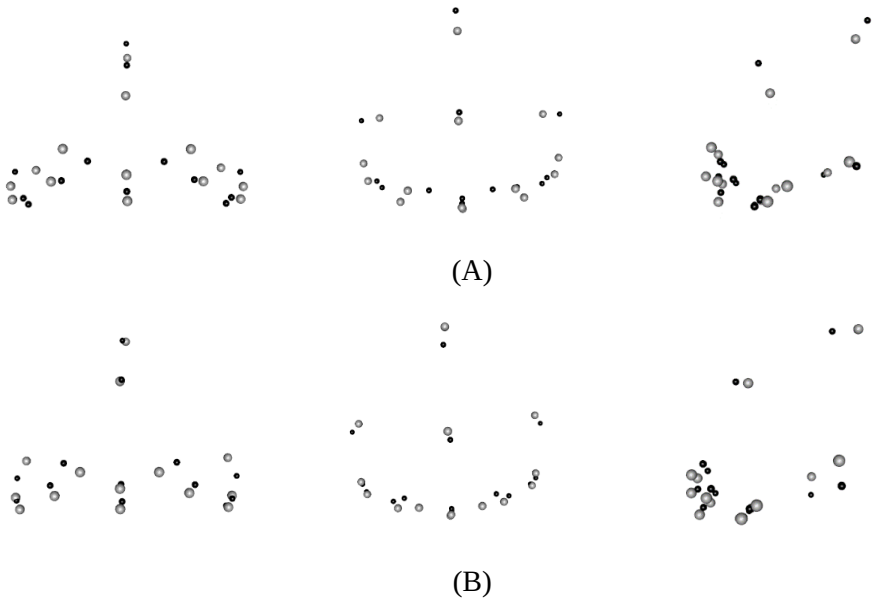

(A)

(B)

Figure 8.27 Shape changes in PC 1 and PC 3 of *H. sapiens* and fossils (discrete landmarks of the frontal region)

(A) The shapes at the two ends of PC 1. (B) The shapes at the two ends of PC 3. The grey points represent the shape at the negative end. The black points represent the shape at the positive end. From left to right: lateral view, superior view and lateral view. The graphs are generated by the Geomorph R. package (Adams et al., 2018).

When using only 15 discrete landmarks placed in the frontal region, PC 1 to PC 3 based on the fossil set are roughly consistent with the corresponding PCs from the maximum-semilandmark set. PC 1 shows a very similar distribution of specimens because these discrete landmarks show similar shape differences revealed by PC 1 of the anchor-point dataset, such as overall thickness of the brow, degree of frontal rise, position of the highest point of the brow and general orientation of glabellar and supraorbital surfaces (Figure 8.24 and Figure 8.25A).

PC 2 is also roughly comparable to PC 2 of the anchor-point set, though the Ngandong specimens overlap with the Neanderthals, ZKD 12 and Petrolona (Figure 8.24 and Figure 8.25B). Again, these discrete landmarks can reflect a decrease in size of the supraorbital region relative to the mediolateral wider frontal squama, a slightly superiorly shift of the glabellar region, and a posterior shift of the glabellar region in a specimen plotted closer to this PC's positive end. However, it cannot capture details such as the concavity at the medial part of the brow because no landmark is placed there.

PC 3 is similar to PC 3 from the previous analysis, but the separation between D2700 and other fossils is greatly reduced (Figure 8.24 and Figure 8.25C). PC 3 continues to show that in a specimen plotted closer to D2700, the brow becomes superoinferiorly thinner, the glabellar profile becomes more posteriorly sloping and bregma lies more posteroinferiorly. It cannot show differences such as a superoinferior lateral thinning of the brow and the formation of the posttoral plane. This probably explains why D2700 is less separated from the other fossils.

PC 4 shows a different distribution of specimens compared to the corresponding PCs from the anchor-point and the maximum-semilandmark dataset, though KNM-ER 3733 remains separated from other fossils (Figure 8.24 and Figure 8.25D). La Ferrassie 1 and KNM-ER 3883 are placed at the opposite end. They are close to the Ngandong-Ngawi specimens and OH 9. This PC shows that in a specimen plotted closer to KNM-ER 3733 end, the highest point of each brow lies more laterally, the brow becomes superoinferiorly thinner overall, the glabellar region lies more inferiorly and frontal rise becomes steeper.

With the large *H. sapiens* sample, PC 1 and PC 3 are comparable to the corresponding PCs in the analysis of anchor-points or semilandmarks (Figure 8.26 and Figure 8.27). PC 1 separates fossil specimens from specimens of the *H. sapiens* sample because the discrete landmarks can capture overall size and protrusion of the supraorbital region and flatness of the frontal bone. PC 2 plots the three Neanderthals at the positive end, well separated from the *H. erectus* specimens. OH 9 is at the opposite end. This PC continues to show a medial shift of the highest point at the superior margin of the brow as well as an anteroposterior elongation of the frontal bone in a specimen plotted closer to OH 9.

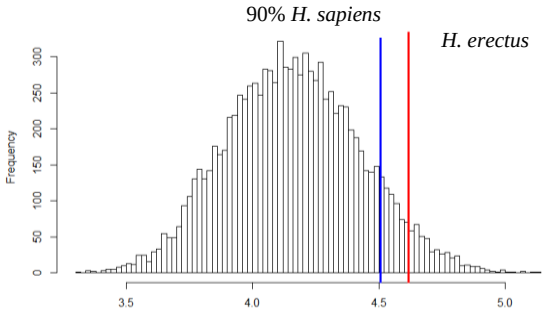

Figure 8.28 The bootstrapped analysis of SSDs based on the discrete landmarks of the frontal region
The red line represents the SSD of the *H. erectus* sample. The blue line indicates the 90th percentile of the bootstrapped *H. sapiens* SSDs.

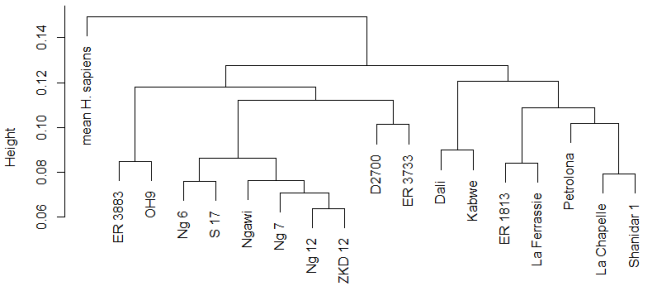

Figure 8.29 The UPGMA dendrogram (the discrete landmarks of the frontal region)

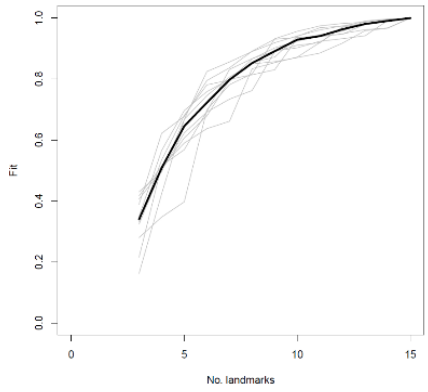

Figure 8.30 The mean LASEC based on the discrete landmarks of the overall cranium

The bootstrap analysis shows that the SSD of the *H. erectus s. l.* sample is still significantly great, as it exceeds 9,537 (95.37%) of the *H. sapiens* SSDs (Figure 8.28). The UPGMA dendrogram shows some differences with that based on the maximum-semilandmark set. In the current analysis, all *H. erectus* specimens group together (Figure 8.29). KNM-ER 1813 and three mid-Pleistocene *Homo* group with Neanderthals in a separate cluster. In this analysis, the mean LASEC obtained with 10 rounds of resampling shows a consistent increase in fit value when the number of landmarks increases (Figure 8.30). This result is similar to the LASEC analysis based on anchor points or surface semilandmarks.

9.0 DISCUSSION AND CONCLUSION

9.1 PROBLEMS OF MORPHOLOGICAL INTERPRETATION IN PCA

The main purpose of this dissertation is to explore whether GMA based on sampling dense semilandmarks is useful to capture and identify specific morphological features of cranial remains commonly allocated to *H. erectus*. In order to fulfill this goal, PCA is used because this is the most popular method for visualizing the degrees and patterns of overall shape differences within a group of specimens. Usually, the distribution of specimens in a few higher ranked PCs that can explain a large proportion of the total variance is an important kind of evidence for classifying fossils.

As discussed in Chapter 4, a PC specifies a direction of shape differences that can be visualized as landmark displacements (Baab et al., 2012; Klingenberg, 2013; Zelditch et al., 2012). Therefore, PCA is usually used to provide a morphological explanation for grouping specimens, based on the degree and patterns of overall similarity. For example, Lordkipanidze et al. (2013, p. 329) believed that PC 1 of their GMA successfully arranged specimens from "large-faced/prognathic" individuals to "small-faced/orthognathic" individuals. Baab (2016) used a few higher-ranked PCs to draw a morphological boundary around *H. erectus*, based on the distribution of specimens commonly allocated to *H. erectus*, *H. habilis*, Mid-Pleistocene *Homo* and *H. neanderthalensis*. Relying on visualizing shape differences in each PC, she concluded that her *H. erectus* sample differed from early *Homo* in having features such as a flatter and anteroposteriorly elongated vault, more posteriorly positioned inion, and mediolaterally wider cranium (Baab, 2016). Terhune et al. (2007) even summarized a list of "features" in the temporal bone according to shape differences demonstrated by PC 1 and PC 2. For example, they concluded that PC 1 and PC 2 jointly show differences in the depth and mediolateral width of the mandibular fossa.

Nevertheless, a PC is essentially an axis in shape space and a mathematical construction (Adams et al., 2011; Zelditch et al., 2012). This is because the generation of PCs is completely free from human intervention, but solely based on the spatial distribution of a group of points (i.e., the shapes of a group of specimens) in shape space (Adams et al., 2011; Zelditch et al., 2012). For example, PC 1 always lies in a direction such that a group of points, after being projected to this PC, is more separated than projections to any other axes (Adams et al., 2011; González-José et al., 2011; Zelditch et al., 2012). Therefore, a PC

is a statistically meaningful variable because it can explain a substantial amount of the total variance within a specific group of landmark configurations.

However, whether a PC is biological meaningful depends on specific biological questions and how researchers interpret it (Zelditch et al., 2012). In paleoanthropology, grouping specimens into species must be based on scrutinizing the morphology of individual specimens (Schwartz & Tattersall, 2002, 2003; Zeitoun, 2009). In particular, an individual specimen, if it presents some unique features, can represent a distinct species (Schwartz & Tattersall, 2002, 2003; Zeitoun, 2009). Therefore, when using spatial distributions of specimens in a PC or in a combination of two PCs to group specimens, one should examine whether visualized shape differences in these PCs can properly represent morphological differences between individual specimens. For example, when a PC appears to demonstrate differences in degree of frontal rise, one should consider whether these differences match those of actual specimens. This does not mean that a PC is morphologically meaningless. It can reveal some morphological differences between some specimens but not others (see later discussion). Furthermore, some specimens may present details that are not demonstrated by some higher-ranked PCs, such as having a post-toral sulcus. In this situation, alternative groupings specimens based on morphological detail should not be ignored.

Nevertheless, as reviewed previously, paleoanthropologists usually directly interpret PCs without carefully comparing individual specimens (e.g., Baab, 2016; Terhune et al., 2007). Though admitting the problem of missing detail, they usually believed that a few higher-ranked PCs, which explain a large proportion of the total variance, can reflect "the most variable aspects of morphology" within a group of specimens (Baab, 2016, p. 8; Harvati et al., 2010; Terhune et al., 2007). As a result, shape differences described by a few higher-ranked PCs were simply treated as major, or at least gross morphological differences between specimens.

A fundamental assumption regarding the use of PCA is that morphological differences between fossil specimens can be treated as geometric differences between shapes. In this way, overall morphological differences can be equated with overall shape differences. This is because PCA operates in the shape space (more accurately, the tangent Euclidean space that preserves nearly identical information in the shape space). In a shape space, the distribution of points (shapes) is determined by Procrustes distances, which measure overall differences between shapes. Thus, overall similar shapes are represented by points that lie close to each other in a shape space. The purpose of applying PCA is to use a few higher-ranked PCs to recapitulate spatial distribution of a group of points in a hyperdimensional shape space (Adams et al., 2011; Slice et al., 2007; Zelditch et al., 2012). This eases the process of interpreting overall shape differences, which are then transformed to morphological differences.

Noteworthy, landmark configurations, after sampled from actual specimens, can be called shapes only when information about sizes, locations, and orientations are removed by Procrustes superimposition, because they are believed to be irrelevant to shape differences in mathematical sense (it should be noted that in some biological studies, such as ontogenetic analysis, size and shape can be associated and can be explored by methods like regression analysis) (Zelditch et al., 2012). The logic is that shape differences, such as those between two triangles, is irrelevant to their sizes, locations, and orientations (Zelditch et al., 2004). Thus, the differences between more complicated biological shapes should also be free from these factors (Zelditch et al., 2004). After this process, the landmark configurations become shapes and are superimposed onto each other (Zelditch et al., 2004). The Procrustes distances between any two shapes are then calculated from the sum of differences between positions of every pair of corresponding landmarks. In this way, the overall shape differences represented by spatial distribution of points in a shape space ultimately reflect the positional differences between every pair of corresponding landmarks in the original superimposed shapes.

Therefore, accepting that a specimen can be treated as a shape is equal to accepting that one can read morphological differences simply from reading differences in landmark locations in a group of Procrustes superimposed shapes. In fact, in order to assess what "morphological differences" can be captured by their landmark data, some researchers only compared Procrustes superimposed shapes without examining actual specimens (e.g., Freidline, Gunz, Harvati, et al., 2012; Freidline, Gunz, Janković, et al., 2012; Harvati et al., 2010)

Nevertheless, when the Procrustes superimposition eliminates the effect of orientation, the sole criterion is to minimize the overall differences, i.e., the sum of squared difference between every pair of corresponding landmarks (Richtsmeier et al., 2002; Zelditch et al., 2012). In this way, the landmark configurations used in an analysis are rotated until their overall differences are minimized. The exact angles that these configurations deviate from each other are unpredictable and uncontrollable (Richtsmeier et al., 2002). This is because the final orientations of configurations totally depend on the specimens brought into an analysis as well as the landmarks sampled from these specimens (Richtsmeier et al., 2002). The process of rotation in the Procrustes superimposition certainly influences positional differences of corresponding landmarks in different landmark configurations, thus influencing the results of Procrustes distances between them (Richtsmeier et al., 2012). Therefore, the distribution of shapes in a shape space is produced by not only their overall morphological differences but also the Procrustes superimposition (Richtsmeier et al., 2012).

Yet, orientation matters when assessing morphological differences. There are many observed morphological features that depend on the orientations of specimens, such as the lateral profile of the frontal bone, the orientation of the supraorbital region, the course of the squamosal suture, and the

inclination of the occipital and nuchal planes. Because shapes are oriented inconsistently by the Procrustes superimposition, positional differences of corresponding landmarks in a group of superimposed shapes may not match observed morphological differences. Consequently, the distribution of these shapes in a shape space and the Procrustes distances that separate them also may not appropriately reflect overall morphological differences. If so, shape differences revealed by PCA, which only operates in the shape space, may not match observed morphological differences, not even gross differences. Consequently, groupings based on Procrustes distances and the spatial distribution of points in higher-ordered PCs may be different from the results of comparative morphology.

In the following text, "shape difference" is used to refer to differences between landmark configurations after the Procrustes superimpositions; "morphological difference" refers to differences between actual specimens aligned consistently by the Frankfurt plane. When interpreting the results of GMAs, especially when using PCA, paleoanthropologists usually ignore the effect of specimen orientation, which result in grouping specimens based on shape rather than actual morphological differences. Richtsmeier et al. (2002) did point out the problem of orientation produced by the Procrustes superimposition. However, they did not offer concrete examples to support their view.

In order to assess whether higher-ranked PCs appropriately reflect observed morphology (both details and gross morphology), it is necessary to compare visualized shape differences between individual specimens in each PC to observed morphological differences. In the following discussion, I carefully compared observed morphology and shape differences visualized by each PC. I particularly provide example to show how Procrustes superimposition may create incompatibility between GMA and observed morphology.

9.1.1 The overall cranial profile

In this study, the semilandmark datasets of entire and posterior crania were designed to capture differences in overall cranial profiles. In the PCA of the posterior cranium, PC 1 primarily separates Neanderthals from *H. erectus* by plotting them at its positive and negative halves, respectively (Figure 6.1). When taking results of visualization for granted, this PC shows that the Asian *H. erectus* specimens and KNM-WT 15000, which are plotted closer to Neanderthals, have more superoinferiorly and mediolaterally expanded posterior vault than KNM-ER 3733, KNM-ER 3883, and D2700 (Figure 6.2 and Figure 9.1). In particular, in the Asian specimens and KNM-WT 15000, the mid-parietal region becomes more bulging superiorly.

However, it is difficult to link these shape differences to actual morphology. When simply looking at the height of the posterior cranium, the Ngandong specimens and KNM-ER 3733 are

moderately tall superoinferiorly (Schwartz & Tattersall, 2003) (Figure 9.2 and Figure 9.5). The crania of other specimens, including KNM-WT 15000, S 17, S 2, and D2700, can be described as fairly low superoinferiorly (Schwartz & Tattersall, 2003) (Figure 9.2 and Figure 9.5). Their lateral profiles are also different. Based on orienting these specimens in the Frankfurt plane, the lateral profiles of all specimens except KNM-ER 3883 peaks at bregma (Schwartz & Tattersall, 2003) (Figure 9.2). In Ngandong and Sangiran specimens, the lateral contours of the anterior parietal bones are relatively straight and slightly downward sloping, while that of KNM-WT 15000 is almost horizontal. Posterior to the parietal bones, the lateral contours of all specimens then gently curve downward toward their occipital flexures. Therefore, the posterior vaults of KNM-WT 15000, and the Sangiran and Ngandong specimens are long and flat overall. On the other hand, in KNM-ER 3733 (especially in left lateral view) and D2700, the lateral profiles curve downward relatively sharply toward the occipital flexure. In particular, KNM-ER 3733's posterior vault is even relatively superoinferiorly short, because its nuchal plane is only moderately downwardly inclined (Schwartz & Tattersall, 2003). The lateral profile peaks well-behind bregma only in KNM-ER 3883 (Figure 9.2). Thus, the posterior vault can be described as superoinferiorly expanded only in KNM-ER 3883 (Schwartz & Tattersall, 2003).

Based on the above summary, it is difficult to understand why PC 1 plots KNM-ER 3733, KNM-3883, and D2700 very close to each other at its negative end, suggesting they all have similarly anteroposteriorly long, superoinferiorly short, and posteriorly flat vaults. Equally confusing is that KNM-WT 15000, S 2 and S 17, regardless of their differences in morphological detail, are plotted close to the Ngandong specimens, indicating that they have similarly superoinferiorly tall vaults.

Some clues for deciphering this intriguing arrangement of specimens can be found in the Procrustes superimposed landmark configurations. The Procrustes superimposition rotates semilandmark configurations to minimize the sum of positional differences between all pairs of corresponding semilandmarks and landmarks. As a result, relative to KNM-ER 3883, both KNM-ER 3733 and D2700 are rotated posterosuperiorly to minimize differences between corresponding landmarks at the vault (Figure 9.2 and Figure 9.4 (A) and (B)). Because of this kind of rotation, the lateral profiles of KNM-ER 3733 and D2700 become well aligned with that of KNM-ER 3883, rather than being more downwardly inclined (Figure 9.2 and Figure 9.4 (A) and (B)). Consequently, it is no surprise that the first PC, which appears to reveal differences in lateral profiles of the posterior vaults, plots these specimens very close to each other.

Meanwhile, KNM-ER 3883 itself also rotates posteroinferiorly in left lateral view relative to the specimens that have low and flat posterior vault, such as S 17 and KNM-WT 15000 (Figure 9.2 and Figure 9.4 (C) and (D)). After this rotation, KNM-ER 3883's vault is also well-aligned with S 17 and KNM-WT 15000. Thus, when only relying on the results of the Procrustes superimposition, one may

conclude that the lateral contour of KNM-ER 3883 does not peak midway along the parietal bone, but gently curves backward and downward from bregma, roughly similar to S 17 and KNM-WT 15000 (Figure 9.2 and Figure 9.4 (C) and (D)). In this way, the posterior vault of KNM-ER 3883 does not appear to be superoinferiorly expanded, but becomes low and flat. As a result, the perplexing arrangement of specimens in PC 1, which suggests that KNM-ER 3883 has an even somewhat superoinferiorly shorter posterior vault than all other *H. erectus* specimens, is probably influenced by the Procrustes superimposition in this study.

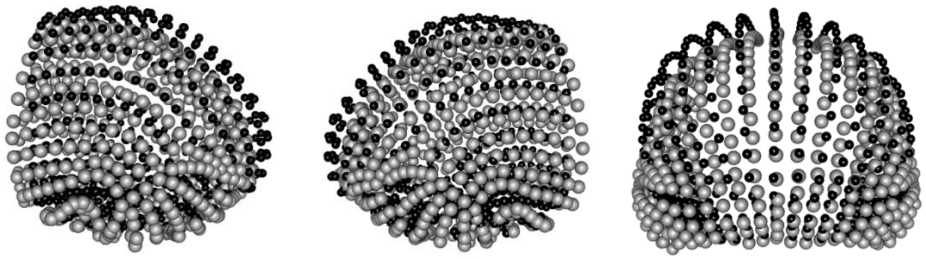

Figure 9.1 The shapes at two ends of PC 1 of entire crania of fossils (the maximum-semilandmark dataset)
The grey dots represent the shape at the negative end of PC 1. The black dots represent the positive end of PC 1. From left to right: left lateral view, right lateral view, and posterior view. Graphs are generated by the Geomorph R package (Adams et al., 2018).

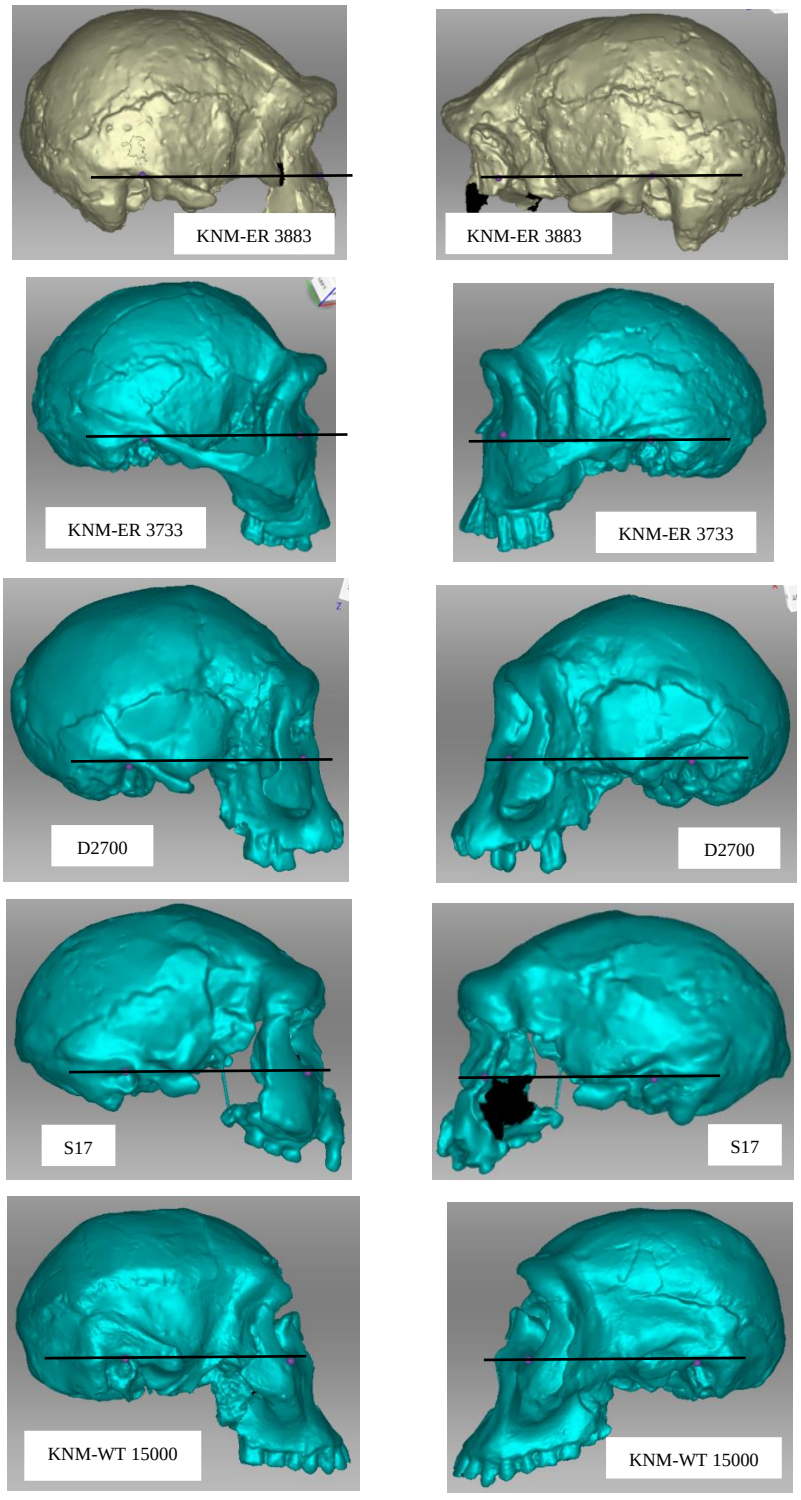

Figure 9.2 The 3D models of KNM-ER 3883, KNM-ER 3733, D2700, S 17 and KNM-WT 15000
The 3D models (Artec 3D Inc., 2018) of these specimens (see Appendix A) are aligned by the Frankfurt plane, which is marked by the black line in each graph.

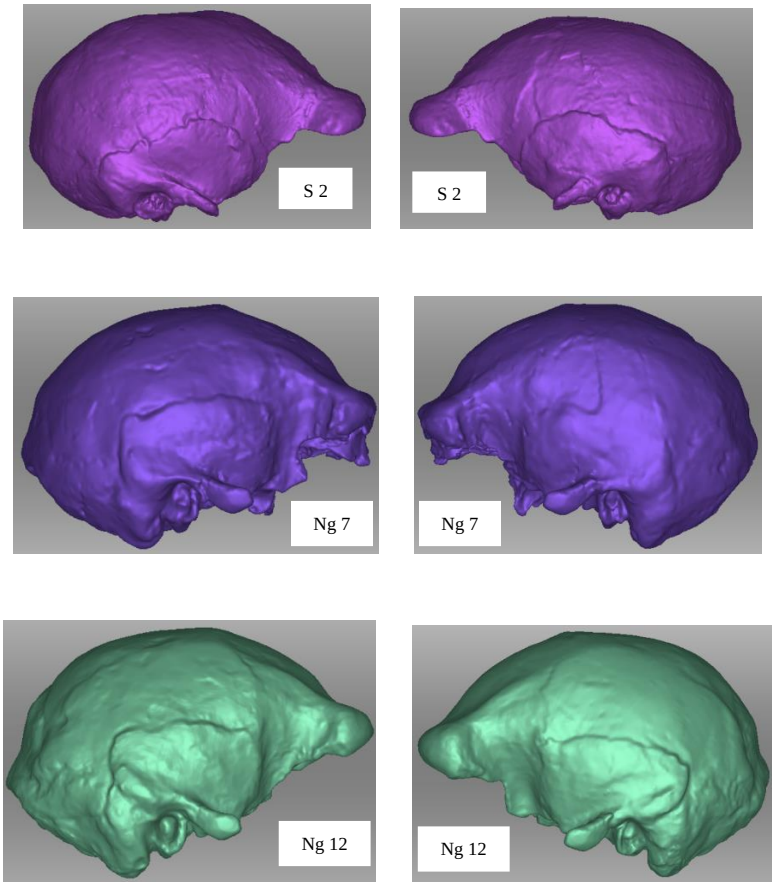

Figure 9.3 The 3D models of S 2, Ng 7 and Ng 12 (Artec 3D Inc., 2018)

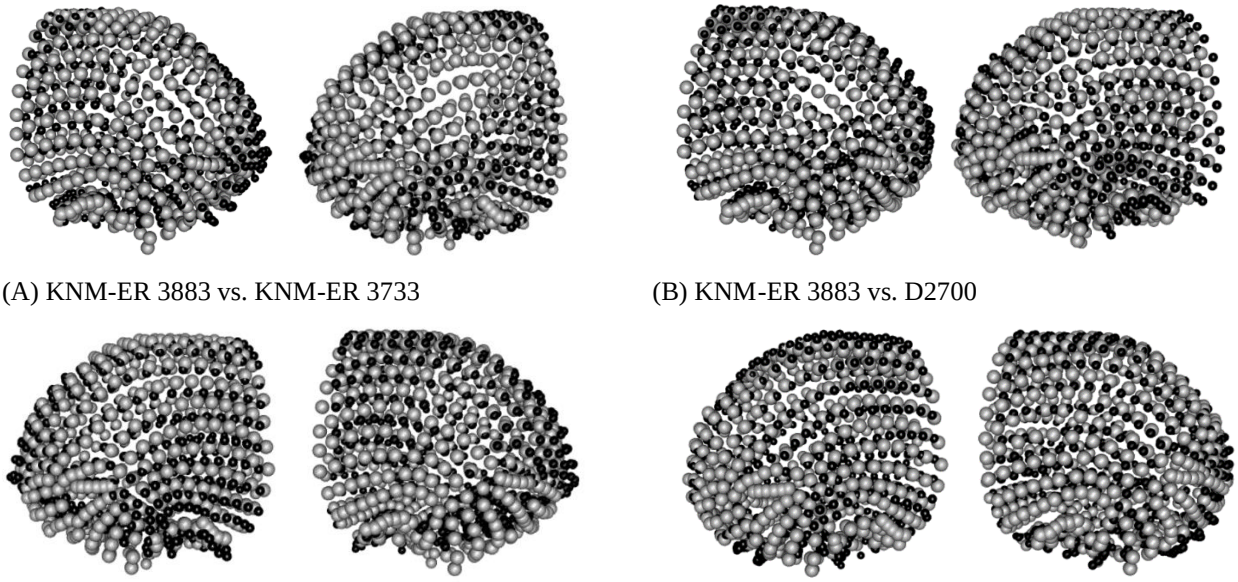

(A) KNM-ER 3883 vs. KNM-ER 3733

(B) KNM-ER 3883 vs. D2700

(C) KNM-ER 3883 vs. S 17

(D) KNM-ER 3883 vs. KNM-WT 15000

Figure 9.4 The Procrustes superimposition of KNM-ER 3883, KNM-ER 3733, D2700, S 17 and KNM-WT 15000

The results of the Procrustes superimposition are based on the maximum landmark dataset of posterior crania of fossils. In each graph, the grey dots represent the semilandmark configuration of KNM-ER 3883. Graphs are generated by the Geomorph R package (Adams et al., 2018).

S 2's position in the PC 1 of the posterior cranium is also intriguing (Figure 6.1). This PC plots S 2 at the positive boundary of the *H. erectus s. l.* cluster, suggesting it has a superiorly and mediolaterally more expanded vault than most other *H. erectus* specimens. However, S 2 has a quite superoinferiorly short posterior vault (Figure 9.3 and Figure 9.5). In particular, its posterior cranial profile is uniquely "much wider than superoinferiorly tall", resembling the type specimen of *H. erectus*, Trinil 2 (Schwartz, 2016, p. 95) (Figure 9.3 and Figure 9.5). To the contrary, the mediolateral widths of all other *H. erectus* cranial specimens are in general less than their superoinferior heights. Therefore, it is unlikely that S 2 should be plotted closer to Neanderthals in PC 1, who have superiorly and mediolaterally more expanded vaults than all other fossils in this study.

The unexpected position of S 2 in PC 1 is probably a joint product of its unique gross cranial morphology and the Procrustes superimposition. After the Procrustes superimposition, the mid-sagittal line in S 2's cranial roof is well aligned with the mid-sagittal lines of the other *H. erectus* specimens, including the Ngandong specimens, which have relatively superoinferiorly tall vault (Figure 9.6). This is partly because the Procrustes superimposition first scales the centroid sizes of all specimens into the unit quantity, hence reducing their differences in absolute heights. It should also be noted that S 2 has a

relatively flat and mediolaterally wide roof, which curves almost at a right angle into the nearly straight and vertical side wall. However, the roofs of other *H. erectus* are more-or-less inferiorly inclined from the peak at the mid-sagittal line and relatively mediolaterally narrow (Figure 9.5). Because the mid-sagittal lines of these specimens are roughly aligned after the Procrustes superimposition, S 2's semilandmarks at the region where the roof curves downward into the side walls side are somewhat more superolaterally positioned than those of the other *H. erectus* (e.g., KNM-ER 3733, KNM-ER 3883, and Ng 12 as shown in Figure 9.6). Recall that PC 1 of the posterior crania of fossils shows that in a specimen plotted closer to its positive end, the vault not only becomes taller superoinferiorly, as semilandmarks at the roof lie more superiorly, but also wider mediolaterally, because semilandmarks at the regions where the roof curves downward into the side walls lie more superolaterally (Figure 9.1). Therefore, the reason that S 2 is plotted closer to the positive end (Neanderthals) of PC 1 of the posterior crania of fossils than the other *H. erectus* is probably caused by differences in semilandmark positions described above. These differences are ultimately a joint of the unique posterior profile of S 2 and the way it is superimposed with the other specimens.

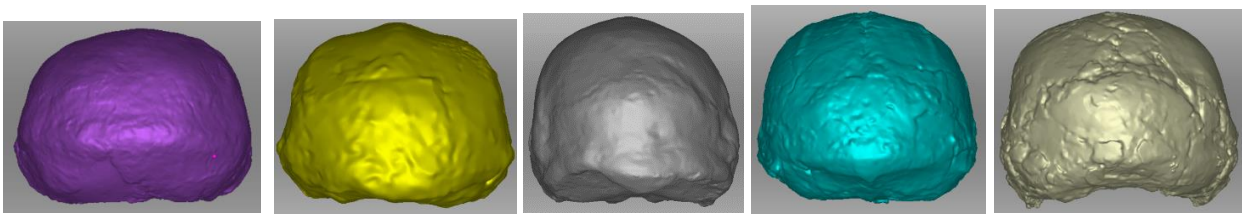

Figure 9.5 The posterior view of 3D models of *H. erectus* specimens
From left to right: S 2, S 17, Ng 12, KNM-ER 3733 and KNM-ER 3883 (Artec 3D Inc., 2018).

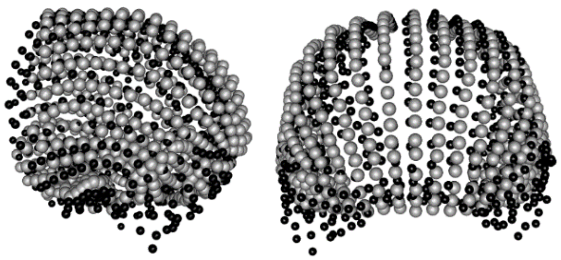

(A) S 2 vs. ER 3883

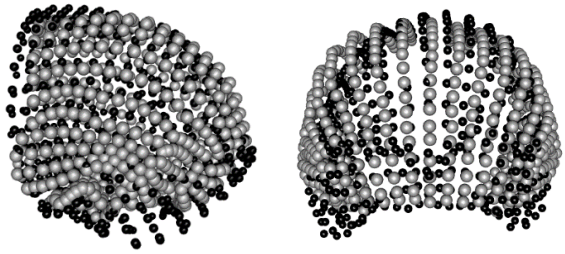

(B) S 2 vs. Ng 12

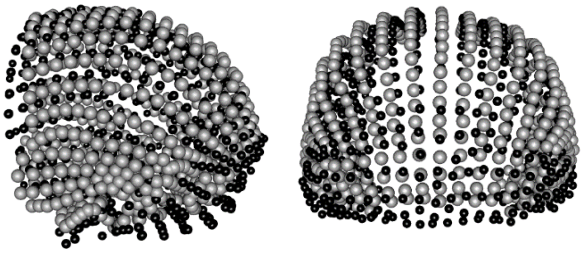

(C) S 2 vs. ER 3733

Figure 9.6 The Procrustes superimposition of S 2 and three other fossils after Procrustes fit
(A) S 2 and ER3883. (B) S 2 and Ng 12. (C) S 2 and ER 3733. The configurations with grey dots are S 2, while the ones with black dots are the others. These configurations are based on the maximum-semilandmark sets of the posterior cranium. The magnitude of differences is amplified 1.5 times for better visualization. Graphs are generated by the Geomorph R package (Adams et al., 2018).

PC 1 of the entire cranium shows a distribution of specimens comparable to that in PC 1 of the posterior cranium (Figure 5.1 and Figure 6.1). Again, Asian *H. erectus* are plotted somewhat closer to Neanderthals than *H. ergaster*. Similar to PC 1 of the posterior cranium, this PC shows that Asian *H. erectus* have slightly more superiorly and mediolaterally expanded posterior vaults than *H. ergaster* (Figure 5.2 and Figure 9.7). These results are likely influenced by the Procrustes superimposition in a way similar to the analysis of the posterior crania of fossils. For example, KNM-ER 3733 and D2700, whose lateral contours of the posterior vaults are more downwardly inclined from bregma, tilt slightly posterosuperiorly (Figure 9.8). Meanwhile, KNM-ER 3883, whose lateral profile peaks behind bregma, tilts somewhat posteroinferiorly (Figure 9.8). Thus, the lateral profiles of the posterior vaults of these specimens become similarly superoinferiorly low and flat like the profiles of S 17 and the Ngandong specimens.

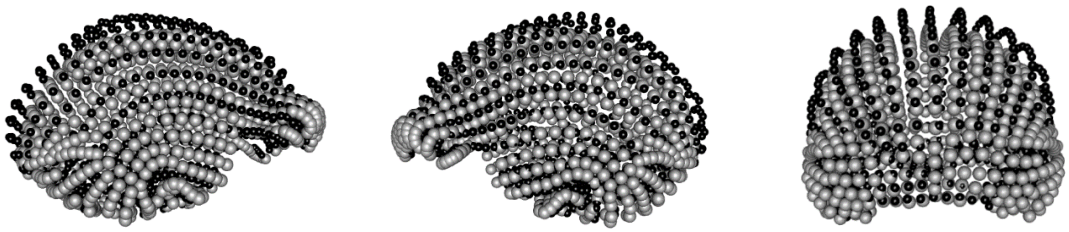

Figure 9.7 The shapes at two ends of PC 1 of entire crania of fossils (the maximum-semilandmark dataset) The grey dots represent the shape at the negative end of PC 1. The black dots represent the positive end of PC 1. From left to right: left lateral view, right lateral view, and posterior view. Graphs are generated by the Geomorph R package (Adams et al., 2018).

Despite the profiles of the posterior vaults, differences in the degrees of frontal rise demonstrated by PC 1 of the entire cranium are also difficult to match with observed morphological conditions. This PC shows that a specimen plotted closer to its positive end has a steeper frontal rise because semilandmarks at the mid-frontal region lie more anterosuperiorly (Figure 5.1, Figure 5.2 and Figure 9.7). It is acceptable to plot the Ngandong specimens to more positive positions than KNM-ER 3883 and D2700 in PC 1, because the former have a steeper frontal rise. However, KNM-ER 3733, which has a relatively steep frontal rise, is plotted very close to KNM-ER 3883 and D2700; whereas S 17, which has a relatively low and flat frontal bone, is plotted very close to the Ngandong specimens.

The influence of the Procrustes superimposition on the relative steepness of frontal rise is complicated. The Procrustes superimposition does alter somewhat the relative steepness of the frontal rise in some specimens by rotating them to different angles. As discussed previously, KNM-ER 3883, which has a relatively flat forehead and gentle frontal rise, slightly tilts posteroinferiorly relative to specimens such as S 17 and D2700 (Figure 9.8). This rotation makes the frontal rise of KNM-ER 3883 somewhat gentler. For example, when aligning KNM-ER 3883 by the Frankfurt plane, this specimen has a slightly steeper frontal rise than S 17. However, after the Procrustes superimposition in this analysis, KNM-ER 3883's lateral frontal rise becomes slightly gentler than that of S 17 (Figure 9.8 (C)). This rotation during the Procrustes superimposition may contribute to plotting KNM-ER 3883 at the negative end of PC 1 of the entire cranium, indicating that it has the least steep frontal rise. Moreover, the Ngandong specimens also appear to slightly tilt posteroinferiorly relative to S 17. Thus, their degrees of frontal rise decrease slightly, so that their frontal bones are well-aligned with S 17's frontal bone (Figure 9.8 (D) and (E)). This perhaps helps to explain why S 17 is plotted very close to the Ngandong specimens, suggesting they have similar frontal rise.

(A) KNM-ER 3883 vs. KNM-ER 3733 (B) KNM-ER 3883 vs. D2700 (C) KNM-ER 3883 vs. S 17

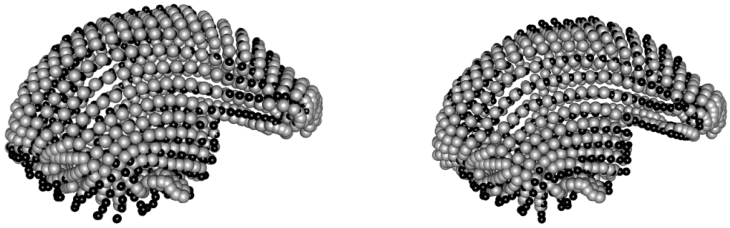

(D) S 17 vs. Ng 7 (E) S 17 vs. Ng 12

Figure 9.8 The Procrustes superimposition of KNM-ER 3883, KNM-ER 3733, D2700, S 17, Ng 7 and Ng 12
The results of the Procrustes superimposition are based on the maximum landmark dataset of entire crania of fossils. In (A), (B) and (C), the configurations with grey dots represent KNM-ER 3883. In (D) and (E), the configurations with black dots represent S 17. Graphs are generated by the Geomorph R package (Adams et al., 2018).

As previously discussed, KNM-ER 3733 is rotated slightly posterosuperiorly relative to most other *H. erectus* specimens, in particular KNM-ER 3883. This rotation also slightly increases the steepness of frontal rise of KNM-ER 3733. Therefore, it is still difficult to decipher why PC 1 of the entire cranium plots KNM-ER 3733 to a position slightly negative to S 17, whose frontal rise is much lower. A possible reason is that KNM-ER 3733 has a distinct post-toral sulcus (Schwartz & Tattersall, 2003) (Figure 9.2). Its frontal squama then rises sharply from behind this sulcus (Schwartz & Tattersall, 2003). Therefore, after the Procrustes superimposition, semilandmarks at the post-toral sulcus and the inferior half of the frontal squama in KNM-ER 3733 are positioned more posteroinferiorly than corresponding semilandmarks of the other *H. erectus* specimens, including S 17 (Figure 9.9 (A)). PC 1 of the entire crania of fossils shows that in a specimen plotted closer to its positive end, semilandmarks at the middle and lower frontal regions lie more anterosuperiorly, resulting in an increase in steepness of frontal rise. Thus, the presence of the posterior sulcus in KNM-ER 3733 and the way its frontal squama is superimposed with other *H. erectus* perhaps contribute to assigning this specimen a very negative position in this particular PC.

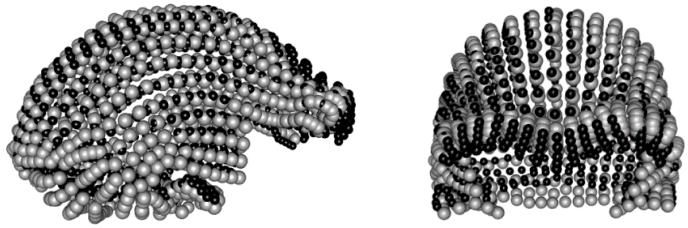

(A) S 17 vs. KNM-ER 3733

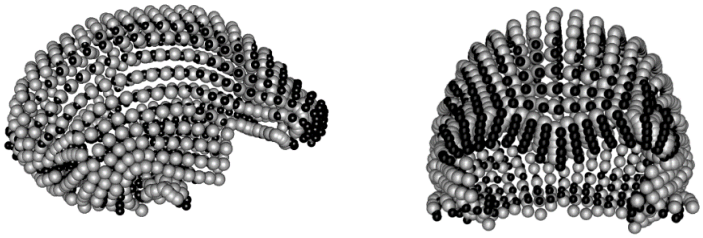

(B) S 17 vs. D2700

Figure 9.9 The Procrustes superimposition of S 17, KNM-ER 3733 and D2700
The results of the Procrustes superimposition are based on the maximum landmark dataset of entire crania of fossils. In each graph, the configuration with black dots represents S 17. Graphs are generated by the Geomorph R package (Adams et al., 2018).

PC 2 of the entire cranium also show some differences in the frontal region (Figure 5.1). These differences are probably influenced by the Procrustes superimposition. This PC shows that in a specimen plotted closer to the positive end, the frontal bone becomes longer anteroposteriorly as semilandmarks at the supraorbital region lie more anteroinferiorly, making the supraorbital region more anteroinferiorly facing (Figure 5.3 and Figure 9.10). Meanwhile, the supraorbital region becomes superoinferiorly thicker. Thus, when literally relying on this PC, the supraorbital regions of *H. ergaster*, which are plotted closer to the negative end of PC 1, are both more anterosuperiorly facing and superoinferiorly thinner than Asian *H. erectus* (Figure 5.1, Figure 5.3 and Figure 9.10). Further, the frontal bones of *H. ergaster* are anteroposteriorly shorter than Asian *H. erectus*.

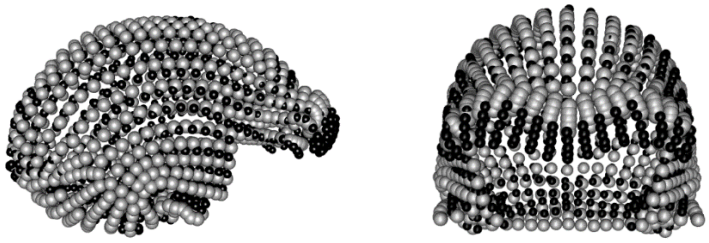

Figure 9.10 The shapes at two ends of PC 2 of entire crania of fossils (the maximum-semilandmark dataset) The grey dots represent the shape at the negative end of PC 1. The black dots represent the positive end of PC 1. From left to right: right lateral view and anterior view. Graphs are generated by the Geomorph R package (Adams et al., 2018).

In *H. ergaster*, KNM-ER 3733's superoinferiorly thin supraorbital tori are indeed anterosuperiorly facing (Figure 9.2). D2700's less developed descending part of the supraorbital region flows backward smoothly into the post-toral plane, hence also somewhat face anterosuperiorly. As discussed previously, the Procrustes superimposition tilts the landmark configurations of KNM-ER 3733 and D2700 slightly posterosuperiorly in order to better align their posterior vaults with the vaults of other *H. erectus*. This kind of rotation makes the supraorbital regions of KNM-ER 3733 and D2700 slightly less superiorly facing. However, compared to S 17, which is plotted closer to PC 2's positive end among *H. erectus*, KNM-ER 3733 and D2700's superoinferiorly thinner supraorbital regions still face more superiorly (Figure 9.9). Furthermore, KNM-ER 3733 and D2700's supraorbital regions are positioned slightly more posterosuperiorly than S 17 when superimposed, because KNM-ER 3733 and D2700 have relatively anteroposteriorly shorter frontal bones (Figure 9.9). Therefore, PC 2 can still reveal that KNM-ER 3733 and D2700 have anteroinferiorly shorter frontal regions and more superiorly faced brows than S 17, even after the Procrustes superimposition slightly alters their orientations.

However, KNM-ER 3883 is plotted to a more negative position than Asian *H. erectus* in PC 2 of the entire cranium (Figure 5.1). This position of KNM-ER 3883 in PC 2 indicates that KNM-ER 3883's frontal bone is somewhat shorter anteroposteriorly, and its supraorbital torus is superoinferiorly thinner and more anterosuperiorly facing than *Asian H. erectus*, in particular S 17 (Figure 5.3 and Figure 9.10). Yet, KNM-ER 3883 actually has a fairly anteroposteriorly long frontal bone, as well as a superoinferiorly thick and anteriorly facing supraorbital torus (Schwartz & Tattersall, 2003) (Figure 9.2). This position of KNM-ER 3883 in PC 2 of the entire cranium is probably influenced by the Procrustes superimposition, which alters its orientation relative to S 17. As previous discussed, KNM-ER 3883 tilts slightly posteroinferiorly relative to specimens with low and flat posterior vaults, such as S 17, for the purpose of reducing their overall shape differences. As a result, KNM-ER 3883's supraorbital torus is rotated slightly

superiorly, thus facing slightly more anterosuperiorly than S 17. In addition, KNM-ER 3883's supraorbital torus becomes increasing superoinferiorly thinner laterally, rather than uniformly thick, as in S 17. PC 2 shows that in a specimen plotted closer to the positive end, the supraorbital region becomes overall thicker superoinferiorly (Figure 5.3 and Figure 9.10). In particular, the descending part lateral to the highest point of each brow thickens superoinferiorly to a slightly higher degree than the ascending part. Therefore, the Procrustes superimposition and KNM-ER 3883's laterally thinning brows jointly contribute to plot KNM-ER 3883 to a more negative position of S 17 in PC 2 (Figure 5.1).

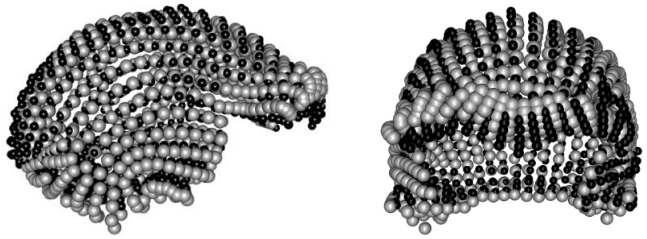

(A) KNM-ER 3883 vs. S 17

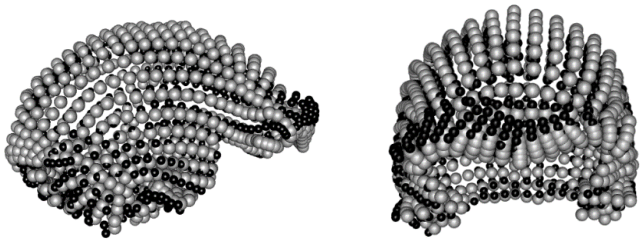

(B) Ng 12 vs. S 17

Figure 9.11 The Procrustes superimposition of KNM-ER 3733, S 17 and Ng 12
The results of the Procrustes superimposition are based on the maximum landmark dataset of the entire crania of fossils. In (A), the configuration with black dots represents S 17. In (B), the configuration with black dots represents S 17. Graphs are generated by the Geomorph R package (Adams et al., 2018).

In addition, KNM-ER 3883 is also plotted to a somewhat more negative position than the Ngandong specimens in PC 2 of the entire cranium (Figure 5.1). Though KNM-ER 3883 and the Ngandong specimens are also rotated slightly relative to each other by the Procrustes superimposition, their supraorbital regions are still well-aligned and anteriorly facing. Thus, the Procrustes superimposition perhaps does not have a strong effect on plotting KNM-ER 3883 to a more negative position than the

Ngandong specimens in this PC. As just discussed, PC 2 shows that in a specimen plotted closer to the positive end, the descending part of each brow becomes slightly more superoinferiorly thicker than the ascending part. Thus, the reason that KNM-ER 3883 is plotted to a more negative position than the Ngandong specimens is more likely that the brows of KNM-ER 3883 are laterally thinning superoinferiorly, whereas the brows of the Ngandong specimens are uniformly thick.

9.1.2 The occipital profiles

In the PCAs of the entire and posterior cranium, some PCs demonstrate differences in occipital profiles (Figure 5.1, Figure 6.1 and Figure 6.3). Yet, not all of these differences can match observed gross morphology. For example, PC 2 of the posterior cranium shows that in a specimen plotted closer to the positive end, inion shifts posterosuperiorly from a position below to above asterion (Figure 6.1 and Figure 6.3). The occipital plane becomes slightly more anteriorly sloping, and the nuchal plane becomes more downwardly inclined. Among *H. erectus* specimens, D2700 has the most negative score, while S 2 has the most positive score in this PC. Most other *H. erectus* specimens are plotted to intermediate positions, which are fairly close to each other.

The contrast of D2700 and S 2 in PC 2 of the posterior cranium match observed morphological differences in their occipital profiles. Relative to S 2, D2700's inion is more anteroinferiorly positioned, well below the position of asterion and close to the bottom of the posterior vault (Figure 9.2 and Figure 9.3). This is because the inferior part of D2700's nearly vertical occipital plane curves slightly anteriorly. Its nuchal plane is only slightly downwardly sloping. However, S 2 develops a "V-shaped" occipital profile, because its flat occipital and nuchal planes form similar angles with the horizontal plane (Schwartz & Tattersall, 2003). S 2's inion lies well above asterion, roughly at the middle of the height of its posterior vault in lateral view.

Nevertheless, differences between other specimens revealed by PC 2 in particular in inclination of the nuchal planes, do not fully conform to their actual morphological conditions. Among these specimens, KNM-WT 15000 is plotted very close to S 2, suggesting its occipital profile is very similar to S 2 (Figure 6.1). KNM-WT 15000's inion lies at the middle of the height of the posterior vault. Its inion also lies at the same height with asterion in lateral view. Because KNM-WT 15000's mastoid part of the temporal bone is tall superoinferiorly, its asterion lies superiorly in its vault relative to most other fossils, but similar to S 2 (Figure 9.2). However, KNM-WT 15000's occipital angle is slightly more obtuse than that of S 2, particularly because KNM-WT 15000's nuchal plane is more downwardly inclined (Figure 9.2 and Figure 9.3).

It should be noted that PC 2 also shows that in a specimen plotted closer to its positive end (S 2 and KNM-WT 15000), the entire nuchal plane not only becomes more downwardly inclined, it also lies more posteriorly. When superimposed, the anterior boundary of the nuchal plane in KNM-WT 15000 lies right beneath the corresponding part of S 2, rather than more anteriorly or posteriorly. This perhaps explains why KNM-WT 15000 is plotted very close to S 2 in PC 2 in the analysis of the posterior crania of fossils.

The position of KNM-ER 3733 in PC 2 is also interesting (Figure 6.1). KNM-ER 3733 is plotted away from both S 2 and KNM-WT 15000 in PC 2, indicating that KNM-ER 3733's inion lies slightly more inferiorly and nuchal plane less downwardly inclined. When comparing actual specimens, KNM-ER 3733's inion is indeed positioned more inferiorly at its vault relative to both S 2 and KNM-WT 15000, and its nuchal plane is not more downwardly inclined than S 2 and KNM-WT 15000. However, as previously discussed, KNM-ER 3733 is rotated slightly posterosuperiorly by the Procrustes superimposition to better align it with specimens with flatter lateral contours, such as S 2 and KNM-WT 15000 (Figure 9.4 and Figure 9.12). After this rotation, KNM-ER 3733's nuchal plane should become slightly more downwardly inclined and its inion slightly more upward positioned than their original positions (Figure 9.12). Because the scale of rotation is small, KNM-ER 3733's inion remains more inferiorly situated than S 2 and KNM-WT 15000 after the Procrustes superimposition. However, KNM-ER 3733's nuchal plane becomes slightly more downwardly inclined than in S 2 and similar to KNM-WT 15000. A possible reason contributing to plotting KNM-ER 3733 away from S 2 and KNM-WT 15000 in PC 2 is that when superimposed, semilandmarks at the nuchal plane of KNM-ER 3733 lie slightly more anteriorly than corresponding semilandmarks in S 2 and KNM-WT 15000. This is because PC 2 also shows that the nuchal plane of KNM-ER 3733 is more anteriorly positioned than those of S 2 and KNM-WT 15000.

S 17 is plotted to a position nearly identical to that of KNM-ER 3733 in PC 2 of the posterior cranium, indicating that S 17 and KNM-ER 3733 have very similar occipital profiles and positions of inions (Figure 6.1). However, S 17 has a nearly horizontal nuchal plane. Thus, S 17's inion lies near the inferior-most side of its vault. After the Procrustes superimposition, difference in inclinations of nuchal planes between S 17 and KNM-ER 3733 is still quite obvious: KNM-ER 3733 has a much more downwardly inclined nuchal plane than S 17 (Figure 9.12). However, when superimposed, KNM-ER 3733's nuchal plane lies more inferiorly but not more posteriorly than the nuchal plane of S 17. This may help to explain why S 17 and KNM-ER 3733 are plotted to nearly identical positions in PC 2.

Overall, differences in inclinations of nuchal planes revealed by PC 2 of the posterior cranium should not be equated to actual morphological conditions. The reason is not likely to be the Procrustes superimposition, which does not significantly alter relative degree of inclinations of nuchal planes in

different specimens. Perhaps PC 2 is more influenced by other differences, such as trajectories of the squamosal and parietomastoid sutures, which are discussed later.

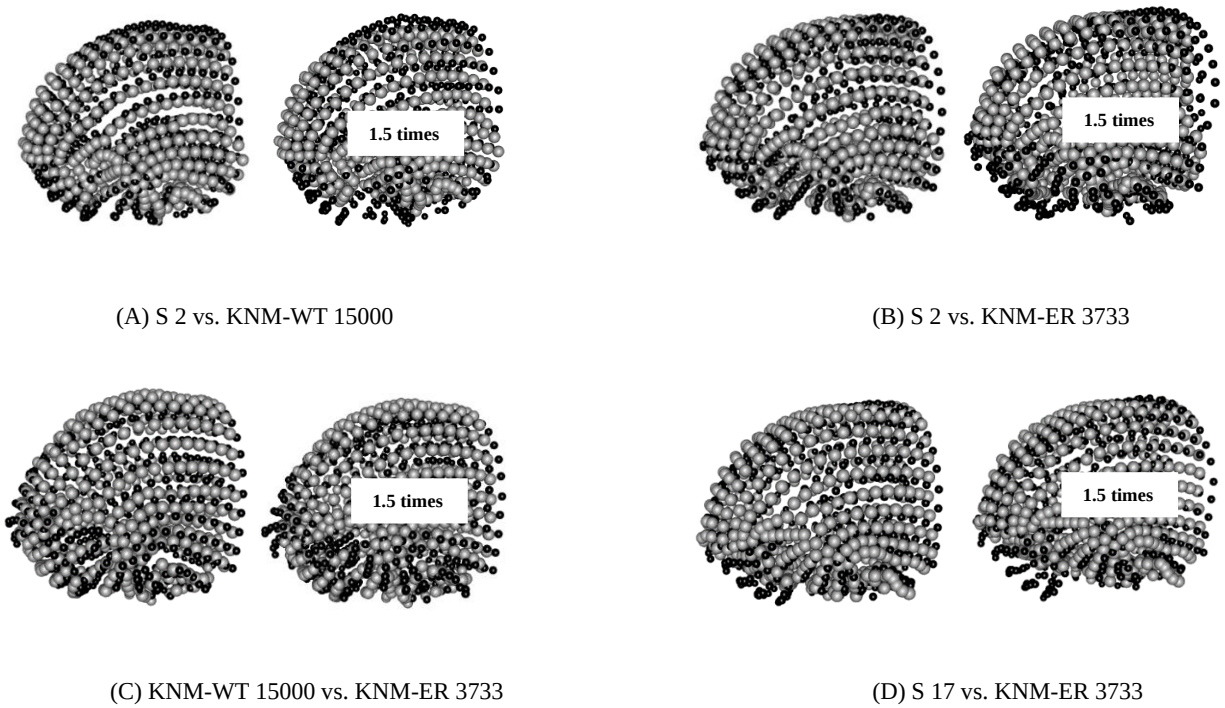

(A) S 2 vs. KNM-WT 15000

(B) S 2 vs. KNM-ER 3733

(C) KNM-WT 15000 vs. KNM-ER 3733

(D) S 17 vs. KNM-ER 3733

Figure 9.12 The Procrustes superimposition of S 2, KNM-WT 15000, KNM-ER 3733 and S 17
The results of the Procrustes superimposition are based on the maximum landmark dataset of the posterior crania of fossils. In the left graph in (A), (B), (C) or (D), the magnitude of differences is amplified **1.5 times** for better visualization. (A) Grey dots represent the S 2; the black dots represent KNM-WT 15000. (B) Grey dots represent the S 2; the black dots represent KNM-ER 3733. (C) Grey dots represent KNM-WT 15000; the black dots represent KNM-ER 3733. (D) Grey dots represent the S 17; the black dots represent KNM-ER 3733. Graphs are generated by the Geomorph R package (Adams et al., 2018).

PC 4 of the posterior cranium shows that in a specimen plotted closer to its positive end, the occipital flexure becomes more obtuse, primarily because semilandmarks at the nuchal plane lie more inferiorly and slightly posteriorly, making the nuchal plane more downwardly inclined (Figure 6.4, Figure 6.5 and Figure 9.13). This PC plots S 17 near its negative end and KNM-WT 15000 at its positive end (Figure 6.4). The other *H. erectus* specimens are at intermediate positions and are fairly close to each other.

The contrast between S 17 and KNM-WT 15000 in PC 4 appears to match observed morphology. As summarized previously, KNM-WT 15000 has a very obtuse occipital angle and a more downwardly sloping nuchal plane than the other *H. erectus* specimens used in this analysis (Figure 9.2). S 17's nuchal

plane is less downwardly sloping than these *H. erectus* specimens (Figure 9.2). These differences in inclinations of the nuchal planes are still preserved after the Procrustes superimposition.

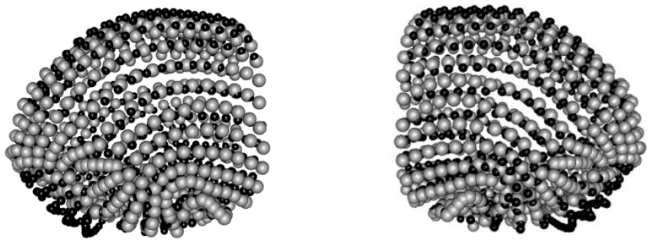

Figure 9.13 The shapes at two ends of PC 2 of the posterior crania of fossils (the maximum-semilandmark dataset)
The grey dots represent the shape at the negative end of PC 1. The black dots represent the positive end of PC 1. From left to right: right lateral view and anterior view. Graphs are generated by the Geomorph R package (Adams et al., 2018).

Among other *H. erectus* specimens, KNM-ER 3733 is plotted closest to the positive end (KNM-WT 15000) in PC 4 of the posterior cranium, while S 2 is plotted closest to the negative end (S 17) (Figure 6.4). As previously discussed, KNM-ER 3733's posterior vault rotates slightly posterosuperiorly relative to specimens such as S 2, KNM-ER 3883, and KNM-WT 15000 (Figure 9.4 and Figure 9.12). This rotation makes the nuchal plane of KNM-ER 3733 even slightly more downwardly sloping than that of S 2 (Figure 9.12). Therefore, it appears that the arrangement of KNM-ER 3733 and S 2 in PC 4 appears to reflect differences in inclinations of their nuchal planes after the Procrustes superimposition.

The fact that D2700 and S 2 are plotted to the nearly identical positions in PC 4 of the posterior cranium is also probably a result of the Procrustes superimposition (Figure 6.4). As discussed previously, S 2's nuchal plane is somewhat more downwardly inclining than the nuchal plane of D2700. However, like KNM-ER 3733, D2700 is rotated posterosuperiorly relative to S 2 by the Procrustes superimposition (Figure 9.4 and Figure 9.14). This rotation makes D2700's nuchal plane slightly more downwardly inclined. As a result, when superimposed, D2700's nuchal plane becomes aligned with S 2's nuchal plane (Figure 9.14). This helps explain why these two specimens are plotted so close to each other in this PC (Figure 6.4). Further, D2700's nuchal plane is also well-aligned with those of the Ngandong specimens. This explains why the Ngandong specimens are plotted very close to D2700 in PC 4, though the Ngandong specimens have more downwardly inclined nuchal planes than D2700's when aligned in the Frankfurt plane (Figure 9.2 and Figure 9.14).

It should be noted that PC 4 of the posterior cranium reflects positions of the entire nuchal plane when configurations are superimposed, in addition to inclinations of the nuchal plane. In a specimen plotted closer to the positive end of PC 4, the entire nuchal plane lies more inferiorly. Consequently, KNM-ER 3733 is plotted to a position closer to the positive end than the Ngandong specimens, probably because the nuchal plane of KNM-ER 3733 lies more inferiorly than those of the Ngandong specimens when superimposed. However, there is no discernable difference in inclinations of the nuchal planes between KNM-ER 3733 and the Ngandong specimens after the Procrustes superimposition (Figure 9.14).

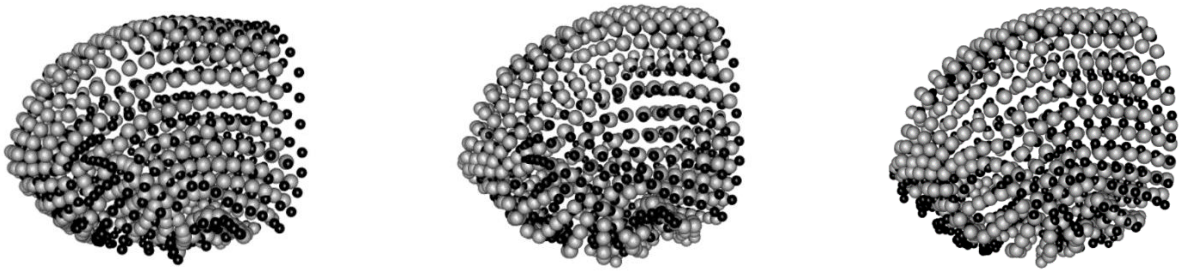

(A) S 2 vs. D2700 (B) Ng 7 vs. D2700 (C) Ng 7 vs. KNM-ER 3733

Figure 9.14 The Procrustes superimposition of S 2, D2700, Ng 7 and KNM-ER 3733
The results of the Procrustes superimposition are based on the maximum landmark dataset of the posterior crania of fossils. (A) Grey dots represent the S 2; the black dots represent D2700. (B) Grey dots represent the Ng 7; the black dots represent D2700. (C) Grey dots represent the Ng 7; the black dots represent KNM-ER 3733. Graphs are generated by the Geomorph R package (Adams et al., 2018).

In the PCA of the entire cranium, PC 2 shows that in a specimen plotted closer to its positive end, the nuchal plane becomes more concave (Figure 5.3). This PC primarily separates KNM-ER 1813 (negative end) and Kabwe 1 (positive end) (Figure 5.1). The *H. erectus* specimens are relatively close to each other. Within *H. erectus*, the Indonesian specimens (S 17 and Ngandong specimens) are plotted closer to the positive end (Kabwe 1) than *H. ergaster* (D2700, KNM-ER 3733 and 3883) (Figure 5.1). Thus, this PC reflects that the nuchal planes of S 17 and the Ngandong specimens are more concave at the superior nuchal line than those of *H. ergaster*.

However, the first two PCs in the analysis of the entire crania of fossils do not show differences in inclinations of the nuchal planes. In the study of the entire cranium, specimens are also rotated relative to each other, so that inclinations of the nuchal planes in some specimens become slightly different. In particular, D2700 rotates slightly superoinferiorly relative to other specimens, such as the Ngandong

specimens and KNM-ER 3883. When aligned in the Frankfurt plane, D2700's nuchal plane is less downwardly inclined than those of the Ngandong specimens. After rotations during the Procrustes superimpositions, inclination of D2700's nuchal plane becomes similar to those of the Ngandong specimens.

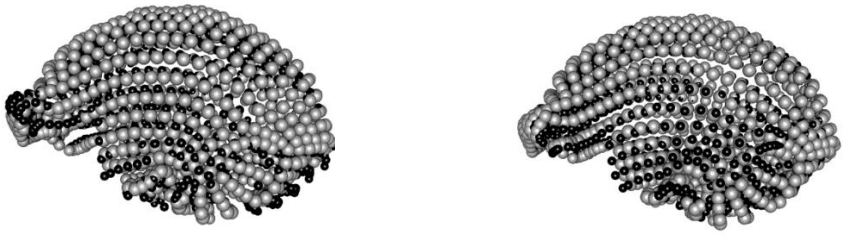

(A) Ng 7 vs. KNM-ER 3733 (B) Ng 7 vs. D2700

Figure 9.15 The Procrustes superimposition of KNM-ER 3733, Ng 7, and D2700
The results of the Procrustes superimposition are based on the maximum landmark dataset of the posterior crania of fossils. (A) Grey dots represent the Ng 7; the black dots represent KNM-ER 3733. (B) Grey dots represent the Ng 7; the black dots represent D2700. Graphs are generated by the Geomorph R package (Adams et al., 2018).

9.1.3 The overall shape of the temporal bone

In the analysis of the temporal bone, PC 2 demonstrates that in a specimen plotted closer to its positive end, the squamosal part of the temporal bone becomes shorter superoinferiorly, because semilandmarks at the region of the squamosal suture roughly above the auditory meatus lie more inferiorly (Figure 7.3 and Figure 9.16). As a result, the squamosal suture becomes less curved. Meanwhile, the mastoid region becomes superoinferiorly taller relative to the squamosal, because semilandmarks at the parietomastoid suture lie more superiorly (Figure 7.3 and Figure 9.16).

PC 2 plots KNM-WT 15000 and S 2 at its positive end by assigning them nearly identical scores, which reflect morphology (Figure 7.1). This is because KNM-WT 15000 and S 2's mastoid regions are superoinferiorly tall relative to the squamosal; their parietomastoid sutures lie only slightly inferior to their squamosal sutures (Figure 9.17). Their squamosal sutures are also fairly straight and nearly horizontally oriented (Figure 9.17). Meanwhile, this PC also plots Kabwe 1 and the Dali skull in nearly identical positions at its negative end, which more-or-less match their morphology (Figure 7.1). This is because, compared to the majority of fossil specimens in this study, Kabwe 1 and the Dali skull's mastoid

regions are much shorter superoinferiorly relative to their squamosals (Figure 9.17). Their parietomastoid sutures lie as low as their auditory meatuses, and their squamosal sutures arc greatly at their midpoints.

Differences between other specimens revealed by PC 2 of the temporal bone do not match actual morphology. KNM-ER 3883, the Ngandong specimens and Neanderthals are plotted very close to each other at the negative half (Figure 7.1). S 17 turns out to be relatively close to the positive end of PC 2 of the temporal bones of fossils (i.e., close to S 2 and KNM-WT 15000). D2700 and KNM-ER 3733 are plotted to nearly identical positions intermediate between S 17 and the cluster of KNM-ER 3883 and the Ngandong specimens (Figure 7.1). If literally interpreting PC 2, this arrangement indicates that the mastoid regions of KNM-ER 3883, the Ngandong specimens and Neanderthals are superoinferiorly short relative to their superoinferiorly tall squamosals, though differences in height between the mastoid regions and squamosals are not as great as the conditions of Kabwe 1 and the Dali skull (Figure 9.16). Meanwhile, according to PC 2, S 17 has a superoinferiorly tall mastoid region relative to its superoinferiorly short squamosal part. Its squamosal suture is straighter than KNM-ER 3883 and Ngandong specimens (Figure 9.16). KNM-ER 3733 and D2700 are intermediate between S 17 and the Ngandong specimens, Neanderthals, and KNM-ER 3883 (Figure 9.16). However, this is not representative of the actual morphology.

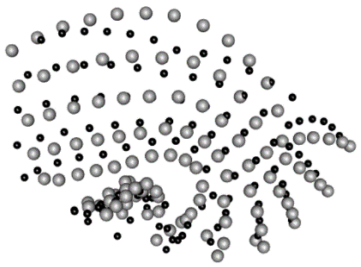

Figure 9.16 The shapes at two ends of PC 2 of the temporal bones of fossils
The configurations are based on the maximum-semilandmark dataset. The grey dots represent the shape at the negative end of PC 2. The black dots represent the positive end of PC 2. Graphs are generated by the Geomorph R package (Adams et al., 2018).

Aligned in the Frankfurt plane, the Ngandong specimens' mastoid regions are superoinferior tall relative to the squamosals (Figure 9.17). Therefore, the parietomastoid sutures of the Ngandong specimens lie somewhat above the middle of the heights of their squamosals and also well above their auditory meatuses (Figure 9.17). However, S 17, KNM-ER 3733 and D2700 all have superoinferiorly short mastoid regions relative to their squamosals (Figure 9.17). The parietomastoid sutures of S 17,

KNM-ER 3733 and D2700 also lie much below the middle of the height of the squamosal part and only slightly above the auditory meatus. Their fairly straight squamosal sutures generally peak near the anterior ends, and slope down toward the shallow parietal notches. Thus, it is difficult to understand why S 17, KNM-ER 3733, and D2700 are plotted closer to the positive end in PC 2 of the temporal bone than the Ngandong specimens.

To decipher the confusing arrangement of specimens in PC 2, it is important to examine the results of the Procrustes superimposition. After the Procrustes superimposition, S 17, KNM-ER 3733 and D2700's temporal configurations are rotated slightly posterosuperiorly relative to specimens that have superoinferiorly tall mastoid regions and horizontally oriented squamosal sutures (i.e., KNM-WT 15000, S 2, and the Ngandong specimens) (Figure 9.18). After these rotations, the positions of parietomastoid sutures of S 17, KNM-ER 3733 and D2700 are shifted more superiorly than their original positions (Figure 9.18). As a result, differences in height between their squamosals and mastoid regions are much reduced, similar to the conditions of KNM-WT 15000, S 2, and the Ngandong specimens (Figure 9.18).

In particular, S 17 appears to be rotated more posterosuperiorly relative to S 2, KNM-WT 15000 and the Ngandong specimens than D2700 and KNM-ER 3733. Thus, S 17's parietomastoid suture is shifted to a position only slightly below the parietomastoid sutures of S 2, KNM-WT 15000 and the Ngandong specimens. Consequently, the squamosal and parietomastoid sutures of S 17 align better with those of S 2 and KNM-WT 15000 than with the corresponding sutures of D2700 and KNM-ER 3733. The close alignment of the squamosal and parietomastoid sutures via Procrustes superimposition probably contributes to plotting S 17 especially closer to S 2 and KNM-WT 15000 in PC 2 than other specimens, including D2700 and KNM-ER 3733.

Nevertheless, after the Procrustes superimposition reduces the overall differences between S 17, KNM-ER 3733, D2700 and the Ngandong specimens, the parietomastoid sutures of S 17, KNM-ER 3733 and D2700 remain situated somewhat more inferiorly than in the Ngandong specimens. Thus, the relative rotation of S 17, KNM-ER 3733 and D2700 in the Procrustes superimposition is still insufficient to explain why S 17, KNM-ER 3733 and D2700 are plotted closer to PC 2's positive end than the Ngandong specimens. One possible reason is associated with the trajectories of the squamosal sutures of the Ngandong specimens as well as how the Ngandong specimens are superimposed with other specimens after the Procrustes superimposition (Figure 9.17 and Figure 9.19).

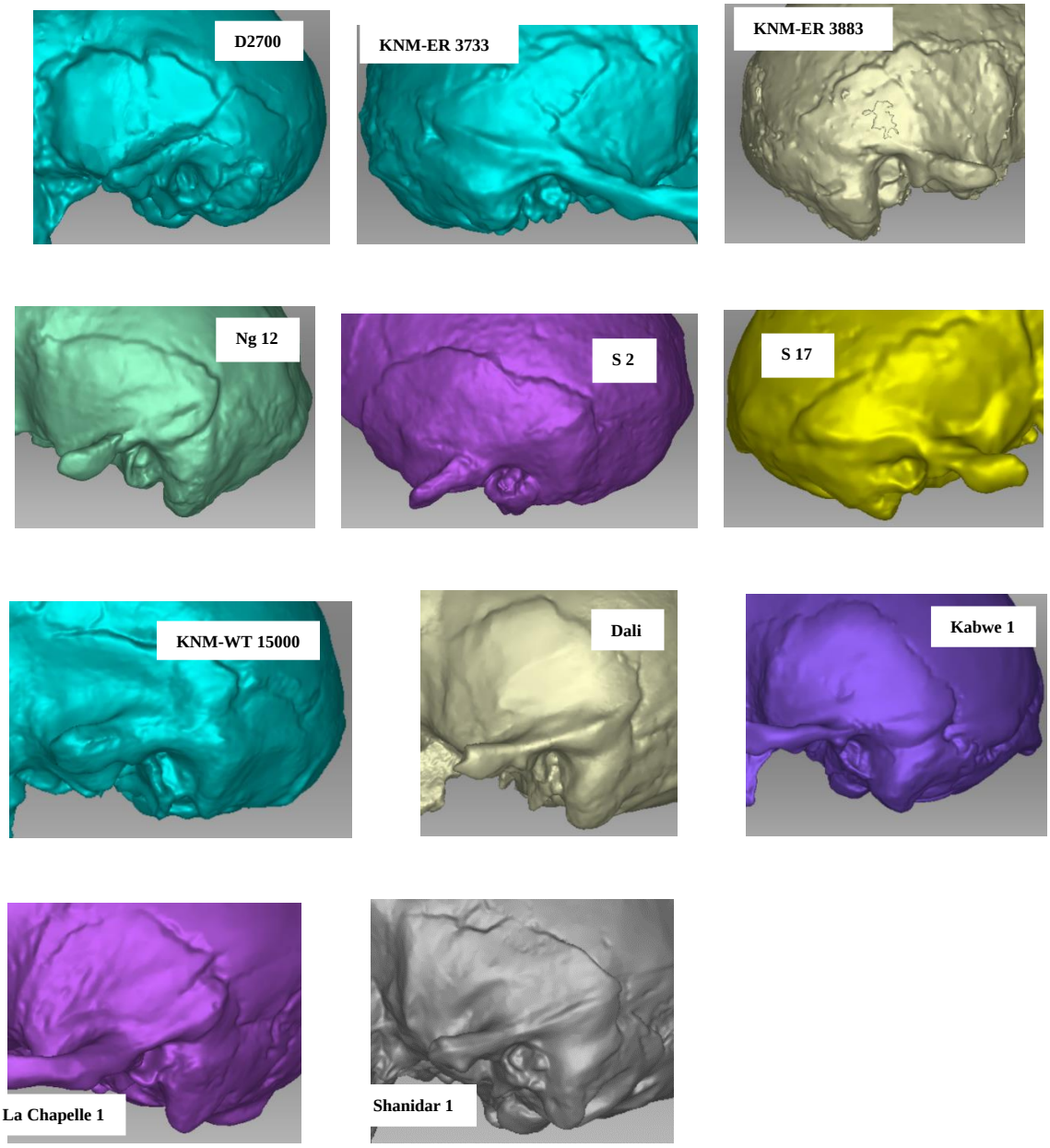

Figure 9.17 The lateral view of 3D models of the temporal bones of fossils (Artec 3D Inc., 2018)

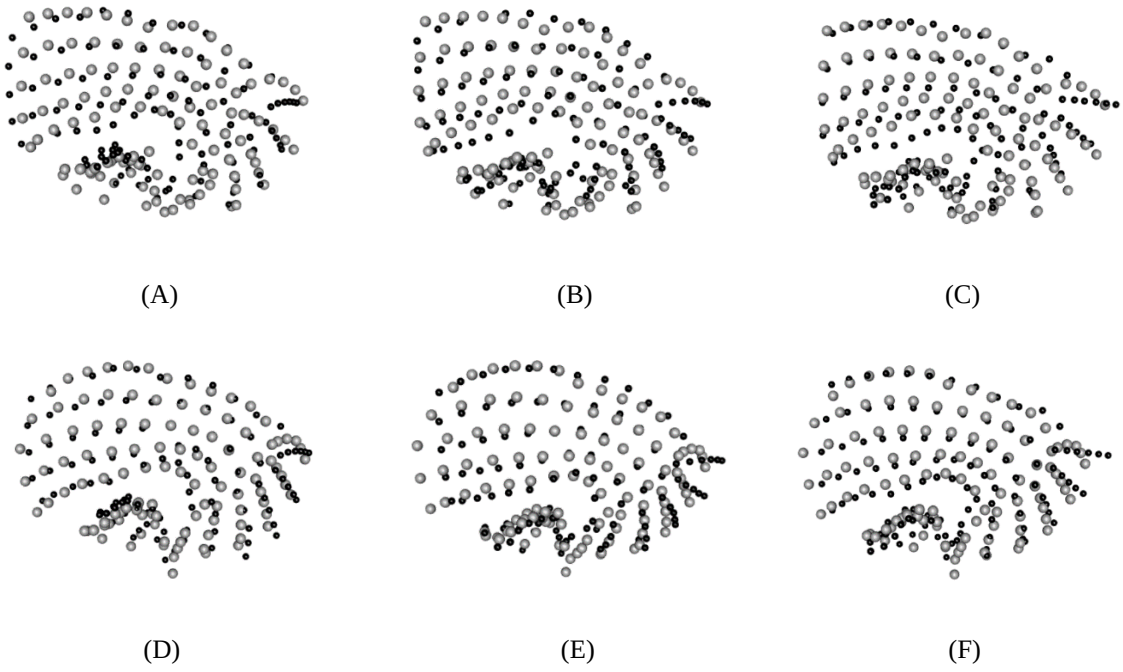

Figure 9.18 The Procrustes superimposition of the temporal configurations of fossils
The results of the Procrustes superimposition are based on the maximum landmark dataset of the posterior crania of fossils. (A) Grey dots: KNM-WT 15000; black dots: D2700. (B) Grey dots: KNM-WT 15000; black dots: KNM-ER 3733. (C) Grey dots: KNM-WT 15000; black dots: S 17. (D) Grey dots: S 2; black dots: D2700. (E) Grey dots: S 2; black dots: KNM-ER 3733. (F) Grey dots: S 2; black dots: S 17. Graphs are generated by the Geomorph R package (Adams et al., 2018).

The squamosal sutures of the Ngandong specimens are essentially straight and horizontally oriented (Figure 9.17). After coursing above the auditory meatuses, the squamosal suture curves sharply inferiorly for a considerable distance to reach relatively deep parietal notch. Different from the squamosal sutures of the Ngandong specimens, the less curved squamosal sutures of D2700, KNM-ER 3733 and S 17 generally peak anteriorly and then slope toward their shallow parietal notches (Figure 9.17). After the Procrustes superimposition, the squamosal sutures of S 17, KNM-ER 3733 and D2700 remain more downwardly sloping than the squamosal sutures of the Ngandong specimens (Figure 9.18 and Figure 9.19). The squamosal sutures of S 2 and KNM-WT 15000 also slope gently down toward their shallow parietal notches (Figure 9.17, Figure 9.18 and Figure 9.19).

When superimposed, semilandmarks at the sections of the squamosal sutures at their midpoints, roughly above the auditory meatuses, in the Ngandong specimens lie slightly more superior than the corresponding semilandmarks in S 17, KNM-ER 3733, D2700, S 2 and KNM-WT 15000 (Figure 9.19). This is because the squamosal sutures in the Ngandong specimens are, in general, more horizontally oriented, while the squamosal sutures in the latter group are slightly more downwardly sloping.

Meanwhile, semilandmarks at the sections of the squamosal sutures behind the auditory meatuses lie more anteroinferiorly in the Ngandong specimens than in S 17, KNM-ER 3733, D2700, S 2 and KNM-WT 15000 (Figure 9.19). This is because the section of the squamosal sutures posterior to the auditory meatus in the former group are more downwardly sloping than those in the latter group. Recall that PC 2 shows that in a specimen plotted closer to its positive end, the squamosal suture appears to become less curved at its midpoint. This is because semilandmarks at the midpoint of the squamosal suture above the auditory meatus lie more inferiorly, while semilandmarks posterior to the auditory meatus lie more posterosuperiorly (Figure 9.16). Thus, positional differences in semilandmarks at the squamosal sutures above and posterior to the auditory meatuses may contribute to plotting the Ngandong specimens further away from S 2 and KNM-WT 15000 at PC 2's positive end than S 17, KNM-ER 3733 and D2700 (Figure 9.19). Overall, the specific positions of the Ngandong specimens in PC 2 should not be interpreted as the squamosal sutures of the Ngandong specimens being more curved than those of S 2, KNM-WT 15000, S 17, KNM-ER 3733 and D2700.

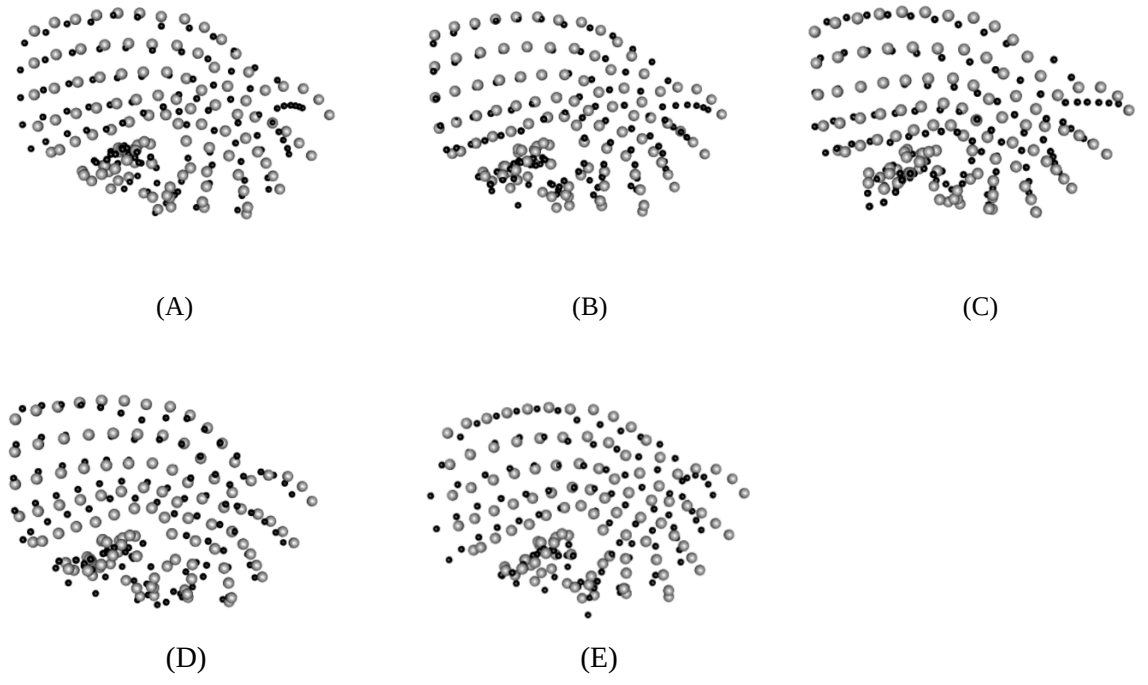

Figure 9.19 The Procrustes superimposition of the temporal configurations of fossils
The results of the Procrustes superimposition are based on the maximum landmark dataset of the temporal bones of fossils. In each, the gray dots represent Ng 12. (A) Ng 12 vs. D2700. (B) Ng 12 vs. KNM-ER 3733. (C) Ng 12 vs. S 17. (D) Ng 12 vs. KNM-WT 15000. (E) Ng 12 vs. S 2. Graphs are generated by the Geomorph R package (Adams et al., 2018).

The three Neanderthal specimens used in this analysis, especially Shanidar 1 and La Chapelle 1, also have relatively superoinferiorly tall squamosals and superoinferiorly short mastoid regions. The temporal configurations of these specimens are also somewhat rotated posterosuperiorly relative to those of S 2, KNM-WT 15000 and the Ngandong specimens, so that their parietomastoid sutures lie slightly closer to the peaks of their squamosal sutures. Overall, after these rotations, the squamosal and parietomastoid sutures become aligned with the corresponding sutures of the Ngandong specimens (Figure 9.20). This alignment helps to explain why the Ngandong and Neanderthal specimens are plotted to very similar positions in PC 2 of the temporal bone. KNM-ER 3883 does not appear to rotate much relative to the Ngandong specimens. After the Procrustes superimposition, KNM-ER 3883's mastoid region is still much shorter superoinferiorly than its squamosal. The parietomastoid suture of KNM-ER 3883 also lies much more inferiorly than in Ngandong specimens. Perhaps because the squamosal suture of KNM-ER 3883 is well aligned with those of the Ngandong specimens, they are plotted very close to each other in PC 2.

In addition to Neanderthals, Kabwe 1 and the Dali skull are also rotated posterosuperiorly, so that their parietomastoid sutures lie closer to the peaks of their squamosal sutures. However, because Kabwe 1 and the Dali skull's squamosals are very tall superoinferiorly relative to their mastoid regions and squamosal sutures highly curved at the midpoints, they are still plotted at the negative end of PC 2 of the temporal bone.

(A) (B) (C)

Figure 9.20 The Procrustes superimposition of the temporal configurations of fossils
The results of the Procrustes superimposition are based on the maximum landmark dataset of the temporal bones of fossils. In each, the gray dots represent Ng 12. (A) Ng 12 vs. La Chapelle 1. (B) Ng 12 vs. KNM-ER 3883. (C) Ng 12 vs. Kabwe 1. Graphs are generated by the Geomorph R package (Adams et al., 2018).

In the analysis of the temporal bone, PC 1 shows that in a specimen plotted closer to the positive end, the parietomastoid suture is anteroposteriorly longer, because the parietomastoid suture lies more anteriorly, closer to the region above the auditory meatus (Figure 7.2 and Figure 9.21). The parietomastoid suture also becomes more curved at its midpoint. Meanwhile, the posterior part of the squamosal suture roughly posterior to the auditory meatus also becomes more downwardly sloping, because semilandmarks in this part of the squamosal suture lie more anteriorly (Figure 7.2 and Figure 9.21). This PC plots KNM-WT 15000 at its positive end. The Ngandong specimens are plotted to very similar positions slightly less negative to KNM-WT 15000 (Figure 7.1). Other specimens are fairly close to each other, located at the negative half of PC 1 of the temporal bones of fossils.

The positions of KNM-WT 15000 and the Ngandong specimens in PC 1 of the temporal bone roughly match their morphology. This PC accurately reveals that the parietomastoid sutures of KNM-WT 15000 and the Ngandong specimens are anteroposteriorly longer and more curved than other specimens (Figure 9.17, Figure 9.18 and Figure 9.19). Furthermore, KNM-WT 15000's parietal notch lies slightly above the posterior margin of the auditory meatus (Figure 9.17). Thus, PC 1 also conforms with the condition in which the parietal notch of KNM-WT 15000 lies more anteriorly than the parietal notches of other specimens (Figure 9.18 and Figure 9.19). The parietal notches of the Ngandong specimens also lie fairly anteriorly, though not as anteriorly as in KNM-WT 15000 (Figure 9.17). In addition, as PC 1 of the temporal bone reveals, KNM-WT 15000 and the Ngandong specimens have fairly straight squamosal sutures that only angle sharply downward toward the parietal notches after their sutures passing their auditory meatuses.

Figure 9.21 The shapes at two ends of PC 1 of the temporal bones of fossils
The configurations are based on the maximum-semilandmark dataset. The grey dots represent the shape at the negative end of PC 1. The black dots represent the positive end of PC 1. Graphs are generated by the Geomorph R package (Adams et al., 2018).

S 17 is plotted at the negative end of PC 1 of the temporal bone (Figure 7.1). KNM-ER 3733, D2700 and S 2 are plotted very close to S 17 (Figure 7.1). Therefore, PC 1 successfully demonstrates that the parietomastoid sutures of S 17, S 2, KNM-ER 3733 and D2700 are relatively straight and anteroposteriorly short (Figure 9.17, Figure 9.18 and Figure 9.21). In addition, the fairly straight squamosal sutures of S 17, S 2, KNM-ER 3733 and D2700 are also somewhat downwardly sloping (S 2's squamosal suture is more horizontally oriented than S 17, KNM-ER 3733 and D2700). Interestingly, in KNM-ER 3733, D2700 and S 17, the squamosal suture angles downward into a very superoinferiorly short and vertically oriented component before reaching their shallow parietal notches (Figure 9.17). This short component of the squamosal suture is marked by only a single semilandmark (Figure 9.18). Therefore, positional differences in the corresponding semilandmarks in different specimens may only have a minimal affect in the computation of overall shape differences. Consequently, PC 1 of the temporal bone does not reflect the possession of a very short vertical component of the posterior squamosal sutures in KNM-ER 3733, D2700 or S17, though this PC shows that KNM-WT 15000 and the Ngandong specimens' posterior squamosal sutures angle sharply inferiorly into relatively superoinferiorly long vertical components (Figure 7.1, Figure 9.18, Figure 9.19 and Figure 9.21).

The similar positions of S 2, KNM-ER 3733, D2700 and S 17 in PC 1 of the temporal bone may also be somewhat influenced by the Procrustes superimposition. As summarized above, S 2's parietomastoid suture lies only slightly inferior to its squamosal suture, while the parietomastoid sutures of KNM-ER 3733, D2700 and S 17 lie much inferior to their squamosal sutures (Figure 9.17). Thus, S 2's parietal notch lies more anterosuperiorly than in KNM-ER 3733, D2700 and S 17, closer to its auditory meatus (Figure 9.17). The Procrustes superimposition rotates KNM-ER 3733, D2700 and S 17's temporal configurations posterosuperiorly (or counterclockwise in left lateral view) relative to S 2 to minimize their overall differences. After these rotations, the parietal notches of KNM-ER 3733, D2700 and D2700 shift somewhat more anterosuperiorly compared to their original positions (Figure 9.18). Thus, the positional differences between the parietal notches in S 2, KNM-ER 3733, D2700 and S 17 are reduced after the Procrustes superimposition (Figure 9.18).

(A) (B) (C) (D)

Figure 9.22 The Procrustes superimposition of the temporal configurations of fossils
The results of the Procrustes superimposition are based on the maximum landmark dataset of the temporal bones of fossils. In each, the gray dots represent KNM-ER 3883. (A) KNM-ER 3883 vs. S 2. (B) KNM-ER 3883 vs. KNM-ER 3733. (C) KNM-ER 3883 vs. D2700. (D) KNM-ER 3883 vs. S 17. Graphs are generated by the Geomorph R package (Adams et al., 2018).

KNM-ER 3883's moderately curved squamosal suture peaks somewhat behind its anterior end and then slopes gently to the parietal notch. Its parietomastoid suture is straight and short anteroposteriorly. However, KNM-ER 3883 is plotted somewhat closer to the positive end of PC 1 of the temporal bone than S 2, S 17, KNM-ER 3733 and D2700, indicating that the posterior part of KNM-ER 3883's squamosal suture curves slightly more steeply downward and the parietomastoid suture is anteroposteriorly longer and more curved. A possible reason is that KNM-ER 3883's squamosal suture is slightly more downwardly inclined than S 2, S 17, KNM-ER 3733 and D2700 (Figure 9.17). When superimposed, the slightly more downwardly sloping posterior squamosal suture of KNM-ER 3883 lies more anteroinferiorly than in S 2, S 17, KNM-ER 3733 and D2700 (Figure 9.22). PC 1 of the temporal bones of fossils shows that in a specimen plotted closer to its positive end, semilandmarks at the posterior part of the squamosal suture lie more anteriorly (Figure 9.21). Therefore, the positional differences at the posterior squamosal sutures, which are results of the Procrustes superimposition, may contribute to plotting KNM-ER 3883 to a somewhat more positive position than S 2, S 17, KNM-ER 3733 and D2700 in PC 1 of the temporal bone.

9.1.4 The mastoid process

Among the fossil specimens used in this analysis, the mastoid processes of KNM-ER 3883, the Ngandong specimens, Neanderthals, Kabwe 1 and the Dali skull are relatively large, and much more inferiorly protruding than their tympanic plates (Figure 9.17). Among the specimens with smaller and less protruding mastoid processes, in S 17 and KNM-ER 1813, they still protrude more inferiorly than their tympanic plates. KNM-ER 3733's mastoid process only minimally protrudes inferiorly beyond its

tympanic plate (Figure 9.17). D2700 does not develop an actual mastoid process, but its bulging mastoid region still distends slightly more inferiorly than the tympanic plate. KNM-WT 15000's small mastoid process terminates level with the tympanic plate. The inferior extremity of S 2's bulging mastoid region terminates above the tympanic plate (Figure 9.17).

In the PCA of the temporal bone, PC 2 demonstrates that in a specimen plotted closer to its positive end, the mastoid process becomes less inferiorly protruding beyond the tympanic plate (Figure 7.3 and Figure 9.16). Kabwe 1 and the Dali skull are plotted at the negative end of PC 2. KNM-ER 3883, KNM-ER 1813, Neanderthals, and the Ngandong specimens are also plotted at PC 2's negative half (Figure 7.1). As just summarized, these specimens' mastoid processes protrude more inferiorly than their tympanic plates (Figure 9.17). S 2 and KNM-WT 15000 are plotted at the positive end of PC 2, which accurately reflects that their mastoid regions do not protrude more inferiorly than their tympanic plates (Figure 7.1 and Figure 9.17). It is also reasonable for KNM-ER 3733 and D2700 to plot at the positive half of PC 2, because their mastoid regions only slightly protrude beyond their tympanic plates (Figure 7.1 and Figure 9.17).

As discussed in the previous section, after the Procrustes superimposition, specimens (e.g., KNM-ER 3733 and S 17), whose parietomastoid sutures lie much more inferiorly than their squamosal sutures are in general rotated posterosuperiorly relative to specimens (e.g., S 2 and KNM-WT 15000), whose parietomastoid sutures lie level with their squamosal sutures (Figure 9.18, Figure 9.19 and Figure 9.20). These rotations tend to reduce the degree of protrusion of the mastoid processes in specimens with relatively inferiorly positioned parietomastoid sutures. Nevertheless, differences in inferior protrusion of the mastoid regions relative to the tympanic plates can still be observed. For example, Kabwe 1 and the Dali skull, which are plotted at the negative end of PC 2 in the analysis of the temporal bones, are rotated posterosuperiorly relative to KNM-WT 15000 and S 2, whose mastoid regions do not protrude beyond their tympanic plates (Figure 9.20). When superimposed, Kabwe 1 and the Dali skull's mastoid processes are still much more downwardly protruding than their tympanic plates, though the degree of protrusion is somewhat reduced (Figure 9.20). KNM-ER 3733 and D2700 are also rotated posterosuperiorly relative to KNM-WT 15000 and S 2 (Figure 9.18). When superimposed, KNM-ER 3733 and D2700's mastoid regions are still minimally more downwardly protruding than their tympanic plates.

On the other hand, the Procrustes superimposition somewhat affects the degree of protrusion of the mastoid processes in S 17 compared to other fossil specimens. S 17 has a small mastoid process that protrudes more inferiorly relative to its tympanic plate than in KNM-ER 3733 and D2700 (Figure 9.17). However, PC 2 of the temporal bone plots S 17 closer to the positive end (KNM-WT 15000 and S 2) than KNM-ER 3733 and D2700 (Figure 7.1). This arrangement indicates that S 17's mastoid process is less inferiorly protruding than the mastoid processes of KNM-ER 3733 and D2700 (Figure 7.3, Figure 9.16

and Figure 9.17). The reason is probably because S 17 is rotated slightly more posterosuperiorly than KNM-ER 3733 and D2700 relative to KNM-WT 15000 and S 2 (Figure 9.18). Thus, the degree of downward protrusion of S 17's mastoid process relative to its tympanic plate is reduced more than in KNM-ER 3733 and D2700.

KNM-ER 3883, the Ngandong specimens and Neanderthals are plotted somewhat closer to the positive end (KNM-WT 15000 and S 2) in PC 2 than Kabwe 1 and the Dali skull (Figure 7.1). This indicates that the mastoid processes of KNM-ER 3883, the Ngandong specimens and Neanderthals protrude beyond their tympanic plates to a lesser degree than in Kabwe 1 and the Dali skull (Figure 7.3 and Figure 9.16). However, KNM-ER 3883, the Ngandong specimens and the Neanderthals' relatively large mastoid processes also protrude much more inferiorly than their tympanic plates, which morphologically, is still obvious after the Procrustes superimposition (Figure 9.17, Figure 9.18, Figure 9.19 and Figure 9.20). It should be noted that PC 2 of the temporal bone is also driven by differences in their overall shapes, such as trajectories of the squamosal suture. These differences, which are analyzed in the previous section, likely explain why KNM-ER 3883, the Ngandong specimens and Neanderthals are plotted closer to the positive end of PC 2 of temporal bones of fossils than Kabwe 1 and the Dali skull.

PC 1 of the temporal bone also shows that in a specimen plotted closer to this PC's positive end, the mastoid process becomes increasingly inferiorly distended (Figure 7.2 and Figure 9.21). However, these visualized differences in the mastoid regions should be interpreted carefully. In particular, this PC plots KNM-WT 15000 at its positive end (Figure 7.1). As just discussed, KNM-WT 15000's small mastoid process does not protrude more inferiorly than its tympanic plate (Figure 9.17).

Rather than revealing differences in the degrees of inferior protrusion of the mastoid processes, PC 1 likely only reflects positional differences of semilandmarks at the inferior extremity of the mastoid regions. In addition, PC 1 of the temporal bone also shows that the tympanic plate becomes more downwardly protruding in a specimen plotted closer to this PC's positive end (Figure 7.2 and Figure 9.21). When superimposed, semilandmarks at the inferior mastoid region of KNM-WT 15000 are well aligned with corresponding semilandmarks of the Ngandong specimens, KNM-ER 3883, Neanderthals, Kabwe 1 and the Dali skull, whose mastoid processes are somewhat more inferiorly distended (Figure 9.23). Meanwhile, semilandmarks at the inferior tympanic plate of KNM-WT 15000 lie even more inferiorly than in most other fossils. Thus, the positions of semilandmarks at the inferior mastoid region and the tympanic plate jointly contribute to plot KNM-WT 15000 at the positive end in PC 1 of the temporal bones of fossils.

Similar to KNM-WT 15000, the Ngandong specimens' tympanic plate is also more inferiorly distended than most specimens when they are superimposed (Figure 9.19). Thus, the Ngandong specimens are plotted much closer to KNM-WT 15000 than other specimens in PC 1 of the temporal bone

(Figure 7.1). Though KNM-ER 3883, Kabwe 1, the Dali skulls, and Neanderthals have quite inferiorly protruding mastoid processes, their tympanic plates lie less inferiorly than in the Ngandong specimens (Figure 9.19). This perhaps contributes to plotting these specimens further away from the positive end (KNM-WT 15000) of PC 1 than the Ngandong specimens (Figure 7.1). Yet, if literally relying on interpreting PC 1 of the temporal bone, one may infer that KNM-ER 3883, Kabwe 1, the Dali skull, and Neanderthals have less inferiorly protruding mastoid regions and less inferiorly situated tympanic plates than the Ngandong specimens and KNM-WT 15000 (Figure 7.2 and Figure 9.21).

Again, it should be noted that the arrangement of specimens in PC 1 of the temporal bone is perhaps also driven by overall shape differences of the entire temporal bones (see the previous section). Therefore, differences in the mastoid region demonstrated by PC 1 of the temporal bone should be interpreted cautiously.

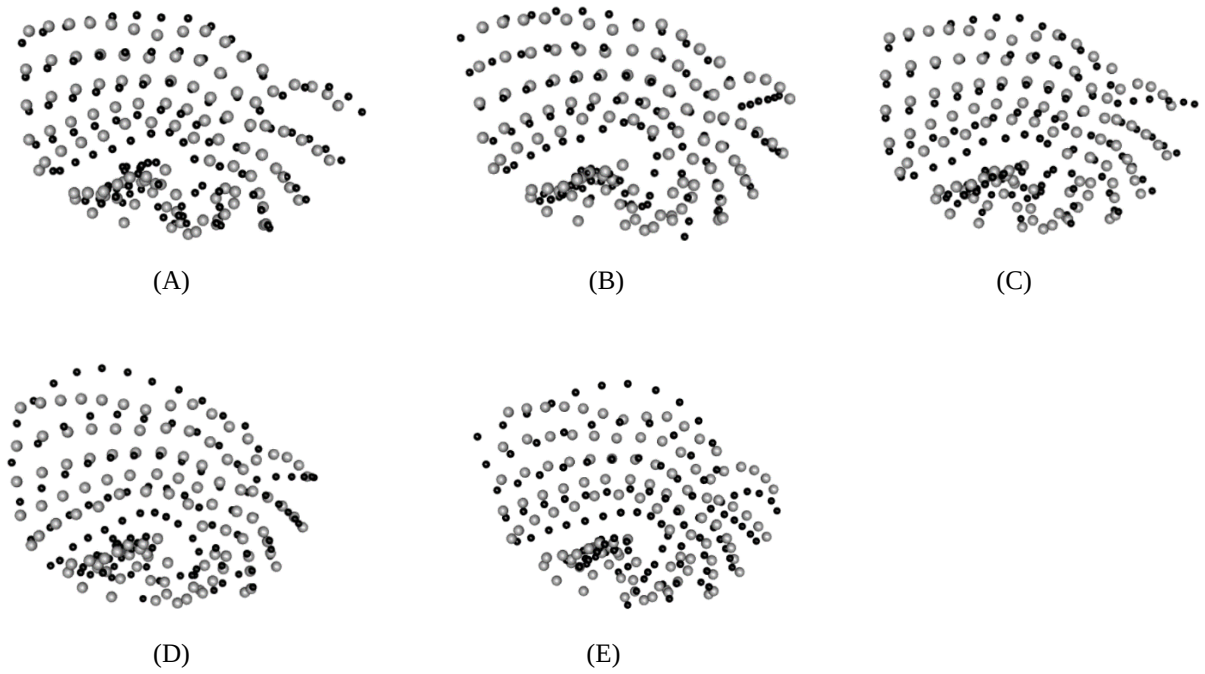

Figure 9.23 The Procrustes superimposition of the temporal configurations of fossils
The results of the Procrustes superimposition are based on the maximum landmark dataset of the temporal bones of fossils. In each, the gray dots represent KNM-WT 15000. (A) KNM-WT 15000 vs. Ng 12. (B) KNM-WT 15000 vs. KNM-ER 3883. (C) KNM-WT 15000 vs. La Chapelle 1. (D) KNM-WT 15000 vs. Kabwe 1. (E) KNM-ET 15000 vs. the Dali skull. Graphs are generated by the Geomorph R package (Adams et al., 2018).

9.1.5 The mandibular fossa

In the PCA of the temporal bone, PC 1 shows that in a specimen plotted closer to the positive end, the mandibular fossa becomes deeper (Figure 7.2 and Figure 9.24). Meanwhile, the tympanic plate, which forms the posterior wall of the mandibular fossa, becomes more inferiorly positioned (Figure 9.24). PC 1 plots KNM-WT 15000 at the positive end (Figure 7.1). The Ngandong specimens lie very close to KNM-WT 15000. Therefore, PC 1 reveals that KNM-WT 15000 and the Ngandong specimens have relatively superoinferiorly deep mandibular fossae (Figure 9.24 and Figure 9.25). Their tympanic plates are more inferiorly positioned than the anterior walls of the mandibular fossae (Figure 9.24 and Figure 9.25). In particular, this PC shows that the lateral profiles of the mandibular fossae in KNM-WT 15000 and the Ngandong specimens are V-shaped, because their fossae are deepest at the posterior margin, along the tympanic plate (Figure 9.24 and Figure 9.25).

Other specimens are plotted fairly close to each other at PC 1's negative half. If reading this PC literally without examining actual specimens, one may conclude that they have superoinferiorly shallower mandibular fossae than KNM-WT 15000 and the Ngandong specimens. However, some specimens plotted near PC 1's negative end, such as S 17 and S 2, actually have quite superoinferiorly deep mandibular fossae. It should be noted that, because semilandmarks at the bottom of the mandibular fossa lie more posterosuperiorly in a specimen plotted closer to PC 1's positive end, the mandibular fossa appears to become deeper superoinferiorly. Thus, what PC 1 really captures appears to be positional differences of corresponding semilandmarks at the top of the mandibular fossa. In addition to the depths of the mandibular fossa, these positional differences of semilandmarks at the tops of the mandibular fossae can be influenced by the relative locations of the entire fossa. These relative locations of the mandibular fossa are results of the Procrustes superimposition of the overall configuration of the temporal bone. For example, when temporal configurations are superimposed, the mandibular fossae of S 17 and S 2 lie more inferiorly than the mandibular fossa of Ng 12. Therefore, semilandmarks at the top of Ng 12's mandibular fossae are positioned more superiorly than corresponding semilandmarks in S 17 and S 2. These positional differences of semilandmarks at the tops of the mandibular fossae perhaps contribute to plotting S 17 and S 2 further away from the positive end of PC 1 than in the Ngandong specimens.

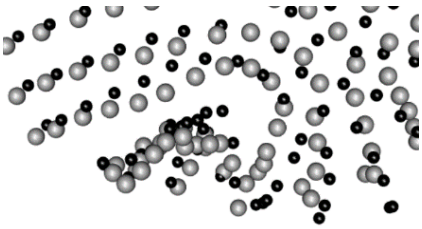

Figure 9.24 The shapes at two ends of PC 1 of the temporal bones of fossils
The configurations are based on the maximum-specimen dataset. The focus of this graph is the mandibular fossa. The grey dots represent the shape at the negative end of PC 1. The black dots represent the positive end of PC 1. Graphs are generated by the Geomorph R package (Adams et al., 2018).

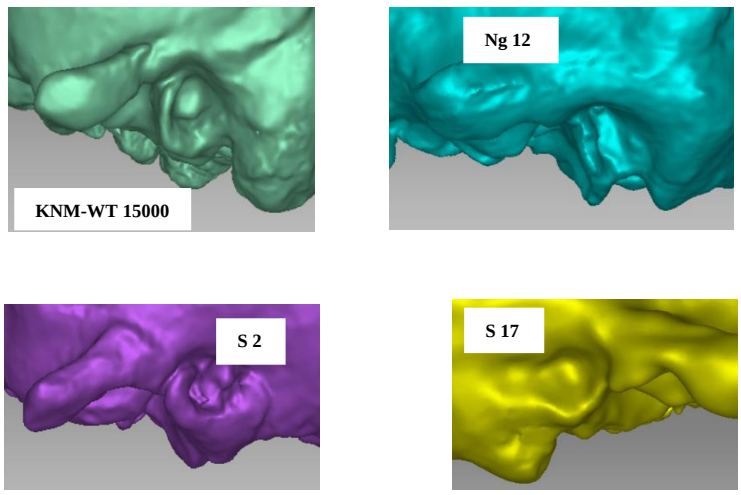

Figure 9.25 The lateral view of 3D models of the mandibular fossae of fossils (Artec 3D Inc., 2018)

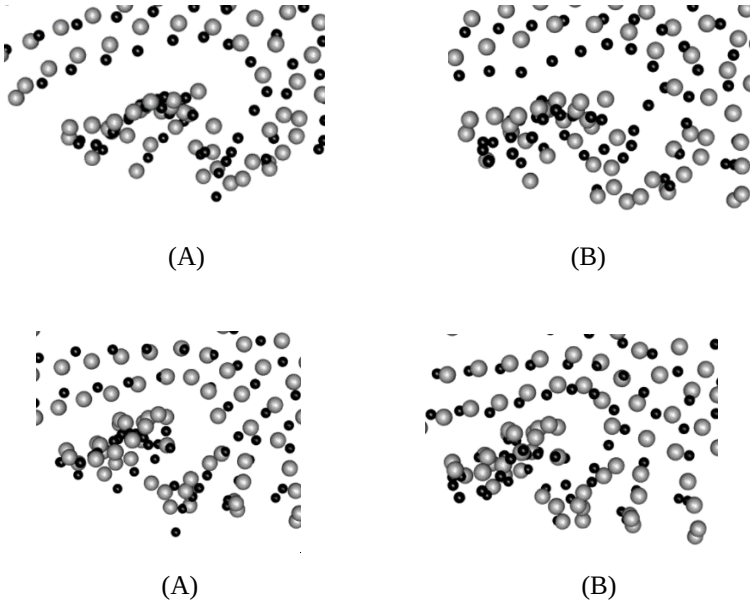

Figure 9.26 The Procrustes superimposition of the mandibular fossae of fossils
The results of the Procrustes superimposition are based on the maximum landmark dataset of the temporal bones of fossils. (A) KNM-WT 15000 (grey) vs. S 2 (black). (B) KNM-WT 15000 (grey) vs. S 17 (black). (C) Ng 12 (grey) vs. S 2 (black). (D) Ng 12 (grey) vs. S 17 (black). Graphs are generated by the Geomorph R package (Adams et al., 2018).

PC 2 of the temporal bone also shows that in a specimen plotted closer to this PC's positive end, the mandibular fossa becomes deeper (Figure 7.3 and Figure 9.27). S 2 is plotted to PC 2's positive end, while S 17 lies very close to S 2. Interestingly, the Ngandong specimens are plotted relatively close to the negative end of PC 2, indicating that they have shallower mandibular fossae than both S 17 and S 2 (Figure 7.1). In PC 2, the mandibular fossa appears to become deeper in a specimen plotted closer to this PC's positive end, because semilandmarks at both the anterior and posterior walls of the mandibular fossa lie more inferiorly, making them appear more inferiorly distended (Figure 7.3 and Figure 9.27). These positional differences in semilandmarks at the anterior and posterior walls of the mandibular fossae can be affected by the relative position of the entire mandibular fossae, as a result of the Procrustes superimposition of the overall temporal configuration.

As just discussed, when superimposed, the mandibular fossae of S 17 and S 2 lie more inferiorly than the mandibular fossae of the Ngandong specimens (Figure 9.26). Consequently, the anterior walls of S 17 and S 2's mandibular fossae lie slightly more inferiorly than in the Ngandong specimens, although the posterior walls of S 17 and S 2 are still less inferiorly distended. In particular, S 17 is rotated posterosuperiorly relative to the Ngandong specimens after the Procrustes superimposition, which reduces differences in overall temporal configuration (Figure 9.18 and Figure 9.19). This rotation further makes

the anterior wall of S 17's mandibular fossa slightly more downwardly positioned (Figure 9.26). Therefore, the positional differences in semilandmarks on the anterior wall of the mandibular fossa, rather than simply the depths of the mandibular fossa, likely contribute to the separation of S 17 and S 2 from the Ngandong specimens in PC 2 in the PCA of the temporal bone.

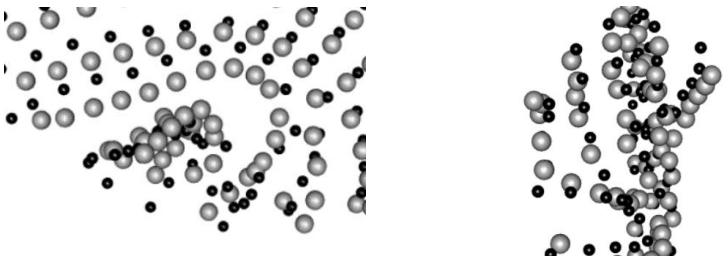

Figure 9.27 The shapes at two ends of PC 2 of the temporal bones of fossils
The configurations are based on the maximum-semilandmark dataset. The focus of this graph is the mandibular fossa. The grey dots represent the shape at the negative end of PC 1. The black dots represent the positive end of PC 2. Graphs are generated by the Geomorph R package (Adams et al., 2018).

PC 2 also shows that in a specimen closer to the positive end, the mandibular fossa becomes anteroposteriorly longer as the lateral half of the anterior wall lies more anteriorly (Figure 7.3 and Figure 9.27). The medial half of the anterior wall becomes more obliquely oriented. Meanwhile, the tympanic plate becomes more mediolaterally oriented as the landmark at the vaginal process lies more posteriorly (Figure 7.3 and Figure 9.27). Thus, the distance between the entoglenoid region and the vaginal process increases. By plotting S 2 at the positive end, PC 2 shows that the anterior wall of S 2's mandibular fossa angles sharply posteriorly into an anteroposteriorly oriented medial wall, while the tympanic plate is oriented mediolaterally (Figure 9.27 and Figure 9.28). This PC also shows that S 2's entoglenoid region is well separated from the vaginal process, because the tympanic plate is anteroposteriorly thick relative to other specimens (Figure 9.27 and Figure 9.28).

However, differences in the mandibular fossae of other specimens demonstrated by PC 2 do not fully match actual morphology. For example, KNM-WT 15000 is plotted to a nearly identical position with S 2 (Figure 7.1). Though the anterior wall of KNM-WT 15000's mandibular fossa also angles posteriorly into a medial wall, as in S 2, KNM-WT 15000's tympanic plate is more obliquely oriented than in S 2 (Figure 9.28 and Figure 9.29). Compared to KNM-ER 3733, D2700's tympanic plate is more obliquely oriented, and its mandibular fossa is anteroposteriorly shorter (Figure 9.28 and Figure 9.29). Yet, D2700 and KNM-ER 3733 are plotted to nearly identical positions in PC 2 (Figure 7.1). Moreover,

the anterior wall KNM-ER 1813's mandibular fossa also angles sharply into an anteroposteriorly oriented medial wall, as in S 2 and KNM-WT 15000 (Figure 9.28 and Figure 9.29). KNM-ER 1813's tympanic plate is mediolaterally oriented. However, KNM-ER 1813 is plotted to PC 2's negative half, indicating that the anterior wall of its mandibular fossa is similarly gently curved and its tympanic plate similarly obliquely oriented, as in KNM-ER 3883, Neanderthals, and the Ngandong specimens (Figure 7.1, Figure 9.27, Figure 9.28 and Figure 9.29). The shape differences in mandibular fossae demonstrated by PC 2 do not match actual morphology, perhaps because this PC is primarily driven by overall shape differences of the temporal regions (see the previous section).

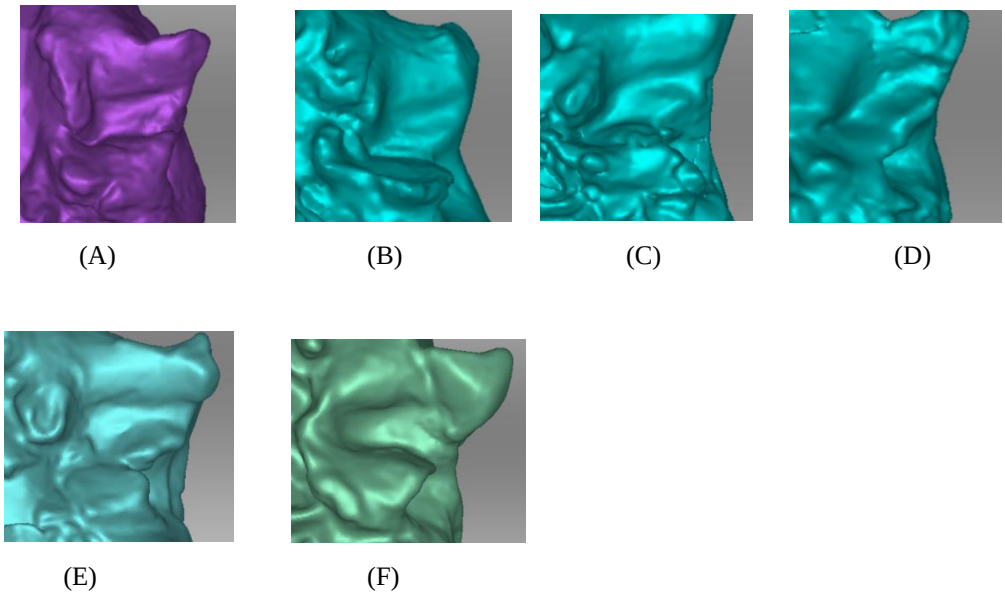

Figure 9.28 The 3D models of the mandibular fossae of fossils (Artec 3D Inc., 2018)
(A) S 2. (B) KNM-WT 15000. (C) KNM-ER 3733. (D) D2700. (E) KNM-ER 1813. (F) Ng 12

(A) (B) (C) (D)

Figure 9.29 The Procrustes superimposition of the mandibular fossae of fossils
The results of the Procrustes superimposition are based on the maximum landmark dataset of the temporal bones of fossils. (A) S 2 (grey) vs. KNM-WT 15000 (black). (B) D2700 (grey) vs. KNM-ER 3733 (black). (C) S 2 (grey) vs. KNM-ER 1813 (black). (D) KNM-ER 1813 (grey) vs. Ng 12 (black). Graphs are generated by the Geomorph R package (Adams et al., 2018).

9.1.6 The frontal squama and the supraorbital region

In the PCA of the frontal bone, PC 1 demonstrates that, in a specimen plotted closer to its positive end, the supraorbital and glabellar regions become superoinferiorly taller (Figure 8.2 and Figure 9.30). The peak of the superior margin of each brow lies more inferomedially. Thus, the ascending part of each brow, which is the section between the glabellar region and the peak of the brow, becomes mediolaterally shorter.

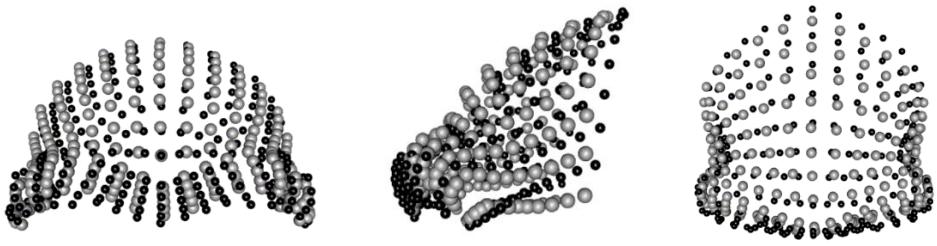

Figure 9.30 The shapes at two ends of PC 1 of the frontal bones of fossils
The grey dots represent the shape at the negative end of PC 1. The black dots represent the positive end of PC 2. Graphs are generated by the Geomorph R package (Adams et al., 2018).

PC 1 plots OH 9 at its positive end. The Ngandong specimens, KNM-ER 3883 and S 17 lie very close to OH 9 (Figure 8.1). The positions of OH 9 and the Ngandong specimens in PC 1 reflect the actual morphology of their supraorbital regions, because the ascending parts of their brows are mediolaterally

short (Figure 9.31 and Figure 9.33). Further, the brows of OH 9 and the Ngandong specimens are, overall, straight and horizontally oriented (Figure 9.31 and Figure 9.33). The ascending parts of KNM-ER 3883's brows are also mediolaterally short, and its brows are only gently curved (Figure 9.31). The ascending parts of KNM-ER 3883's brows are superoinferiorly tall. It should be noted that KNM-ER 3883's brows become superoinferiorly thinner laterally (Figure 9.31). The laterally thinning brows of KNM-ER 3883 are not revealed by PC 1. S 17's brows are uniformly tall superoinferiorly (Figure 9.31 and Figure 9.33). This may help to plot S 17 close to KNM-ER 3883, OH 9 and the Ngandong specimens. However, PC 1 does not reveal that S 17's brows are somewhat more arched than the brows of the Ngandong specimens, KNM-ER 3883 and OH 9 (Figure 9.31 and Figure 9.33). The peaks of S 17's brows also lie more laterally than in the Ngandong specimens, KNM-ER 3883 and OH 9 (Figure 9.31 and Figure 9.33).

Neanderthals, who have double-arched brows, are placed at the negative end of PC 1 (Figure 9.32). When superimposed, the highest points of the brows of Neanderthals are more superolaterally placed than those of OH 9, KNM-ER 3883, S 17 and the Ngandong specimens (Figure 9.33). The brows of Neanderthals are also superoinferiorly thinner than the brows of OH 9, KNM-ER 3883, S 17, and the Ngandong specimens. Thus, PC 1 captures these differences between the brows of Neanderthals at PC 1's negative end and the brows of OH 9, KNM-ER 3883, S 17, and the Ngandong specimens at PC 1's positive end.

KNM-ER 3733 is plotted to a position intermediate between Neanderthals at PC 1's negative end and OH 9, KNM-ER 3883, S 17 and the Ngandong specimens at PC 1's positive end (Figure 8.1). KNM-ER 3733's brows are also double-arched, though slightly less arched than the brows of Neanderthals (Figure 9.31, Figure 9.32, Figure 9.33). When superimposed, the peaks of KNM-ER 3733's brows also lie slightly medial to those of Neanderthals (Figure 9.33). Therefore, PC 1 demonstrates differences in the arc of the brows between Neanderthals and KNM-ER 3733. However, KNM-ER 3733's brows are superoinferiorly very thin (Figure 9.31). After the Procrustes superimposition, KNM-ER 3733's brows become as superoinferiorly thin as the brows of Neanderthals (Figure 9.33). Thus, PC 1 does not reveal the actual superoinferiorly thickness of the brows of KNM-ER 3733 and Neanderthals.

KNM-ER 3733 also lies very close to D2700 in PC 1 (Figure 8.1). The brows of D2700 are as superoinferiorly thin as the brows of KNM-ER 3733. When superimposed, the peaks of D2700's brows lie more medially than in KNM-ER 3733, because the ascending parts of the former are shorter than in KNM-ER 3733. Therefore, PC 1 does not demonstrate differences in the mediolateral lengths of the ascending parts of the brows in D2700 and KNM-ER 3733.

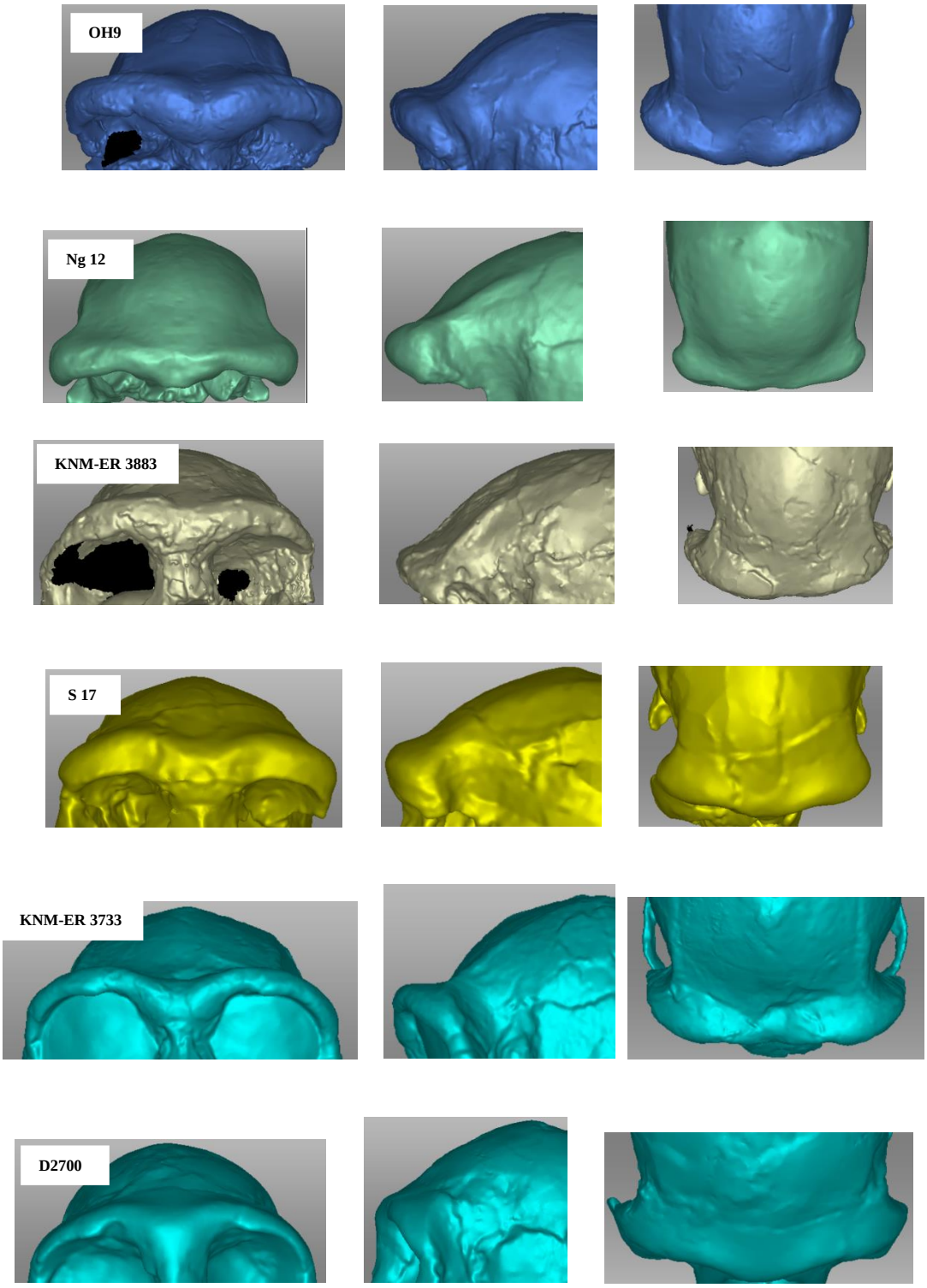

Figure 9.31 The 3D models of the frontal regions of fossils (part 1) (Artec 3D Inc., 2018)

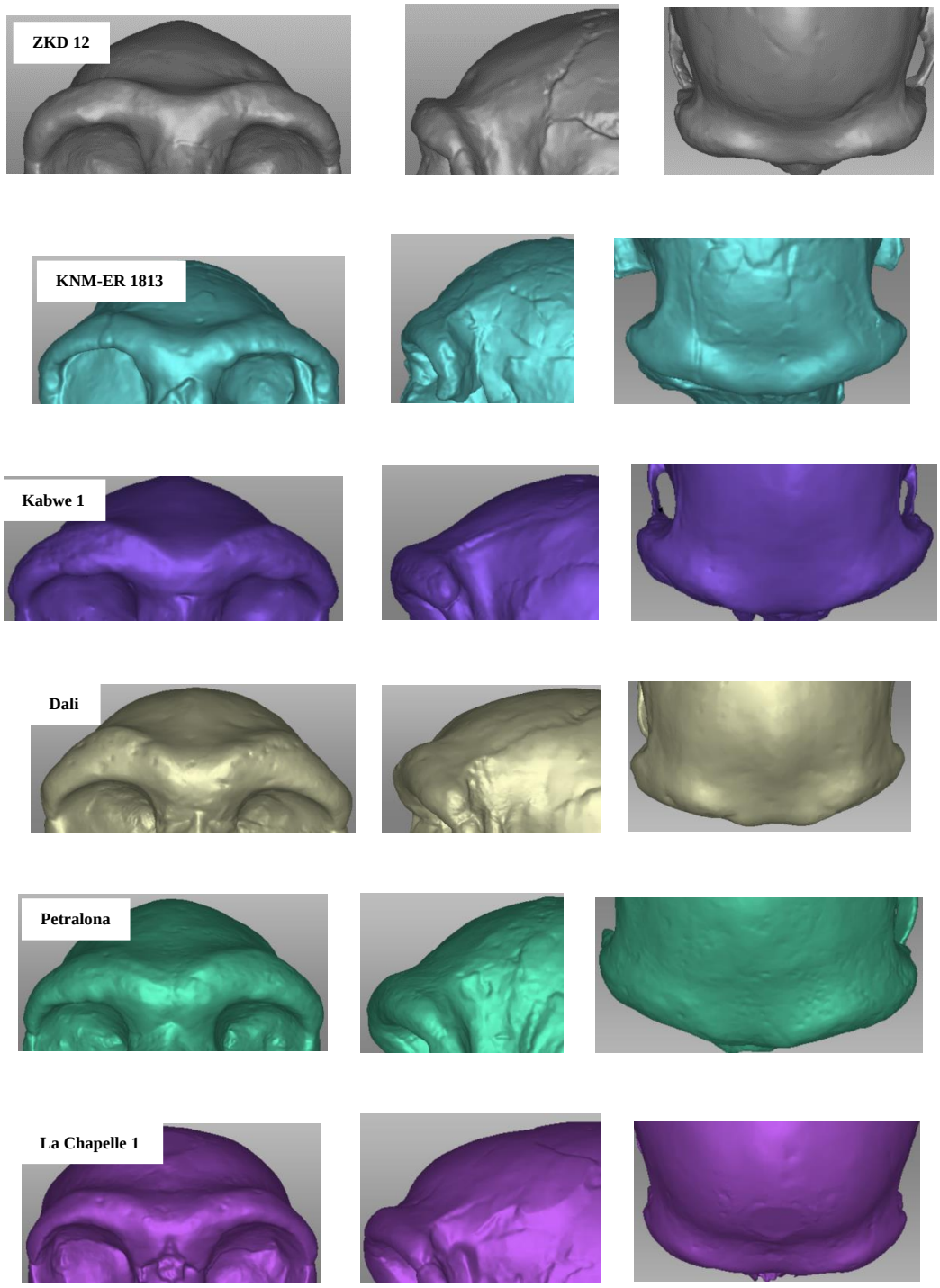

Figure 9.32 The 3D models of the frontal regions of other fossils (part 2) (Artec 3D Inc., 2018)

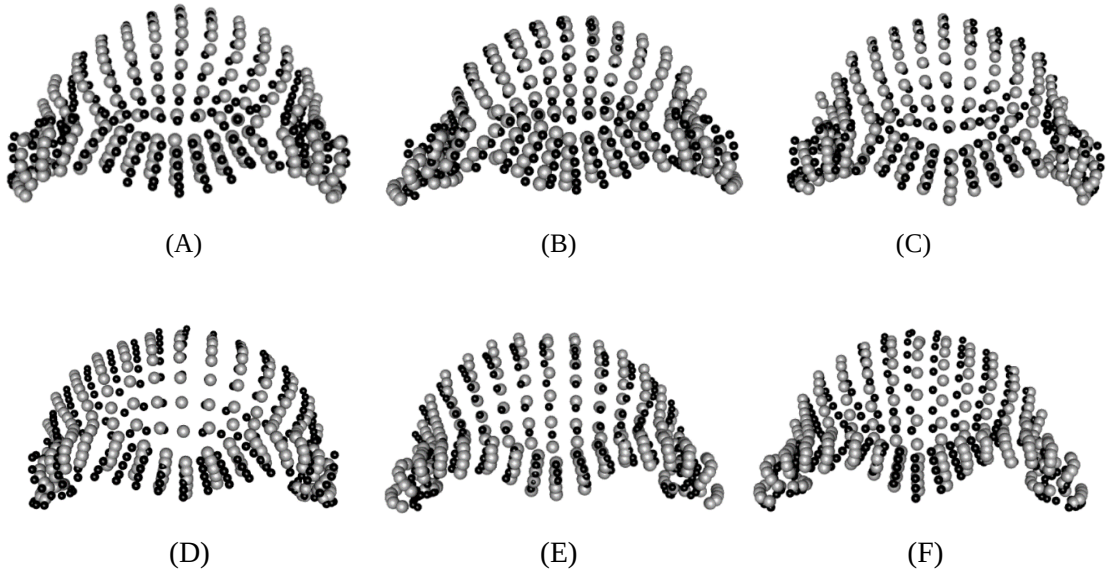

Figure 9.33 The Procrustes superimposition of the frontal bones of fossils (part 1)
The results of the Procrustes superimposition are based on the dataset of the frontal bones of fossils. (A) Ng 12 (grey) vs. OH 9 (black). (B) KNM-ER 3883 (grey) vs. OH 9 (black). (C) S 17 (grey) vs. OH 9 (black). (D) La Chapelle 1 (grey) vs. S 17 (black). (E) KNM-ER 3733 (grey) vs. La Chapelle 1 (black). (F) KNM-ER 3733 vs. D2700. Graphs are generated by the Geomorph R package (Adams et al., 2018).

PC 1 also shows that in a specimen plotted closer to its positive end, the frontal bone becomes mediolaterally narrower, such that the brows flare more laterally from the frontal squama (Figure 9.30). OH 9, KNM-ER 3883 and S 17, which are plotted at PC 1's positive end, have more laterally flaring brows and mediolaterally narrower frontal squama than the Neanderthals, which are plotted at PC 1's negative end (Figure 8.1, Figure 9.31, Figure 9.32 and Figure 9.34). However, differences demonstrated by PC 1 in lateral flaring of the brows between other specimens do not accurately match actual morphological differences. For example, KNM-ER 1813's brows flare more laterally than the brows of Neanderthals, but they are plotted very close to each other in PC 1 (Figure 8.1, Figure 9.31, Figure 9.32 and Figure 9.34). The brows of the Ngandong specimens are less laterally flaring than in D2700 and KNM-ER 3733 (Figure 9.31 and Figure 9.34). The frontal squamae of the Ngandong specimens are also mediolaterally wider than in D2700 and KNM-ER 3733. Yet, the Ngandong specimens are plotted very close to OH 9 and KNM-ER 3883 at the positive end of PC 1, suggesting that the Ngandong specimens' brows are more laterally flaring and their frontal squamae mediolaterally narrower than in D2700 and KNM-ER 3733 (Figure 8.1 and Figure 9.30).

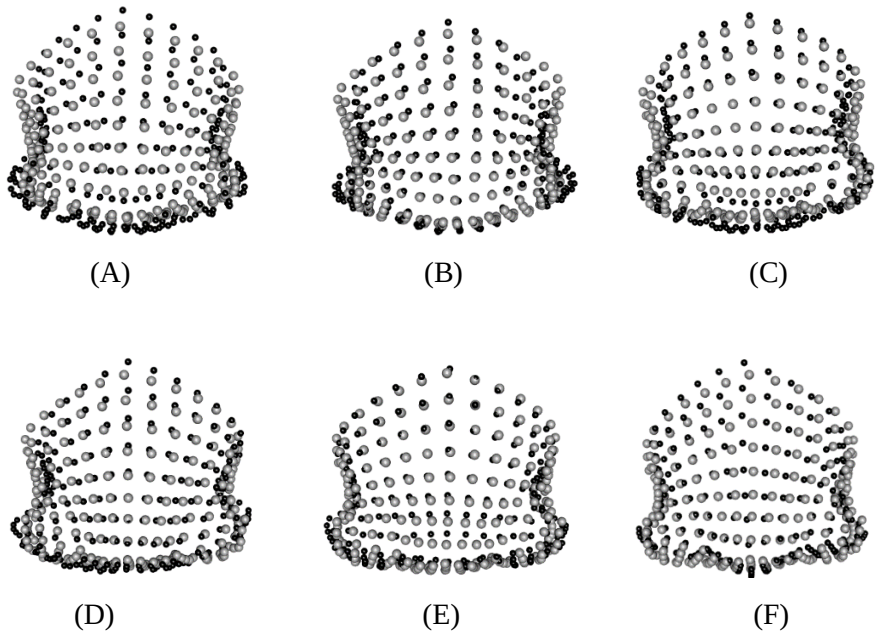

Figure 9.34 The Procrustes superimposition of the frontal bones of fossils (part 2)
The results of the Procrustes superimposition are based on the dataset of the frontal bones of fossils. (A) La Chapelle 1 (grey) vs. OH 9 (black). (B) KNM-ER 3883 (grey) vs. La Chapelle (black). (C) Ng 12 (grey) vs. OH 9 (black). (D) Ng 12 (grey) vs. KNM-ER 3883 (black). (E) Ng 12 (grey) vs. KNM-ER 3733 (black). (F) Ng 12 vs. D2700. Graphs are generated by the Geomorph R package (Adams et al., 2018).

Differences in the steepness of frontal rise demonstrated by PC 1 also do not accurately reflect actual morphological differences. In a specimen plotted closer to the positive end of PC 1, the frontal rise becomes less steep, and the lateral profile of the frontal squama becomes flatter (Figure 8.2 and Figure 9.30). Therefore, the separation between Neanderthals at PC 1's negative end and OH 9, KNM-ER 3883 and S 17 at PC 1's positive end reveals that Neanderthals have steeper frontal rise and more bulging frontal profiles in lateral view than OH 9, KNM-ER 3883 and S17 (Figure 9.31, Figure 9.32, and Figure 9.35). Among other *H. erectus* specimens, Ng 7, Ng 12 and ZKD 12 have steeper frontal rises and more curved lateral profiles of the frontal squamae than D2700 (Figure 9.31 and Figure 9.32). However, they are plotted very close to D2700 and even slightly closer to PC 1's positive end than D2700 (Figure 8.1 and Figure 9.30). The Procrustes superimposition appears to slightly rotate D2700 anteroinferiorly relative to Ng 7, Ng 12, and ZKD 12. Thus, the frontal rise of D2700 becomes slightly steeper than its original condition. When superimposed, the frontal rises of Ng 7, Ng 12, and ZKD 12 are only minimally steeper than in D2700 (Figure 9.31, Figure 9.32 and Figure 9.35). Thus, perhaps the Procrustes superimposition, which reduces differences in the degrees of frontal rise, contributes to plotting Ng 7, Ng 12, ZKD 12 and D2700 very close to each other in PC 1.

KNM-ER 3733, as another *H. erectus* that has a relatively steep frontal rise, is plotted very close to D2700 in PC 1 (Figure 8.1 and Figure 9.31). These differences in the frontal rise between D2700 and KNM-ER 3733 can still be detected when superimposed (Figure 9.35). Thus, PC 1 does not reveal the differences in the degrees of frontal rise between D2700 and KNM-ER 3733. The frontal rise of KNM-ER 1813 is roughly similar to that of Ng 7 and Ng 11 and slightly less steep than that of ZKD 12 (Figure 9.31, Figure 9.32 and Figure 9.35). However, KNM-ER 1813 is plotted very close to Neanderthals at PC 1's negative end, though its frontal rise is slightly less steep than the Neanderthals' (Figure 9.32 and Figure 9.35). Therefore, PC 1 also does not capture the degree of frontal rise in KNM-1813.

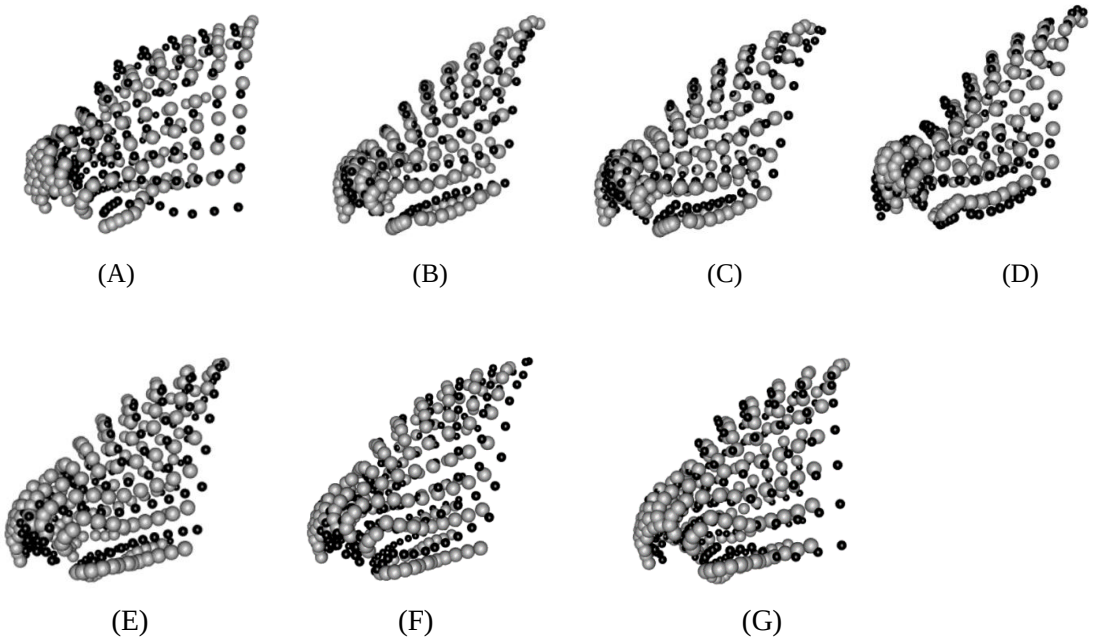

Figure 9.35 The Procrustes superimposition of the frontal bones of fossils (part 3)
The results of the Procrustes superimposition are based on the dataset of the frontal bones of fossils. (A) S 17 (grey) vs. La Chapelle (black). (B) D2700 (grey) vs. OH 9 (black). (C) D2700 (grey) vs. ZKD 12 (black). (D) KNM-ER 3733 (grey) vs. D2700 (black). (E) KNM-ER 1813 (grey) vs. Ng 12 (black). (F) KNM-ER 1813 (grey) vs. ZKD 12 (black). (G) KNM-ER 1813 (grey) vs. La Chapelle 1 (black). Graphs are generated by the Geomorph R package (Adams et al., 2018).

PC 2 in the PCA of the frontal bone shows that in a specimen plotted closer to its positive end, the glabellar region lies slightly more superiorly, while the peak of each brow lies more inferiorly and slightly medially (Figure 8.3 and Figure 9.36). Thus, the brows become less arched. In particular, the ascending part of each brow rises less steeply from the glabellar region. Through the plotting of the

Ngandong specimens at its positive end, PC 2 demonstrates that their brows are overall straighter and more horizontal across the glabellar regions than in other fossils (Figure 8.1 and Figure 9.31).

Kabwe 1 is plotted at PC 2's negative end (Figure 8.1). Kabwe 1's brows are more arched than in the Ngandong specimens (Figure 9.31, Figure 9.32 and Figure 9.37). The ascending parts of Kabwe 1's brows also rise quite steeply from the glabellar region to the peaks of its brows. In particular, the superior margin of the ascending parts of Kabwe 1's brows rise somewhat more steeply than most *H. erectus* specimens, such as OH 9, D2700, KNM-ER 3733, KNM-ER 3883, ZKD 12 and S 17 (Figure 9.37). This is because Kabwe 1's brows are tallest superoinferiorly at their mid-supraorbital regions (Figure 9.32). These differences between Kabwe 1 and *H. erectus* are still obvious when their configurations are Procrustes superimposed, because Kabwe 1's glabellar region lies slightly more inferiorly, and peaks of the brows lie slightly more superiorly than the corresponding parts of *H. erectus* specimens (Figure 9.37).

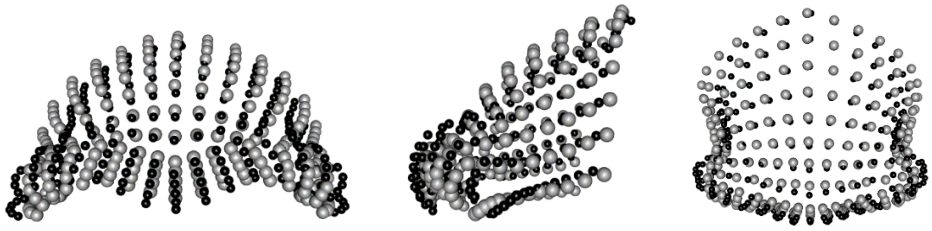

Figure 9.36 The shapes at two ends of PC 2 of the frontal bones of fossils
The black dots represent the shape at the negative end of PC 2. The grey dots represent the positive end of PC 2. Graphs are generated by the Geomorph R package (Adams et al., 2018).

Among other specimens, KNM-ER 1813 and OH 9 are plotted very close to Kabwe 1, suggesting that the ascending parts of their brows rise steeply from the glabellar region (Figure 8.1, Figure 8.3 and Figure 9.36). Similar to Kabwe 1, KNM-ER 1813's brows are also tallest superoinferiorly at the mid-regions (Schwartz & Tattersall, 2003) (Figure 9.32). Thus, the superior margins of the ascending parts of KNM-ER 1813's brows also rise somewhat more steeply from the glabellar region than in most *H. erectus* specimens (Figure 9.37). OH 9 has overall straight and bar-like brows (Figure 9.31). However, the mediolaterally short ascending parts of OH 9's brows rise steeply from the glabellar region (Figure 9.37).

The arrangement of other specimens in PC 2 does not match differences in the steepness of the ascending parts of their brows. For example, Neanderthals have double-arched brows, such that their ascending parts of the brows rise more steeply from the glabellar region than do the corresponding parts of the Ngandong specimens (Figure 9.32 and Figure 9.37). However, Neanderthals are plotted very close

to the Ngandong specimens near PC 2's positive end (Figure 8.1). The ascending parts of the Dali skull's brows also rise steeply from the glabellar region, as in Kabwe 1 and KNM-ER 1813 (Figure 9.32 and Figure 9.37). However, Dali is plotted much closer to the Ngandong specimens than Kabwe 1 and KNM-ER 1813 (Figure 8.1).

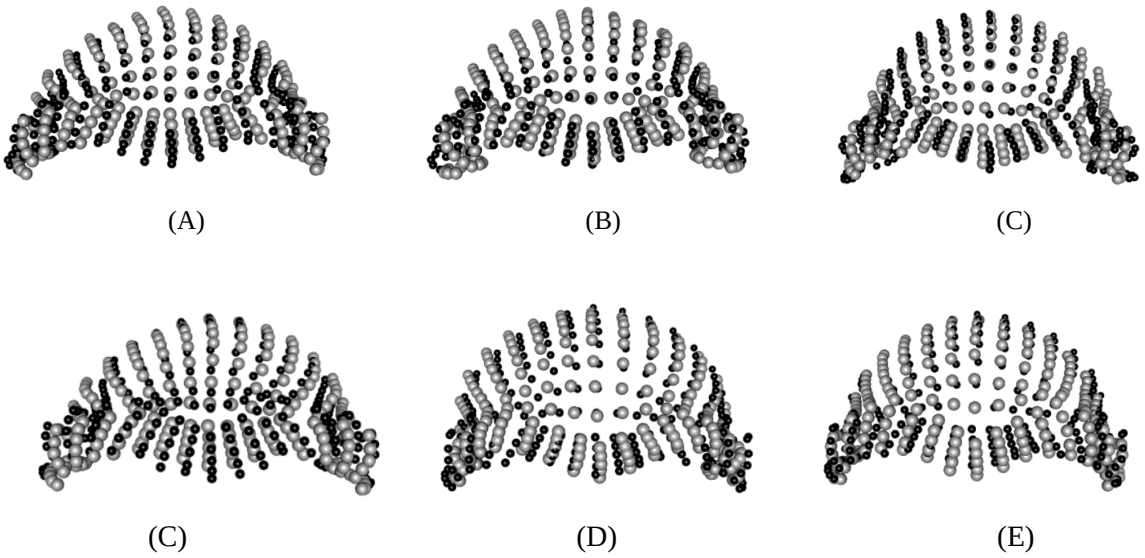

Figure 9.37 The Procrustes superimposition of the frontal bones of fossils (part 4)
The results of the Procrustes superimposition are based on the dataset of the frontal bones of fossils. (A) Ng 12 (grey) vs. Kabwe 1 (black). (B) Ng 12 (grey) vs. S 17 (black). (C) Ng 12 (grey) vs. KNM-ER 1813 (black). (D) Ng 12 (grey) vs. OH 9 (black). (E) La Chapelle 1 (grey) vs. Ng 12 (black). (F) Dali (grey) vs. Ng 12 (black). Graphs are generated by the Geomorph R package (Adams et al., 2018).

PC 2 also shows that in a specimen plotted closer to its positive end, the brows flare less laterally from the frontal squama, and the frontal squama becomes mediolaterally narrower (Figure 8.3 and Figure 9.36). The contrast between Kabwe 1 and the Ngandong specimens at PC 2's negative and positive end reveals that Kabwe 1's supraorbital region flares much more away from the frontal squama than do the supraorbital regions of the Ngandong specimens (Figure 8.1, Figure 9.31, Figure 9.32 and Figure 9.38). OH 9 and KNM-ER 1813 are plotted very close to Kabwe 1, indicating that OH 9 and KNM-ER 1813's brows flare significantly away from their frontal squamae to the degree Kabwe 1's brows do (Figure 8.1, Figure 9.31, Figure 9.32 and Figure 9.38). Neanderthals are plotted very close to the Ngandong specimens, which demonstrates that their brows flare away from their frontal squamae to the same degree as the brows of the Ngandong specimens (Figure 9.38).

However, the arrangement of other specimens in PC 2 does not reflect differences in actual degree of lateral flaring of their brows. According to PC 2, the brows of the Dali skull and Petralona 1 flare as much out from their frontal squamae as in KNM-ER 3883, but much more than in the Ngandong specimens (Figure 8.1). However, when comparing the actual specimens, the brows of the Dali and Petralona skulls flare out from the frontal squamae as much as in the Ngandong specimens, but much less than in KNM-ER 3883 (Figure 9.31, Figure 9.32 and Figure 9.38).

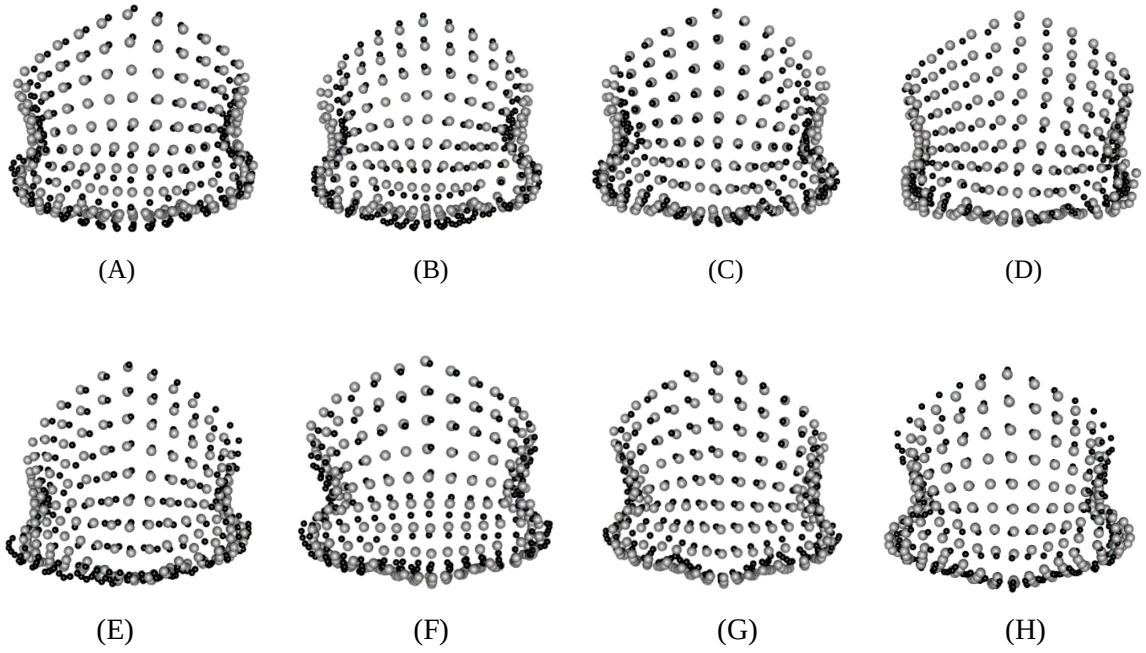

Figure 9.38 The Procrustes superimposition of the frontal bones of fossils (part 5)
The results of the Procrustes superimposition are based on the dataset of the frontal bones of fossils. (A) Ng 12 (grey) vs. Kabwe 1 (black). (B) Ng 12 (grey) vs. OH 9 (black). (C) Ng 12 (grey) vs. KNM-ER 1813 (black). (D) Ng 12 (grey) vs. La Chapelle 1 (black). (E) Dali (grey) vs. KNM-ER 3883 (black). (F) S 17 (grey) vs. KNM-ER 3733 (black). (G) S 17 (grey) vs. D2700 (black). (H) Dali (grey) vs. S 17 (black). Graphs are generated by the Geomorph R package (Adams et al., 2018).

PC 2 also plots S 17, ZKD 12, KNM-ER 3733 and D2700 to nearly identical positions closer to Neanderthals and the Ngandong specimens than to the Dali and Petralona skulls (Figure 8.1). This arrangement suggests that the brows of S 17, ZKD 12, KNM-ER 3733 and D2700 flare out from their frontal squamae to nearly the same degrees. It also shows that S 17, ZKD 12, KNM-ER 3733 and D2700's brows flare laterally slightly more than in Neanderthals and less than in the Dali and Petralona skulls (Figure 8.3 and Figure 9.36). However, when comparing actual specimens, KNM-ER 3733 and

D2700's brows flare more laterally than the brows of S 17 and ZKD 12 (Figure 9.31, Figure 9.32 and Figure 9.38). Furthermore, the brows of S 17, ZKD 12, KNM-ER 3733 and D2700 all flare much more out from their frontal squamae than the brows of Neanderthals, the Dali and Petralona skulls (Figure 9.31, Figure 9.32 and Figure 9.38).

Differences in brow thickness demonstrated by PC 2 also do not accurately reflect actual morphological differences. PC 2 shows that in a specimen closer to its positive end (the Ngandong specimens), the brows become superoinferiorly thinner (Figure 8.3 and Figure 9.36). Kabwe 1 and OH 9, which are plotted at PC 2's negative end, indeed have superoinferiorly taller brows than the Ngandong specimens', which are plotted at PC 2's positive end (Figure 8.1, Figure 9.31, Figure 9.32 and Figure 9.37). However, KNM-ER 3733 and D2700 are plotted very close to S 17 and ZKD 12, though their brows are much superoinferiorly thinner (Figure 8.1, Figure 9.31, Figure 9.32 and Figure 9.39).

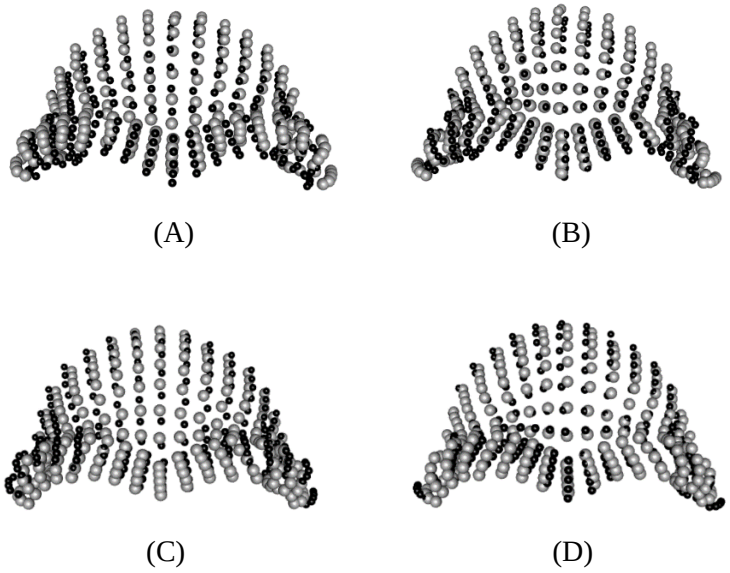

Figure 9.39 The Procrustes superimposition of the frontal bones of fossils (part 6)
The results of the Procrustes superimposition are based on the dataset of the frontal bones of fossils. (A) KNM-ER 3733 (grey) vs. S 17 (black). (B) D2700 (grey) vs. S17 (black). (C) ZKD 12 (grey) vs. KNM-ER 3733 (black). (D) ZKD 12 (grey) vs. D2700 (black). Graphs are generated by the Geomorph R package (Adams et al., 2018).

PC 3 of the frontal bone plots D2700 and KNM-ER 3733 in nearly identical positions at its positive end, well separated from other specimens (Figure 8.4). This PC shows that the brows of KNM-ER 3733 and D2700 are superoinferiorly short and much shorter than the glabellar region relative to the conditions of other fossils (Figure 8.5, Figure 9.31 and Figure 9.40). PC 3 also reveals that they have a

mediolaterally wide supraorbital notch at each side (Figure 8.5, Figure 9.31 and Figure 9.40). Thus, in superior view, the surface of the ascending part of each brow becomes more concave relative to the glabellar region and the descending part of the brow (Figure 9.31 and Figure 9.40).

Other shape differences demonstrated by PC 3 do not match the actual morphology of D2700 and KNM-ER 3733. For example, PC 3 shows that the glabellar lateral profiles of both D2700 and KNM-ER 3733 are similarly vertical (Figure 8.5). However, though D2700's glabellar profile is nearly vertical, the glabellar profile of KNM-ER 3733 bulges out and then curves posteriorly toward nasion, which is depressed (Figure 9.31). After the Procrustes superimposition, these differences in glabellar profile are preserved. However, PC 3, and other PCs, do not demonstrate this difference (Figure 9.40).

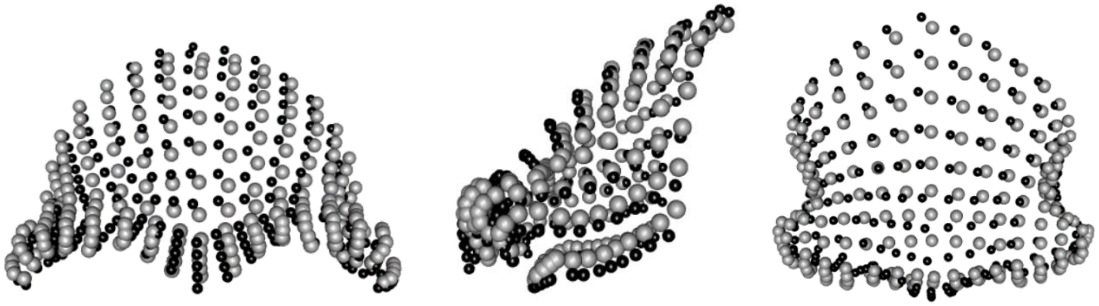

Figure 9.40 The Procrustes superimposition of the KNM-3733 and D2700
The results of the Procrustes superimposition are based on the dataset of the frontal bones of fossils. The gray dots represent KNM-ER 3733. The black dots represent D2700. Graphs are generated by the Geomorph R package (Adams et al., 2018).

PC 3 also shows that both KNM-ER 3733 and D2700 have an anteroposteriorly long and horizontal postorbital plane, because semilandmarks behind the glabellar and supraorbital regions lie more inferiorly than corresponding semilandmarks in other specimens (Figure 8.5). Further, the frontal rises of KNM-ER 3733 and D2700 are steeper than other specimens (Figure 8.5). When examining the specimens, KNM-ER 3733 presents an anteroposteriorly long post-toral sulcus (Figure 9.31 and Figure 9.40). KNM-ER 3733's frontal rise is also quite steep. However, D2700's frontal squama is confluent with the glabellar and supraorbital regions via a slightly sloped, anteroposteriorly short post-toral plane (Figure 9.31 and Figure 9.40). D2700's frontal rise is also less steep than KNM-ER 3733's. Overall, the closeness of KNM-ER 3733 and D2700 in PC 3 cannot be interpreted as morphological similarity in the supraorbital and frontal regions.

PC 4 separates KNM-ER 3733 from other specimens, and reveals some interesting features (Figure 8.6, Figure 8.7, Figure 9.31 and Figure 9.41). For example, PC 4 shows that the surface of the brows is more anterosuperiorly facing than in other fossils. Further, compared to other specimens, semilandmarks at the post-toral region lie more posteroinferiorly, revealing that KNM-ER 3733 develops an anteroposteriorly long post-toral sulcus. In addition, PC 4 also demonstrates that semilandmarks along the sagittal midline anterior to bregma lie more anteriorly than corresponding semilandmarks in other specimens, indicating that KNM-ER 3733 develops a bulging area anterior to its bregma (Figure 8.7, Figure 9.31 and Figure 9.41).

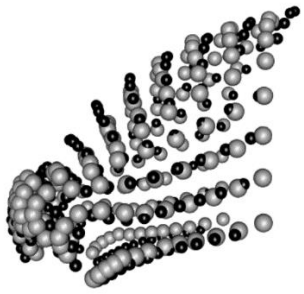

Figure 9.41 The shapes at two ends of PC 4 of the frontal bones of fossils
The black dots represent the shape at the negative end of PC 4. The grey dots represent the positive end of PC 4. Graphs are generated by the Geomorph R package (Adams et al., 2018).

9.2 SEMILANDMARK DENSITIES

One goal of this dissertation is to examine whether using dense surface semilandmarks can capture more morphological details, which may influence results of GMA and associated statistical analyses that are commonly used for testing the validity of *H. erectus*. For this purpose, LASEC analysis was employed. The results of this analysis suggest that all semilandmark datasets used in this study are oversampled, because a much smaller number of semilandmarks can capture similar "shape information" (Watanabe, 2018, p. 12). Indeed, when only using anchor point datasets, the PCAs, UPGMA and statistical analyses that assess overall variability of a sample yield results very similar to those based on the original semilandmark datasets.

The anchor point datasets and original semilandmark datasets appear to capture nearly equivalent "shape information" primarily because the former datasets, though much less dense than the latter

datasets, are still sufficient to include many gross shape differences. These differences are associated with the relative sizes of major cranial bones, overall cranial contours, degree of frontal rise, sizes of the supraorbital regions, and occipital flexure angles.

However, some detailed shape differences are not captured by the anchor point datasets, because there are not enough anchor points on cranial structures or regions where these differences are located. For example, anchor point datasets cannot capture differences between the post-toral planes, such as the presence of a post-toral sulcus in KNM-ER 3733 and ZKD 12, because there are no anchor points on the post-toral region. The concavity of the nuchal plane near the superior nuchal line (e.g., in Kabwe 1 and the Ngandong specimens), indicating strong nuchal muscle attachment, also cannot be captured by using only anchor points, again because there are no anchor points on this region. Furthermore, because only a few anchor points are placed on the mandibular fossa and mastoid region, detailed differences of the mandibular fossae, such as the orientations of the anterior and posterior walls, as well as the degree of downward protrusion of the mastoid processes cannot be included.

Nevertheless, detailed differences, which are only represented by a small number of semilandmarks in the original semilandmark datasets placed at localized structures or small cranial regions, tend to contribute little to overall shape differences. This is because in GMA, overall shape differences, which are calculated as Procrustes distances, are achieved from summarizing positional differences of all corresponding semilandmarks within a group of specimens. Therefore, not including details does not affect most overall shape difference. Furthermore, because statistical analyses commonly used for testing the validity of species are based on assessing overall variability, the results of these analyses are also not likely influenced by omitting some detailed differences, such as downward extensions of the mastoid processes and shapes of the mandibular fossae.

In contrast, gross shape differences tend to contribute substantially to the calculation of overall shape difference, because these differences are usually large-scale and involve many semilandmarks. Even when the datasets used in this study contain a large number of semilandmarks, the calculation of overall shape differences still places more weight on gross shape than detail. In particular, researchers usually pick up a few higher-ranked PCs to interpret shape differences, because these PCs can explain a large proportion of overall shape differences. These higher-ranked PCs also tend to emphasize gross shape differences rather than morphological detail. This explains why the first two to three PCs in each analysis based on anchor points demonstrate shape differences and distributions of specimens comparable to the corresponding PCs based on semilandmarks. However, it should be noted that, as discussed in section 9.1, even gross shapes differences captured by GMA should not be directly equated with actual morphology.

The emphasis on gross shape differences also explains why GMAs based on the maximum-semilandmark and maximum-specimen datasets yield essentially similar results. In the analyses of the entire and posterior cranium, the maximum-specimen datasets do not include semilandmarks placed on the mandibular fossae and the mastoid processes. In the analysis of the temporal bone, the maximum-specimen dataset omits semilandmarks on the mastoid processes. However, the results of the PCAs and other statistical analyses remain essentially comparable to those based on the maximum-semilandmark datasets, primarily because the number of semilandmarks on the mandibular fossa and mastoid processes are very small compared to the number of semilandmarks in the entire dataset. Therefore, not including semilandmarks on the mandibular fossa and mastoid process only has little effect on gross cranial shapes, hence the calculation of overall shape differences.

Although a large number of semilandmarks are sampled, some features still cannot be included. For example, in ZKD 11, ZKD 12, and the Ngandong specimens, the occipital torus is present at the region of occipital flexure. However, semilandmarks placed there are insufficient to capture the occipital tori of these specimens. The trajectories of the suprameatal crests also cannot in this study be captured by semilandmarks. Increasing semilandmark density can potentially include these features. However, because GMA tends to emphasize gross shape differences, including these features is not likely to have a remarkable effect on the results of GMA.

Even when only using discrete landmarks, some gross shape differences can still be captured, such as the overall dimensions of the vault and major cranial bones, the size of the supraorbital region, the arc of the brow, and the relative sizes of the squamosal and the mastoid region of the temporal bone. Thus, in the PCA of each cranial region based on discrete landmarks, the first two PCs that explain a substantial amount of overall shape differences continue to show distributions of specimens roughly similar to those based on semilandmarks or anchor points. The statistical analyses that compare the overall variabilities of the *H. erectus* and *H. sapiens* samples also yield results roughly similar to those based on the semilandmark or anchor point datasets.

Using discrete landmarks certainly cannot capture many shape differences, including some gross shape differences that can be recorded by using either semilandmarks or anchor points. This is because only a small number of discrete landmarks are sampled from the entire cranium. For example, all shape information from the cranial regions where no discrete landmarks are sampled—such as the cranial walls, the nuchal planes, the frontal and occipital squamae, the contours of the squamosal sutures, and the surfaces of the supraorbital and glabellar regions—are not included because no discrete landmarks are sampled from these regions. The LASEC analyses confirm that the discrete landmark datasets can only include a fraction of the shape differences captured by either the semilandmarks or the anchor points. Because of substantial information loss due to sampling a small number of discrete landmarks, some

statistical analyses give results that differ from those based on the semilandmark and anchor point datasets. For example, in the analyses of the entire and posterior cranium, PC 1 based on discrete landmarks places Neanderthals much closer to other specimens than in PC 1 based on the semilandmark or anchor point datasets. Further, Kabwe 1 falls into the Neanderthal cluster in PC 1 based on discrete landmarks, rather than the Asian *H. erectus* cluster as in PC 1 based on either semilandmarks or anchor points. The reason is probably because no discrete landmarks are placed on the vault except for a few along the sagittal suture. Thus, the discrete landmarks cannot capture the mediolateral width of the vault, probably contributing to plotting Neanderthals closer to other specimens in PC 1. This is because PC 1 based on semilandmarks (or anchor points) shows that the vaults of Neanderthals are not only more superoinferiorly taller, but that they are also mediolaterally wider than the vaults of other specimens. In the analysis of the frontal bone, no PC especially separates KNM-ER 3733 from other fossils, likely because very few discrete landmarks are sampled from the surface of the supraorbital region and frontal squama. Therefore, the morphological features that separate KNM-ER 3733 from most other specimens, such as a mediolaterally wide supraorbital notch, a posttoral sulcus, anterosuperiorly facing brows, and a steep frontal rise, are not included in the analysis.

9.3 DIFFERENT CRANIAL REGIONS

This dissertation examines whether analyzing different cranial regions can yield different results of statistical analyses. In this study, semilandmark datasets were sampled from the entire and posterior cranium, and the temporal and frontal bones. The statistical analyses based on datasets sampled from these cranial regions do yield some incompatible results.

In general, the bootstrap analyses of the entire and posterior cranium show that the variability in *H. erectus* and its subsets (*H. ergaster* and Asian *H. erectus*) in Procrustes distances are not significantly greater than in *H. sapiens*. The sum of Procrustes squared distances (SSDs) and mean pairwise distances, which represent the overall variability of *H. erectus* and its subsets, all fall around the 50th percentile of the *H. sapiens* values. Even when adding Kabwe 1 and KNM-ER 1813, which group with *H. erectus* in the UPGMA dendrogram, *H. erectus* is still not significantly more variable in distances than *H. sapiens*. However, the analyses based on the temporal and frontal bones show that the overall variability of *H. erectus* and its subsets (except Asian *H. erectus*) are all significantly greater than in *H. sapiens*. In particular, for the dataset of the frontal bone, the SSD and mean pairwise distances of the *H. erectus* s. l. sample exceed all 10,000 bootstrapped *H. sapiens* values.

Interestingly, Asian *H. erectus* is much less variable in Procrustes distances than other *H. erectus* subsets throughout the analyses of different cranial regions. Even for the analyses of the temporal and frontal bones, the SSDs and mean pairwise distances of Asian *H. erectus* are not significantly greater than in *H. sapiens*. The relatively small variability of Asian *H. erectus* is primarily due to small pairwise Procrustes distances between the late Indonesian specimens (i.e., the Ngandong specimens, Ngawi 1 and SM 3). In the analyses of the entire and posterior cranium as well as the temporal bone, the majority of pairwise distances between the late Indonesian specimens fall below the 25th percentile of bootstrapped distances within *H. sapiens*. In the analyses of the frontal bone, the pairwise distances between the late Indonesian specimens fall below the 50th percentile of bootstrapped *H. sapiens* values.

Except for the late Indonesian specimens, pairwise Procrustes distances between other fossils are incompatible with the analyses that focus on different cranial regions. For example, in the analyses of the entire and posterior cranium, except for Kabwe 1 and KNM-ER 1813, *H. erectus* is well separated from Neanderthals, Petralona 1 and the Dali skull in the UPGMA dendrogram constructed from pairwise Procrustes distances between specimens. The analyses of the temporal bone show that the temporal configurations of KNM-WT 15000, Petralona 1, and the late Indonesian specimens are, in general, well separated from other specimens. In fact, the overall variability of temporal bone configurations of *H. erectus* and its subsets is significantly greater than in *H. sapiens*. This is primarily because the distances between KNM-WT 15000 and other *H. erectus* specimens, especially the Ngandong specimens, are great. Other than the late Indonesian specimens, the distances between KNM-ER 3733, D2700 and OH 9 are relatively small. In addition, the pairwise distances do not show a clear separation between *H. erectus* and other specimens, because the UPGMA dendrogram shows that Neanderthals, the Ngandong specimens, the Dali skull, KNM-ER 1813, and KNM-ER 3883 group into the same cluster.

Regarding the frontal bones, except for the late Indonesian specimens, the distances between most *H. erectus* specimens are greater compared to distances between *H. sapiens* specimens. The distance between OH 9 and other *H. erectus* specimens is particularly great, though OH 9 is somewhat closer to KNM-ER 3883. The distance between KNM-ER 3733 and D2700 is also relatively small compared to distances between other *H. erectus*. Similar to the late Indonesian specimens, the frontal configurations of Neanderthals are, in general, close to each other in distances and well separated from other specimens.

The statistical tests of differences between mean shapes of geographical subsets are also different in the analyses of different cranial regions. In the analyses of the entire and posterior cranium, the bootstrap analyses show that distances between means of geographical subsets of *H. erectus* (*H. ergaster* and Asian *H. erectus*) are insignificant compared to distances between geographical subsets of *H. sapiens*. This is most likely because pairwise distances between *H. erectus* specimens are very small, compared to the distances within *H. sapiens*. Contradictory to the bootstrap analyses, the Procrustes ANOVAs show

that a significant amount of the total variance within *H. erectus* is associated with the separation of geographical groups. However, when evaluating individual pairwise distances, in general, the *H. ergaster* specimens are separated from each other as much as they are from the Asian *H. erectus* specimens. Further, when using the distances between the late Indonesian specimens as references, *H. ergaster* specimens are not close to each other. Thus, *H. ergaster* specimens do not constitute a group well-separated from Asian *H. erectus*. It should be noted that the majority of Asian *H. erectus* are the late Indonesian specimens. Therefore, the detection of geographical groups by the Procrustes ANOVAs might be driven by small distances between the late Indonesian specimens, which are relatively more separated from *H. ergaster*.

The bootstrap analyses of the temporal bone show that the distances between geographical subsets are not significantly greater than those between geographical subsets of *H. sapiens*. The Procrustes ANOVAs also indicate that only an insignificant amount of the total variance within *H. erectus* is associated with a separation of geographical groups. The Procrustes distances between individual specimens also do not show that specimens belonging to *H. ergaster*, African *H. erectus*, or Asian *H. erectus* are particularly closer to each other than to other specimens in Procrustes distances, though distances between the late Indonesian specimens are still relatively small.

The bootstrap analyses and Procrustes ANOVAs of the frontal bone all support a separation of an African-Dmanisi group and an Asian group. A clear separation between means of geographical groups of *H. erectus* revealed by the bootstrap analyses is primarily due to the pairwise distances between most *H. erectus* specimens being significantly greater than those between *H. sapiens* specimens. Further, S 17 and ZKD 12 are somewhat closer to the Indonesian specimens than they are to the African and Dmanisi specimens. However, patterns of Procrustes distances between African and Dmanisi specimens are complicated. Though the distance between OH 9 and KNM-ER 3883 is relatively small, African and Dmanisi specimens are not particular closer to each other than to Asian *H. erectus*. Thus, the existence of geographical groups indicated by Procrustes ANOVA is due primarily to relatively small distances between Asian specimens. Overall, based on Procrustes distances alone, African and Dmanisi specimens do not constitute a coherent group.

In general, the incompatible results of the statistical analyses of different cranial regions are probably because they emphasize different shape information. As demonstrated by PCAs, the analyses of the entire and posterior cranium emphasize large-scale, gross differences that involve many semilandmarks, such as proportions between cranial bones and overall cranial contours. For example, in the analysis of the entire cranium, PC 1 demonstrates gross differences, such as overall size of the vault relative to the temporal bone, degree of postorbital constriction, and overall cranial profile. PC 2 shows

differences in anteroposterior length of the frontal and occipital bones relative to the parietal bone, and size and positions of the supraorbital region relative to the vault.

The large-scale, gross shape differences of the entire cranium certainly cannot be captured by the analyses based on semilandmarks sampled from isolated temporal and frontal bones. Rather, the analyses of the temporal and frontal bones place more weight on localized shape differences. For example, in the temporal bone analyses, PC 1 and PC 2 demonstrate differences in the course of the squamosal and parietomastoid sutures, and size of the squamosal part of the temporal bone relative to the mastoid region. In the frontal bone analyses, the first four PCs demonstrate differences such as the arc of the brow, orientation of the supraorbital and glabellar surfaces, and the presence of a horizontal post-toral plane and posttoral sulcus. These differences in the temporal and frontal bones are potentially included by the datasets of the entire and posterior cranium. This is because semilandmarks in the datasets of the temporal and frontal bones are simply those placed on the temporal and frontal regions in the datasets of the entire and posterior crania. However, as previously discussed, in the analyses of the entire and posterior cranium, localized differences in individual cranial bones tend to contribute less to overall shape differences than large-scale, gross shape differences.

9.4 SAMPLE SIZES OF *H. SAPIENS*

Paleoanthropologists usually include a large sample of *H. sapiens* for exploring differences between fossil hominids and *H. sapiens*, and for increasing sample sizes for statistical analyses (e.g., Freidline, Gunz, Janković, et al., 2012; Lordkipanidze et al., 2013). However, when the sample size of *H. sapiens* is much larger than the fossils, higher-ranked PCs that explain a substantial amount of the total variance may only demonstrate differences within *H. sapiens*. This is because differences within a relatively small sample of fossils tend to contribute little to overall shape differences within a pooled sample that includes both *H. sapiens* and fossils. Therefore, to assess effect of sample sizes of *H. sapiens* on statistical analyses, especially PCA, this study includes a large and small sample of *H. sapiens* (35 and 8 respectively).

In the PCAs of each cranial region that include the large *H. sapiens* sample and fossils, the first PC shows that fossils differ from *H. sapiens* in having anteroposteriorly longer and superoinferiorly lower vaults, steeper occipital flexures, gentler frontal rise, larger mandibular fossae and more lateral flaring brows. In general, the second or third PC only focus on differences within *H. sapiens*, whereas fossil specimens are grouped into a relatively tight cluster.

Though higher-ranked PCs that include the large *H. sapiens* sample with fossils only focus on differences within *H. sapiens*, a few lower-ranked PCs are roughly comparable to higher-ranked PCs in the analyses that only include the fossils. For example, in the analyses of the entire cranium, PC 4 and PC 5 that include both *H. sapiens* and fossils describe nearly the same shape differences between fossils as do PC 1 and PC 2 that only include the fossils. In the analyses of the temporal bone that include both the large sample of *H. sapiens* and fossils, PC 2 and PC 4 demonstrate shape differences that separate the Petralona skull from all others, comparable to PC 1 in the analysis that only include fossils. PC 3 in the analyses that includes both *H. sapiens* and fossils are roughly compatible with PC 2 in the analysis that only includes fossils. In the analyses of the frontal bone that includes both *H. sapiens* and fossils, only PC 2 describes the same shape differences as PC 1 in the analysis of fossils.

When including only the small *H. sapiens* sample together with fossil hominids, the PCAs are, in general, still consistent with those in the analyses that include the large *H. sapiens* sample and fossils. The first PC in each PCA continues to separate *H. sapiens* from the fossils. However, the second or third PCs cease to focus on differences within *H. sapiens*, likely because the sample size of *H. sapiens* is small. Instead, the second or third PCs become roughly compatible with the first two PCs in the analyses of fossil hominids. For example, in the analyses of entire cranium that include the large *H. sapiens* sample and fossils, PC 4 and PC 5 are roughly consistent with PC 1 and PC 2 in the analyses that only include fossils. However, with the small *H. sapiens* sample and fossils, PC 2 and PC 3 become roughly consistent with PC 1 and PC 2 in the analyses that only include fossils.

9.5 CONCLUSION

This dissertation assesses whether GMA based on surface semilandmarks can capture more observed morphological features than analyses based on discrete landmarks. This study also assesses whether these details, if captured, can be properly identified from results of PCA. Semilandmark datasets used in this study can potentially capture many observed features, including cranial profile, the morphology of the post-toral plane, muscle markings of the nuchal muscles, morphology of the supraorbital region, courses of the squamosal and parietomastoid sutures, and shapes of the mandibular fossa. This is because semilandmarks are placed on cranial regions where these features are located.

However, many shape differences demonstrated by PCAs between hominids do not match observed morphology. Even some gross cranial shape differences, including lateral cranial profile, occipital profile, size of the supraorbital region, and overall shape of the temporal bone, are not compatible with actual morphological differences. Procrustes superimposition is identified as an

important, yet usually ignored, factor that underlies these incompatibilities between the shape differences demonstrated by PCA and actual morphology. This is because this procedure determines how semilandmark configurations are superimposed, which then determines results of GMA. In particular, during the process of Procrustes superimposition, superimposed semilandmark configurations of specimens are rotated to slightly different angles to minimize overall shape differences calculated as Procrustes sum of squares. However, observed morphology is based on aligning specimens in the Frankfurt plane. The different ways of orienting specimens probably contribute to the incompatibility between shape differences revealed by PCA and actual gross morphological differences.

Overall, this study suggests that shape differences read either from superimposed configurations or the results of PCA should not be treated as representing actual morphological differences. Though Gunz and Mitteroecker (2013) suggested that using dense surface semilandmarks can facilitate interpretation, shape differences revealed by GMAs should be read cautiously. When interpreting results of GMA, it is crucial to first have a thorough understanding of cranial morphology based on examining actual specimens. These observed morphological differences should then serve as a basis from which to assess whether shape differences captured and revealed by GMA have real morphological meaning.

An important goal of this dissertation is to test whether increasing semilandmark densities can capture more features, hence affect results of statistical analyses that test hypotheses of *H. erectus*. These hypotheses are 1) *H. erectus* is more variable than *H. sapiens*, 2) the overall variability in Asian *H. erectus* and *H. ergaster* exceeds that of *H. sapiens*, and 3) the difference between Asian *H. erectus* and *Homo ergaster* exceeds that between geographical subsets of *H. sapiens*.

Although dense surface semilandmarks can potentially capture more morphological differences than using discrete landmarks, they do not appear to remarkably affect statistical analyses of overall variability. In fact, semilandmark datasets used in this study also appear to be oversampled for commonly used statistical analyses based on computing overall shape differences. A much lower density of surface semilandmarks can yield nearly identical results. Consequently, other than difficulty in associating shape differences captured and visualized by GMA with observed morphology, this study also demonstrates that including detailed shape differences may not affect statistical analyses. The reason is that since GMA quantifies overall shape differences, it tends to place more weight on large-scale, gross shape differences that involve a large number of semilandmarks than on details. However, discrete landmarks cannot even sufficiently capture gross cranial shapes. Overall, if the purpose is to compute overall shape differences, it is better to experimenting on different densities of semilandmarks in order to determine the number of semilandmarks one needs to sample.

This study also shows that statistical analyses of different cranial regions can yield incompatible results of overall variability. The analyses of the entire and posterior cranium show that *H. erectus* and its

subsets are not more variable than *H. sapiens*. These results are consistent with previous GMAs that place discrete landmarks across the entire cranium (e.g., Baab, 2008a). However, the analyses of the frontal and temporal bones suggest that *H. erectus* and its subsets are significantly more variable in Procrustes distances than *H. sapiens*. One possible reason for this is that localized shape differences may place more weight on calculating overall shape differences in the analyses of individual bones than entire crania. The majority of GMAs that aims to quantify the overall variability of *H. erectus* only focuses on overall cranial configurations by sampling landmarks across the calvaria (e.g., Baab, 2008b; Lordkipanidze et al., 2013). In general, these studies show that *H. erectus* is not more variable than *H. sapiens* or extant great apes (e.g., Baab, 2008b; Lordkipanidze et al., 2013). This is likely because these studies only focus on gross shapes of the entire cranium rather than shapes of individual bones or localized structures.

Another sampling factor worth noticing is the sample size of *H. sapiens*. This study shows that in PCAs based on a large sample of *H. sapiens* and fossils, a few higher-ranked PCs, such as PC 2 and PC 3 in the analyses of the entire cranium, only focus on differences within *H. sapiens*. However, there are still lower-ranked PCs that are roughly consistent with the first two PCs in PCAs of fossils. Therefore, when including a large sample of *H. sapiens* with fossils in a PCA, it is also important to examine lower-ranked PCs.

Overall, this study suggests that current methods for analyzing landmark and semilandmark data, although robust in quantifying overall shape differences, fall short in identifying morphological detail. Although usually criticized as subjective because they rely on visual analysis and verbal description, conventional comparative morphological analyses are flexible in searching for and comparing between specific features across an array of specimens. Through orienting specimens consistently via the Frankfurt plane, morphological descriptions can also be relatively consistent. As species recognition in paleoanthropology must be based on a comprehensive analysis of morphology, GMA should work with, rather than replace, conventional morphological analysis, in order to contribute to a more holistic understanding of hominid morphology, which can then serve as a basis for testing hypotheses of hominid taxic diversity. Recently, through analyzing gross shape differences of the entire cranial vault, GMA has contributed significantly to the suggestion that *H. erectus* is a highly variable species (e.g., Baab, 2008a, 2016; Lordkipanidze et al., 2013). Detailed morphological analyses as well as GMAs of different individual cranial bones should also be carried out to provide a comprehensive assessment about the taxonomic validity of *H. erectus*.

9.6 FUTURE DIRECTIONS

This study suggests that Procrustes superimposition may underlie incompatibilities between shape differences revealed by PCA and observed morphological differences, because the Procrustes superimposition rotates specimens to different orientations until overall shape differences are minimized. However, observed morphology is based on aligning specimens in the Frankfurt plane. In order to have a thorough understanding of influences of orientations on GMA, it is necessary to compare analyses that align specimens by Procrustes superimposition and those that align specimens in the Frankfurt plane. Therefore, the next step of this study is to assess how different ways of aligning specimens may affect results of GMA, based on landmark or semilandmark data. Further, it would be especially interesting to sample more fossil specimens and specimens of extant apes in order to explore whether including different specimens may affect results of the Procrustes superimposition, which would then influence the results of GMA.

It is also crucial to continue developing methods for detecting specific features from landmark data. This will improve the contribution of GMA to the study of hominid systematics. As discussed in this dissertation, current methods that analyze landmark data primarily focus on capturing patterns of overall similarity, not specific morphological features (Adams et al., 2004; Zelditch et al., 2012). However, the foundation of systematics is to properly recognize detailed morphological features, because the study of systematics is about discovering unique morphological features as a basis for recognizing groups and their phylogenetic relationships (Andrews, 1984; Schwartz & Tattersall, 2002, 2003; Tattersall, 2000; Zeitoun, 2009). Therefore, a quantitative method that can contribute to systematics must be able to recognize specific morphological features.

A particular method, machine learning, which is a subset of artificial intelligence, might be promising for the study of systematics. Machine learning is a category of algorithms that trains computers to make decisions from existing data and past experience (Alpaydın, 2010; Sajda, 2006). In recent years, machine learning has been developed for various kinds of biomedical research because of its great potential in automatically recognizing biological features from 2D and 3D images of specimens (Bäckström et al., 2018; Sajda, 2006; Shahri, 2015; Sommer & Gerlich, 2013; Zhang et al., 2014). For example, some researchers developed machine learning algorithms for recognizing abnormal anatomical features indicated ocular disease from scanned 2D and 3D images of eyeballs commonly used in visual diagnoses (Zhang et al., 2014). Another group developed algorithms of deep learning, a subdiscipline of machine learning, in order to recognize markers of Alzheimer's disease from brain scans (Bäckström et al., 2018). Other studies aim to develop machine-learning systems to recognize features of cells from microscopic images for purposes of cell-type classification (Sommer & Gerlich, 2013). In these

experiments, computer systems are trained with a large amount of existing data about diagnostic features of diseases or certain cell types (Bäckström et al., 2018; Sommer & Gerlich, 2013; Zhang et al., 2014). Here, the decision-making ability of these computer systems is based on the knowledge and experiences of biomedical researchers. Further, with the supervision of experts, the more disease features the systems successfully identify via new cases, the more experience the computer systems will gain. As a result, the systems are expected to become more accurate and efficient in disease diagnosis and cell classification (Bäckström et al., 2018; Shahri, 2015; Sommer & Gerlich, 2013; Zhang et al., 2014).

If techniques of machine learning can be used to train computer systems to recognize and extract biological features for disease diagnosis or cell classification, these techniques have the potential to identify specific morphological features from fossil remains. In particular, recent advances in facial recognition techniques enable using machine learning to identify individuals from geometric properties in high-resolution 3D scans of human faces (Kesterke et al., 2019; Kim et al., 2017). High-resolution 3D scans are accurate virtual replicas of biological specimens, such as the 3D models of hominid crania used in this dissertation for sampling landmarks and semilandmarks. Though directly using 3D scans of fossils requires powerful computers, these scans can preserve most morphological detail of original specimens.

Machine learning also offers unique advantages for studying systematics because this technique enables computer systems to learn from prior "experiences" with morphology as well as to deal efficiently with a huge amount of data. In hominid systematics, groups are defined by unique morphological features. Because unique features of any hominid or group of hominids are recognized by comparing these specimens with a large outgroup, the study of hominid systematics requires a substantial knowledge and data base of mammalian morphology (Schwartz, 2004; Schwartz & Tattersall, 2002, 2003). For example, a potentially new species must possess some unique features not present in other mammals. Ideally, computer systems can learn from systematists' knowledge of mammalian comparative morphology, just as computer systems in biomedical researches can gain knowledge of diagnostic features of disease from medical experts. For example, when training computer systems with existing data, researchers can employ the techniques called supervising learning to determine if features extracted by computers match actual morphology (Shahri, 2015). In this way, researchers can correct mistakes computer systems make in recognizing specific features (Shahri, 2015). Based on acquired knowledge of mammalian morphology, computer systems can then make decisions about whether recognized features of a newly added fossil specimen are unique to it or not. Theoretically, by continually adding specimens with different features into a data base, computer systems can keep accumulating data in mammalian morphology, thereby increasing the accuracy of determining whether a newly observed feature is unique or not.

Some authors have proposed developing algorithms of machine learning to facilitate automatic species recognition. For example, MacLeod et al. (2016) experimented with algorithms of machine learning to recognize planktonic foraminiferal species from a set of 2D images. Ellen et al. (2015) also attempted to apply machine learning to identify plankton species from their 2D images. However, these analyses only focus on discriminating known taxa of organisms. Currently, no study specifically focuses on developing techniques of machine learning to recognize unique features in order to study hominid systematics. Therefore, techniques of machine learning that can work with high-resolution 3D scans of hominid remains should be developed to contribute to the study of hominid systematics.

Overall, the results of this dissertation suggest that methods of GMA are designed for computing overall shape differences. Even when dense surface semilandmarks are used, these methods are not as efficient in extracting and comparing specific morphological features as visual comparative method is. In order to develop quantitative techniques suitable for hominid systematics, these techniques should be able to appropriately recognize and compare individual morphological features within a large group of organisms. Though highly challenging, future studies should focus on developing techniques of artificial intelligence, especially machine learning, to meet the methodological requirements of systematics.

APPENDIX A MATERIALS AND SEMILANDMARK DATASETS

A.1 SPECIMENS

Table A.1 Fossil specimens used in the analysis

Specimens	Self-scanned (S) or acquired (A)[1]	Taxon[3]	Site[3]	Preservation condition[3]	Dating[3] (million years ago (Ma))
D2700	A	*H. erectus* or *H. ergaster*	Dmanisi, the Republic of Georgia	Face and vault are well preserved	~1.7 Ma
KNM-ER 3733	A	*H. erectus* or *H. ergaster*	Koobi Fora, Kenya	Face and vault are well preserved; the area of bregma is damaged	~ 1.8 Ma
KNM-ER 3883	S	*H. erectus* or *H. ergaster*	Koobi Fora, Kenya	The vault is well preserved but distorted; only a relatively small portion of right face is preserved	~ 1.6 Ma
Ngandong 6 (Ng 6)	S	*H. erectus*	Ngandong, Indonesia	The vault is largely preserved. Missing face, lateral end of right brow, right mandibular fossa, right mastoid process and the tip of left mastoid process.	< 0.1 Ma
Ngandong 7 (Ng 7)	S	*H. erectus*	Ngandong, Indonesia	The vault is fairly complete. Missing face. The end of the right brow is damaged. The lateral half of the left brow is broken. The lateral end of each mandibular fossa is broken.	< 0.1 Ma

Table A.1 (continued)

Specimens	Self-scanned (S) or acquired (A)[1]	Taxon[3]	Site[3]	Preservation condition[3]	Dating[3] (million years ago (Ma) or thousand years ago (Ka))
Ngandong 10 (Ng 10)	S	*H. erectus.*	Ngandong, Indonesia	The vault is largely preserved. Missing face, inferior part of each brow, lateral end of each mandibular fossa, left mastoid process and tympanic region, inferior tip of the right mastoid process	< 0.1 Ma
Ngandong 12 (Ng 12)	S	*H. erectus*	Ngandong, Indonesia	The vault is nearly complete. Face is missing. The lateral end of the left mandibular fossa is broken. The inferior tip of each mastoid process is broken.	< 0.1 Ma
Ngawi 1	S	*H. erectus*	Ngawi, Indonesia	The vault is fairly complete. The cranial base is heavily weathered. The face is missing.	
OH 9	S	*H. erectus*	Olduvai Gorge, Tanzania	The vault is heavily reconstructed. Missing face and a large portion cranial roof. The inferior portion of each mastoid process is broken.	1.4 to 1.5 Ma
Sangiran 2 (S 2)	S	*H. erectus*	Sangiran, Indonesia	Missing face and right brow region. Right mandibular fossa, tympanic tube, and left mastoid region are damaged.	0.9 to 1.6 Ma
Sangiran 17 (S 17)	A	*H. erectus*	Sangiran, Indonesia	Fairly complete. Face is preserved. The cranial roof is cracked. The lateral end of left mandibular fossa is broken.	0.9 to 1.6 Ma
Sambungmaçan 3 (SM 3)	A	*H. erectus*	Sambungmaçan, Indonesia	The vault is fairly complete. Missing face. The medial part of right brow is damaged. The lateral end of each mandibular fossa and the inferior tip of each mastoid process are broken.	< 0.1 Ma
KNM-WT 15000	A	*H. erectus* or *H. ergaster*	Nariokotome, Kenya	The skull is fairly complete. The face is preserved. A large portion of the brows and glabellar region are broken.	~1.6 Ma
Zhoukoudian Skull XI (ZKD 11)	S	*H. erectus*	Zhoukoudian, China	The vault is fairly complete. Missing face, lateral end of each brow, lateral end of each mandibular fossa, and inferior tip of each mastoid process.	0.2 to 0.6 Ma
Zhoukoudian Skull XII (ZKD 12)	A/S[2]	*H. erectus*	Zhoukoudian, China	The vault is fairly complete. Missing face and right temporal region. The lateral end of the left mandibular fossa and the inferior tip of the left mastoid process are broken.	0.2 to 0.6 Ma

Table A.1 (continued)

Specimens	Self-scanned (S) or acquired (A)[1]	Taxon[3]	Site[3]	Preservation condition[3]	Dating[3] (million years ago (Ma) or thousand years ago (Ka))
KNM-ER 1813	A	*H. habilis*	Koobi Fora, Kenya	The skull is fairly complete. Missing part of left brow region and part of cranial base.	~1.9 Ma
The Dali skull	A	Mid-Pleistocene *Homo*	Dali, China	Fairly complete skull. Part of right occipital and parietal regions are reconstructed.	~180 to 230 Ka
Petralona 1	A	*Homo heidelbergensis*/Mid-Pleistocene *Homo*	Petralona, Greece	Well-preserved skull	150 to 250 Ka
The La Chapelle skull	A	*Homo neanderthelansis*	La Chapelle-aux-Saints, France	Fairly complete skull. Missing part of right vault.	>125 Ka
La Ferrassie 1	A	*Homo neanderthelansis*	Savignac du Bugue, France	Fairly complete skull.	~70 Ka
Shanidar 1	A	*Homo neanderthelansis*	Greater Zab river valley, Iraq	A reconstructed cranium. The skull is fairly complete.	~60 Ka

1. All the specimens scanned by the author are well-made casts generously provided by Dr. Ian Tattersall of the American Museum of Natural History (AMNH). The scanning facility and instruction are offered by Dr. William Harcourt-Smith of AMNH. The 3D models of the other specimens are kindly offered by Dr. Eric Delson of AMNH.

2. One 3D model of ZKD 12 is scanned from the cast made by Weidenreich from Dr. Ian Tattersall's collection. Another 3D model is the cast reconstructed by Tattersall and Sawyer (1996). The vault and the left temporal of this cast comes from ZKD 12. The right temporal comes from the Skull III. Because the authors also reconstructed the lateral end of the mandibular fossa, this study uses this reconstructed cast. The left temporal of Skull III is deleted.

3. The commonly used classification, preservation condition and dating are cited from Rightmire (1993, 1998), Marquez et al. (2001), Vekua et al. (2002), Rightmire et al. (2006), Anton (2002, 2003) and Schwartz and Tattersall (2002, 2003)

Table A.2 Fossil specimens included in the analyses of different cranial regions

Specimens	Taxon[3]	Overall cranium[4]		Posterior cranium		Temporal		Frontal
		Max landmark	Max specimen	Max landmark	Max specimen	Max landmark	Max specimen	
D2700	*H. erectus s. l.*	✓	✓	✓	✓	✓	✓	✓
KNM-ER 3733	*H. erectus s. l.*	✓	✓	✓	✓	✓	✓	✓
KNM-ER 3883	*H. erectus s. l.*	✓	✓	✓	✓	✓	✓	✓
Ngandong 6	*H. erectus s. l.*		✓		✓		✓	✓
Ngandong 7	*H. erectus s. l.*	✓	✓	✓	✓	✓	✓	✓
Ngandong 10	*H. erectus s. l.*				✓			✓
Ngandong 12	*H. erectus s. l.*	✓	✓	✓	✓	✓	✓	✓
Ngawi 1	*H. erectus s. l.*		✓		✓			✓
OH 9	*H. erectus s. l.*						✓	✓
Sangiran 2	*H. erectus s. l.*			✓	✓	✓	✓	
Sangiran 17	*H. erectus s. l.*	✓	✓	✓	✓	✓	✓	✓
Sambungmaçan 3	*H. erectus s. l.*				✓			
KNM-WT 15000	*H. erectus s. l.*			✓	✓	✓	✓	
Zhoukoudian Skull XI	*H. erectus s. l.*				✓			
Zhoukoudian Skull XII	*H. erectus s. l.*		✓		✓		✓	✓
KNM-ER 1813	*H. habilis*	✓	✓	✓	✓	✓	✓	✓

Table A.2 (continued)

Specimens	Taxon[3]	Overall cranium[4]		Posterior cranium		Temporal		Frontal
		Max landmark	Max specimen	Max landmark	Max specimen	Max landmark	Max specimen	
Sambungmaçan 3	*H. erectus s. l.*				✓			
KNM-WT 15000	*H. erectus s. l.*			✓	✓	✓	✓	
Zhoukoudian Skull XI	*H. erectus s. l.*				✓			
Zhoukoudian Skull XII	*H. erectus s. l.*		✓		✓		✓	✓
KNM-ER 1813	*H. habilis*	✓	✓	✓	✓	✓	✓	✓
The Dali skull	*Homo. heidelbergensis/* Mid-Pleistocene *Homo*	✓	✓	✓	✓	✓	✓	✓
Kabwe 1	*Homo heidelbergensis/* Mid-Pleistocene *Homo*	✓	✓	✓	✓	✓	✓	✓
Petralona 1	*Homo heidelbergensis/* Mid-Pleistocene *Homo*		✓		✓		✓	✓

Table A.2 (continued)

Specimens	Taxon[1]	Overall cranium[2]		Posterior cranium		Temporal		Frontal
		Max landmark	Max specimen	Max landmark	Max specimen	Max landmark	Max specimen	
The La Chapelle skull	*Homo neanderthalensis*	✓	✓	✓	✓	✓	✓	✓
La Ferrassie 1	*Homo neanderthalensis*	✓	✓	✓	✓	✓	✓	✓
Shanidar 1	*Homo neanderthalensis*	✓	✓	✓	✓	✓	✓	✓

1. The commonly used classification, preservation condition and dating are cited from Rightmire (1993, 1998), Marquez et al. (2001), Vekua et al. (2002), Rightmire et al. (2006), Anton (2002, 2003) and Schwartz and Tattersall (2002, 2003)

2. This study analyzed four cranial regions: the overall calvaria, the posterior calvaria, the temporal region, and the frontal region. For each cranial region, two landmark sets are used. The first landmark set is the maximum landmark set. The second landmark set is the maximum specimen set.

Table A.3 The *Homo sapiens* sample

Population	Source[1]	Number
Egypt	AMNH	8
Ethiopia	AMNH	5
Mongolia	AMNH	5
Australian Aborigine	AMNH	17

1. All the *H. sapiens* 3D models are adult specimens generously provided by Dr. William Harcourt-Smith and Dr. Eric Delson from the American Museum of Natural History (AMNH).

Table A.4 The geographical subsets of the H. erectus s. l. sample

Specimens	African *H. ergaster*	*H. ergaster*	African *H. erectus*	Asian *H. erectus*
D2700		✓		
ER 3733	✓	✓	✓	
ER 3883	✓	✓	✓	
Ng 6				✓
Ng 7				✓
Ng 10				✓
Ng 12				✓
Ngawi 1				✓
OH 9			✓	
S 2				✓
S 17				✓
SM 3				✓
WT 15000	✓	✓	✓	
ZKD 11				✓
ZKD 12				✓

A.2 VIRTUAL RECONSTRUCTION OF HOMINID SPECIMENS

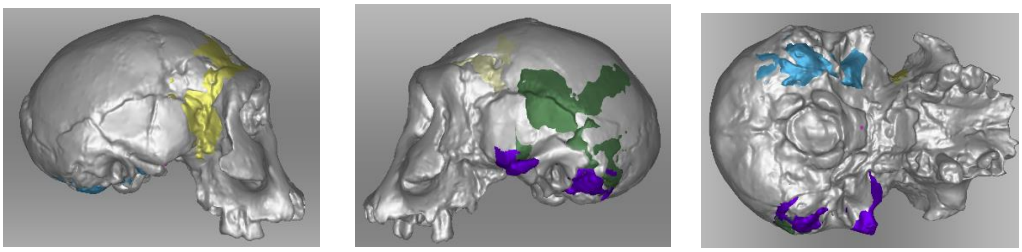

Figure A.1 The reconstruction of D2700
This cracked surface is reconstructed by reflecting patches of the counterparts at the better-preserved other side as indicated by colored patches.

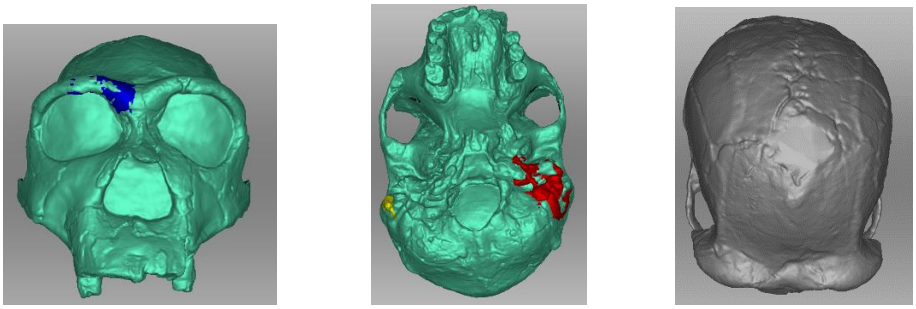

Figure A.2 The reconstruction ER 3733
Left: The crack at the right brow is fixed by a patch of the left brow (blue). Middle: The cracked surface at the right mastoid process is fixed by a patch of the right mastoid process, while the damaged left tympanic and mastoid region is fixed by a patch of the right counterpart (red). Right: the hole at the bregmatic region is filled.

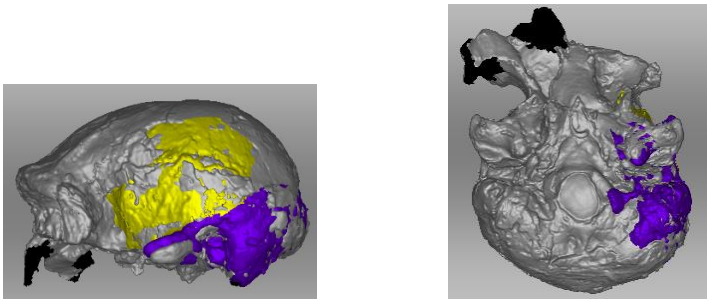

Figure A.3 The reconstruction ER 3883
The damaged left mandibular fossa and mastoid portion is fixed by a patch of the left counterpart (blue). The cracked surface at the left cranial wall is fixed by a patch of the right counterpart (yellow).

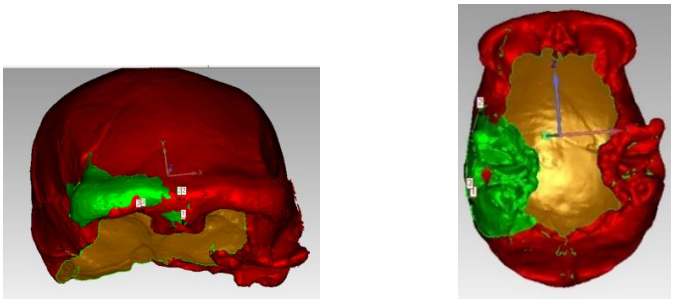

Figure A.4 The reconstruction Ng 6
Left: The broken right brow is fixed by the mirror image of the patch of the right counterpart (green). Right: The broken right temporal region is fixed by a patch of the left counterpart (green).

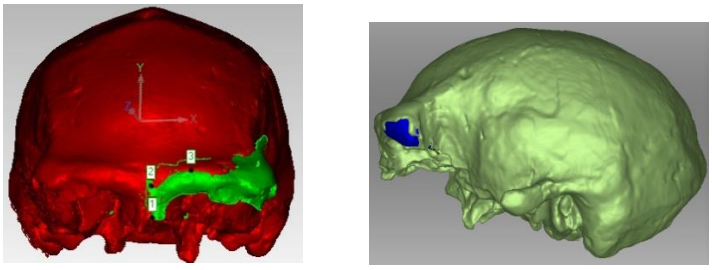

(A) (B)

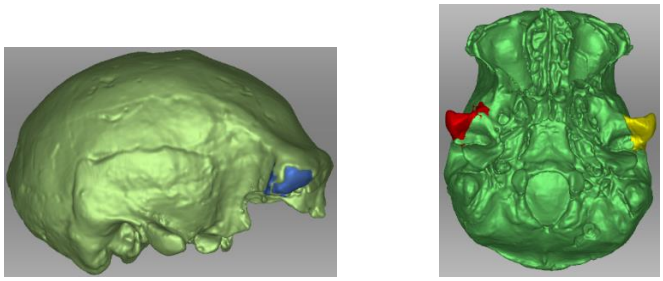

(C) (D)

Figure A.5 The reconstruction of Ng 7
(A) The left brow of Ng 7 is first reconstructed by reflecting a patch of the right brow (green). (B) The damaged part at the lateral end of the left brow is then repaired by a patch of the counterpart from Ng 12 (blue). (C) The fixed left brow is then reflected to repair the damaged surface at the right brow (purple). (D) The broken lateral end of the mandibular fossa at each side is reconstructed by using the counterpart from Ng 12 (yellow and red).

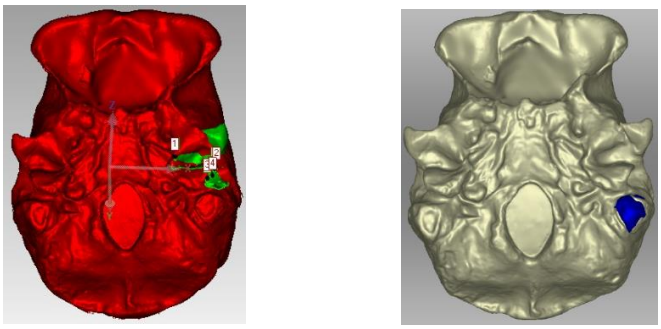

Figure A.6 The reconstruction of Ng 12
Left: the broken lateral end of the left mandibular fossa is repaired by a patch of the right counterpart (green). Right: the broken left mastoid process is reconstructed by a patch of the left counterpart from Ng 7 (blue). The reconstructed left mastoid process is then flipped to the other side to reconstruct the right mastoid process.

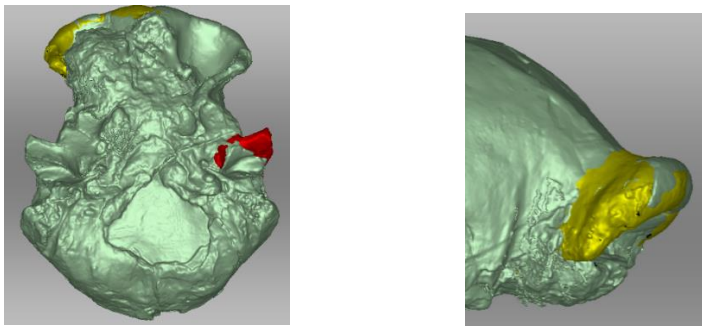

Figure A.7 The reconstruction of OH 9
Left: the broken lateral end of the left mandibular fossa is reconstructed by a patch of the right counterpart (red). Right: the missed lateral end of the right brow is reconstructed by a patch of the left counterpart (yellow).

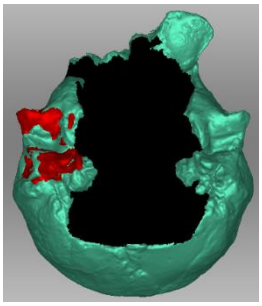

Figure A.8 The reconstruction of S 2
The damaged right mandibular and tympanic region is reconstructed by a patch of the left counterpart (red).

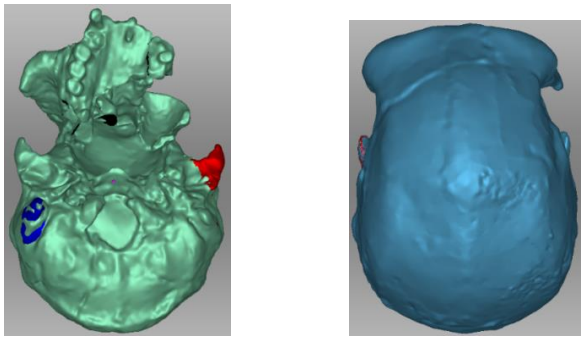

Figure A.9 The reconstruction of S 17
Left: The missed lateral end of the left mandibular fossa and the broken right mastoid processes are reconstructed by patches of the right (red) and left (blue) counterparts respectively. Right: The cracked surface on the vault are repaired by both patches from the non-cracked counterparts at the opposite side as well as the "defeature" function in the Artec Studio 13.

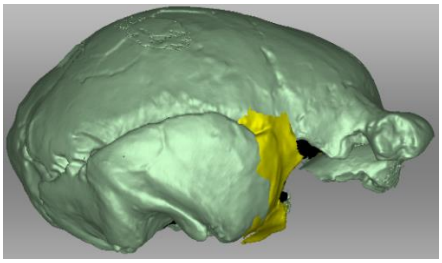

Figure A.10 The reconstruction of ZKD 11
The broken anterior margin of the right squamosal portion is reconstructed by a patch of the left counterpart (yellow).

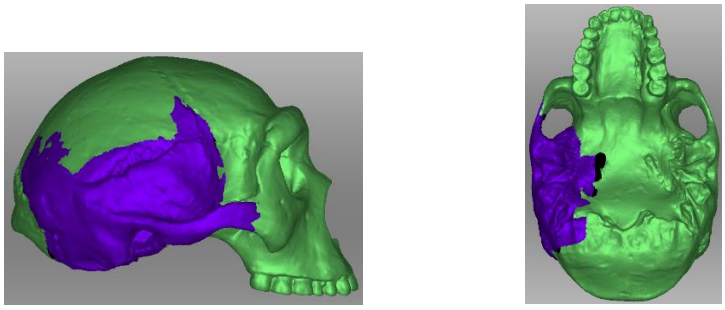

Figure A.11 The reconstruction of ZKD 12
The right temporal bone of ZKD 3 in Tattersall and Sawyer's (1996) reconstruction is removed. The left temporal region (blue) is then flipped to the right. This makes assure that the vault is exclusively ZKD 12.

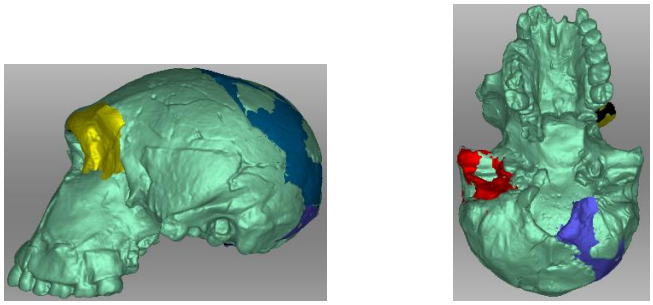

Figure A.12 The reconstruction of ER 1813
Left: The broken lateral part of the left brow and damaged surface of the left vault are reconstructed by their right counterparts (yellow and purple respectively). Right: The broken right mandibular fossa and the tympanic tube is reconstructed by a patch of the left counterpart (red), while the damaged surface of the left nuchal plane is reconstructed by a patch of its right counterpart (blue).

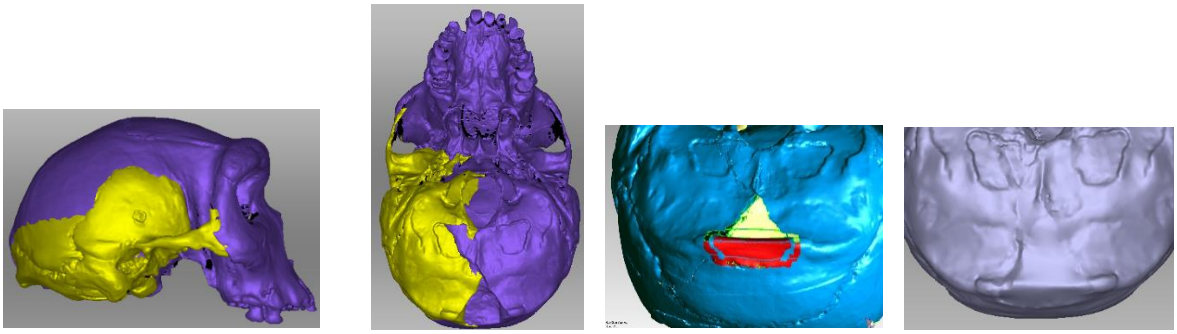

(A) (B) (C) (D)

Figure A.13 The reconstruction of Kabwe
(A) and (B) show that the broken right temporal region is reconstructed by the counterpart at the left side (yellow). As (C) shows, to repair the damaged surface at the joint of the superior nuchal lines, this region is first deleted. The function "Bridge" in the Geomagic Studio (Geomagic Inc., 2015) is applied to create bridges (red) across the deleted region. The hole between pairs of "bridges" are then filled as (D) shows.

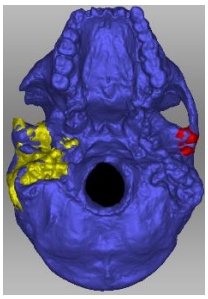

Figure A.14 The reconstruction of Petrolona
The damaged tympanic region at the right side and the lateral end of the mandibular fossa at the left side are reconstructed by their counterparts at the opposite sides (yellow and red).

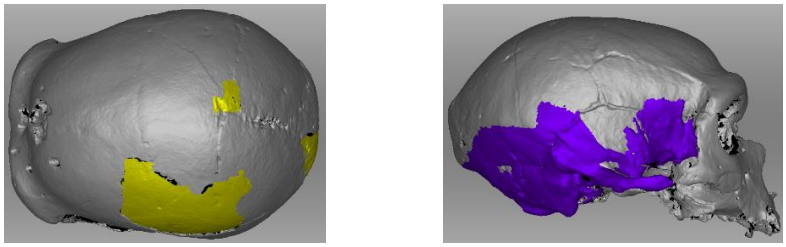

Figure A.15 The reconstruction of La Chapelle
Left: The damaged area at the vault are repaired by a patch from the opposite side (yellow). The other holes are also filled by the Artec Studio 13 software. Right: The somewhat right crushed temporal region is reconstructed by the left counterpart (blue).

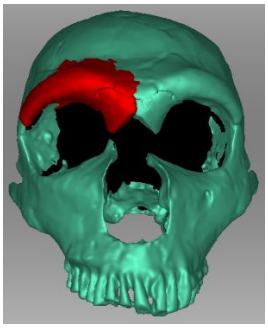

Figure A.16 The reconstruction of La Ferrassie 1
The damaged right brow is reconstructed by its counterpart at the left side (red).

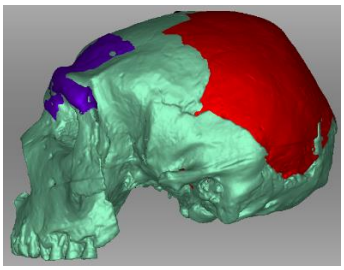

Figure A.17 The reconstruction of La Ferrassie
The damaged left brow is reconstructed by the mirror image of its right brow (blue). The damaged left vault is reconstructed by flipping its counterpart (red).

A.3 ANCHOR POINTS OF SEMILANDMARK PATCHES

A.3.1 The landmark sets of the overall calvaria

A.3.1.1 The maximum landmark data set

This dataset contains 32 patches of semilandmarks that cover the overall calvaria. Overall, 767 points are sampled after deleting replicate points at the boundary of adjacent patches. Among these points, 40 are discrete landmarks that do not slide, 183 are treated as curve semilandmarks, and 544 are surface semilandmarks.

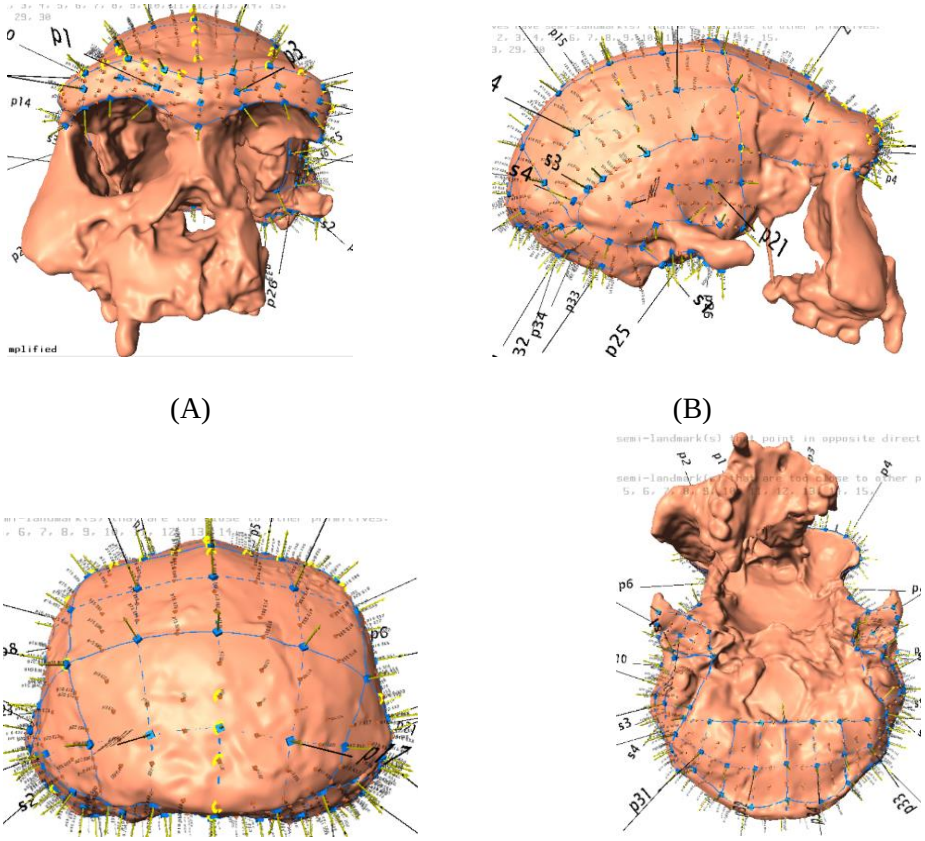

Figure A.18 The patches of semilandmarks placed on the 3D model of S 17

Table A.5 Patch 1 (R) and patch 3 (L) at the medial supraorbital and glabellar regions (density: 5×5)

Anchor point	Discrete landmark[1]	No sliding[2]	Definition
1	Glabellar (GL)	✓	The point along the midline where the post-glabellar plane curves downward. In many specimens, it is roughly the anterior-most point of the frontal bone
2			Midpoint between Anchor point 1 and Anchor point 3
3	Nasion (NA)	✓	The point at the intersection between the midline plane and the frontonasal suture, located at the frontal bone (Howells, 1973).
4			Midpoint between the Anchor point 3 and 7 along the superior margin of the supraorbital rim.
5			Midpoint between the Anchor point 4 and 6.
6			Midpoint between Anchor point 3 and 9
7[3]	✓	✓	The highest point at the superior margin of the supraorbital rim.
8			Midpoint between Anchor point 7 and 9
9	Midtorus inferior		The midpoint along the superior orbital margin, roughly above the center of the orbit.

1. These points marked as "discrete landmark" either by a name or the "✓" sign are used in the analyses that only employ discrete landmarks.

2. Some points marked as "discrete landmarks" are still allowed to slide as semilandmarks when using the semilandmark sets or anchor point sets.

3. The commonly used "mid-torus superior" is not applied in this study (Baab, 2008a, 2008b, 2016; Harvati et al., 2010; McNulty, 2004). The first reason is that this point does not convey information such as the highest point of the brow. Second, *Homo sapiens* is unique in developing bipartite brows (Tattersall and Schwartz, 2008). The short medial part is a lateral extension of a mount of bone at the glabellar region. The long lateral part is a plate-like supraorbital rim. Therefore, there is no way to place a mid-torus superior.

Table A.6 Patch 2 (R) and patch 4 (L) at the lateral supraorbital region (density: 9×5)

Anchor point	Discrete landmark	No sliding	Definition
1	✓	✓	The same point with Anchor point 7 of Patch 1.
2			The same point with Anchor point 8 of Patch 1.
3	✓		The same point with Anchor point 9 of Patch 1.
4			The midpoint between anchor point 1 and Anchor point 7 roughly on the superior margin of the supraorbital rim.
5			The midpoint between Anchor point 4 and 6.
6			The midpoint between Anchor point 3 and 9 at the superior orbital margin.
7	Frontomalare tempolare (FMT)	✓	The intersection between the orbit rim and the frontozygomatic suture (Baab, 2016)
8			The midpoint between FMT and the FMO
9	Frontomalare orbitale (FMO)	✓	The intersection between the orbital rim and the frontozygomatic suture (Baab, 2016)

Table A.7 Patch 5 (R) and 7 (L) at the frontal bone (density: 9×5)

Anchor point	Discrete landmark	No sliding	Definition
1	GL	✓	The same point as the anchor point 1 of patch 1 (R) or 3 (L).
2			The same point as the anchor point 4 of patch 1 (R) or 3(L).
3			The same point as anchor point 7 of patch 1 (R) or 3(L)
4			The midpoint between the GL and BR roughly along the sagittal midline of the vault.
5			The midpoint between Anchor point 2 and Anchor point 8.
6			The midpoint between Anchor point 3 and Anchor point 9.
7	Bregma (BR)	✓	The intersection between the coronal suture and sagittal suture at the posterior border of the frontal bone (Baab, 2016; Howells, 1973)
8			The midpoint between BR and anchor point 9
9			Midpoint between BR and the pterion

Table A.8 Patch 6 and 8 at the frontal region (density: 9×5)

Anchor point	Discrete landmark	No sliding	Definition
1	✓	✓	The same point as the anchor point 7 of patch 1 (R) or 3(L).
2			The same point as anchor point 4 of patch 2 (R) or 4 (L).
3	FMT	✓	The same point as anchor point 7 of patch 2 (R) or 4 (L).
4			The same point as anchor point 6 of Patch 5 (R) or 7 (L).
5			The midpoint between anchor point 2 and 8.
6			The midpoint between anchor point 3 (FMT) and 9 (Pterion).
7			The same point as anchor point 9 of Patch 5 (R) or 7 (L)
8			The midpoint between anchor point 7 and anchor point 9 (Pterion)
9	Pterion (PT)[1]	✓	The point where the anterior margin of the temporal bone curves back into the squamosal suture.

1. The pterion region is where frontal, temporal, sphenoid, and parietal bones meet. The intersections of these bones are highly variable in primate species (Schwartz, 2006; Wang et al., 2006). In this study, PT is defined to ease the task of the describing the trajectory of the squamosal suture. When the angle at the anterosuperior corner of the squamosal portion is rounded, such as in some *H. sapiens* specimen, this point is put at intersection between the spheno-frontal suture and the squamosal suture. If the spheno-frontal suture is not apparent, such as in S 2, the point is roughly located at the center of the section where the anterior margin of the temporal bone curves into the squamosal suture.

Table A.9 Patch 9 (R) and patch 11 (L) at the parietal bone (density: 5×7)

Anchor point	Discrete landmark	No sliding	Definition
1	BR	✓	
2			The same as the anchor point 8 of Patch 5 (R) or 7 (L)
3			The same as Anchor point 9 of Patch 5 (R) or 7 (L)
4			The midpoint between BR and Anchor point 7 on the sagittal suture.
5			The midpoint between anchor point 4 and 6
6			The midpoint between anchor point 4 and anchor point 6 of Patch 10 (R) and Patch 12 (L).
7	✓	✓	The midpoint between BR and Lambda on the sagittal suture
8			The midpoint between BR and anchor point 9
9			Midpoint between anchor point 7 of this patch and anchor point 9 of Patch 10 (R) and Patch 12 (L).

Table A.10 Patch 9 (R) and patch 11 (L) at the parietal bone (density: 5×7)

Anchor point	Discrete landmark	No sliding	Definition
1			The same point as anchor 3 of Patch 9(R) and Patch 11(L).
2			The same point as anchor 8 of Patch 6(R) and Patch 8 (L).
3	PT	✓	
4			The same point as anchor point 6 of Patch 9(R) and Patch 11(L).
5			The midpoint between Anchor point 4 and Anchor point 6.
6			The midpoint between anchor point 3 (PT) and anchor point 9 on the squamosal suture.
7			The same point as anchor point 9 of Patch 9(R) and Patch 11(L)
8			The midpoint between anchor point 7 and anchor point 9
9	✓	✓	The midpoint between PT and PN (Parietal notch) on the squamosal suture.

Table A.11 Patch 13 (R) and patch 15 (L) at the parietal bone (density: 7×5)

Anchor point	Discrete landmark	No sliding	Definition
1	✓	✓	The same point as anchor point 7 of Patch 9(R) and Patch 11(L).
2			The same point as anchor point 8 of Patch 9(R) and Patch 11(L).
3			The same point as anchor point 9 of Patch 9(R) and Patch 11(L).
4			The midpoint between anchor point 1 and the lambda roughly on the sagittal suture
5			The midpoint between anchor point 4 and 6
6			The midpoint between anchor point 4 of this patch and anchor point 6 of patch 14 (R) and 16 (L).
7	Lambda (LA)	✓	The apex of occipital bone at its junction with the sagittal suture (Howells, 1973)
8			The midpoint between anchor point 7 and anchor point 9
9			The midpoint between the LA and the parietal notch

Table A.12 Patch 14 (R) and patch 16 (L) at the parietal bone (density: 5×7)

Anchor point	Discrete landmark	No sliding	Definition
1			The same point as anchor point 3 of Patch 13(R) and Patch 15(L).
2			The same as anchor point 8 of Patch 10 (R) and Patch 12(L).
3	✓	✓	The same as anchor point 9 of Patch 10 (R) and Patch 12(L).
4			The same point as anchor point 6 of Patch 13(R) and Patch 15(L).
5			The midpoint between anchor point 4 and 6.
6			The midpoint between anchor point 3 and 9 on the squamosal suture.
7			The same point as anchor point 9 of Patch 13(R) and Patch 15(L).
8			The midpoint between anchor point 7 and 9.
9	Parietal notch (PN)	✓	The deepest point of the parietal notch.

Table A.13 Patch 17 (R) and 19 (L) at the occipital squama (density: 5×7)

Anchor point	Discrete landmark	No sliding	Definition
1	LA	✓	
2			The same point as anchor point 8 of Patch 13(R) and 15(L)
3			The same point as anchor point 9 of Patch 13(R) and 15(L)
4			The midpoint between LA and inion
5			The midpoint between anchor point 2 and 8
6			The midpoint between anchor point 3 and 9
7	Inion (IN)	✓	The intersection of the left and right superior nuchal lines roughly at the midline.
8			The midpoint between IN and anchor point 9 on the superior nuchal line.
9	Mid-nuchal line	✓	The midpoint between IN and AST (asterion) on the superior nuchal line[1].

1. This point is taken on the superior nuchal line when the chord distances between it to IN as well as that between it and AST are approximately equal to each other. If the superior nuchal line is very short, the point is put at the lateral extension of this line.

Table A.14 Patch 18 (R) and 20 (L) at the occipital squama (density: 5×6)

Anchor point	Discrete landmark	No sliding	Definition
1			The same point as anchor point 7 of patch 14 (R) and 16(L).
2			The same point as anchor point 8 of patch 14 (R) and 16 (L).
3	PN	✓	
4			The same point as anchor point 6 of patch 17(R) and 19(L).
5			The midpoint between anchor point 2 and 8.
6			The midpoint between anchor point 3 and 9 on the parietomastoid suture.
7		✓	The same point as anchor point 9 of patch 17(R) and 19(L).
8			The midpoint between anchor point 7 and 9.
9	Asterion (AST)	✓	The intersection of occipital, parietal and the mastoid region of the temporal (Howells, 1973).

Table A.15 Patch 21(R) and 23 (21) at the squamosal portion (density: 5×6)

Anchor point	Discrete landmark	No sliding	Definition
1	PT	✓	
2			The midpoint between Anchor point 1 and 3 on the sphenotemporal suture
3	Infratemporal crest	✓	This point is defined as the point where the sphenotemporal suture enters the cranial base and is usually placed on the infratemporal crest (Baab, 2016).
4			The midpoint between anchor point 1 and 7 on the squamosal suture.
5			The midpoint between anchor point 4 and 6.
6			The midpoint between anchor point 3 and 9
7	✓		The midpoint between PT and PN on the squamosal suture.
8			The midpoint between anchor point 7 and 9.
9			The midpoint between anchor point 3 and auriculare (AU).

Table A.16 Patch 22(R) and 24(L) at the squamosal portion (density: 5×6)[1]

Anchor point	Discrete landmark	No sliding	Definition
1	✓		The same point as anchor point 7 of patch 21(R) and 23(L)
2			The same point as anchor point 8 of patch 21(R) and 23(L).
3			The same point as anchor point 9 of patch 21(R) and 23(L).
4			The midpoint between anchor point 1 and PN on the squamosal suture
5			The midpoint between anchor point 4 and 6.
6	Auriculare[2] (AU)		The point at the suprameatal crest superior to the highest point of the auditory meatus (Baab, 2008).
7	PN		
8			The midpoint between anchor point 7 and 9.
9	✓	✓	The midpoint of the posterior margin of the auditory meatus

1. In some specimens, like the Ngandong specimens, S 17, WT 15000 and the Mid-Pleistocene *Homo*, the squamosal suture sharply curves downward toward the parietal notch. In this situation, the upper boundary of this patch cannot fully capture the trajectory of the posterior squamosal suture. Therefore, a few semilandmarks at the boundary are replaced by manually placed landmarks (Figure A.19).

2. Because of the semilandmark density, the AU is eliminated in the associated analyses. This point is still used in the anchor point and discrete landmark sets.

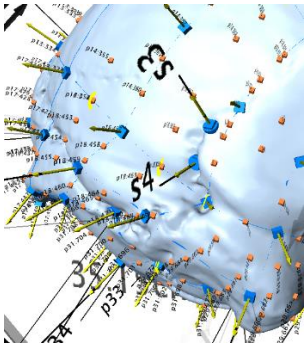

Figure A.19 The two discrete landmarks placed at the posterior squamosal suture of Kabwe
These two points are marked as S 3 and S 4. This is because semilandmarks at the upper boundary of patch 22 cannot capture the trajectory of that section. After that, the original semilandmarks are manually deleted.

Table A.17 Patch 25(R) and 26 (L) at the mandibular fossa (density: 5×5)

Anchor point	Discrete landmark	No sliding	Definition
1	✓	✓	The inferior most point on the Lateral most portion of the anterior wall of the mandibular fossa (Schoeder et al., 2017)
2	✓	✓	The midpoint at the anterior wall of the articular fossa.
3	✓	✓	The medial most point on the anterior border of the fossa (Schroeder et al., 2017)
4			The mid-point between anchor point 1 and 7
5			The mid-point between anchor point 4 and 6
6			The mid-point between anchor point 7 and 9
7	✓	✓	The lateral most point of the posterior border.
8	✓	✓	The midpoint at the anterior boundary of the auditory meatus
9	✓	✓	The vaginal process[1]

1. If the vaginal process is not existed, the point is put at the inferior border of the tympanic plate anterior to the styloid pit.

Table A.18 Patch 27 (R) and 28 (L) at the mastoid portion (density: 6×6)

Anchor point	Discrete landmark	No sliding	Definition
1	✓	✓	The same point as anchor point 9 of Patch 22 (R) and 24 (L)
2			The same point as anchor point 8 as Patch 22 (R) and 24 (L)
3	PN	✓	
4	✓	✓	The inferior tip of the auditory meatus[1]
5	The vaginal process[1]	✓	
6			The midpoint between anchor point 2 and 6
7			The midpoint between anchor point 5 and asterion along the medial border of the mastoid process
8			The midpoint between the parietal notch and asterion on the parietomastoid notch
9	Asterion (AST)	✓	

1. This landmark is also manually placed because the density of the patch eliminates the original point at the inferior tip of the auditory meatus.

Table A.19 Patch 29 (R) and 31 (L) at the nuchal plane (density: 5×5)[1]

Anchor point	Discrete landmark	No sliding	Definition
1			The intersection between the transverse line across the opisthion and the medial border of patch 29 and 30.
2			The midpoint between anchor point 1 and 3
3			The midpoint between anchor point 1 and opisthion
4			The midpoint between anchor point 1 and 7
5			The midpoint between anchor point 2 and 8
6			The midpoint between anchor point 3 and Inion
7	AST	✓	
8			The same point as anchor point 8 of patch 18 (R) and 20 (L)
9	✓	✓	The same point as anchor point 7 of patch 18 (R) and 20 (L)

1. The points at the lateral border of this patch are deleted.

Table A.20 Patch 30 (R) and 32 (L) at the nuchal plane (density: 5×5)

Anchor point	Discrete landmark	No sliding	Definition
1			The same point as anchor point 3 of patch 29 (R) and 31 (L)
2			The midpoint between anchor point 1 and 3
3	Opisthion (OPS)	✓	The midline point at the posterior margin of the foramen magnum (Baab, 2016)
4			The same point as anchor point 6 of patch 29 (R) and 31 (L).
5			The midpoint between anchor point 2 and 8
6			The midpoint between anchor point 3 and 9
7	✓	✓	The same point as anchor point 9 of patch 17 (R) and 19 (L)
8			The same point as anchor point 6 of patch 17 (R) and 19 (L)
9	IN	✓	

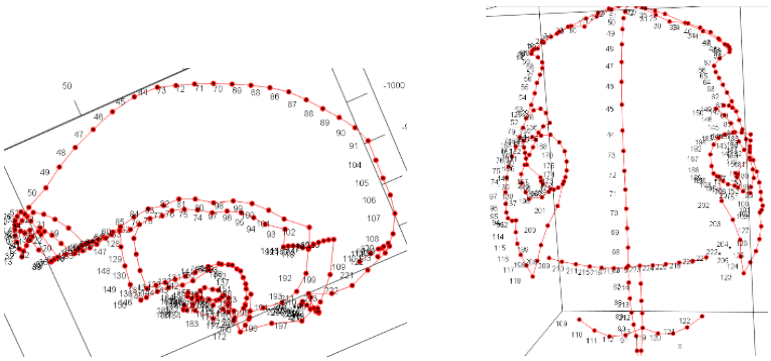

Figure A.20 Curve semilandmarks
Curve semilandmarks manually picked up from the maximum specimen landmark set of the overall calvaria using the geomorph package in R.

A.3.1.2 The maximum-specimen dataset

To include more fossil specimens, the maximum specimen datasets of the overall cranium takes out the patches at the mandibular fossa. The original patch in the maximum-semilandmark set that covers the mastoid region is modified to avoid the mastoid process (Figure A.). The definitions of the other patches remain the same. Therefore, there are 30 patches of 697 points in this data set. Among them, 510 are surface semilandmarks, 159 are curvature semilandmarks, and 28 are discrete landmarks.

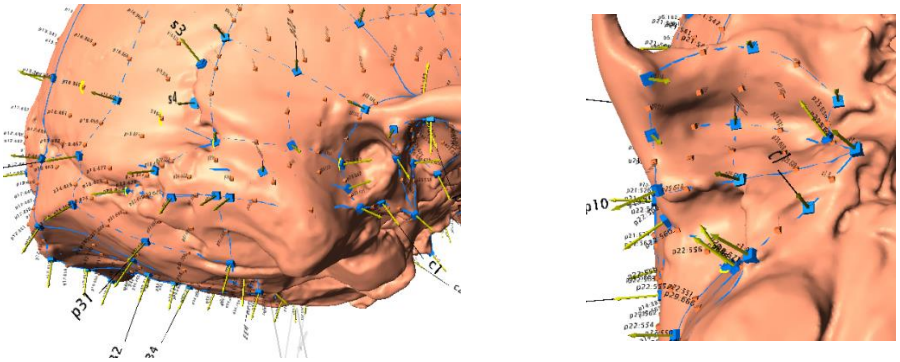

Figure A.21 The patch at the mastoid portion for the maximum-specimen set
(A) The patch at the mastoid portion in lateral view. (B) The curvature semilandmarks along the inferior border of the tympanic tube (B). The region in the pictures is from the right side of the Kabwe cranium.

Table A.21 The new patch at the mastoid portion (density: 6×4) for the maximum-specimen set

Anchor point	Discrete landmark	No sliding	Definition
1	✓	✓	The midpoint at the posterior boundary of the auditory meatus
2			The same point as anchor point 8 as Patch 22 (R) and 24 (L)
3	PN	✓	
4			The midpoint between anchor point 1 and 5
5	✓	✓	The inferior tip of the auditory meatus
6			The midpoint between anchor point 2 and 7
7			The midpoint between anchor point 5 and asterion roughly along the lateral border of the base of the mastoid process
8			The midpoint between the parietal notch and asterion on the parietomastoid notch
9	Asterion (AST)	✓	

A.3.2 The semilandmark sets of the posterior cranium

For the maximum landmark data set of the posterior calvaria, the patch 1 to 8 are deleted so that the frontal region is removed. Overall, there are 563 sampled points. Among them, there are 390 surface semilandmarks, 141 curve semilandmarks, and 32 discrete landmarks.

For the maximum specimen data set of the posterior calvaria, the patch 1 to 8 are also deleted. Overall, there are 493 sampled points. Among them, there are 356 surface semilandmarks, 117 curve semilandmarks and 20 discrete landmarks.

A.3.3 The landmark sets of the temporal region

The analyses only focus on the left temporal bone because this side is better preserved in a majority of hominid casts. ER 3733 and ER 3883's better preserved left temporal bones are flipped to the right side. Consequently, for both the maximum landmark and maximum specimen landmark set, patch 23, 24, 26, and 28 at the left temporal region are selected from the correspondent landmark sets of the overall calvaria respectively. An extra series of curvature semilandmarks is put along the inferior margin of the tympanic plate between.

For the maximum landmark set, there are 112 sampled points. Among these points, 67 are surface semilandmarks, 31 are curve semilandmarks, and 14 are discrete landmarks. For the maximum specimen set, there are 103 sampled points. Among these points, 59 are surface semilandmarks, 31 are curve semilandmarks, and 13 are discrete landmarks.

A.3.4 The landmark set of the frontal region

For the frontal region, patch 1 to 8 of the maximum landmark set of the overall calvaria are selected. Overall, there are 221 sampled points. Among them, 140 are surface semilandmarks, 70 are curve semilandmarks, and 11 are discrete landmarks.

A.3.5 Discrete landmarks used in each analysis

Table A.22 Discrete landmarks in patch 1 to 8 of the overall cranium

Discrete landmarks[1]	Bilateral	Overall cranium	Posterior cranium	The temporal region	Frontal
GL		✓			✓
NA		✓			✓
The highest point at the superior margin of the brow	✓	✓			✓
Mid-torus inferior	✓	✓			✓
FMT	✓	✓			✓
FMO	✓	✓			✓
BR		✓	✓		✓

Table A.23 Discrete landmarks in patch 9 to patch 24, patch 29 to patch 32

Discrete landmarks	Bilateral	Overall cranium	Posterior cranium	The temporal region
Midpoint between BR and LA		✓	✓	
LA		✓	✓	
PT	✓	✓	✓	✓
Midpoint between PT and PN along the squamosal suture	✓	✓	✓	✓
PN	✓	✓	✓	✓
IN		✓	✓	
Mid-nuchal line	✓	✓	✓	
OPN		✓	✓	
Infratemporal crest	✓	✓	✓	✓
Asterion	✓	✓	✓	✓
Auriculare	✓	✓	✓	✓

Table A.24 Discrete landmarks in patch 25 to patch 28

Discrete landmarks[1]	Bilateral	Overall cranium	Posterior cranium	The temporal region
Mid-point at the posterior auditory meatus	✓	✓	✓	✓
Inferior tip of the meatus	✓	✓	✓	✓
Mid-point at the anterior auditory meatus	✓	✓	✓	✓
The lateral most point at the anterior wall of the mandibular fossa	✓	✓	✓	✓
The mid-point at the anterior wall of the mandibular fossa	✓	✓	✓	✓
The medial most point of the anterior wall of the mandibular fossa	✓	✓	✓	✓
Vaginal process	✓	✓	✓	✓

1. The definitions of these landmarks refer to Table A.1 to Table A.20 of the maximum-semilandmark set.

A.4 THE RECONSTRUCTION OF MISSING LANDMARKS

Table A.25 The cranial measurements used in reconstructing missing landmarks

Measurements[1]	ER 1813		ER 3883		OH 9[3]	S 2		S 17	
	Cited[2]	Actual	Cited[3]	Actual		Cited[2]	Actual	Cited[5]	Actual
GL-BR chord	80	77.14	101	98.71	120				
BR-LA chord	74	72.84	86	86.22		98	97.36	106	105
LA-IN	55	55.69							
Bi-AST chord	93	91.60	121	123.9					
LA-AST chord	64	L: 64.5 R: 64.25				82	L: 82.0 R: 84.5		
LA-OPN chord			75	75[4]					
BR-AST chord			L: 119 R: 118	L: 121.5 R: 120.7					

1. Usually, around 1 to 2mm error is allowed for each actual measurement taken from the 3D models because this small amount of error likely not create much differences in computing overall shape variability. The unit for the cited metrical data is mm. The unit for the actual measurements is in cm.

2. The metrical data of ER 1813 S2 are from Rightmire (1993). These measurements are used to estimate the positions of lambda, bregma, and asterion of ER 1813, as well as the lambda in S 2. In particular, the bregma of S 2 is put at the center of the faint bregmatic eminence.

3. The metrical data of ER 3883 is from Wood (1991). These measurements are used to estimate the positions of bregma on ER 3883 and OH 9.

4. The LA-OPN chord of ER 3883 is set to the published value in order to scale the 3D model.

5. The position of landmark and bregma is estimated from Kaifu et al. (2008). Consequently, the bregma is put at the center of the bregmatic eminence. The lambda is first located by following Kaifu et al.'s (2008) diagram. The position is then slightly adjusted to roughly meet the value of BR-LA chord published by Kaifu et al. 2008).

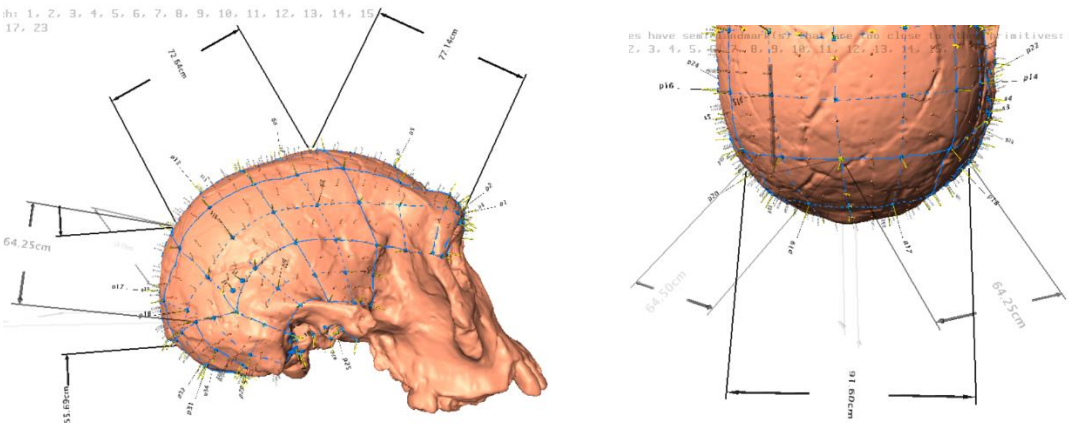

Figure A.22 The cranial measurements taken from ER 1813
These measurements are used to determine the position of unclear bregma, lambda, and asterion.

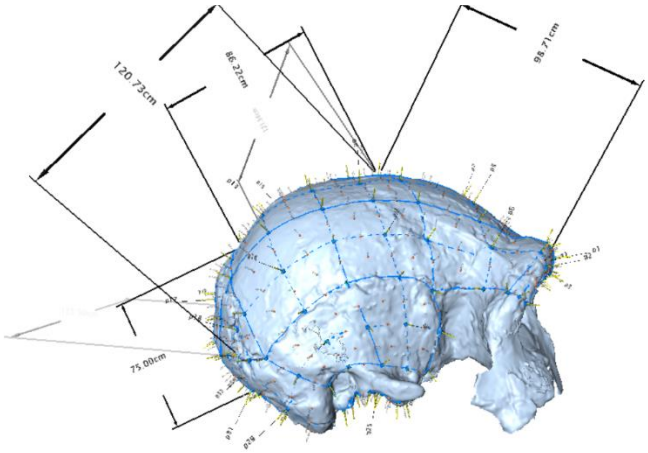

Figure A.23 The cranial measurements taken from ER 3883
These measurements are used to determine the position of the bregma.

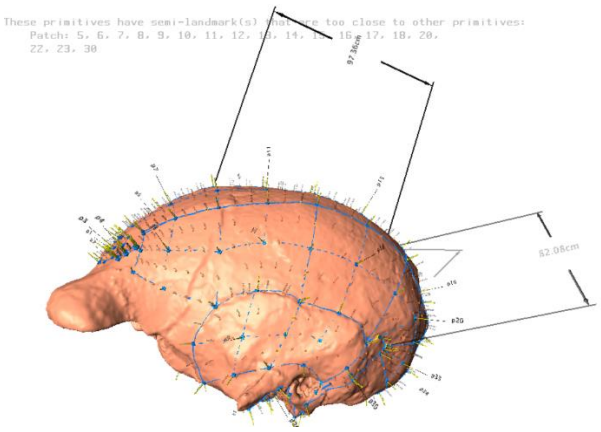

Figure A.24 The cranial measurements taken from S 2
These measurements are used to determine the position of the lambda.

APPENDIX B STATISTICAL ANALYSIS

B.1 THE OVERALL CRANIUM

B.1.1 Principal component analysis (PCA)

B.1.1.1 The first PCA

Table B.1 The size-shape relationship of the first seven PCs in the first PCA (the overall cranium)

	Sample size	r square value	F value	p-value
PC1 vs. centroid size	12	0.4032	6.0308	0.0265
PC 2 vs. centroid size	12	0.3048	4.384	0.0662
PC 3 vs. centroid size	12	0.04528	0.4744	0.5099
PC 4 vs. centroid size	12	0.03752	0.3899	0.5465
PC 5 vs. centroid size	12	0.000003853	0.00003853	0.9953
PC 6 vs. centroid size	12	0.02277	0.233	0.633
PC 7 vs. centroid size	12	0.04604	0.4826	0.5088

B.1.1.2 The second PCA

Table B.2 The size-shape relationship of the first seven PCs in the second PCA (the overall cranium)

	Sample size	r square value	F value	p-value
PC1 vs. centroid size	47	0.03436	1.6011	0.201
PC 2 vs. centroid size	47	0.0001922	0.0008649	0.9759
PC 3 vs. centroid size	47	0.0007943	0.03578	0.8556
PC 4 vs. centroid size	47	0.1381	7.21	0.0198
PC 5 vs. centroid size	47	0.1648	8.879	0.0048
PC 6 vs. centroid size	47	0.03947	1.8492	0.173
PC 7 vs. centroid size	47	0.02909	1.349	0.243

B.1.1.3 The third PCA

Table B.3 The size-shape relationship of the first seven PCs in the third PCA (the overall cranium)

	Sample size	r square value	F value	p-value
PC1 vs. centroid size	20	0.05578	1.063	0.03273
PC 2 vs. centroid size	20	0.2194	5.058	0.0405
PC 3 vs. centroid size	20	0.2233	5.176	0.0378
PC 4 vs. centroid size	20	0.000001858	0.00003346	0.9954
PC 5 vs. centroid size	20	0.01699	0.3111	0.5644
PC 6 vs. centroid size	20	0.1924	4.302	0.0509
PC 7 vs. centroid size	20	0.002465	0.04448	0.8247

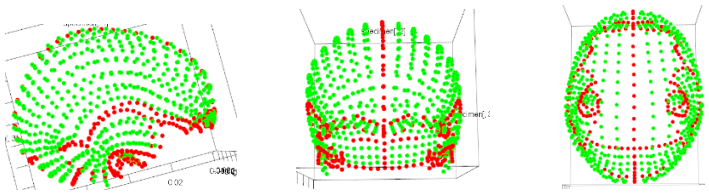

(A)

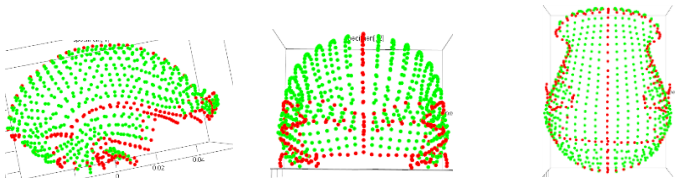

(B)

Figure B.1 PC 1 of the third PCA of the overall cranium
(A) The shape at the negative end. (B) The shape at the positive end. From left to right: lateral view, anterior view, and inferior view.

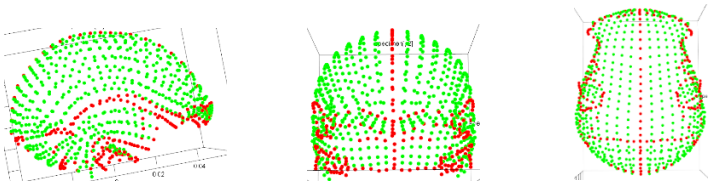

(A)

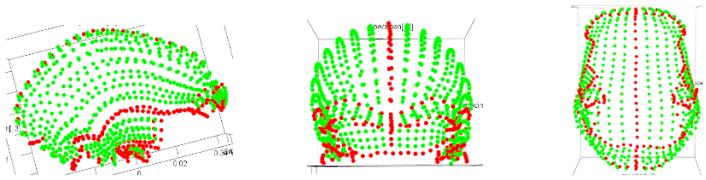

(B)

Figure B.2 PC 2 of the third PCA of the overall cranium
(A) The shape at the negative end. (B) The shape at the positive end. From left to right: lateral view, anterior view, and inferior view.

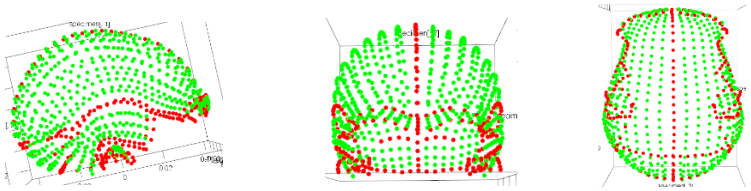

(A)

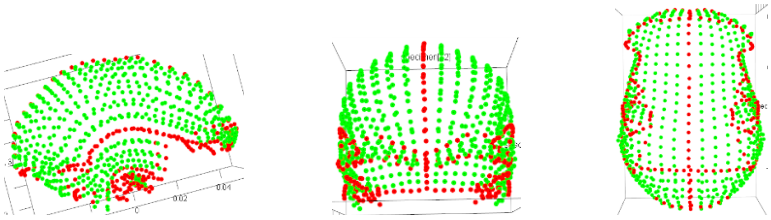

(B)

Figure B.3 PC 2 of the third PCA of the overall cranium
(A) The shape at the negative end. (B) The shape at the positive end. From left to right: lateral view, anterior view, and inferior view.

B.1.1.4 The fourth PCA of the overall cranium

Table B.4 The size-shape relationship of the first seven PCs in the fourth PCA (the overall cranium)

	Sample size	r square value	F value	p-value
PC1 vs. centroid size	16	0.3248	6.735	0.0247
PC 2 vs. centroid size	16	0.3853	8.774	0.0085
PC 3 vs. centroid size	16	0.01038	0.1468	0.7058
PC 4 vs. centroid size	16	0.09604	1.488	0.2301
PC 5 vs. centroid size	16	0.003892	0.05468	0.8248
PC 6 vs. centroid size	16	0.01445	0.2053	0.6407
PC 7 vs. centroid size	16	0.001018	0.01462	0.9133

B.1.1.5 The fifth PCA of the overall cranium

Table B.5 The size-shape relationship of the first seven PCs in the fifth PCA (the overall cranium)

	Sample size	r square value	F value	p-value
PC1 vs. centroid size	24	0.01859	0.4167	0.5273
PC 2 vs. centroid size	24	0.2493	7.305	0.0185
PC 3 vs. centroid size	24	0.2265	6.441	0.0175
PC 4 vs. centroid size	24	0.004175	0.09223	0.7531
PC 5 vs. centroid size	24	0.03116	0.7078	0.4106
PC 6 vs. centroid size	24	0.06203	1.453	0.2342
PC 7 vs. centroid size	24	0.003119	0.06883	0.7962

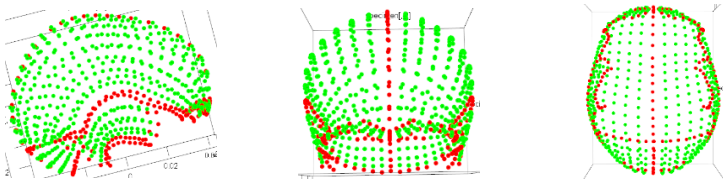

(A)

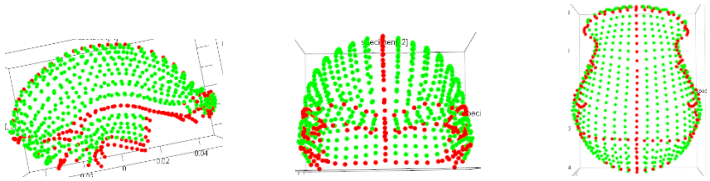

(B)

Figure B.4 PC 2 of the fifth PCA of the overall cranium
(A) The shape at the negative end. (B) The shape at the positive end. From left to right: lateral view, anterior view, and inferior view.

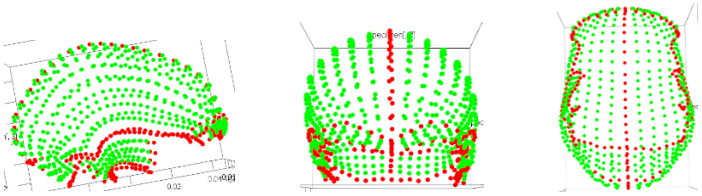

(A)

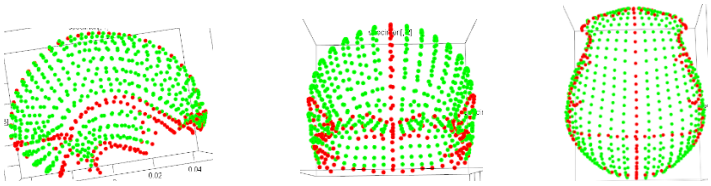

(B)

Figure B.5 PC 4 of the fifth PCA of the overall cranium
(A) The shape at the negative end. (B) The shape at the positive end. From left to right: lateral view, anterior view, and inferior view.

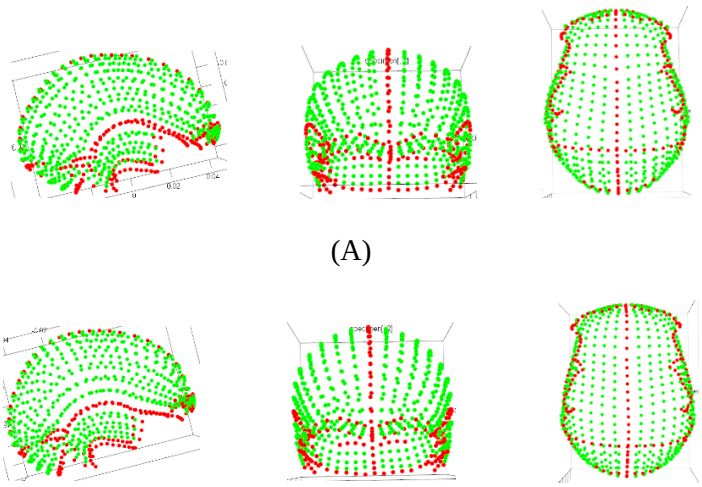

Figure B.6 PC 5 of the fifth PCA of the overall cranium
(A) The shape at the negative end. (B) The shape at the positive end. From left to right: lateral view, anterior view, and inferior view.

B.1.1.6 The sixth PCA of the overall cranium

Table B.6 The size-shape relationship of the first seven PCs in the sixth PCA (the overall cranium)

	Sample size	r square value	F value	p-value
PC1 vs. centroid size	51	0.01057	0.5232	0.484
PC 2 vs. centroid size	51	0.00081	0.0399	0.853
PC 3 vs. centroid size	51	0.00037	0.0184	0.879
PC 4 vs. centroid size	51	0.17417	10.373	0.006
PC 5 vs. centroid size	51	0.13301	7.5174	0.009
PC 6 vs. centroid size	51	0.04313	2.2087	0.137
PC 7 vs. centroid size	51	0.0231	1.1584	0.267

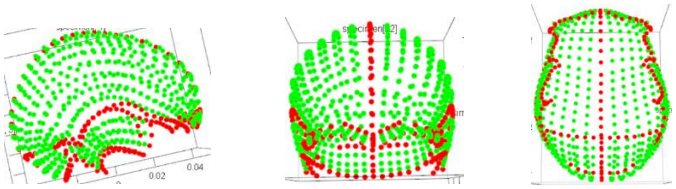

(A)

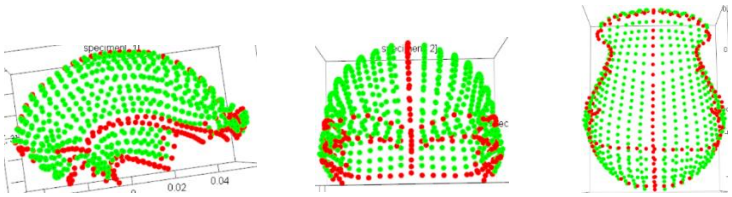

(B)

Figure B.7 PC 1 of the sixth PCA of the overall cranium
(A) The shape at the negative end. (B) The shape at the positive end. From left to right: lateral view, anterior view, and inferior view.

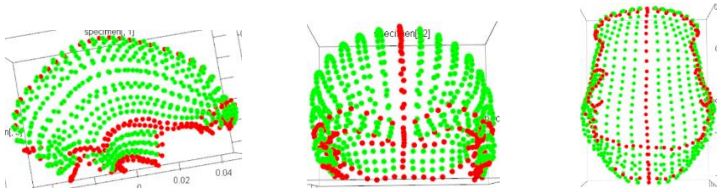

(A)

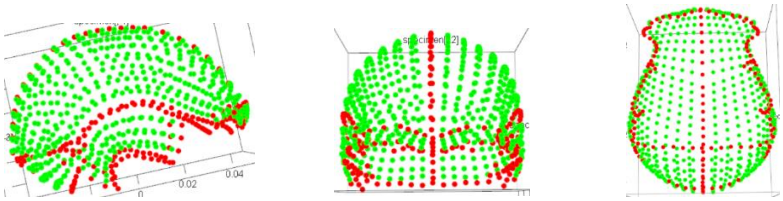

(B)

Figure B.8 PC 2 of the sixth PCA of the overall cranium
(A) The shape at the negative end. (B) The shape at the positive end. From left to right: lateral view, anterior view, and inferior view.

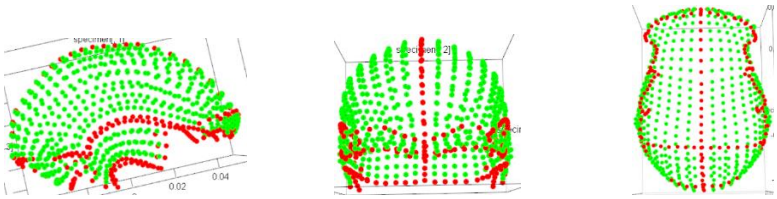

(A)

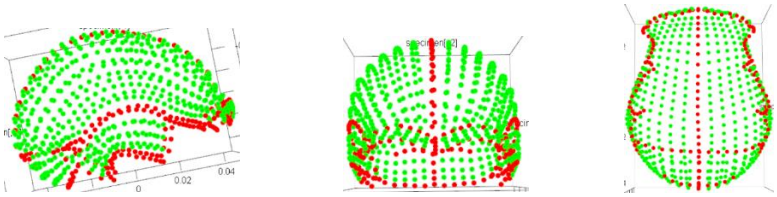

(B)

Figure B.9 PC 3 of the sixth PCA of the overall cranium
(A) The shape at the negative end. (B) The shape at the positive end. From left to right: lateral view, anterior view, and inferior view.

B.1.2 The bootstrap analysis of SSDs

Table B.7 The SSDs of *H. erectus* and its subsets compared to *H. sapiens*
(A) *H. erectus s. l.* (maximum-semilandmark set). (B) *H. erectus s. l.* (maximum-specimen set. (C) *H. ergaster* (with D2700) (maximum-semilandmark set). (C) *H. ergaster* (with D2700) (maximum-specimen set. (D) Asian *H. erectus* (maximum-semilandmark set). (E) Asian *H. erectus* (maximum-specimen set).

(A)

	Average SSD	25th percentile	50th percentiles	75th percentiles	90th percentiles	95th percentiles
Homo sapiens	1.118	1.038	1.116	1.201	1.271	1.312
Homo erectus s. l. (SSD)	1.103					

(B)

	Average SSD	25th percentile	50th percentiles	75th percentiles	90th percentiles	95th percentiles
Homo sapiens	2.651	2.496	2.653	2.809	2.943	3.020
Homo erectus s. l. (SSD)	2.503					

(C)

	Average SSD	25th percentile	50th percentiles	75th percentiles	90th percentiles	95th percentiles
Homo sapiens	0.230	0.204	0.226	0.252	0.277	0.293
H. ergaster with D2700 (SSD)	0.228					

(D)

	Average SSD	25th percentile	50th percentiles	75th percentiles	90th percentiles	95th percentiles
Homo sapiens	0.228	0.201	0.225	0.252	0.276	0.291
H. ergaster with D2700 (SSD)	0.216					

(E)

	Average SSD	25th percentile	50th percentiles	75th percentiles	90th percentiles	95th percentiles
Homo sapiens	0.230	0.204	0.227	0.252	0.277	0.293
Asian *H. erectus*	0.189					

(F)

	Average SSD	25th percentile	50th percentiles	75th percentiles	90th percentiles	95th percentiles
Homo sapiens	1.137	1.059	1.133	1.211	1.279	1.319
Asian *H. erectus*	0.935					

B.1.3 Bootstrapped analyses of mean pairwise distances

Table B.8 The mean pairwise distance of *H. erectus* and its subsets compared to *H. sapiens*
(A) *H. erectus s. l.* (maximum-semilandmark set). (B) *H. erectus s. l.* (maximum-specimen set. (C) *H. ergaster* (no D2700) (maximum-semilandmark set). (D) *H. ergaster* (no D2700) (maximum-specimen set. (E) *H. ergaster* (with D2700) (maximum-semilandmark set). (F) *H.* ergaster (with D2700) (maximum-specimen set. (G) Asian *H. erectus* (maximum-semilandmark set). (H) Asian *H. erectus* (maximum-specimen set).

(A)

	Mean pairwise distance	25th percentile	50th percentiles	75th percentiles	90th percentiles	95th percentiles
H. sapiens	0.0766	0.0716	0.0762	0.0813	0.0859	0.0885
H. erectus s. l.	0.0736					

(B)

	Mean pairwise distance	25th percentile	50th percentiles	75th percentiles	90th percentiles	95th percentiles
H. sapiens	0.0759	0.0721	0.0758	0.0796	0.0829	0.0848
H. erectus s. l.	0.0695					

(C)

	Average SSD	25th percentile	50th percentiles	75th percentiles	90th percentiles	95th percentiles
Homo sapiens	0.0770	0.0644	0.0751	0.0872	0.0987	0.109
ER 3733 vs. ER 3883	0.0803					

(D)

	Average SSD	25th percentile	50th percentiles	75th percentiles	90th percentiles	95th percentiles
Homo sapiens	0.0756	0.0629	0.0731	0.0859	0.0994	0.110
ER 3733 vs. ER 3883	0.0741					

(E)

	Mean pairwise distance (sample size 4)	25th percentile	50th percentiles	75th percentiles	90th percentiles	95th percentiles
H. sapiens	0.0768	0.0683	0.0758	0.0841	0.0927	0.978
H. ergaster (with D2700)	0.759					

(F)

	Mean pairwise distance	25th percentile	50th percentiles	75th percentiles	90th percentiles	95th percentiles
H. sapiens	0.0757	0.0668	0.0749	0.0833	0.0915	0.969
H. ergaster (with D2700)	0.719					

(G)

	Mean pairwise distance	25th percentile	50th percentiles	75th percentiles	90th percentiles	95th percentiles
H. sapiens	0.0770	0.0683	0.0759	0.0845	0.0928	0.0977
Asian *H. erectus*	0.0631					

(H)

	Mean pairwise distance	25th percentile	50th percentiles	75th percentiles	90th percentiles	95th percentiles
H. sapiens	0.0758	0.0706	0.0756	0.0808	0.0853	0.0877
Asian *H. erectus*	0.0624					

B.1.4 Lower landmark densities

B.1.4.1 One hundred-fifty-nine anchor points

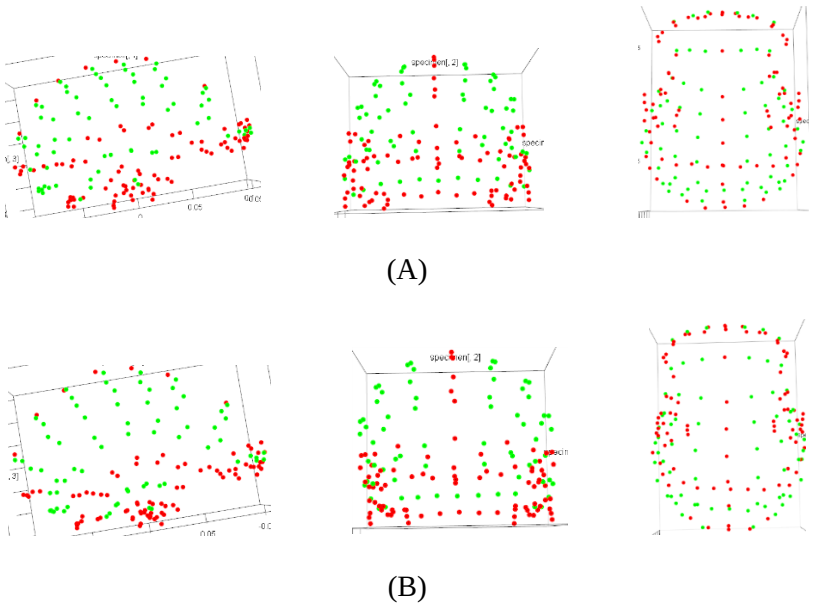

(A)

(B)

Figure B.10 PC 1 of fossil set (anchor points of the overall cranium)
(A) The shape at the negative end. (B) The shape at the positive end. From left to right: lateral view, anterior view, and inferior view.

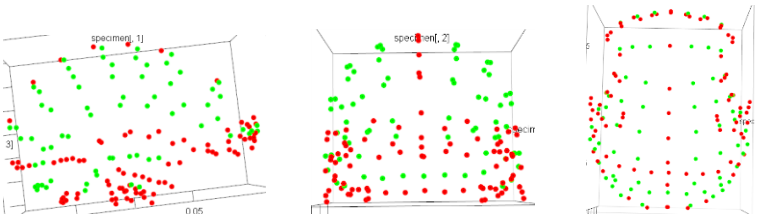

(A)

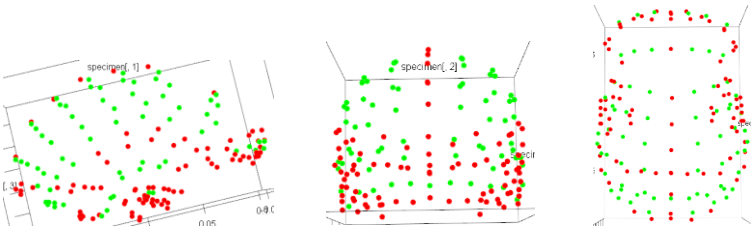

(B)

Figure B.11 PC 2 of fossil set (anchor points of the overall cranium)
(A) The shape at the negative end. (B) The shape at the positive end. From left to right: lateral view, anterior view, and inferior view.

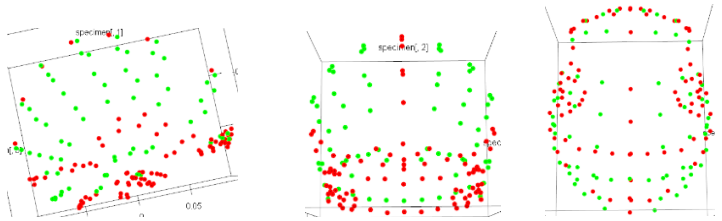

(A)

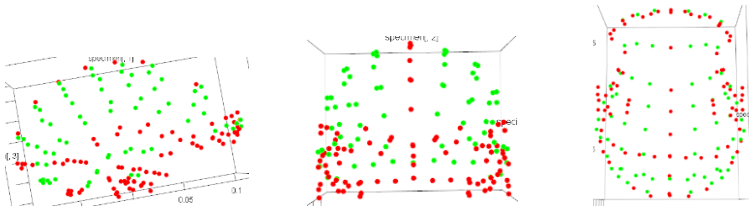

(B)

Figure B.12 PC 1 of fossils and *H. sapiens* (anchor points of the overall cranium)
(A) The shape at the negative end. (B) The shape at the positive end. From left to right: lateral view, anterior view, and inferior view.

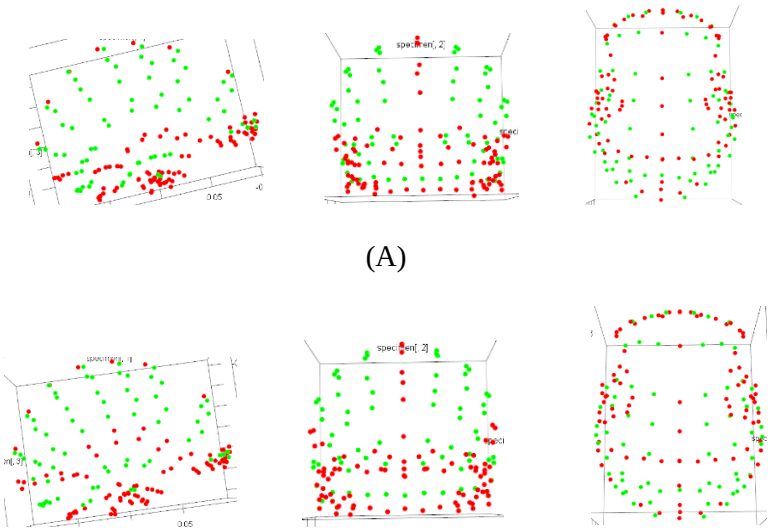

Figure B.13 PC 4 of fossils and *H. sapiens* (anchor points of the overall cranium)
(A) The shape at the negative end. (B) The shape at the positive end. From left to right: lateral view, anterior view, and inferior view.

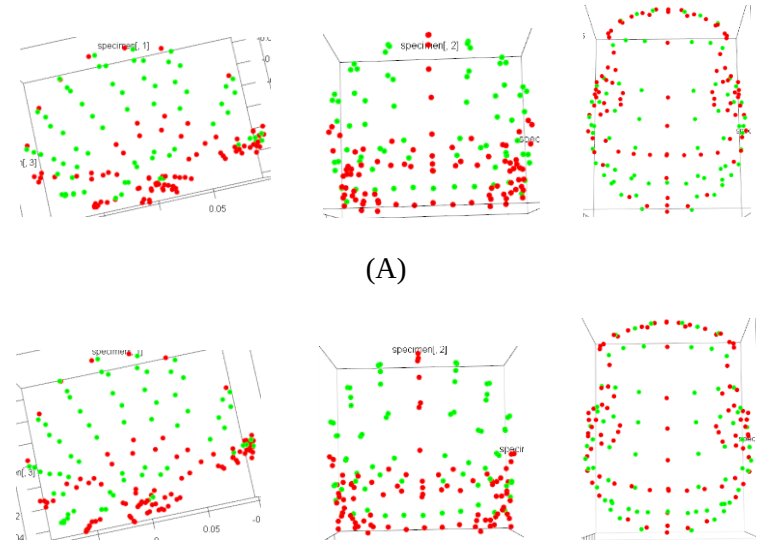

Figure B.14 PC 5 of fossils and *H. sapiens* (anchor points of the overall cranium)
(A) The shape at the negative end. (B) The shape at the positive end. From left to right: lateral view, anterior view, and inferior view.

B.1.4.2 Discrete landmarks

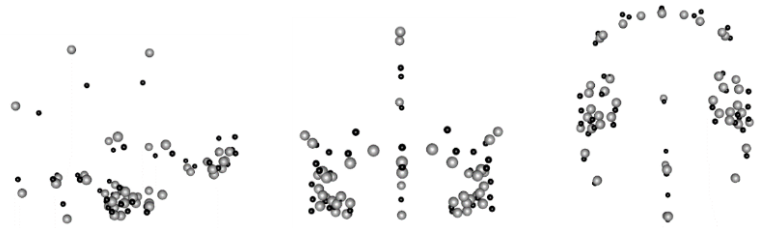

Figure B.15 PC 1 of fossils and *H. sapiens* (discrete landmarks of the overall cranium)
The configuration with grey dots is the shape at the negative end. The configuration with black dots is the shape at the positive end. From left to right: lateral view, anterior view, and inferior view.

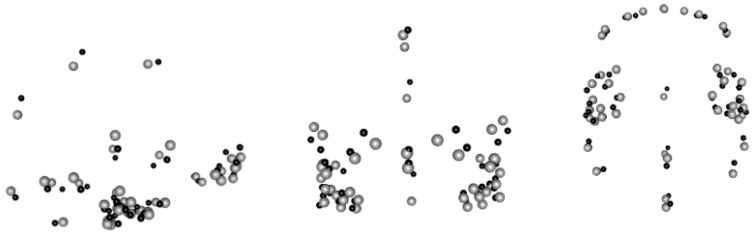

Figure B.16 PC 4 of fossils and *H. sapiens* (discrete landmarks of the overall cranium)
The configuration with grey dots is the shape at the negative end. The configuration with black dots is the shape at the positive end. From left to right: lateral view, anterior view, and inferior view.

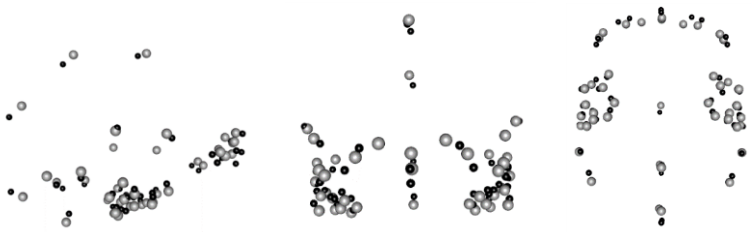

Figure B.17 PC 5 of fossils and *H. sapiens* (discrete landmarks of the overall cranium)
The configuration with grey dots is the shape at the negative end. The configuration with black dots is the shape at the positive end. From left to right: lateral view, anterior view, and inferior view.

B.2 THE POSTERIOR CRANIUM

B.2.1 PCA

B.2.1.1 The first PCA

Table B.9 The size-shape relationship of the first seven PCs in the first PCA (the posterior cranium)

	Sample size	R square	F value	p-value
PC1 vs. centroid size	14	0.5203	13.02	0.0031
PC 2 vs. centroid size	14	0.002278	0.0274	0.8735
PC 3 vs. centroid size	14	0.1054	1.413	0.2514
PC 4 vs. centroid size	14	0.1147	1.555	0.2409
PC 5 vs. centroid size	14	8.494×10^{-7}	1.09×10^{-5}	0.9979
PC 6 vs. centroid size	14	0.01376	0.1674	0.6882
PC 7 vs. centroid size	14	0.03834	0.4784	0.4931

B.2.1.2 The second PCA

Table B.10 The size-shape relationship of the first seven PCs in the second PCA (the posterior cranium)

	Sample size	R square	F value	p-value
Full Procrustes sum of squares	49	0.07691	3.9158	0.004
PC1 vs. centroid size	49	0.1194	6.371	0.0162
PC 2 vs. centroid size	49	0.001696	0.07986	0.775
PC 3 vs. centroid size	49	0.1750	9.968	0.0036
PC 4 vs. centroid size	49	0.02477	1.194	0.2885
PC 5 vs. centroid size	49	0.00966	0.4585	0.4962
PC 6 vs. centroid size	49	0.1660	9.352	0.005
PC 7 vs. centroid size	49	0.000550	0.02586	0.8711

B.2.1.3 The third PCA

Table B.11 The size-shape relationship of the first seven PCs in the third PCA (the posterior cranium)

	Sample size	R square	F value	p-value
PC1 vs. centroid size	22	0.207	5.221	0.0326
PC 2 vs. centroid size	22	0.2328	6.068	0.0262
PC 3 vs. centroid size	22	0.01675	0.3407	0.5669
PC 4 vs. centroid size	22	0.002714	0.05441	0.8175
PC 5 vs. centroid size	22	0.1726	4.171	0.0532
PC 6 vs. centroid size	22	4.6756×10^{-5}	0.000935	0.978
PC 7 vs. centroid size	22	0.08671	1.899	0.1835

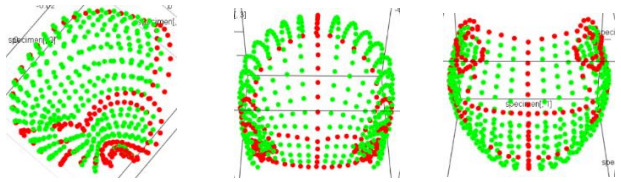

(A)

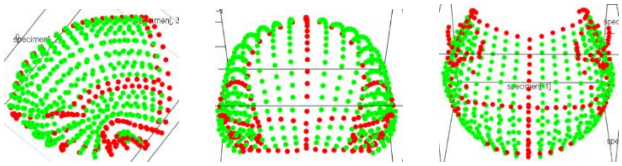

(B)

Figure B.18 PC 1 of the third PCA of the posterior cranium
(A) The shape at the negative end. (B) The shape at the positive end. From left to right: lateral view, anterior view, and inferior view.

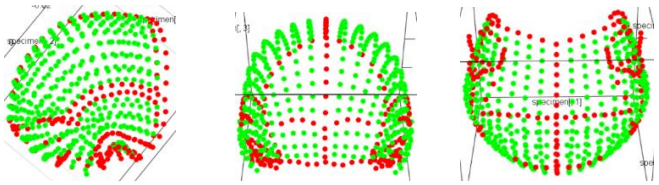

(A)

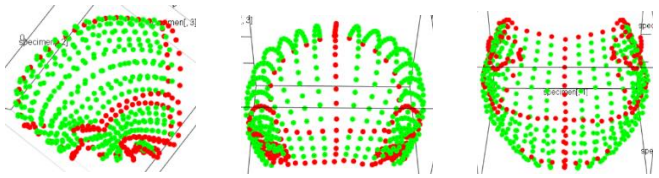

(B)

Figure B.19 PC 2 of the third PCA of the posterior cranium
(A) The shape at the negative end. (B) The shape at the positive end. From left to right: lateral view, anterior view, and inferior view.

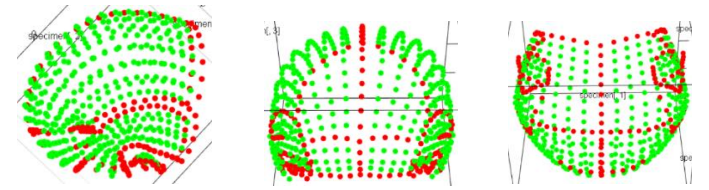

(A)

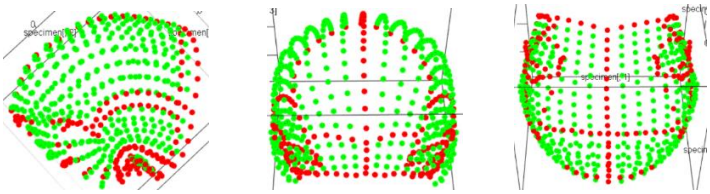

(B)

Figure B.20 PC 3 of the third PCA of the posterior cranium
(A) The shape at the negative end. (B) The shape at the positive end. From left to right: lateral view, anterior view, and inferior view.

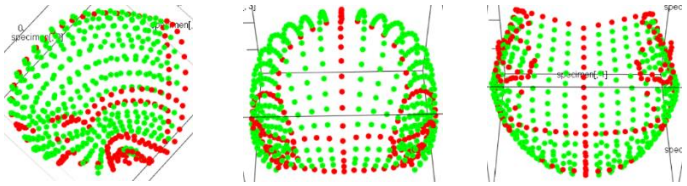

(A)

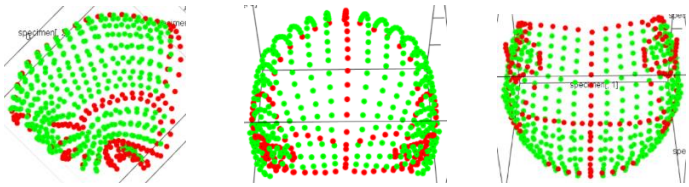

(B)

Figure B.21 PC 5 of the third PCA of the posterior cranium
(A) The shape at the negative end. (B) The shape at the positive end. From left to right: lateral view, anterior view, and inferior view.

B.2.1.4 The fourth PCA

Table B.12 The size-shape relationship of the first seven PCs in the fourth PCA (the posterior cranium)

	Sample size	R square	F value	p-value
PC1 vs. centroid size	21	0.4644	16.48	0.04
PC 2 vs. centroid size	21	0.01222	0.2352	0.6347
PC 3 vs. centroid size	21	0.1193	2.573	0.1224
PC 4 vs. centroid size	21	0.0752	1.545	0.2234
PC 5 vs. centroid size	21	0.03189	0.6258	0.436
PC 6 vs. centroid size	21	0.08182	1.693	0.2059
PC 7 vs. centroid size	21	0.01325	0.02522	0.8785

B.2.1.5 The fifth PCA

Table B.13 The size-shape relationship of the first seven PCs in the fifth PCA (the posterior cranium)

	Sample size	R square	F value	p-value
PC1 vs. centroid size	56	0.1008	6.053	0.0156
PC 2 vs. centroid size	56	0.001761	0.09525	0.7581
PC 3 vs. centroid size	56	0.1666	10.79	0.003
PC 4 vs. centroid size	56	0.0418	0.4363	0.549
PC 5 vs. centroid size	56	0.0528	3.135	0.0846
PC 6 vs. centroid size	56	0.01568	0.08483	0.7758
PC 7 vs. centroid size	56	0.2164	14.91	0.0006

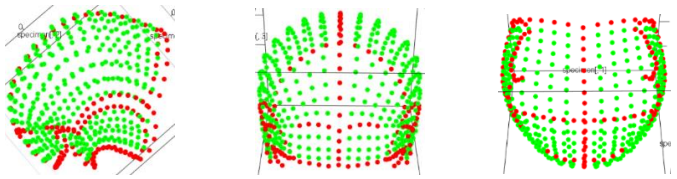

(A)

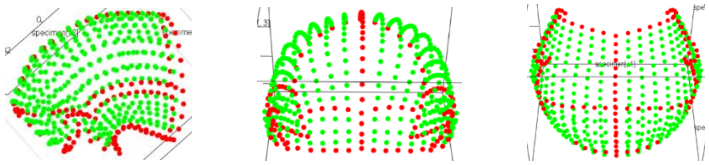

(B)

Figure B.22 PC 1 of the fifth PCA of the posterior cranium
(A) The shape at the negative end. (B) The shape at the positive end. From left to right: lateral view, anterior view, and inferior view.

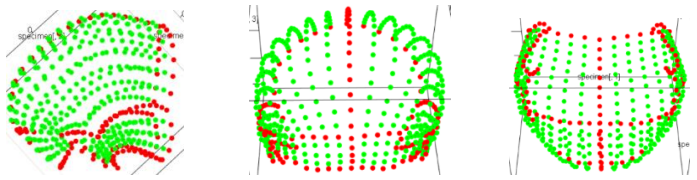

(A)

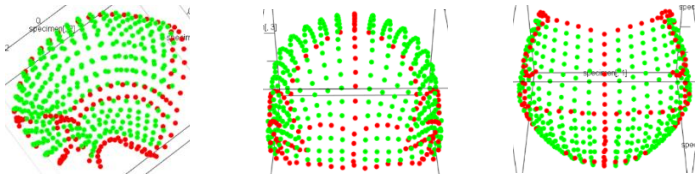

(B)

Figure B.23 PC 3 of the fifth PCA of the posterior cranium
(A) The shape at the negative end. (B) The shape at the positive end. From left to right: lateral view, anterior view, and inferior view.

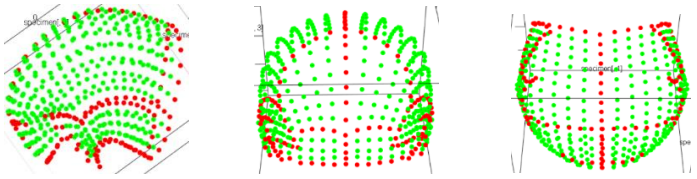

(A)

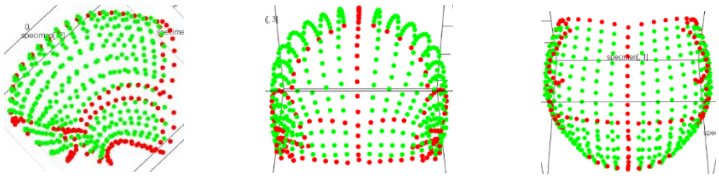

(B)

Figure B.24 PC 5 of the fifth PCA of the posterior cranium
(A) The shape at the negative end. (B) The shape at the positive end. From left to right: lateral view, anterior view, and inferior view.

B.2.1.6 The sixth PCA of the posterior cranium

Table B.14 The size-shape relationship of the first seven PCs in the sixth PCA (the posterior cranium)

	Sample size	R square	F value	p-value
PC1 vs. centroid size	56	0.1008	6.053	0.0156
PC 2 vs. centroid size	56	0.001761	0.09525	0.7581
PC 3 vs. centroid size	56	0.1666	10.79	0.003
PC 4 vs. centroid size	56	0.0418	0.4363	0.549
PC 5 vs. centroid size	56	0.0528	3.135	0.0846
PC 6 vs. centroid size	56	0.01568	0.08483	0.7758
PC 7 vs. centroid size	56	0.2164	14.91	0.0006

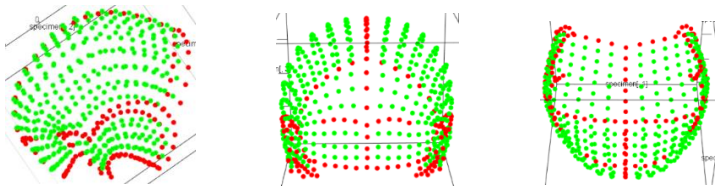

(A)

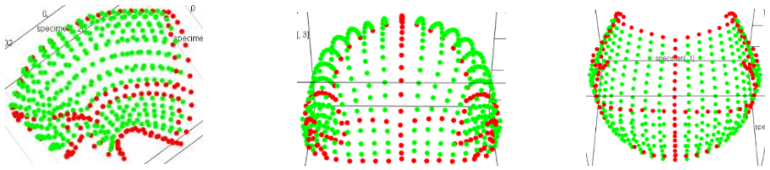

(B)

Figure B.25 PC 1 of the sixth PCA of the posterior cranium
(A) The shape at the negative end. (B) The shape at the positive end. From left to right: lateral view, anterior view, and inferior view.

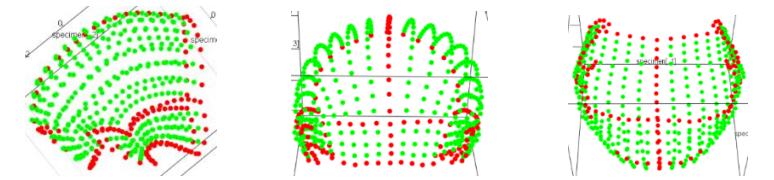

(A)

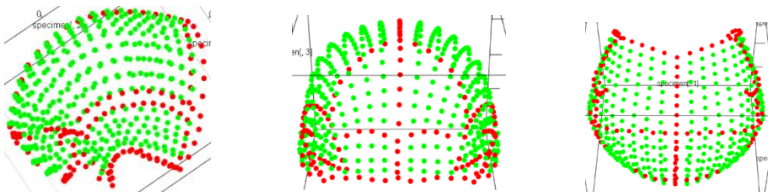

(B)

Figure B.26 PC 2 of the sixth PCA of the posterior cranium
(A) The shape at the negative end. (B) The shape at the positive end. From left to right: lateral view, anterior view, and inferior view.

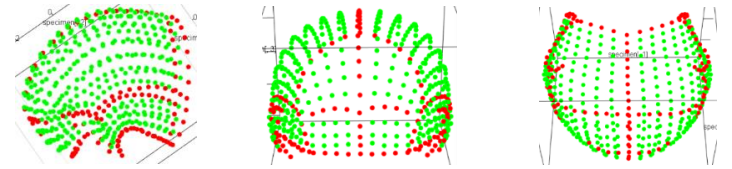

(A)

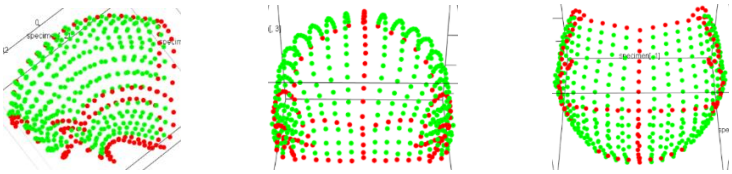

(B)

Figure B.27 PC 6 of the sixth PCA of the posterior cranium
(A) The shape at the negative end. (B) The shape at the positive end. From left to right: lateral view, anterior view, and inferior view.

B.2.2 Bootstrapped analyses of SSDs

Table B.15 The SSDs of *H. erectus* and its subsets compared to *H. sapiens* (the posterior cranium)
(A) *H. erectus s. l.* (maximum-semilandmark set). (B) *H. erectus s. l.* (maximum-specimen set. (C) *H. ergaster* (no D2700) (maximum-semilandmark set). (D) *H. ergaster* (no D2700) (maximum-specimen set. (E) *H. ergaster* (with D2700) (maximum-semilandmark set). (F) *H. ergaster* (with D2700) (maximum-specimen set. (G) Asian *H. erectus* (maximum-semilandmark set). (H) Asian *H. erectus* (maximum-specimen set).

(A)

	Average SSD	25th percentile	50th percentiles	75th percentiles	90th percentiles	95th percentiles
Homo sapiens	2.287	2.155	2.281	2.416	2.534	2.607
Homo erectus s. l. (SSD)	4.598					

(B)

	Average SSD	25th percentile	50th percentiles	75th percentiles	90th percentiles	95th percentiles
Homo sapiens	7.194	6.839	7.192	7.550	7.869	8.063
Homo erectus s. l. (SSD)	7.158					

(C)

	Average SSD	25th percentile	50th percentiles	75th percentiles	90th percentiles	95th percentiles
Homo sapiens	0.245	0.215	0.240	0.271	0.300	0.320
H. ergaster without D2700 (SSD)	0.245					

(D)

	Average SSD	25th percentile	50th percentiles	75th percentiles	90th percentiles	95th percentiles
Homo sapiens	0.243	0.210	0.238	0.272	0.300	0.320
H. ergaster without D2700 (SSD)	0.235					

(E)

	Average SSD	25th percentile	50th percentiles	75th percentiles	90th percentiles	95th percentiles
Homo sapiens	0.491	0.444	0.486	0.533	0.580	0.607
H. ergaster with D2700 (SSD)	0.498					

(F)

	Average SSD	25th percentile	50th percentiles	75th percentiles	90th percentiles	95th percentiles
Homo sapiens	0.487	0.444	0.483	0.533	0.580	0.607
H. ergaster with D2700 (SSD)	0.478					

(G)

	Average SSD	25th percentile	50th percentiles	75th percentiles	90th percentiles	95th percentiles
Homo sapiens	0.490	0.441	0.484	0.531	0.577	0.604
Asian *H. erectus*	0.460					

(H)

	Average SSD	25th percentile	50th percentiles	75th percentiles	90th percentiles	95th percentiles
Homo sapiens	3.661	3.475	3.624	3.842	4.008	4.115
Asian *H. erectus*	3.304					

B.2.3 Bootstrapped analyses of mean pairwise distances

Table B.16 The mean pairwise distance of *H. erectus* subsets compared to *H. sapiens* (the posterior cranium) (A) *H. erectus s. l.* (maximum-semilandmark set). (B) *H. erectus s. l.* (maximum-specimen set. (C) *H. ergaster* (no D2700) (maximum-semilandmark set). (D) *H. ergaster* (no D2700) (maximum-specimen set. (E) *H. ergaster* (with D2700) (maximum-semilandmark set). (F) *H. ergaster* (with D2700) (maximum-specimen set. (G) Asian *H. erectus* (maximum-semilandmark set). (H) Asian *H. erectus* (maximum-specimen set).

(A)

	Mean pairwise distance (sample size 3)	25th percentile	50th percentiles	75th percentiles	90th percentiles	95th percentiles
H. sapiens	0.0817	0.0768	0.0815	0.0862	0.0904	0.0929
H. erectus s. l.	0.0821					

(B)

	Mean pairwise distance (sample size 3)	25th percentile	50th percentiles	75th percentiles	90th percentiles	95th percentiles
H. sapiens	0.0814	0.0783	0.0815	0.0846	0.0873	0.0889
H. erectus s. l.	0.0787					

(C)

	Mean pairwise distance	25th percentile	50th percentiles	75th percentiles	90th percentiles	95th percentiles
Homo sapiens	0.0820	0.0719	0.0803	0.0909	0.100	0.107
H. ergaster (no D2700)	0.0817					

(D)

	Mean pairwise distance	25th percentile	50th percentiles	75th percentiles	95th percentiles	Max
Homo sapiens	0.0814	0.0703	0.0799	0.0912	0.105	0.129
H. ergaster (no D2700)	0.0783					

(E)

	Mean pairwise distance (sample size 4)	25th percentile	50th percentiles	75th percentiles	90th percentiles	95th percentiles
H. sapiens	0.0817	0.0736	0.0808	0.0888	0.964	0.101
H. ergaster (with D2700)	0.0829					

(F)

	Mean pairwise distance	25th percentile	50th percentiles	75th percentiles	90th percentiles	Max
Homo sapiens	0.0813	0.0727	0.0806	0.0888	0.971	0.123
H. ergaster (with D2700)	0.0796					

(G)

	Mean pairwise distance	25th percentile	50th percentiles	75th percentiles	90th percentiles	95th percentiles
H. sapiens	0.0818	0.0738	0.0810	0.0887	0.0966	0.101
Asian *H. erectus*	0.0767					

(H)

	Mean pairwise distance (sample size 4)	25th percentile	50th percentiles	75th percentiles	90th percentiles	95th percentiles
H. sapiens	0.0814	0.0772	0.0814	0.0854	0.0892	0.0912
Asian *H. erectus*	0.0734					

B.2.4 Bootstrap analyses of distance between geographical group means

Table B.17 The distances between means of geographical subsets (the posterior cranium)
(A) *H. ergaster* (no D2700) vs. Asian *H. erectus* (maximum-semilandmark set). (B) *H. ergaster* (no D2700) vs. Asian *H. erectus* (maximum-specimen set) (C) *H. ergaster* (with D2700) vs. Asian *H. erectus* (maximum-semilandmark set). (D) *H. ergaster* (with D2700) vs. Asian *H. erectus* (maximum-specimen set)

(A)

	Mean pairwise distance	25th percentile	50th percentile	75th percentile	90th percentiles	95th percentile
Homo sapiens	0.0611	0.0523	0.0601	0.0689	0.0771	0.0822
H. ergaster (no D2700) vs. *H. erectus*	0.0499					

(B)

	Mean pairwise distance	25th percentile	50th percentiles	75th percentile	90th percentile	95th percentile
Homo sapiens	0.0572	0.0500	0.0573	0.0651	0.0716	0.0753
H. ergaster (no D2700) vs. *H. erectus*	0.0577					

(C)

	Mean pairwise distance	25th percentile	50th percentile	75th percentile	90th percentile	95th percentile
Homo sapiens	0.0592	0.0511	0.0584	0.0663	0.0743	0.0790
H. ergaster (with D 2700) vs. Asian *H. erectus*	0.0469					

(D)

	Mean pairwise distance	25 percentiles	50 percentiles	75 percentiles	90 percentiles	95 percentiles
Homo sapiens	0.0563	0.0496	0.0561	0.0627	0.0685	0.0720
H. ergaster (no D2700) vs. *H. erectus*	0.0490					

B.2.5 The anchor points

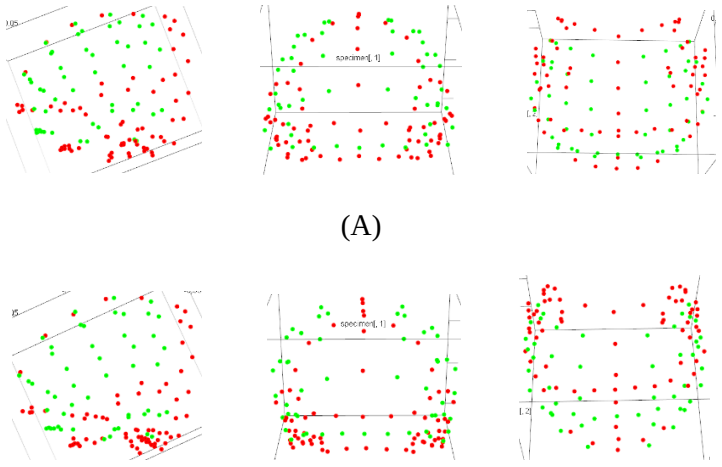

(A)

(B)

Figure B.28 PC 1 of the fossils sample (anchor points of the posterior cranium)
(A) The shape at the negative end. (B) The shape at the positive end. From left to right: lateral view, anterior view, and inferior view.

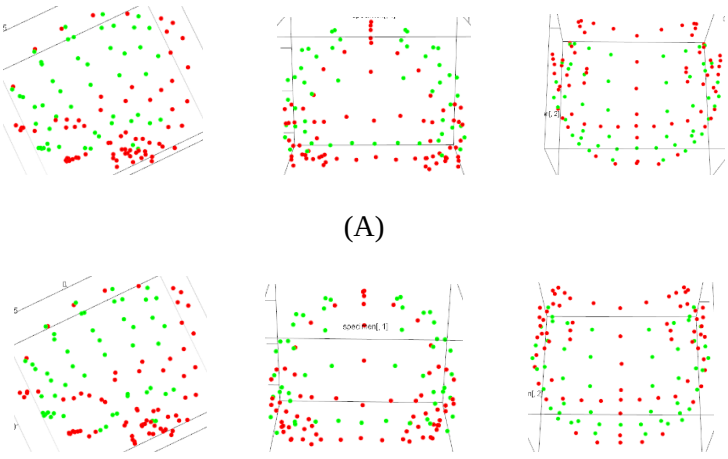

(A)

(B)

Figure B.29 PC 2 of the fossils sample (anchor points of the posterior cranium)
(A) The shape at the negative end. (B) The shape at the positive end. From left to right: lateral view, anterior view, and inferior view.

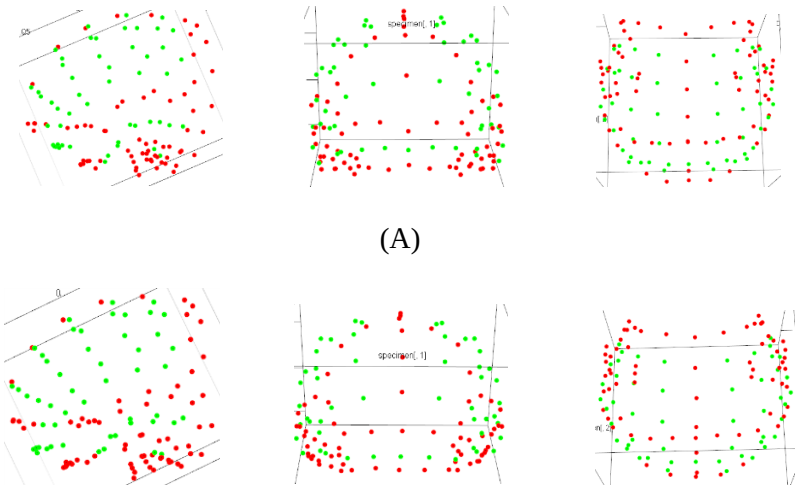

(A)

(B)

Figure B.30 PC 3 of the fossils sample (anchor points of the posterior cranium)
(A) The shape at the negative end. (B) The shape at the positive end. From left to right: lateral view, anterior view, and inferior view.

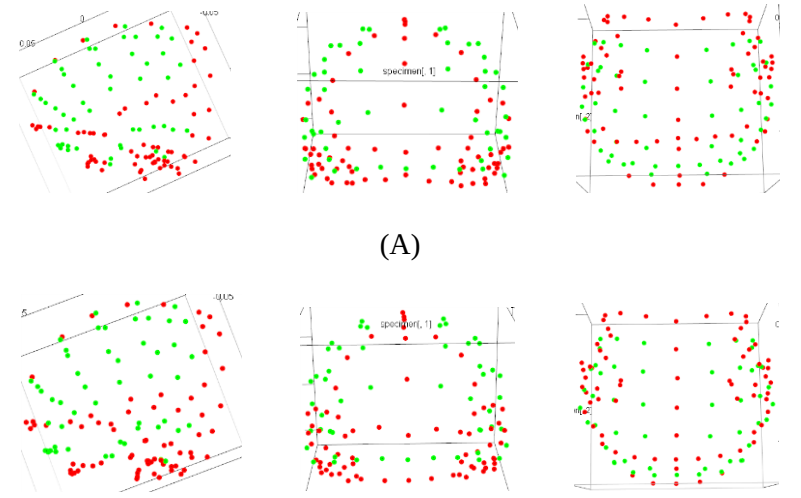

(A)

(B)

Figure B.31 PC 4 of the fossils sample (anchor points of the posterior cranium)
(A) The shape at the negative end. (B) The shape at the positive end. From left to right: lateral view, anterior view, and inferior view.

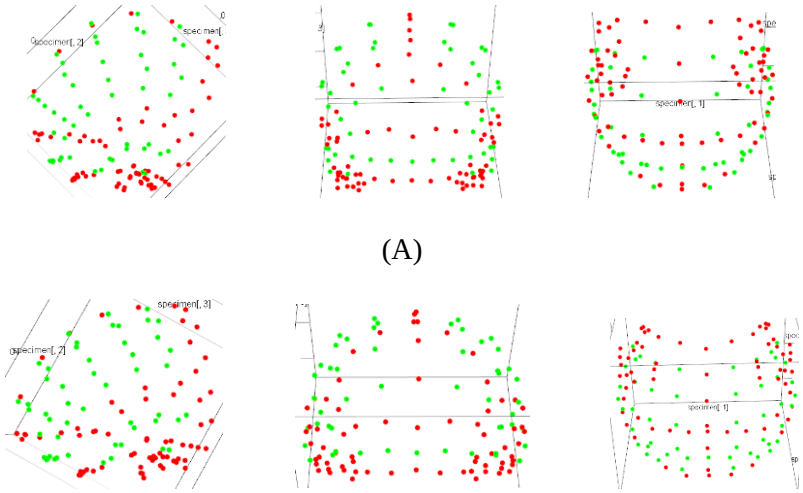

(A)

(B)

Figure B.32 PC 1 of fossils and *H. sapiens* (anchor points of the posterior cranium)
(A) The shape at the negative end. (B) The shape at the positive end. From left to right: lateral view, anterior view, and inferior view.

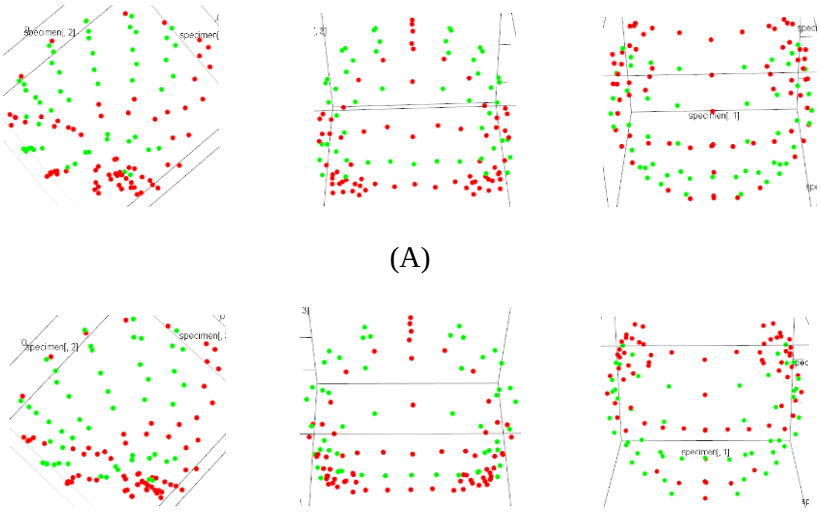

(A)

(B)

Figure B.33 PC 3 of fossils and *H. sapiens* (anchor points of the posterior cranium)
(A) The shape at the negative end. (B) The shape at the positive end. From left to right: lateral view, anterior view, and inferior view.

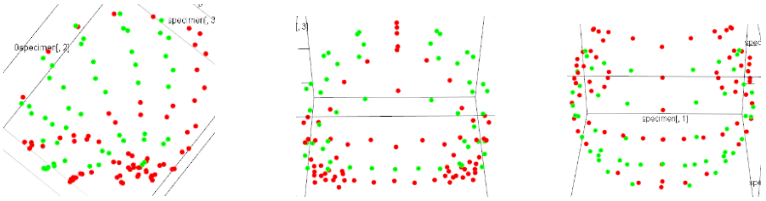

(A)

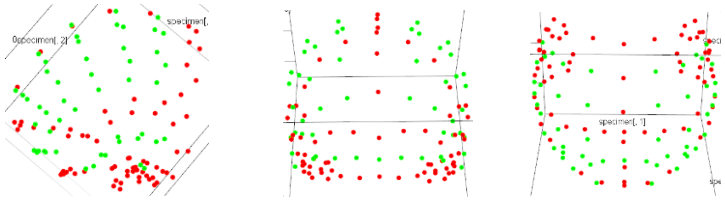

(B)

Figure B.34 PC 4 of fossils and *H. sapiens* (anchor points of the posterior cranium)
(A) The shape at the negative end. (B) The shape at the positive end. From left to right: lateral view, anterior view, and inferior view.

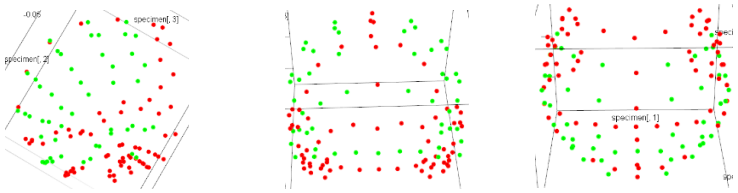

(A)

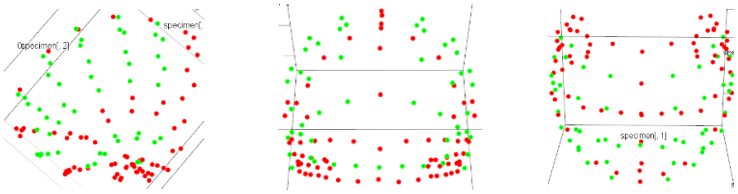

(B)

Figure B.35 PC 6 of fossils and *H. sapiens* (anchor points of the posterior cranium)
(A) The shape at the negative end. (B) The shape at the positive end. From left to right: lateral view, anterior view, and inferior view.

B.2.6 The discrete landmarks

Figure B.36 PC 1 of fossils and *H. sapiens* (discrete landmarks of the posterior cranium)
The configuration of grey dots represents the shape at the negative end. The configuration of black dots represents the shape at the positive end. From left to right: lateral view, anterior view, and inferior view.

Figure B.37 PC 3 of fossils and *H. sapiens* (discrete landmarks of the posterior cranium)
The configuration of grey dots represents the shape at the negative end. The configuration of black dots represents the shape at the positive end. From left to right: lateral view, anterior view, and inferior view.

Figure B.38 PC 4 of fossils and *H. sapiens* (discrete landmarks of the posterior cranium)
The configuration of grey dots represents the shape at the negative end. The configuration of black dots represents the shape at the positive end. From left to right: lateral view, anterior view, and inferior view.

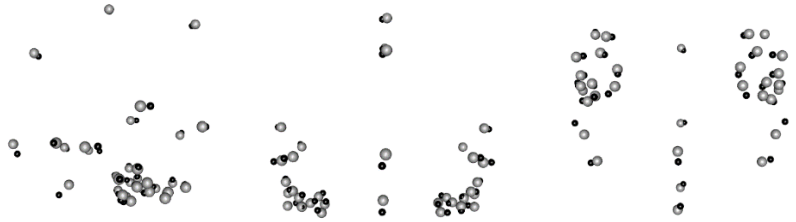

Figure B.39 PC 6 of fossils and *H. sapiens* (discrete landmarks of the posterior cranium)
The configuration of grey dots represents the shape at the negative end. The configuration of black dots represents the shape at the positive end. From left to right: lateral view, anterior view, and inferior view.

B.3 TEMPORAL REGION

B.3.1 PCA

B.3.1.1 The first PCA

Table B.18 The size-shape relationship of the first seven PCs in the first PCA (the temporal region)

	Sample size	R square	F value	p-value
PC1 vs. centroid size	14	0.2009	3.017	0.1152
PC 2 vs. centroid size	14	0.2701	4.441	0.0548
PC 3 vs. centroid size	14	0.181	2.652	0.1266
PC 4 vs. centroid size	14	0.01809	0.221	0.6801
PC 5 vs. centroid size	14	0.02513	0.3093	0.5905
PC 6 vs. centroid size	14	0.06149	0.7862	0.3868
PC 7 vs. centroid size	14	1.964×10^{-6}	2.357×10^{-5}	0.9961

B.3.1.2 The second PCA

Table B.19 The size-shape relationship of the first seven PCs in the second PCA (the temporal region)

	Sample size	R square	F value	p-value
PC1 vs. centroid size	49	4.92×10^{-5}	0.002313	0.959
PC 2 vs. centroid size	49	0.02226	1.07	0.3018
PC 3 vs. centroid size	49	0.05368	0.5672	0.455
PC 4 vs. centroid size	49	0.04000	1.958	0.1656
PC 5 vs. centroid size	49	0.000636	0.02989	0.8589
PC 6 vs. centroid size	49	0.00409	0.1929	0.6614
PC 7 vs. centroid size	49	0.001908	0.08084	0.7654

B.3.1.3 The third PCA

Table B.20 The size-shape relationship of the first seven PCs in the third PCA (the temporal region)

	Sample size	R square	F value	p-value
Full Procrustes sum of squares	22	0.04673	0.9805	0.434
PC1 vs. centroid size	22	0.01225	0.2481	0.6244
PC 2 vs. centroid size	22	0.06159	1.313	0.2647
PC 3 vs. centroid size	22	0.1026	2.287	0.1567
PC 4 vs. centroid size	22	0.03334	0.6899	0.4179
PC 5 vs. centroid size	22	0.1675	4.024	0.0588
PC 6 vs. centroid size	22	0.005986	0.1204	0.7327
PC 7 vs. centroid size	22	0.0021	0.0421	0.8357

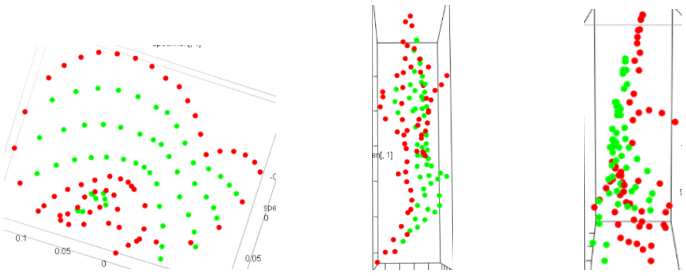

(A)

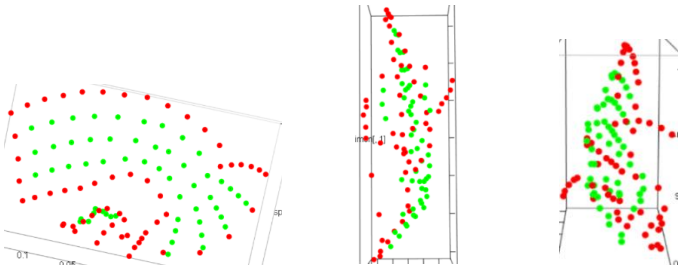

(B)

Figure B.40 Shape changes in PC 1 of the third PCA of the temporal region
(A) The shape at the negative end. (B) The shape at the positive end. From left to right: lateral view, inferior view, and posterior view.

B.3.1.4 The fourth PCA

Table B.21 The size-shape relationship of the first seven PCs in the fourth PCA (the temporal region)

	Sample size	R square	F value	p-value
PC1 vs. centroid size	18	0.00527	0.08477	0.7933
PC 2 vs. centroid size	18	0.00218	0.03497	0.8517
PC 3 vs. centroid size	18	0.05085	0.8572	0.3748
PC 4 vs. centroid size	18	0.01637	0.2662	0.6161
PC 5 vs. centroid size	18	0.04958	0.8347	0.3638
PC 6 vs. centroid size	18	0.02861	0.4714	0.509
PC 7 vs. centroid size	18	0.0307	0.5067	0.4826

B.3.1.5 The fifth PCA

Table B.22 The size-shape relationship of the first seven PCs in the fifth PCA (the temporal region)

	Sample Size	R Squared	F-value	p-value
PC 1 vs. centroid size	53	0.00293	0.1499	0.7005
PC 2 vs. centroid size	53	0.000794	0.04502	0.8445
PC 3 vs. centroid size	53	0.1281	7.494	0.0099
PC 4 vs. centroid size	53	0.00996	0.5132	0.4829
PC 5 vs. centroid size	53	0.0701	3.846	0.0547
PC 6 vs. centroid size	53	0.0151	0.7841	0.3813
PC 7 vs. centroid size	53	0.00106	0.05432	0.8201

B.3.1.6 The sixth PCA

Table B.23 The size-shape relationship of the first seven PCs in the sixth PCA (the temporal region)

	Sample size	R square	F value	p-value
PC1 vs. centroid size	26	0.00685	0.1655	0.6915
PC 2 vs. centroid size	26	0.001918	0.04613	0.8291
PC 3 vs. centroid size	26	0.0511	1.292	0.275
PC 4 vs. centroid size	26	0.0626	1.602	0.2091
PC 5 vs. centroid size	26	0.0289	0.715	0.4146
PC 6 vs. centroid size	26	0.0151	0.7841	0.3813
PC 7 vs. centroid size	26	0.263	8.564	0.0065

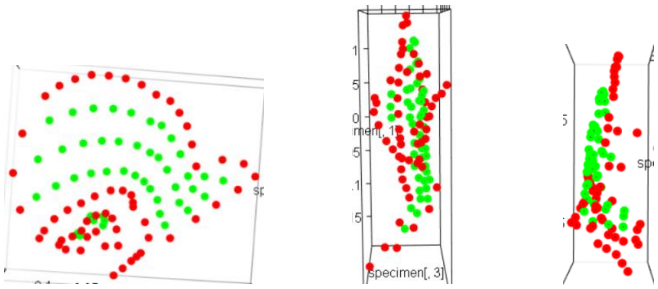

(A)

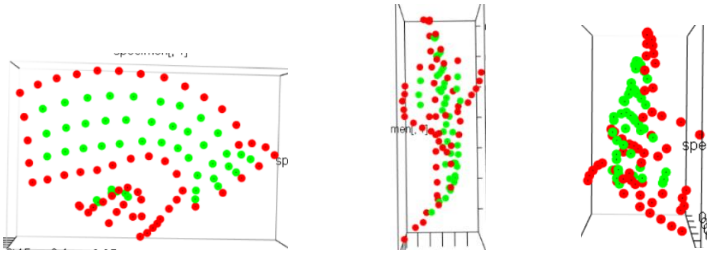

(B)

Figure B.41 Shape changes in PC 1 of the sixth PCA of the temporal region
(A) The shape at the negative end. (B) The shape at the positive end. From left to right: lateral view, inferior view, and posterior view.

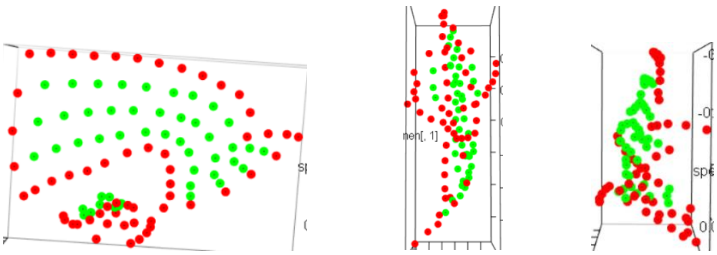

(A)

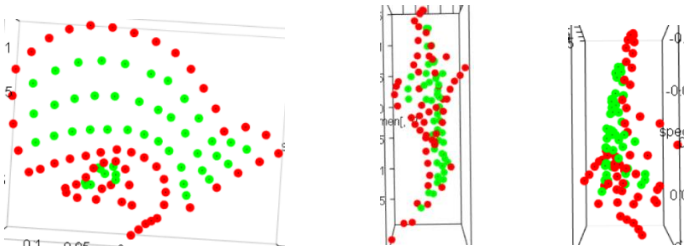

(B)

Figure B.42 Shape changes in PC 2 of the sixth PCA of the temporal region
(A) The shape at the negative end. (B) The shape at the positive end. From left to right: lateral view, inferior view, and posterior view.

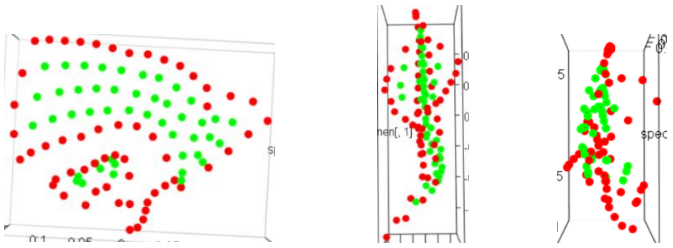

(A)

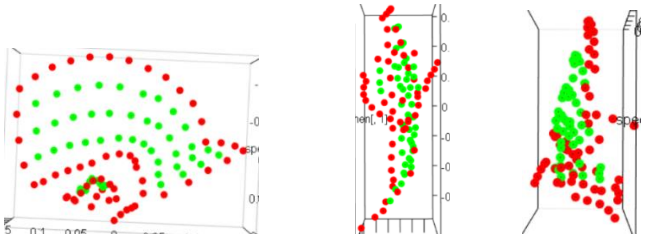

(B)

Figure B.43 Shape changes in PC 3 of the sixth PCA of the temporal region
(A) The shape at the negative end. (B) The shape at the positive end. From left to right: lateral view, inferior view, and posterior view.

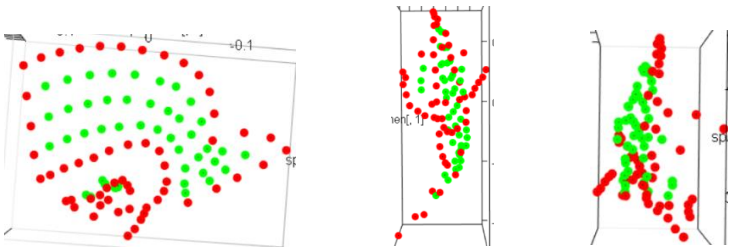

(A)

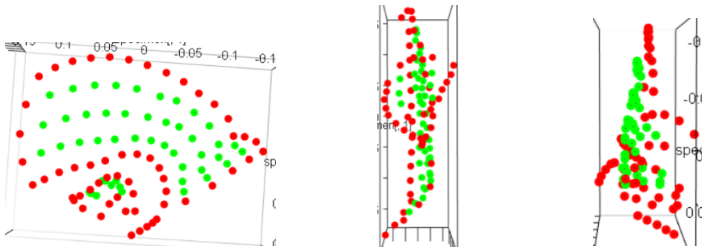

(B)

Figure B.44 Shape changes in PC 4 of the sixth PCA of the temporal region
(A) The shape at the negative end. (B) The shape at the positive end. From left to right: lateral view, inferior view, and posterior view.

B.3.2 Bootstrapped analysis of SSDs

Table B.24 The SSDs of *H. erectus* and its subsets compared to *H. sapiens* (the temporal region)
(A) *H. erectus s. l.* (maximum-semilandmark set). (B) *H. erectus s. l.* (maximum-specimen set. (C) *H. ergaster* (no D2700) (maximum-semilandmark set). (D) *H. ergaster* (no D2700) (maximum-specimen set. (E) *H. ergaster* (with D2700) (maximum-semilandmark set). (F) *H. ergaster* (with D2700) (maximum-specimen set. (G) African *H. erectus* (maximum-specimen set). (H) Asian *H. erectus* (maximum-semilandmark set). (I) Asian *H. erectus* (maximum-specimen set).

(A)

	Average SSD	25th percentile	50th percentiles	75th percentiles	90th percentiles	95th percentiles
Homo sapiens	3.804	3.591	3.775	4.004	4.215	4.336
Homo erectus s. l. (SSD)	4.321					

(B)

	Average SSD	25th percentile	50th percentiles	75th percentiles	90th percentiles	95th percentiles
Homo sapiens	7.595	7.260	7.573	7.913	8.22	8.394
Homo erectus s. l. (SSD)	8.288					

(C)

	Average SSD	25th percentile	50th percentiles	75th percentiles	90th percentiles	95th percentiles
Homo sapiens	0.409	0.367	0.402	0.441	0.496	0.532
H. ergaster without D2700 (SSD)	0.512					

(D)

	Average SSD	25th percentile	50th percentiles	75th percentiles	90th percentiles	95th percentiles
Homo sapiens	0.414	0.370	0.405	0.449	0.506	0.536
H. ergaster without D2700 (SSD)	0.503					

(E)

	Average SSD	25th percentile	50th percentiles	75th percentiles	90th percentiles	95th percentiles
Homo sapiens	0.814	0.744	0.800	0.873	0.958	1.008
H. ergaster with D2700 (SSD)	0.999					

(F)

	Average SSD	25th percentile	50th percentiles	75th percentiles	90th percentiles	95th percentiles
Homo sapiens	0.829	0.757	0.817	0.890	0.974	1.020
H. ergaster with D2700 (SSD)	0.987					

(G)

	Average SSD	25th percentile	50th percentiles	75th percentiles	90th percentiles	95th percentiles
Homo sapiens	0.830	0.756	0.818	0.894	0.977	1.023
African *H. erectus* (with OH 9)	0.927					

(H)

	Average SSD	25th percentile	50th percentiles	75th percentiles	90th percentiles	95th percentiles
Homo sapiens	0.818	0.748	0.805	0.876	0.963	1.013
Asian *H. erectus*	0.898					

(I)

	Average SSD	25th percentile	50th percentiles	75th percentiles	90th percentiles	95th percentiles
Homo sapiens	2.075	1.933	2.059	2.208	2.347	2.425
Asian *H. erectus*	2.183					

B.3.3 Bootstrapped analysis of mean pairwise distances

Table B.25 The mean pairwise distance of *H. erectus* subsets compared to *H. sapiens* (the temporal region) (A) *H. erectus s. l.* (maximum-semilandmark set). (B) *H. erectus s. l.* (maximum-specimen set. (C) *H. ergaster* (no D2700) (maximum-semilandmark set). (D) *H. ergaster* (no D2700) (maximum-specimen set. (E) *H. ergaster* (with D2700) (maximum-semilandmark set). (F) *H. ergaster* (with D2700) (maximum-specimen set. (G) African *H. erectus* (maximum-specimen set). (H) Asian *H. erectus* (maximum-semilandmark set). (I) Asian *H. erectus* (maximum-specimen set).

(A)

	Mean pairwise distance	25th percentile	50th percentiles	75th percentiles	90th percentiles	95th percentiles
H. sapiens	0.136	0.128	0.140	0.143	0.151	0.155
H. erectus s. l.	0.154					

(B)

	Mean pairwise distance	25th percentile	50th percentiles	75th percentiles	90th percentiles	95th percentiles
H. sapiens	0.138	0.132	0.138	0.144	0.150	0.153
H. erectus s. l.	0.151					

(C)

	Mean within-sample distance	25th percentile	50th percentiles	75th percentiles	90th percentiles	95th percentiles
Homo sapiens	0.136	0.122	0.133	0.147	0.164	0.177
H. ergaster (no D2700)	0.171					

(D)

	Mean within-sample distance	25th percentile	50th percentiles	75th percentiles	90th percentiles	95th percentiles
Homo sapiens	0.139	0.124	0.136	0.158	0.168	0.180
H. ergaster (no D2700)	0.168					

(E)

	Mean within-sample distance	25th percentile	50th percentiles	75th percentiles	90th percentiles	95th percentiles
H. sapiens	0.136	0.124	0.134	0.146	0.160	0.169
H. ergaster (with D2700)	0.167					

(F)

	Mean within-sample distance	25th percentile	50th percentiles	75th percentiles	90th percentiles	95th percentiles
H. sapiens	0.138	0.126	0.136	0.148	0.163	0.170
H. ergaster (with D2700)	0.165					

(G)

	Mean within-sample distance	25th percentile	50th percentiles	75th percentiles	90th percentiles	95th percentiles
H. sapiens	0.136	0.126	0.136	0.148	0.162	0.170
African *H. erectus* (with OH 9)	0.155					

(H)

	Mean pairwise distance (sample size 4)	25th percentile	50th percentiles	75th percentiles	90th percentiles	95th percentiles
H. sapiens	0.0818	0.0738	0.0810	0.0887	0.0966	0.101
Asian *H. erectus*	0.0767					

(I)

	Mean pairwise distance (sample size 4)	25th percentile	50th percentiles	75th percentiles	90th percentiles	95th percentiles
H. sapiens	0.138	0.127	0.137	0.146	0.156	0.162
Asian *H. erectus*	0.146					

B.3.4 Bootstrap analyses of distance between geographical group means

Table B.26 The distances between means of geographical subsets (the temporal region)
(A) *H. ergaster* (no D2700) vs. Asian *H. erectus* (maximum-semilandmark set). (B) *H. ergaster* (no D2700) vs. Asian *H. erectus* (maximum-specimen set) (C) *H. ergaster* (with D2700) vs. Asian *H. erectus* (maximum-semilandmark set). (D) *H. ergaster* (with D2700) vs. Asian *H. erectus* (maximum-specimen set); African *H. erectus* (with OH 9) vs. Asian *H. erectus* (maximum-specimen set).

(A)

	Mean pairwise distance	25 percentiles	50 percentiles	75 percentiles	90 percentiles	95 percentiles
Homo sapiens	0.0797	0.0717	0.0788	0.0869	0.0950	0.101
H. ergaster (no D2700) vs. *H. erectus*	0.0672					

(B)

	Mean pairwise distance	25 percentiles	50 percentiles	75 percentiles	90 percentiles	95 percentiles
Homo sapiens	0.0765	0.0689	0.0756	0.0830	0.0910	0.0967
H. ergaster (no D 2700) vs. Asian *H. erectus*	0.0744					

(C)

	Mean pairwise distance	25 percentiles	50 percentiles	75 percentiles	90 percentiles	95 percentiles
Homo sapiens	0.0754	0.0674	0.0746	0.0821	0.0900	0.0954
H. ergaster (with D 2700) vs. Asian *H. erectus*	0.0625					

(D)

	Mean pairwise distance	25 percentiles	50 percentiles	75 percentiles	90 percentiles	95 percentiles
Homo sapiens	0.0717	0.0647	0.0711	0.0778	0.0848	0.0897
H. ergaster (with D 2700) vs. Asian *H. erectus*	0.0691					
African (with OH 9) vs. Asian *H. erectus*	0.0700					

B.4 THE FRONTAL REGION

B.4.1 PCA

B.4.1.1 The first PCA

Table B.27 The size-shape relationship of the first seven PCs in the first PCA (the frontal region)

	Sample size	R square	F value	p-value
PC1 vs. centroid size	17	0.01727	0.2636	0.6143
PC 2 vs. centroid size	17	0.02641	0.4069	0.5293
PC 3 vs. centroid size	17	0.6704	30.51	0.0004
PC 4 vs. centroid size	17	0.001510	0.02268	0.8746
PC 5 vs. centroid size	17	0.00862	0.1305	0.7205
PC 6 vs. centroid size	17	0.0903	1.488	0.2459
PC 7 vs. centroid size	17	0.0109	0.1654	0.6839

B.4.1.2 The second PCA

Table B.28 The size-shape relationship of the first seven PCs in the second PCA (the frontal region)

	Sample size	R square	F value	p-value
PC1 vs. centroid size	52	0.00126	0.06337	0.8031
PC 2 vs. centroid size	52	0.0107	0.5426	0.4667
PC 3 vs. centroid size	52	0.4318	37.99	0.0004
PC 4 vs. centroid size	52	0.0249	1.28	0.2619
PC 5 vs. centroid size	52	0.00654	0.3291	0.5771
PC 6 vs. centroid size	52	0.02452	1.257	0.269
PC 7 vs. centroid size	52	0.0903	4.691	0.0328

B.4.1.3 The third PCA

Table B.29 The size-shape relationship of the first seven PCs in the third PCA (the frontal region)

	Sample size	R square	F value	p-value
PC1 vs. centroid size	25	0.0009083	0.2072	0.654
PC 2 vs. centroid size	25	0.0109	0.2531	0.6242
PC 3 vs. centroid size	25	0.344	12.06	0.0023
PC 4 vs. centroid size	25	0.249	7.637	0.0113
PC 5 vs. centroid size	25	0.0271	0.6404	0.4253
PC 6 vs. centroid size	25	0.119	3.091	0.0912
PC 7 vs. centroid size	25	0.0273	0.6458	0.04333

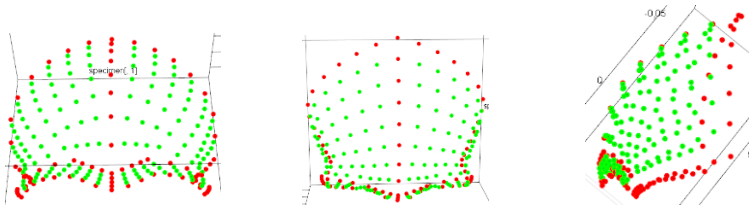

(A)

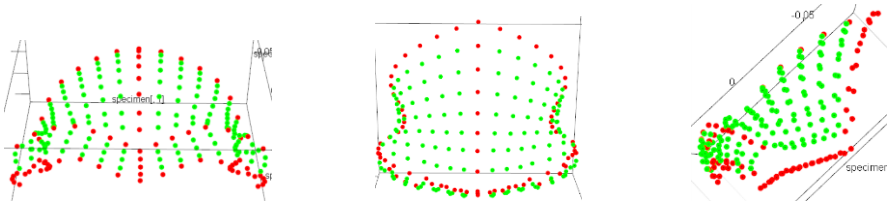

(B)

Figure B.45 Shape changes in PC 1 of the third PCA of the frontal region
(A) The shape at the negative end. (B) The shape at the positive end. From left to right: anterior view, superior view, and lateral view.

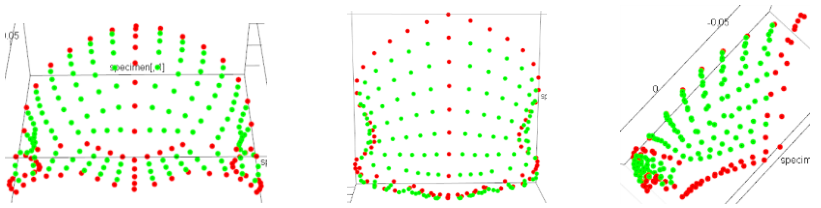

(A)

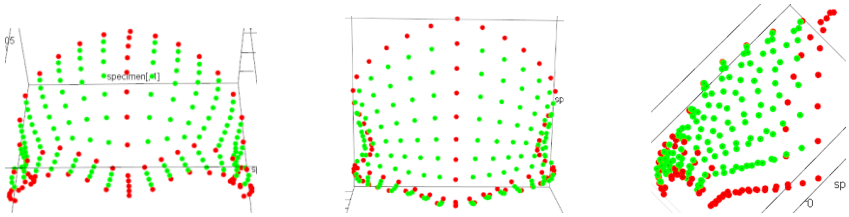

(B)

Figure B.46 Shape changes in PC 2 of the third PCA of the frontal region
(A) The shape at the negative end. (B) The shape at the positive end. From left to right: anterior view, superior view, and lateral view.

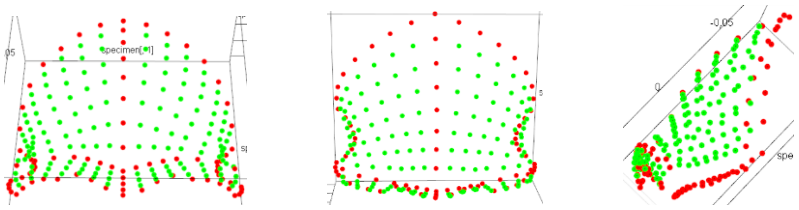

(A)

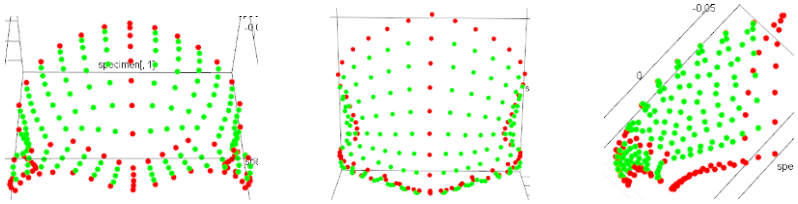

(B)

Figure B.47 Shape changes in PC 3 of the third PCA of the frontal region
(A) The shape at the negative end. (B) The shape at the positive end. From left to right: anterior view, superior view, and lateral view.

B.4.2 Bootstrapped analyses of SSDs

Table B.30 The SSDs of *H. erectus* and its subsets compared to *H. sapiens* (the frontal region)
(A) *H. erectus s. l.* (B) *H. ergaster* (with D2700). (C) African *H. erectus* (with D2700). (D) Asian *H. erectus* (maximum-specimen set).

(A)

	Average SSD	25th percentile	50th percentiles	75th percentiles	90th percentiles	95th percentiles
Homo sapiens	3.483	3.336	3.475	3.626	3.767	3.849
Homo erectus s. l. (SSD)	3.343					

(B)

	Average SSD	25th percentile	50th percentiles	75th percentiles	90th percentiles	95th percentiles
Homo sapiens	0.232	0.208	0.229	0.253	0.277	0.294
H. ergaster with D2700 (SSD)	0.323					

(C)

	Average SSD	25th percentile	50th percentiles	75th percentiles	90th percentiles	95th percentiles
Homo sapiens	0.232	0.208	0.229	0.253	0.277	0.294
African H. erectus with OH 9	0.332					

(D)

	Average SSD	25th percentile	50th percentiles	75th percentiles	90th percentiles	95th percentiles
Homo sapiens	1.160	1.089	1.155	1.225	1.296	1.339
Asian H. erectus	1.192					

B.4.3 Bootstrapped analysis of mean pairwise Procrustes distances

Table B.31 The mean pairwise distances of *H. erectus* subsets compared to *H. sapiens* (the frontal region)
(A) *H. erectus s. l.* (B) *H. ergaster* (no D2700). (C) *H. ergaster* (with D2700). (D) African *H. erectus* (with D2700). (E) Asian *H. erectus* (maximum-specimen set).

(A)

	Mean pairwise distance	25^{th} percentile	50^{th} percentiles	75^{th} percentiles	90^{th} percentiles	95^{th} percentiles
H. sapiens	0.0774	0.0740	0.0772	0.0806	0.0837	0.0854
H. erectus s. l.	0.0965					

(B)

	Average SSD	25^{th} percentile	50^{th} percentiles	75^{th} percentiles	90^{th} percentiles	95^{th} percentiles
Homo sapiens	0.0774	0.0662	0.0756	0.0878	0.0980	0.105
ER 3733 vs. ER 3883	0.119					

(C)

	Mean pairwise distance (sample size 4)	25th percentile	50th percentiles	75th percentiles	90th percentiles	95th percentiles
H. sapiens	0.0777	0.0697	0.0767	0.0849	0.0920	0.979
H. ergaster (with D2700)	0.108					

(D)

	Mean pairwise distance (sample size 4)	25th percentile	50th percentiles	75th percentiles	90th percentiles	95th percentiles
H. sapiens	0.0774	0.0694	0.0765	0.0843	0.0918	0.0973
African *H. erectus*	0.111					

(E)

	Mean pairwise distance	25th percentile	50th percentiles	75th percentiles	90th percentiles	95th percentiles
H. sapiens	0.0774	0.0726	0.0771	0.0817	0.0864	0.0894
Asian *H. erectus*	0.0795					

B.4.4 The bootstrapped analyses of distances between geographic group means

Table B.32 The distances between means of geographical subsets (the frontal region)
(A) *H. ergaster* (no D2700) vs. Asian *H. erectus* (maximum-semilandmark set). (B) *H. ergaster* (with D2700) vs. Asian *H. erectus* (maximum-specimen set); African *H. erectus* (with OH 9) vs. Asian *H. erectus* (maximum-specimen set).

(A)

	Mean pairwise distance	25 percentiles	50 percentiles	75 percentiles	90 percentiles	95 percentiles
Homo sapiens	0.0545	0.0473	0.0542	0.0615	0.0682	0.0721
H. ergaster (no D2700) vs. *H. erectus*	0.0699					

(B)

	Mean pairwise distance	25 percentiles	50 percentiles	75 percentiles	90 percentiles	95 percentiles
Homo sapiens	0.0506	0.0432	0.0503	0.0565	0.0618	0.0647
H. ergaster (with D 2700) vs. Asian *H. erectus*	0.0651					
African (with OH 9) vs. Asian *H. erectus*	0.0700					

B.4.5 The 45-anchor point set

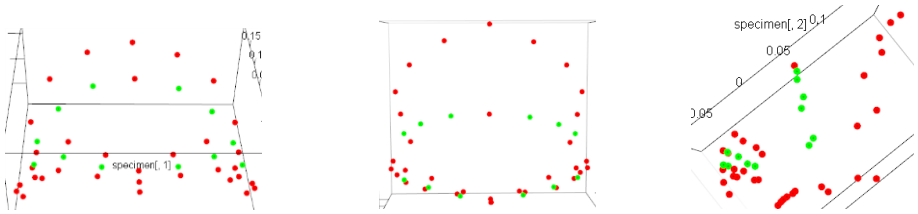

(A)

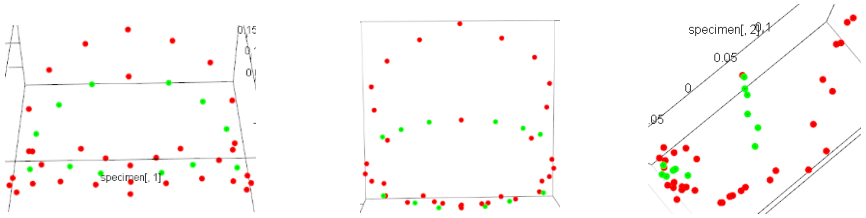

(B)

Figure B.48 PC 1 of the fossil sample (discrete landmarks of the frontal region)
(A) The shape at the negative end. (B) The shape at the positive end. From left to right: anterior view, superior view, and lateral view.

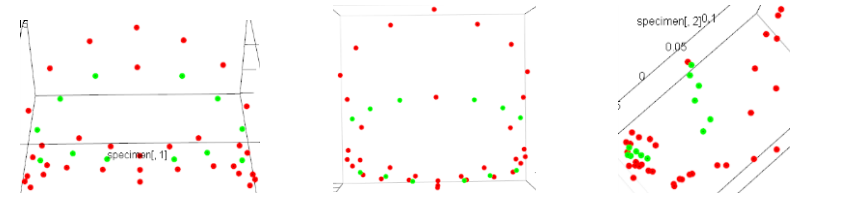

(A)

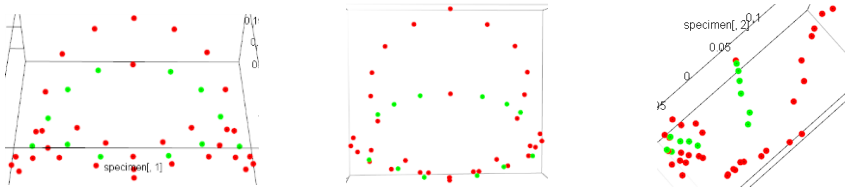

(B)

Figure B.49 PC 2 of the fossil sample (discrete landmarks of the frontal region)
(A) The shape at the negative end. (B) The shape at the positive end. From left to right: anterior view, superior view, and lateral view.

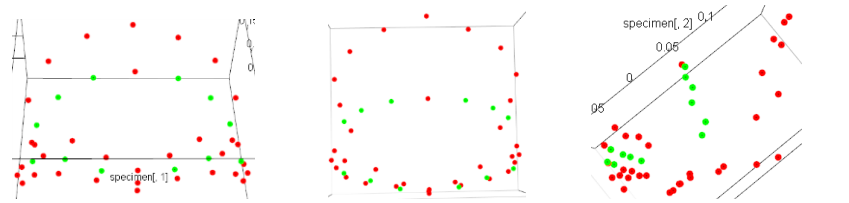

(A)

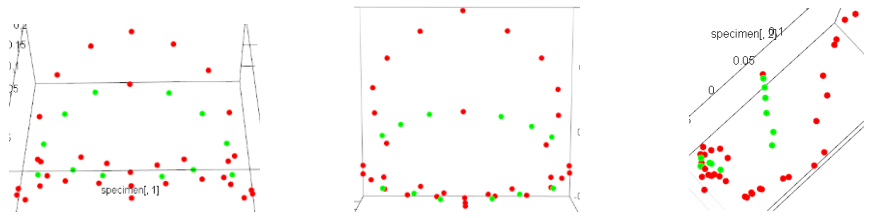

(B)

Figure B.50 PC 3 of the fossil sample (discrete landmarks of the frontal region)
(A) The shape at the negative end. (B) The shape at the positive end. From left to right: anterior view, superior view, and lateral view.

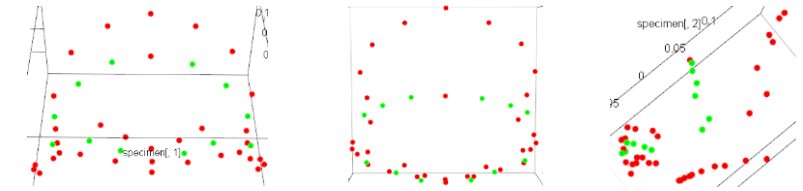

(A)

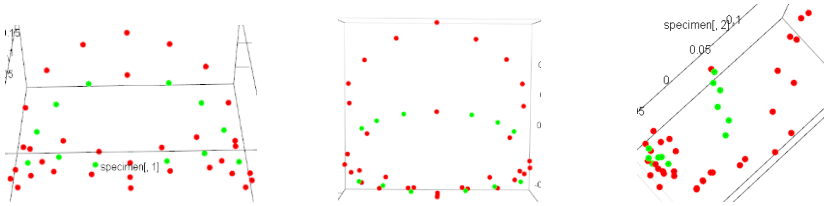

(B)

Figure B.51 PC 4 of the fossil sample (discrete landmarks of the frontal region)
(A) The shape at the negative end. (B) The shape at the positive end. From left to right: anterior view, superior view, and lateral view.

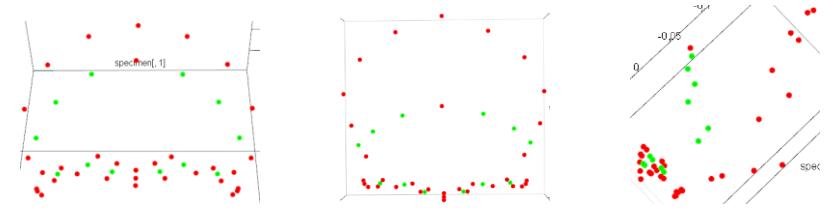

(A)

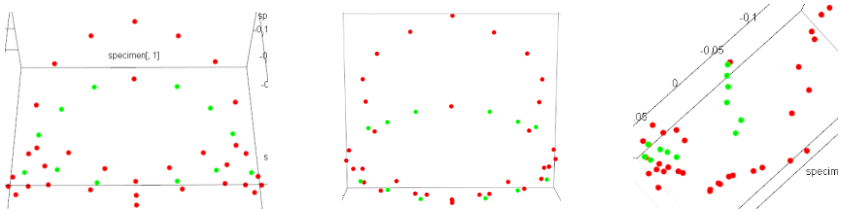

(B)

Figure B.52 PC 1 of fossils and *H. sapiens* (discrete landmarks of the frontal region)
(A) The shape at the negative end. (B) The shape at the positive end. From left to right: anterior view, superior view, and lateral view.

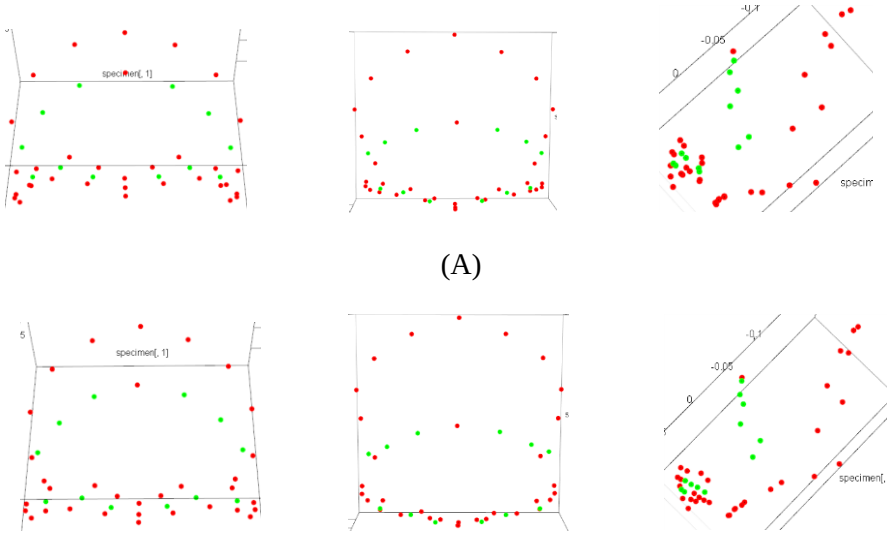

Figure B.53 PC 4 of fossils and *H. sapiens* (discrete landmarks of the frontal region)
(A) The shape at the negative end. (B) The shape at the positive end. From left to right: anterior view, superior view, and lateral view.

BIBLIOGRAPHY

Ackermann, R. R. (2002). Patterns of covariation in the hominoid craniofacial skeleton: implications for paleoanthropological models. *Journal of Human Evolution, 43*(2), 167-187.

Adams, D. C., Cardini, A., Monteiro, L., O'higgins, P., & Rohlf, F. J. (2011). Morphometrics and phylogenetics: principal components of shape from cranial modules are neither appropriate nor effective cladistic characters. *Journal of Human Evolution, 60*(2), 240-243.

Adams, D. C., Collyer, M. L., & Kaliontzopoulou, A. (2018). Geomorph: Software for geometric morphometric analyses (Version 3.0.6). Retrieved from https://cran.r-project.org/package=geomorph

Adams, D. C., Rohlf, F. J., & Slice, D. E. (2004). Geometric morphometrics: ten years of progress following the 'revolution'. *Italian Journal of Zoology, 71*(1), 5-16.

Adams, D. C., Rohlf, F. J., & Slice, D. E. (2013). A field comes of age: geometric morphometrics in the 21st century. *Hystrix, 24*(1), 7.

Aigner, J. S., & Laughlin, W. S. (1973). The dating of Lantian man and his significance for analyzing trends in human evolution. *American Journal of Physical Anthropology, 39*(1), 97-109.

Alpaydın, E. (2010). *Introduction to machine learning* (2 ed.). Cambridge, Massachusetts: The MIT Press.

Andrews, P. (1984). On the characters that define *Homo Erectus*. In P. Andrews & J. L. Franzen (Eds.), *The Early Evolution of Man: With Special Empahsis on Southeast Asia and Africa* (Vol. 69, pp. 167-178). Frankfurt am Main: Senckenbergischen Naturforschenden Gesellschaft.

Antón, S. C. (2002). Evolutionary significance of cranial variation in Asian *Homo erectus*. *American Journal of Physical Anthropology, 118*(4), 301-323.

Antón, S. C. (2003). Natural history of *Homo erectus*. *American Journal of Physical Anthropology, 122*(S37), 126-170.

Arif, J., Kaifu, Y., Baba, H., Suparka, M. E., Zaim, Y., & Setoguchi, T. (2002). Preliminary observation of a new cranium of *Homo erectus* (Tjg-1993.05) from Sangiran, Central Jawa. *Anthropological Science, 110*(2), 165-177.

Artec 3D Inc. (2018). Artec Studio (Version 13). Luxembourg: Artec 3D Inc.

Asfaw, B. (2008). *Homo erectus* cranial anatomy. In B. Asfaw & W. H. Gilbert (Eds.), *Homo erectus: Pleistocene Evidence from the Middle Awash, Ethiopia* (pp. 265-327). Berkeley and Los Angeles: University of California Press.

Ashton, E. H., Healy, M. J. R., & Lipton, S. (1957). The descriptive use of discriminant functions in physical anthropology. *Proceedings of the Royal Society of London. Series B-Biological Sciences, 146*(925), 552-572.

Baab, K. L. (2008a). A re-evaluation of the taxonomic affinities of the early *Homo* cranium KNM-ER 42700. *Journal of Human Evolution, 55*(4), 741.

Baab, K. L. (2008b). The taxonomic implications of cranial shape variation in *Homo erectus*. *Journal of Human Evolution, 54*(6), 827-847.

Baab, K. L. (2016). The role of neurocranial shape in defining the boundaries of an expanded *Homo erectus* hypodigm. *Journal of Human Evolution, 92*, 1-21.

Baab, K. L., McNulty, K. P., & Rohlf, F. J. (2012). The shape of human evolution: a geometric morphometrics perspective. *Evolutionary Anthropology: Issues, News, and Reviews, 21*(4), 151-165.

Baba, H., Aziz, F., Kaifu, Y., Suwa, G., Kono, R. T., & Jacob, T. (2003). *Homo erectus* calvarium from the Pleistocene of Java. *Science, 299*(5611), 1384-1388.

Bäckström, K., Nazari, M., Gu, I. Y.-H., & Jakola, A. S. (2018). *An efficient 3D deep convolutional network for Alzheimer's disease diagnosis using MR images.* Paper presented at the 2018 IEEE 15th International Symposium on Biomedical Imaging (ISBI 2018).

Bae, C. J. (2010). The late Middle Pleistocene hominin fossil record of eastern Asia: synthesis and review. *American Journal of Physical Anthropology, 143*(S51), 75-93.

Bilsborough, A. (1971). Evolutionary change in the hominoid maxilla. *Man, 6*(3), 473-485.

Bilsborough, A. (1973). A multivariate study of evolutionary change in the hominid cranial vault and some evolution rates. *Journal of Human Evolution, 2*(5), 387-403.

Bilsborough, A. (1984). Multivariate analysis and cranial diversity in Plio-Pleistocene hominids. In G. N. van Vark & W. W. Howells (Eds.), *Multivariate Statistical Methods in Physical Anthropology* (pp. 351-375). Dordrecht: D. Reidel Publishing Company.

Bilsborough, A., & Wood, B. (1988). Cranial morphometry of early hominids: facial region. *American Journal of Physical Anthropology, 76*(1), 61-86.

Black, D. (1927). On a lower molar hominid tooth from the Chou Kou Tien Deposit. *Palaeontologia Sinica, VII*, 1-28.

Blackith, R. E. (1957). Polymorphism in some Australian locusts and grasshoppers. *Biometrics, 13*(2), 183-196.

Blackith, R. E., & Reyment, R. A. (1971). *Multivariate morphometrics*. London and New York: Academic Press.

Bookstein, F. L. (1997). *Morphometric tools for landmark data: geometry and biology*: Cambridge University Press.

Bookstein, F. L. (1998). A hundred years of morphometrics. *Acta Zoologica Academiae Scientiarum Hungaricae, 44*(1-2), 7-59.

Bräuer, G. (1990). The occurrence of some controversial *Homo erectus* cranial features in the Zhoukoudian and East African hominids. *Acta Anthropologica Sinica, 9*, 352-358.

Bräuer, G. (1994). How different are Asian and African *Homo erectus*. In J. L. Franzen (Ed.), *100 years of Pithecanthropus: the Homo erectus problem* (Vol. 171, pp. 159-165). Frankfurt am Main: Senckenbergischen Naturforschenden Gesellschaft.

Bräuer, G., & Mbua, E. (1992). *Homo erectus* features used in cladistics and their variability in Asian and African hominids. *Journal of Human Evolution, 22*(2), 79-108.

Bronowski, J., & Long, W. (1952). Statistics of discrimination in anthropology. *American Journal of Physical Anthropology, 10*(4), 385-394.

Campbell, B. (1963). Quantitative taxonomy and human evolution. In S. L. Washburn (Ed.), *Classification and human evolution* (pp. 50-74). Chicago: Aldine Publishing Company.

Campbell, N. A., & Atchley, W. R. (1981). The geometry of canonical variate analysis. *Systematic Biology, 30*(3), 268-280.

Cartmill, M., & Smith, F. H. (2009). *The human lineage*. Hoboken, New Jersey: John Wiley & Sons.

Cignoni, P., Callieri, M., Corsini, M., Dellepiane, M., Ganovelli, F., & Ranzuglia, G. (2008). *Meshlab: an open-source mesh processing tool.* Paper presented at the Eurographics Italian chapter conference.

Clark, W. E. L. G. (1940). The relationship between *Pithecanthropus* and *Sinanthropus*. *Nature, 145*(3663), 70.

Clark, W. E. L. G. (1957). *The fossil evidence for human evolution: An introduction to the study of paleoanthropology*. Chicago: University of Chicago Press.

Clark, W. E. L. G. (1964). *The fossil evidence for human evolution: An introduction to the study of paleoanthropology* (2 ed.). Chicago: University of Chicago Press.

Collyer, M. L., Sekora, D. J., & Adams, D. C. (2015). A method for analysis of phenotypic change for phenotypes described by high-dimensional data. *Heredity, 115*(4), 357.

Corruccini, R. S. (1975). Multivariate analysis in biological anthropology: some considerations. *Journal of Human Evolution, 4*(1), 1-19.

Cranston, P. S., & Humphries, C. J. (1988). Cladistics and computers: a chironomid conundrum? *Cladistics, 4*(1), 72-92.

Delson, E., Eldredge, N., & Tattersall, I. (1977). Reconstruction of hominid phylogeny: a testable framework based on cladistic analysis. *Journal of Human Evolution, 6*(3), 263-278.

Delson, E., Harvati, K., Reddy, D., Marcus, L. F., Mowbray, K., Sawyer, G., . . . Márquez, S. (2001). The Sambungmacan 3 *Homo erectus* calvaria: a comparative morphometric and morphological analysis. *The Anatomical Record: An Official Publication of the American Association of Anatomists, 262*(4), 380-397.

Dubois, E. (1892). Paleontological Investigations on Java. In M. E. Meikle & S. T. Parker (Eds.), *Naming our ancestors* (pp. 37-40). Prospect Heights, Illinois: Waveland Press. Inc.

Dubois, E. (1896). The Place of "*Pithecanthropus*" in the Genealogical Tree. *Nature, 53*, 245-246.

Dubois, E. (1898). *Pithecanthropus erectus* - a form from the ancestral stock of Mankind. In L. S. B. Leakey, J. Prost, & S. Prost (Eds.), *Adam, or ape: A sourcebook of discoveries about early man* (pp. 165-175). Cambridge, Massachusetts, U.S.A. and London, England: Schenkman Publishing Company.

Durband, A. C. (2008). The enigma of the Sangiran 4 palate revisited. *Homo, 59*(2), 111-122.

Ellen, J., Li, H., & Ohman, M. D. (2015). *Quantifying California current plankton samples with efficient machine learning techniques.* Paper presented at the OCEANS 2015-MTS/IEEE Washington.

Etler, D. A. (1996). The fossil evidence for human evolution in Asia. *Annual Review of Anthropology, 25*(1), 275-301.

Fisher, R. A. (1936). The use of multiple measurements in taxonomic problems. *Annals of Eugenics, 7*(2), 179-188.

Fisher, R. A. (1938). The statistical utilization of multiple measurements. *Annals of eugenics, 8*(4), 376-386.

Freidline, S. E., Gunz, P., Harvati, K., & Hublin, J.-J. (2012). Middle Pleistocene human facial morphology in an evolutionary and developmental context. *Journal of Human Evolution, 63*(5), 723-740.

Freidline, S. E., Gunz, P., Janković, I., Harvati, K., & Hublin, J.-J. (2012). A comprehensive morphometric analysis of the frontal and zygomatic bone of the Zuttiyeh fossil from Israel. *Journal of Human Evolution, 62*(2), 225-241.

Frossard, J., & Renaud, O. (2019). R package permuco (Version 1.0.2). Retrieved from https://cran.r-project.org/package=permuco

Gabunia, L., Vekua, A., Lordkipanidze, D., Swisher, C. C., Ferring, R., Justus, A., . . . Bosinski, G. (2000). Earliest Pleistocene hominid cranial remains from Dmanisi, Republic of Georgia: taxonomy, geological setting, and age. *Science, 288*(5468), 1019-1025.

Geomagic Inc. (2015). Geomagic Studio (Version 2015). Morrisville, North Carolina: Geomagic, Inc.

Gilbert, W. H. (2008). Hominid systematics. In B. Asfaw & W. H. Gilbert (Eds.), *Homo erectus: Pleistocene Evidence from the Middle Awash, Ethiopia* (pp. 349-372). Berkeley and Los Angeles: University of California Press.

Godfrey, L., & Marks, J. (1991). The nature and origins of primate species. *American Journal of Physical Anthropology, 34*(S13), 39-68.

Gómez-Robles, A., Olejniczak, A. J., Martinón-Torres, M., Prado-Simón, L., & Bermúdez de Castro, J. M. (2011). Evolutionary novelties and losses in geometric morphometrics: a practical approach through hominin molar morphology. *Evolution: International Journal of Organic Evolution, 65*(6), 1772-1790.

González-José, R., Escapa, I., Neves, W. A., Cúneo, R., & Pucciarelli, H. M. (2008). Cladistic analysis of continuous modularized traits provides phylogenetic signals in Homo evolution. *Nature, 453*(7196), 775.

González-José, R., Escapa, I., Neves, W. A., Cúneo, R., & Pucciarelli, H. M. (2011). Morphometric variables can be analyzed using cladistic methods: A reply to Adams et al. *Journal of Human Evolution, 60*(2), 244-245.

Goodall, C. (1991). Procrustes methods in the statistical analysis of shape. *Journal of the Royal Statistical Society: Series B (Methodological), 53*(2), 285-321.

Grine, F. E., Jungers, W., & Schultz, J. (1996). Phenetic affinities among earlyHomocrania from East and South Africa. *Journal of Human Evolution, 30*(3), 189-225.

Groves, C. P., & Mazak, V. (1975). An approach to the taxonomy of the hominidae: gracile villafranchian hominids of Africa. *Casopis pro Mineralogii a Geologii, 20*(3), 225-247.

Gunz, P., & Mitteroecker, P. (2013). Semilandmarks: a method for quantifying curves and surfaces. *Hystrix, the Italian Journal of Mammalogy, 24*(1), 103-109.

Harcourt-Smith, W. E. H. (2003). *Form and function in the hominoid tarsal skeleton.* (Doctor of Philosophy). University College London, London.

Harrison, T. (1993). Cladistic concepts and the species problem in hominoid evolution. In W. H. Kimbel & L. B. Martin (Eds.), *Species, species concepts and primate evolution* (pp. 345-371). New York: Plenum Press.

Harvati, K., Hublin, J.-J., & Gunz, P. (2010). Evolution of middle-late Pleistocene human cranio-facial form: A 3-D approach. *Journal of Human Evolution, 59*(5), 445-464.

Hennig, W. (1966). *Phylogenetic systematics*. Urbana: University of Illinois Press.

Hesterberg, T., Monaghan, S., Moore, D. S., Clipson, A., & Epstein, R. (2003). *Bootstrap methods and permutation tests: Companion chapter 18 to the practice of business statistics*. New York: W. H. Freeman and Company.

Howells, W. W. (1969). The use of multivariate techniques in the study of skeletal populations. *American Journal of Physical Anthropology, 31*(3), 311-314.

Howells, W. W. (1972). Analysis of patterns of variation in crania of recent man. In R. H. Tuttle (Ed.), *The functional and evolutionary biology of primates* (pp. 123-151). Chicago: Aldine-Atherton.

Howells, W. W. (1973). *Cranial variation in man: a study by multivariate analysis of patterns of difference among recent human populations*. Cambridge: Harvard University.

Howells, W. W. (1976). *Homo erectus* in human descent: ideas and problems. In B. A. Sigmon & J. S. Cybulski (Eds.), *Homo erectus: Papers in Honor of Davidson Black* (pp. 63-86). Toronto: University of Toronto Press.

Howells, W. W. (1980). *Homo erectus*—who, when and where: a survey. *American Journal of Physical Anthropology, 23*(S1), 1-23.

Howells, W. W. (1984). Introduction. In G. N. van Vark & W. W. Howells (Eds.), *Multivariate statistical methods in physical anthropology: a review of recent advances and current developments* (pp. 1-11). Dordrecht: D. Reidel Publishing Company.

Hublin, J. J. (1986). Some comments on the diagnostic features of Homo erectus. *Anthropos (Brno), 23*, 175-187.

Humphries, C. J. (2002). Homology, characters and continuous variables. In N. MacLeod & P. L. Forey (Eds.), *Morphology, shape and phylogeny* (Vol. 64, pp. 8-26). London: Taylor and Francis Inc.

Jacob, T. (1972). New Hominid Finds in Indonesia and their Affinitics. *The Australian Journal of Anthropology, 8*(3), 176-181.

Jacob, T. (1973). Palaeoanthropological discoveries in Indonesia with special reference to the finds of the last two decades. *Journal of Human Evolution, 2*(6), 473-485.

Kaifu, Y., Aziz, F., & Baba, H. (2005). Hominid mandibular remains from Sangiran: 1952–1986 collection. *American Journal of Physical Anthropology: The Official Publication of the American Association of Physical Anthropologists, 128*(3), 497-519.

Kaifu, Y., Aziz, F., Indriati, E., Jacob, T., Kurniawan, I., & Baba, H. (2008). Cranial morphology of Javanese *Homo erectus*: new evidence for continuous evolution, specialization, and terminal extinction. *Journal of Human Evolution, 55*(4), 551-580.

Kay, R. F. (1982). *Sivapithecus simonsi*, a new species of Miocene hominoid, with comments on the phylogenetic status of the Ramapithecinae. *International Journal of Primatology, 3*(2), 113-173.

Kennedy, G. E. (1991). On the autapomorphic traits of *Homo erectus*. *Journal of Human Evolution, 20*(5), 375-412.

Kesterke, M. J., Sankaranarayanan, G., Sautter, M., Bhattacharya, R., Bhattacharjee, R., Read-Fuller, A., & Reddy, L. V. (2019). *Saving face: the role of artificial intelligence in evaluating craniofacial variation for the treatment of orofacial dysfunction.* Paper presented at the American Journal of Physical Anthropology.

Kim, D., Hernandez, M., Choi, J., & Medioni, G. (2017). *Deep 3D face identification.* Paper presented at the 2017 IEEE International Joint Conference on Biometrics (IJCB).

Kimbel, W. H., & White, T. D. (1988). Variation, sexual dimorphism and the taxonomy of *Australopithecus*. In F. E. Grine (Ed.), *Evolutionary History of the ''Robust''Australopithecines* (pp. 175-192). New York: Aldine de Gruyter.

Klingenberg, C. P. (2013). Visualizations in geometric morphometrics: how to read and how to make graphs showing shape changes. *Hystrix, the Italian Journal of Mammalogy, 24*(1), 15-24.

Klingenberg, C. P. (2015). Analyzing fluctuating asymmetry with geometric morphometrics: concepts, methods, and applications. *Symmetry, 7*(2), 843-934.

Klingenberg, C. P. (2016). Size, shape, and form: concepts of allometry in geometric morphometrics. *Development genes and evolution, 226*(3), 113-137.

Kowalski, C. J. (1972). A commentary on the use of multivariate statistical methods in anthropometric research. *American Journal of Physical Anthropology, 36*(1), 119-131.

Kramer, A. (1993). Human taxonomic diversity in the Pleistocene: Does *Homo erectus* represent multiple hominid species? *American Journal of Physical Anthropology, 91*(2), 161-171.

Kramer, A., Donnelly, S. M., Kidder, J. H., Ousley, S. D., & Olah, S. M. (1995). Craniometric variation in large-bodied hominoids: testing the single-species hypothesis for *Homo habilis*. *Journal of Human Evolution, 29*(5), 443-462.

Krantz, G. S. (1975). An explanation for the diastema of Javan erectus Skull IV. In R. H. Tuttle (Ed.), *Paleoanthropology, Morphology and Paleoecology* (pp. 361-372). Paris: Mouton Publisher.

Krantz, G. S. (1994). The palate of skull Sangiran 4 from Java. In J. L. Franzen (Ed.), *100 years of Pithecanthropus: The Homo erectus problem* (Vol. 171, pp. 69-74). Frankfurt am Main: Senckenbergischen Naturforschenden Gesellschaft.

Leakey, L. S. B. (1961). New finds at Olduvai gorge. *Nature, 189*(4765), 649.

Leakey, M. G., & Leakey, R. E. (1978). *Koobi Fora research project* (Vol. 1). Oxford: Clarendon Press.

Leakey, R. E., & Walker, A. C. (1976). *Australopithecus, Homo erectus* and the single species hypothesis. *Nature, 261*(5561), 572.

Lele, S. R., & Richtsmeier, J. T. (2001). *An invariant approach to statistical analysis of shapes*: Chapman and Hall/CRC.

Li, T., & Etler, D. A. (1992). New middle Pleistocene hominid crania from Yunxian in China. *Nature, 357*(6377), 404.

Lieberman, D. E., Pilbeam, D. R., & Wood, B. (1988). A probabilistic approach to the problem of sexual dimorphism in *Homo habilis*: a comparison of KNM-ER 1470 and KNM-ER 1813. *Journal of Human Evolution, 17*(5), 503-511.

Lieberman, D. E., Wood, B., & Pilbeam, D. R. (1996). Homoplasy and early *Homo*: an analysis of the evolutionary relationships of *H. habilis sensu stricto* and *H. rudolfensis*. *Journal of Human Evolution, 30*(2), 97-120.

Liu, W., Zhang, Y., & Wu, X. (2005). Middle Pleistocene human cranium from Tangshan (Nanjing), Southeast China: a new reconstruction and comparisons with *Homo erectus* from Eurasia and Africa. *American Journal of Physical Anthropology: The Official Publication of the American Association of Physical Anthropologists, 127*(3), 253-262.

Lockwood, C. A., Lynch, J. M., & Kimbel, W. H. (2002). Quantifying temporal bone morphology of great apes and humans: an approach using geometric morphometrics. *Journal of Anatomy, 201*(6), 447-464.

Lockwood, C. A., Richmond, B. G., Jungers, W. L., & Kimbel, W. H. (1996). Randomization procedures and sexual dimorphism in *Australopithecus afarensis*. *Journal of Human Evolution, 31*(6), 537-548.

Lordkipanidze, D., de León, M. S. P., Margvelashvili, A., Rak, Y., Rightmire, G. P., Vekua, A., & Zollikofer, C. P. (2013). A complete skull from Dmanisi, Georgia, and the evolutionary biology of early *Homo*. *Science, 342*(6156), 326-331.

Lordkipanidze, D., Vekua, A., Ferring, R., Rightmire, G. P., Zollikofer, C. P., Ponce de León, M. S., . . . Nioradze, M. (2006). A fourth hominin skull from Dmanisi, Georgia. *The Anatomical Record Part A: Discoveries in Molecular, Cellular, and Evolutionary Biology: An Official Publication of the American Association of Anatomists, 288*(11), 1146-1157.

Macintosh, N. W. G., & Larnach, S. L. (1972). The Persistence of" *Homo erectus*" Traits in Australian Aboriginal Crania. *Archaeology & Physical Anthropology in Oceania, 7*(1), 1-7.

MacLeod, N., & Forey, P. L. (2002). Introduction: morphology, shape, and phylogenetics. In N. MacLeod & P. L. Forey (Eds.), *Morphology, shape and phylogeny* (Vol. 64, pp. 1-7). London: Taylor and Francis Inc.

MacLeod, N., O'Neill, M., & Walsh, S. A. (2016). A Comparison between. Morphometric. and. Artificial. Neural. Network. Approaches. to. the. Automated. Species. Recognition. Problem. in. Systematics. In *Biodiversity Databases* (pp. 49-74): CRC Press.

Mahalanobis, P. C. (1936). On the generalized distance in statistics. *Journal of asiatic society of bangladesh, 2*(1), 49-55.

Mahalanobis, P. C. (1949). Historical note on the D^2-statistics, appendix I. anthropological survey of United Provinces, 1941: a statistical study. *The Indian Journal of Statistics, 9*, 239.

Márquez, S., Mowbray, K., Sawyer, G., Jacob, T., & Silvers, A. (2001). New fossil hominid calvaria from Indonesia—Sambungmacan 3. *The Anatomical Record: An Official Publication of the American Association of Anatomists, 262*(4), 344-368.

Martin, L. B. (1983). *The relationships of the later Miocene Hominoidea.* (Doctor of Philosophy). University College London, London.

Mayr, E. (1950). *Taxonomic categories in fossil hominids.* Paper presented at the Cold Spring Harbor Symposia on Quantitative Biology, Cold Spring Harbor

Mayr, E. (1963). The taxonomic evaluation of fossil hominids. In S. L. Washburn (Ed.), *Classification and human evolution* (pp. 332-346). Chicago: Aldine Publishing Company.

O'Higgins, P., & Jones, N. (2006). Morphologika (Version 2.4). York: Hull York Medical School.

Oakley, K. P., Campbell, B., & Molleson, T. I. (1976). Catalogue of Fossil Hominids, Part III: Americas, Asia, Australasia. *Asian Perspectives, 19*(2), 324.

Oppenoorth, W. F. F. (1932). The place of *Homo Soloensis* among fossil Men. In G. G. MacCurdy (Ed.), *Early Man* (pp. 349-360). Philadelphia and New York: J. B. Lippincott Company.

Oxnard, C. E. (1968a). The architecture of the shoulder in some mammals. *Journal of Morphology, 126*(3), 249-290.

Oxnard, C. E. (1968b). Primate evolution—a method of investigation. *American Journal of Physical Anthropology, 28*(3), 289-301.

Oxnard, C. E. (1972). Functional morphology of primates: Some mathematical and physical methods. In R. H. Tuttle (Ed.), *The functional and evolutionary biology of primates* (pp. 305-336). Chicago: Aldine-Atherton.

Oxnard, C. E. (1983). Multivariate statistics in physical anthropology: testing and interpretation. *Zeitschrift für Morphologie und Anthropologie*, 237-278.

Pearson, K. (1926). On the coefficient of racial likeness. *Biometrika*, 105-117.

Pimentcl, R. A., & Riggins, R. (1987). The nature of cladistic data. *Cladistics, 3*(3), 201-209.

Pope, G. G. (1992). Craniofacial evidence for the origin of modern humans in China. *American Journal of Physical Anthropology, 35*(S15), 243-298.

R Core Team. (2018). R: A language and environment for statistical computing. Vienna, Austria: R Foundation for Statistical Computing. Retrieved from https://www.R-project.org/

Rao, C. R. (1948). The utilization of multiple measurements in problems of biological classification. *Journal of the Royal Statistical Society. Series B (Methodological), 10*(2), 159-203.

Rao, C. R. (1952). *Advanced statistical methods in biometric research*. New York: Hafner Press.

Reyment, R. A. (2010). Morphometrics: an historical essay. In *Morphometrics for nonmorphometricians* (pp. 9-24): Springer.

Richtsmeier, J. T., Burke Deleon, V., & Lele, S. R. (2002). The promise of geometric morphometrics. *American Journal of Physical Anthropology, 119*(S35), 63-91.

Rightmire, G. P. (1970a). Bushman, Hottentot and South African Negro crania studied by distance and discrimination. *American Journal of Physical Anthropology, 33*(2), 169-195.

Rightmire, G. P. (1970b). Iron age skulls from Southern Africa re-assessed by multiple discriminant analysis. *American Journal of Physical Anthropology, 33*(2), 147-167.

Rightmire, G. P. (1979). Cranial remains of Homo erectus from Beds II and IV, Olduvai Gorge, Tanzania. *American Journal of Physical Anthropology, 51*(1), 99-115.

Rightmire, G. P. (1993). *The evolution of Homo erectus: comparative anatomical studies of an extinct human species*. Cambridge: Cambridge University Press.

Rightmire, G. P. (1998). Human evolution in the Middle Pleistocene: the role of *Homo heidelbergensis*. *Evolutionary Anthropology: Issues, News, and Reviews: Issues, News, and Reviews, 6*(6), 218-227.

Rightmire, G. P., Lordkipanidze, D., & Vekua, A. (2006). Anatomical descriptions, comparative studies and evolutionary significance of the hominin skulls from Dmanisi, Republic of Georgia. *Journal of Human Evolution, 50*(2), 115-141.

Robinson, J. T. (1953). Meganthropus, australopithecines and hominids. *American Journal of Physical Anthropology, 11*(1), 1-38.

Rohlf, F. J., & Marcus, L. F. (1993). A revolution morphometrics. *Trends in ecology & evolution, 8*(4), 129-132.

Rosenberg, K. R., & Wu, X. (2013). A river runs through it: modern human origins in East Asia. In F. H. Smith & J. Ahern (Eds.), *The origins of modern humans: Biology reconsidered* (pp. 89-121). Hoboken, New Jersey: John Wiley & Sons.

Saitou, N., & Nei, M. (1987). The neighbor-joining method: a new method for reconstructing phylogenetic trees. *Molecular biology and evolution, 4*(4), 406-425.

Sajda, P. (2006). Machine learning for detection and diagnosis of disease. *Annu. Rev. Biomed. Eng., 8*, 537-565.

Santa Luca, A. P. (1980). *The Ngandong fossil hominids: a comparative study of a far eastern Homo erectus group* (Vol. 78). New Haven: Department of Anthropology, Yale University.

Sartono, S. (1971). *Observations on a skull of Pithecanthropus erectus (Pithecanthropus VIII) from Sangiran, Central Java.* Paper presented at the Proceedings of the Koninklijke Nederlandse Akademie van Wetenschappen, Amsterdam.

Sartono, S. (1982). Sagittal cresting in *Meganthropus palaeojavanicus* von Koenigswald. *Modern Quaternary Research in Southeast Asia, 7*, 201-210.

Schwartz, J. H. (2004). Getting to know *Homo erectus*. *Science, 305*(5680), 53-54.

Schwartz, J. H. (2016). *Beyond Homo erectus: Sangiran is key to deciphering the Asian human fossil record and re-evaluating Homo*. Paper presented at the Homenaje al Dr. José Gibert Clols, Granada.

Schwartz, J. H., & Tattersall, I. (2000). What constitutes *Homo erectus*. *Acta Anthropologica Sinica, 19*, 18-22.

Schwartz, J. H., & Tattersall, I. (2002). *The human fossil record: terminology and craniodental morphology of genus Homo (Europe)* (Vol. 1): John Wiley & Sons.

Schwartz, J. H., & Tattersall, I. (2003). *The human fossil record: craniodental morphology of genus Homo (Africa and Asia)* (Vol. 2): John Wiley & Sons.

Schwartz, J. H., Tattersall, I., & Chi, Z. (2014). Comment on "A Complete Skull from Dmanisi, Georgia, and the Evolutionary Biology of Early *Homo*". *Science, 344*(6182), 360. doi:10.1126/science.1250056

Shahri, S. H. (2015). *Applications Of Machine Learning In Biology And Medicine.* Wayne State University, Detroit, Michigan.

Sherratt, E. (2014). Quick guide to Geomorph v. 2.0. *Quick Guide to Geomorph.[Online][Accessed 5 July 2016] Available from: http://www. public. iastate. edu.*

Simpson, G. G. (1943). Criteria for genera, species, and subspecies in zoology and paleozoology. *Annals of the New York Academy of Sciences, 44*(2), 145-178.

Simpson, G. G. (1963). The meaning of taxonomic statements. In S. L. Washburn (Ed.), *Classification and human evolution* (pp. 1-31). Chicago: Aldine Publishing Company.

Sommer, C., & Gerlich, D. W. (2013). Machine learning in cell biology–teaching computers to recognize phenotypes. *Journal of Cell Science, 126*(24), 5529-5539.

Spoor, F. (2013). Palaeoanthropology: Small-brained and big-mouthed. *Nature, 502*(7472), 452.

Spoor, F., Leakey, M. G., Antón, S. C., & Leakey, L. N. (2008). The taxonomic status of KNM-ER 42700: A reply to Baab (2008a). *Journal of Human Evolution, 4*(55), 747-750.

Strait, D. S., & Grine, F. E. (1999). Cladistics and early hominid phylogeny. *Science, 285*(5431), 1209-1209.

Strait, D. S., Grine, F. E., & Moniz, M. A. (1997). A reappraisal of early hominid phylogeny. *Journal of Human Evolution, 32*(1), 17-82.

Straus Jr, W. L. (1956). *Pithecanthropus* in Africa? *Science, 123*, 498.

Stringer, C. B. (1984). The definition of *Homo erectus* and the existence of the species in Africa and Europe. In P. Andrews & J. L. Franzen (Eds.), *The Early Evolution of Man: With Special Empahsis on Southeast Asia and Africa* (Vol. 69, pp. 131-143). Frankfurt am Main: Senckenbergischen Naturforschenden Gesellschaft.

Tattersall, I., & Schwartz, J. H. (2009). Evolution of the genus *Homo*. *Annual Review of Earth and Planetary Sciences, 37*, 67-92.

Terhune, C. E., Kimbel, W. H., & Lockwood, C. A. (2007). Variation and diversity in *Homo erectus:* a 3D geometric morphometric analysis of the temporal bone. *Journal of Human Evolution, 53*(1), 41-60.

Thorne, A. G., & Wolpoff, M. H. (1981). Regional continuity in Australasian Pleistocene hominid evolution. *American Journal of Physical Anthropology, 55*(3), 337-349.

Tobias, P. V., & von Koenigswald, G. H. R. (1964). A comparison between the Olduvai hominines and those of Java and some implications for hominid phylogeny. *Current Anthropology, 6*(4), 427-431.

Trinkaus, E. (1990). Cladistics and the hominid fossil record. *American Journal of Physical Anthropology, 83*(1), 1-11.

Turner, A., & Chamberlain, A. (1989). Speciation, morphological change and the status of African *Homo erectus*. *Journal of Human Evolution, 18*(2), 115-130.

Tyler, D. E. (1994). The taxonomic status of "*Meganthropus*". In J. L. Franzen (Ed.), *100 years of Pithecanthropus: The Homo erectus problem* (Vol. 171, pp. 115-121). Frankfurt am Main: Senckenbergischen Naturforschenden Gesellschaft.

Tyler, D. E. (1996). The taxonomic status of the" *Meganthropus*" cranium Sangiran 31 and the" *Meganthropus*" occipital fragment III. *Bulletin of the Indo-Pacific Prehistory Association, 15*, 235-241.

van Vark, G. N. (1984). On the determination of hominid affinities. In G. Van Vark & W. W. Howells (Eds.), *Multivariate statistical methods in physical anthropology* (pp. 323-349). Dordrecht: D. Reidel Publishing Company.

Vekua, A., Lordkipanidze, D., Rightmire, G. P., Agusti, J., Ferring, R., Maisuradze, G., . . . Tappen, M. (2002). A new skull of early *Homo* from Dmanisi, Georgia. *Science, 297*(5578), 85-89.

Villmoare, B. (2005). Metric and non-metric randomization methods, geographic variation, and the single-species hypothesis for Asian and African *Homo erectus*. *Journal of Human Evolution, 49*(6), 680-701.

von Koenigswald, G. H. R. (1948). Fossil hominids from the Lower Pleistocene of Java. *Report of the Eighteeth International Geological Conference, 9*(9), 59-61.

von Koenigswald, G. H. R. (1968). Observations upon 2 *Pithecanthropus* mandibles from Sangiran, central Java. *Proceedings of the Koninklijke Nederlandse Akademie van Wetenschappen. Series B, Physical sciences, 71*(2), 1-9.

von Koenigswald, G. H. R., & Weidenreich, F. (1939). The relationship between *Pithecanthropus* and *Sinanthropus*. *Nature, 144*, 926-929.

Walker, A. C., & Leakey, R. E. (1993). *The nariokotome Homo erectus skeleton*. Cambridge: Harvard University Press.

Washburn, S. L. (1963). *Classification and human evolution*. Chicago: Aldine Publishing Company.

Watanabe, A. (2017). LaMBDA: LandMark-Based Data Assessment.

Watanabe, A. (2018). How many landmarks are enough to characterize shape and size variation? *PloS One, 13*(6), e0198341.

Weidenreich, F. (1936). Sinanthropus pekinensis and its position in the line of human evolution. *Peking Natural History Bulletin, 10*, 281-291.

Weidenreich, F. (1943). *The skull of Sinanthropus pekinensis: a comparative study on a primitive hominid skull* (Vol. 10). Chuengking: Geological Survey of China.

Weidenreich, F. (1944). Giant early man from Java and South China. *Science, 99*(2581), 479-482.

Weidenreich, F. (1945). The puzzle of *Pithecanthropus*. In P. Honig & F. Verdoom (Eds.), *Science and Scientists in the Netherlands Indies* (pp. 380-390). New York: Board for the Netherlands Indies, Surnam and Curacao.

Wiley, D. F., Amenta, N., Alcantara, D. A., Ghosh, D., Kil, Y. J., Delson, E., . . . Hamann, B. (2005). *Evolutionary morphing.* Paper presented at the VIS 05. IEEE Visualization, 2005.

Wolpoff, M. H., Thorne, A. G., Jelinek, J., & Yinyun, Z. (1994). The case for sinking *Homo erectus*: 100 years of *Pithecanthropus* is enough. In J. L. Franzen (Ed.), *100 years of Pithecanthropus: The Homo erectus problem* (Vol. 171, pp. 341-361). Frankfurt am Main: Senckenbergischen Naturforschenden Gesellschaft.

Wood, B. (1984). The origin of *Homo erectus*. In P. Andrews & J. L. Franzen (Eds.), *The Early Evolution of Man, with Special Emphasis on Southeast Asia and Africa* (Vol. 69, pp. 99-111). Frankfurt am Main: Courier Forschungsinstitut Senckenberg.

Wood, B. (1991a). *Koobi Fora research project: Hominid cranial remains* (Vol. 4): Oxford University Press, USA.

Wood, B. (1991b). A palaeontological model for determining the limits of early hominid taxonomic variability. *Palaeontologica Africana, 28*, 71-77.

Wood, B. (1993). Early *Homo*: How many species? In W. H. Kimbel & L. B. Martin (Eds.), *Species, species concepts and primate evolution* (pp. 485-522). New York: Plenum Press.

Wood, B., Li, Y., & Willoughby, C. (1991). Intraspecific variation and sexual dimorphism in cranial and dental variables among higher primates and their bearing on the hominid fossil record. *Journal of Anatomy, 174*, 185.

Wu, R. (1964). A newly discovered mandible of the *Sinanthropus* type-*Sinanthropus lantianensis*. *Scientia Sinica, 13*(8), 801-811.

Wu, R. (1966). The skull of Lantian man. *Current Anthropology, 7*(1), 83-86.

Wu, R., & Dong, X. (1985). *Homo erectus* in China. In R. Wu & J. W. Olsen (Eds.), *Palaeonanthropology and Palaeolithic Archaeology in the People's Republic of China* (pp. 79-90). New York: Academic Press.

Wu, X. (1996). The mosaic evolution of humankind in China. *Bulletin of the Indo-Pacific Prehistory Association, 15*, 225-228.

Wu, X., & Poirier, F. E. (1995). *Human evolution in China: a metric description of the fossils and a review of the sites*. New York: Oxford University Press.

Wu, X., & Wu, M. (1985). Early *Homo sapiens* in China. In R. Wu & J. W. Olsen (Eds.), *Palaeonanthropology and Palaeolithic Archaeology in the People's Republic of China* (pp. 91-106). New York: Academic Press.

Zeitoun, V. (2009). *The human canopy: Homo erectus, Homo soloensis, Homo pekinensis and Homo floresiensis*. Oxford: John and Erica Hedges Ltd.

Zelditch, M. L., Swiderski, D. L., & Sheets, H. D. (2012). *Geometric morphometrics for biologists: a primer* (2 ed.): Academic Press.

Zelditch, M. L., Swiderski, D. L., & Sheets, H. D. (2019). A Practical Companion to Geometric Morphometrics for Biologists: Running analyses in freely-available software (revised edition). *Free download from https://booksite. elsevier. com/9780123869036/(18 June 2013)*.

Zhang, Z., Srivastava, R., Liu, H., Chen, X., Duan, L., Wong, D. W. K., . . . Liu, J. (2014). A survey on computer aided diagnosis for ocular diseases. *BMC Medical Informatics and Decision Making, 14*(1), 80.

Zuckerman, S. (1933). *Sinanthropus* and other fossil men: their relations to each other and to modern types. *The Eugenics Review, 24*(4), 273.

Zuckerman, S. (1940). Human genera and species. *Nature, 145*(3674), 510.

Zuckerman, S. (1950). Taxonomy and human evolution. *Biological Reviews, 25*(4), 435-485.

Zuckerman, S. (1951). An ape or the ape. *Journal of the Anthropological Institute of Great Britain and Ireland, 81*(1), 57-68.